AFAPL-TR-78-85
VOLUME I

LEVEL III

A064 685

AD A065020

THE GENERATION, RADIATION AND PREDICTION OF SUPERSONIC JET NOISE VOLUME I

LOCKHEED-GEORGIA COMPANY
MARIETTA, GEORGIA 30063

DDC FILE COPY

OCTOBER 1978

TECHNICAL REPORT AFAPL-TR-78-85
FINAL REPORT FOR PERIOD 1 DECEMBER 1975 – 1 SEPTEMBER 1978

Approved for public release; distribution unlimited

AIR FORCE AERO-PROPULSION LABORATORY
AIR FORCE WRIGHT AERONAUTICAL LABORATORIES
AIR FORCE SYSTEMS COMMAND
WRIGHT-PATTERSON AIR FORCE BASE, OHIO 45433

NOTICE

When Government drawings, specifications, or other data are used for any purpose other than in connection with a definitely related Government procurement operation, the United States Government thereby incurs no responsibility nor any obligation whatsoever; and the fact that the government may have formulated, furnished, or in any way supplied the said drawings, specifications, or other data, is not to be regarded by implication or otherwise as in any manner licensing the holder or any other person or corporation, or conveying any rights or permission to manufacture, use, or sell any patented invention that may in any way be related thereto.

This report has been reviewed by the Information Office (OI) and is releasable to the National Technical Information Service (NTIS). At NTIS, it will be available to the general public, including foreign nations.

This technical report has been reviewed and is approved for publication.

Robert M. McGregor

ROBERT M. McGREGOR, 1Lt, USAF
Project Engineer

Robert E. Henderson

ROBERT E. HENDERSON
Manager, Combustion Technical Area

FOR THE COMMANDER

H. I. Bush

H. I. BUSH
Deputy Director
Turbine Engine Division

"If your address has changed, if you wish to be removed from our mailing list, or if the addressee is no longer employed by your organization please notify AFAPL/TBC *, W-PAFB, OH 45433 to help us maintain a current mailing list".*

Copies of this report should not be returned unless return is required by security considerations, contractual obligations, or notice on a specific document.

UNCLASSIFIED

SECURITY CLASSIFICATION OF THIS PAGE (When Data Entered)

(11) REPORT DOCUMENTATION PAGE

READ INSTRUCTIONS BEFORE COMPLETING FORM

1. REPORT NUMBER (12) AFAPL-TR-78-85-Vol-I	2. GOVT ACCESSION NO.
3. RECIPIENT'S CATALOG NUMBER	
4. TITLE (and Subtitle) (1) THE GENERATION, RADIATION AND PREDICTION OF SUPERSONIC JET NOISE, Volume I	5. TYPE OF REPORT & PERIOD COVERED (9) FINAL TECHNICAL REPORT, Dec 1975 - 1 Sept 1978
	6. PERFORMING ORG. REPORT NUMBER (14) LG78ER0262-Vol-I
7. AUTHOR(s) (10) B. J. Tester, P. J. Morris, J. C. Lau and H. K. Tanna	8. CONTRACT OR GRANT NUMBER(s) (15) F33615-76-C-2021
9. PERFORMING ORGANIZATION NAME AND ADDRESS Lockheed-Georgia Company Marietta, Georgia 30063	10. PROGRAM ELEMENT, PROJECT, TASK AREA & WORK UNIT NUMBERS (16) Project 3066 (17) Task 14
11. CONTROLLING OFFICE NAME AND ADDRESS Air Force Aero Propulsion Laboratory/TBC Wright-Patterson Air Force Base, Ohio 45433	12. REPORT DATE (11) Oct[illegible]978
	13. NUMBER OF PAGES 485 (12) 509 p.
14. MONITORING AGENCY NAME & ADDRESS (if different from Controlling Office)	15. SECURITY CLASS. (of this report) Unclassified
	15a. DECLASSIFICATION/DOWNGRADING SCHEDULE

16. DISTRIBUTION STATEMENT (of this Report)

Approved for Public Release; Distribution Unlimited

17. DISTRIBUTION STATEMENT (of the abstract entered in Block 20, if different from Report)

18. SUPPLEMENTARY NOTES

19. KEY WORDS (Continue on reverse side if necessary and identify by block number)

Acoustics, Turbulence, Jet Noise, Laser Velocimeter, Supersonic Jets, Shock Noise, Noise Prediction

20. ABSTRACT (Continue on reverse side if necessary and identify by block number)

The work presented in this report forms a continuation of the fundamental studies on the generation and radiation of supersonic jet noise, reported in technical reports AFAPL-TR-72-53 (six volumes), AFAPL-TR-74-24, and AFAPL-TR-76-65 (four volumes). The total noise from a supersonic jet is taken to consist of contributions from three independent noise sources: (1) small-scale turbulent mixing noise, (2) noise from large-scale turbulence

(Continued)

DD FORM 1 JAN 73 1473 EDITION OF 1 NOV 65 IS OBSOLETE

UNCLASSIFIED

SECURITY CLASSIFICATION OF THIS PAGE (When Data Entered)

20. ABSTRACT (Continued)

structure, and (3) shock-associated noise. The generation, radiation and prediction of each of these noise components is described in this report. In addition, the mean and turbulent flow characteristics of heated and unheated, subsonic and supersonic jets, measured by a laser velocimeter system, are also presented. Finally, a computer program for the prediction of jet noise, based on fundamental principles as far as possible at the present time, is presented and described in the form of a user's guide. A complete listing of this computer program is given in the Appendix volume (Volume II) of this report.

LEVEL II

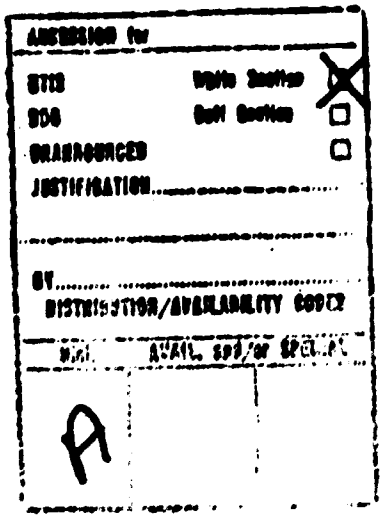

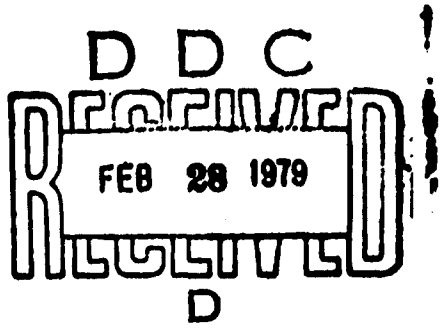

PREFACE

This report was prepared by the Lockheed-Georgia Company, Marietta, Georgia, for the Air Force Aero Propulsion Laboratory, Wright-Patterson Air Force Base under Contract F33615-76-C-2021 (Project 3066, Task 14). The report describes work conducted during the period 1 December 1975 through 1 September 1978. The work described herein is part of the Air Force Aero Propulsion Laboratory's program to define and control the noise emission of aircraft propulsion systems, and forms a continuation of the studies conducted at Lockheed under two previous contracts (F33615-71-C-1663 and F33615-73-C-2032), which were reported in technical reports AFAPL-TR-72-53 (six volumes) and AFAPL-TR-76-65 (four volumes), respectively.

Mr. Paul Shahady was the Air Force Aero Propulsion Laboratory's Project Engineer for the first two contracts, and he also initiated the third (i.e. the present) contract. Lt. Robert McGregor was the AFAPL's Program Manager for the present contract. Lockheed's Program Manager for all three contracts was Dr. Harry E. Plumblee, Jr.

The work on turbulent mixing noise prediction was conducted in collaboration with the University of Southampton (England), and the contributions of Dr. Michael J. Fisher, Dr. Christopher L. Morfey, and Dr. Victor M. Szewczyk (now at Rolls-Royce) of Southampton University are gratefully acknowledged.

The authors are also grateful to the following individuals who participated in the performance of this research: Mr. Dennis F. Blakney for modifying, maintaining and running the computer programs and generating the computer plots throughout the contract; Mr. David M. Smith and Mr. M. Clay Whiffen for their contributions in developing and maintaining the laser velocimeter system and the associated data processing systems and programs; Mr. W. H. Brown, Mr. J. Mehta, and Mr. A. Thomas for their assistance in the LV measurements; and Mr. Robert H. Burrin, Dr. Peter D. Dean, and Dr. M. Salikuddin for their contributions in the source location experiments and data reduction.

Finally, the efforts of Mr. Robert H. Burrin in preparing this report and Mrs. Barbara C. Reagan in typing the manuscripts are sincerely acknowledged.

This report was submitted by the authors on 15 September 1978.

TABLE OF CONTENTS

TABLE OF CONTENTS (Cont'd)

TABLE OF CONTENTS (Cont'd)

TABLE OF CONTENTS (Cont'd)

LIST OF FIGURES

1. INTRODUCTION

In late 1970, in recognition of the need to better understand the generation mechanisms of supersonic jet noise, the U. S. Air Force and the U. S. Department of Transportation jointly initiated a series of research contracts directed toward this need. During the first phase, three contractors examined three different models proposed for explaining the generation and radiation of supersonic jet noise. The results were presented periodically to an invited audience of about 100 persons from university, government, and industry. At these meetings, a panel of experts also critically reviewed and assessed the contract findings. At the end of the Phase I study contracts, Phase II contract awards were made for continued research and development on the two most promising models. This Phase II work continued for three years during which semi-annual progress reviews were given to an audience of similar size and composition to that above. Following that Phase II work, a Phase III contract of three years duration was awarded to Lockheed-Georgia to complete work initiated during the first two phases. This report details the work accomplished in that Phase III contract.

The primary objective of this program (and the prior studies) was to develop the technology to significantly reduce supersonic jet noise with minimum penalties. The specific objectives were to refine and experimentally verify the jet noise theory developed in the two earlier programs; to provide the necessary turbulence and mean flow data required by this refined jet noise theory; and, to develop a unified jet noise prediction model based on the fundamental theory developed.

As a result of these objectives and the objectives of the previous studies by Lockheed, the Lockheed team adopted a philosophy early in the work. This philosophy was to keep the program centered upon fundamental understanding. This philosophy guided the planning and implementation of both the theoretical and experimental tasks to be described in the following.

As a result of the objectives and philosophy stated above, there were several significant accomplishments during the span of these programs. Some of the more noteworthy ones are given below.

A new jet noise theory - the Lilley theory - was developed during this study. The Lilley theory properly identifies and separates generation and flow/acoustic interaction propagation effects. Thus, the theory provides the insight needed to understand jet noise generation and the mechanisms that potentially lead to jet noise reduction.

Another new theory, based on the unstable solutions of Lilley's equation, was used to explain supersonic jet noise generation inside the "cone of silence." (The cone of silence terminology is a misnomer since the peak noise angle lies within this region for many supersonic operationg conditions.) This theory on large-scale structure noise was verified by the measured jet noise data, both in the near and far field in the regime of the spectral peak.

A third development was the improvement of an existing theory and prediction method for shock-associated noise. The method developed has been adopted by the SAE A-21 Jet Noise Subcommittee as the standard shock-associated noise prediction method.

In another phase of the program a new laser velocimeter was developed for measuring the important flow parameters for input to the noise theories. This instrument accurately measures mean and turbulence velocity at two independent points in the flow simultaneously, with two orthogonal components measured at each point. The quantities that are measured are mean velocity, turbulence intensity, turbulence spectra, cross-spectra, convection speed and scale. With this instrument, the first accurate measurements of turbulence (and mean flow) velocity were made in a supersonic heated jet flow and relevant scaling relationships were derived to show the effects of velocity and temperature.

Finally, a unified jet noise prediction program has been developed, based on the theoretical and experimental program to be described in the following. This prediction is based on fundamental concepts and scaling parameters and is not simply an exercise in curve fitting. As an example, temperature effects are described by a second source (identified during this program) rather than a variable (empirical) density exponent. While this prediction method may not be as accurate in some areas as some others available (as a result of lack of resort to gross empiricism), it is valid over a broad range of parameters since it models the physical laws derived from the theory.

Thus, in what follows, we describe the final results of a fundamental theoretical and experimental program on jet noise that (i) separates and identifies the three major sources of noise, (ii) describes the generation and then the radiation of each of those sources separately, and (iii) assesses the validity of the result. The results presented do not complete the work on supersonic jet noise, however. Much remains to be done in properly defining the fluid dynamics of the source region both experimental and theoretical means. This work is required if the acoustic sources are to be adequately defined. Then with this more accurate definition of the sources, the acoustic theory presented in the following will provide an accurate method of determining optimum ways of reducing jet noise. Future expansion of the work could be used to determine optimum conditions for designing inverted profile coannular flow jets or mixer nozzle suppressors.

2. TURBULENT MIXING NOISE

The Lilley equation jet noise model has been substantially developed during this contract phase with attention focussed on the *prediction* of jet mixing noise. The major outcome is a very efficient prediction method for jet mixing noise which although partly empirical, retains a sufficient degree of physical modeling to allow a simple interpretation of results and a future straightforward extension to more complex flows including coannular jets. Temperature effects are modeled by an additional (dipole) noise source which can be justified on theoretical grounds, rather than a purely empirical approach like that adopted in the SAE method of a "density exponent."

The efficiency of the prediction method is largely due to the utilization of the high-frequency approximate solutions to the Lilley equation [2.1, 2.2] *and* a high-frequency approximate model of transverse noncompactness effects; hence numerical solutions to Lilley's equation have been generated mainly to establish the accuracy and range of validity of these high-frequency approximations. A prediction method based directly on numerical solutions to Lilley's equation *has* been derived, but this does require a relatively large amount of computation time and, it is suggested, would be useful only from a research viewpoint (with variable turbulence data inputs, for example).

In Section 2.1.1 the present Lilley equation model is described up to the point where the source function statistics are required to proceed further. Here, the definition of the source function is now effectively the original version given by Lilley – modified by the additional dipole source if the jet flow is non-isothermal – and not the displacement source type proposed in our earlier work [2.2], which has now been discarded. As a result, a significant shear noise term arises, which is similar to the source term utilized by Ribner [2.3], for example, in jet noise analysis and prediction, and consequently the high-frequency solutions are somewhat less accurate, compared to the cases when the displacement source was used.

In Section 2.1.2, the model is essentially completed by specifying the "standard" Gaussian correlation function for the source strength and an alternative form (Exponential-Gaussian), which is preferable in certain respects in the context of absolute noise spectrum level calculations (as described in Section 2.4).

The high-frequency approximate solutions to the Lilley equation are described and compared with numerical solutions in Sections 2.1.3 and 2.1.4.

With the standard correlation function, noncompactness effects (radial-azimuthal coherence, radial source distribution) are investigated in Section 2.1.5, and the results expressed relative to that obtained with the high-frequency (noncompact) approximation. It is found that this approximation is quite accurate for radiation outside the cone of silence but needs to be modified inside the cone of silence.

Section 2.1.6 shows some direct comparisons between the measured data, the high-frequency and the numerical Lilley equation solutions, and reveals the influence of the shear noise terms. Ideally, our high-frequency analysis of

the turbulent mixing noise data should be repeated as soon as possible with (a) a corrected noncompactness model for radiation inside the cone of silence and (b) a modification to the high-frequency solution to allow for the contribution of the shear noise terms. This would certainly yield more physically realistic inferred values of the various turbulence source parameters in the mid-to-low Strouhal number range.

Azimuthal mode spectrum measurements are described in Section 2.2 and compared with the calculated azimuthal spectrum of the Lilley equation solutions. The general lack of agreement could be the result of some deficiency in the theoretical model but bearing in mind the limited (unpublished) results obtained elsewhere the measured results are suspect. The investigation should be repeated, it is recommended, since the validity of the now widely used Lilley equation solutions should be confirmed (or otherwise) experimentally in this respect at the earliest opportunity.

Section 2.3 presents results of an experimental program to determine axial source distributions based on two-point far-field measurements and a transformation or data processing procedure known as the Polar Correlation Technique. Results from this and other programs have been used to judge the physical validity of the shear layer thickness (or "shielding") parameter values inferred from the measured acoustic data and to guide our modeling of the source correlation function for the purposes of calculating the absolute noise spectrum at 90° to the jet axis. The latter exercise, based on LV turbulence data, is described in Section 2.4, where it is shown that the standard Gaussian correlation function model (with measured turbulence data) can be used to give accurate predictions, but the so-called Exponential-Gaussian model can provide a better representation of the correlation data and, in same cases, of the axial source distributions. The sensitivity of each model to the turbulence parameters (length and time scales, convection velocity) is significantly different and it is vital that the correct model be determined. One feature of the Exponential-Gaussian model is that it has, in effect, a different convective amplification law from the standard form, which offers the prospect that the residual under-prediction at high speed, small angles and medium-to-high Strouhal numbers might be corrected with a new convective amplification factor. This aspect was revealed only towards the end of the present program and has not been investigated in any detail.

Finally, the prediction methods are described in Section 2.5. A description of the actual prediction program and a user's guide is given in Section 6.

2.1 FURTHER DEVELOPMENTS OF THE JET NOISE MODEL BASED UPON THE LILLEY EQUATION

2.1.1 Lilley Equation Solution Formulation

The unsteady pressure field of a turbulent shear layer is regarded in the present model as a set of small-amplitude waves, with real values of frequency ω and axial wavenumber k_x, superimposed on a steady axisymmetric parallel shear flow with velocity $[V(r),0,0]$, sound speed $\bar{a}(r)$ and density $\bar{\rho}(r)$ as sketched in Figure 2.1 (a list of symbols is given in Appendix 2B).

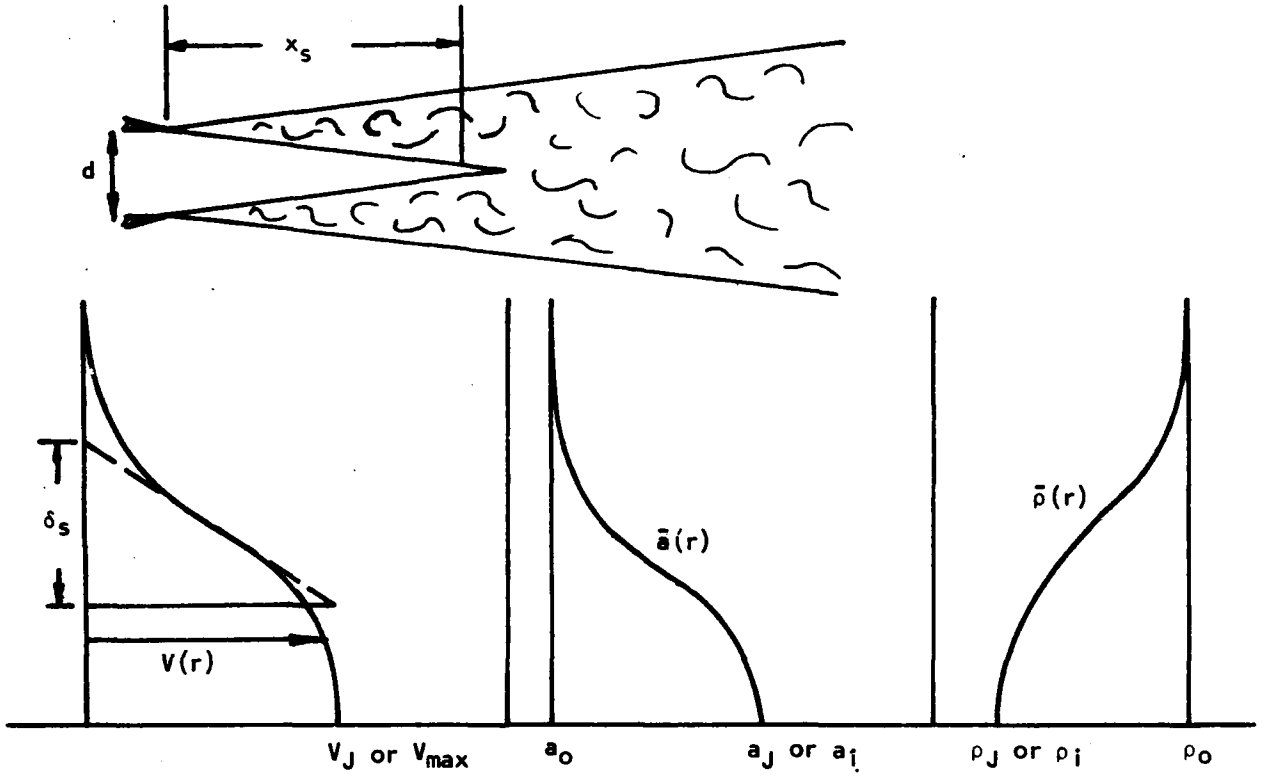

Figure 2.1 Typical Flow Profiles Used in the Lilley Equation, Showing Relation to Actual Jet Flow.

The governing equation for the pressure p (relative to the uniform pressure in the assumed basic flow) is the Lilley equation [2.2], written as

$$L(p) = \bar{\rho} Q, \tag{2-1}$$

with the linear operator L defined by

$$L \equiv \frac{1}{\bar{a}^2} \frac{\bar{D}^3}{Dt^3} - \frac{\bar{D}}{Dt} \nabla^2 + \frac{1}{\bar{\rho}} \frac{d\bar{\rho}}{dr} \frac{D}{Dt} \frac{\partial}{\partial r} + 2 \frac{dV}{dr} \frac{\partial^2}{\partial x \partial r} \tag{2-2a}$$

and

$$\frac{\bar{D}}{Dt} \equiv \frac{\partial}{\partial t} + V \frac{\partial}{\partial x} . \tag{2-2b}$$

The fluid is represented as inviscid and nonconducting but is not limited to a perfect gas.

The source term Q is a complicated function of the turbulent velocity fluctuations v_i [relative to the local basic flow V(r)], density (ρ) and pressure (p) fluctuations. The source function is equivalent to the form derived by Lilley [2.1] for isothermal flows, viz. (reverting to cartesian coordinates)

$$Q = \frac{\bar{D}}{Dt} \left(\frac{\partial^2 v_i v_j}{x_i x_j} \right) - 2 \frac{dV}{dx_2} \frac{\partial^2 v_2 v_k}{\partial x_1 \partial x_k} - 2 \frac{dV}{dx_3} \frac{\partial^2 v_3 v_\ell}{\partial x_1 \partial x_\ell} \tag{2-3}$$

but for non-isothermal flows an additional, independent source term arises, Q_e, given by

$$Q_e = - \frac{\bar{D}}{Dt} \left| \frac{\partial}{\partial x_j} \left| -\left(\frac{1}{\rho} - \frac{1}{\rho_o}\right) \frac{\partial p}{\partial x_j} \right| \right| + 2 \frac{dV}{dx_2} \frac{\partial}{\partial x_1} \left| -\left(\frac{1}{\rho} - \frac{1}{\rho_o}\right) \frac{\partial p}{\partial x_2} \right|$$

$$+ 2 \frac{dV}{dx_3} \frac{\partial}{\partial x_1} \left| -\left(\frac{1}{\rho} - \frac{1}{\rho_o}\right) \frac{\partial p}{\partial x_3} \right| \tag{2-4}$$

The "isothermal source term," Q, given above is also used by Mani† [2.4] as the basis for the G.E. jet noise prediction method [2.6] but it is not clear what source term is used (if any) to model the excess noise that occurs when

---

†*Mani also gives a concise summary of the approximations used by Lilley [2.1] to obtain this source function and thus details of the various approximations are not given here. However, in one respect, those approximations are incorrect and this concerns the excess noise source term identified by Morfey [2.5] in the Lighthill analogy, involving interactions between density and pressure fluctuations. The source strength is of the same order, i.e. $O(v^2)$ as the isothermal source and must be retained when the jet mean flow is non-isothermal.*

the jet is non-isothermal (jet static exit temperature different from ambient temperature). In earlier work at Lockheed [2.2], different expressions were used for Q and Q_e, in the form of displacement source functions, but these have now been discarded since (a) an error was found in the basic analysis, and (b) it has been established that when the so-called shear noise source terms are included (the second and third terms in Q above) the correct V_J^8 scaling law *is* obtained at low Mach numbers for isothermal jets. Without these terms (the above-mentioned error had caused these to be neglected), the self-noise source term alone gives rise to an unacceptable V_J^6 dependence at low Mach numbers and this was the original reason which led to the utilization of an alternative source - the displacement source - which (also) has the correct asymptotic dependence on jet exit velocity.

The source distribution Q of Equation (2-3) in cylindrical coordinates is given by

(quadrupole type)

$$Q = \frac{\bar{D}}{Dt}\left(\frac{\partial^2 v_x^2}{\partial x^2}\right) \qquad \textit{axial-axial}$$

$$+ 2\,\frac{\bar{D}}{Dt}\left(\frac{1}{r}\,\frac{\partial^2 r v_x v_r}{\partial x \partial r}\right) - 2\,\frac{dV}{dr}\,\frac{\partial^2 v_x v_r}{\partial x^2} \qquad \textit{axial-radial}$$

$$+ 2\,\frac{\bar{D}}{Dt}\left(\frac{\partial^2 (v_x v_\phi / r)}{\partial x \partial \phi}\right) \qquad \textit{axial-azimuthal}$$

$$+ \frac{\bar{D}}{Dt}\left(\frac{1}{r}\,\frac{\partial^2 (r v_r^2)}{\partial r^2}\right) - 2\,\frac{dV}{dr}\,\frac{1}{r}\,\frac{\partial^2 (r v_r^2)}{\partial x \partial r} \qquad \textit{radial-radial}$$

$$+ 2\,\frac{\bar{D}}{Dt}\left(\frac{1}{r^2}\,\frac{\partial^2 (r v_r v_\phi)}{\partial r \partial \phi}\right) - 2\,\frac{dV}{dr}\,\frac{1}{r}\,\frac{\partial^2 (v_r v_\phi)}{\partial x \partial \phi} \qquad \textit{azimuthal-radial}$$

$$+ \frac{\bar{D}}{Dt}\left(\frac{\partial^2 (v_\phi^2 / r^2)}{\partial \phi^2} - \frac{1}{r}\,\frac{\partial v_\phi^2}{\partial r}\right) + 2\,\frac{dV}{dr}\,\frac{\partial}{\partial x}\left(\frac{v_\phi^2}{r}\right) \qquad \textit{azimuthal-azimuthal} \qquad (2\text{-}5)$$

and the source distribution Q_e of Equation (2-4) by

$$Q_e = -\frac{\bar{D}}{Dt}\left(\frac{\partial f_x}{\partial x}\right) - \frac{\bar{D}}{Dt}\left(\frac{1}{r}\,\frac{\partial}{\partial r}\,(r f_r)\right) + 2\,\frac{dV}{dr}\,\frac{\partial f_r}{\partial x} - \frac{\bar{D}}{Dt}\left(\frac{1}{r}\,\frac{\partial f_\phi}{\partial \phi}\right) \qquad (2\text{-}6a)$$

where $$f_\alpha = -\left|\left(\frac{1}{\rho} - \frac{1}{\rho_o}\right)\frac{\partial p}{\partial x},\quad \left(\frac{1}{\rho} - \frac{1}{\rho_o}\right)\frac{\partial p}{\partial r},\quad \left(\frac{1}{\rho} - \frac{1}{\rho_o}\right)\frac{1}{r}\,\frac{\partial p}{\partial \phi}\right|. \qquad (2\text{-}6b)$$

The Fourier transform of Equation (2-1) with respect to x, ϕ and t is

$$\frac{1}{r}\frac{d}{dr}\left(r\frac{d\tilde{p}}{dr}\right) + \left(-\frac{1}{\bar{\rho}}\frac{d\bar{\rho}}{dr} - \frac{2}{D}\frac{dD}{dr}\right)\frac{d\tilde{p}}{dr}$$

$$+ \left|k_o^2\left(\frac{a_o^2\ D2}{\bar{a}^2} - \frac{k_x^2}{k_o^2}\right) - \frac{n^2}{r^2}\right|\tilde{p} = -\bar{\rho}\left(\frac{\tilde{Q}+\tilde{Q}_e}{j\omega D}\right) \qquad (2\text{-}7)$$

where

$$D(r) = 1 - \frac{k_x V(r)}{\omega} \qquad (2\text{-}8a)$$

$$k_o = \frac{\omega}{a_o} \qquad (2\text{-}8b)$$

and

$$\tilde{p}(k_x,r,n,\omega) = \int_{-\infty}^{+\infty} dx \int_{-\pi}^{+\pi} d\phi \int_{-\infty}^{+\infty} dt\ p(x,r,\phi,t)e^{j(k_x x + n\phi - \omega t)} \qquad (2\text{-}9)$$

and similarly for $\tilde{Q}$, $\tilde{Q}_e$.

The solution of Equation (2-7) is

$$\tilde{p}(k_x,r,n,\omega) = \int_0^{\infty} r'dr'\ G(r|r')\ (j\omega D(r'))^{-3}\ (\tilde{Q}(r') + \tilde{Q}_e(r')) \qquad (2\text{-}10)$$

where $G(r|r')$ is the solution of

$$\frac{d}{dr}\left|\frac{r}{\bar{\rho}\omega^2 D^2}\frac{dG(r|r')}{dr}\right| + \frac{rG(r|r')}{\bar{\rho}\omega^2 D^2}\left|k_o^2\kappa^2 - \frac{n^2}{r^2}\right| = \delta(r-r') \qquad (2\text{-}11)$$

satisfying the finiteness condition at $r=0$ and the radiation condition. In Equations (2-10) and (2-11) the dependence of $\tilde{Q}$, $\tilde{Q}_e$ and G on k_x,n and ω has been suppressed and here

$$\kappa = \{a_o^2 D^2/\bar{a}^2 - (k_x/k_o)^2\}^{\frac{1}{2}} \qquad (2\text{-}12)$$

After the usual manipulation in which the spatial derivatives are transferred from the source function, $\tilde{Q}$, to the Green function (see ref. [2.2] for details), Equation (2-10) can be written as

$$\tilde{p} = \int_0^{\infty} \frac{r'\,dr'}{(j\omega D)^2} G(r|r')\ \{I(r') + I_e(r')\} \qquad (2\text{-}13)$$

where†

$$I(r) = -k_x^2\,\widetilde{v_x^2} + 2jk_x\left(\frac{1}{G}\frac{dG}{dr} - \frac{M_o'\,k_x/k_o}{D}\right)\widetilde{v_x v_r}$$

$$-\left|\left(k_o^2\kappa^2 - \frac{n^2}{r^2}\right) + \left(\frac{1}{r} - \frac{1}{\bar{\rho}}\frac{d\bar{\rho}}{dr}\frac{1}{G}\frac{dG}{dr}\right)\right|\widetilde{v_r^2} - 2k_x n\left(\frac{1}{r\,G}\frac{dG}{dr}\right)\widetilde{v_x v_\phi}$$

$$+ 2jn\left|\frac{1}{r}\left(\frac{1}{G}\frac{dG}{dr} - \frac{M_o'\,k_x/k_o}{D}\right) - \frac{1}{r^2}\right|\widetilde{v_r v_\phi} + \left|\frac{1}{r}\left(\frac{1}{G}\frac{dG}{dr} - \frac{n^2}{r^2}\right)\right|\widetilde{v_\phi^2} \qquad (2\text{-}13a)$$

and

$$I_e(r) = jk_x\tilde{f}_x + \left(\frac{1}{G}\frac{dG}{dr}\right)\tilde{f}_r + \left(\frac{jn}{r}\right)\tilde{f}_\phi \qquad (2\text{-}13b)$$

The Green function solution to Equation (2-11) is written as

$$G(r|r') = \omega^2\,\frac{j\pi}{2}\,p_o(r)\,p_i(r')\left[\frac{2\bar{\rho}(r')D^2(r')}{j\pi r' W\{p_i(r'),\,p_o(r')\}}\right] \quad (r \geq r') \qquad (2\text{-}14)$$

$$= \omega^2\,\frac{j\pi}{2}\,p_o(r)\;\;C(r')$$

where

$$C(r) = p_i(r)\left[\frac{2\bar{\rho}(r)D^2(r)}{j\pi r W\{p_i(r),\,p_o(r)\}}\right] \qquad (2\text{-}15)$$

and p_i, p_o are the two independent solutions to the homogeneous Equation (2-11), satisfying, respectively, the finiteness condition as $r \to 0$, and the radiation condition as $r \to \infty$. Outside the jet in the ambient medium, the latter solution is simply

$$p_o(r) = p_o^{\frac{1}{2}}\,H_n^{(2)}\,(k_o\kappa_o r) \qquad (2\text{-}16)$$

and here the complete solution is given by

$$\tilde{p} = -\omega^2\,\frac{j\pi}{2}\,\rho_o^{\frac{1}{2}}\,H_n^{(2)}(k_o\kappa_o r)\int_0^\infty r'dr'\,\{C_{\alpha\beta}\widetilde{v_\alpha v_\beta} + C_\alpha\tilde{f}_\alpha\} \qquad (2\text{-}17)$$

where

$$C_{xx} = -k_x^2\;C/D^2 \qquad (2\text{-}18a)$$

$$C_{xr} = j\,k_x\left(\frac{dC}{dr} - \frac{M_o'\,k_x/k_o}{D}\,C\right)/D^2 \qquad (2\text{-}18b)$$

†*Here* $M_o' \equiv d(V(r)/a_o)/dr$.

$$C_{rr} = -\left|\left(k_o^2\kappa^2 - \frac{n^2}{r^2}\right) C + \left(\frac{1}{r} - \frac{1}{\bar{\rho}}\frac{d\bar{\rho}}{dr}\right)\frac{dC}{dr}\right| / D^2 \qquad (2\text{-}18c)$$

$$C_{x\phi} = -\left(k_x n \frac{C}{r}\right)/D^2 \qquad (2\text{-}18d)$$

$$C_{r\phi} = jn\left|\frac{1}{r}\left(\frac{dC}{dr} - \frac{M_o' k_x/k_o}{D} C\right) - \frac{C}{r^2}\right| / D^2 \qquad (2\text{-}18e)$$

$$C_{\phi\phi} = \left(\frac{1}{r}\frac{dC}{dr} - \frac{n^2 C}{r^2}\right) / D^2 \qquad (2\text{-}18f)$$

and

$$C_x = jk_x C/D^2 \qquad (2\text{-}19a)$$

$$C_r = (dC/dr)/D^2 \qquad (2\text{-}19b)$$

$$C_\phi = jn(C/r)/D^2 \qquad (2\text{-}19c)$$

After Fourier inversion with respect to k_x and n, the far-field ($k_o R_r \to \infty$) acoustic pressure is obtained as

$$p(R_r,\theta_o,\phi_o,\omega) = \rho_o^{\frac{1}{2}} \frac{\exp[-jk_o R_r]}{4\pi R_r} \sum_{n=-\infty}^{\infty} a_n e^{jn\pi/2} e^{-jn\phi_o} \qquad (2\text{-}20)$$

where

$$a_n = \int_0^\infty r'dr' \{C_{\alpha\beta}\widetilde{v_\alpha v_\beta} + C_\alpha \tilde{f}_\alpha\} \qquad (2\text{-}20a)$$

with

$$k_x/k_o = \cos\theta_o . \qquad (2\text{-}21)$$

In what follows, all quantities are evaluated with this particular value of the axial wavenumber; R_r is the distance along a line joining the far-field observer and the axial center of the source region, and θ_o is the angle between the line and the (downstream) jet axis.

The power spectral density of the far-field pressure, P, follows immediately from Equation (2-20)

$$\frac{(4\pi R_r)^2}{\rho_o} P(R_r,\theta_o,\phi_o,\omega) = \sum_{n=-\infty}^{\infty} \sum_{m=-\infty}^{\infty} P_{nm} e^{-j(m-n)\phi_o} \qquad (2\text{-}22)$$

where $$P_{nm} = \int_{-\infty}^{\infty} dx \int_{-\infty}^{\infty} dx' \int_{0}^{\infty} r\,dr \int_{0}^{\infty} r'dr' \int_{-\pi}^{+\pi} d\phi \int_{-\pi}^{+\pi} d\phi'$$

$$C^{*}_{\alpha\beta}(r)\, C_{\delta\gamma}(r')\Phi_{\alpha\beta\delta\gamma}(\omega|x,r,\phi;\, x',r',\phi')$$

$$\cdot \exp[-jk_x(x-x')] \exp[-jn\phi + jm\phi'] \qquad (2\text{-}23)$$

[NB. $C_{\alpha\beta}(r) \equiv C_{\alpha\beta}(k_x,r,n,\omega)$]

and

$$\Phi_{\alpha\beta\delta\gamma}(\omega|x,r,\phi;\, x',r',\phi') = \int_{-\infty}^{+\infty} R_{\alpha\beta\delta\gamma}(\tau|x,r,\phi;\, x',r',\phi')e^{j\omega\tau}\, d\tau \qquad (2\text{-}24)$$

where $R_{\alpha\beta\delta\gamma}$ is the cross-correlation function of the velocity fluctuation product $v_\alpha v_\beta$, defined as

$$R_{\alpha\beta\delta\gamma}(\tau|x,r,\phi;\, x',r',\phi')$$

$$= \lim_{T\to\infty} \frac{1}{2T} \int_{-T}^{+T} v_\alpha v_\beta(x,r,\phi,t) \cdot v_\alpha v_\gamma(x',r',\phi',t+\tau)dt \qquad (2\text{-}25)$$

Equations (2-23) through (2-25) follow from the definition

$$\widetilde{v_\alpha v_\beta} = \int_{-\infty}^{+\infty} dt \int_{-\infty}^{+\infty} dx \int_{-\pi}^{+\pi} d\phi\; v_\alpha v_\beta(x,r,\phi,t)e^{j(k_x x + n\phi - \omega t)} \qquad (2\text{-}26)$$

and similar expressions apply to the dipole source – which is assumed to be statistically independent of the quadrupole source – except $v_\alpha v_\beta$ is replaced by f_α.

2.1.2 Turbulence Source Function Models

In the following description of the two source function models that have been employed in the present work, only the *quadrupole* turbulence source function is considered; however, in the prediction method the dipole turbulence source function is assumed to have the same statistical properties (i.e. length and time scales, convection velocity, etc.).

2.1.2.1 Statistical axisymmetry

The correlation function of the source strength is assumed to be dependent only upon the azimuthal separation and not the absolute azimuthal positions of the two measurement points, viz.;

$$R_{\alpha\beta\delta\gamma}(\tau|x,r,\phi;\ x',r',\phi') \rightarrow R_{\alpha\beta\delta\gamma}(\tau,\Delta\phi|x,r;\ x',r') \tag{2-27}$$

and the same must hoid for its spectrum,

$$\Phi_{\alpha\beta\delta\gamma}(\omega|x,r,\phi;\ x',r',\phi') \rightarrow \Phi_{\alpha\beta\delta\gamma}(\omega,\Delta\phi|x,r;\ x',r') \tag{2-28}$$

It follows from Equation (2-23) that P_{nm} is zero unless $n=m$ and hence Equation (2-22) reduces to

$$\frac{(4\pi R_r)^2}{\rho_o} P(R_r,\theta_o,\omega) = \sum_{n=-\infty}^{\infty} P_n \tag{2-29}$$

where

$$P_n = \int_{-\infty}^{+\infty} dx \int_{-\infty}^{+\infty} dx' \int_0^{\infty} 2\pi r dr \int_0^{\infty} r'dr'\ C^*_{\alpha\beta}(r)\ C_{\delta\gamma}(r')\ \exp[-jk_x(x-x')]$$

$$\cdot \int_{-\pi}^{+\pi} \Phi_{\alpha\beta\delta\gamma}(\omega,\Delta\phi|x,r;\ x',r') e^{jn\Delta\phi}\ d(\Delta\phi). \tag{2-30}$$

2.1.2.2 Normal joint probability

The assumption of normal joint probability

$$R_{\alpha\beta\delta\gamma}(\tau) = R_{\alpha\delta}(\tau)\ R_{\beta\gamma}(\tau) + R_{\alpha\gamma}(\tau)\ R_{\beta\delta}(\tau) + R_{\alpha\beta}(0)\ R_{\alpha\gamma}(0) \tag{2-31}$$

is extended so that

$$R_{\alpha\beta\delta\gamma}(\tau) = R_{\alpha\delta}(\tau)\ R_{\beta\gamma}(\tau)\ \delta_{\alpha\delta}\delta_{\beta\gamma} + R_{\alpha\gamma}(\tau)\ R_{\beta\delta}(\tau)\ \delta_{\alpha\gamma}\delta_{\beta\delta}$$

$$+ R_{\alpha\beta}(0)\ R_{\delta\gamma}(0) \tag{2-32}$$

(where $\delta_{\alpha\beta}$ is the Kronecker delta) and Equation (2-30) reduces to

$$P_n = \int_{-\infty}^{+\infty} dx \int_{-\infty}^{+\infty} dx' \int_0^{\infty} 2\pi r dr \int_0^{\infty} r' dr\, C^*_{\alpha\beta}(r)\, C_{\alpha\beta}(r')\, \exp[-jk_x(x-x')]$$

$$\int_{-\pi}^{+\pi} 2\phi^{(2)}_{\alpha\beta}(\omega,\Delta\phi|x,r;\, x',r') e^{jn\Delta\phi}\, d(\Delta\phi) \qquad (2\text{-}33)$$

where

$$\phi^{(2)}_{\alpha\beta}(\omega|x,r,\phi;\, x',r',\phi') = \int_{-\infty}^{+\infty} d\tau e^{-j\omega\tau}\{\langle v_\alpha(x,r,\phi,t)\, v_\beta(x,r,\phi,t+\tau)\rangle_t\}^2 \qquad (2\text{-}34)$$

is the spectrum of the *square* of the velocity fluctuation cross-correlation function.

2.1.2.3 Axial coherence length scale smaller than power spectral density length scale

This assumption precludes the modeling of fluctuations that are coherent for axial distances over which the power spectral density of the fluctuations and/or the jet mean profiles vary significantly. The coherent large-scale component is dealt with separately in Section 3. The small-scale assumption allows us to utilize the concept of "noise generated per unit slice of turbulence" since the source spectrum can be written as

$$\phi^{(2)}_{\alpha\beta}(\omega,\Delta\phi|x,r;\, x',r') \rightarrow \phi^{(2)}_{\alpha\beta}(\omega,\Delta\phi|x,r;\, \Delta x,r') \qquad (2\text{-}35)$$

and Equation (2-33) reduces again to

$$P_n = \int_{-\infty}^{+\infty} dx \int_0^{\infty} 2\pi r dr \int_0^{\infty} r' dr'\, C^*_{\alpha\beta}(r)\, C_{\alpha\beta}(r')$$

$$\cdot \int_{-\pi}^{+\pi} d(\Delta\phi) e^{jn\Delta\phi} \int_{-\infty}^{+\infty} d(\Delta x) e^{jk_x\Delta x}\, 2\phi^{(2)}_{\alpha\beta}(\omega,\Delta\phi|x,r;\Delta x,r') \qquad (2\text{-}36)$$

or

$$P_n = \int_{-\infty}^{\infty} dx \int_0^{\infty} 2\pi r dr \int_0^{\infty} r' dr'\, C^*_{\alpha\beta}(r)\, C_{\alpha\beta}(r') 2\phi^{(2)}_{\alpha\beta}(\omega,n|x,r;k_x,r') \qquad (2\text{-}37)$$

where

$$\phi^{(2)}_{\alpha\beta}(\omega,n|x,r;\ k_x,r')$$

$$= \int_{-\pi}^{+\pi} d(\Delta\phi) e^{jn\Delta\phi} \int_{-\infty}^{\infty} d(\Delta x)\ \phi^{(2)}_{\alpha\beta}(\omega,\Delta\phi|x,r;\ \Delta x,r') e^{jk_x\Delta x} \qquad (2\text{-}37a)$$

2.1.2.4 Correlation function models

Two models have been utilized to collapse the measured LV turbulence correlation data and to provide the necessary Fourier transformed expressions for noise spectrum calculations. The first is the "standard" model referred to as the Gaussian model and has been utilized by Ribner [2.3] and Ffowcs Williams [2.7], among others, while the second was first used by Harper-Bourne* and is referred to as the Exponential-Gaussian model. The latter bears some resemblance to models introduced by Ribner [2.3] and Maestrello [2.8].

The Gaussian model is utilized for all the numerical and analytical work performed with Lilley equation solutions, although it does not appear to provide a very satisfactory model for the turbulence data and hence the introduction of an alternative model. The changes that may occur in our directivity predictions with the Lilley equation solutions using the Exponential-Gaussian model have not been considered as yet, but it is possible that improvements could be obtained, particularly for high-speed jets at small angles.

Gaussian Correlation Function Model

This is defined as

$$R_{\alpha\beta}(\tau,\Delta\phi|x,r;\ \Delta x,r') = \{\overline{v_\alpha^2}(x,r)\ \overline{v_\beta^2}(x,r')\}^{\frac{1}{2}}$$

$$\cdot \exp\left[-(\tau/\tau_o)^2\right]$$

$$\cdot \exp[-\pi(\Delta x - V_c\tau)^2/L_x^2 - \pi(r^2 + r'^2 - 2rr'\cos\Delta\phi)/L_t^2] \qquad (2\text{-}38)$$

where the time scale τ_o and length scales, L_x, L_t are functions of x but are independent of the other spatial coordinates. (The convection velocity V_c may also vary with x.)

The corresponding spectrum is given by

---

*Personal communication.

$$\phi_{\alpha\beta}^{(2)}(\omega,n|x,r';k_x,r') = \overline{v_\alpha^2}(x,r)\ \overline{v_\beta^2}(x,r')\ \sqrt{\pi}\ \frac{L_x\tau_o}{2}\ \exp\ [-\omega_{mx}^2\ \tau_o^2/8]$$

$$\cdot\ \exp[-2\pi(r^2+r'^2)/L_t^2]\ 2\pi I_n(4\pi rr'/L_t^2) \qquad (2\text{-}39)$$

where

$$\omega_{mx}^2 = \omega^2\{(1-M_c k_x/k_o)^2 + (L_x/\tau_o a_o)^2\ (1/\pi)\ (k_x/k_o)^2\} \qquad (2\text{-}40)$$

and I_n is the modified Bessel function.

Exponential-Gaussian Correlation Model

This is defined as

$$R_{\alpha\beta}(\tau,\Delta\phi|x,r;\ \Delta x,r') = \{v_\alpha^2(x,r)\ v_\beta^2(x,r')\}^{\frac{1}{2}}$$

$$\cdot\ \exp\ [-\{(\Delta x/V_c\tau_o)^2 + \pi^2(r^2+r'^2-2rr'\ \cos\Delta\phi)^2/L_t^4\}^{\frac{1}{2}}]$$

$$\cdot\ \exp\ [-\pi(\Delta x - V_c\tau)^2/L_x^2]. \qquad (2\text{-}41)$$

The spectrum, integrated over the radius is obtained as

$$\int_0^\infty r'dr'\phi_{\alpha\beta}^{(2)}\ (\omega,\Delta\phi|x,r;\ k_x,r') = \overline{v_\alpha^2}(x,r)\ \overline{v_\beta^2}(x,r)$$

$$\frac{\sqrt{2}\pi}{4}\ L_x\left(\frac{L_t^2}{2}\right)\frac{\tau_o}{2}\ \frac{\exp[-\omega^2 L_x^2/8\pi V_c^2]}{\{1+\omega'^2\tau_o^2/4\}^{3/2}} \qquad (2\text{-}42)$$

where ω' is the frequency in the moving frame

$$\omega' = \omega - k_x\ V_c\ .$$

This is the form used in the absolute noise spectrum calculations of Section 2.4 in which transverse noncompactness effects are neglected.

2.1.2.5 Application to the no-flow problem

To demonstrate how these correlation functions are used to obtain the radiated noise spectrum, consider the simple case of radiation from the axial-axial quadrupole in the zero (mean) flow or Lighthill problem, with the Gaussian correlation function model. In this case Equation (2.18a) becomes

$$C_{xx} = -\ k_x^2\ \rho_o^{\frac{1}{2}}\ J_n(k_2 r) \qquad (2\text{-}43)$$

where

$$k_2 = \{k_o^2 - k_x^2\}^{\frac{1}{2}} \tag{2-44}$$

and from Equations (2-37) and (2-39)

$$P_{nxx} = k_x^4 \rho_o \int_{-\infty}^{\infty} dx\ 2\left(\frac{\sqrt{\pi} L_x \tau_o}{2}\right) \exp[-\omega_{mx}^2\ \tau_o^2/8]$$

$$\cdot\ 2\pi \int_0^{\infty} rdr\ J_n(k_2 r)\ e^{-2\pi r^2/L_t^2}\ \overline{v_x^2}^2\ (x,r)$$

$$\cdot \int_0^{\infty} r'dr'\ J_n(k_2 r')\ e^{-2\pi r'^2/L_t^2}\ 2\pi I_n(4\pi r r'/L_t^2) \tag{2-45}$$

where it has been assumed, as in the axial direction, that the radial coherence length scale is much smaller than the radial psd length scale. Using a standard integral [2.9]

$$\int_0^{\infty} r'dr' J_n(k_2 r') e^{-2\pi r'^2/L_t^2}\ 2\pi\ I_n(4\pi r r'/L_t^2)$$

$$= \frac{L_t^2}{2} \exp\ [-k_2^2\ L_t^2/8\pi]\ J_n(k_2 r) \tag{2-46}$$

so that

$$P_{nxx} = k_x^4 \rho_o \int_{-\infty}^{\infty} dx\ 2\left(\frac{\sqrt{\pi} L_x \tau_o}{2}\right) \exp\ [-\omega_{mo}^2\ \tau_o^2/8]$$

$$\cdot\ 2\pi\ \frac{L_t^2}{2} \int_0^{\infty} rdr\ J_n^2\ (k_2 r)\ \overline{v_x^2}^2\ (x,r) \tag{2-47}$$

and

$$\bar{P} \equiv (4\pi R_r)^2 \, P(R_r, \theta_o, \omega)/\rho_o$$

$$= \sum_n P_{nxx}$$

$$= k_x^4 \rho_o \int_{-\infty}^{\infty} dx \left(\frac{\sqrt{\pi}}{2} L_x \tau_o\right) \left(\frac{L_t^2}{2}\right) \exp\left[-\omega_{mo}^2 \tau_o^2/8\right] \int_o^{\infty} 2\pi r dr \, \overline{v_x^2}^2 (x,r) \qquad (2\text{-}48)$$

where

$$\omega_{mo}^2 = \omega^2 \{(1 - M_c \cos\theta_o)^2 + (L_x/\tau_o a_o)^2 \, (1/\pi) \, (k_x/k_o)^2$$

$$+ (L_t/\tau_o a_o)^2 \, (1/\pi) \, (k_2/k_o)^2\} \qquad (2\text{-}49)$$

Hence, in this case, the power spectral density of the noise radiated per unit volume ignoring noncompactness effects (i.e. neglecting the exponential factor) is given by

$$k_x^4 \left(\sqrt{\pi} L_x \tau_o \frac{L_t^2}{2}\right) \rho_o^2 \, \overline{v_x^2}^2 \qquad (2\text{-}50)$$

omitting the constant $(4\pi R_r)^2$. (Incidentally Ribner's [2.3] result is a factor of two smaller than this, and this arises because of the special form the correlation function should take if an incompressible, isotropic turbulence model is assumed. However, this factor of two appears to be the net difference and *is* incorporated in the noise spectrum calculations of Section 2.4.)

2.1.3 High-Frequency Lilley Equation Solutions Outside the Cone of Silence

Outside the cone of silence† a high-frequency (Green function) solution can be obtained to the Lilley equation by simply defining the radiated intensity or pressure amplitude to depend only upon mean flow conditions at the effective source radius and to be otherwise completely independent of the flow field (profile shapes, etc.). Under these conditions the *modulus* of the factor in square brackets in Equation (2-15) is unity. The high-frequency or geometric acoustics solution is

$$p_I(r) = (\rho_s D_s^2)^{\frac{1}{2}} \, J_n(k_o \kappa_s r) \qquad (2\text{-}51)$$

and thus from Equation (2-15)

$$C(r) = (\rho_s D_s^2)^{\frac{1}{2}} \, J_n(k_o \kappa_s r) \, e^{j\psi} \qquad (2\text{-}52)$$

---

†*Defined as* $\kappa_s^2 \geq 0$.

where the phase ψ is independent of r and n. Here subscript "s" denotes mean flow conditions at the source radius $V = V_s$, $\bar{\rho} = \rho_s$, $\bar{a} = a_s$, $D_s = 1 - k_x V_s/\omega$, $\kappa_s^2 = a_o^2 D_s^2/a_s^2 - (k_x/k_o)^2$; the high-frequency approximation outside the cone of silence is to use mean flow conditions at this radius to define V_s, ρ_s, a_s and to *assume* those flow conditions hold throughout the source volume – for a particular frequency or a band of frequencies. This approach cannot be extended to radiation *inside* the cone of silence without some modification, as discussed below.

We can now illustrate how a simple description emerges – from the Lilley equation in the high-frequency limit – of acoustic-mean flow interactions for both compact and noncompact source distributions. This is demonstrated with the so-called Gaussian model of the source strength correlation function and the axial-axial quadrupole source, viz. from Equations (2-18a) and (2-52).

$$C_{xx} = - k_x^2 \ (\rho_s D_s^2)^{\frac{1}{2}} \ J_n(k_o \kappa_s r) \ e^{j\psi}/D_s^2 \tag{2-53}$$

and with Equation (2-39), Equation (2-37) becomes

$$P_{nxx} = \int_{-\infty}^{\infty} dx \int_{0}^{\infty} 2\pi r dr \ k_x^2 \ \frac{(\rho_s D_s)^{\frac{1}{2}}}{D_s^2} \ J_n(k_o \kappa_s r) e^{-j\psi}$$

$$\int_{0}^{\infty} r' dr' \ k_x^2 \ \frac{(\rho_s D_s^2)^{\frac{1}{2}}}{D_s^2} \ J_n(k_o \kappa_s r') e^{j\psi}$$

$$2 \ \overline{v_x^2}(x,r) \ \overline{v_x^2}(x,r') \ \frac{\sqrt{\pi} L_x \tau_o}{2} \ \exp\left[-\omega_{mx}^2 \ \tau_o^2/8\right]$$

$$\exp[-2\pi(r^2 + r'^2)/L_t^2] \ 2\pi \ I_n(4\pi r r'/L_t^2) \tag{2-54}$$

The integration with respect to r' can be carried out provided it is assumed (as in the zero flow case given in the previous section) that $\overline{v_x^2}(x,r')$ varies slowly over the coherence length scale, L_t, and can be therefore omitted from the integration. Making this assumption (and noting that ρ_s, D_s are independent of r over the source region as discussed above) gives the same intermediate result as in the zero flow case except k_2 is replaced by $k_o \kappa_s$ and ρ_o by ρ_s/D_s^2.

$$P_{nxx} = k_x^4 \frac{\rho_s}{D_s^2} \int_{-\infty}^{\infty} dx\ 2\left(\frac{\sqrt{\pi}}{2} L_x \tau_o\right) \exp\left[-\omega_{mx}^2 \tau_o^2/8\right]$$

$$2\pi \int_0^{\infty} rdr\ J_n(k_o \kappa_s r) e^{-2\pi r^2/L_t^2} \left[\overline{v_x^2}(x,r)\right]^2$$

$$\int_0^{\infty} r'dr'\ J_n(k_o \kappa_s r') e^{-2\pi r'^2/L_t^2}\ 2\pi\ I_n(4\pi r r'/L_t^2) \qquad (2\text{-}55)$$

As before, the second integral is standard (from ref. [2.9], p. 718, 6.633, #4), viz.

$$\int_0^{\infty} r'dr'\ J_n(k_o \kappa_s r') e^{-2\pi r'^2/L_t^2}\ 2\pi\ I_n(4\pi r r'/L_t^2)$$

$$= \frac{L_t^2}{2} \cdot \exp[2\pi r^2/L_t^2]\ J_n(k_o \kappa_s r)\ \exp\left[-k_o^2 \kappa_s^2 L_t^2/8\pi\right] \qquad (2\text{-}56)$$

so that

$$P_{nxx} = k_x^4 \frac{\rho_s}{D_s^2} \int_{-\infty}^{\infty} dx\ 2\left(\frac{\sqrt{\pi}}{2} L_x \tau_o\right) \exp\left[-\omega_{mx}^2 \tau_o^2/8\right] \exp[-k_o^2 \kappa_s^2 L_t^2/8\pi] \cdot \frac{L_t^2}{2}$$

$$2\pi \int_0^{\infty} rdr\ J_n^2\ (k_o \kappa_s r)\ \left[\overline{v_x^2}(x,r)\right]^2 \qquad (2\text{-}57)$$

The axial and transverse (i.e. radial-azimuthal) factors can be combined into a single factor

$$\exp\left[-\omega_m^2 \tau_o^2/8\right] \qquad (2\text{-}58)$$

where

$$\omega_m^2 = \omega^2 \left| (1 - k_x M_c/k_o)^2 + \left(\frac{L_x}{\tau_o a_o}\right)^2 \frac{1}{\pi} \left(\frac{k_x}{k_o}\right)^2 + \left(\frac{L_t}{\tau_o a_o}\right)^2 \frac{1}{\pi}\ \kappa_s^2 \right| \qquad (2\text{-}59)$$

Finally, the summation over all azimuthal mode numbers gives, substituting for k_x from Equation (2-21)

$$\bar{P} \equiv (4\pi R_r)^2 \frac{P}{\rho_o} = k_o^4 \cos^4\theta_o \frac{\rho_s}{D_s^2} \int_{-\infty}^{\infty} dx\, 2\left(\frac{\sqrt{\pi}}{2} L_x \tau_o\right)\left(\frac{L_t^2}{2}\right)\exp[-\omega_m^2\tau_o^2/8]$$

$$\int_0^{\infty} 2\pi r dr\, [\overline{v_x^2}(x,r)]^2 \qquad (2\text{-}60)$$

where ω_m is understood to be evaluated with $k_x/k_o = \cos\theta_o$ also, i.e. $\omega_m = \omega D_m$ where

$$D_m = \left|(1 - M_c\cos\theta_o)^2 + \left(\frac{L_x}{\tau_o a_o}\right)^2 \frac{\cos^2\theta_o}{\pi} + \left(\frac{L_t}{\tau_o a_o}\right)^2 \frac{\kappa_s^2}{\pi}\right|^{\frac{1}{2}} \qquad (2\text{-}61)$$

and

$$D_s = 1 - M_s \cos\theta_o \qquad (2\text{-}62)$$

$$\kappa_s = \{a_o^2 D_s^2/a_s^2 - \cos^2\theta_o\}^{\frac{1}{2}} \qquad (2\text{-}63)$$

This result together with the corresponding expressions for the other quadrupole components is, in effect, the basis for the high-frequency prediction methods (outside the cone of silence) described in Section 2.5, although the integration over the source volume is not carried out *per se*.

Provided the dependence on radiation angle (θ_o), jet exit velocity (V_J) and jet exit temperature (T_J) can be extracted from the integrand, the volume integration is not required, that is, as long as the derived scaling laws are used only to predict radiation *directivity* or the *variation* of spectrum levels with velocity and temperature, as in the prediction methods of Section 2.5. If *absolute* noise level predictions are to be attempted, as in Section 2.4, then in principle the volume integral has to be evaluated.

In the case of the Gaussian model the variation of the integrand with θ_o can be suppressed if ω_m, the modified radian frequency which appears in the exponential argument, is held constant (or $\omega_m d/V_J \equiv 2\pi S_m$ since $\tau_o \propto d/V_J$ at a given value of x/d). The directivity of the radiated noise in proportional bandwidths, $\omega\bar{P}(\omega)$, is then governed by (1) the inherent zero-flow directivity of each quadrupole component (in the example given above, $\cos^4\theta_o$), (2) the effect of the acoustic-mean flow interactions (ρ_s/D_s^2) and (3) the convective amplification - modified by noncompactness effects - represented by a factor D_m^{-5} for all quadrupole components; this factor appears *via* the frequency dependence $\omega\bar{P}(\omega) \propto \omega(\omega/a_o)^4$; the relation $\omega = \omega_m/D_m$ and the requirement ω_m = constant. With regard to the latter, a more general approach has been utilized in the past [2.10] which does not rely on a specific form for the correlation function, or its Fourier transform, but simply *assumes* the scaling law

$$\Phi_{\alpha\beta}^{(2)}\ (\omega,n|x,r;\ k_x,r') = \Phi_{\alpha\beta}^{(2)}(\omega_m,0|x,r;0,r') \tag{2-64}$$

with ω_m as defined above. The transform of the *Gaussian* correlation function is a special case of this scaling law. When the directivity of the radiated sound is analyzed in the general case, the functional dependence of ω_m is unknown and hence ω_m *must* be held constant as the angle is varied. More precisely the directivity of the radiated sound intensity is given by (for the above example)

$$\omega P(\omega) \propto \left[\omega^5 \cos^4\theta_o\ \frac{\rho_s}{D_s^2}\right]_{\omega_m = \text{constant}} \tag{2-65}$$

or

$$\omega P(\omega) \propto \frac{\cos^4\theta_o}{D_m^5}\ \frac{\rho_s}{D_s^2} \tag{2-66}$$

The time (τ_o) and length scales (L_x, L_t) are roughly proportional to the distance from the nozzle exit plane and the integrand in Equation (2-60) reaches a pronounced maximum at an axial location largely determined by $S_m = f_m d/V_j$. Thus, the value of S_m also determines the axial location and hence the local shear layer thickness δ_s of an "effective" axial source position. This concept is used to determine the "true" polar radiation distance and angle when analyzing mixing noise data and more significantly to analyze data inside the cone of silence in that δ_s is assumed to be only a function of S_m.

The above result for $\bar{P}$, given by Equation (2-60), can now be generalized to include all the other quadrupole components, viz.

$$\bar{P} = \int_{-\infty}^{+\infty} dx\ 2\left(\frac{\sqrt{\pi}}{2} L_x \tau_o\right) \frac{L_t^2}{2} \exp\left[-\omega_m^2\ \tau_o^2/8\right]$$

$$\int_0^{\infty} 2\pi r dr \sum_{n=-\infty}^{\infty} |C_{\alpha\beta}|^2\ \overline{v_\alpha^2}(x,r)\ \overline{v_\beta^2}(x,r). \tag{2-67}$$

Substitution of Equation (2-52) for C into Equation (2-18) allows the azimuthal sums to be expressed in closed form as follows:

$$\sum_n |C_{xx}|^2 = \rho_s D_s^2\ \frac{k_o^4 \cos^4\theta_o}{D_s^4} \sum_n J_n^2(k_o \kappa_s r) = k_o^4\ \frac{\rho_s}{D_s^2} \cos^4\theta_o \tag{2-68a}$$

$$\sum_n |C_{xr}|^2 = \rho_s D_s^2\ \frac{k_o^2 \cos^2\theta_o}{D_s^4}\ k_o^2 \kappa_s^2 \sum_n J_n'^2(k_o \kappa_s r) = k_o^4\ \frac{\rho_s}{D_s^2} \cos^2\theta_o\ \kappa_s^2 \cdot \frac{1}{2} \tag{2-68b}$$

$$\sum_n |C_{rr}|^2 = \rho_s D_s^2 \frac{(k_o^2 \kappa_s^2)^2}{D_s^4} \sum_n J_n''^2 (k_o \kappa_s r) = k_o^4 \frac{\rho_s}{D_s^2} (\kappa_s^2)^2 \cdot \frac{3}{8} \qquad (2\text{-}68c)$$

$$\sum_n |C_{x\phi}|^2 = \rho_s D_s^2 k_o^2 \frac{\cos^2\theta_o}{D_s^4} \frac{1}{r^2} \sum_n n^2 J_n^2 (k_o \kappa_s r) = k_o^4 \frac{\rho_s}{D_s^2} \cos^2\theta_o \frac{\kappa_s^2}{2} \qquad (2\text{-}68d)$$

$$\sum_n |C_{r\phi}|^2 = \frac{\rho_s}{D_s^2} \sum_n n^2 \left| k_o \kappa_s \frac{J_n'(k_o \kappa_s r)}{r} - \frac{J_n(k_o \kappa_s r)}{r^2} \right|^2 = k_o^4 \frac{\rho_s}{D_s^2} \frac{\kappa_s^4}{8} \qquad (2\text{-}68e)$$

$$\sum_n |C_{\phi\phi}|^2 = \frac{\rho_s}{D_s^2} \sum_n \left| \frac{k_o \kappa_s}{r} J_n'(k_o \kappa_s r) - \frac{n^2}{r^2} J_n(k_o \kappa_s r) \right|^2 = k_o^4 \frac{\rho_s}{D_s^2} \frac{3\kappa_s^4}{8} \qquad (2\text{-}68f)$$

Hence, we obtain

$$\tilde{P} = \int_{-\infty}^{\infty} dx\, 2 \left(\frac{\sqrt{\pi}}{2} L_x \tau_o \right) \frac{L_t^2}{2} \exp\left[-\omega_m^2 \tau_o^2/8\right] k_o^4 \int_0^{\infty} \frac{2\pi r\, dr}{D_s^2} \rho_s \Big| \overline{v_x^2}^2 \cos^4\theta_o$$

$$+ \overline{v_x^2}\, \overline{v_r^2}\, \kappa_s^2 \cos^2\theta_o + \overline{v_x^2}\, \overline{v_\phi^2}\, \kappa_s^2 \cos^2\theta_o$$

$$\frac{3}{8} \overline{v_r^2}^2 \kappa_s^4 + \frac{1}{4} \overline{v_r^2}\, \overline{v_\phi^2} \kappa_s^4 + \overline{v_\phi^2}^2 \kappa_s^4 \Big| \qquad (2\text{-}69)$$

and *if* $\overline{v_r^2} = \overline{v_\phi^2} = \overline{v_t^2}$, then this simplifies to

$$\tilde{P} = \int_{-\infty}^{\infty} dx\, 2 \left(\frac{\sqrt{\pi}}{2} L_x \tau_o \right) \frac{L_t^2}{2} \exp\left[-\omega_m^2 \tau_o^2/8\right]$$

$$k_o^4 \int_0^{\infty} \frac{2\pi r dr}{D_s} \rho_s \left[\overline{v_x^2}^2 \cos^4\theta_o + \overline{v_x^2}\, \overline{v_t^2}\, 2 \cos^2\theta_o \kappa_s^2 + \overline{v_t^2}^2 \kappa_s^4 \right] \qquad (2\text{-}70)$$

If it is assumed also that the turbulence *is* statistically isotropic (SI) i.e.

$$\overline{v_x^2} = \overline{v_t^2} = \overline{v^2}$$

then Equation (2-70) reduces to

$$\bar{P} = \omega^4 \frac{\rho_s D_s^2}{a_s^4} \int_{-\infty}^{+\infty} dx\ 2\left(\frac{\sqrt{\pi}}{2} L_x \tau_o\right) \frac{L_t^2}{2} \exp\left[-\omega_m^2 \tau_o^2/8\right]$$

$$\cdot \int_0^{\infty} 2\pi r dr\ [\overline{v^2}(x,r)]^2 \qquad (2\text{-}71)$$

but this is not supported by turbulence measurements and for this and other reasons the high-frequency prediction model is written in a form allowing for an arbitrary axial-axial quadrupole "weighting":

$$\bar{P} = \omega^4 \left| \frac{\rho_s D_s^2}{a_s^4} + C_q \frac{\rho_s}{a_o^4 D_s^2} \cos^4\theta_o \right|$$

$$\int_{-\infty}^{\infty} dx\ 2\left(\frac{\sqrt{\pi}}{2} L_x \tau_o\right) \frac{L_t^2}{2} \exp\left[-\omega_m^2 \tau_o^2/8\right] \int_0^{\infty} 2\pi r dr\ [\overline{v^2}\ (x,r)]^2 \qquad (2\text{-}72)$$

and similarly for the dipole source. The isotropic case corresponds to $C_q = 0$ (or $C_d = 0$ for the dipole source).

The accuracy of the high-frequency, approximate description of acoustic-mean flow interactions represented by the factor

$$\frac{\rho_s D_s^2}{a_s^4}$$

in Equation (2-71) for the *isotropic* quadrupole ring-source model is illustrated in Figure 2.2 which shows the ratio (in dB) of the corresponding *numerical* solution to Lilley's equation and the expression given above, as a function of velocity ratio V_J/a_o. The angle parameter θ_s is the emission angle at the effective source position which is related to the radiation angle, θ_o, by

$$\cos\theta_s = \frac{(a_s/a_o)\cos\theta_o}{(1 - V_s\cos\theta_o/a_o)} \qquad (2\text{-}73)$$

Real values of θ_s automatically exclude radiation from sources inside the cone of silence. For these calculations and those to follow the mean flow and source parameter values assumed are given in Table 2.1. The flow profiles used for the numerical solutions are described in Appendix 2A; the value of V_s/V_{max} given in Table 2.1 determines the ring source radius for these solutions at each Strouhal number.

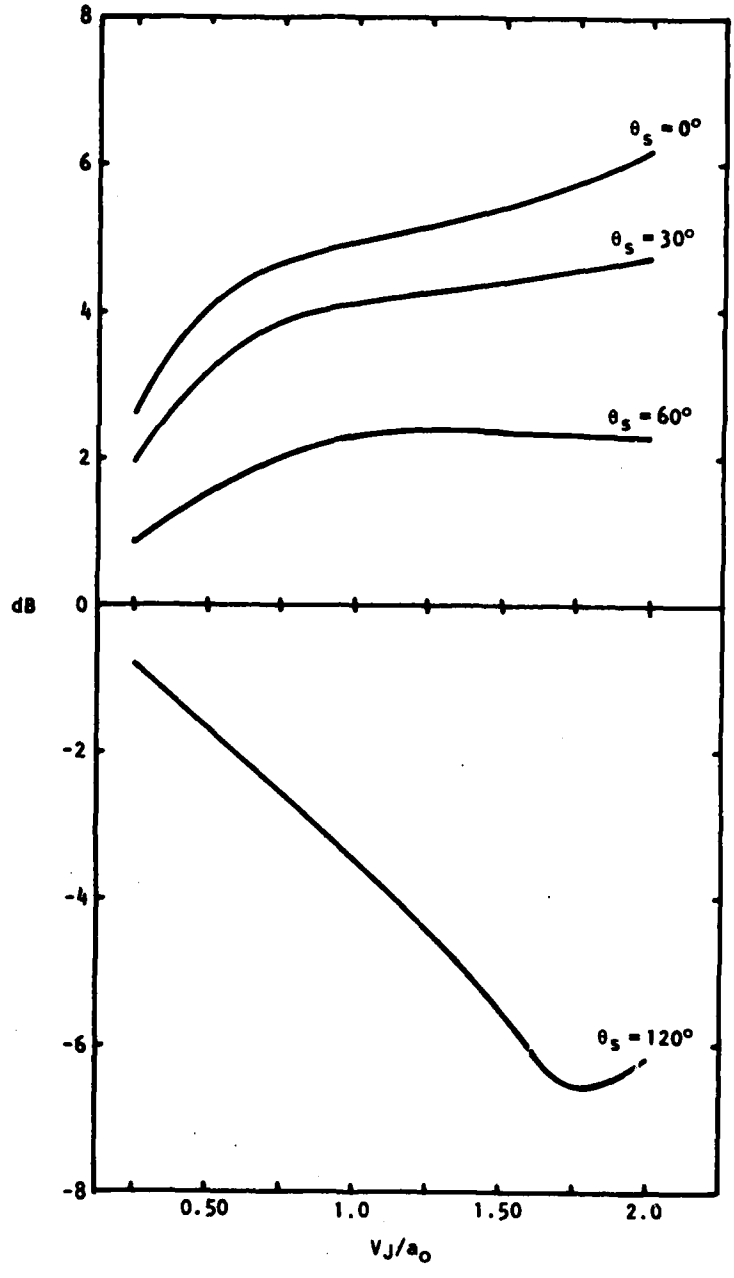

Figure 2.2 Ratio of Numeric and High-Frequency Lilley Equation Solutions at Constant Values of Source Emission Angle θ_s for Isotropic Quadrupole Ring-Source Model. Flow/Source Parameters Given in Table 2.1; $S_m = 0.1$.

Figure	2.2/2.3	2.4/2.5	2.6	2.7
S_m	0.1	0.316	1.0	3.16
δ_s/r_J	2.818 1.432	1.818 1.612	1.024	0.460
V_{max}/V_J	0.5 1.0	0.9 1.0	1.0	1.0
V_s/V_{max}	0.99 0.5	0.663 0.6	0.6	0.6
V_c/V_{max}	2.0 1.0	0.8111 0.7300	0.6	0.6

Table 2.1 Shear layer thickness of velocity profiles and centerline, source region and convection velocities ($T_s/T_o = 1, \gamma = 1.4$) for Lilley equation numeric *versus* high-frequency solution comparisons.

The values of δ_s/r_J, V_s/V_{max} and V_{max}/V_J are based upon source location data (e.g. Polar Correlation Technique, see Section 2.3) and measured turbulence data. The alternative value of δ_s/r_J shown for $S_m = 0.1$ corresponds to the value inferred from a high-frequency analysis of the Lockheed data (see Section 2.5) and the comparison in this case, referred to as "inferred δ_s/r_J" is shown in Figure 2.3. These large deviations are due to the shear noise source terms as discussed in Section 2.1.6 below and indicate that the unrealistic δ_s/r_J value obtained in the high-frequency analysis, which neglects all shear noise source terms, is due to the exclusion of this effect from the high-frequency, approximate solutions. Similar results are presented for $S_m = 0.316$ in Figures 2.4 and 2.5; although the shear noise effect is weaker at this higher frequency, the deviation is quite appreciable for the standard axial source location ($\delta_s/r_J = 1.818$). At the highest Strouhal numbers the inferred values of δ_s/r_J from the high-frequency analysis agree very well with source location data and here the deviations are much smaller as shown in Figures 2.6 and 2.7, although there are still some significant variations with V_J/a_o at small angles over the velocity range.

As might be expected, the largest deviations (of the high-frequency from the numeric Lilley equation solutions) occur at low Strouhal numbers and here a high-frequency analysis of jet mixing noise data can lead to erroneous conclusions. On the other hand provided that the deviations do not *vary* appreciably over a useful range of jet velocities (or jet temperatures but temperature effects are not considered here), then the mean deviation can be incorporated in a "source directivity" parameter [i.e. C_q as defined by Equation (2-72)] and this has been the approach adopted by Szewczyk [2.11] and in our high-frequency analysis. These aspects are discussed further in Section 2.5.

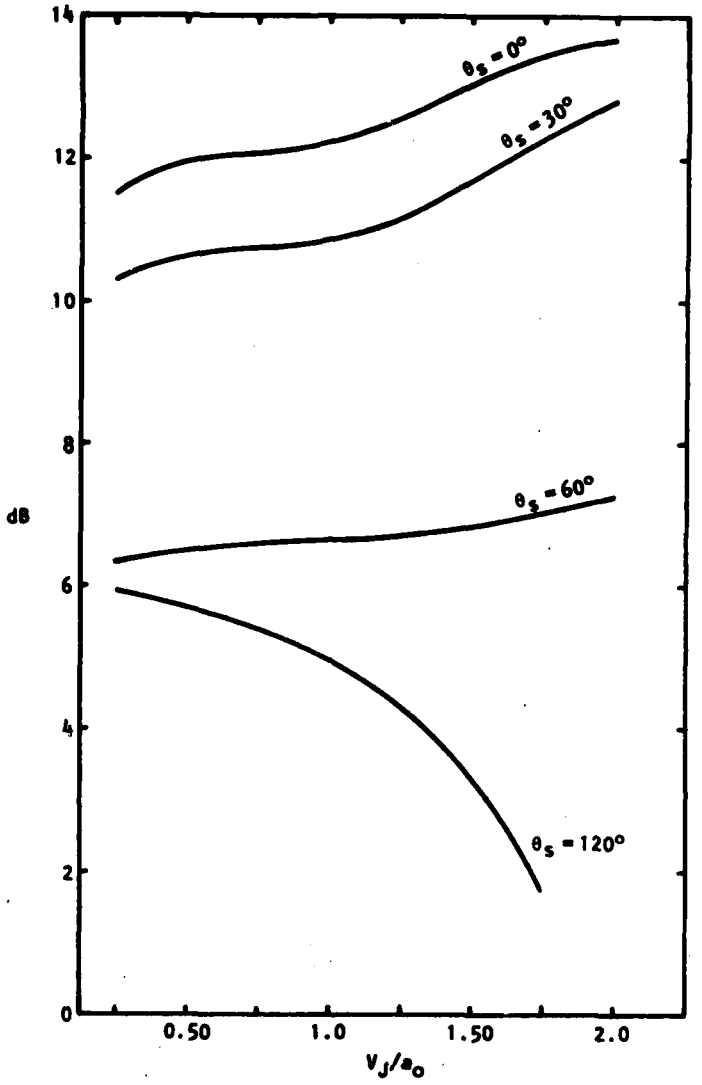

Figure 2.3 Ratio of Numeric and High-Frequency Lilley Equation Solutions at Constant Values of Source Emission Angle θ_s for Isotropic Quadrupole Ring-Source Model. Flow/Source Parameters Given in Table 2.1; $S_m = 0.1$ (Inferred δ_s/r_j).

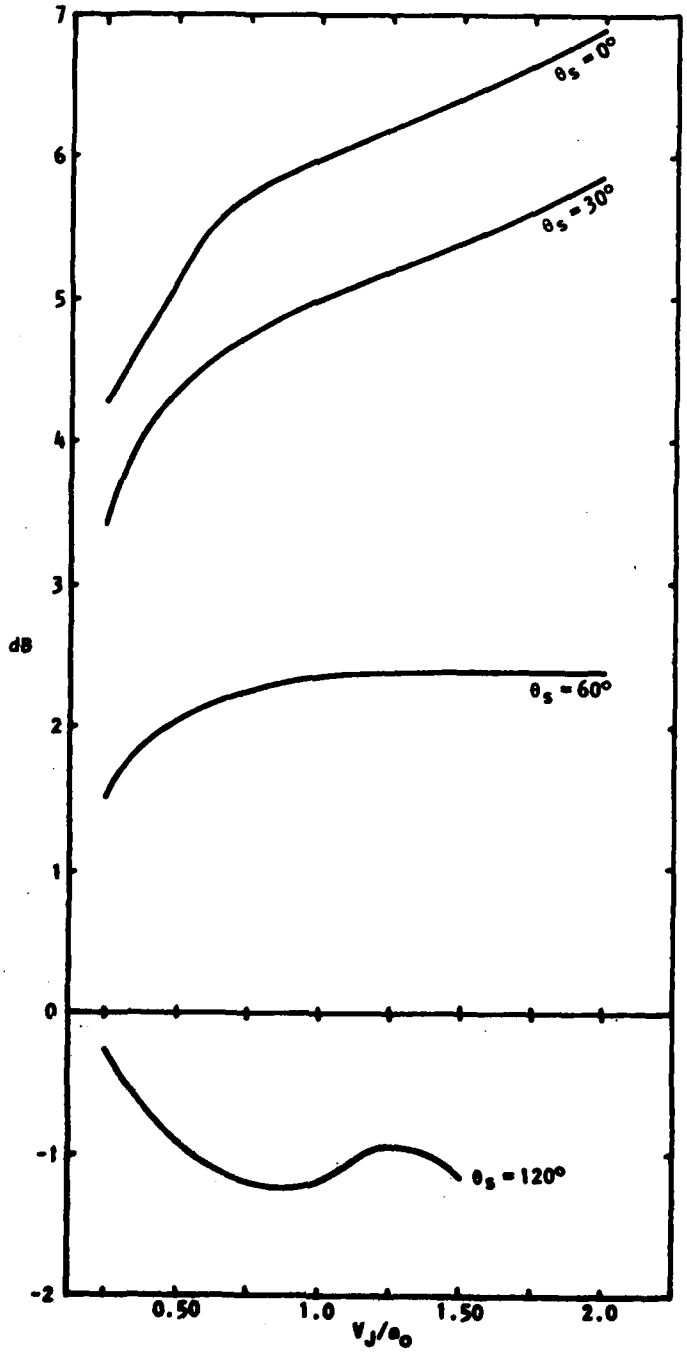

Figure 2.4 Ratio of Numeric and High-Frequency Lilley Equation Solutions at Constant Values of Source Emission Angle θ_s for Isotropic Quadrupole Ring-Source Model. Flow/Source Parameters Given in Table 2.1; $S_m = 0.316$.

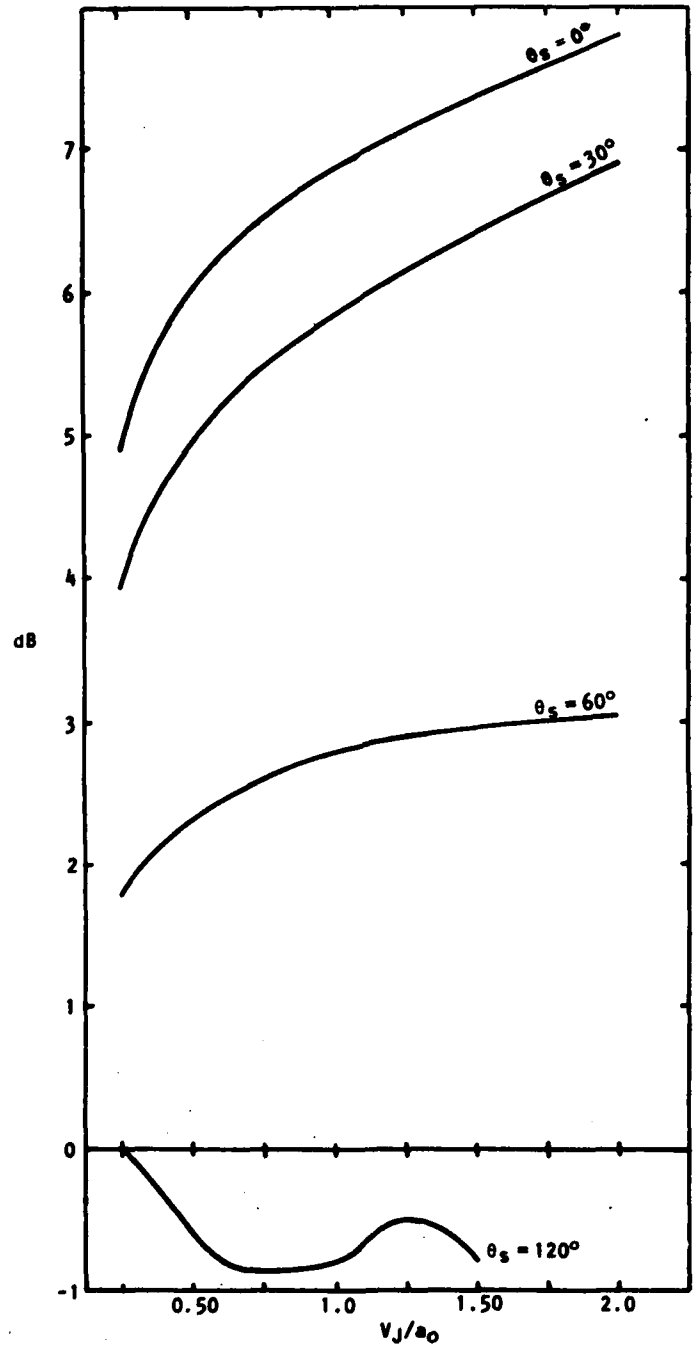

Figure 2.5 Ratio of Numeric and High-Frequency Lilley Equation Solutions at Constant Values of Source Emission Angle θ_s for Isotropic Quadrupole Ring-Source Model. Flow/Source Parameters Given in Table 2.1; $S_m = 0.316$ (Inferred δ_s/r_J)

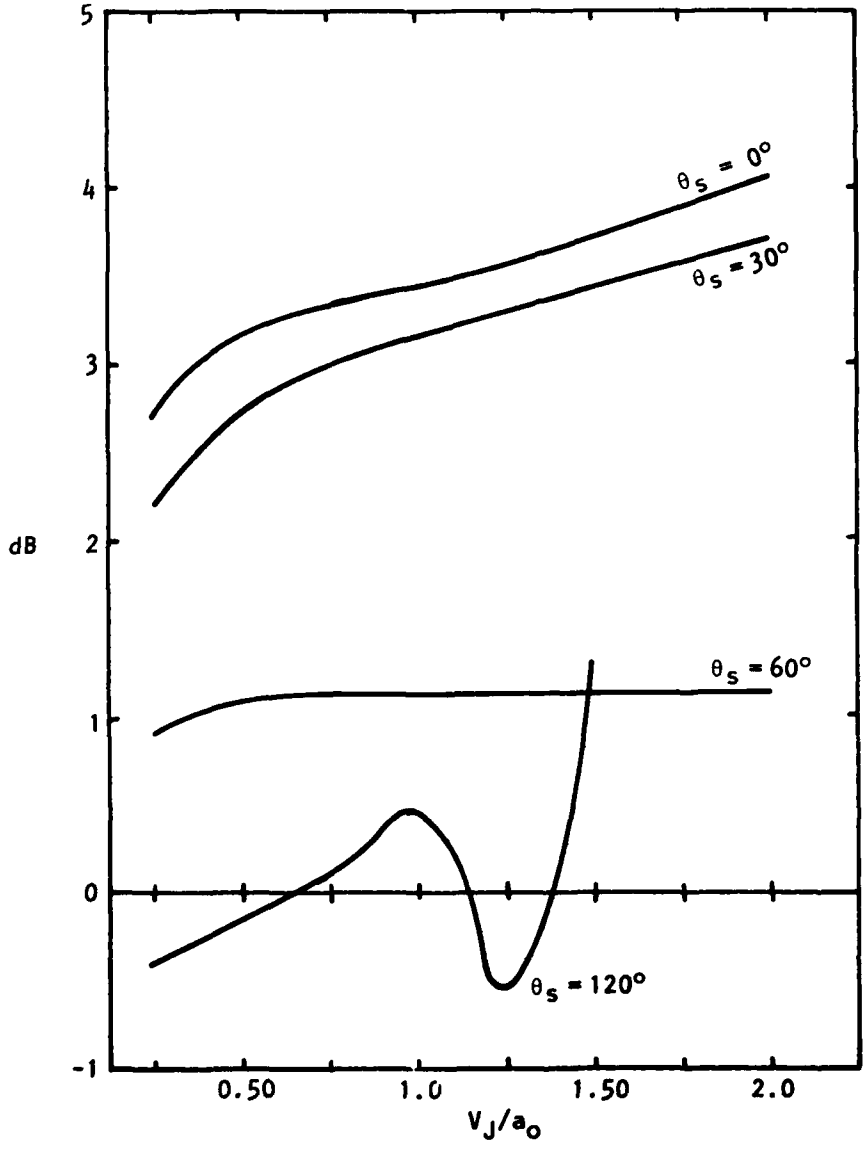

Figure 2.6 Ratio of Numeric and High-Frequency Lilley Equation Solutions at Constant Values of Source Emission Angle θ_s for Isotropic Quadrupole Ring-Source Model. Flow/Source Parameters Given in Table 2.1; $S_m = 1.0$.

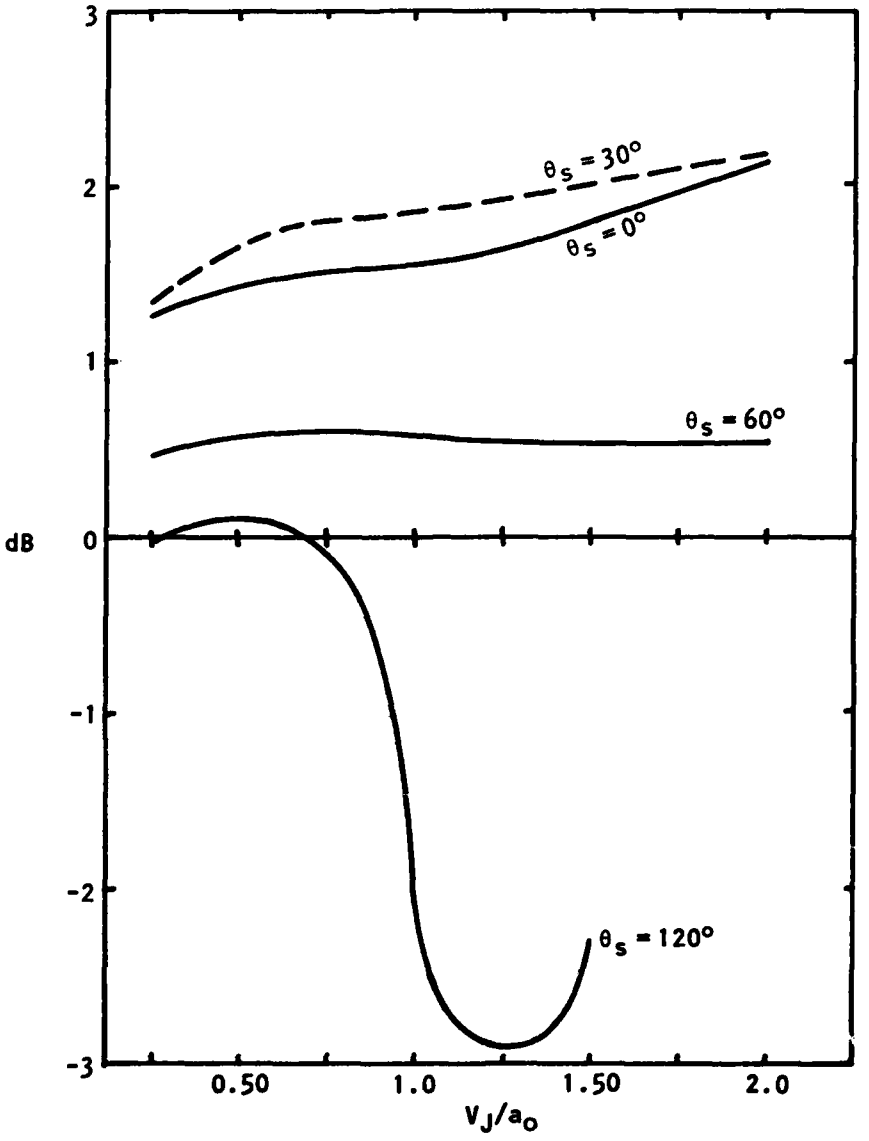

Figure 2.7 Ratio of Numeric and High-Frequency Lilley Equation Solutions at Constant Values of Source Emission Angle θ_s for Isotropic Quadrupole Ring-Source Model. Flow/Source Parameters Given in Table 2.1; $S_m = 3.16$.

2.1.4 High-Frequency Lilley Equation Solutions Inside the Cone of Silence

The high-frequency or WKB Green function solution to Lilley's equation *inside* the cone of silence was derived at Lockheed under the previous contract [2.2] and in the present notation (source position $r = r_s$), its modulus squared is determined by

$$|C(r_s)|^2 = \frac{\rho_o \rho_s D_s^{-2}}{2\pi r_s} \frac{1}{k_o |q_s|} \exp\left[-2 k_o \int_{r_s}^{r_{Tq}} |q| dr\right] \qquad (2\text{-}74)$$

where

$$q^2(r) = \kappa^2 - (n^2 - \tfrac{1}{4})/(k_o r)^2 \qquad (q^2 < 0) \qquad (2\text{-}75)$$

and r_{Tq}, the transition point radius, is defined by

$$q^2(r_{Tq}) = 0 \qquad \text{(a simple zero is assumed).} \qquad (2\text{-}76)$$

This solution was obtained using an effective wavenumber substitution suggested by Lilley [2.1] – given by Equation (2-75) – and is one of the highlights of the work covered in this and the previous contract. It also provided the foundation for Szewczyk's [2.11] original high-frequency analysis of the Lockheed mixing noise data (inside the cone of silence) and gives a simple but quantitatively realistic estimate of the so-called shielding effect, as indicated by the comparisons with numerical solutions in Table 2.2. For this comparison the isotropic quadrupole ring-source model has been used with $S_m = 1$, $\delta_s/r_J = 1.05$, $V_s/V_J = 0.6$ and $\gamma = 1.4$.

V_J/a_o	T_J/T_o	θ_o	20°	30°	40°
0.5	1.0	Numerical	-9.8	-6.9	--
		WKB	-10.7	-8.0	--
0.9	2.2	Numerical	-31.5	-25.2	-19.2
		WKB	-32.3	-26.2	-20.6

Table 2.2 Numerical and WKB Lilley Equation Solutions at $S_m = 1.0$

The dipole and quadrupole solutions are easily obtained from the basic Green function solution of Equation (2-74), ignoring all mean flow gradient terms as before.

Although Equation (2-74) is straightforward to evaluate by numerical integration and the azimuthal summations can be performed numerically also,

it is desirable for analysis and prediction purposes to have an even simpler expression for the required solutions. (Analysis of measured data often involves highly repetitive evaluation of the acoustic solutions with different parameter values at each test condition.) Thus, ideally, the integral should be replaced by a reasonably accurate, closed-form expression and similarly for the azimuthal mode summation although this is not so crucial since only a relatively small number of modes are involved inside the cone of silence. Both these steps were accomplished under the previous contract (ref. [2.2], Appendix 3D). There the integrand was replaced by a rectangular distribution of effective width $\bar{y}$ and height κ_s, following the work of Fisher et al. [2.12]. However, some detailed evaluations of $|q|$ in the vicinity of the transition point, $r = r_{Tq}$, suggested a parabolic behavior and this encouraged Szewczyk [2.11] to improve the integral evaluation accordingly. The azimuthal summation approximation was also modified to allow for the revised integral expression. Both these approximations were performed on the monopole solution; the dipole and quadrupole solutions are obtained by analogy with the corresponding expressions outside the cone of silence (i.e. without rigorous proof) and the final expressions for the quadrupole radiation is

$$\bar{P} = \int_{-\infty}^{\infty} dx\ 2\left(\frac{\sqrt{\pi}}{2} L_x \tau_o\right) \frac{L_t^2}{2} \exp[-\omega_m^2 \tau_o^2/8]$$

$$k_o^4 \int_0^{\infty} 2\pi r dr\ \frac{\bar{\rho}(r)}{D^2(r)}\ [\overline{v_x^2}^2 \cos^4\theta_o + 2\ \overline{v_x^2}\ \overline{v_t^2}\ \cos^2\theta_o\ |\kappa^2(r)|$$

$$+ \overline{v_t^2}^2\ |\kappa^2(r)|^2]\ N_\infty(r) \qquad (2\text{-}77)$$

where

$$N_\infty(r) = \frac{0.392}{\{3(2A|\kappa^2(r)|^{3/2}) + 1\}^{\frac{1}{2}}} \exp\ [-2A|\kappa^2(r)|^{3/2}],\quad (2A|\kappa^2(r)|^{3/2} > 0.6)$$

$$= 1 \qquad \text{if} \qquad \kappa^2 \geq 0 \qquad (2\text{-}77a)$$

and in the intermediate region:

$X \equiv 2A\lvert\kappa^2\rvert^{3/2}$	0.0	0.1	0.2	0.3	0.4	0.5	0.6
N_∞	1.0	0.59	0.4	0.28	0.2	0.158	0.128

(2-77b)

The quantity A is defined by

$$A = (-2/3)k_o \left[d(-\kappa^2)/dr\right]^{-1}_{r=r_T} \qquad (2\text{-}77c)$$

and is a function of the mean velocity and temperature and their gradients at the transition radius, r_T, defined by $\kappa^2(r_T) = 0$.

Notice that when $r > r_T$, N_∞ is equal to unity, κ^2 is positive and the expression for $\bar{P}$ Equation (2-77) reduces to that derived outside the cone of silence [Equation (2-70)]. In deriving Equation (2-77) the same assumptions have been employed as before concerning the slow variation of $\overline{v^2}$ on the coherence length scale and the noncompactness effect based on the Gaussian correlation model. Notice though here the flow parameters vary over the source region whereas in the previous case *constant* values (V_s,ρ_s,a_s) were assigned. That approach cannot be used here, as such, since that would lead to the classical geometric acoustics result of *zero* radiation inside the cone of silence.

The intermediate region for which N_∞ is defined numerically arises because the original WKB solution (itself an approximation) has a singularity at the transition point, $r = r_T$, and consequently cannot be used at and near this point. This applies to any approximate evaluation of the solution as well and hence the need for the table of numerical values in this region to link (empirically) the geometric acoustic and WKB solutions.

The accuracy of this approximate method of evaluating the WKB solution is illustrated in Table 2.3 at four subsonic jet flow conditions; clearly its accuracy is reasonable at radiation angles greater than or equal to 30° but at smaller angles the errors become unacceptable. However, this allows a wide, useful range of angles and the approximation has been extensively utilized.

V_J/a_o	T_J/T_o	$\theta_o = 20°$	30°	40°	50°
0.5	1.0	-4.4	-1.5	--	--
0.9	1.0	-19.7	-2.8	-0.8	--
0.5	2.2	-6.8	-1.1	-1.4	-1.0
0.9	2.2	-19.4	-0.9	+1.3	-1.1

Table 2.3 Errors (in dB) due to approximate evaluation of the WKB isotropic quadrupole ring source solution at $S_m = 3.0$ ($\delta_s/r_J = 0.2625$, $V_s/V_J = 0.6$, $\gamma = 1.4$).

The basic solution given by Equation (2-74) and the above approximation, given by Equation (2-77), show quite clearly that the magnitude of the exponential decay or *noise reduction* inside the cone of silence is directly proportional to the shear layer thickness on the wavelength scale. It is

therefore natural to raise the question whether the single profile Lilley equation approach is sufficiently accurate in this context. The axially distributed source could radiate without significant exponential decay from the thinner shear layer region between the nozzle exit plane and the axial peak location, thereby short-circuiting a larger exponential decay at the peak. However, a preliminary investigation of this effect with the aid of polar correlation measurements of the axial source distribution (see Section 2.3) and the approximate form of the WKB solution given above was conducted, and it was found that this was quite a small effect, although that investigation was based upon the displacement source model (now discarded in favor of the original Lilley equation source function). A further investigation into this effect would therefore be desirable.

The High-Frequency Solution at the Mach Angle

The WKB solution is also singular at the Mach angle, i.e. when radiation at an angle θ_o is received from a source located radially in the flow where

$$D = 1 - V(r_c)\cos\theta_o/a_o = 0 \tag{2-78}$$

but this singularity arises from the governing differential equation and is not a feature of the approximate solution alone. When solving the Lilley equation *numerically* the integration contour is taken into the complex r plane where the mean velocity is obrained via a Taylor expansion [2.13], viz.

$$V(r) = V(r_c) + (r - r_c)\, V'(r_c) + O((r - r_c)^2) \tag{2-79}$$

and the radius $|r - r_c|$ has been found (empirically) to be

$$|r - r_c| = \beta_c \delta_s, \qquad 0.06 \le \beta_c \le 0.12 \tag{2-80}$$

so that on this contour the Doppler factor is approximately

$$D = -\beta_c \delta_s \; V'(r_c) \; \cos\theta_o/a_o$$

$$\doteq -\beta_c \; V_J(r_c)\cos\theta_o/a_o \tag{2-81}$$

(since $V' \doteq V_J/\delta_s$ if r_c is at or near the radius of maximum shear). Thus, the singularity caused by Doppler factor D inside the cone of silence has been removed by replacing D in the denominator of Equations (2-74) and (2-77) by

$$\tilde{D}^2 = D^2 + \beta_c^2 \,(V_J \cos\theta_o/a_o)^2 \tag{2-82}$$

with $\beta_c = 0.06$ (the lowest value has been found to give the most acceptable behavior of the high-frequency solutions at and near the Mach angle).

2.1.5 Noncompactness Effects

2.1.5.1 Comparison of high-frequency and numerical solutions to Lilley's equation outside the cone of silence

For the purposes of comparing numerical and high-frequency solutions to Lilley's equation, it *is* assumed for simplicity that the turbulence source is isotropic but it should be emphasized that this was *not* assumed in our high-frequency analysis of the mixing noise data nor in the prediction programs (see Section 2.5).

In this comparison we are mainly concerned with identifying non-geometric acoustics effects in the numerical solutions in order to guide the application of high-frequency data analysis and to establish its accuracy over a wide range of flow parameters. In principle, we wish to compare, for the Gaussian correlation model, the numerical value of the quantity

$$f(x) = \sum_n f_n(x)$$

where

$$f_n(x) = 2\pi \int_0^\infty r\,dr\; C^*_{\alpha\beta}(k_x,r,n,\omega) \int_0^\infty r'dr' C_{\alpha\beta}(k_x,r',n,\omega)\; 2\phi^{(2)}_{\alpha\beta}(\omega,n|x,r;k_x,r') \tag{2-83}$$

which appears in Equation (2-37) as

$$P_n = \int_{-\infty}^{+\infty} dx\; f_n(x) \tag{2-84}$$

with the high-frequency result given by Equation (2-71), *viz.*

$$f_\infty(x) = \omega^4 \frac{\rho_s D_s^2}{a_s^4} \cdot 2\left(\frac{\sqrt{\pi}}{2} L_x \tau_o\right) \frac{L_t^2}{2} \exp\left[-\omega_m^2 \tau_o^2/8\right] \int_0^\infty 2\pi r\,dr\; [\overline{v^2}(x,r)]^2 \tag{2-85}$$

Substituting Equation (2-39) for $\phi^{(2)}_{\alpha\beta}$ – the Gaussian model – into Equation (2-83) gives

$$f(x) = 4\pi \left(\frac{\sqrt{\pi}}{2} L_x \tau_o\right) \exp\left[-\omega_{mx}^2 \tau_o^2/8\right] \sum_n \int_o^\infty r dr\, C^*_{\alpha\beta}(k_x, r, n, \omega)\, \overline{v_\alpha^2}\,(x,r)$$

$$\cdot \int_o^\infty r' dr'\, C_{\alpha\beta}(k_x, r', n, \omega)\, \overline{v_\beta^2}\,(x,r')$$

$$\cdot \exp\left[-2\pi(r^2 + r'^2)/L_t^2\right] 2\pi\, I_n(4\pi r r'/L_t^2) \qquad (2\text{-}86)$$

or, with the statistically isotropic assumption and in terms of ω_m in place of ω_{mx}:

$$f(x) = 4\pi \left(\frac{\sqrt{\pi}}{2} L_x \tau_o\right) \exp\left[-\omega_m^2 \tau_o^2/8\right] \sum_n \exp[k_o^2 \kappa_s^2 L_t^2/8\pi]$$

$$\int_o^\infty r dr\, C^*_{\alpha\beta}\,(k_x, r, n, \omega)\, \overline{v^2}\,(x,r) \int_o^\infty r' dr'\, C_{\alpha\beta}(k_x, r', n, \omega)\, \overline{v^2}(x,r')$$

$$\cdot \exp\left[-2\pi(r^2 + r'^2)/L_t^2\right] 2\pi\, I_n\,(4\pi r r'/L_t^2) \qquad (2\text{-}87)$$

The model adopted for $\overline{v^2}$ is of the usual Gaussian form (see Section 5)

$$\{\overline{v^2}(x,r)\}^{\frac{1}{2}} = \{\overline{v^2}(x)\}^{\frac{1}{2}}_{max} \exp\left\{-\left[\frac{0.8326}{\eta_{hw}}(\eta - \eta_s)\right]^2\right\} \qquad (2\text{-}88)$$

where

$$\eta = (r - r_j)/x \qquad (2\text{-}88a)$$

and

$$\{\overline{v^2}(x,r)\}^{\frac{1}{2}} = \{\overline{v^2}(x)\}^{\frac{1}{2}}_{max} \qquad \text{at} \qquad \eta = \eta_s \qquad (2\text{-}88b)$$

$$\frac{\{\overline{v^2}(x,r)\}^{\frac{1}{2}}}{\{\overline{v^2}(x)\}^{\frac{1}{2}}_{max}} = 0.5 \qquad \text{at} \qquad \eta = \eta_s \pm \eta_{hw} \qquad (2\text{-}88c)$$

The radial center of the source distribution η_s is defined here by the value adopted for V_s in the high-frequency analysis as a function of axial position (i.e. of Strouhal number). The half width has been taken to be $\eta_{hw} = 0.1$ (corresponding to $c \sim 72$ from turbulence data at the subsonic condition

$V_J/a_o \sim 0.5$, see Section 2.4). The integral of this distribution over its radial extent in Equation (2-85) for the high-frequency solution is obtained from the standard integral

$$\int_0^\infty rdr\, e^{-(r-a)^2/b^2} = \frac{b^2}{2}\{e^{-a^2/b^2} + \frac{a}{b}\sqrt{\pi}[1 + \text{erf}\,(a/b)]\}\,. \qquad (2\text{-}89)$$

Thus, we are essentially concerned with the ratio

$$\frac{f(x)}{f_\infty(x)} = \left|\frac{\rho_s D_s^2}{\rho_o}\left(\frac{a_o}{a_s}\right)^4 \exp[-k_o^2\kappa_s^2 L_t^2/8\pi]\,\frac{L_t^2}{2}\int_0^\infty rdr\,[\overline{v^2}(x,r)]^2\right|^{-1}$$

$$\sum_n \int_0^\infty rdr\,\frac{C^*_{\alpha\beta}}{\rho_o^{\frac{1}{2}}k_o^2}(k_x,r,n,\omega)\,\overline{v^2}(x,r)\int_0^\infty r'dr'\,\frac{C_{\alpha\beta}}{\rho_o^{\frac{1}{2}}k_o^2}(k_x,r',n,\omega)\,\overline{v^2}(x,r')$$

$$\cdot \exp\,[-2\pi(r^2 + r'^2)/L_t^2]\;2\pi\, I_n(4\pi rr'/L_t^2) \qquad (2\text{-}90)$$

and its deviation from unity at a fixed modified Strouhal number, S_m, as a function of radiation angle, θ_o, and velocity ratio, V_J/a_o (for the isothermal case – the only one that will be considered here). The ratio is evaluated at $x = x_s$, the axial position where f (and f_∞) reaches a maximum for the chosen value of S_m. The deviations are associated with

(a) non-geometric acoustics or finite wavelength effects causing a deviation from the high-frequency factor

$$\frac{\rho_s D_s^2}{\rho_o}\left(\frac{a_o}{a_s}\right)^4; \qquad (2\text{-}91)$$

(b) similarly for the radial-azimuthal noncompactness factor

$$\exp[-k_o^2\kappa_s^2 L_t^2/8\pi]; \qquad (2\text{-}92)$$

(c) the assumption that the $\overline{v^2}(x,r)$ varies sufficiently slowly over the coherence length scale to be omitted from the integral with respect to r, and

(d) the high frequency assumption that the flow conditions are radially uniform throughout the source region.

At the radiation angle of $\theta_o = 90°$ and for isothermal conditions, there is no effect of flow on the radiated sound field (according to the present parallel flow model) so (a) and (d) can be ignored and the evaluation of the ratio $f(x_s)/f_\infty(x_s)$ can be used to determine whether noncompactness effects

(b) and (c) are important. For this exercise the following parameter values are chosen:

$\theta_o = 90°$

$S_m = 1$

$\delta_s/r_J = 1.050$ (i.e. $x_s = 4d$ with $\sigma = 13.5$)

$V_J/a_o = 0.25\ (0.25)\ 2.0$

T_J/T_o calculated from $T_s/T_o = 1$ at $\eta = \eta_s$ and $\gamma = 1.4$ (uniform)

$\eta_{hw} = 0.1$, η_s corresponding to $V_s/V_J = 0.6$

$L_t = 0.38\ r_J$

and it is assumed that

$$(a_o/a_s)^2 = \rho_s/\rho_o = T_o/T_s \tag{2-93}$$

so that

$$\frac{\rho_s D_s^2}{\rho_o}\left(\frac{a_o}{a_s}\right)^4 = \left(\frac{T_o}{T_s}\right)^3 = 1 \tag{2-94}$$

and the results are given in Table 2.4

V_J/a_o	f/f_∞ (dB)
0.25	-.62
0.5	-.56
0.75	-.46
1.0	-.32
1.25	-.16
1.5	.03
1.75	.23
2.0	.44

Table 2.4 Noncompactness effects: Velocity dependence of high frequency solution deviations from numerical solutions to Lilley's equations at $\theta_o = 90°$, $S_m = 1$.

The variation is ~1 dB over the range covered by the high-frequency analysis and this is expected to be typical of results at all other Strouhal numbers of interest. Thus, the high-frequency noncompactness effect at 90° and at constant S_m for proportional bandwidth data, given by D_m^{-5} where

$$D_m = \left| 1 + \left(\frac{L_t}{\tau_o a_c}\right)^2 \frac{\kappa_s^2}{\pi} \right|^{\frac{1}{2}}, \qquad (2\text{-}95)$$

is reasonably accurate. However, values of L_t/τ_o inferred from our high-frequency analysis of the mixing noise data may be subject to significant error because of the deviations indicated above. (It is only the relatively small departure from the V_j^8 scaling law that is used to infer values of L_t/τ_o.)

In order to uncover the significance of the non-geometric acoustic and nonuniform flow effects (a) and (d) mentioned above – without the complexity of effects (b) and (c) – the results in Table (2.4) are used to justify the next step in which it is assumed that the noncompactness effects (b) and (c) in the numerical solutions can be modeled analytically with the high-frequency result, viz. we adopt the assumption (c):

$$\int_0^\infty r dr\, C^*_{\alpha\beta}\,(k_x,r,n,\omega)\, \overline{v^2}(x,r)$$

$$\cdot \int_0^\infty r' dr'\, C^*_{\alpha\beta}(k_x,r',n,\omega)\, \overline{v^2}(x,r')\, \exp[-2\pi(r^2+r'^2)/L_t^2]\, 2\pi\, I_n(4\pi rr'/L_t^2)$$

$$\rightarrow \int_0^\infty r dr\, C^*_{\alpha\beta}\,(k_x,r,n,\omega)\, [\overline{v^2}(x,r)]^2$$

$$\cdot \int_0^\infty r' dr'\, C_{\alpha\beta}(k_x,r',n,\omega)\, \exp\,[-2\pi(r^2+r'^2)/L_t^2]\, 2\pi\, I_n(4\pi\, rr'/L_t^2) \qquad (2\text{-}96)$$

and the high-frequency radial-azimuthal noncompactness factor (b) derived in Equation (2-56):

$$\rightarrow \exp[-k_o^2\kappa_s^2 L_t^2/8\pi] \cdot \frac{L_t^2}{2} \cdot \int_0^\infty r dr\, |C_{\alpha\beta}(k_x,r,n,\omega)|^2\, [\overline{v^2}(x,r)]^2 \qquad (2\text{-}97)$$

This means that we now need only consider the simpler ratio

$$\frac{f(x)}{f_\infty(x)} = \left| \frac{\rho_s D_s^2}{\rho_o} \left(\frac{a_o}{a_s}\right)^4 \int_0^\infty r dr\, [\overline{v^2}(x,r)]^2 \right|^{-1}$$

$$\sum_n \int_0^\infty r dr\, \frac{C^*_{\alpha\beta}}{\rho_o^{\frac{1}{2}} k_o^2}\,(k_x,r,n,\omega)\, \frac{C_{\alpha\beta}}{\rho_o^{\frac{1}{2}} k_o^2}\,(k_x,r,n,\omega)\, [\overline{v^2}(x,r)]^2 \qquad (2\text{-}98)$$

This ratio is calculated for the same conditions as before except now results are given for other angles outside the cone of silence in the rear arc. The radiation angle actually varies with velocity here since it is the emission angle, θ_s, defined as

$$\cos\theta_s = (a_s/a_o)\cos\theta_o/D_s \qquad (2\text{-}99)$$

which is held constant. This minimizes the deviation of the high-frequency solution from its numerical counterpart over the velocity range as demonstrated in previous work [2.2]; the high-frequency analysis of the mixing noise data has been conducted on this basis outside the cone of silence. The results are given in Table 2.5 where the value of the ratio f/f_∞ is also given for the case when $\eta_{hw} \to 0$ (i.e. a ring source). The results for $\theta_s = 0°$ – on the cone of silence boundary – are also plotted in Figure 2.8 to show that the results are similar over the whole velocity range.

It is concluded that *outside the cone of silence* the most significant error incurred by using the high-frequency or geometric acoustic solutions is that due to non-geometric acoustic or finite wavelength effects in the basic Green function solution to Lilley's equation. The high-frequency modeling of noncompactness effects and the uniform flow assumption do not appear to be serious sources of error.

Thus, the detailed evaluation of the ratio of numeric and high-frequency solutions, f/f_∞, described earlier in Section 2.1.3 and shown in Figures 2.2 through 2.7 was carried out with the ring source model (the model used in previous work [2.2]).

	$\theta_s = 0°$		$\theta_s = 30°$		$\theta_s = 60°$	
V_J/a_o	Dist.	Ring	Dist.	Ring	Dist.	Ring
0.25	2.27	2.66	1.87	2.17	0.80	0.89
0.5	2.68	3.11	2.32	2.67	0.98	1.06
0.75	2.85	3.34	2.57	2.92	1.08	1.09
1.0	3.00	3.34	2.74	3.07	1.17	1.09
1.25	3.16	3.45	2.89	3.20	1.25	1.07
1.50	3.36	3.58	3.04	3.31	1.33	1.04
1.75	3.58	3.73	3.20	3.43	1.41	1.00
2.00	3.82	3.92	3.42	3.59	1.52	0.99

Table 2.5 Ratio of numerical and high-frequency Lilley equation solutions (dB) for radially distributed and ring sources.

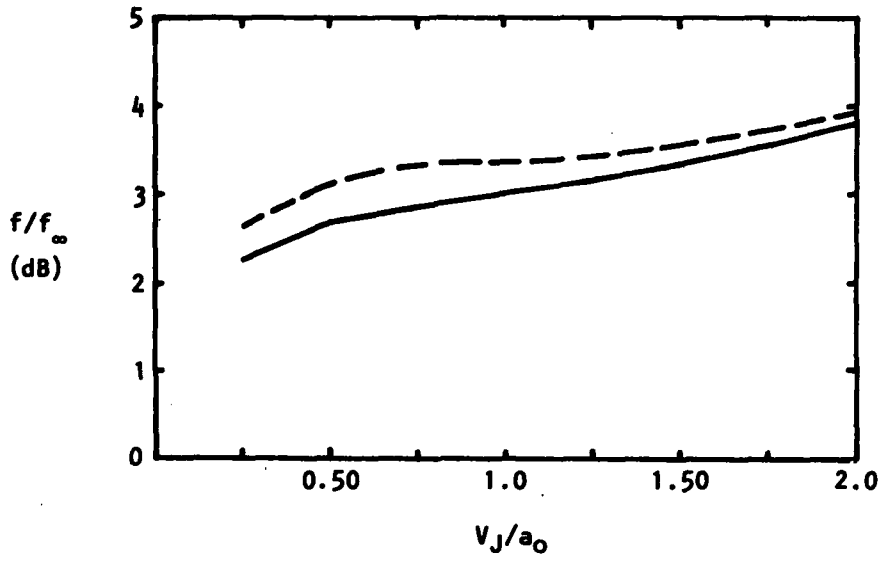

Figure 2.8 Ratio of Numeric and High-Frequency Lilley Equation Solutions on the Cone of Silence Boundary ($\theta_s = 0$) for Isotropic Quadrupole Source Model. Flow/Source Parameters as for Table 2.4; $S_m = 1.0$. Code: —— Radially Distributed; ---- Ring Source.

2.1.5.2 Comparison of high-frequency and numerical solutions to Lilley's equation *inside* the cone of silence

It has been possible to evaluate only a limited number of comparisons between numerical and high-frequency Lilley equation solutions inside the cone of silence, partly because computation time becomes rather excessive, especially if a critical layer (i.e. Mach angle) exists. Some of these comparisons are presented in Section 2.5.3. However, two striking features of the results are that (1) unlike those obtained earlier with the displacement source, the effects of radially distributed *versus* ring source solutions are somewhat less significant with the present source model and (2) the radial noncompactness factor assumed in the high-frequency analysis†, viz. $\exp[-k_o^2\kappa_s^2 L_t^2/8\pi]$, does *not* appear to be quite correct, in that inside the cone of silence ($\kappa_s^2 < 0$) the *modulus* of κ_s^2 should be utilized. Some numerical results with and without the modulus sign have demonstrated this quite clearly for subsonic Mach number jets. Thus, it would be desirable to repeat our high-frequency analysis with this change incorporated in the D_m factor, i.e.

$$D_m = \left| (1 - M_c\cos\theta_o)^2 + \left(\frac{L_x}{\tau_o a_o}\right)^2 \frac{1}{\pi}\cos^2\theta_o + \left(\frac{L_t}{\tau_o a_o}\right)^2 \frac{1}{\pi}\,|\kappa_s^2| \right|^{\frac{1}{2}} \qquad (2\text{-}100)$$

as well as with the shear noise components mentioned in Sections 2.1.3 and 2.1.6.

2.1.6 Comparison of Numerical and High-Frequency Lilley Equation Solutions with Measured Data

The detailed comparison described in Section 2.1.3 between numerical and high-frequency solutions is extended here to the general case of angles both outside and inside the cone of silence and to comparisons with *measured* data. The high-frequency solutions presented here correspond to the prediction method defined in Section 2.5.1 while the numerical solutions correspond to the method defined in Section 2.5.3.1 with $C_q = 0$ (isotropic ring-source model). The first set of comparisons in Figure 2.9 refer to a modified Strouhal number of unity and cover the isothermal velocity range in the Lockheed mixing noise test data [2.14]. Flow parameter details are given in Table 2.6.

---

†*Or rather indirectly assumed via the wavenumber scaling law assumption and modified Doppler factor.*

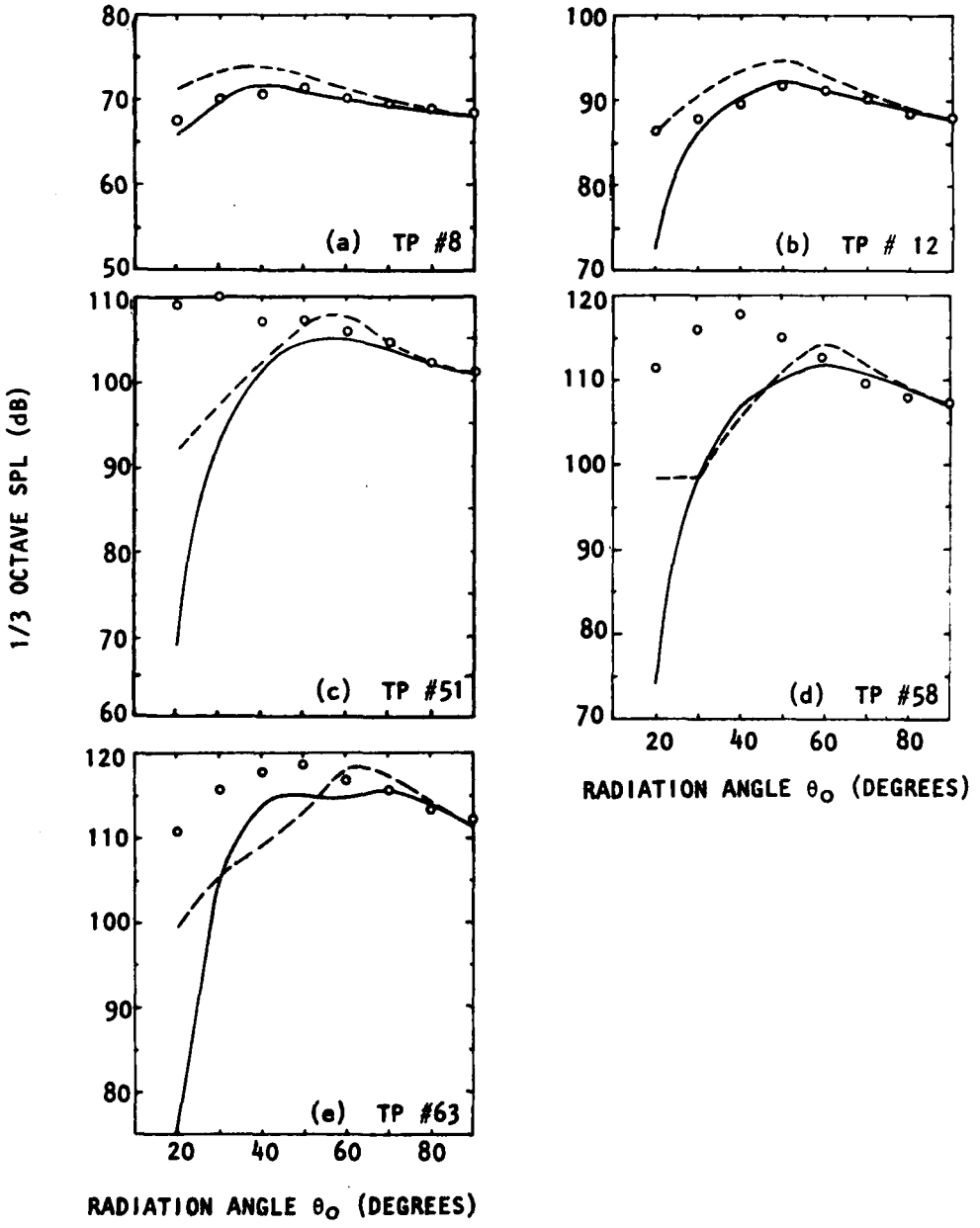

Figure 2.9 Comparison of Numeric (— — —) and High-Frequency Solutions (——) With Lockheed Isothermal Mixing Noise Data (O) for $S_m = 1$. (Jet Exit Conditions are given in Table 2.6.)

Figure	TP	V_J/a_o	T_J/T_o
2.9a	8	0.501	0.978
2.9b	12	0.900	0.976
2.9c	51	1.334	0.941
2.9d	58	1.650	0.977
2.9e	63	1.950	0.988

Table 2.6 Jet exit conditions utilized for comparisons shown in Figure 2.9 ($S_m = 1$, $\delta_s/r_J = 1.05$)

The high-frequency solutions are reasonably accurate, being generally smaller in magnitude than the numerical solutions. The agreement between *measurements* and high-frequency solutions is better here, of course, because the source parameters, including the axial source location defined by δ_s/r_J, have been adjusted to match the data.

Underprediction by both types of solutions always occurs at small angles when $V_J/a_o > 1$ although for angles less than 30° the high-frequency approximation breaks down at all velocities.

The same kind of comparisons at a lower modified Strouhal number ($S_m = 0.1$) in Figure 2.10 for the two subsonic test points reveals quite a large discrepancy between the two solutions, as might be expected from the comparisons presented in Section 2.1.3. In Figure 2.10, the same δ_s/r_J value is used for each solution ($\delta_s/r_J = 1.43$), whereas in Figure 2.11 a different value is used for the numerical solution ($\delta_s/r_J = 2.81$) which corresponds to a value implied by far-field source location data. Here the agreement between the solutions is excellent suggesting, indirectly, that the acoustic data *does* imply a realistic δ_s/r_J value but the high-frequency approximation without the shear-noise source terms leads to incorrect inferred values.

2.2 FAR-FIELD AZIMUTHAL MODE DETECTION RESULTS

The theoretical jet noise model described in previous sections is based upon solutions to the Lilley equation which must be obtained for each azimuthal (circumferential) mode number $n = 0, \pm 1, \pm 2, \ldots N_{max}$. The resulting solution for the far-field radiation is expressed in terms of an incoherent sum of contributions from each mode; the incoherency follows from the fact that the turbulence and hence the far-field radiation is (statistically) axisymmetric.† One way to check the validity of the theoretical model is to transform far-field cross-correlation measurements and obtain the azimuthal spectrum for comparison with the corresponding calculated spectrum. In this case the far-field acoustic pressure cross-correlation is required

†*This was checked out experimentally in the tests described below.*

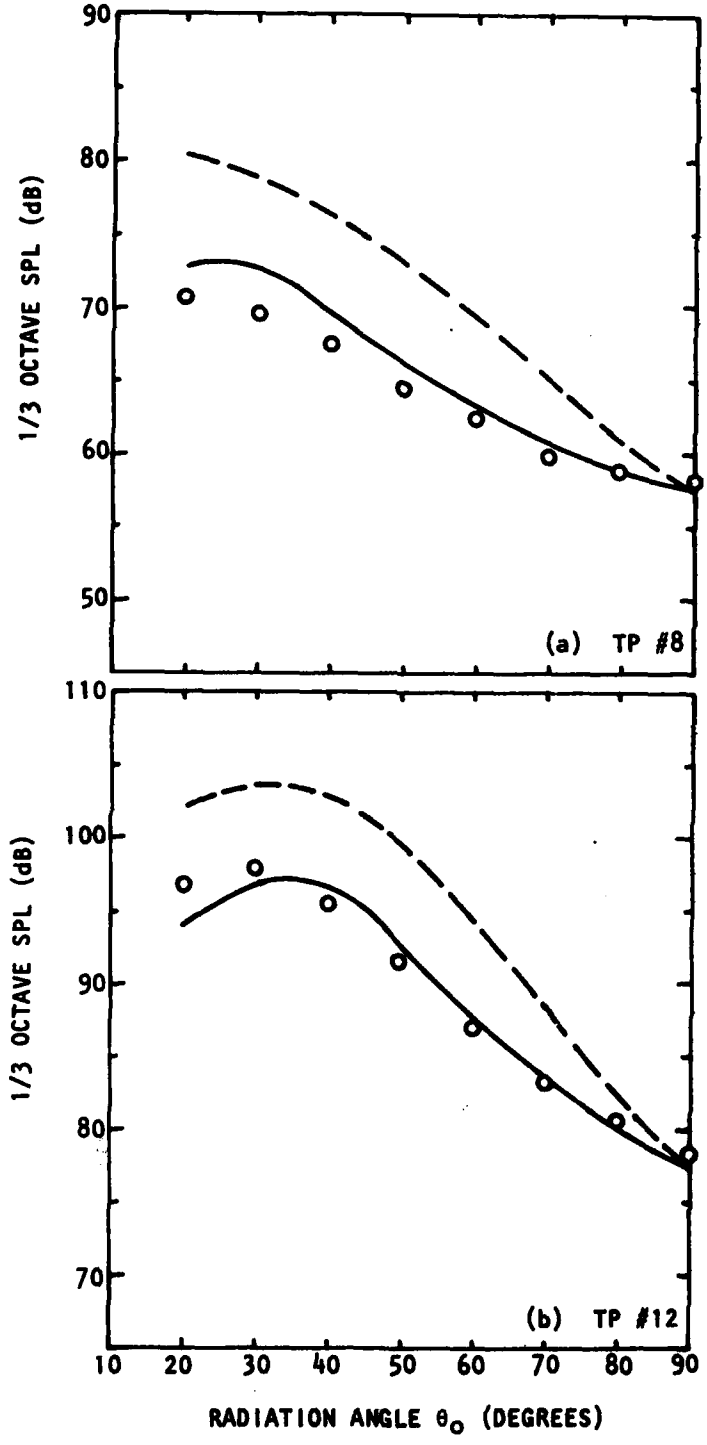

Figure 2.10 Comparison of Numeric (– – –) and High Frequency Solutions (———) with Lockheed Isothermal Mixing Noise Data (O) for $S_m = 0.1$; $\delta_s/r_J = 1.43$ (Jet Exit Conditions are given in Table 2.6.)

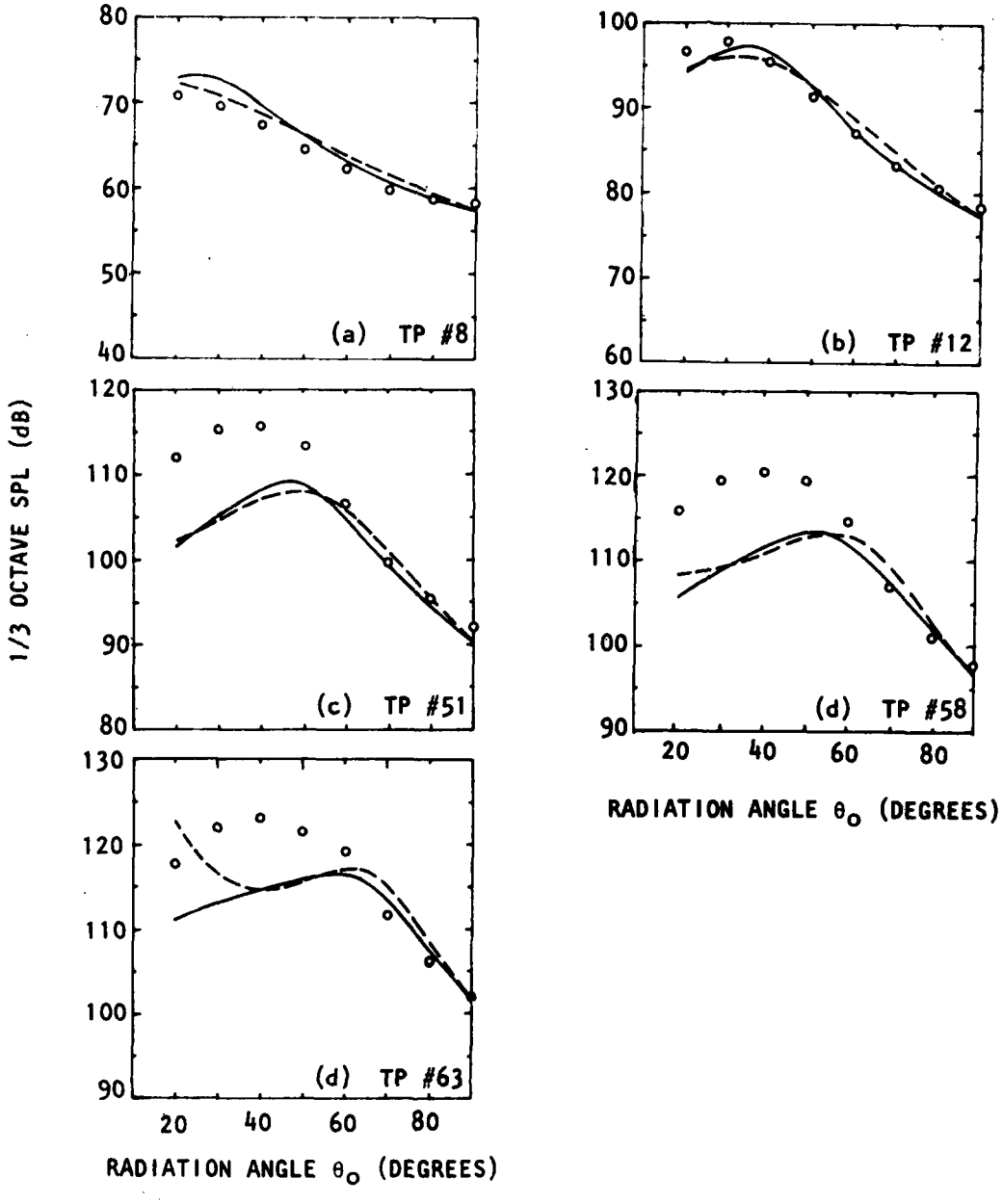

Figure 2.11 Comparison of Numeric (– – –) and High-Frequency Solutions (———) with Lockheed Isothermal Mixing Noise Data (0) for $S_m = 0.1$; $\delta_s/r_J = 2.81$ and 1.43 Respectively, in Calculated Results. (Jet Exit Conditions are given in Table 2.6.)

as a function of temporal (τ) and azimuthal ($\Delta\phi$) separation but with zero radial and polar angle separation. The Fourier transforms are with respect to the time delay τ and azimuthal separation $\Delta\phi$, yielding an azimuthal spectrum at any desired frequency. In practice, the time delay transform yields a coherence spectrum, $\gamma^2(f)$, for each pair of azimuthally separated measurement points and the variation of $\sqrt{\gamma^2(f)}$, at a given frequency, with azimuthal separation, $\Delta\phi$, when transformed with respect to $\Delta\phi$, yields the discrete azimuthal spectrum.

Measurements were conducted at seven different jet exit conditions corresponding to selected test points in the Lockheed mixing noise test point matrix [2.14], as defined in Table 2.7 below.

TP #	V_J/a_o	T_J/T_o	
36	0.9	2.27	CONVERGENT NOZZLE
39	1.47	2.27	
51	1.37	1.0	
52	1.47	1.15	
53	1.62	1.40	CON-DIV
54	1.84	1.80	MACH 1.4 NOZZLE
55	2.06	2.27	

Table 2.7 Jet exit conditions for azimuthal mode detection experiments.

Eleven microphones were used in three separate configurations corresponding to a semi-circular azimuthal array at the polar angles† $\theta_m = 22\frac{1}{2}°$, 45°, and 90° ($R_m$ = 72, 32, and 21 jet diameters, respectively). The microphones were equally spaced at an azimuthal angular interval of $22\frac{1}{2}°$ (that is, one reference microphone and 8 microphones equally spaced out), plus two extra microphones located at $11\frac{1}{4}°$ and $33\frac{3}{4}°$ from the reference microphone (a "shaded microphone array"). Calculated azimuthal spectrum shapes had already indicated that the amplitude of the azimuthal mode of order eight *should* be insignificant relative to that of the plane mode at most conditions of interest and hence, eight equally spaced microphones were judged sufficient to avoid aliasing problems. However, the equal microphone spacing angle was effectively reduced to $11\frac{1}{4}°$ (so N_{max} = 16) by using data from the two microphones and by *estimating* data at the remaining points ($56\frac{1}{4}°$ [$22\frac{1}{2}°$] $168\frac{3}{4}°$) through linear interpolation of the measured data at adjacent points.

The measured data were analyzed in detail at only one test condition (TP #51) and for two polar angles θ_m = 45° and 90°. The *lack* of agreement described below between the measured and calculated spectrum shapes does not warrant analysis of data at other test conditions, since that also involves

†*Origin centered at the nozzle exit plane.*

the complication of the additional source (which is significant at non-isothermal exit conditions). The smallest polar angle was excluded since the Lilley equation solutions for the small-scale mixing noise source do not agree with measured data at small angles for supersonic ($V_J/a_o > 1$) conditions.

Some typical coherence spectra are shown in Figures 2.12 and 2.13. Three frequencies were selected for transformation corresponding to the Strouhal numbers $S = 0.113$, 0.339 and 1.13 (where $S = fd/V_J$). The azimuthal spectra (in dB referenced to the plane mode level) at each frequency for $\theta_m = 90°$ are shown in Figures 2.14 through 2.16 and in Figures 2.17 through 2.19 for $\theta_m = 45°$. The calculated spectra shown in each figure were obtained with the parameter values given in Table 2.8. The lack of agreement between measured and calculated spectrum shapes cannot be explained at this time. It is recommended that this be the subject of further investigation since the Lilley equation solutions are now widely used in aeroacoustic calculations (either in approximate or numerical form) and the validity of these solutions should be confirmed experimentally in this fundamental respect.

S	V_{max}/a_o	T_J/T_o	$\gamma = C_p/C_v$	δ_s/r_J	η_{hw}	V_s/V_{max}
0.113	0.667	1.015	1.4	2.818	0.1	0.500
0.339	1.201	1.000	1.4	1.970	0.1	0.663
1.13	1.334	0.941	1.4	1.050	0.1	0.663

Table 2.8 Parameters for Lilley equation solutions (zero radial-azimuthal coherence, radially distributed source, $\eta_{hw} = 0.1$) corresponding to TP #51.

2.3 AXIAL SOURCE DISTRIBUTION MEASUREMENTS BY THE POLAR CORRELATION TECHNIQUE

The basic philosophy of our jet noise research programs has been to obtain detailed measurements of (a) the mean and turbulent structure of the jet flow with the laser velocimeter and (b) the amplitude and directivity of the radiated far-field noise spectra and to link these theoretically with solutions to the Lilley equation. In the present program the acoustic far-field experiments have been extended from single-point to two-point measurements. The objective was to provide more detailed evidence that the link between the cause and effect (turbulence→noise) *is* understood, that the Lilley equation (or the Lighthill analogy in the special case of radiation normal to the jet axis from a true isothermal jet) *does* describe the relation between the turbulence structure and radiated noise with a reasonable degree of accuracy.

In the previous section, two-point, far-field measurements with azimuthal separation were used to infer the azimuthal spectrum for comparison with that calculated from the Lilley equation. Here, we consider far-field measurements at *zero* azimuthal separation (and zero separation in polar radius) but variable polar angle separation and processing of these measured data by the

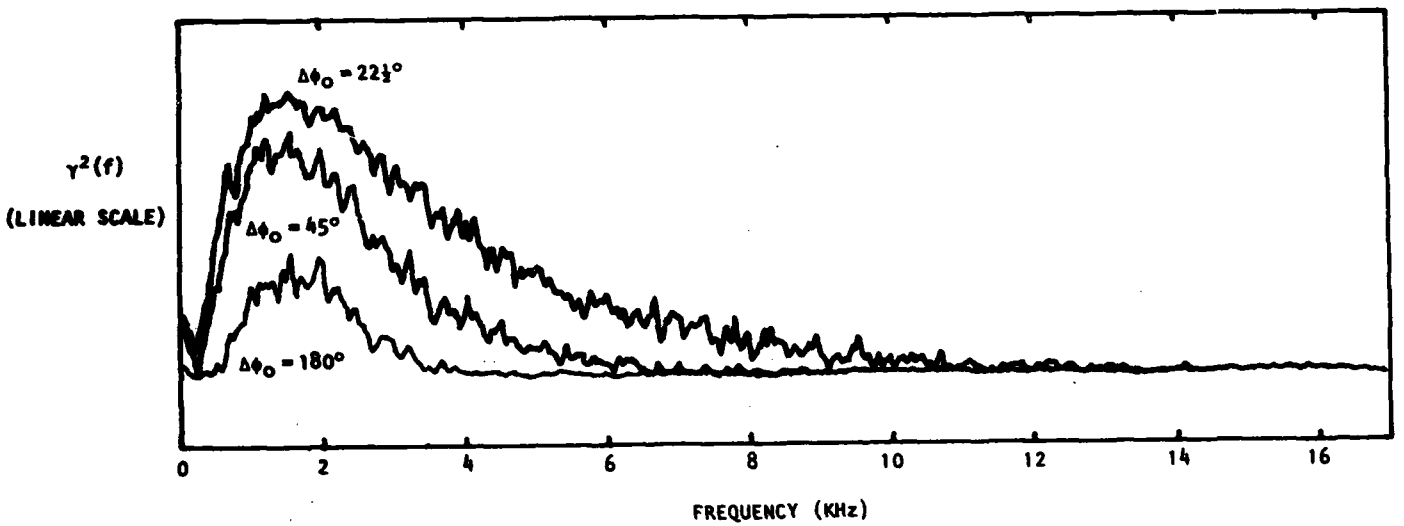

Figure 2.12 Measured Far-Field Coherence Spectrum at three Azimuthal Separations; TP #51, Polar Angle $\theta_m = 45°$.

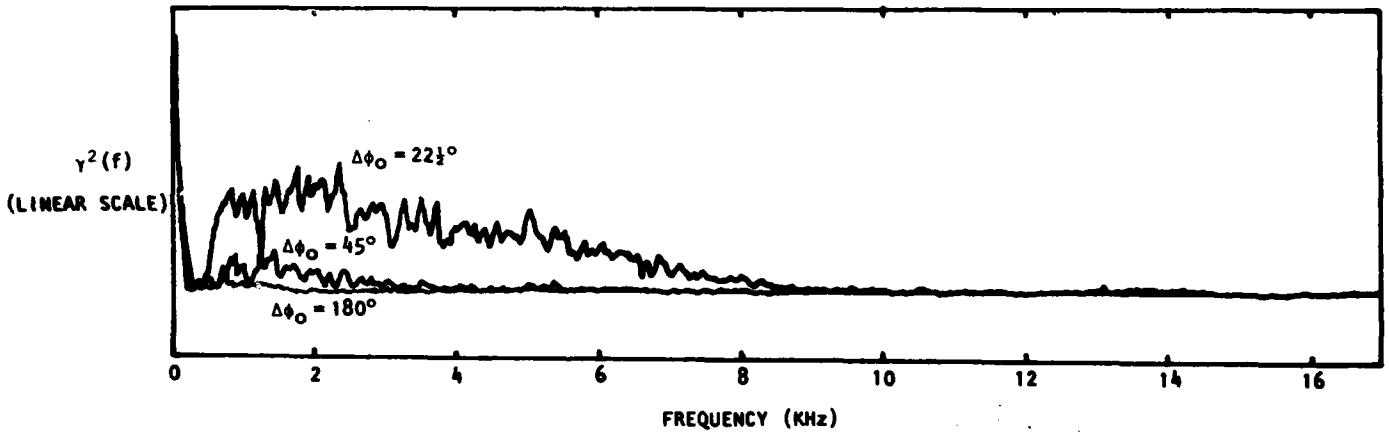

Figure 2.13 Measured Far-Field Coherence Spectrum at Three Azimuthal Separations; TP #51, Polar Angle $\theta_m = 90°$.

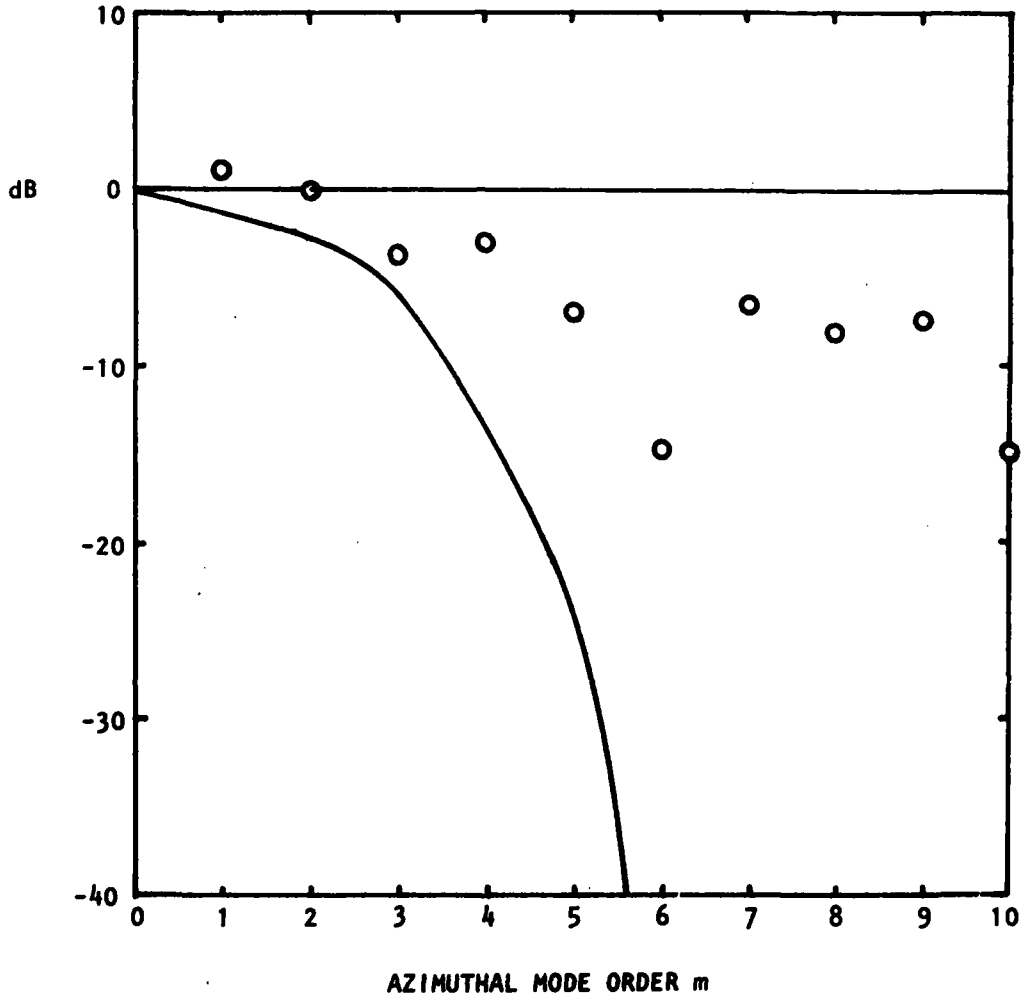

Figure 2.14 Comparison of Measured (O) and Calculated (——) Spectra, TP #51; θ_m, $\theta_o = 90°$, $S = 0.113$. (Calculation Parameters are given in Table 2.8.)

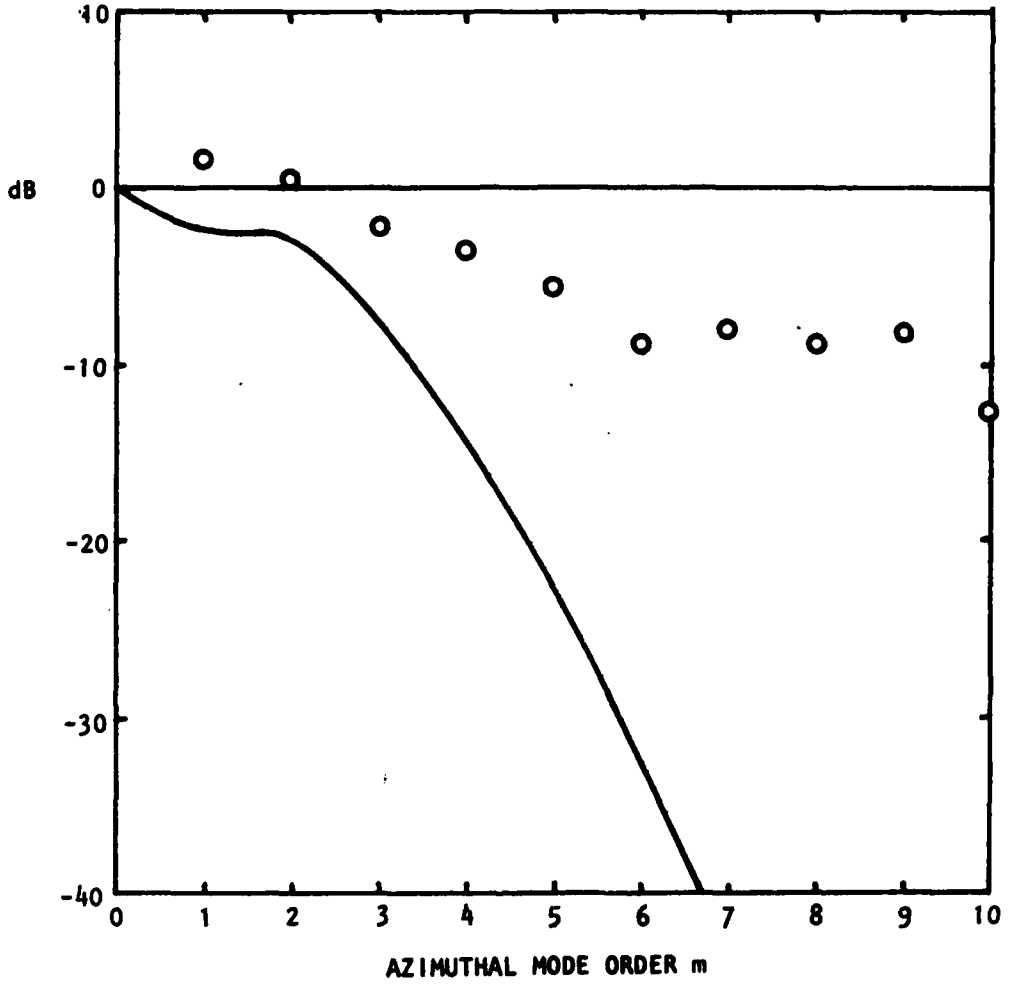

Figure 2.15 Comparison of Measured (O) and Calculated (——) Spectra, TP #51; θ_m, $\theta_o = 90°$, S = 0.339. (Calculation Parameters are given in Table 2.8.)

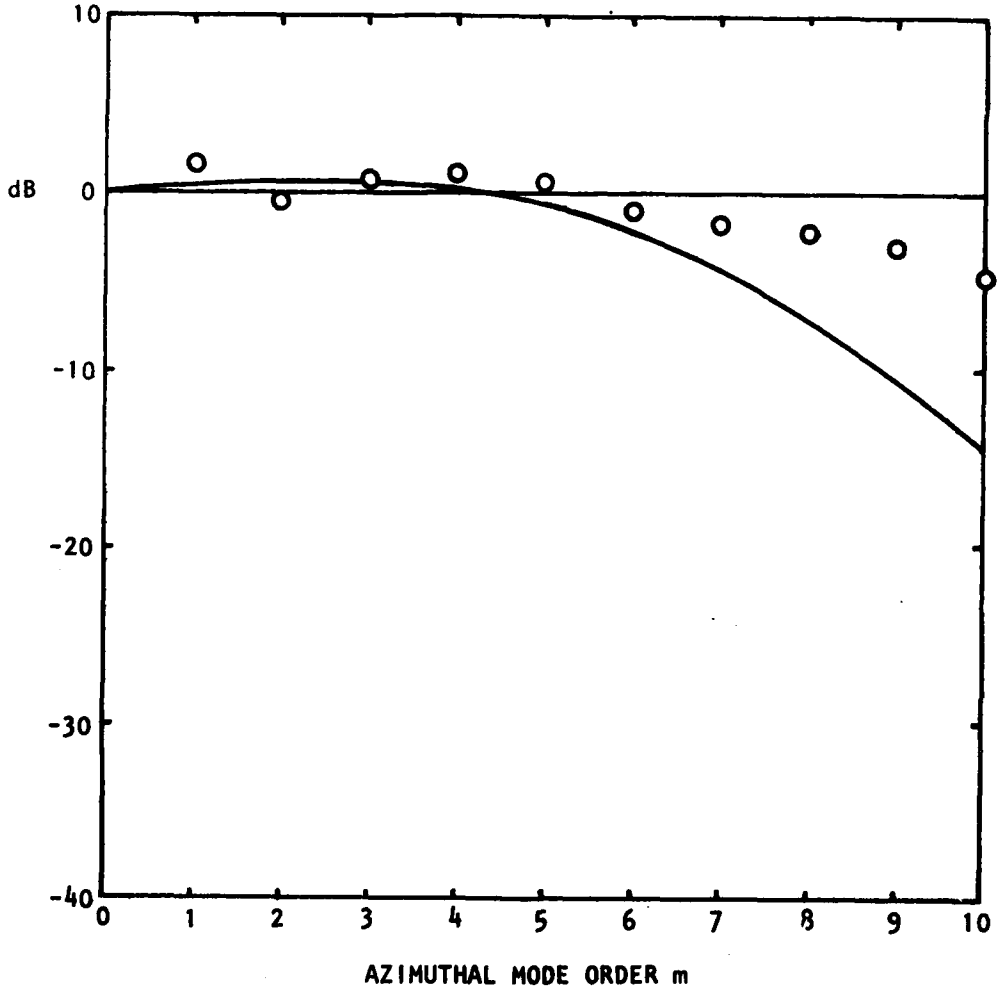

Figure 2.16 Comparison of Measured (O) and Calculated (——) Spectra, TP #51; θ_m, $\theta_o = 90°$, $S = 1.13$. (Calculated Parameters are given in Table 2.8.)

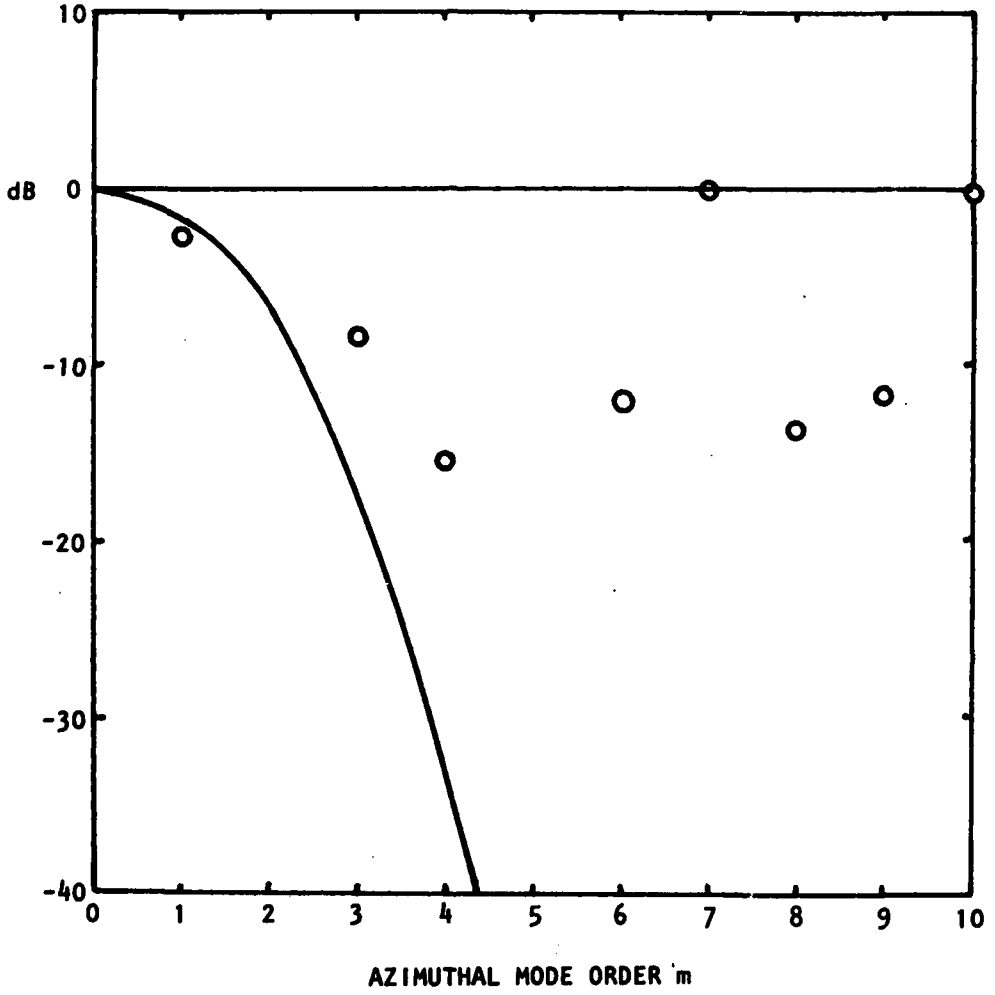

Figure 2.17 Comparison of Measured (O) and Calculated (——) Spectra, TP #51; θ_m, $\theta_o = 45°$, $S = 0.113$. (Calculation Parameters are given in Table 2.8.)

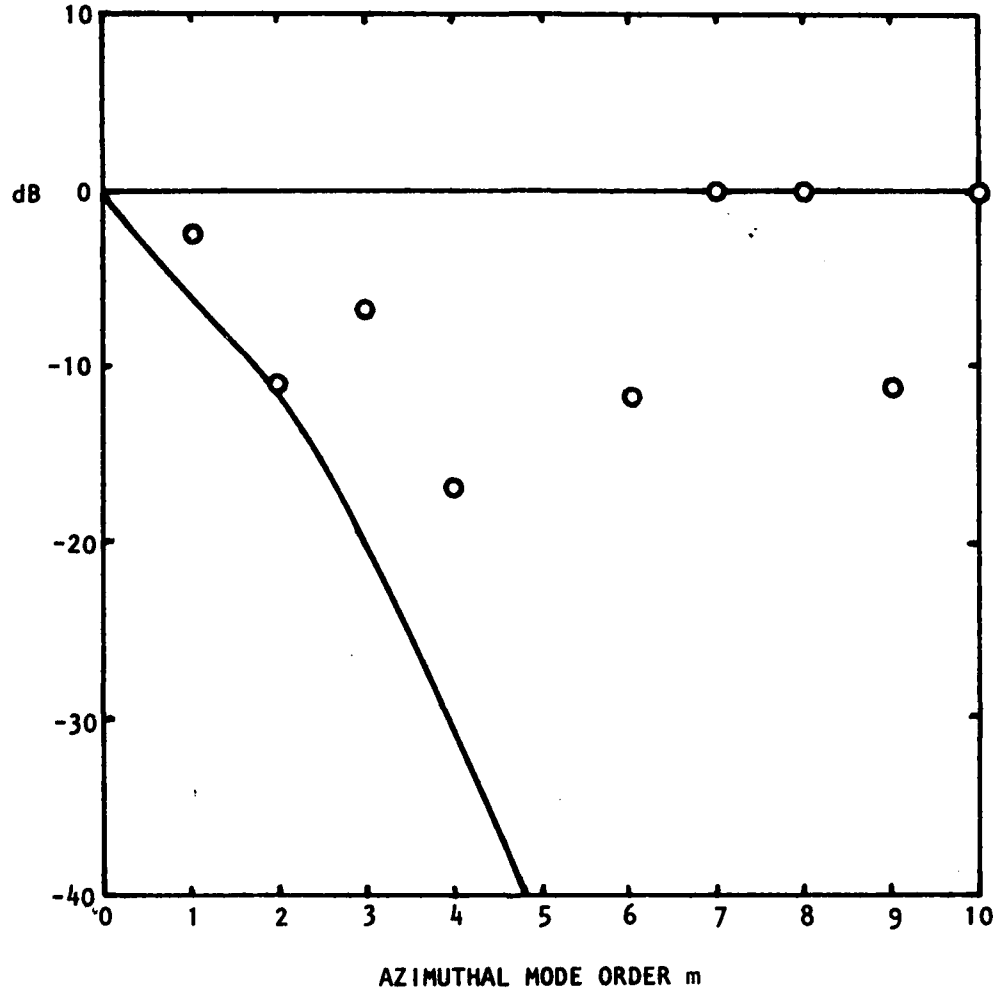

Figure 2.18 Comparison of Measured (O) and Calculated (——) Spectra, TP #51; θ_m, $\theta_o = 45°$, $S = 0.339$. (Calculation Parameters are given in Table 2.8.)

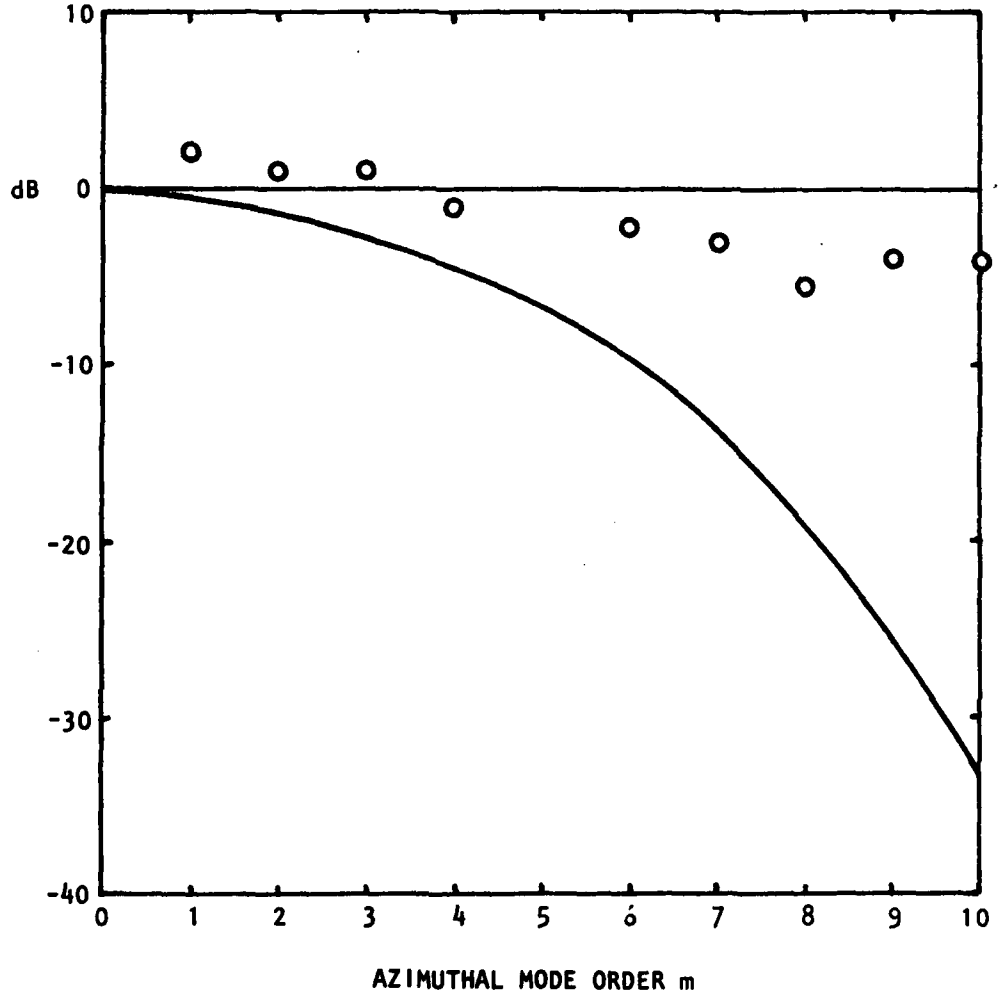

Figure 2.19 Comparison of Measured (O) and Calculated (——) Spectra, TP #51; θ_m, $\theta_o = 45°$, $S = 0.113$. (Calculation Parameters are given in Table 2.8.)

"Polar Correlation Technique." This technique has been fully described by Fisher et al. [2.15] who have shown that the measured correlation or cross-power spectral density can be transformed to yield a "diffraction limited image" of the "source strength per unit axial slice" of the jet, or in other words, of the integrand that appears in expressions for the far-field radiated noise, for example, in Equation (2-48) (after integration with respect to r). The technique cannot, as yet, yield a radial source strength distribution nor, of course, can it separate out the quadrupole and dipole source contributions for hot jets, although a separation can be attempted (after processing) on the final results by comparing, for example, isothermal and hot jet axial source distributions of the same exit velocity.

This kind of experimental evidence (taken from earlier work by Laufer [2.16] and Grosche [2.17]) has already been used in the Lilley equation calculations: at a given frequency or Strouhal number, the axial location of the source distribution peak is used to define the mean velocity and temperature profiles for the Lilley equation, which strictly can only describe the effect of an infinite, parallel constant-profile shear layer on the radiation from multipole sources within that shear layer. This approach is judged to be adequate from the point of view of calculating acoustic-mean flow interaction effects; on the other hand, calculation of the (absolute) noise spectrum, as described in the following section, probably requires a more realistic distributed source model. In either case, the polar correlation technique offers a means of testing jet noise calculations at an intermediate stage between the cause - the turbulent flow, as measured by the laser velocimeter - and the effect, the measured far-field (single-point) acoustic data.

Four jet operating conditions were selected for the polar correlation test program as indicated in Table 2.9. Polar microphone arrays were arranged in two configurations, one with the reference microphone at the polar angle†, $\theta_m = 90°$ and one with $\theta_m = 22\frac{1}{2}°$. At the chosen frequencies (Table 2.9) the measured†† coherence function, $\gamma^2(f)$, and phase of the cross-power spectral density, $\phi(f)$, for each microphone pair are plotted as a function of microphone separation, α. After processing according to the theory given by Fisher et al. [2.15] (a discrete Fourier transform of $\{\sqrt{\gamma^2(f)}, \phi(f)\}$ with respect to $k_o \sin\alpha$), the axial source distributions are obtained at each frequency and can be displayed in the form shown in Figure 2.20a. (The distribution at a Strouhal number $S \triangleq 3$ has been omitted here and in the other cases to follow since the results are unsatisfactory at this frequency). The axial peak locations, x_{peak}/d, are reasonably consistent with those obtained from previously published results as indicated in Table 2.10, the exception being the result for $S = 1.0$. The results for the $22\frac{1}{2}°$ reference angle are shown in Figure 2.20b and the peak locations are also given in Table 2.10. At the highest Strouhal number, $S = 0.3$ ($S = 1.0$ is omitted) there is a clear shift of peak location towards the nozzle, but at the lower Strouhal numbers there is little change. These results, however, substantially agree with the

---

†*Origin centered at the nozzle exit plane.*
††*Constant bandwidth, 60 Hz.*

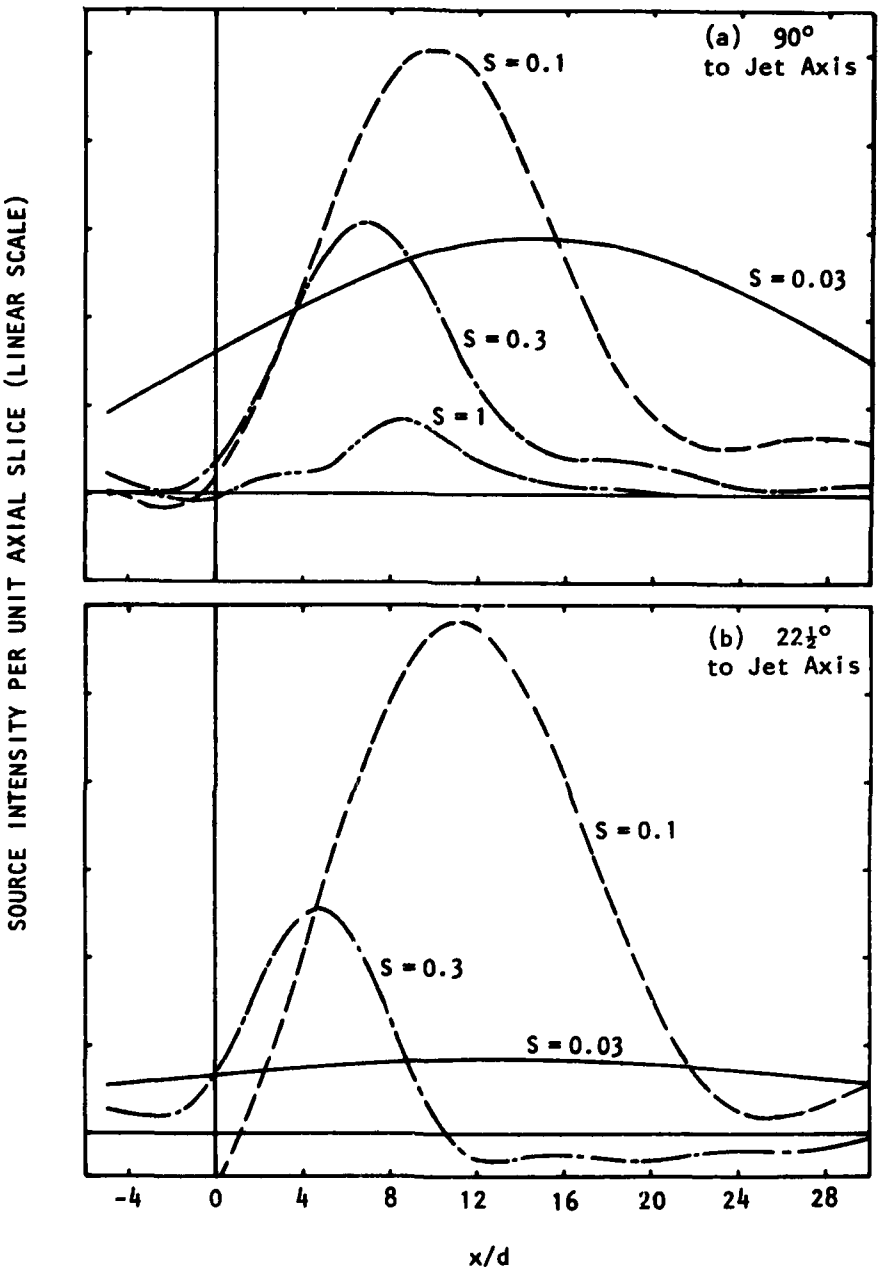

Figure 2.20 Axial Source Distribution Measured with the Polar Correlation Technique. TP #51.

Test Points	V_J/a_o	T_J/T_o	FREQUENCIES IN Hz				
			$S_1 = .03$	$S_2 = .1$	$S_3 = .3$	$S_4 = 1.0$	$S_5 = 3$
36	0.9	2.27	240	600	1860	6240	18840
39	1.47	2.27	300	1020	3060	10200	24000
51	1.37	1.00	300	960	2820	9360	24000
55	2.06	2.27	420	1440	4260	14280	24000

Table 2.9 Test conditions and selected frequencies for Polar Correlation analysis.

S	Laufer et al. [2.16]	Ref. Angle 90° Present Results	Ref. Angle 22½° Present Results
0.03	24	15	13
0.1	13	10	11
0.3	7½	7	4½
1.0	3½	8½	--

Table 2.10 Comparison of axial peak locations, x_{peak}/d, for TP ≠ 51 with previous results

Laufer [2.16] data which has been used in the prediction methods† in the form of an empirical curve fit

$$x_{peak}/d \equiv x_S/d = \{.021\ S^2 + 0.057\ S\}^{-\frac{1}{2}} \qquad (2\text{-}101)$$

as illustrated in Figure 2.21. This has been used in two ways: (1) to allow for source location effects directly (to define the true polar radius and radiation angle) and (2) to define the profiles for the Lilley equation solutions, assuming a relation between the profiles and the distance from the nozzle exit plane (see Appendix 2A).

The remaining polar correlation results given in this section refer largely to the hot-jet tests (TP nos. 36, 39 and 55) and have not been analyzed or related to the prediction model, mainly because there is the complication of separating out the quadrupole and dipole source contributions at each frequency. These figures are simply listed in Table 2.11.

†*There the Strouhal number S has been replaced by the modified Strouhal number, S_m, for the reasons discussed in Section 2.1.3.*

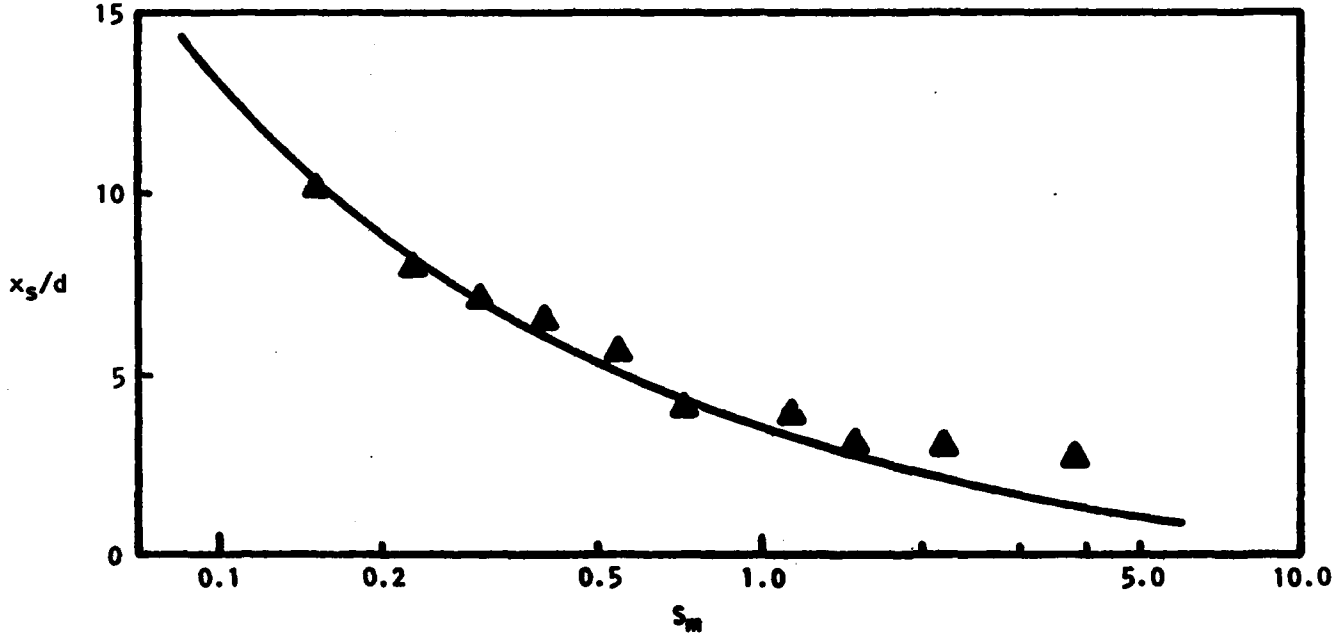

Figure 2.21 Axial Peak Location (▲) of Source Distributions Measured by Laufer et al [2.16]; ——, Empirical Line Used in Present Work [Equations (2-101), (2-115)].

Figure	TP#	Ref. Angle	Parameters
2.22	36	90°	S = .03, .1, .3, 1.0
2.23	39	↓	↓
2.24	55	↓	↓
2.25	36	22½°	S = .03, .1, 0.3
2.26	39	↓	↓
2.27	55	↓	↓
2.28	36,39,55	90°	S = .03, V_J/a_o = 0.9, 1.47, 2.06
2.29	↓	↓	S = .1
2.30	↓	↓	S = .3
2.31	↓	↓	S = 1.0
2.32	↓	22½°	S = .03
2.33	↓	↓	S = .1
2.34	↓	↓	S = .3
2.35	↓	↓	S = 1.0
2.36	39,51	90°	S = .03: T_J/T_o = 1.0, 2.27
2.37	↓	↓	S = .1
2.38	↓	↓	S = .3
2.39	↓	↓	S = 1.0
2.40	39,51	22½°	S = .03
2.41	↓	↓	S = .1
2.42	↓	↓	S = .3
2.43	↓	↓	S = 1.0

Table 2.11 Summary of axial source distribution results from Polar Correlation analysis

2.4 CALCULATION OF ABSOLUTE JET NOISE SPECTRUM LEVELS FROM LV MEAN FLOW AND TURBULENCE DATA (ISOTHERMAL JETS)

The calculation of the shape *and* level of the jet noise spectrum radiated in the direction normal to the jet axis ($\theta_o = 90°$) has been the subject of an investigation based upon the *Lighthill analogy* rather than upon the Lilley equation. The reason is that acoustic-mean flow interactions vanish at $\theta_o = 90°$ if the mean flow is *truly* isothermal (provided, of course, that it is a parallel sheared flow). Although, in practice, there are quite significant temperature variations *within the shear layer* of high-speed isothermal jets (i.e. when the static exit temperature equals the ambient temperature) these give rise to fairly small changes† from the Lighthill prediction and were judged to be unimportant at the present stage. To our knowledge, a successful prediction of absolute spectrum levels had not been achieved in the past and therefore acoustic-mean flow interactions effects could be included later as a fine tuning exercise *if* the Lighthill analogy proved to be approximately valid. The same argument was applied to transverse

†*Approximately 2 dB reduction when* $V_J/a_o \doteq 2$ *(TP# 63).*

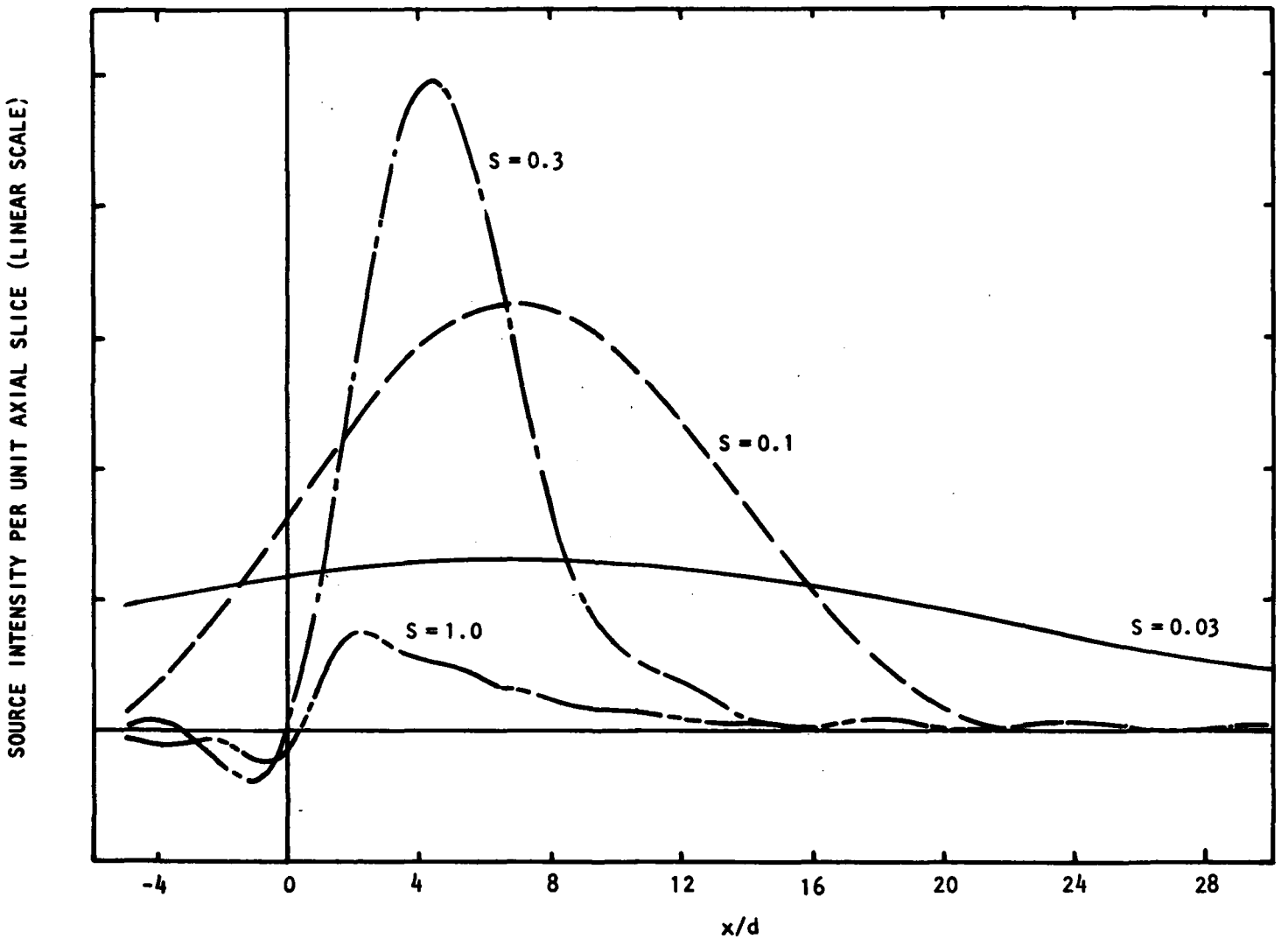

Figure 2.22 Axial source distributions measured with the polar correlation technique at 90° to the jet axis; TP #36.

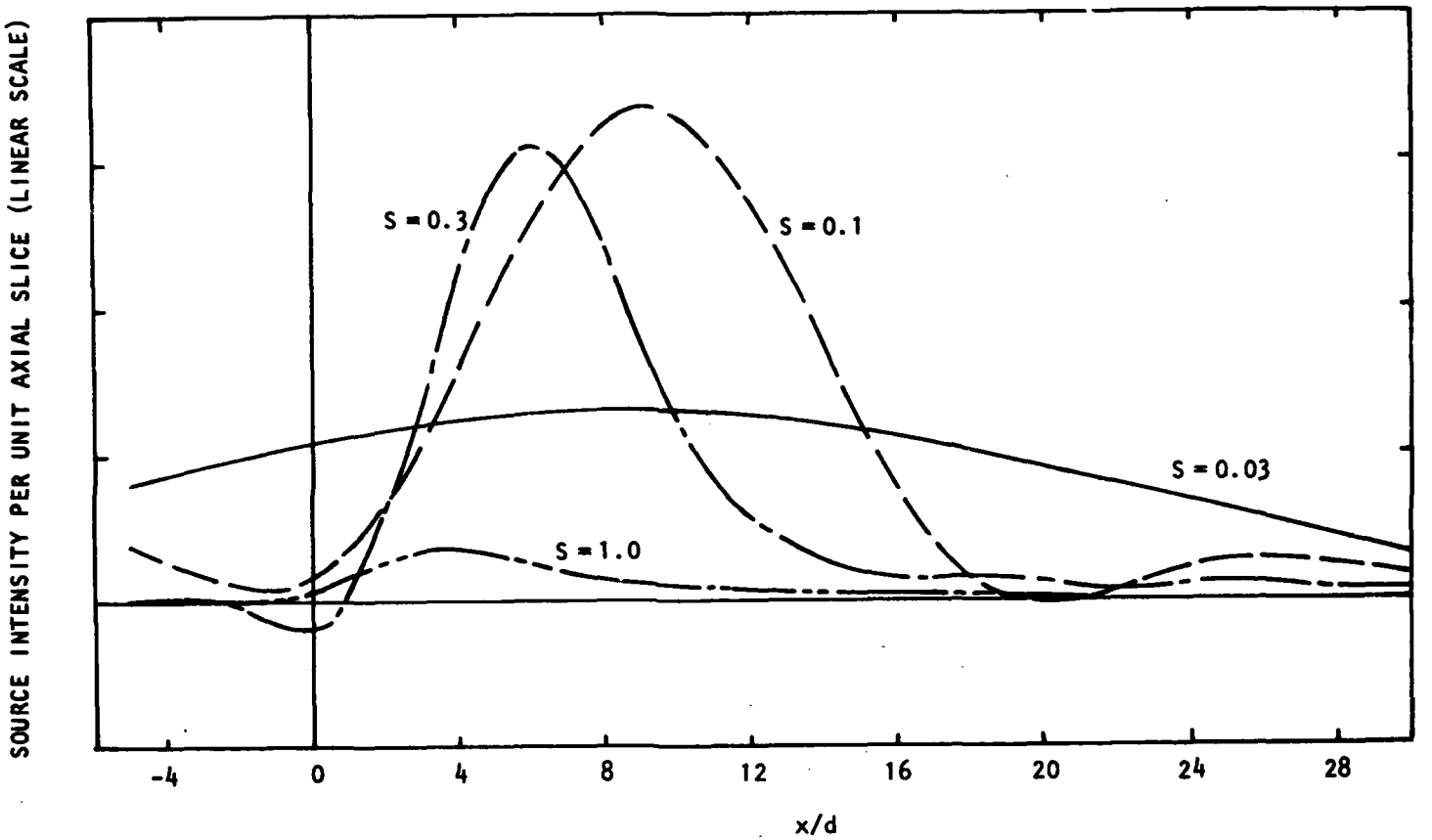

Figure 2.23 Axial source distributions measured with the polar correlation technique at 90° to the jet axis; TP #39.

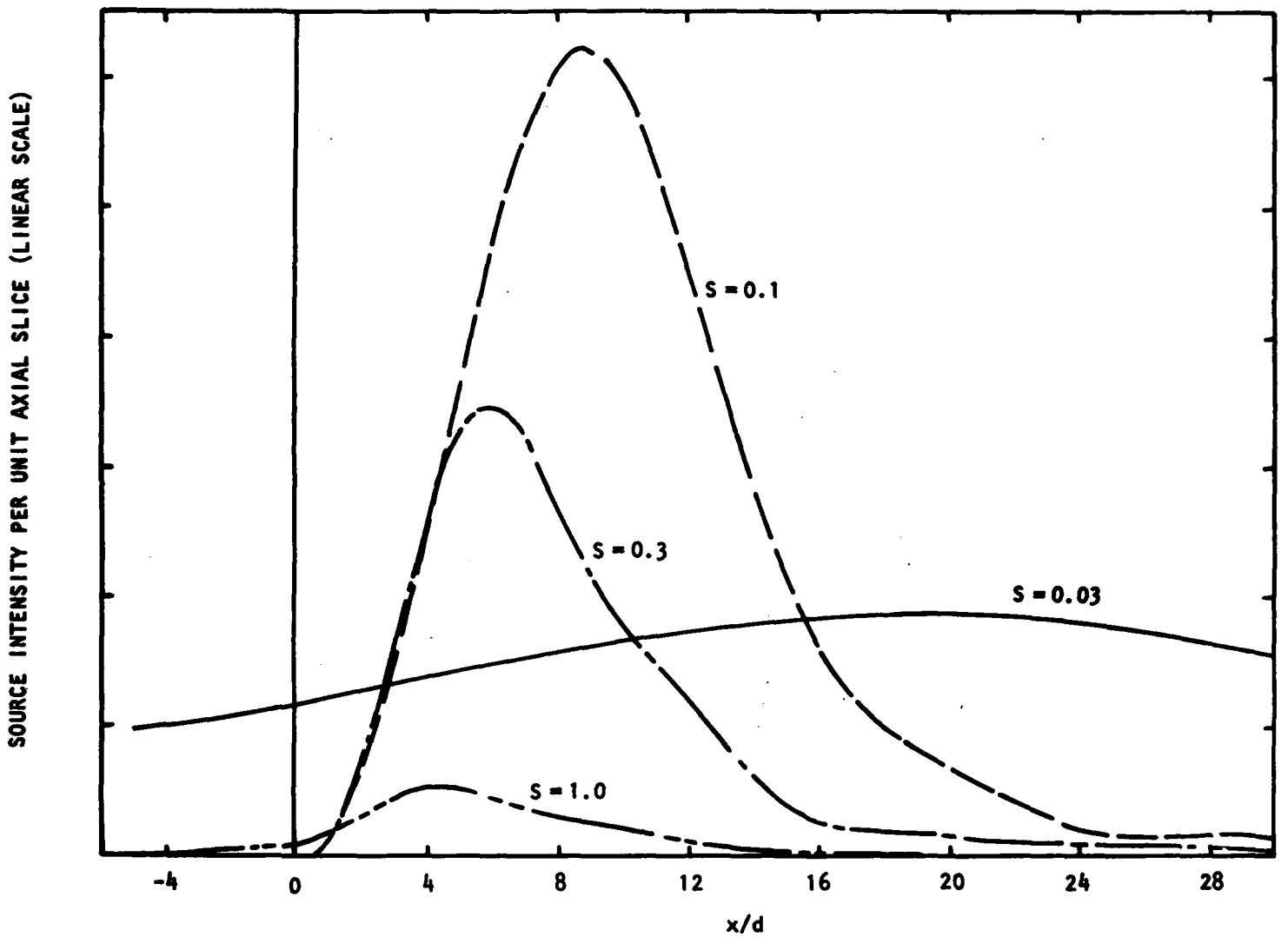

Figure 2.24 Axial source distributions measured with the polar correlation technique at 90° to the jet axis; TP #55.

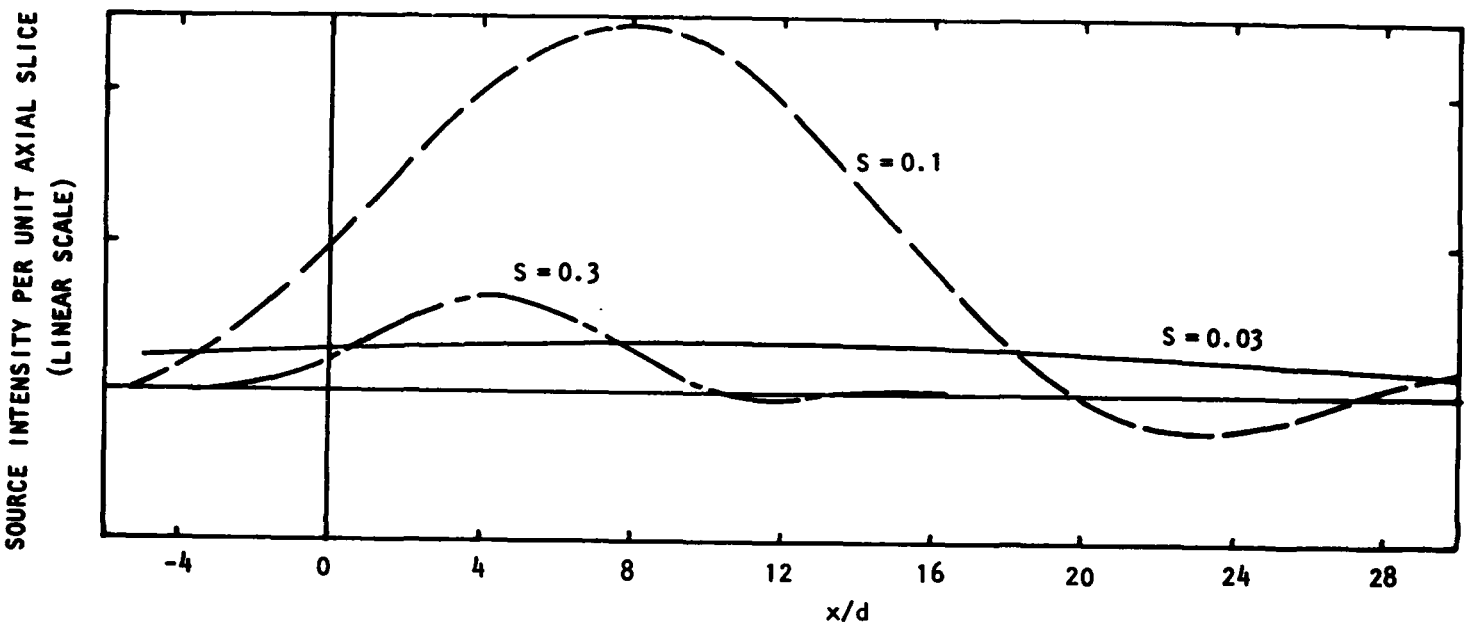

Figure 2.25 Axial source distributions measured with the polar correlation technique at 22½° to the jet axis, TP #36.

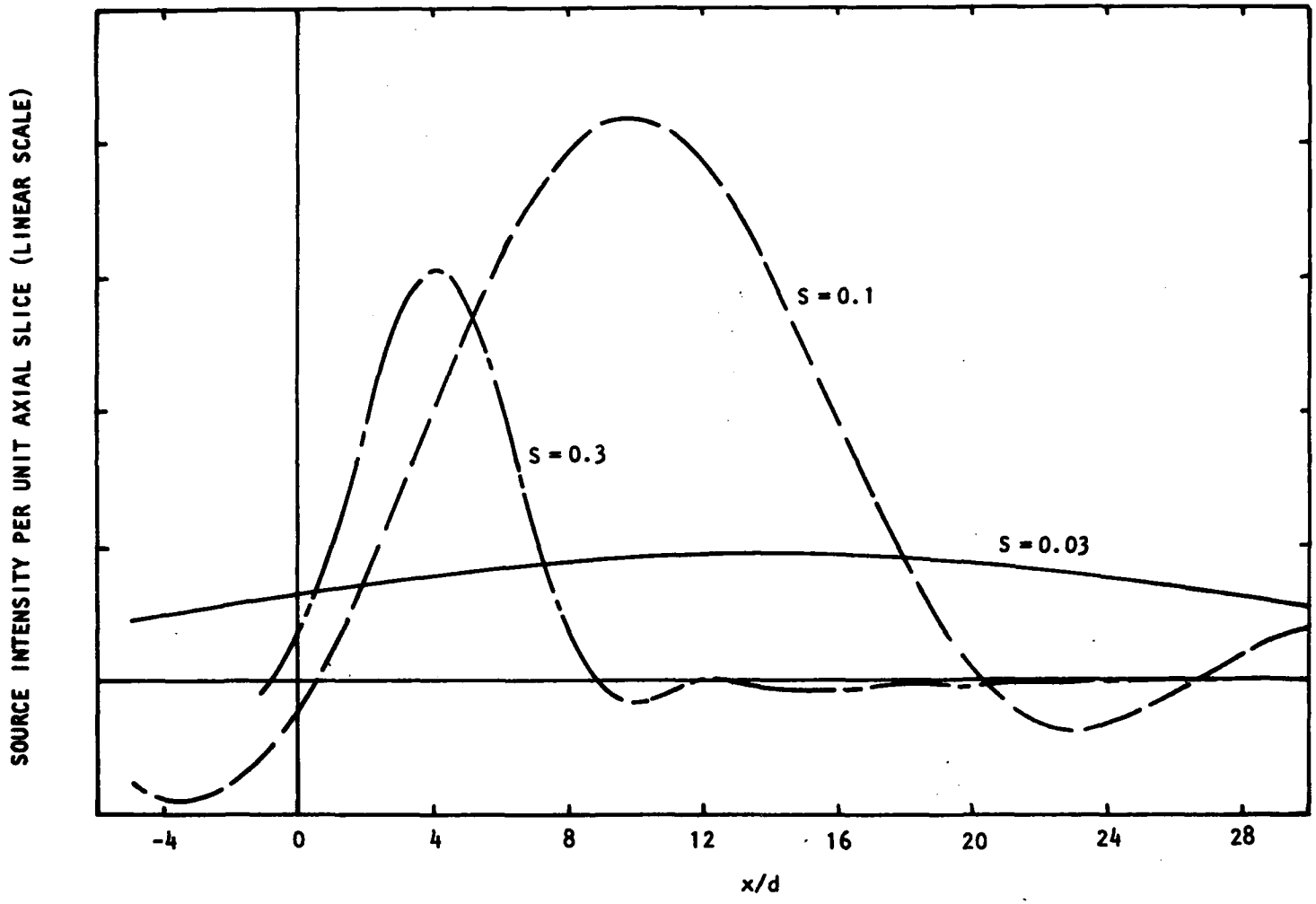

Figure 2.26 Axial source distributions measured with the polar correlation technique at 22½° to the jet axis, TP #39.

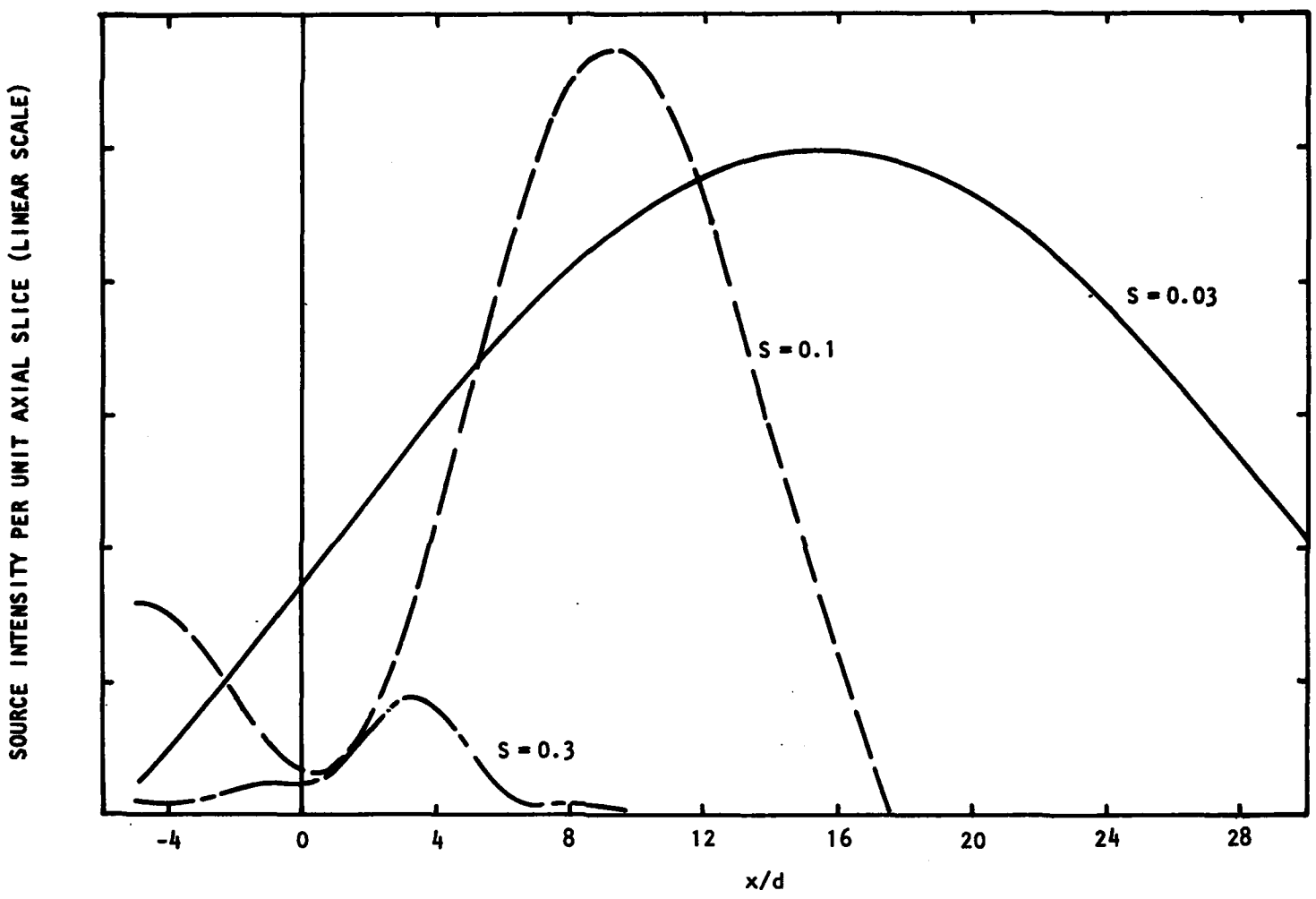

Figure 2.27 Axial source distributions measured with the polar correlation technique at 22½° to the jet axis; TP #55.

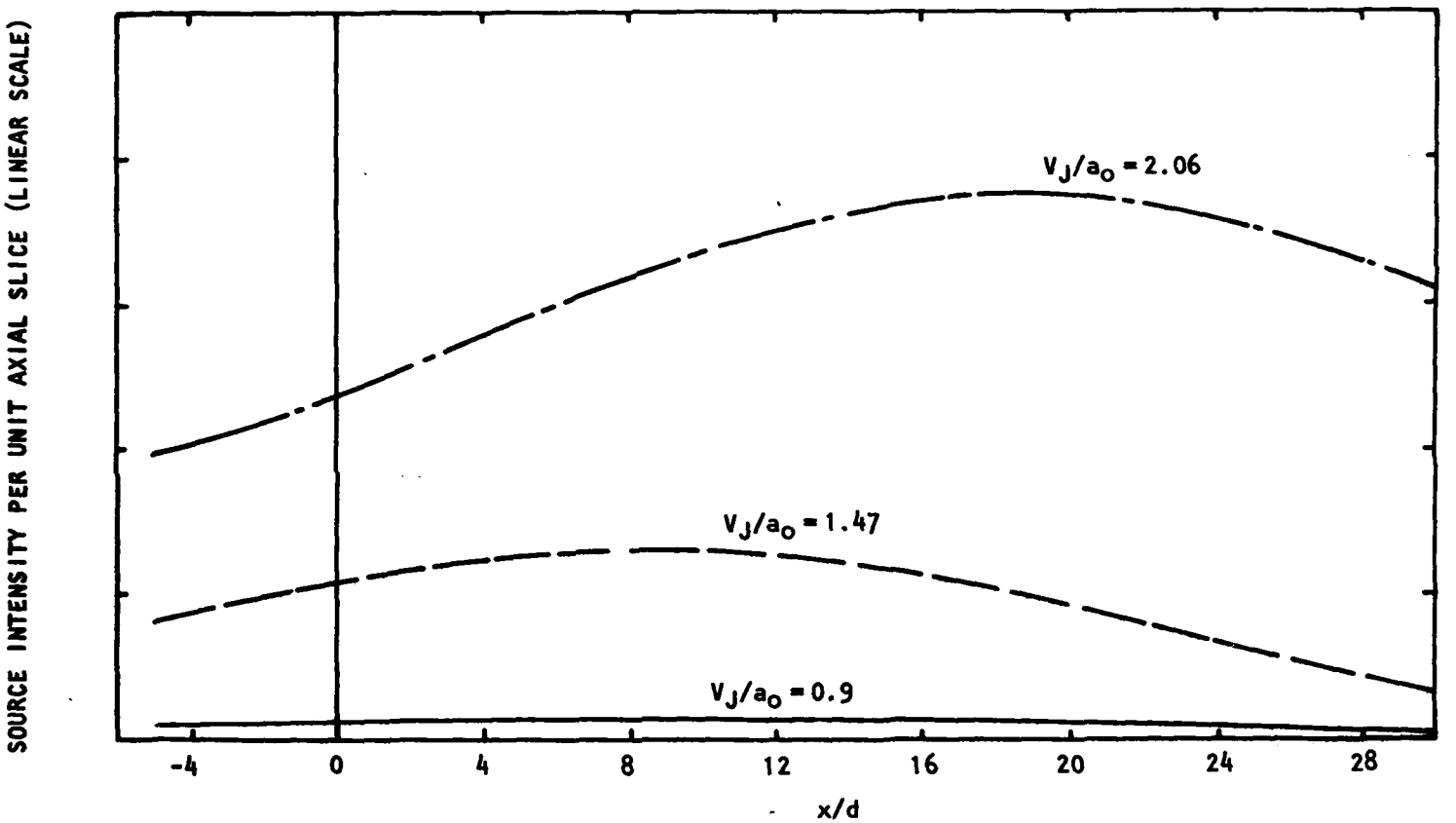

Figure 2:28 Axial source distributions measured with the polar correlation technique at 90° to the jet axis; S = 0.03; TP #36, 39, 55.

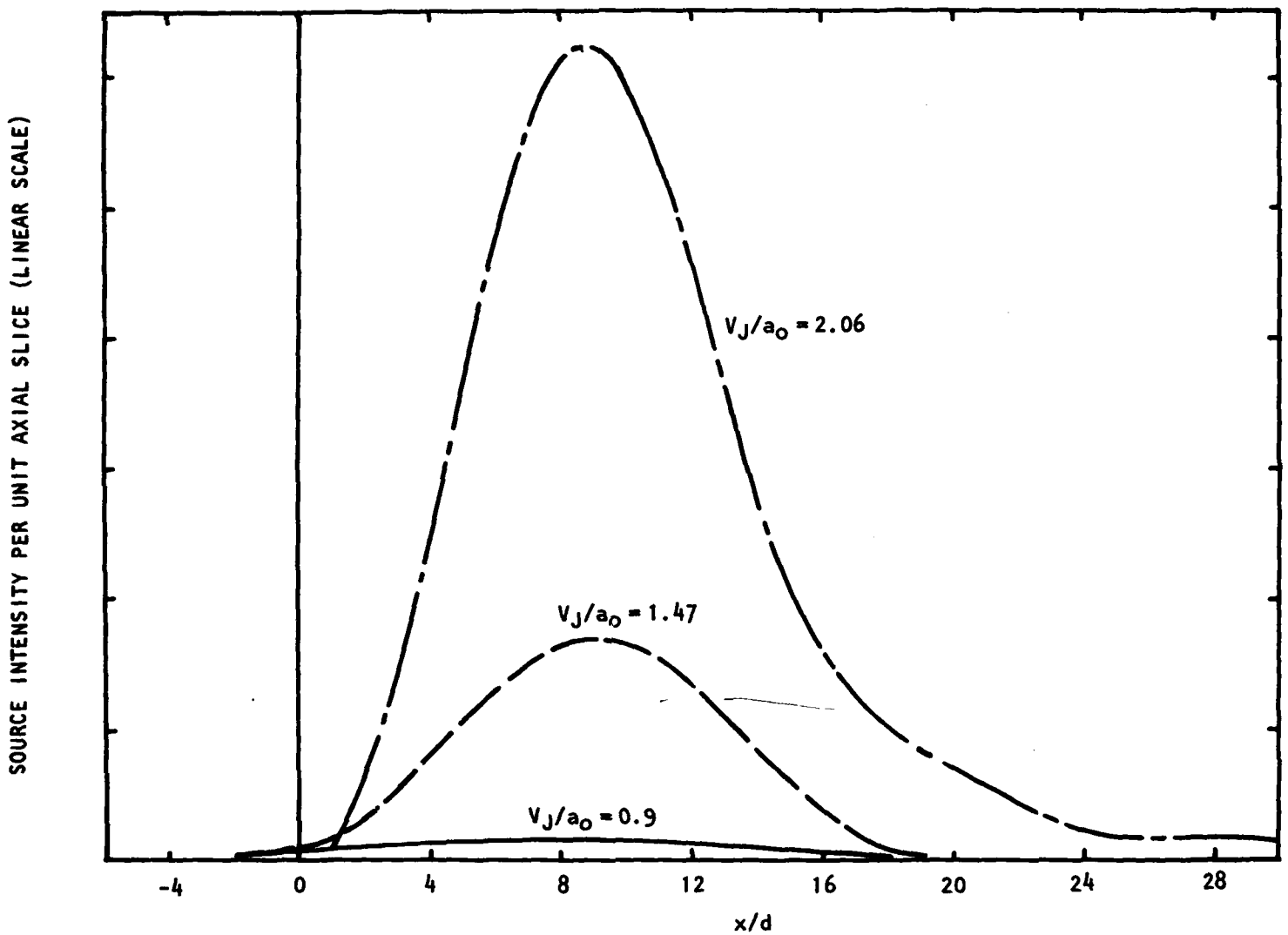

Figure 2.29 Axial source distributions measured with the polar correlation technique at 90° to the jet axis; S = 0.1, TP #36, 39, 55.

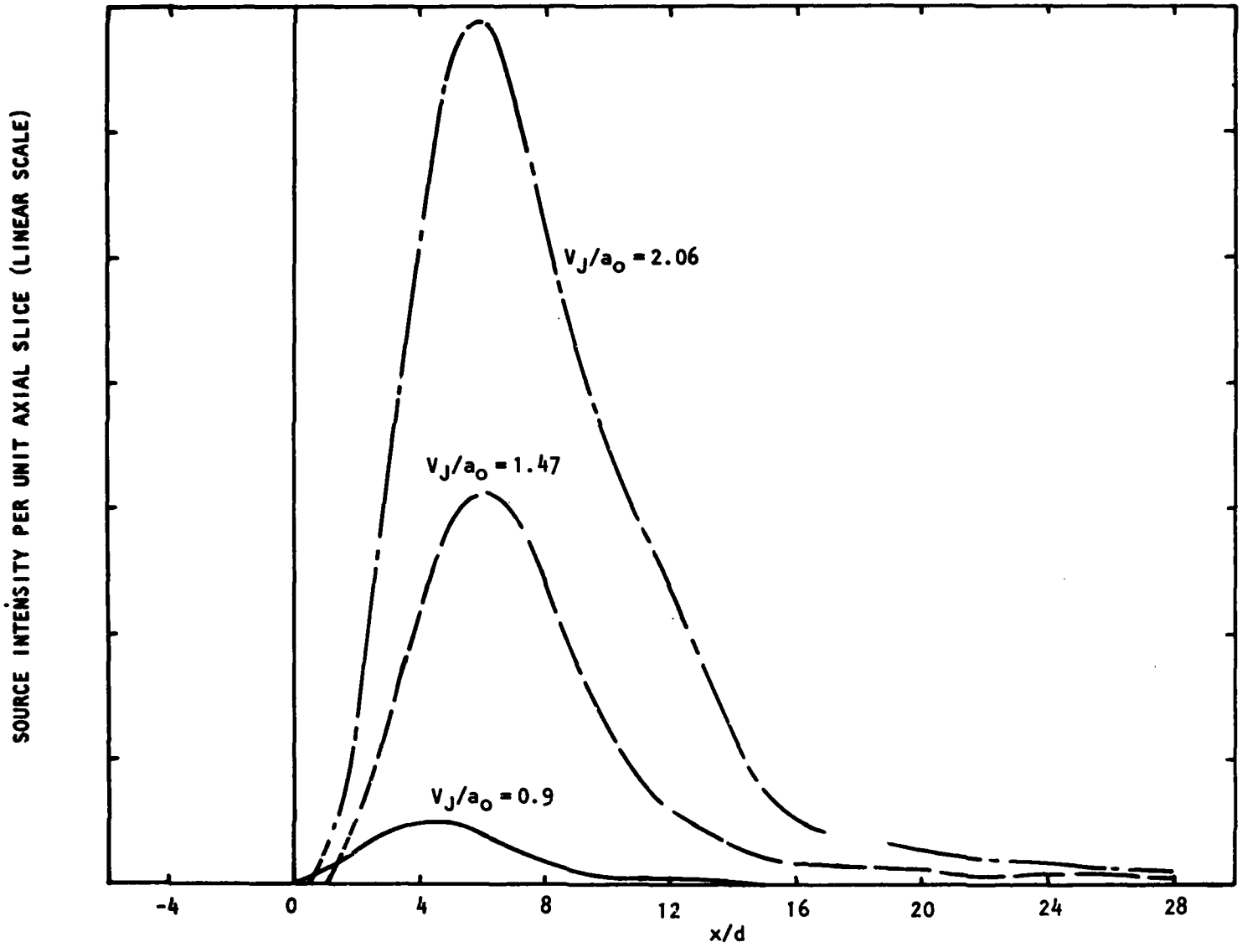

Figure 2.30 Axial source distributions measured with the polar correlation technique at 90° to the jet axis; S = 0.3; TP #36, 39, 55.

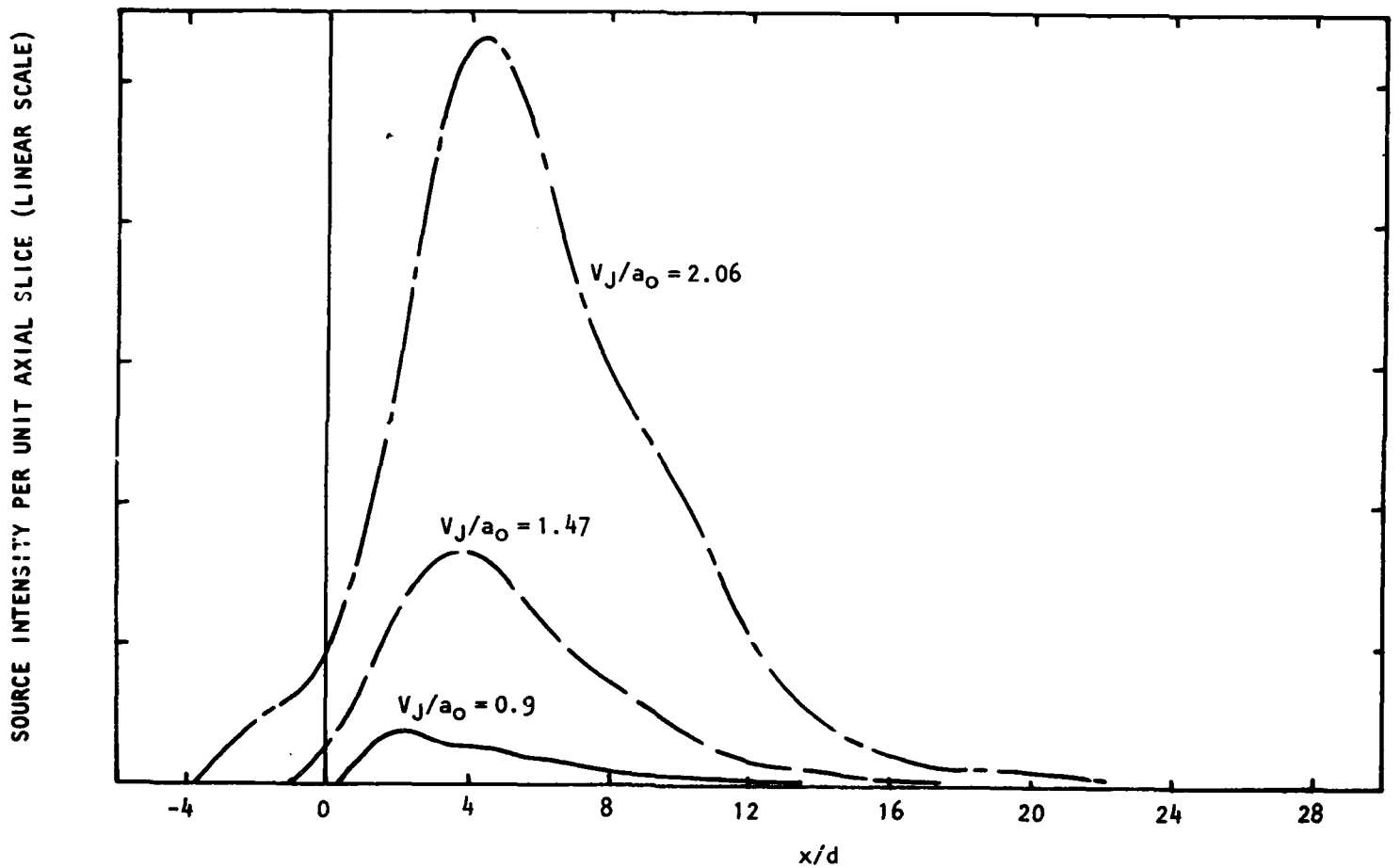

Figure 2.31 Axial source distributions measured with the polar correlation technique at 90° to the jet axis; S = 1.0; TP #36, 39, 55.

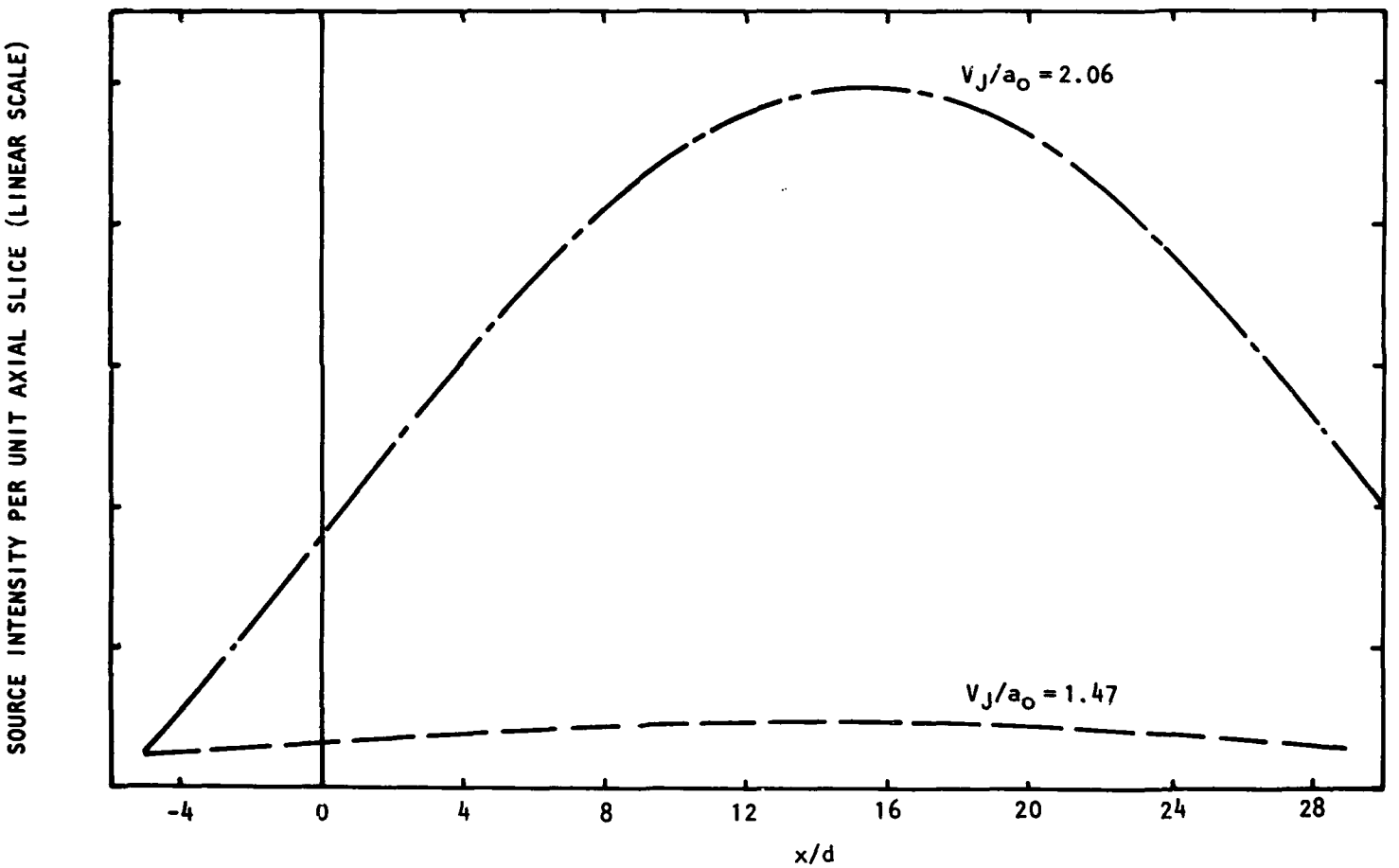

Figure 2.32 Axial source distributions measured with the polar correlation technique at 22½° to the jet axis; S = 0.03; TP #36, 39, 55.

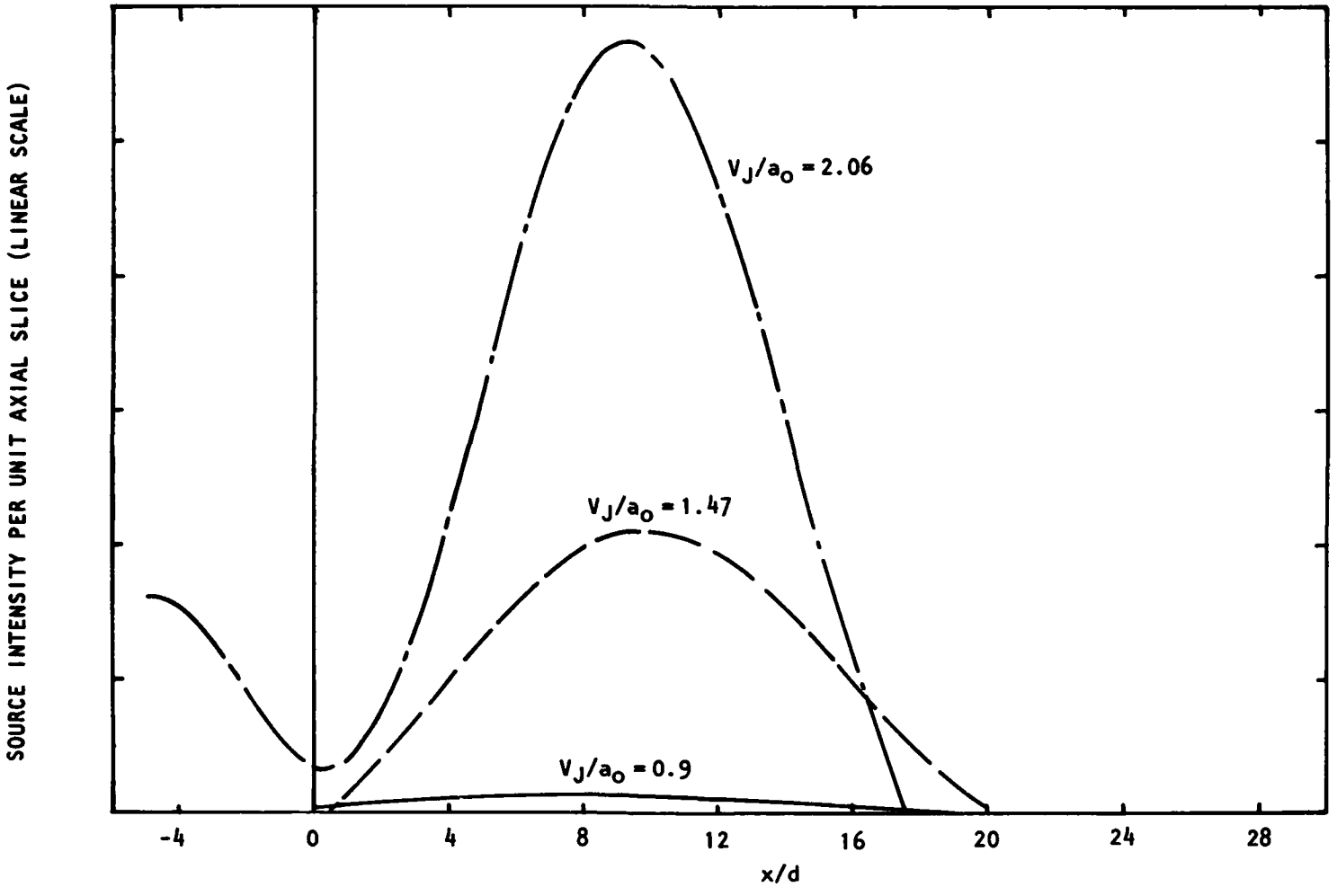

Figure 2.33 Axial source distributions measured with the polar correlation technique at 22½° to the jet axis; S = 0.1; TP #36, 39, 55.

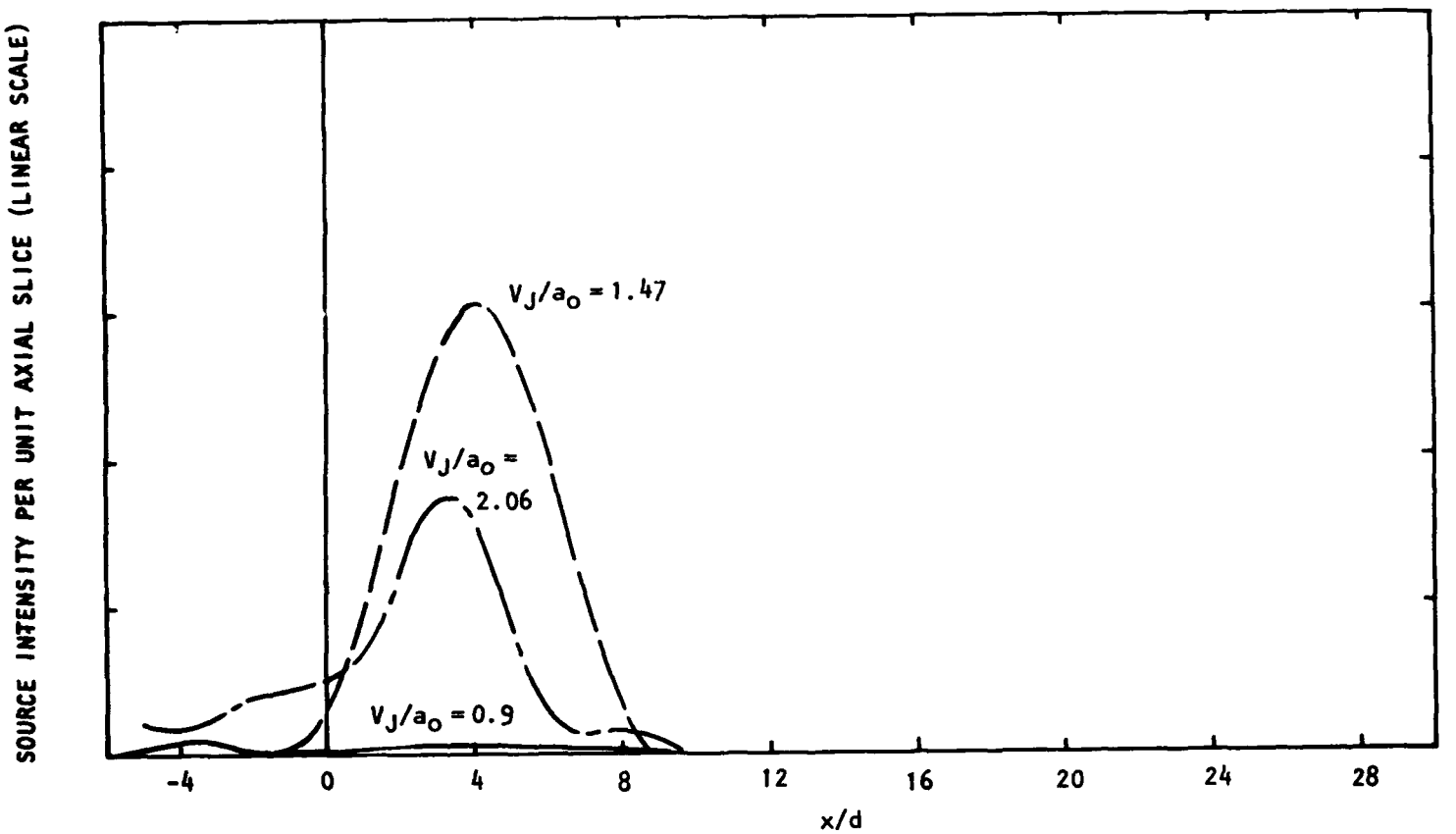

Figure 2.34 Axial source distributions measured with the polar correlation technique at 22½° to the jet axis; S = 0.3; TP #36, 39, 55.

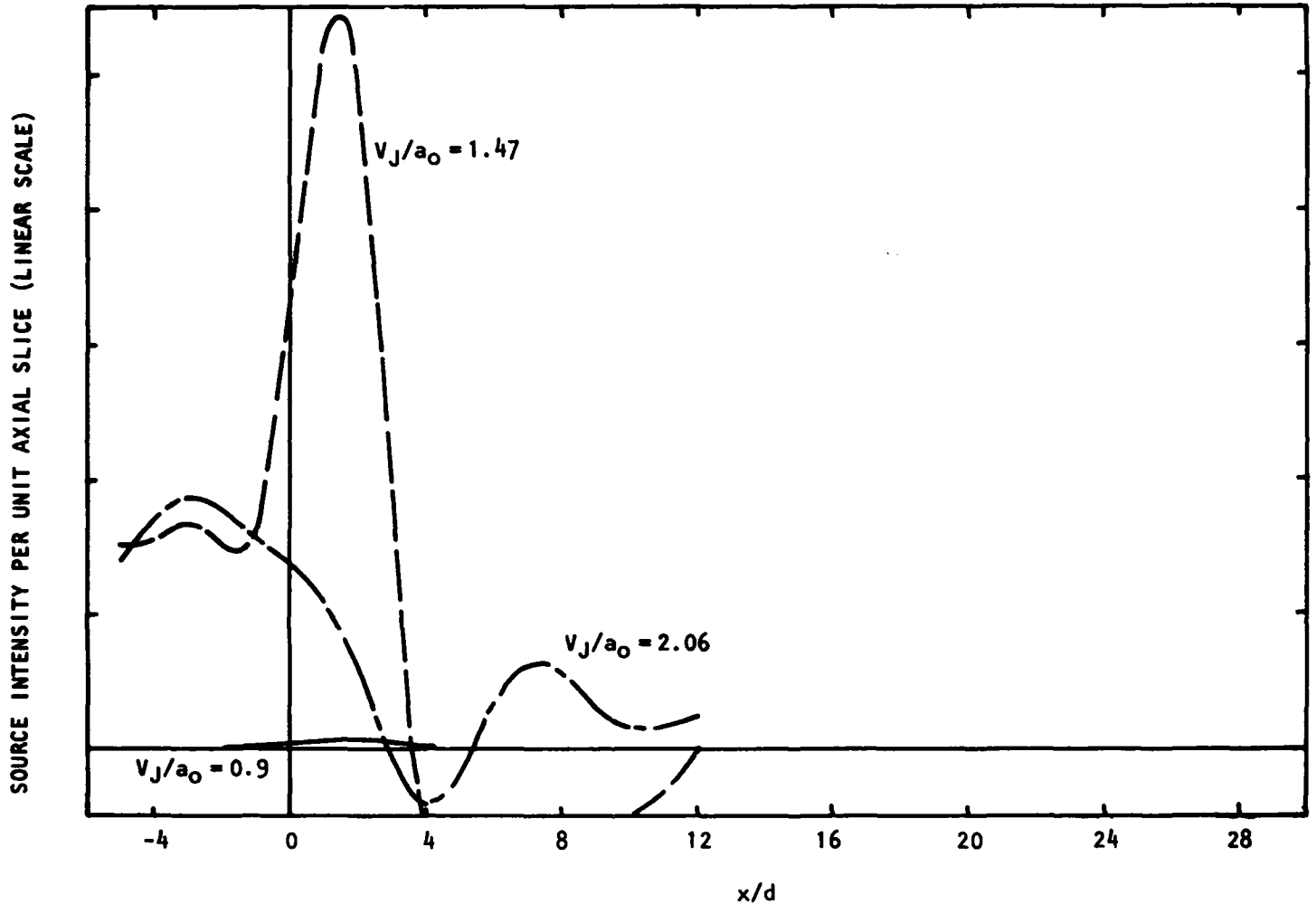

Figure 2.35 Axial source distributions measured with the polar correlation technique at 22½° to the jet axis; S = 1.0; TP #36, 39, 55.

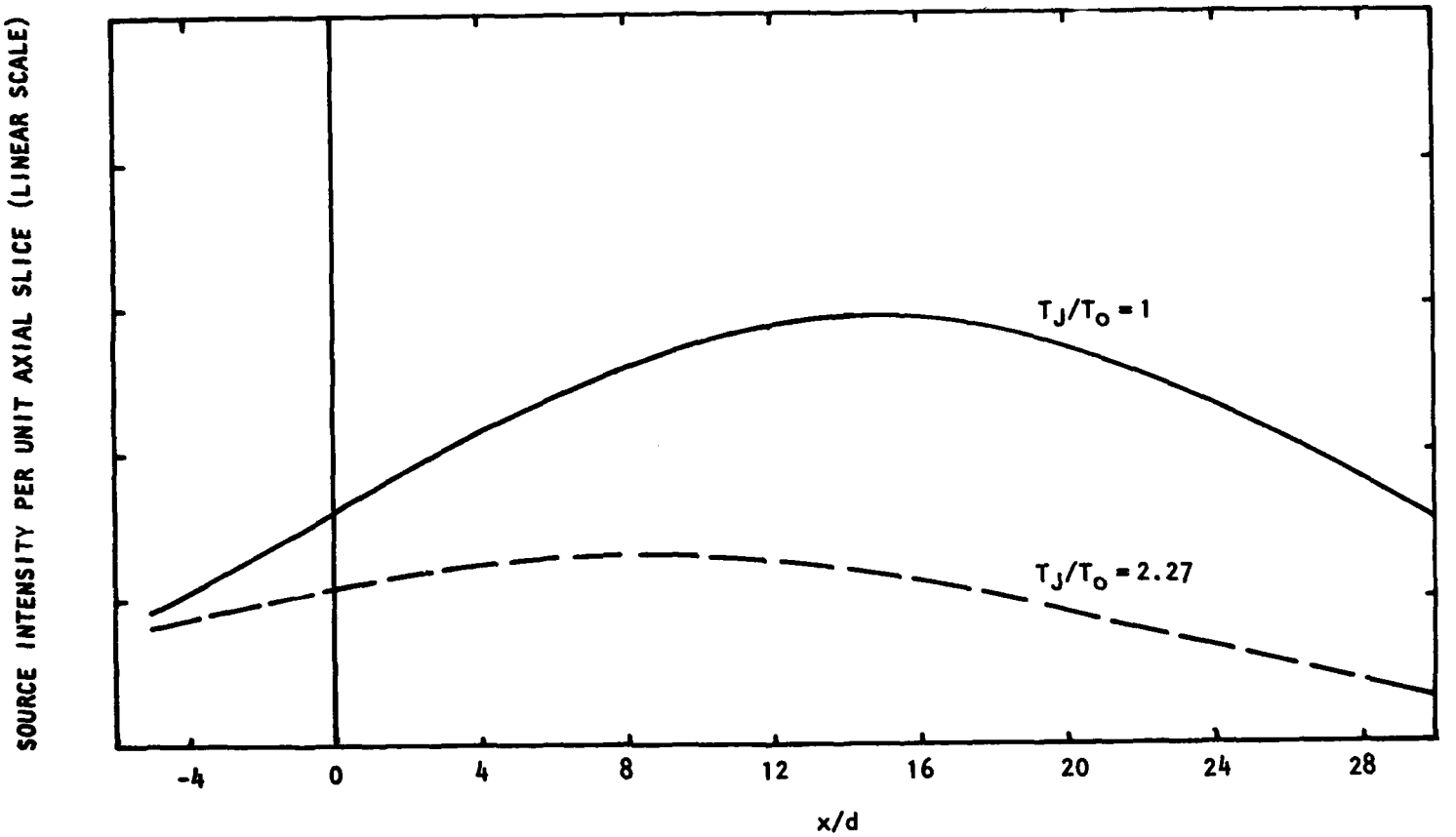

Figure 2.36 Axial source distributions measured with the polar correlation technique at 90° to the jet axis; S = 0.03; TP #39, 51.

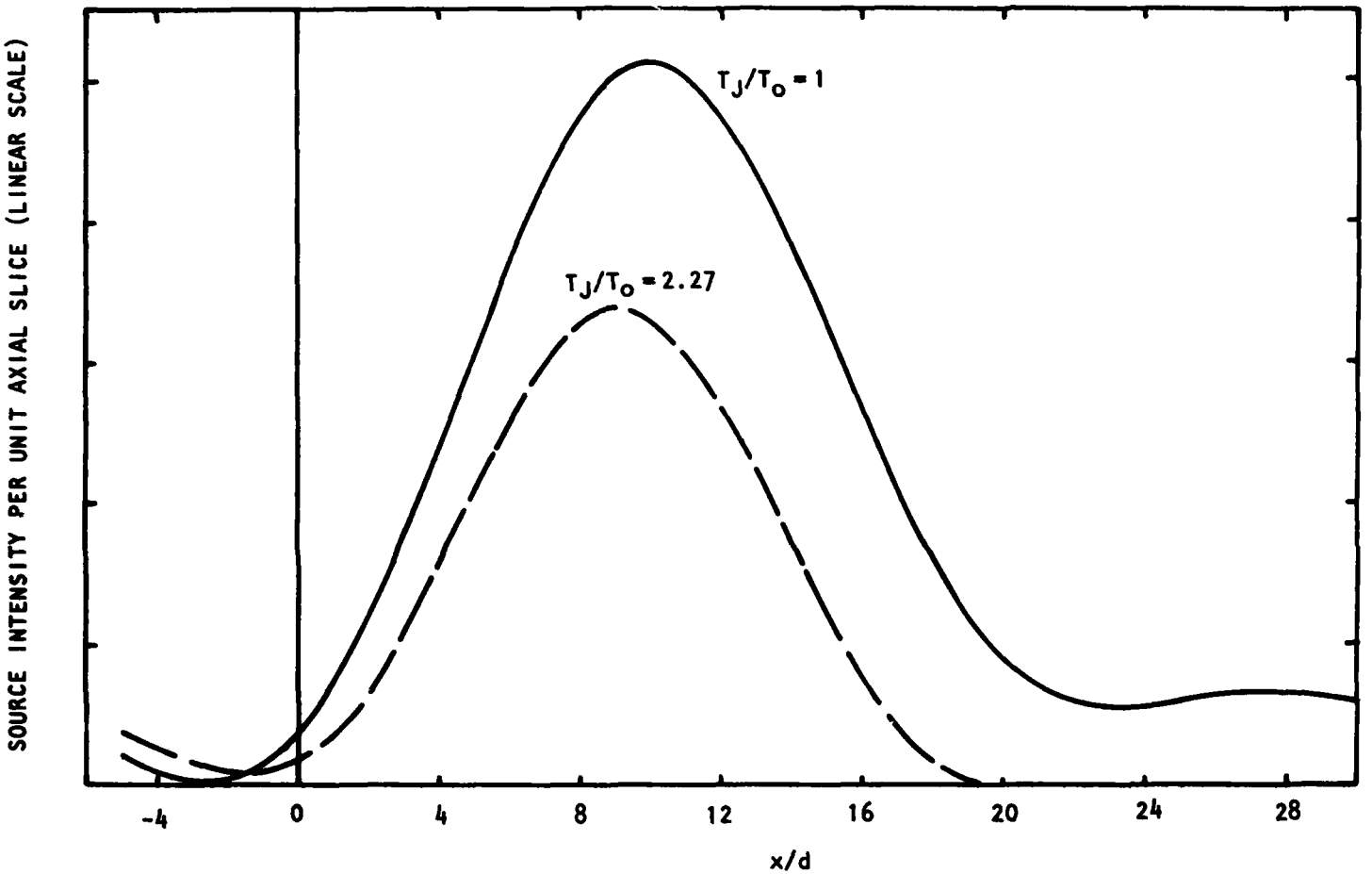

Figure 2.37 Axial source distributions measured with the polar correlation technique at 90° to the jet axis; S = 0.1; TP #39, 51.

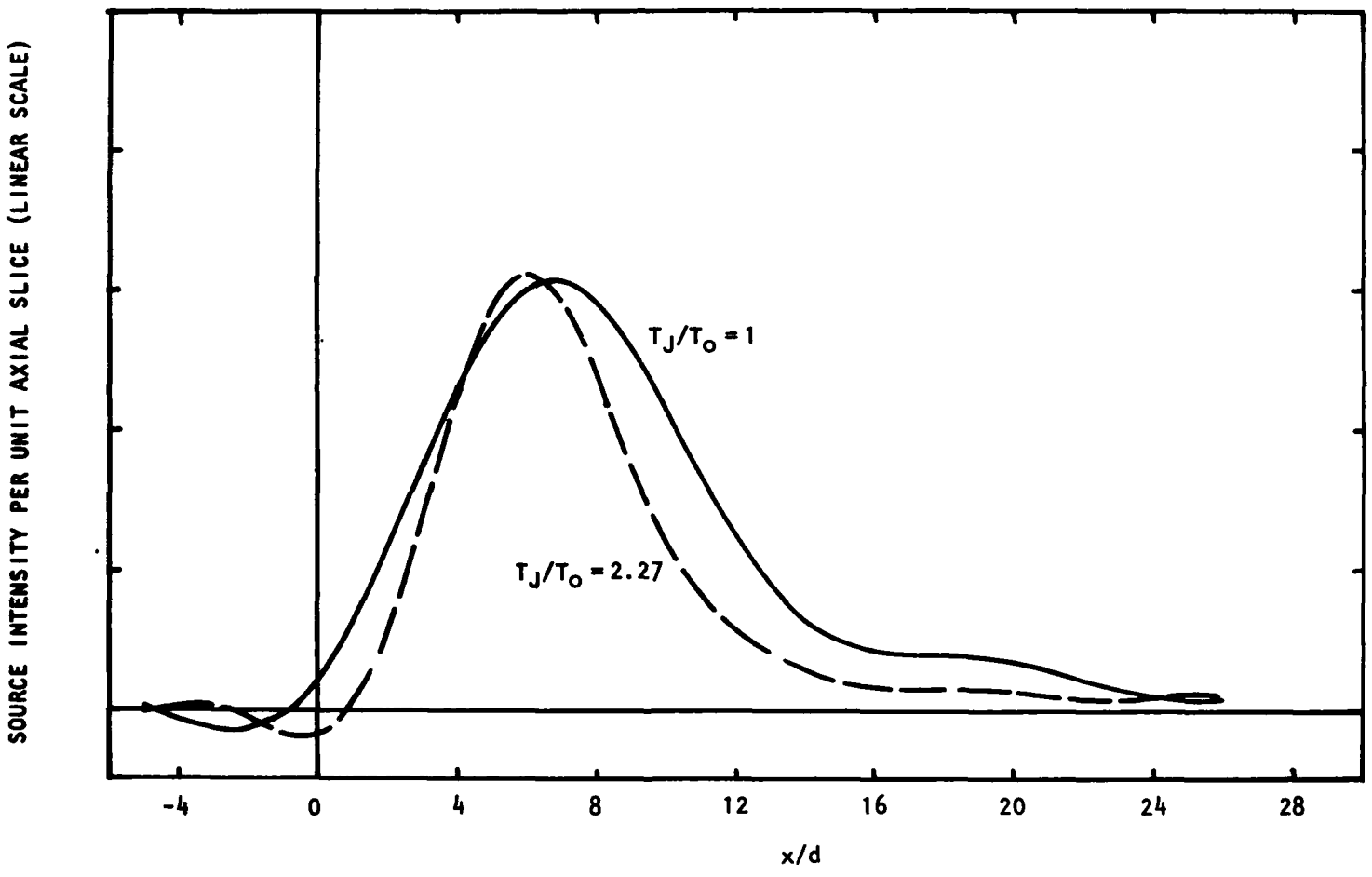

Figure 2.38 Axial source distributions measured with the polar correlation technique at 90° to the jet axis; S = 0.3; TP #39, 51.

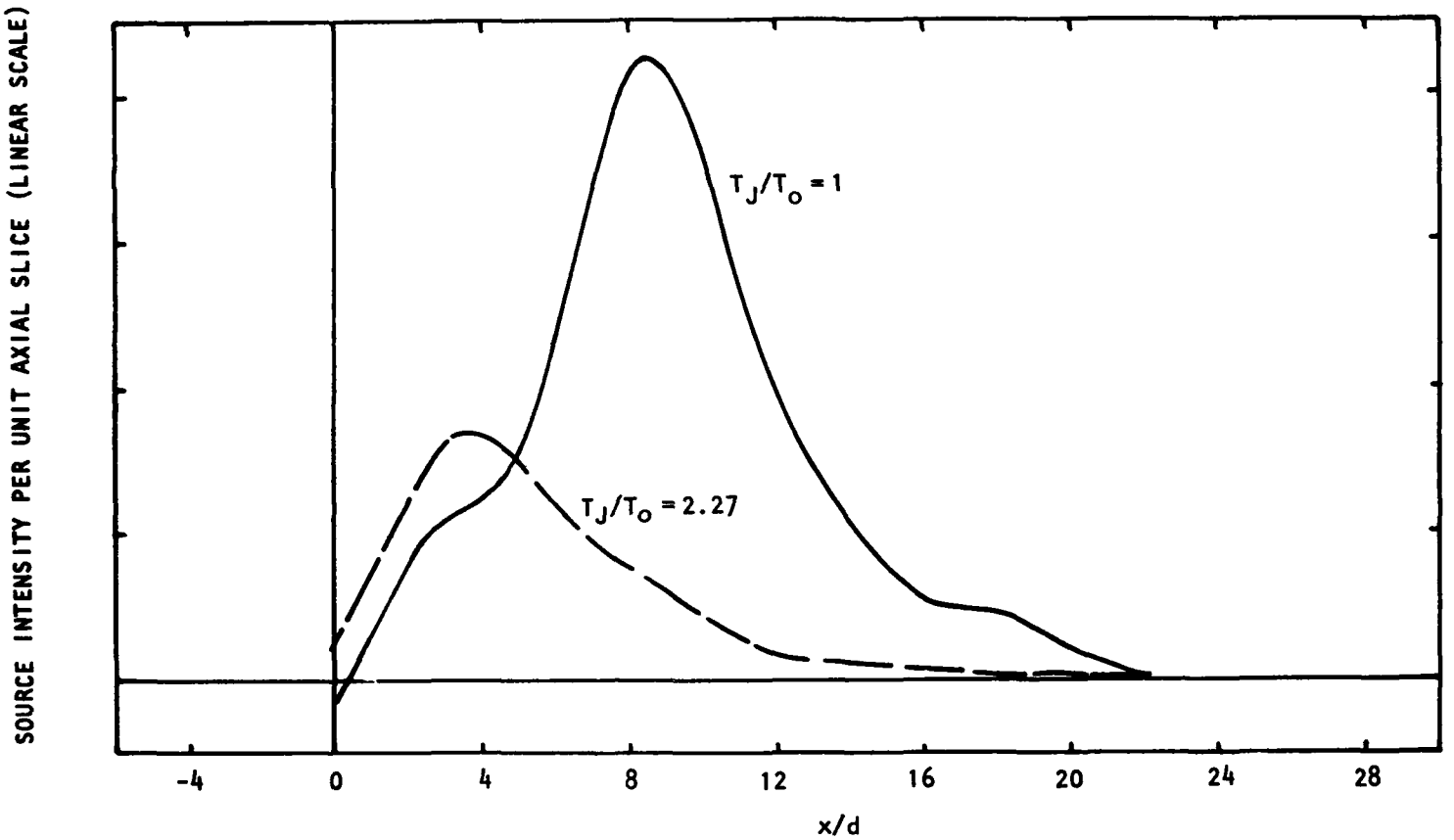

Figure 2.39 Axial source distributions measured with the polar correlation technique at 90° to the jet axis; S = 1.0; TP #39, 51.

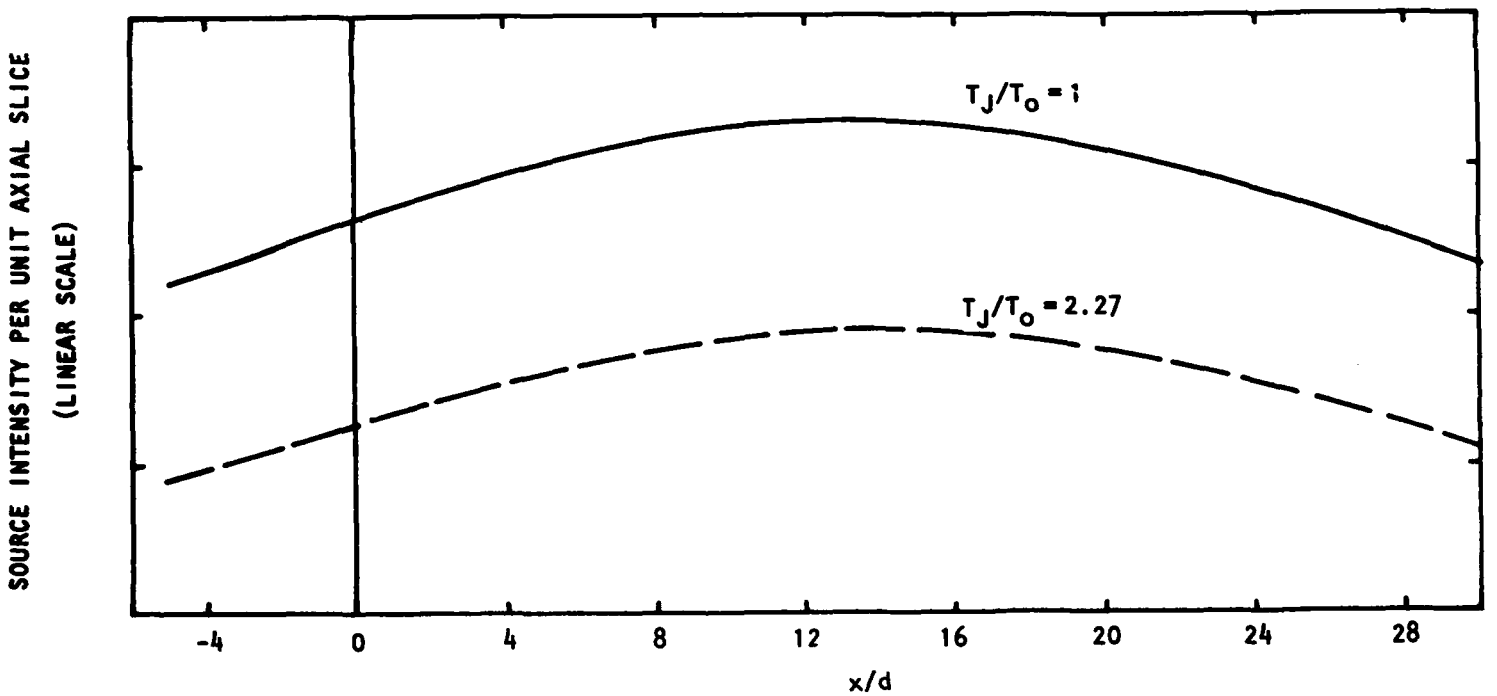

Figure 2.40 Axial source distributions measured with the polar correlation technique at 22½° to the jet axis; S = 0.03; TP #39, 51.

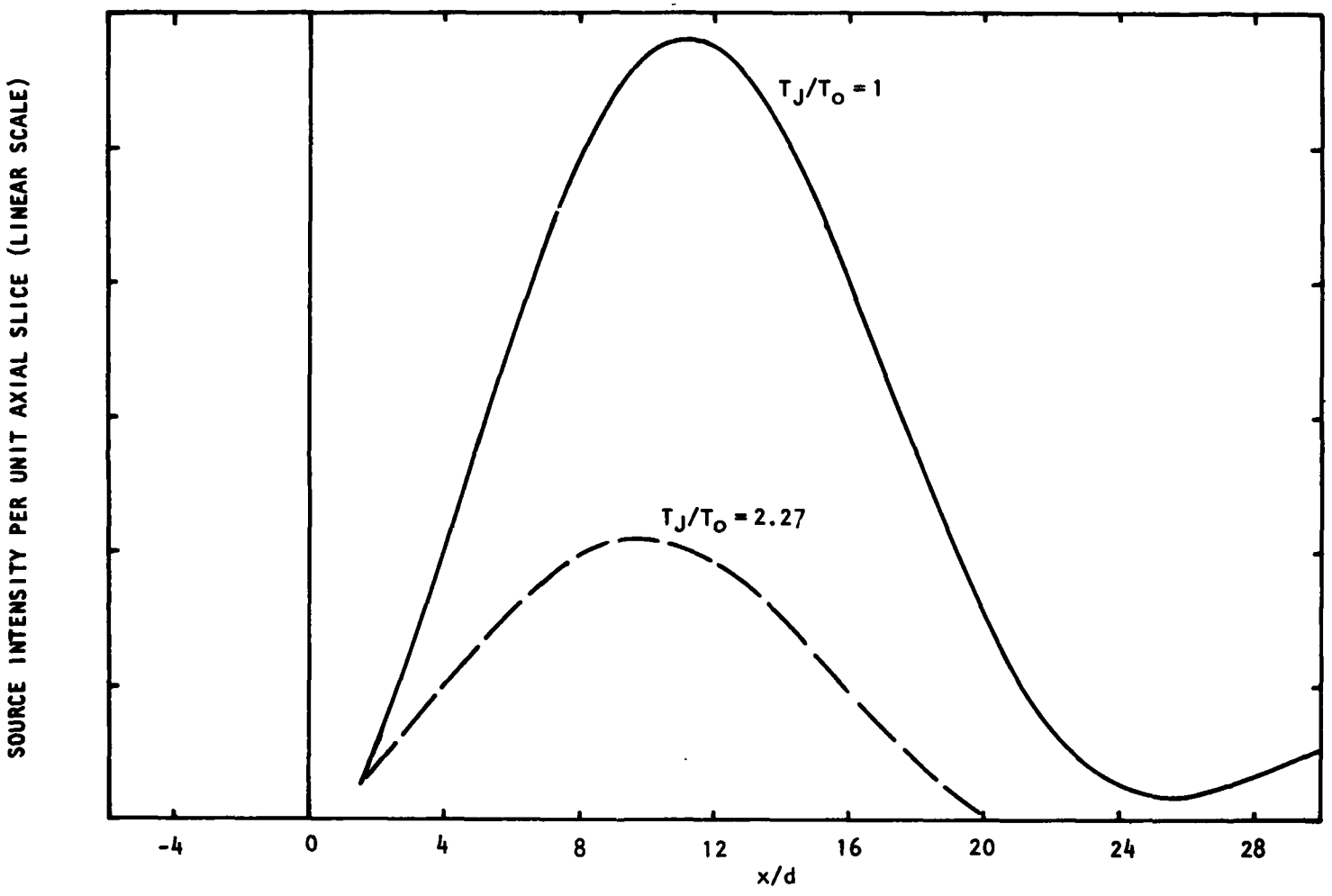

Figure 2.41 Axial source distributions measured with the polar correlation technique at $22\frac{1}{2}^{\circ}$ to the jet axis; S = 0.1, TP #39, 51.

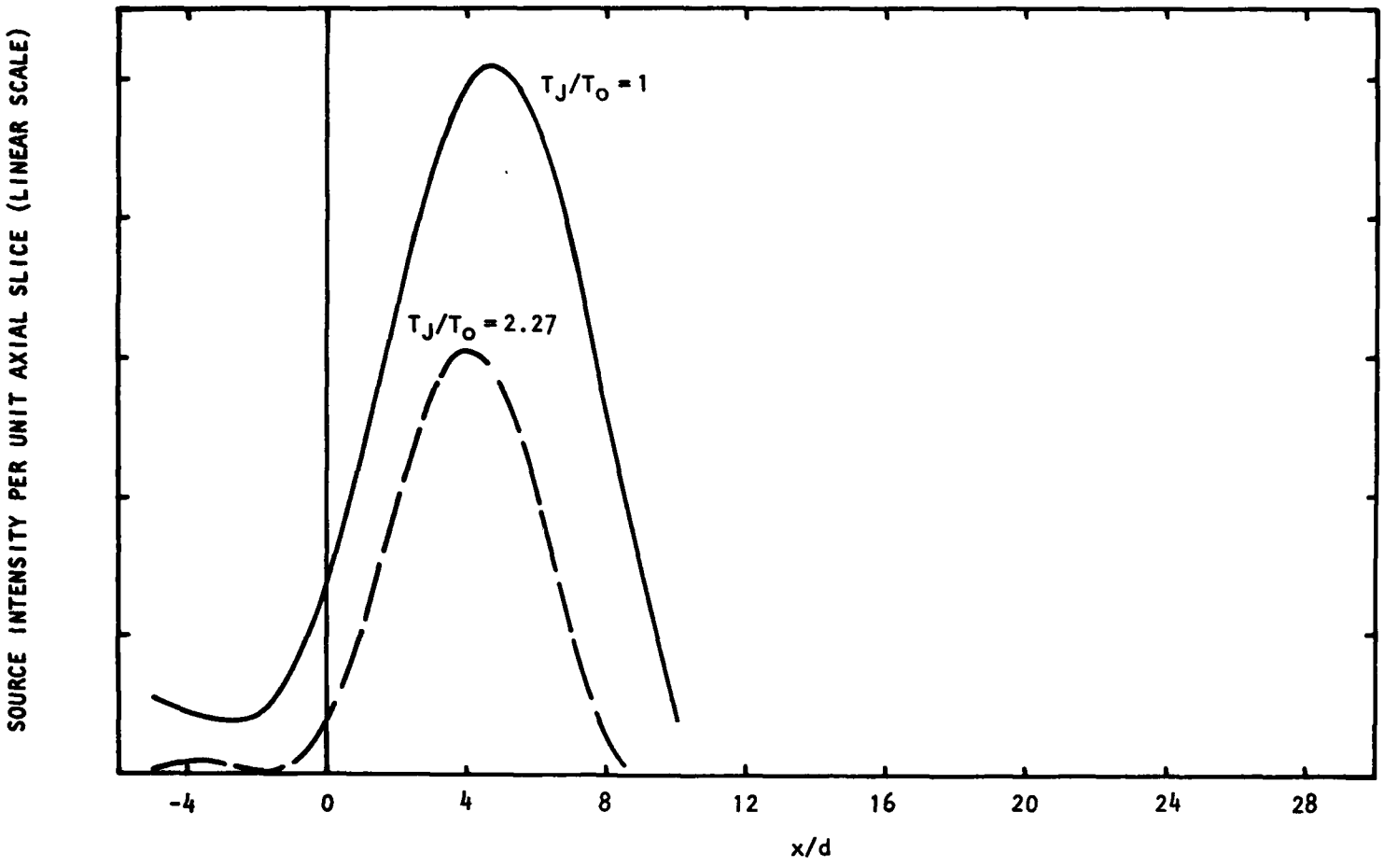

Figure 2.42 Axial source distributions measured with the polar correlation technique at $22\frac{1}{2}^{\circ}$ to the jet axis; S = 0.3; TP #39, 51.

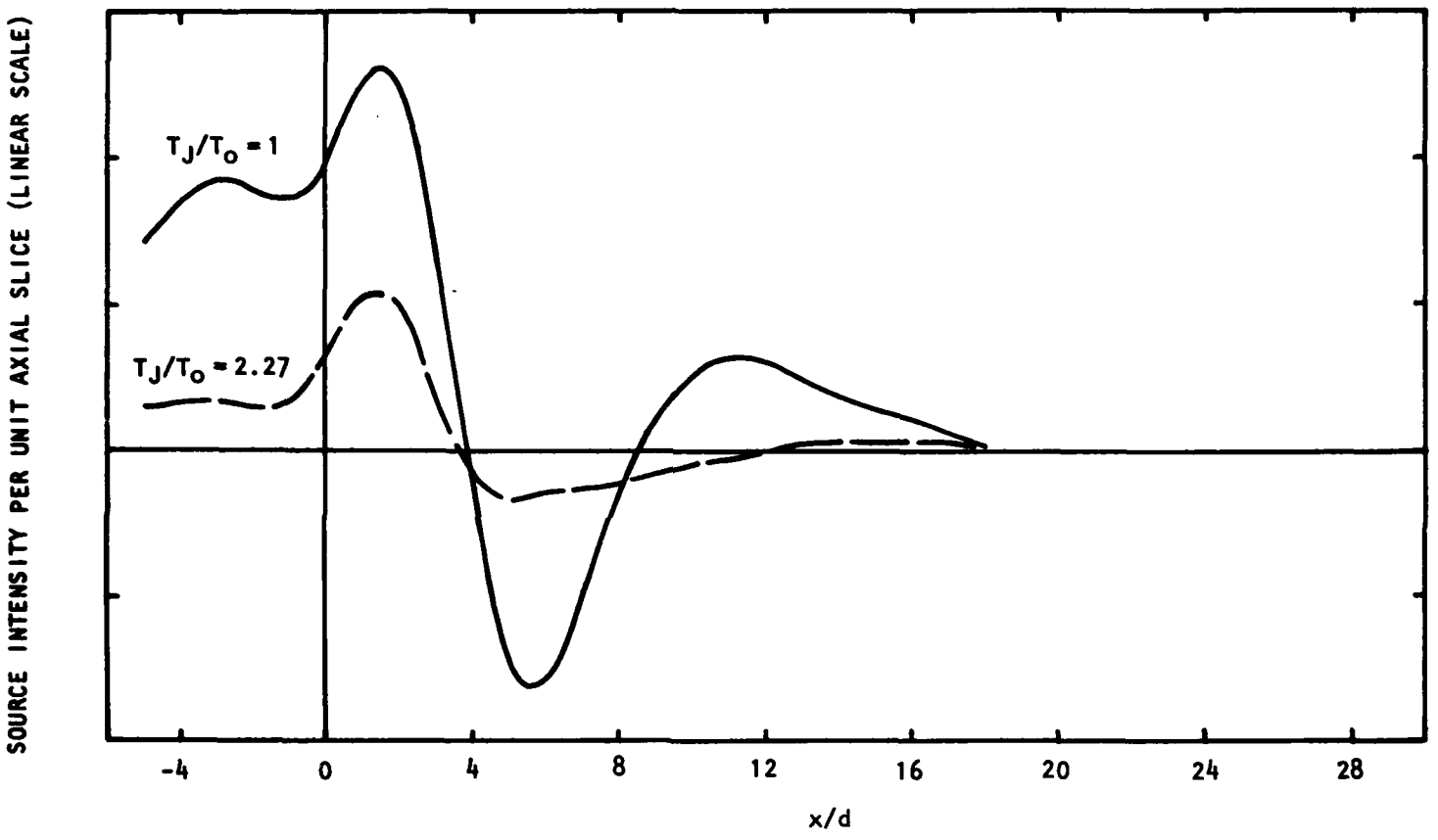

Figure 2.43 Axial source distributions measured with the polar correlation technique at 22½° to the jet axis; S = 1.0; TP #39, 51.

(i.e. radial-azimuthal) noncompactness effects. Thus, the investigation has concentrated on the radiation from a compact source distribution defined by measured *turbulence* data, at 90° to the axis of a "true" isothermal jet.

The starting point is Equation (2-29)

$$P(R_r,\theta_o,\omega) = \frac{\rho_o}{(4\pi R_r)^2} \sum_n P_n \tag{2-102}$$

and Equation (2-37)

$$P_n = \int_{-\infty}^{\infty} dx \int_0^{\infty} 2\pi r dr\, C^*_{\alpha\beta} \quad (k_x,r,n,\omega)$$

$$\cdot \int_0^{\infty} r'dr'\, C_{\alpha\beta}(k_x,r',n,\omega)\; 2\phi^{(2)}_{\alpha\beta}(\omega,n|x,r;k_x,r') \tag{2-103}$$

and since flow effects are being neglected, the appropriate solutions are:

$$C_{rr} = -\left| k_o^2\kappa^2 - \frac{n^2}{r^2} + \frac{k_2}{r}\frac{J_n'(k_2r)}{J_n(k_2r)} \right| \rho_o^{\frac{1}{2}}\, J_n(k_2r) \tag{2-104a}$$

$$C_{r\phi} = jn\left| \frac{k_2}{r}\frac{J_n'(k_2r)}{J_n(k_2r)} - \frac{1}{r} \right| \rho_o^{\frac{1}{2}}\; J_n(k_2r) \tag{2-104b}$$

$$C_{\phi\phi} = \left| \frac{k_2}{r}\frac{J_n'(k_2r)}{J_n(k_2r)} - \frac{n^2}{r^2} \right| \rho_o^{\frac{1}{2}}\; J_n(k_2r) \tag{2-104c}$$

where $$k_2 = (k_o^2 - k_x^2)^{\frac{1}{2}}. \tag{2-104d}$$

By neglecting the noncompactness effects, Equation (2-103) simplifies – for the "Gaussian" model defined by Equation (2-39), neglecting psd variations over the coherence volume – to

$$P_n = \int_{-\infty}^{+\infty} dx\; 2\left(\frac{\sqrt{\pi}}{2} L_x\tau_o\right) \frac{L_t^2}{2}\; \exp[-\omega_{mx}^2\tau_o^2/8]$$

$$\cdot \int_0^{\infty} 2\pi r\, dr\, |C_{\alpha\beta}|^2\, \overline{v_\alpha^2}(x,r)\, \overline{v_\beta^2}(x,r) \tag{2-105a}$$

and for the "Exponential-Gaussian" model - defined by Equation (2-42) - to

$$P_n = \int_{-\infty}^{\infty} dx\ 2\left(\frac{\sqrt{2\pi}}{8}\ L_x\tau_o\right)\frac{L_t^2}{2}\ \frac{\exp[-\omega^2 L_x^2/8\pi V_c^2]}{\{1+\omega'^2\tau_o^2/4\}^{3/2}}$$

$$\cdot\int_0^{\infty} 2\pi r dr\ |C_{\alpha\beta}|^2\,\overline{v_\alpha^2}(x,r)\ \overline{v^2}_\beta(x,r) \qquad (2\text{-}105b)$$

With noncompactness effects neglected so that the summation of n can be performed using the standard sums given in Section 2.1.3, we obtain from Equations (2-102) and (2-105a) the result

$$P(R_r,\theta_o,\omega) = \frac{\rho_o^2 k_o^4}{(4\pi R_r)^2}\int_{-\infty}^{+\infty} dx\ 2\left(\frac{\sqrt{\pi}}{2}L_x\tau_o\right)\frac{L_t^2}{2}\exp[-\omega_{mx}^2\tau_o^2/8]$$

$$\cdot\int_0^{\infty} 2\pi r dr\left|\frac{3}{8}\overline{v_r}^2{}^2 + \frac{1}{4}\overline{v_r^2}\ \overline{v_\phi^2} + \frac{3}{8}\overline{v_\phi}^2{}^2\right| \qquad (2\text{-}106)$$

and similarly for the Exponential-Gaussian model. It is assumed here, following the experimental results of Bradshaw et al. [2.18], for example, that

$$\overline{v_r^2}(x,r) = \overline{v_\phi^2}(x,r) = \overline{v_t^2}(x,r),$$

so that

$$P(R_r,\theta_o,\omega) = \frac{\rho_o^2\ k_o^4}{(4\pi R_r)^2}\int_{-\infty}^{\infty} dx\ 2\left(\frac{\sqrt{\pi}}{2}L_x\tau_o\right)\frac{L_t^2}{2}\exp\ [-\omega_{mx}^2\tau_o^2/8]$$

$$\cdot\int_0^{\infty} 2\pi r dr\ \overline{v_t}^2{}^2(x,r) \qquad (2\text{-}107a)$$

for the Gaussian model, or

$$P(R_r,\theta_o,\omega) = \frac{\rho_o^2 k_o^4}{(4\pi R_r)^2} \int_{-\infty}^{\infty} dx\ 2\sqrt{\frac{\pi}{2}}\ \left(\frac{\sqrt{\pi}}{2} L_x \tau_o\right)\left(\frac{L_t^2}{2}\right)\frac{\exp[-\omega^2 L_x^2/8\pi V_c^2]}{\{1+\omega'^2\tau_o^2/4\}^{3/2}}$$

$$\int_0^{\infty} 2\pi r dr\ \overline{v_t^2}^2(x,r) \qquad (2\text{-}107b)$$

for the Exponential-Gaussian model. The radial integral

$$I_r = 2\pi \int_0^{\infty} r dr\ \overline{v_t^2}^2(x,r).$$

has been calculated with the following expression based on LV measured data (see Section 5).

$$I_r = 2\pi\ \overline{v_t^2}^2_{peak}\ e^{-.0016\ (x/r_J)^2} \cdot r_{\frac{1}{2}} \cdot x\ \frac{\sqrt{\pi}}{2\sqrt{c}} \qquad x < x_{c,eff} \qquad (2\text{-}108a)$$

(see Figure 5.26)

$$= 2\pi\ \overline{v_t^2}^2_{peak}\ \left(\frac{x_{c,eff}}{x}\right)^4 \cdot e^{-.0016\ (x_{c,eff}/r_J)^2} \cdot x^2\ \frac{1}{8c} \qquad x > x_{c,eff} \qquad (2\text{-}108b)$$

where

$$(\overline{v_{t_{peak}}^2})^{\frac{1}{2}} = (2/3)\ (.179)\ V_J\ M_J^{-.1028} \qquad \textit{(Figure 5.26)} \qquad (2\text{-}109a)$$

$$x_{c,eff} \triangleq 2\ x_c \qquad \textit{(Figure 5.26)} \qquad (2\text{-}109b)$$

$$x_c = 2\ r_J\ (4.3 + 1.1\ M_J^2) \qquad \textit{(Figure 5.15)} \qquad (2\text{-}109c)$$

$$r_{\frac{1}{2}} \triangleq r_J \qquad \textit{(Figure 5.25)} \qquad (2\text{-}109d)$$

where $M_J = V_J/a_J$ and c, representing the radial width of the source distribution, is specified with sample calculations given below. The axial integrals have been calculated numerically† as a function of frequency with the following expressions for the time and length scales and convection velocity, obtained from LV data (see Section 5).

---

†*With a computer program (INTEG) which is described in Section 6.*

$$L_x = 0.042\ x + 0.48\ (\equiv 2L_x') \qquad \textit{(Figure 5.52)} \qquad (2\text{-}110a)$$

or

$$L_x = 0.12\ x^{\dagger} \qquad (2\text{-}110b)$$

$$L_t = 0.028\ x + 0.28\ (\equiv 2L_r') \qquad \textit{(Figure 5.53)} \qquad (2\text{-}110c)$$

or

$$L_t = 0.06\ x^{\dagger\dagger} \qquad (2\text{-}110d)$$

$$\tau_o = \{(0.63)(2)\ V_J(1.1 + 0.9\ M_J)\}^{-1} x \qquad \textit{(Figure 5.42)} \qquad (2\text{-}110e)$$

$$V_c = 0.63\ V_J \qquad \textit{(Figure 5.45)} \qquad (2\text{-}110f)$$

The results are expressed in the form of 1/3-octave SPL's defined as

$$SPL = 10 \log_{10} \left\{ .2316 \left(\frac{\omega}{2\pi}\right) \frac{P(R_r, \theta_o = 90^\circ, \omega)}{(2 \times 10^{-5})^2} \right\} \qquad (2\text{-}111)$$

with the power spectral density, P, calculated in MKS units, and R_r the polar radius set equal to 72 jet diameters, the measurement distance of the Lockheed mixing noise data [2.14].

Three isothermal jet operating conditions were chosen for detailed comparisons of measured noise spectrum levels and values calculated according to the two source function models described above. These are referred to as test point numbers 8, 12 and 51 in the Lockheed mixing noise test data [2.14]; the jet exit and ambient conditions are given in Table 2.12, together with values of the parameter c calculated from the turbulence data (see Section 5).

---

†*Best fit to measured data passing through origin in Figure 5.51 from $x = 0$ to $x = 4d$.*

††*Best fit to measured data passing through origin in Figure 5.53 from $x = 0$ to $x = 4d$.*

TP	M_J	V_J/a_o	T_J/T_o	T_o (F)	P_o (psia)	c
8	0.506	0.501	0.980	70.0	14.20	72.0
12	0.911	0.900	0.976	72.0	14.20	110.0
51	1.370	1.334	0.941	81.0	14.26	285.0

Table 2.12 Jet exit conditions for 90° spectrum level comparisons

The first set of results presented in Figure 2.44 were calculated with the expression for the axial length scale L_x given by Equation (2-110a) and the transverse length scale by Equation (2-110c), which have non-zero values at the exit plane. The calculated spectrum (solid curve) bears little resemblance to the measured spectrum (symbols) in any of these cases although the Gaussian model spectrum is close to the measured spectrum below its peak frequency and the "peak frequency" is predicted quite well by the Exponential-Gaussian model, about 1 octave below the measured value, the peak level being about 2 dB too high at all three test points. The Gaussian model spectrum does not exhibit a maximum within the frequency range considered. The spectra labelled DBU and DBD in these figures correspond to the "upstream" and "downstream" integrals, that is the axial integration of Equation (2-107) is calculated in two parts, from $x = 0$ to $x = x_{c,eff}$ (upstream) and from $x = x_{c,eff}$ to $x = \infty$ (downstream).

It has been found that these poor predictions, particularly at high frequencies can be rectified to a large extent by using, in the first instance, the alternative expressions for L_x and L_t [Equations (2-110b), (2-110d)] which yield a zero value for the length scales at the exit plane. The results are shown in Figure 2.45. Clearly, the spectrum calculated with the Exponential-Gaussian model and the alternative L_x, L_t expressions has many features in common with the measured spectrum. The low and high-frequency slopes agree fairly well although the calculated rise at low frequencies is somewhat steeper than that of the measured spectrum.

Nevertheless, the general qualitative agreement is quite encouraging, when the Exponential-Gaussian model is utilized. One of the reasons for this can be seen by plotting the integrand in Equation (2-107b) (after the integration with respect to r) as a function of distance from the exit plane as in Figure 2.47. Here, the results are shown for four frequencies corresponding (approximately) to the Strouhal numbers $S = 0.1$, 0.3, 1, and 3 at TP #8 ($V_J/a_o = .501$, $T_J/T_o = 0.980$). This "source strength per unit slice of jet" is the quantity that can be obtained with the polar correlation technique or more precisely a diffraction limited image of that quantity. Results of the polar correlation measurement program are given in the previous section. A detailed comparison of the calculated and measured axial "source strength" distribution has not been possible but the calculated results in Figure 2.46 clearly exhibit one of the required features, i.e. approximately the correct axial peak locations as a function of frequency (high frequencies close to the nozzle, low frequencies far downstream $x_{peak}/d \doteq 2$, 4, 7, and 13 for $S = 3$, 1, 0.3, and 0.1, respectively). Also, there is a slight but noticeable asymmetry of the distribution about the axial peak, as found in the polar correlation results. In distinct contrast, the corresponding Gaussian model

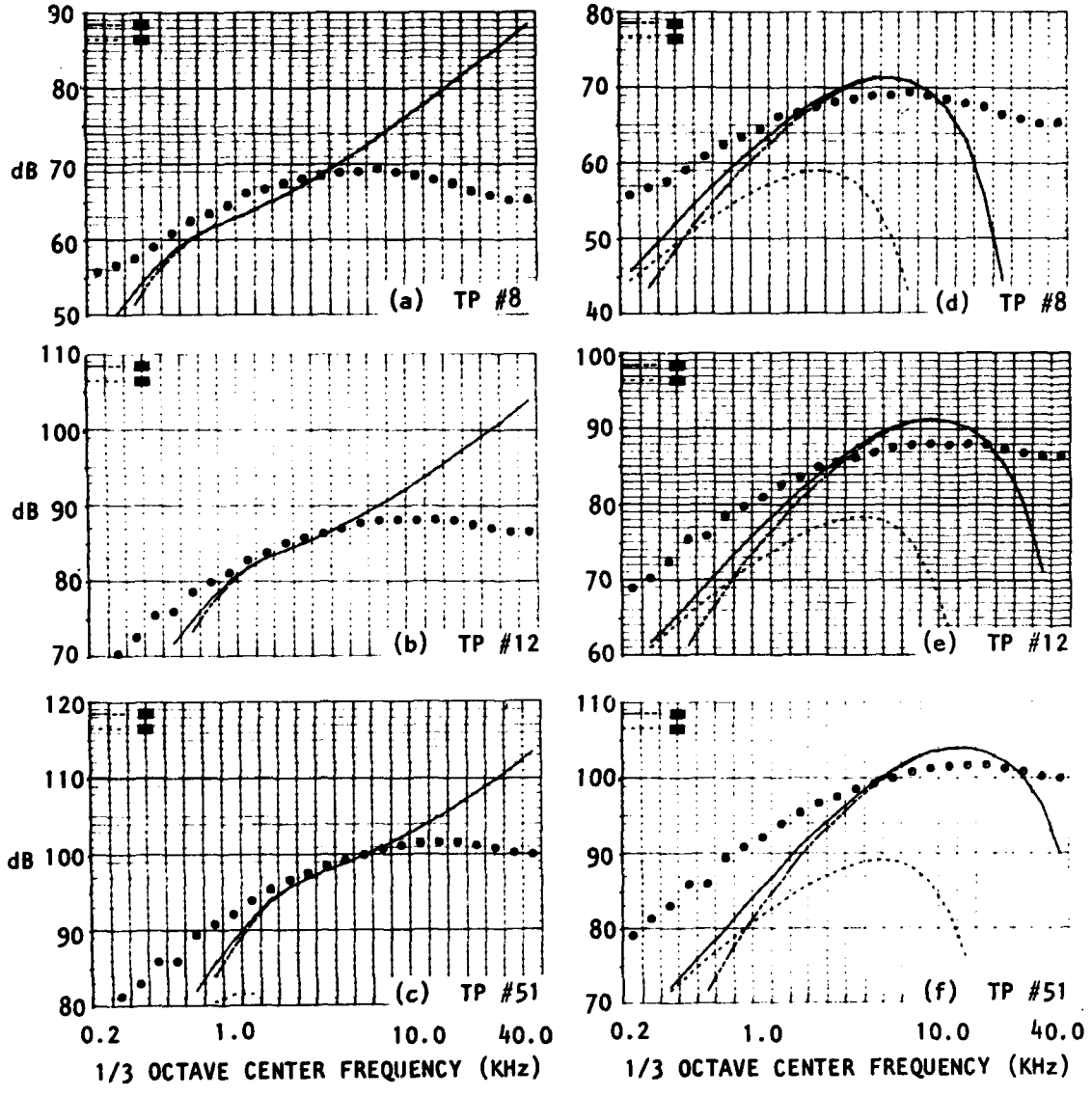

Figure 2.44 Measured and Calculated Jet Mixing Noise Spectrum Levels at 90° to the Jet Axis

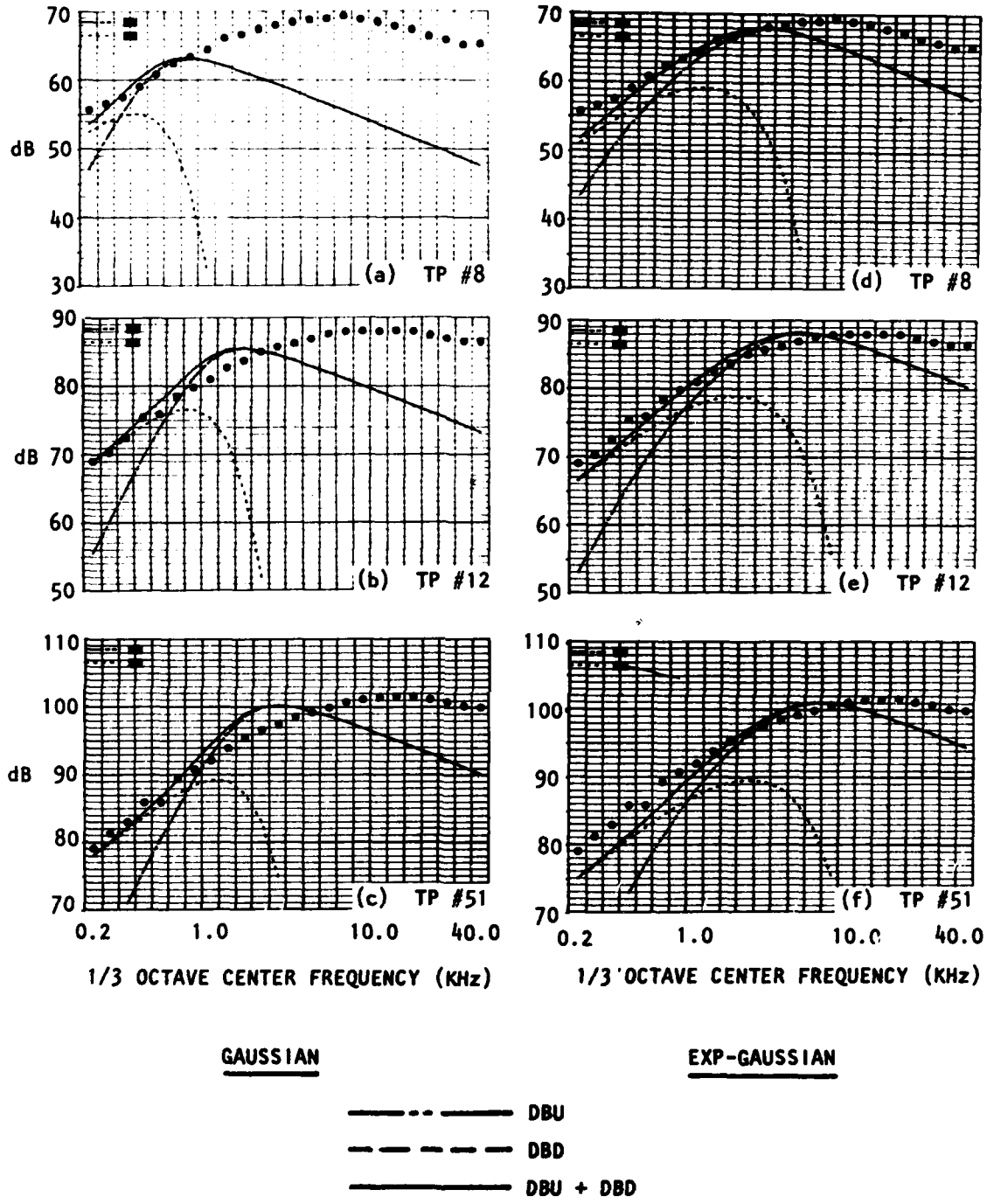

Figure 2.45 Measured and Calculated Jet Mixing Noise Spectrum Levels at 90° to the Jet Axis (Alternative L_x, L_t Expressions)

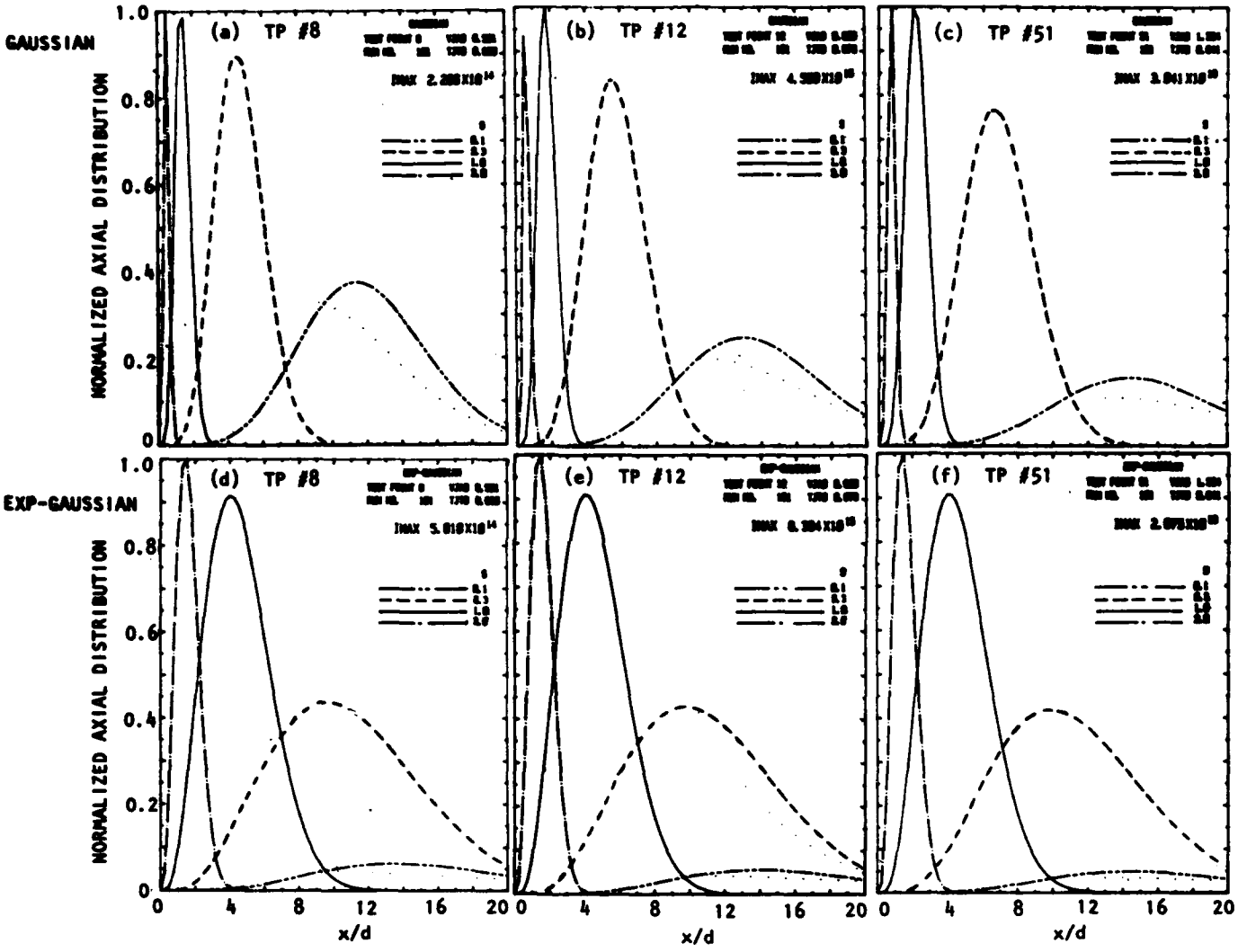

Figure 2.46 Calculated Axial Source Distributions at Different Strouhal Numbers in the Corresponding Spectra of Figure 2.45; —·—·— , S = 0.1; – – – – , 0.3; ——— , 1.0; ——·——, 3.0.

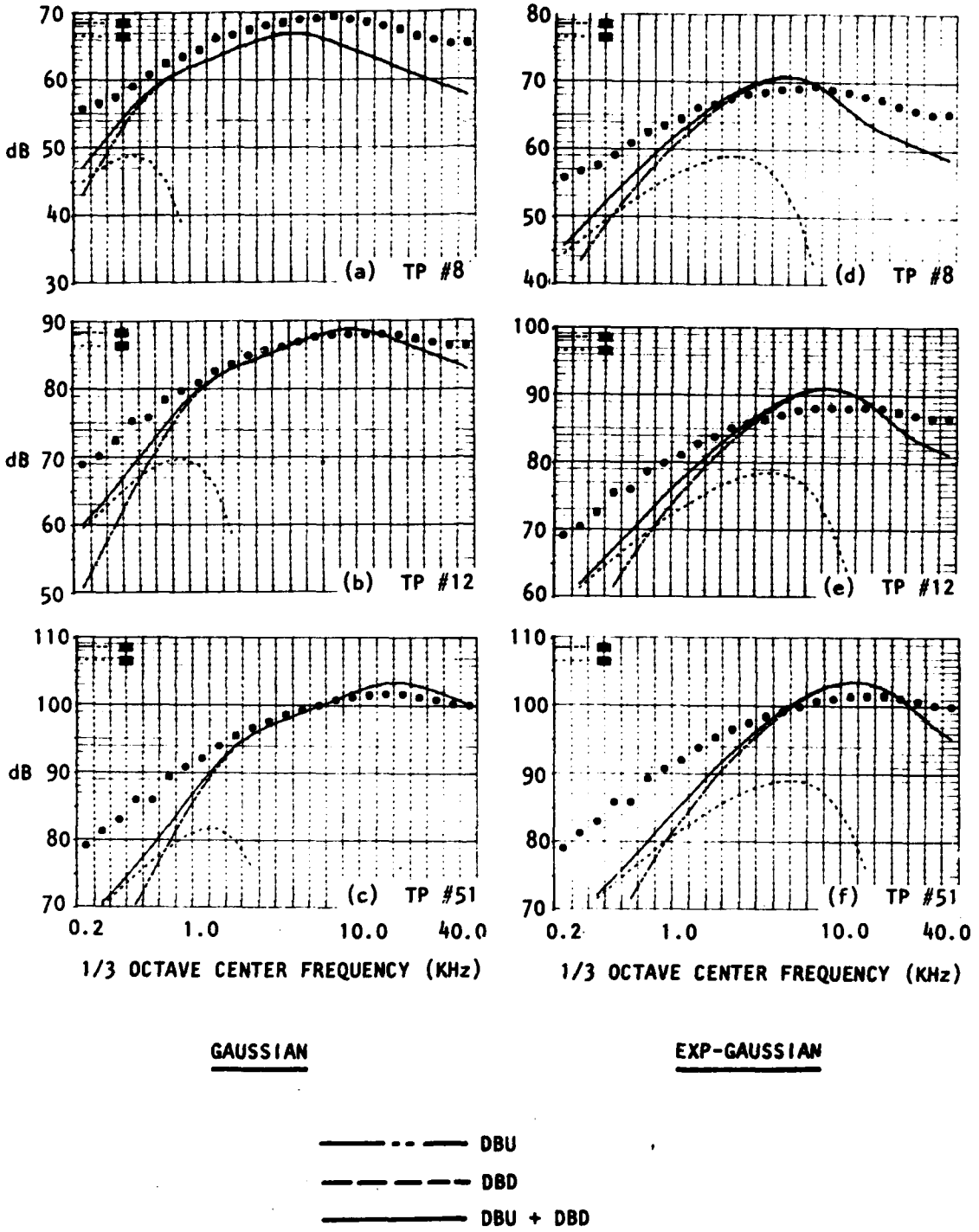

Figure 2.47 Measured and Calculated Jet Mixing Noise Spectrum Levels at 90° to the Jet Axis

axial distributions, also shown in Figure 2.47, do *not* give the correct peak locations except at the lowest Strouhal number.

Yet another approach at representing L_x and L_t is to assume that these length scales *are zero* at the exit plane and rise linearly with x until they intersect the corresponding lines given by Equations (2-110a) and (2-110c), respectively at $x/d = 1.25$. This is the approximate position where the initially laminar shear layer of the jet apparently undergoes transition (Lau, to be published). The results are shown in Figure 2.47. There is a noticeable improvement in the spectra at the high frequencies (compare Figure 2.44) and this is especially marked in the results for the Gaussian model. The predicted values from this model follow the experimental results very closely, and it is believed that with fine "tuning" of some of the variables used in the model, the prediction would be further improved.

Figure 2.48 shows the corresponding source distributions for both models at Strouhal numbers of 0.1, 0.3, 1.0, and 3.0, and exhibit the essential characteristics mentioned earlier (i.e. the higher frequencies lie close up to the nozzle and the distributions have a somewhat skewed appearance). However, the respective peaks lie further upstream than where source location techniques would seem to indicate. The reasons for this apparent discrepancy would need to be explored.

To summarize, the standard, Gaussian correlation function model can yield a good noise spectrum prediction (at 90°), but the corresponding axial source distributions do not tie in very well with (far-field) source location data nor – as often pointed out in the past (e.g. Ribner [2.3]) – does the Gaussian model fit the measured turbulence correlation data particularly well with regard to the moving frame decay envelope. The so-called Exponential-Gaussian model with the same length scale assumptions offers an improvement with regard to the latter deficiency and possibly a slight improvement in the axial source distribution (see Figure 2.48), but the penalty is a degraded noise spectrum prediction (see Figure 2.47). On the other hand, with the simplest length scale assumptions [Equations (2-110b), (2-110d)], the axial distributions agree almost perfectly with far-field source location data (Figure 2.46) and the noise spectrum predictions improve also (Figure 2.45), but still do not reach the same standard as those of the best Gaussian model predictions. Clearly, the choice of length scale assumptions is important and could be resolved by further LV turbulence measurements near the nozzle exit plane. More detailed analysis of turbulence and acoustic far-field correlation data may help to resolve the correlation function issue and possibly lead to further improvements in the modeling of those data as well as in noise spectrum predictions. Once satisfactory agreement had been reached in *all three areas*, it would then be reasonable to assume that the link between the fluctuating velocity field of an isothermal jet and its radiated noise field had been finally quantified.

A similar exercise is now required for the dipole source that arises in hot jets, together with further refinements to the quadrupole source spectrum calculations (e.g. include noncompactness and temperature effects at $\theta_o = 90°$) which will probably lead to an improvement in the prediction accuracy. Once that is done, the calculation method could be incorporated into the UNIJET prediction program, in place of the present empirically determined master spectra.

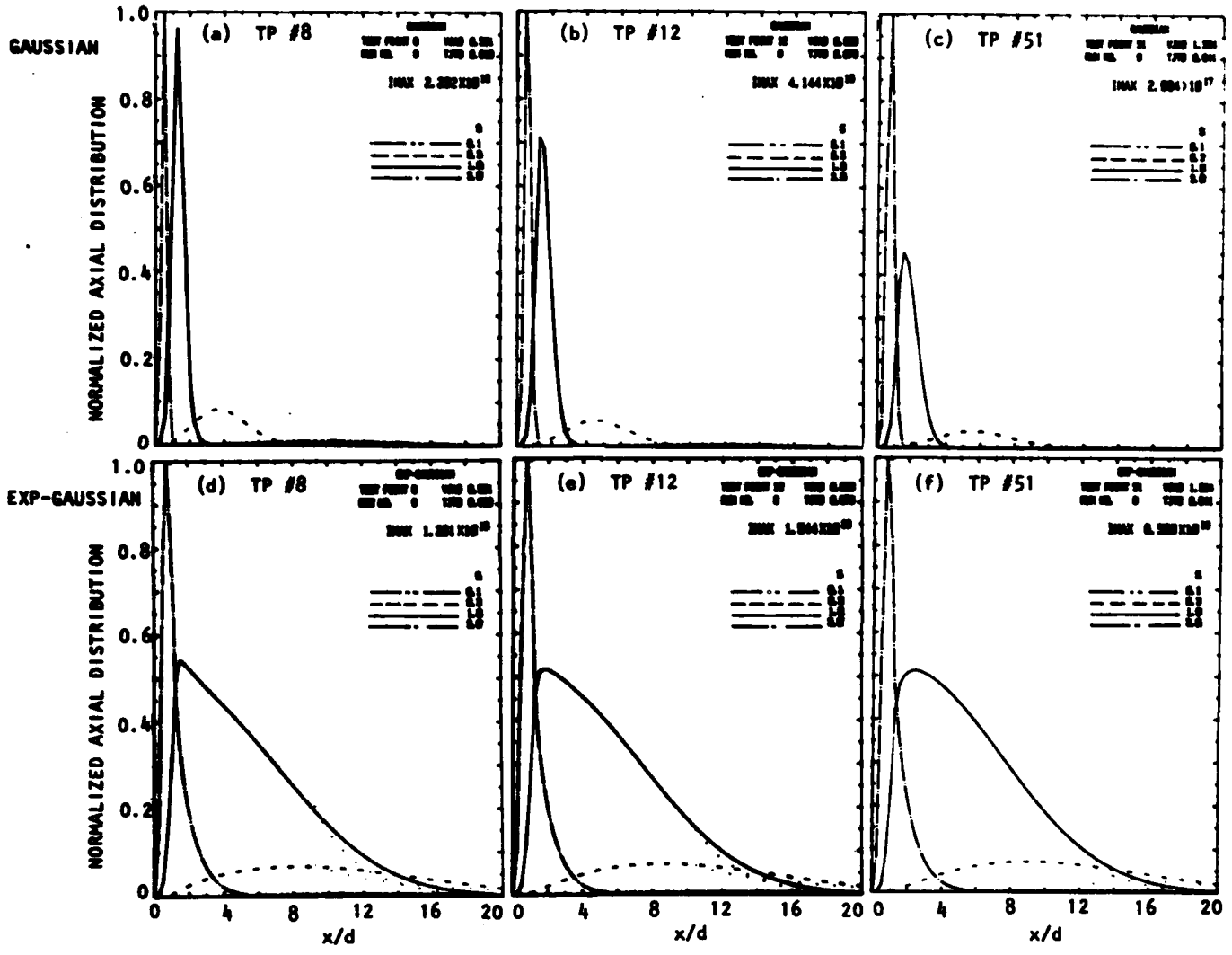

Figure 2.48 Calculated Axial Source Distributions at Different Strouhal Numbers in the Corresponding Spectra of Figure 2.47. Code: As in Figure 2.46.

2.5 THE JET MIXING NOISE PREDICTION METHODS

Three "small-scale" mixing noise prediction methods have been obtained from the Lilley equation solutions. The first and second are based on the high-frequency closed-form solutions and the third upon numeric solutions. Methods 1 and 2 are the result of a detailed, high-frequency analysis of our mixing noise data conducted at Lockheed in which parameters such as: the noise spectrum at 90° under isothermal conditions (or the quadrupole master spectrum), the eddy convection velocity, V_c, and other turbulence source parameters are *inferred* from the measured data. This approach serves three purposes: (1) it provides an efficient, accurate prediction method, unless the model is clearly inapplicable (in the present case at high speeds, small angles); (2) it allows *measurements* of turbulence parameters to be compared with values "implied" by the far-field noise data and (3) it links our results with earlier work, e.g. Ribner [2.3] where that has been the standard approach.

The third prediction method is *research oriented*, allowing specification of some or all of the important turbulence parameters and these are used with *numeric* solutions to Lilley's equation to calculate the far-field noise spectra. Although this third method has the advantage of being more "realistic," particularly at low frequencies, the disadvantage is that considerable computational time is required. (It is possible to specify turbulence data for the first two methods although it is expected that these are to be used for general prediction purposes where a minimum of information is available.)

2.5.1 The High-Frequency Jet Mixing Noise Prediction Methods (Methods 1 and 2)

These prediction methods are based upon the high-frequency solutions to the Lilley equation described in Sections 2.1.3 and 2.1.4 and a ring-source model for the quadrupole and dipole source distributions. For example, Equation (2-77) - with Equation (2-82) - leads almost directly to Equation (2-112) below for the quadrupole source component when the ring source assumption is employed (flow conditions at the ring source being denoted by subscript s). The other assumptions involved are discussed in Section 2.1.3; as usual the jet flow and surrounding medium (at constant pressure) are assumed to obey the laws for a perfect gas, that is $\rho_s/\rho_o = T_o/T_s$ and $a_s^2/a_o^2 = (\gamma_s T_s)/\gamma_o T_o)$.

The far-field noise spectrum in 1/3-octave bandwidths is given by the "dB-addition" of the SPL due to the quadrupole source, SPL_q, and that due to the dipole source, SPL_d. The calculation procedure for both methods is the same (1 and 2); only one of the source parameters is different.

2.5.1.1 The quadrupole source component

The 1/3-octave SPL of center frequency f, at a measurement point (R_m, θ_m) due to the quadrupole source component of the noise radiated by a jet, nozzle diameter d, exit velocity V_J and exit temperature T_J, exhausting into a stationary atmosphere at temperature T_o (speed of sound a_o) and a pressure of 14.7 psia, is given by

$$SPL_q = 10 \log_{10} I_q \qquad \textit{(Master spectrum at } R_r/d = 72\textit{)}$$

$$+ 10 \log_{10} \left(\frac{72}{R_r/d}\right)^2 \qquad \textit{(Inverse square law based on effective source location)}$$

$$+ 10 \log_{10} \left(\frac{V_J}{a_o}\right)^8 \qquad \textit{(Lighthill scaling law)}$$

$$+ 10 \log_{10} \left(\frac{1}{D_m{}^5}\right) \qquad \textit{(Ribner [2.3] - Ffowcs Williams [2.7] convective amplification)}$$

$$+ 10 \log_{10} \left| \frac{1}{\bar{D}_s{}^2} \frac{N_\infty}{(\bar{T}_s/\bar{T}_o)} \left[\cos^4\theta_o (1 + C_q) + 2|\kappa_s{}^2|\cos^2\theta_o + |\kappa_s{}^2|^2\right]\right| \qquad \textit{(High frequency Lilley equation solutions)} \qquad (2\text{-}112)$$

where I_q is the quadrupole master spectrum referred to a true measurement distance of 72 diameters ($R_r = 72d$) and C_q is the axial-axial quadrupole weighting or anisotropy coefficient such that $C_q = 0$ for the statistically isotropic (SI) quadrupole source model. In Methods 1 and 2, both I_q and C_q have values determined empirically for the Lockheed mixing noise data, as a function of the *modified Strouhal number* $S_m = D_m f d/V_J$ (see Section 2.5.1.3).

The radiation distance and polar angle (R_r, θ_o) are related to the measurement point coordinates (R_m, θ_m) by (see Figure 2.49)

$$R_r/d = \{(R_m/d)^2 + (x_s/d)^2 - 2(x_s/d)\ (R_m/d)\ \cos\theta_m\}^{\frac{1}{2}} \qquad (2\text{-}113)$$

$$\cos(\theta_o - \theta_m) = \{(R_m/d)^2 + (R_r/d)^2 - (x_s/d)^2\}/\{2(R_m/d)\ (R_r/d)\} \qquad (2\text{-}114)$$

where

$$x_s/d = \{0.057\ S_m + 0.021\ S_m{}^2\}^{-\frac{1}{2}}\ . \qquad (2\text{-}115)$$

The modified Doppler factor, D_m, is given by

$$D_m = \{D_c{}^2 + \beta^2 (V_J/a_o)^2\ \cos^2\theta_o + \alpha^2 (V_J/a_o)^2 \kappa_s{}^2\}^{\frac{1}{2}} \qquad (2\text{-}116)$$

and the square of the transverse (nondimensional) wavenumber by

$$\kappa_s{}^2 = \frac{D_s{}^2}{(\gamma_s/\gamma_o)\ (\bar{T}_s/\bar{T}_o)} - \cos^2\theta_o. \qquad (2\text{-}117)$$

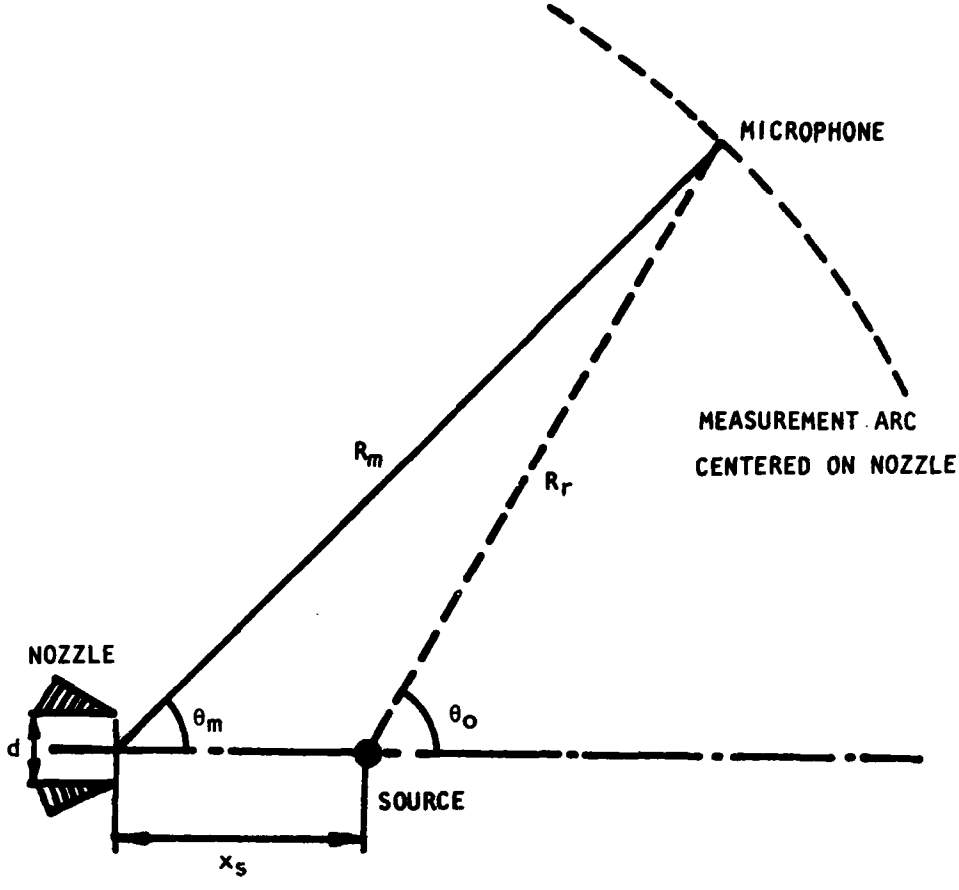

Figure 2.49 Definition of Angles Used in Analysis and Prediction of Jet Mixing Noise. Measurement Angle θ_m Differs from θ_o Because of Finite x_s/R_m.

The Doppler factors based on the eddy convection velocity V_c and the flow velocity in the source region V_s are defined as

$$D_c = 1 - V_c \cos\theta_o/a_o = 1 - \varepsilon_c V_J \cos\theta_o/a_o \qquad (2\text{-}118)$$

$$(\varepsilon_c \equiv V_c/V_J)$$

and

$$D_s = 1 - V_s \cos\theta_o/a_o = 1 - \varepsilon_s V_J \cos\theta_o/a_o. \qquad (2\text{-}119)$$

$$(\varepsilon_s \equiv V_s/V_J)$$

The transverse and axial noncompactness parameters are assumed to vary with the source region temperature, T_s, in the form

$$\alpha = \alpha_o \, (T_s/T_o)^p \qquad (2\text{-}120)$$

$$\beta = \beta_o \, (T_s/T_o)^q \, . \qquad (2\text{-}121)$$

In Methods 1 and 2, ε_c, ε_s, α_o, p, β_o and q have values determined empirically from the Lockheed mixing noise data (see Section 2.5.1.3).

The temperature ratio T_s/T_o is calculated with the empirical formulae

$$T_s/T_o = 1 + \{(T_s/T_o)_{max} - 1\}/(0.98 + 0.073/S_m^2)^{0.25} \qquad (2\text{-}122)$$

where the maximum value is given by

$$(T_s/T_o)_{max} = 1 + 0.6 \, (T_J/T_o - 1) + (V_J/a_o)^2 \, 0.2 \, (0.6 - 0.6^2). \qquad (2\text{-}123)$$

The ratio of specific heats is calculated from the expression

$$\gamma = 1.421 - (T/11800) + \exp\{-|T - 450|/200\}/80 \qquad (2\text{-}124)$$

where $T = T_s$ is used to obtain $\gamma = \gamma_s$ and $T = T_o$ to obtain $\gamma = \gamma_o$.

The "non-zero Doppler factor" $\tilde{D}_s$ is given by

$$\tilde{D}_s^2 = D_s^2 + \beta_c^2 \, (V_J \cos\theta_o/a_o)^2 \qquad (2\text{-}125)$$

with $\beta_c = 0.06$, as explained in Section 2.1.4.

Finally, the decay factor is defined as

$$N_\infty = 1 \qquad \text{if} \qquad \kappa_s^2 \geq 0 \qquad \textit{(Outside cone of silence)} \tag{2-126a}$$

$$N_\infty = \frac{0.392}{\{3(2A|\kappa_s^2|^{3/2}) + 1\}^{\frac{1}{2}}} \exp\left[-2A|\kappa_s^2|^{3/2}\right] \tag{2-126b}$$

if $2A|\kappa_s^2|^{3/2} > 0.6$, and in the intermediate region $0 < 2A|\kappa_s^2|^{3/2} < 0.6$ is given by

$X = 2A\|\kappa_s^2\|^{3/2}$	0.0	0.1	0.2	0.3	0.4	0.5	0.6
N_∞	1.0	0.59	0.4	0.28	0.2	0.158	0.128

(2-127c)

Outside the cone of silence† the last factor in Equation (2-112) can be simplified to $\{D_s^4/(\gamma_s T_s/\gamma_o T_o)^2 + C_q \cos^4\theta_o\}/(\tilde{D}_s^2 T_s/T_o)$ since $\kappa_s^2 \geq 0$; this is the form actually used in the prediction program (see Section 6) for angles outside the cone of silence.

The parameter A is defined as

$$A = -(2/3)k_o\delta_s\left[d(-\kappa^2)/d(r/\delta_s)\right]^{-1}_{r=r_T} \tag{2-128}$$

where

$$\left[\frac{d(-\kappa^2)}{d(r/\delta_s)}\right]_{r=r_T} = \cos^2\theta_o \left[\frac{d\phi}{dx}\right]_{r=r_T} \left\{ \frac{2}{(T_T/T_o)^{\frac{1}{2}}} \left(\frac{V_J}{a_o}\right) + \frac{1}{(T_T/T_o)} \left[\left(\frac{T_J}{T_o} - 1\right) + \frac{\gamma - 1}{2}\left(\frac{V_J}{a_o}\right)^2 (1 - 2\phi_T)\right]\right\} \tag{2-129}$$

and subscript T denotes evaluation at $r = r_T$; in deriving Equation (2-129) the temperature profile equation (2A-13) has been used with $V_{max} = V_J$, that is, only "initial mixing region" profiles are assumed.

The value of $\phi_T \equiv V_T/V_J$ is obtained by solving a quadratic equation for V_T/V_s:

$$\phi_T = \frac{V_T}{V_s}\frac{V_s}{V_J} \equiv \frac{V_T}{V_s}\epsilon_s \tag{2-130}$$

---

†*This terminology is borrowed from geometric acoustics and is used only to describe the condition $\kappa_s^2 \geq 0$; it does <u>not</u> imply that there is a real cone of silence when $\kappa_s^2 \leq 0$.*

where

$$V_T/V_s = [a_1 - \{a_1^2 - 4\, a_2 a_3\}^{\frac{1}{2}}]/2a_2 \tag{2-131}$$

$$a_1 = 2\varepsilon_s (V_J/a_o)/\cos\theta_o + (T_s/T_o - 1) + \varepsilon_s^2 (V_J/a_o)^2\ (\gamma - 1)/2 \tag{2-132}$$

$$a_2 = \varepsilon_s^2\, (V_J/a_o)^2\ (\gamma + 1)/2 \tag{2-133}$$

$$a_3 = \tan^2\theta_o\ . \tag{2-134}$$

In Equations (2-129), (2-132), and (2-133), a constant value is used for $\gamma = 1.4$.

Given ϕ_T, χ_T is found (by iteration) from†

$$\phi = 0.5\ \{1 - \text{erf}\ (\sqrt{\pi}\chi)\} \tag{2-135}$$

and the gradient required in Equation (2-129) follows immediately from

$$\frac{d\phi}{d(r/\delta_s)} = \frac{d\phi}{d\chi} = -\ \exp\ (-\pi\chi^2) \tag{2-136}$$

The frequency parameter $k_o\delta_s$ in Equation (2-128) can be written either as

$$k_o\delta_s = \left(\frac{\omega_m\delta_s}{V_J}\right)\left(\frac{V_J}{a_o}\right)\frac{1}{D_m} \tag{2-137}$$

or as

$$k_o\delta_s = \pi S_m \left(\frac{\delta_s}{r_J}\right)\left(\frac{V_J}{a_o}\right)\frac{1}{D_m}\ . \tag{2-138}$$

The former was used in the high-frequency analysis of the Lockheed mixing noise data, $\omega_m\delta_s/V_J$ being the "empirical parameter" for which values were inferred from the measured data at each modified Strouhal number. The latter form allows a more direct physical interpretation since δ_s/r_J is the normalized vorticity thickness of the shear layer of maximum sound emission at a given modified Strouhal number (see Section 2.5.1.3).

The transition radius temperature ratio T_T/T_o in Equation (2-129) is evaluated from Equation (2A-13) with $\phi = \phi_T$, $V_{max} = V_J$, $T_j = T_J$ and $\gamma = \gamma_o$.

---

†*The error function (erf) is calculated with the rational approximation 7.1.27 of reference* [2.19].

2.5.1.2 The dipole source component

The 1/3-octave sound pressure level at a measurement point (R_m, θ_m) due to the dipole source component is given by

$$SPL_d = 10 \log_{10} \left| I_d \left(\frac{72}{R_r/d}\right)^2 \cdot \left(\frac{V_J}{a_o}\right)^6 \left(\frac{1}{D_m}\right)^3 \left(\frac{T_s - T_o}{T_s}\right)^2 \right|$$

$$+ 10 \log_{10} \left| \frac{1}{\tilde{D}_s^2} \frac{N_\infty}{(T_s/T_o)} [\cos^2\theta_o (1 + C_d) + |\kappa_s^2|] \right| \qquad (2\text{-}139)$$

where I_d is the dipole master spectrum referred to a true measurement distance of 72 diameters and C_d is the axial dipole weighting or anisotropy coefficient such that $C_d = 0$ for the statistically isotropic (SI) dipole source model. In Methods 1 and 2, both I_d and C_d have values determined empirically from the Lockheed mixing noise data, as a function of the modified Strouhal number, S_m. All the other parameters in Equation (2-139) are defined above under the quadrupole source heading. Outside the cone of silence, the last factor in Equation (2-139) reduces to $\{D_s^2/(\gamma_s T_s/\gamma_o T_o) + C_d \cos^2\theta_o\}/(\tilde{D}_s^2 T_s/T_o)$ since $\kappa_s^2 \geq 0$; this is the form actually used in the prediction program (see Section 6) for angles outside the cone of silence.

2.5.1.3 Determination of empirical parameters

The empirical parameters in the equations given above have been determined from the Lockheed mixing noise data, along the lines followed by Szewczyk [2.11]. These inferred parameters describe in effect the statistical properties of the turbulence source function; on the other hand, the mean flow properties in the source region (V_s, T_s) and the location of the source region (x_s) are *assumed* known at the outset. That is, x_s is calculated from Equation (2-115) which is based on the Laufer data (see Figure 2.21), while V_s is determined from LV data and data published elsewhere (e.g. Bradshaw et al. [2.18], Witze [2.22]); the assumed values of x_s and V_s are given in Table 2.13. The source region temperature is calculated from Equations (2-122) and (2-123) as discussed in Appendix 2A.

Data Analysis Outside the Cone of Silence. The (isothermal) transverse noncompactness parameter α_o is determined from the isothermal data ($T_J/T_o \doteq 1$, see Figure 2.50). At $\theta_o = 90°$ the modified Doppler factor reduces to (with γ_s/γ_o set equal to unity)

$$D_m = \{1 + (\alpha V_J/a_o)^2 (T_o/T_s)\}^{\frac{1}{2}} \qquad (2\text{-}140)$$

so the predicted quadrupole mean velocity dependence is

$$I_{90°} \propto \left(\frac{T_o}{T_s}\right)^3 \left(\frac{V_J}{a_o}\right)^8 \frac{1}{\{1 + (\alpha V_J/a_o)^2 (T_o/T_s)\}^{5/2}} \qquad (2\text{-}141)$$

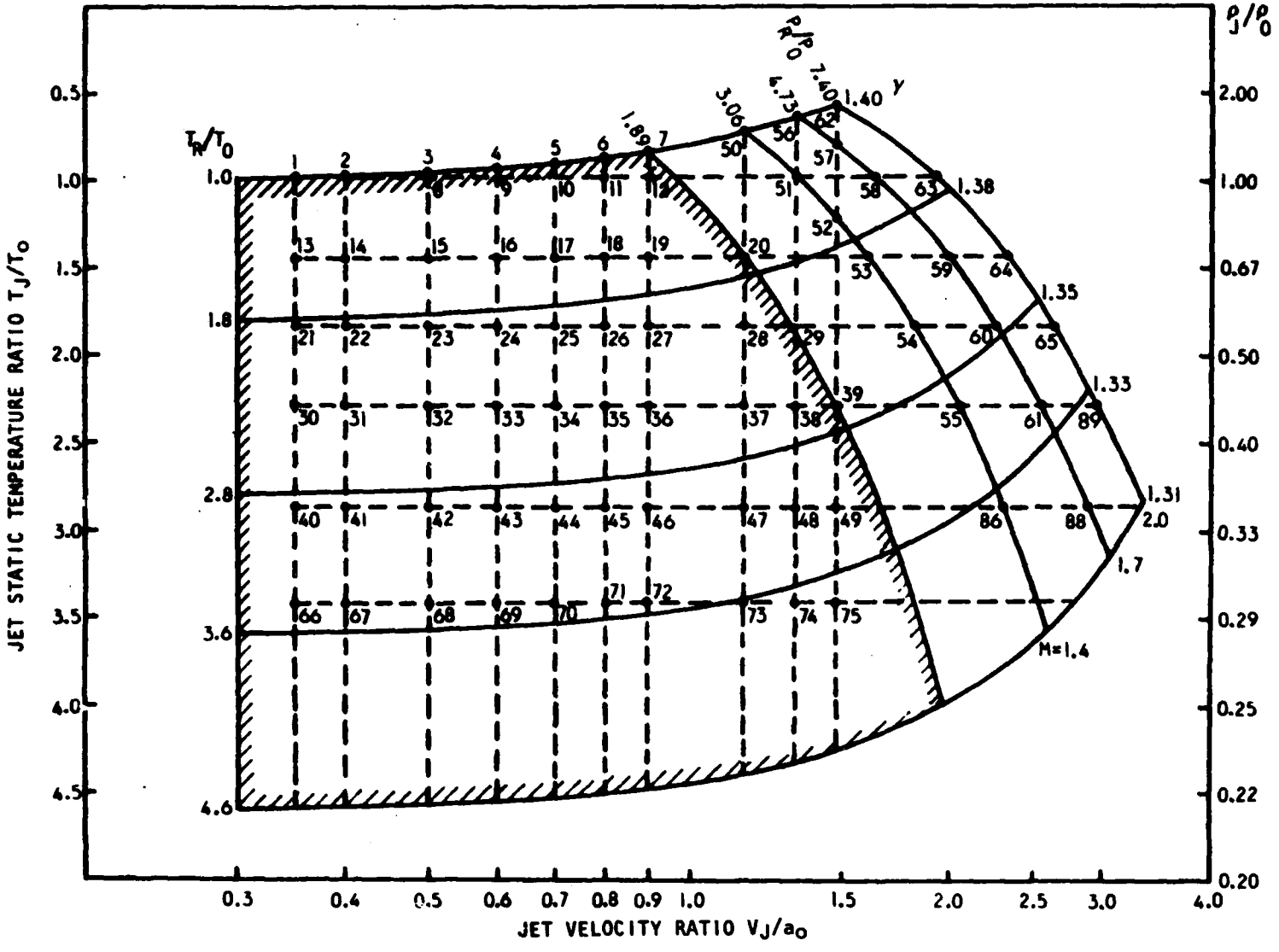

Figure 2.50 Range of Jet Exit Conditions Covered by Lockheed Jet Mixing Noise Program [2.14]

S_m	x_s/d	$\varepsilon_s \equiv V_s/V_J$
0.0316	23.4	0.32
0.04	20.8	0.36
0.05	18.6	0.40
0.063	16.5	0.44
0.08	14.6	0.47
0.1	13.0	0.50
0.125	11.6	0.52
0.16	10.2	0.54
0.2	9.0	0.56
0.25	8.0	0.57
0.316	7.1	0.58
0.4	6.2	0.585
0.5	5.4	0.59
0.63	4.8	0.595
0.8	4.1	0.598
1.0	3.6	0.6
1.25	3.1	0.6
1.6	2.6	0.6
2.0	2.2	0.6
2.5	1.9	0.6
3.16	1.6	0.6
4.0	1.3	0.6
5.0	1.1	0.6
6.3	1.0	0.6
8.0	0.7	0.6
10.0	0.6	0.6
12.5	0.5	0.6
16.0	0.4	0.6

Table 2.13 Assumed values of axial source location (x_s) and source region flow velocity (V_s) for high-frequency analysis of Lockheed mixing noise data.

S_m	10 $\log_{10} I_q$	$\varepsilon_c \equiv V_c/V_J$	C_q	10 $\log_{10} I_d$	C_d
0.0316	70.5	1.0	7.0	82.0	15.0
0.04	73.5	1.0	5.0	84.4	10.0
0.05	75.5	1.0	4.0	86.6	10.0
0.063	78.0	1.0	3.0	88.8	7.5
0.08	79.9	1.0	3.0	91.0	6.0
0.1	81.5	1.0	2.3	93.1	4.5
0.125	83.1	1.0	1.5	95.2	3.0
0.16	84.6	1.0	1.0	97.0	1.7
0.2	86.2	0.9	1.0	98.3	1.3
0.25	87.7	0.8	1.2	99.4	1.0
0.316	89.0	0.73	1.2	100.1	0.8
0.4	90.0	0.68	1.0	100.6	0.6
0.5	90.7	0.65	0.9	101.0	0.3
0.63	91.3	0.63	0.7	101.1	0.2
0.8	91.8	0.6	0.6	101.0	0.0
1.0	92.1	0.6	0.3	100.6	-.15
1.25	92.1	0.6	0.1	100.0	-.2
1.6	92.0	0.6	0.0	99.3	-.3
2.0	91.9	0.6	-.15	98.5	-.3
2.5	91.7	0.6	-.25	97.6	-.4
3.16	91.4	0.6	-.4	96.6	-.4
4.0	90.8	0.6	-.4	95.8	-.5
5.0	90.3	0.6	-.5	94.9	-.55
6.3	89.7	0.6	-.55	94.0	-.6
8.0	89.2	0.6	-.6	93.0	-.62
10.0	88.6	0.6	-.65	92.0	-.62
12.5	88.1	0.6	-.7	91.0	-.65
16.0	87.5	0.6	-.7	90.0	-.7

Table 2.14 Convection velocities (V_c), quadrupole and dipole master spectra (I_q, I_d) and anisotropy coefficients (C_q, C_d) inferred from Lockheed mixing noise data.

Depending on the choice of α, the velocity variation at 90° for each Strouhal number will be more or less closely matched by the predicted scaling law; a value of $\alpha = 0.2$ was found to be a reasonable, optimum value or, more precisely, the value $\alpha_o = 0.2$ was adopted for prediction methods 1 and 2. It must be noted at this stage that an *alternative explanation* of deviations from the V_J^8 law exhibited by the measurement acoustic data is the Mach number dependence of the turbulence intensity and other parameters [see Section 2.4, Equations (2-109) and (2-110)] uncovered by the LV turbulence measurements. This is largely confirmed in Section 2.4 where transverse noncompactness effects are neglected but the Mach number dependence of the turbulence parameters which control the quadrupole radiation is sufficient to produce, approximately, the correct dependence on V_J up to $V_J/a_o \approx 1.4$. (When the absolute *dipole* spectrum levels can be calculated with the same accuracy, prediction methods 1 and 2 could be revised to incorporate the turbulence intensity variation etc., and the value of α_o would be either revised or a value could be calculated from the measured turbulence data.) However, at present *no* turbulence variations with Mach number are included in the predicton methods; e.g. the classical V_J^2 scaling law is assumed for the quadrupole source strength.

At angles other than $\theta_o = 90°$, the modified Doppler factor D_m depends additionally on the parameter β (which allows for axial noncompactness of the sources) and the convection velocity ratio ε. Optimum values have been determined from the rear-arc isothermal data outside the cone of silence: $\beta_o = 0.55$ for all Strouhal numbers, while $\varepsilon_c (= V_c/V_J)$ varies as shown in Figure 2.51a and in Table 2.14. It is encouraging that ε_c as determined from far-field noise measurements lies in the commonly accepted range based on turbulence measurements, except perhaps at the lowest Strouhal numbers. Here, the optimum values of ε_c exceeded unity but the maximum value adopted for prediction purposes was $\varepsilon_c = 1$.

The isothermal rear-arc data analysis also yields the quadrupole anisotropy coefficient C_q and master spectrum I_q (as a function of S_m) as shown in Figures 2.51b and 2.51c and in Table 2.14.

In a similar fashion the *temperature* dependence on the noncompactness parameters α and β, represented by p and q in Equations (2-120), (2-121), was determined from the non-isothermal Lockheed mixing noise data, respectively, at $\theta_o = 90°$ and at rear-arc angles outside the cone of silence. The optimum values were found to be $p = 1.2$, $q = 0.2$. Again, any variation of quadrupole or dipole source strength scaling with temperature (i.e. apart from that already specified for the dipole source) is not incorporated in the prediction methods. In this case, trends in the measured LV data, e.g. turbulence intensity variation with temperature, are not so pronounced and furthermore the *dipole* source strength is a function of the turbulent density and pressure fluctuations, quantities not included in the flow measurement program.

It should be emphasized that the dipole and quadrupole source components are both assumed to have the same noncompactness parameters, that is, ε_c, α and β.

The non-isothermal rear-arc data analysis also yields the dipole anisotropy coefficient C_d and master spectrum I_d as shown in Figures 2.51b and 2.51c and in Table 2.14.

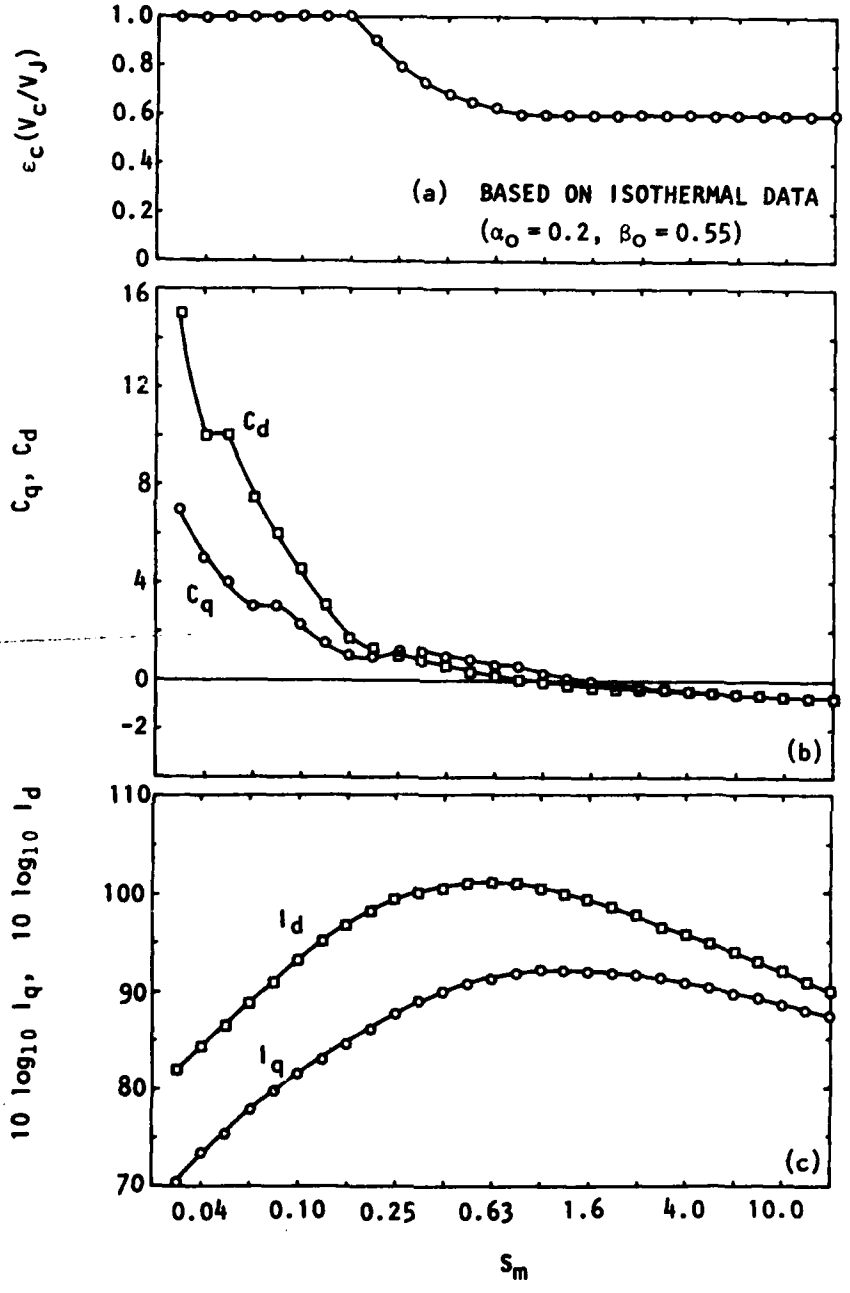

Figure 2.51 Dependence of (a) Source Convection Velocity Ratio $\varepsilon_c (= V_c/V_j)$, (b) Quadrupole ($C_q$) and Dipole ($C_d$) Anisotropy Coefficients, (c) Master Spectra of Quadrupole (I_q) and Dipole (I_d) Sources on Modified Strouhal Number S_m.

To summarize, the transverse and (moving-frame) axial noncompactness parameters have been empirically determined as

$$\alpha = 0.20\ (T_s/T_o)^{1.2} \tag{2-142}$$

$$\beta = 0.55\ (T_s/T_o)^{0.2} \tag{2-143}$$

and ε_c, C_q, l_q, C_d and l_d are given in Table 2.14.

Data Analysis Inside the Cone of Silence. Outside the cone of silence ($\kappa_s^2 \geq 0$) the factor N_∞ (the "shielding factor") in Equation (2-112) is unity and the shear layer thickness (δ_s) – in the high-frequency limit – cannot influence the far-field sound pressure. The shear layer thickness parameter is determined from measured data *inside* the cone of silence by assuming (1) that all of the other parameters remain unchanged in this angular region and (2) δ_s is only a function of S_m (as with all the other parameters but the assumption is possibly more critical in this case as will be illustrated below). Inferred values of δ_s are given in Table 2.15, normalized by the nozzle radius r_J although in the prediction program (Section 6) it is $\omega_m\delta_s/V_J \equiv \pi S_m(\delta_s/r_J)$ which is stored as empirical data.

It is these empirically determined δ_s values which distinguish Method 1 from Method 2, as indicated in Table 2.15. The first set (Method 1) were obtained from the measured data at subsonic conditions ($V_J/a_o < 1$), since these data collapse in a convincing manner inside the cone of silence (at radiation angles greater than or equal to 30°) against these scaling laws based on *approximate* high-frequency solutions to Lilley's equation. The second set (Method 2) were obtained from all the test points, supersonic as well as subsonic and even though the data do not collapse as well as with the subsonic data alone, the resulting Method 2 does yield more acceptable predictions than Method 1 over the whole velocity range. On the other hand, the inferred δ_s/r_J values for Method 2 do not line up as well with far-field source location data as do those of Method 1, especially in the case of isothermal jets. Values of δ_s/r_J implied by source location data are shown for comparison in Table 2.15; these have been calculated from Equation (2-115) and Equations (2A-8) or (2A-11) with the assumption† that $\delta_s \propto (T_J/T_o)^{\frac{1}{4}}$. All three sets of δ_s/r_J values are compared for the isothermal case in Figure 2.52a ($T_J/T_o \doteq 1$) and for the medium temperature case $T_J/T_o \doteq 2.2$ in Figure 2.52b. The actual temperature dependence of Method 1 – δ_s values is shown in Figure 2.53.

The first of these methods is therefore physically justified – at least with regard to δ_s values at medium to high Strouhal numbers – whereas the second method, or average yields better predictions, as illustrated below. A physical interpretation of the smaller δ_s values used in Method 2 is suggested at the end of Section 2.5.3.4.

---

†*Szewczyk [2.11] suggested that this temperature dependence could be used to collapse the inferred values of δ_s; here it is adopted as an (unverified) scaling law for δ_s as implied by far-field source location data.*

S_m	T_J/T_o = 0.980			T_J/T_o = 1.770			T_J/T_o = 2.209			T_J/T_o = 3.330		
	1	2	Source Location	1	2	Source Location	1	2	Source Location	1	2	Source Location
0.0316	1.11	0.10	4.51	1.11	0.81	5.23	1.11	2.01	5.53	1.11	2.52	6.13
0.04	1.11	0.08	4.08	1.11	0.72	4.73	1.11	1.75	5.00	1.11	2.23	5.54
0.05	1.15	0.06	3.72	1.15	0.70	4.31	1.15	1.59	4.55	1.15	2.04	5.04
0.063	1.16	0.05	3.38	1.16	0.61	3.92	1.26	1.41	4.14	1.26	1.82	4.59
0.08	1.23	0.04	3.07	1.23	0.60	3.55	1.39	1.23	3.76	1.39	1.79	4.16
0.1	1.43	0.03	2.81	1.43	0.73	3.25	1.59	1.24	3.44	1.59	1.81	3.81
0.125	1.66	0.13	2.57	1.66	0.81	2.98	1.78	1.35	3.15	1.96	1.91	3.49
0.16	1.69	0.26	2.34	1.69	0.90	2.71	1.89	1.39	2.87	2.19	1.89	3.18
0.2	1.75	0.48	2.16	1.75	1.03	2.50	1.99	1.51	2.64	2.39	1.99	2.93
0.25	1.72	0.66	1.99	1.72	1.15	2.30	1.97	1.59	2.44	2.36	2.04	2.70
0.316	1.61	0.81	1.83	1.61	1.21	2.12	1.91	1.61	2.24	2.27	2.01	2.48
0.4	1.47	0.84	1.62	1.47	1.19	1.87	1.79	1.55	1.98	2.19	1.87	2.19
0.5	1.40	0.83	1.42	1.43	1.15	1.65	1.75	1.43	1.74	2.07	1.72	1.93
0.63	1.29	0.76	1.24	1.36	1.06	1.44	1.64	1.29	1.52	1.92	1.52	1.69
0.8	1.19	0.70	1.08	1.25	0.94	1.25	1.49	1.13	1.32	1.71	1.31	1.46
1.0	1.05	0.60	0.94	1.11	0.81	1.08	1.34	0.97	1.15	1.51	1.15	1.27
1.25	0.92	0.52	0.81	1.01	0.69	0.94	1.17	0.84	0.99	1.32	0.98	1.10
1.6	0.77	0.43	0.69	0.86	0.58	0.80	0.99	0.70	0.84	1.10	0.82	0.93
2.0	0.65	0.37	0.59	0.75	0.48	0.68	0.85	0.59	0.72	0.93	0.68	0.80
2.5	0.57	0.31	0.50	0.64	0.40	0.58	0.72	0.50	0.61	0.78	0.57	0.68
3.16	0.48	0.25	0.42	0.53	0.33	0.49	0.60	0.41	0.51	0.64	0.47	0.57
4.0	0.41	0.21	0.35	0.44	0.27	0.40	0.50	0.34	0.43	0.54	0.38	0.47
5.0	0.34	0.17	0.29	0.37	0.23	0.34	0.42	0.28	0.36	0.45	0.32	0.39
6.3	0.28	0.14	0.24	0.31	0.19	0.28	0.34	0.23	0.29	0.37	0.26	0.32
8.0	0.23	0.11	0.19	0.25	0.15	0.23	0.28	0.19	0.24	0.30	0.22	0.26
10.0	0.19	0.09	0.16	0.20	0.12	0.19	0.23	0.15	0.20	0.25	0.18	0.22
12.5	0.15	0.08	0.13	0.17	0.10	0.15	0.19	0.13	0.16	0.20	0.14	0.18
16.0	0.12	0.06	0.10	0.13	0.08	0.12	0.15	0.10	0.13	0.16	0.12	0.14

Table 2.15 Inferred shear layer thickness values δ_s/r_J from (1) *subsonic* mixing noise data (2) all data; third column gives values implied by far-field source location data multiplied by $(T_J/T_o)^{\frac{1}{2}}$.

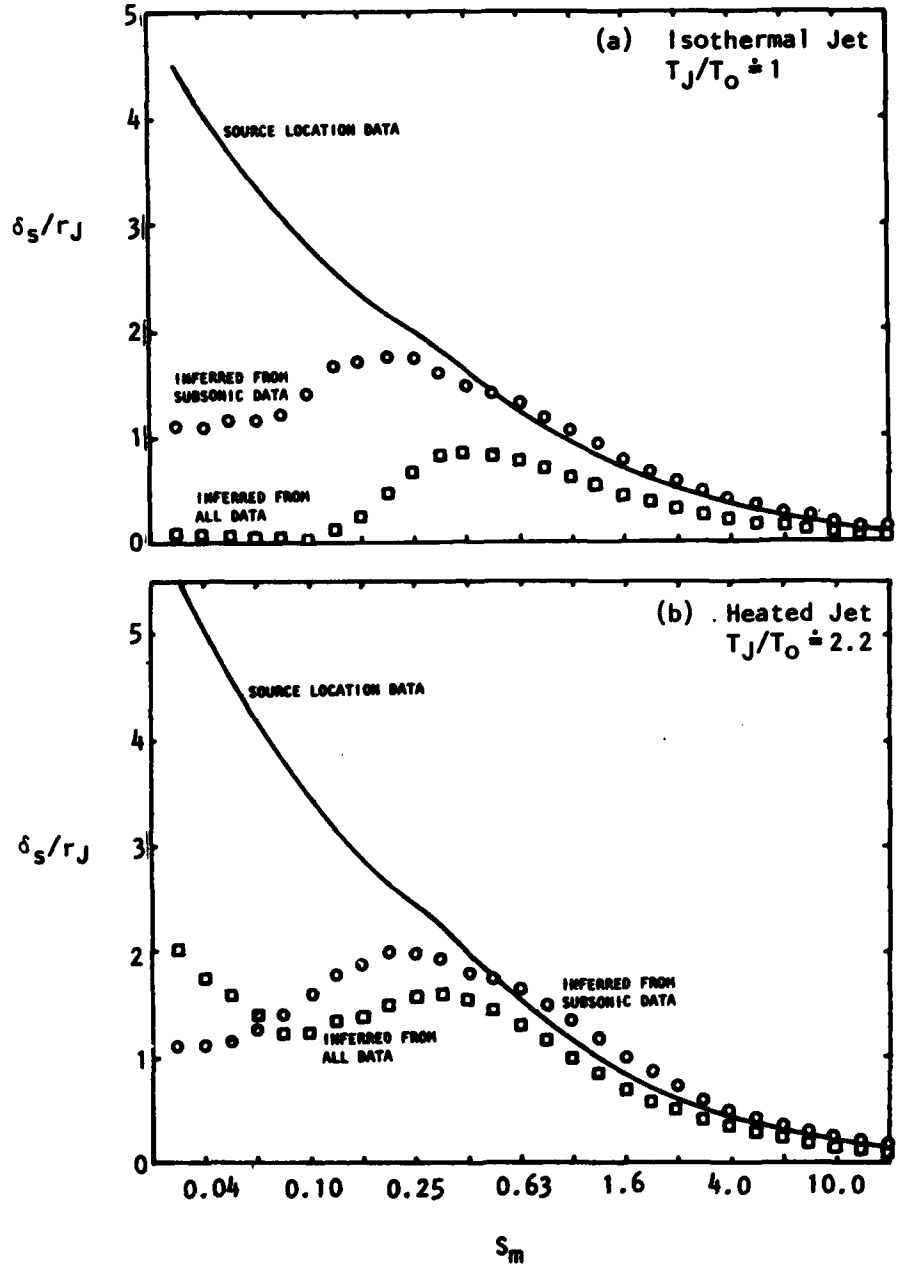

Figure 2.52 Shear Layer Thickness $_s$ at Source Position as a Function of Modified Strouhal Number S_m; ——— as Implied by Far-Field *Source Location* Data;
o Inferred from Subsonic Mixing Noise Data;
□ Inferred from All Mixing Noise Data.

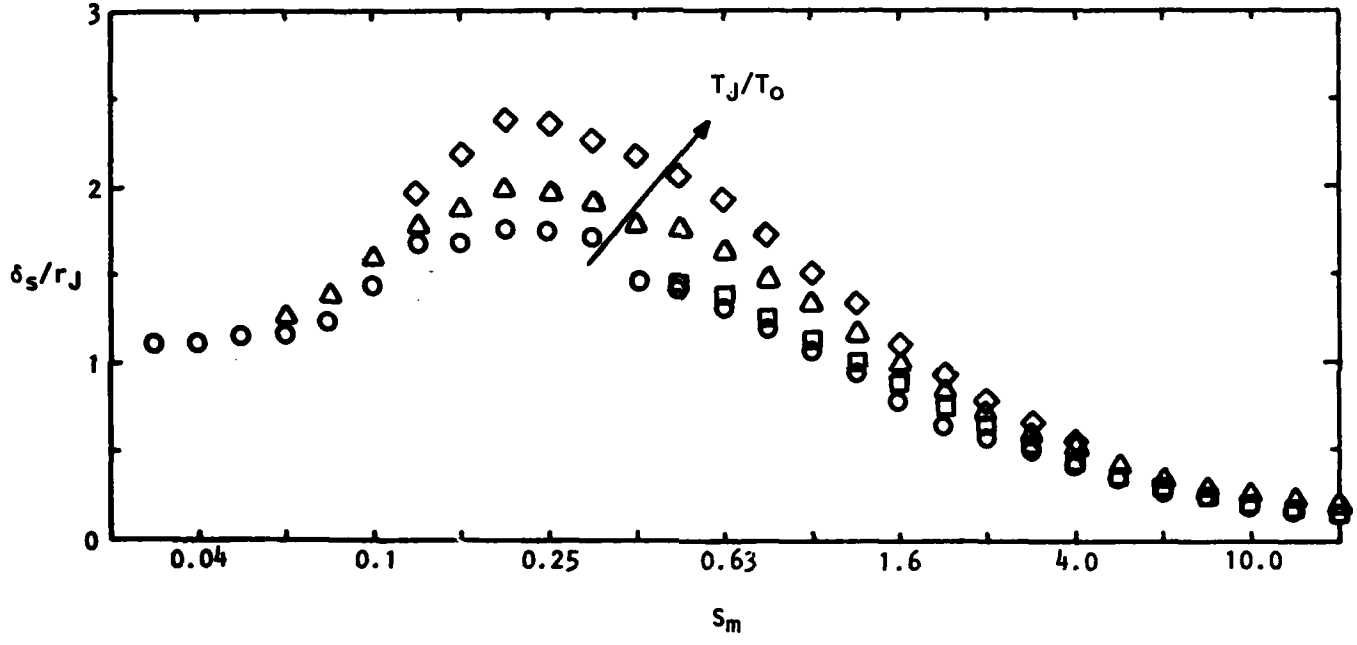

Figure 2.53 Variation with Temperature of Shear Layer Thickness Values Inferred from Subsonic Mixing Noise Data. Code: O , $T_J/T_o \doteq 1$; □ 1.8; △ 2.2; ◇ 3.3.

It should be emphasized that N_∞, the exponential decay or shielding factor, is evaluated with Equations (2-126b) through (2-137) assuming an "initial mixing region" (error function) velocity profile [Equation (2-135)]. In fact, Szewczyk [2.11] was able to modify these equations to include the effect of centerline velocity decay ($V_{max} \neq V_J$) although the velocity profile shape was *not* changed. Bearing in mind that this exercise was performed with the earlier displacement-source model, the effect of centerline velocity decay on values of δ_s inferred from the Lockheed mixing noise data is shown in Table 2.16, with δ_s given in the two forms, normalized by V_J/ω_m and r_J.

S_m	V_{max}/V_J	No Decay $\omega_m\delta_s/V_J$	Decay $\omega_m\delta_s/V_J$	No Decay δ_s/r_J	Decay δ_s/r_J
0.1	0.58	0.67	0.45	2.13	1.43
0.125	0.65	0.80	0.50	2.04	1.27
0.16	0.74	0.95	0.70	1.89	1.39
0.2	0.82	1.18	0.90	1.88	1.43
0.25	0.90	1.43	1.20	1.82	1.53
0.316	0.95	1.70	1.55	1.71	1.56
0.4	0.99	2.00	1.90	1.59	1.51

Table 2.16 Comparison of shear layer thickness parameter values inferred with (1) $V_{max} = V_J$ (no decay) and (2) V_{max}/V_J as given in second column (decay).

It is clear from Table 2.16 that the inferred δ_s/r_J values are even more unrealistic when the centerline velocity decay is included.† The question remains whether the velocity profile *shape* would have any significant influence on inferred values of δ_s at low Strouhal numbers. A comparison of the values of $[d\phi/d(r/\delta_s)]_{r=r_T}$ obtained from each profile shape at one typical value of r_T indicates that this may not be a significant effect. That is, when $r_T = r_{\frac{1}{2}}$ – the half-velocity point where $V/V_{max} = 0.5$ – the gradient of the error function profile Equation [(2A-1]

$$\frac{d\phi}{d(r/\delta_s)} \equiv \frac{d\phi}{d\chi} = -\exp(-\pi\chi^2) \tag{2-144}$$

yields a value of -1 since $\chi \equiv (r - r_{\frac{1}{2}})/\delta_s = 0$, and the gradient of the Gaussian profile [Equation (2A-4)]

$$\frac{d\phi}{d(r/\delta_s)} = -e\left(\frac{r}{\delta_s}\right)\exp\{-(r/\delta_s)^2\,(e/2)\} \tag{2-145}$$

yields a value $-\sqrt{(e/2)\ell n 2} \doteq -0.97$ since

†*In fact, Szewczyk [2.11] uses the original no-decay values in the figures of his thesis.*

$$\frac{r_{\frac{1}{2}}}{\delta_s} = \sqrt{\frac{2}{e}\ \ell n\ 2} \qquad (2\text{-}146)$$

which differs by only 3% from the error function profile gradient.

2.5.1.4 Comparison of inferred noncompactness parameter values with measured turbulence data

Length and Time Scales. According to the results of Section 2.1.3, which are based on the assumption that each coherence length scale is much smaller than the corresponding power spectral density length scale, the noncompactness parameters α_o and β_o are related to the coherence length and time scales – under isothermal conditions – through Equations (2-61) and (2-116), by

$$\alpha_o = \frac{1}{\sqrt{\pi}}\ \frac{L_t}{\tau_o V_J} \qquad (2\text{-}147)$$

$$\beta_o = \frac{1}{\sqrt{\pi}}\ \frac{L_x}{\tau_o V_J} \qquad (2\text{-}148)$$

Two alternative expressions for L_t and L_x are derived from the measured (LV) turbulence data and one for τ_o which is Mach number dependent; in the zero Mach number limit Equation (2-110e) yields

$$\tau_o = x/1.386\ V_J \qquad (2\text{-}149)$$

and in the first alternative (the simplest case) the length scales are given by [Equations (2-110d), (2-110b)]

$$L_t = 0.06\ x \qquad (2\text{-}150)$$

and

$$L_x = 0.12\ x \qquad (2\text{-}151)$$

from which we obtain

$$\alpha_o = \frac{1}{\sqrt{\pi}}\ (0.06)\ (1.386) \doteq 0.05\ (0.20) \qquad (2\text{-}152)$$

$$\beta_o = \frac{1}{\sqrt{\pi}}\ (0.12)\ (1.386) \doteq 0.09\ (0.55) \qquad (2\text{-}153)$$

The figures in brackets are those inferred from the far-field noise data with our high-frequency analysis, as described above.

The alternative expressions for the length scales

$$L_t = 0.028\,x + 0.28 \quad (\triangleq 0.25d) \tag{2-154}$$

$$L_x = 0.042\,x + 0.48 \quad (\triangleq 0.40d) \tag{2-155}$$

evaluated at $x = 4d$, for example, are almost identical to those given above and hence the above comparison is essentially unchanged.

If the Mach number dependence of τ_o is evaluated at the highest possible value ($M_J = 1.7$ in the Lockheed mixing noise data), the measured and inferred values still differ by a factor of two.

Ffowcs Williams [2.7] recommended the values $\alpha_o \triangleq 0.04$, $\beta_o \triangleq 0.13$ based on turbulence data available at the time which correspond closely to values obtained above from LV data. Ribner [2.23], on the other hand, assumed that $\alpha_o = \beta_o$ and obtained a value of 0.28 from his analysis of the far-field acoustic data. This falls between our inferred values of $\alpha_o = 0.2$, $\beta_o = 0.55$.

The significant difference between turbulence-based noncompactness parameter values and those inferred from the mixing noise data lends weight to the idea that noncompactness effects are only partly responsible for the observed deviation from the V_J^8 law. Possibly, a more important effect is the Mach number dependence of the turbulence intensity and, as shown in Section 2.4, when this is taken into account, together with the Mach number dependence of other parameters such as the time scale, the velocity dependence of radiated spectrum levels at 90° can be predicted fairly accurately *without* transverse noncompactness effects. Thus, if the high-frequency analysis were to be repeated and the above factors incorporated, it is likely that α_o and β_o would be somewhat smaller and probably much closer to their turbulence-based values.

2.5.2 Comparison of Jet Mixing Noise Prediction Methods 1 and 2 with Lockheed Measured Data

Since Methods 1 and 2 rely quite extensively on parameters determined from the Lockheed mixing noise data, the comparison that follows, it could be argued, only serves as a check on the original analysis. While it is true that comparisons serve the non-trivial purpose of checking the extensive data processing involved (e.g. there are 3711 data points outside the cone of silence over the range $0.1 \leq S_m \leq 3.16$) three points must be emphasized. First, the mean velocity and mean temperature scaling laws assigned to the noise source strengths in these prediction methods are not arbitrary but follow more or less directly from a dimensional analysis of the (extended) Lighthill aerodynamic noise analogy [2.5]. Second, the convective amplification factors (D_m^{-5}, D_m^{-3}) although arising from an apparently arbitrary, i.e. convenient choice of source correlation function (or of axial-wavenumber frequency spectrum) only contain parameters that can be directly related to the statistical properties of the turbulence. Finally, the most recent development (and therefore possibly over-emphasized to some degree), the prediction of acoustic-mean flow interaction effects is described by either numerical or

approximate closed-form solutions to an inhomogeneous differential equation based on a parallel flow description of the jet mean flow field.

Thus, the prediction methods described in this report have *not* been derived from a blind curve-fitting exercise, involving arbitrary functions and adjustable constants (e.g. the density exponent of the SAE method [2.20]) which, to our knowledge, has not been assigned any physical meaning. As a consequence, the *quality* of our prediction accuracy implies a certain degree of physical understanding and it also follows that the methods described here can be used in a logical fashion as building blocks for the prediction of noise from more complex flows such as coannular jets, provided, of course, the prediction is successful for the single round jet.

A comprehensive set of comparisons between (Lockheed) measured and predicted mixing noise spectra is presented in Figures 2.54 through 2.85. Table 2.17 specifies the test conditions covered in these results, which fall into three parts: isothermal ($T_J/T_O \doteq 1$) Figures 2.54 through 2.63, medium temperature ($T_J/T_O \doteq 2.2$) Figures 2.64 through 2.75, and high temperature ($T_J/T_O \doteq 3.3$) Figures 2.76 through 2.85. Within each part the velocity ratio is varied between $V_J/a_O \doteq 0.5$ and the supersonic values, 1.95, 2.01 and 1.42, respectively. Each figure consists of measured and predicted spectra at the observer or measurement angles $\theta_m = 30°$, 45°, 60°, 75° and 90° (observer distance $R_m = 72d$). Three calculated spectra are shown in each case, that is, the quadrupole component, the dipole component and the (incoherent) sum of these two components – the predicted spectrum. For each test point the comparison is shown with both Method 1 and 2 predictions; results are given at all angles although the methods only differ inside the cone of silence.

The prediction quality of Method 1 is excellent at all subsonic velocities ($V_J/a_O < 1$) and, with the exception of angles $\theta_m = 30°$ and 45° at supersonic velocities also. At those angles, once the velocity ratio exceeds unity, the prediction accuracy of Method 1 begins to deteriorate, although it does not degrade uniformly with V_J/a_O. For example, consider the isothermal conditions at the smallest angle $\theta_m = 30°$: the errors are largest when $V_J/a_O = 1.65$ (Figure 2.60) and reduce somewhat at the highest velocity ($V_J/a_O = 1.95$, Figure 2.62). Of course, it is at these supersonic conditions ($\theta_m \leq 45°$), it can be argued, that the direct radiation from the large-scale structure is expected to be significant (see Sections 3 and 6), but for a number of reasons, it is desirable to press the small-scale prediction methodology to its limits.

The prediction accuracy *can* be improved inside the cone of silence at high speeds by using Method 2 (compare, for example, Figures 2.60 and 2.61, $\theta_m = 30°$, 45°) but the penalty is a degradation of prediction accuracy at the subsonic conditions (compare Figures 2.56 and 2.57). Thus, to use the *same* δ_s/r_J *versus* S_m law for both subsonic and supersonic jet exit conditions appears to compromise prediction accuracy. Bearing in mind the large variation of jet spread rate with Mach number (see Figure 5.6), it is not inconceivable that a different law *does* apply to each velocity regime. On the other hand, available source location results (as viewed from $\theta_m = 90°$) do not indicate such a trend (see, for example, Figure 2.31).

Figure	TP	Method	V_J/a_o	T_J/T_o
2.54	8	1	0.501	0.978
2.55	8	2		
2.56	12	1	0.900	0.975
2.57	12	2		
2.58	51	1	1.334	0.941
2.59	51	2		
2.60	58	1	1.650	0.977
2.61	58	2		
2.62	63	1	1.950	0.988
2.63	63	2		
2.64	32	1	0.481	2.166
2.65	32	2		
2.66	36	1	0.888	2.276
2.67	36	2		
2.68	37	1	1.147	2.285
2.69	37	2		
2.70	38	1	1.315	2.284
2.71	38	2		
2.72	39	1	1.463	2.283
2.73	39	2		
2.74	55	1	2.012	2.217
2.75	55	2		
2.76	68	1	0.484	3.339
2.77	68	2		
2.78	72	1	0.872	3.341
2.79	72	2		
2.80	73	1	1.134	3.353
2.81	73	2		
2.82	74	1	1.276	3.274
2.83	74	2		
2.84	75	1	1.423	3.300
2.85	75	2		

Table 2.17 List of figures showing comparisons between measured spectra and high-frequency predictions, giving jet exit conditions at each test point (TP).

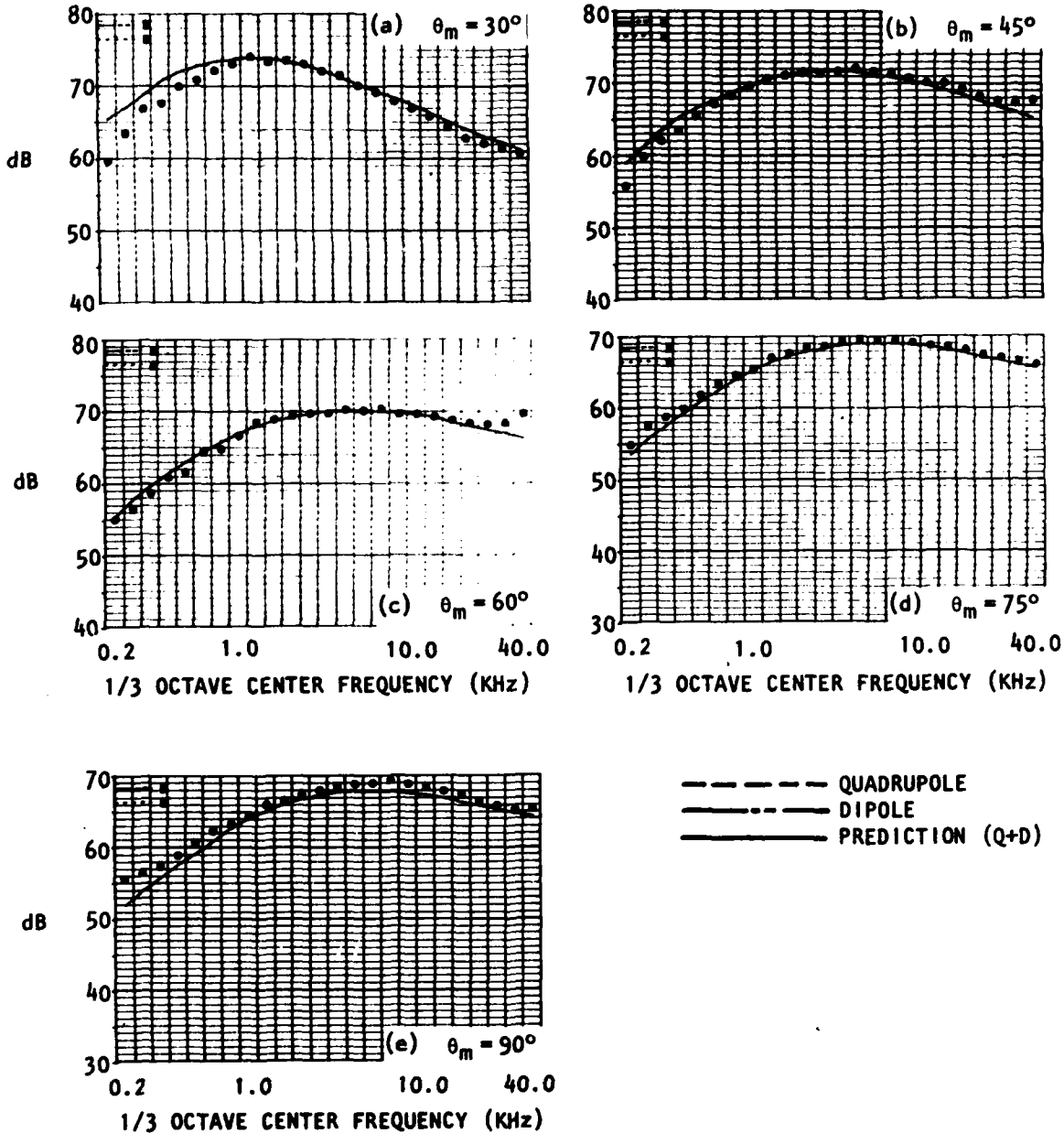

Figure 2.54
Comparison of Measured Mixing Noise Spectra and Predictions Based on High-Frequency Lilley Equation Solutions. Isothermal Jet,.TP #8. Method 1.

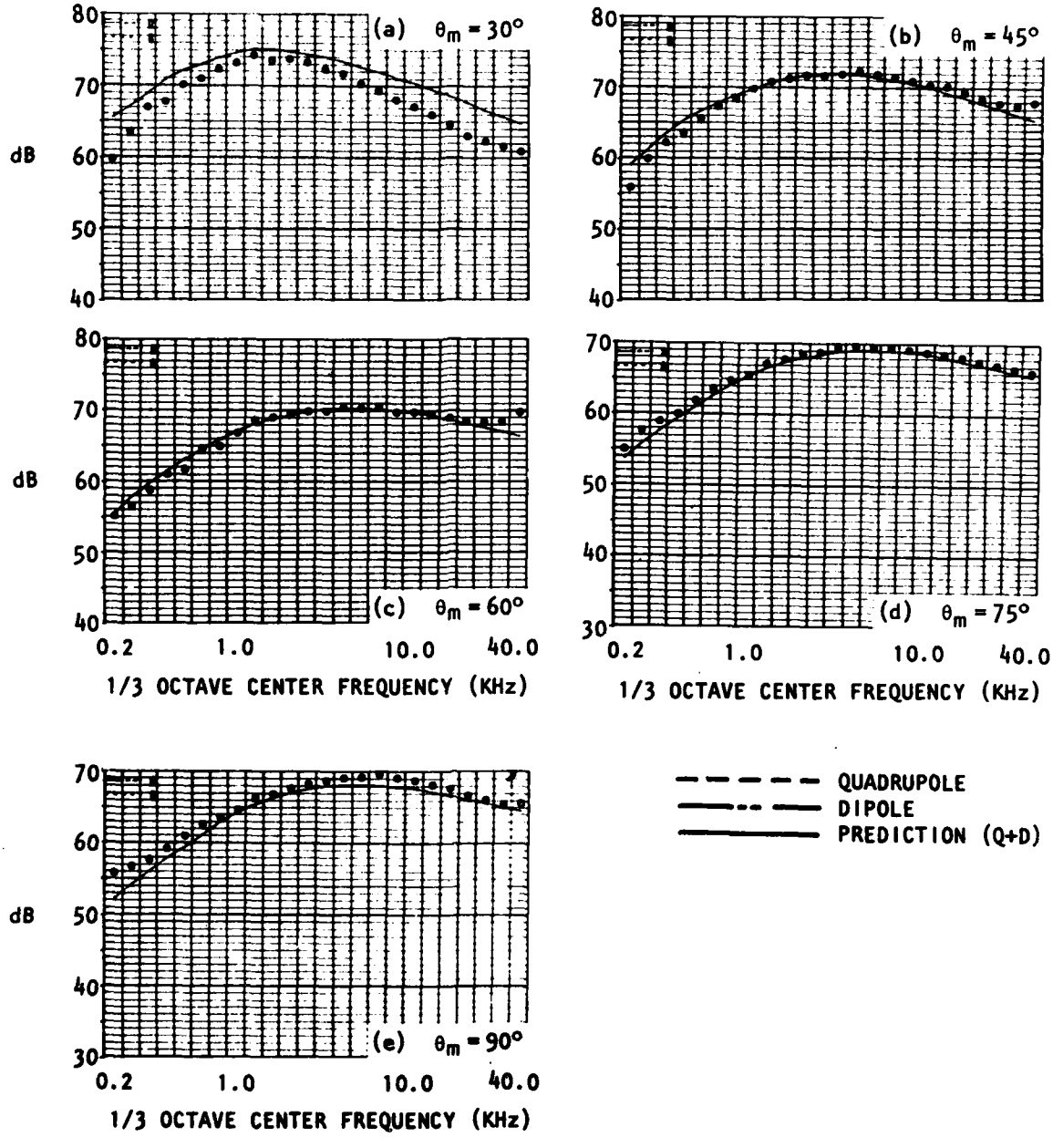

Figure 2.55
Comparison of Measured Mixing Noise Spectra and Predictions Based on High-Frequency Lilley Equation Solutions. Isothermal Jet, TP #8. Method 2.

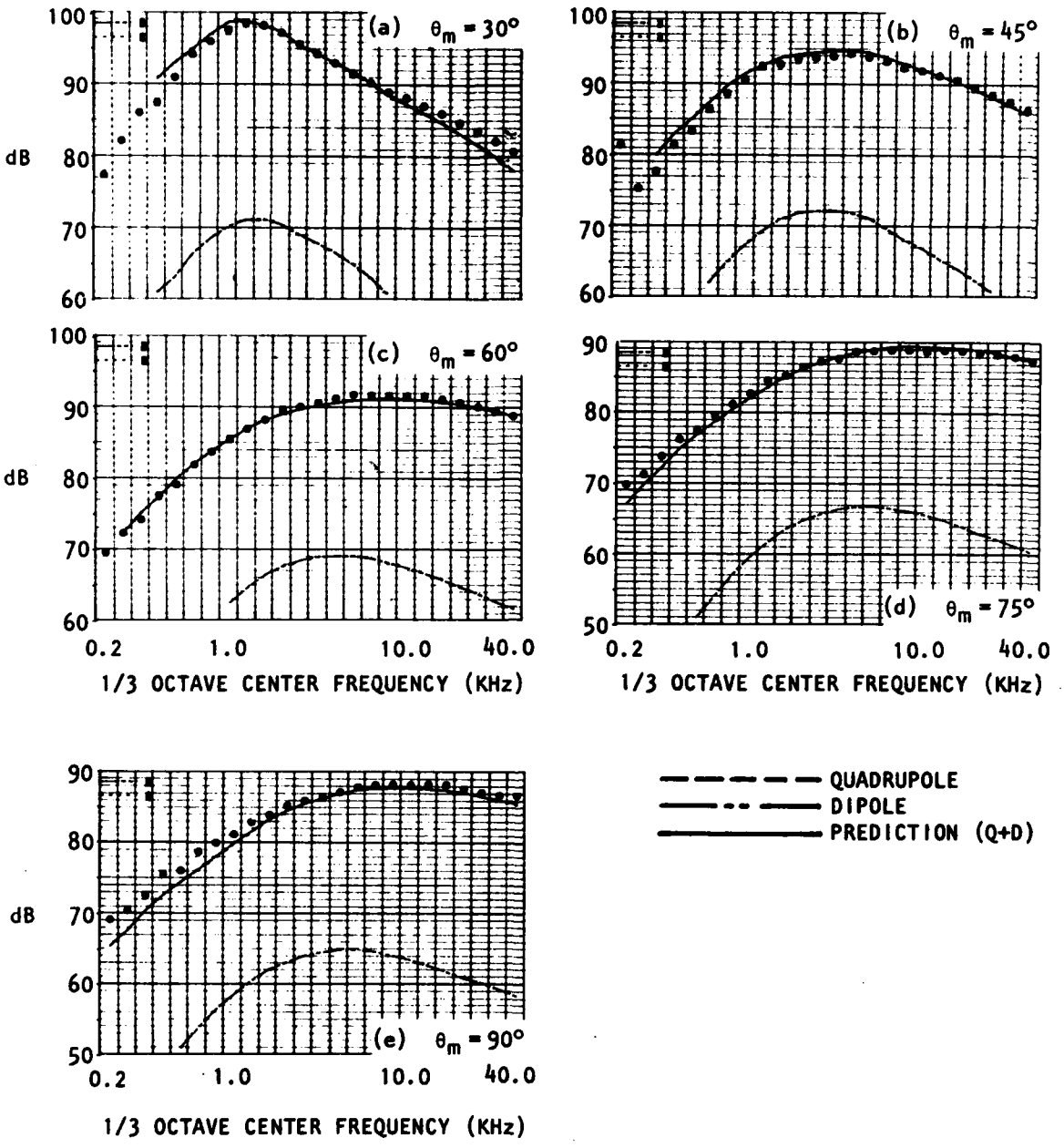

Figure 2.56
Comparison of Measured Mixing Noise Spectra and Predictions Based on High-Frequency Lilley Equation Solutions. Isothermal Jet, TP #12. Method 1.

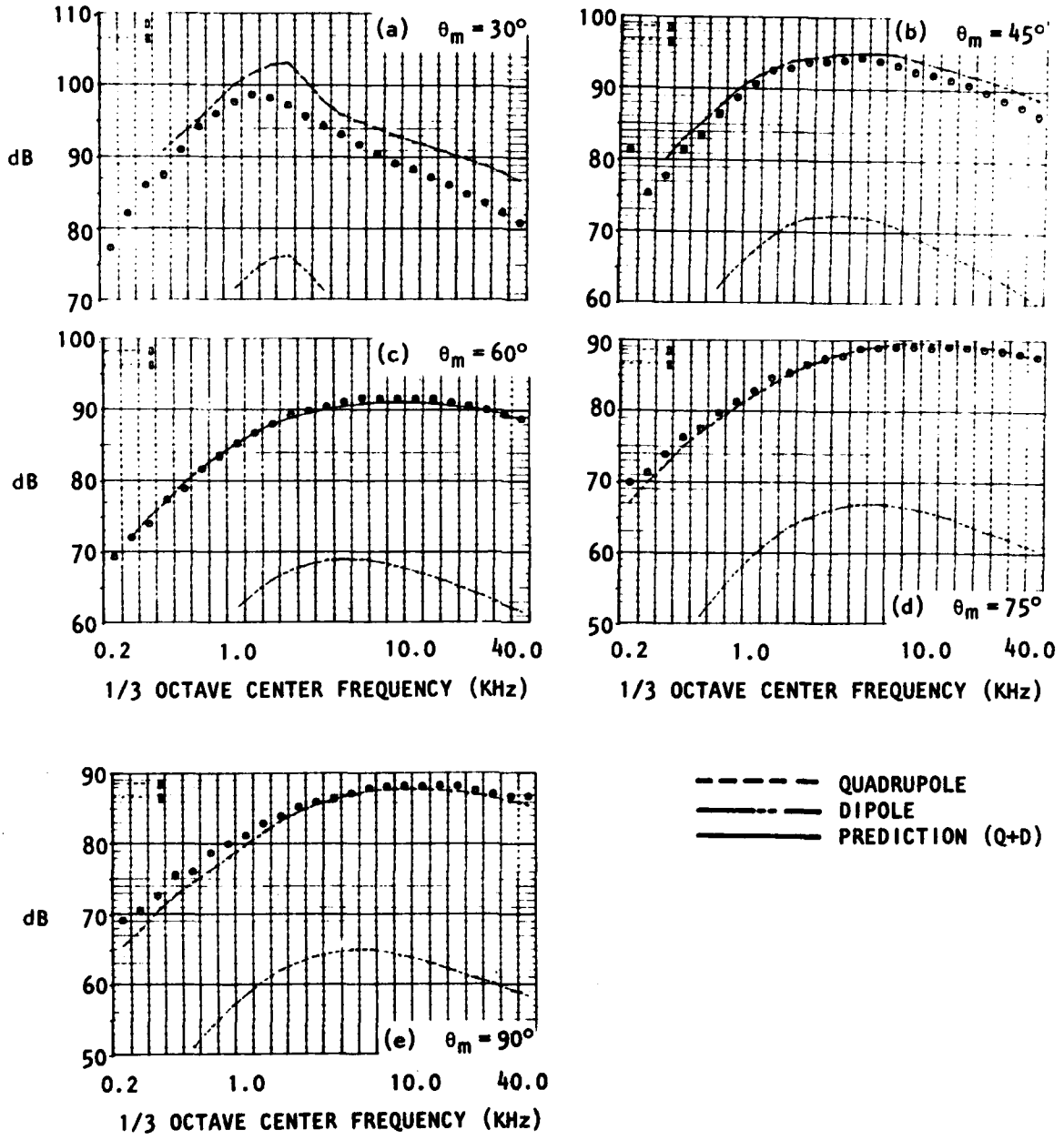

Figure 2.57
Comparison of Measured Mixing Noise Spectra and Predictions Based on High-Frequency Lilley Equation Solutions. Isothermal Jet, TP #12. Method 2.

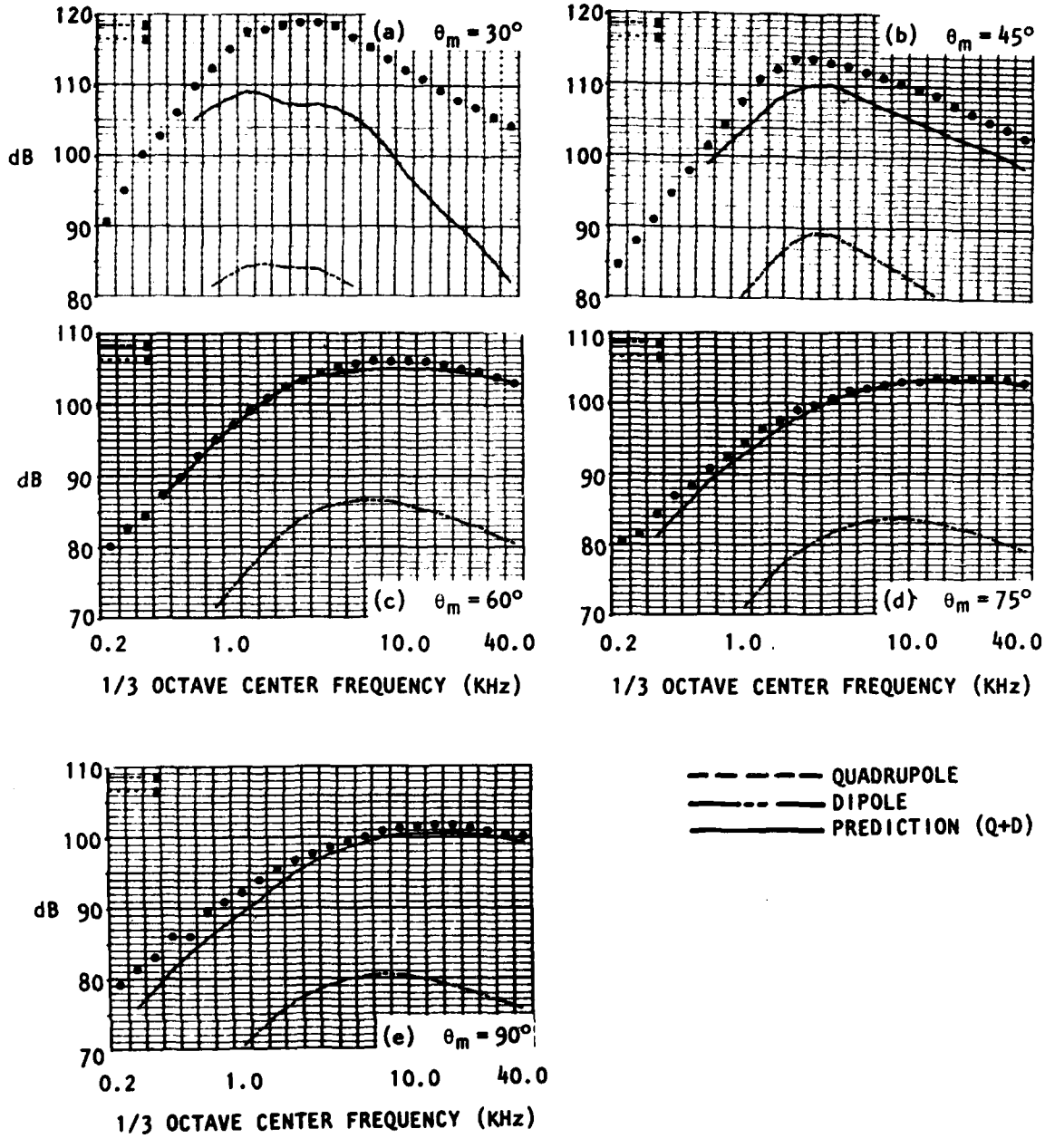

Figure 2.58
Comparison of Measured Mixing Noise Spectra and Predictions Based on High-Frequency Lilley Equation Solutions. Isothermal Jet, TP #51. Method 1.

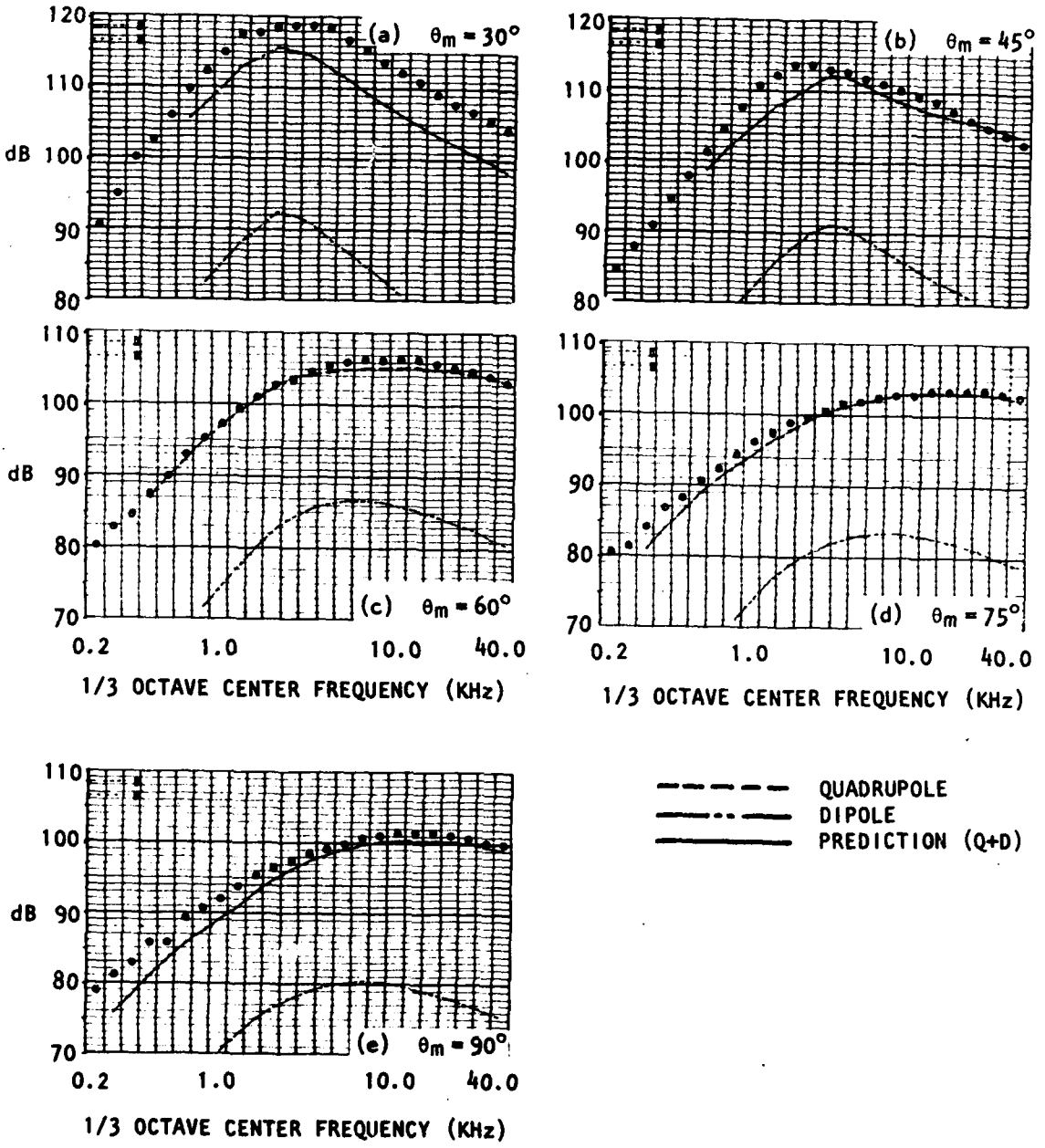

Figure 2.59
Comparison of Measured Mixing Noise Spectra and Predictions Based on High-Frequency Lilley Equation Solutions. Isothermal Jet, TP #51, Method 2.

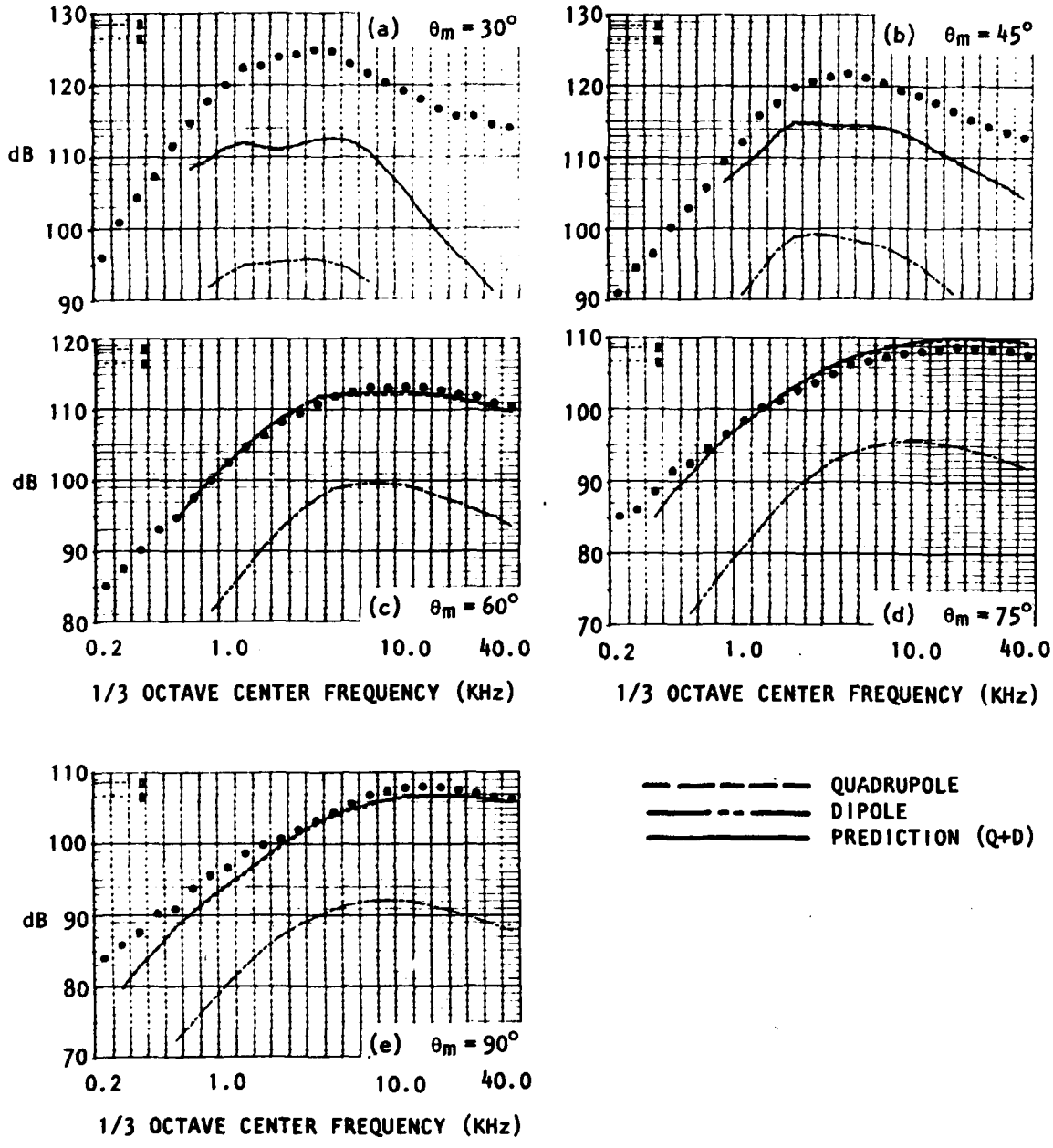

Figure 2.60
Comparison of Measured Mixing Noise Spectra and Predictions Based on High-Frequency Lilley Equation Solutions. Isothermal Jet, TP #58. Method 1.

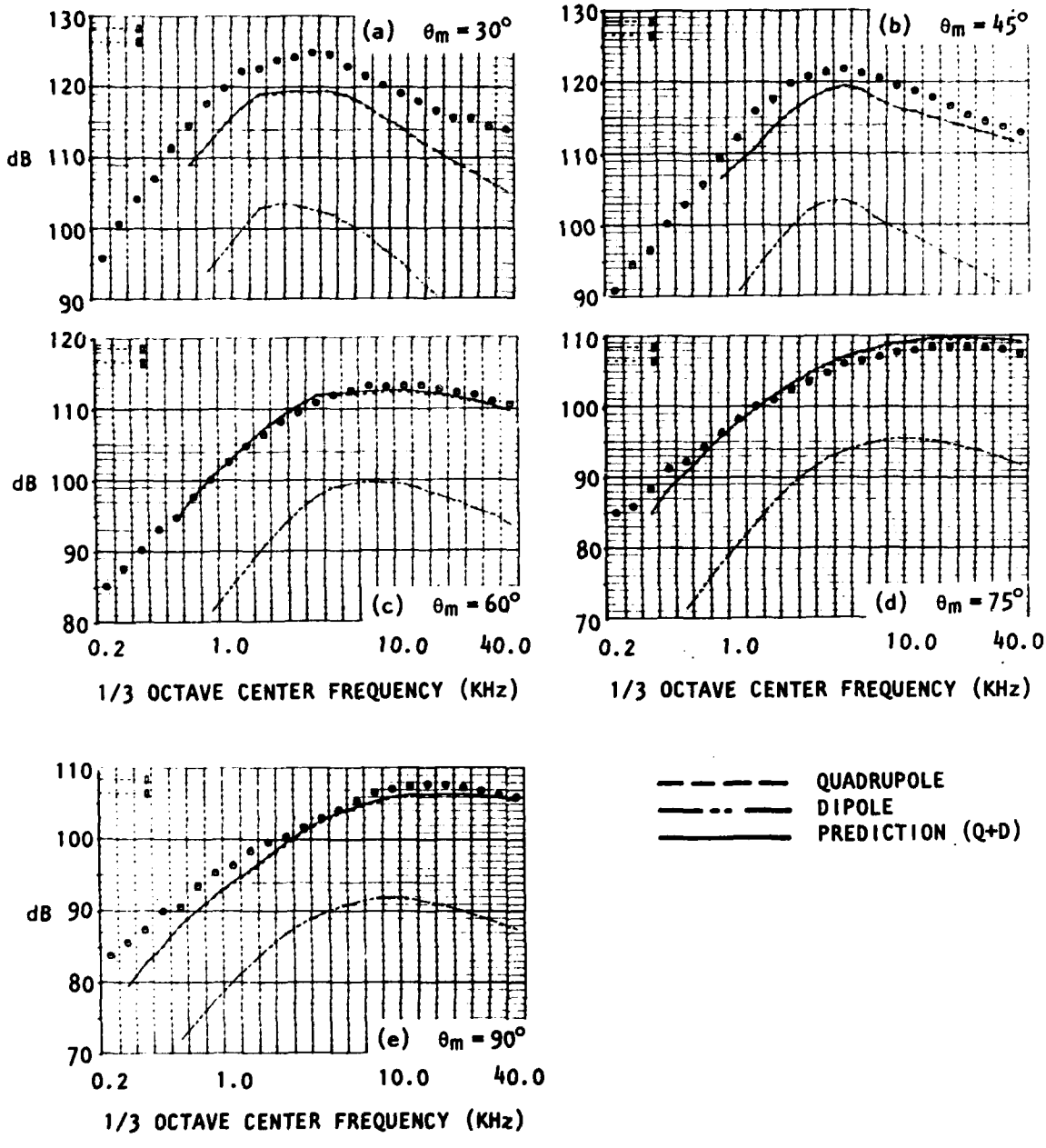

Figure 2.61
Comparison of Measured Mixing Noise Spectra and Predictions Based on High-Frequency Lilley Equation Solutions. Isothermal Jet, TP #58. Method 2.

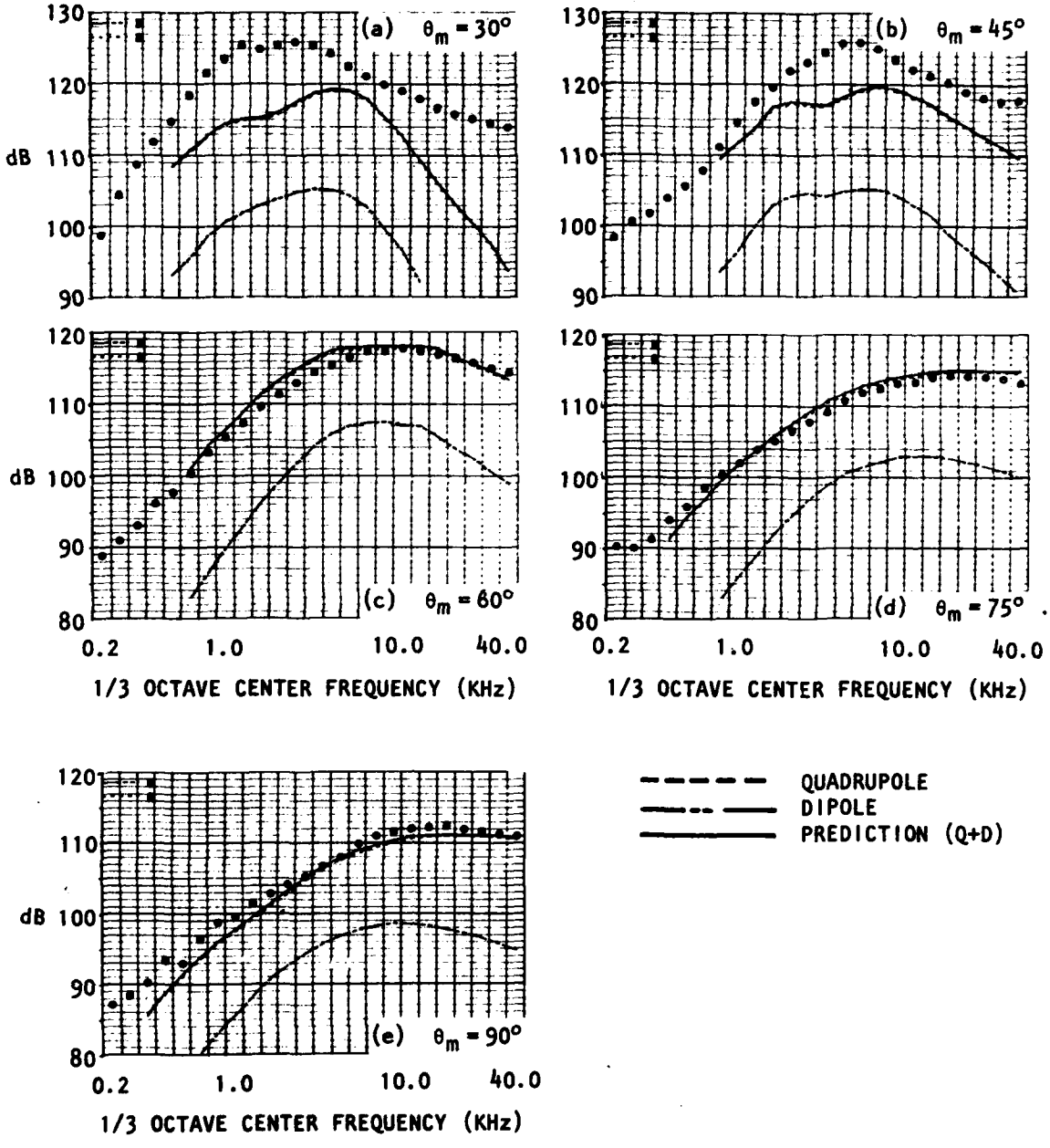

Figure 2.62
Comparison of Measured Mixing Noise Spectra and Predictions Based on High-Frequency Lilley Equation Solutions. Isothermal Jet, TP #63. Method 1.

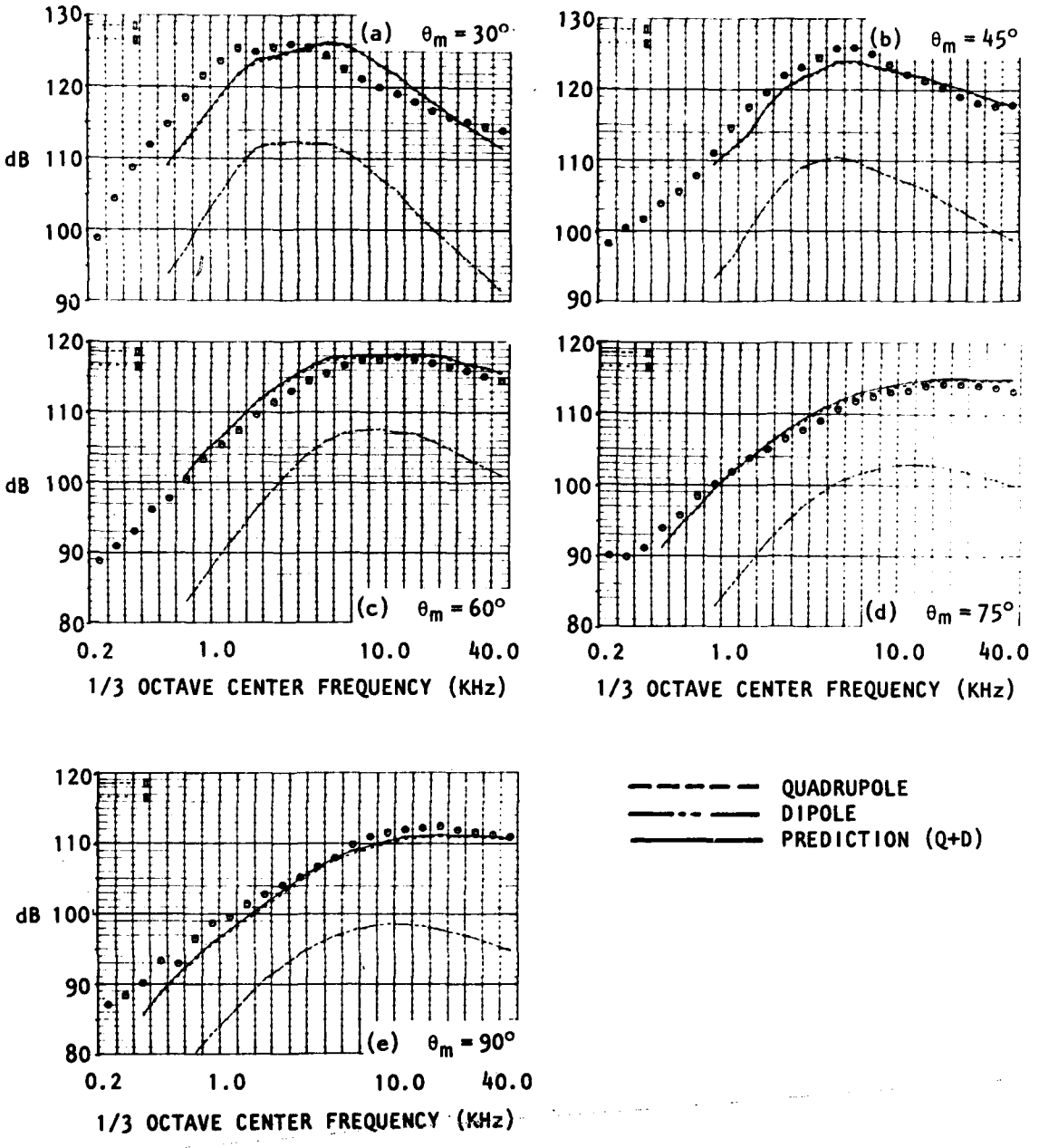

Figure 2.63
Comparison of Measured Mixing Noise Spectra and Predictions Based on High-Frequency Lilley Equation Solutions. Isothermal Jet, TP #63. Method 2.

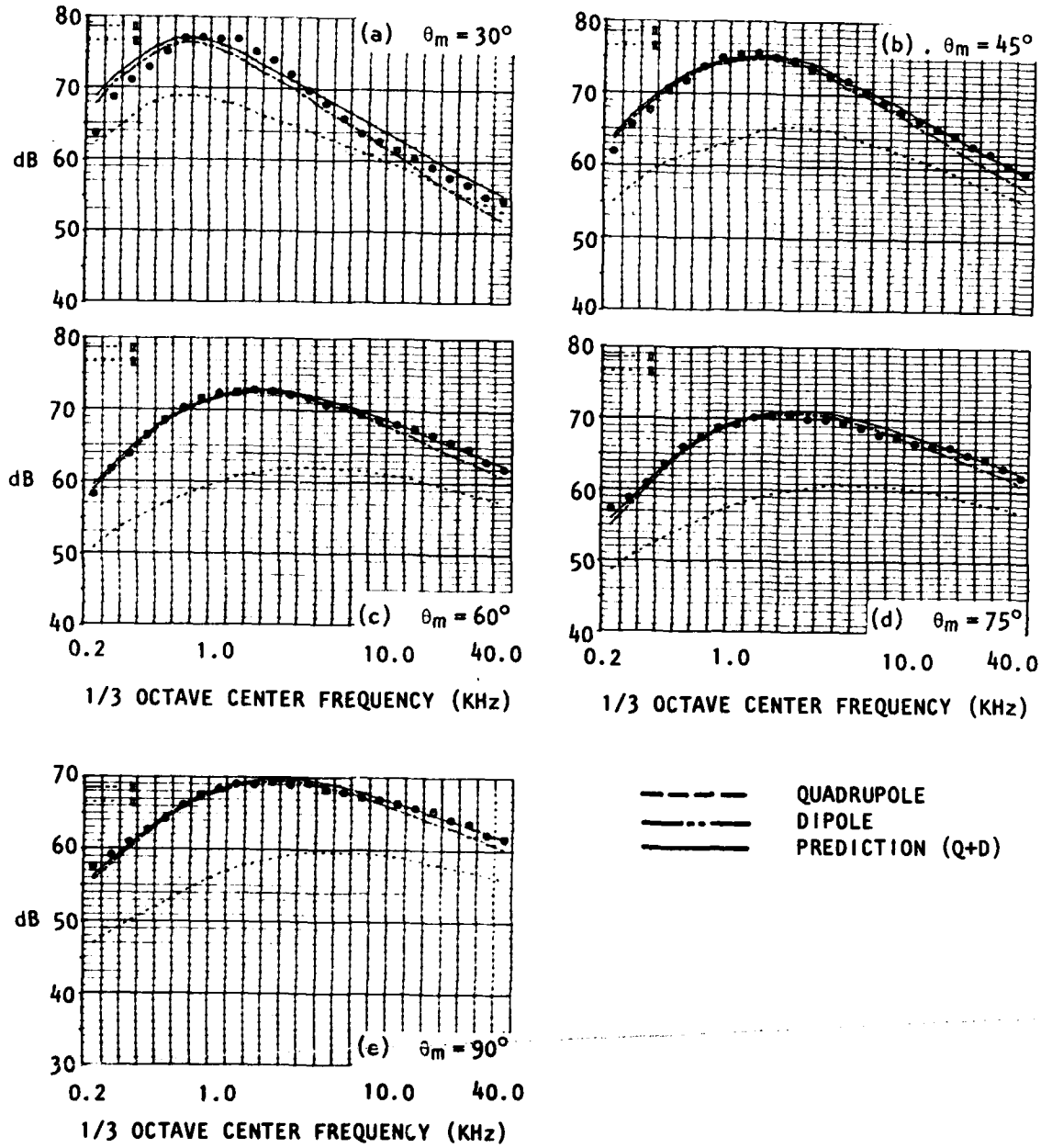

Figure 2.64
Comparison of Measured Mixing Noise Spectra and Predictions Based on High-Frequency Lilley Equation Solutions. Medium-Temperature Jet, TP #32. Method 1.

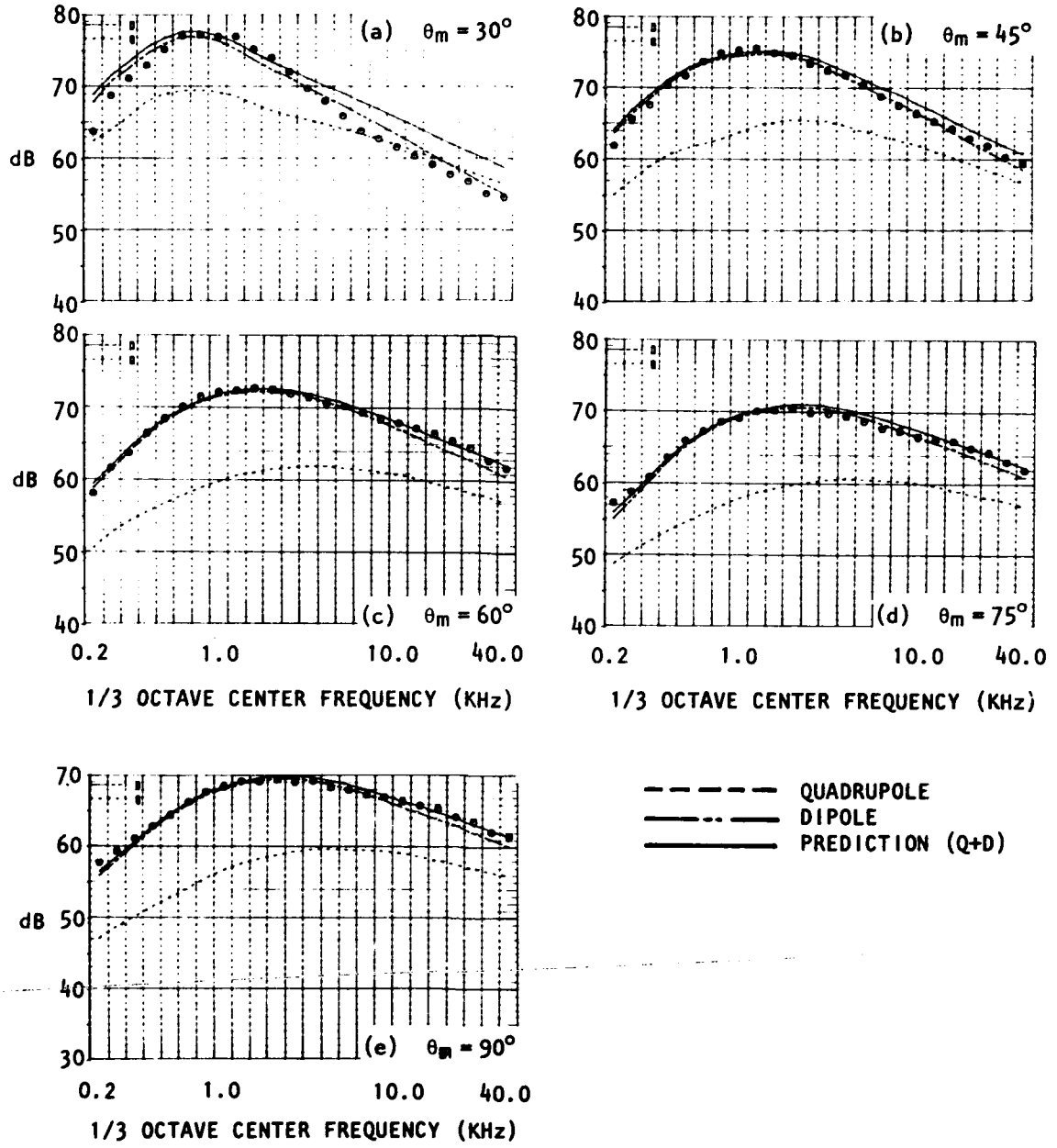

Figure 2.65
Comparison of Measured Mixing Noise Spectra and Predictions Based on High-Frequency Lilley Equation Solutions: Medium-Temperature Jet, TP #32. Method 2.

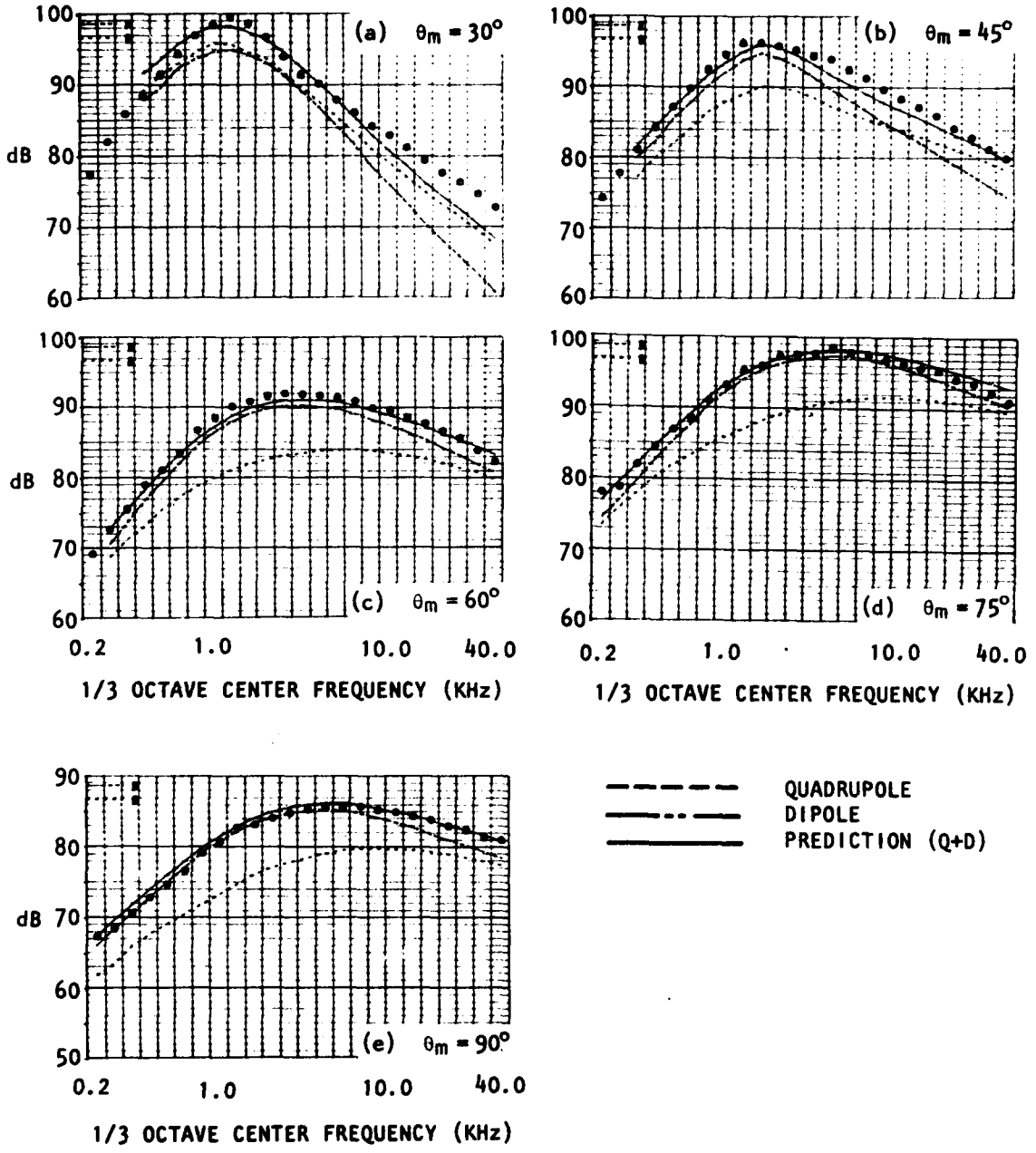

Figure 2.66
Comparison of Measured Mixing Noise Spectra and Predictions Based on High-Frequency Lilley Equation Solutions. Medium-Temperature Jet, TP #36. Method 1.

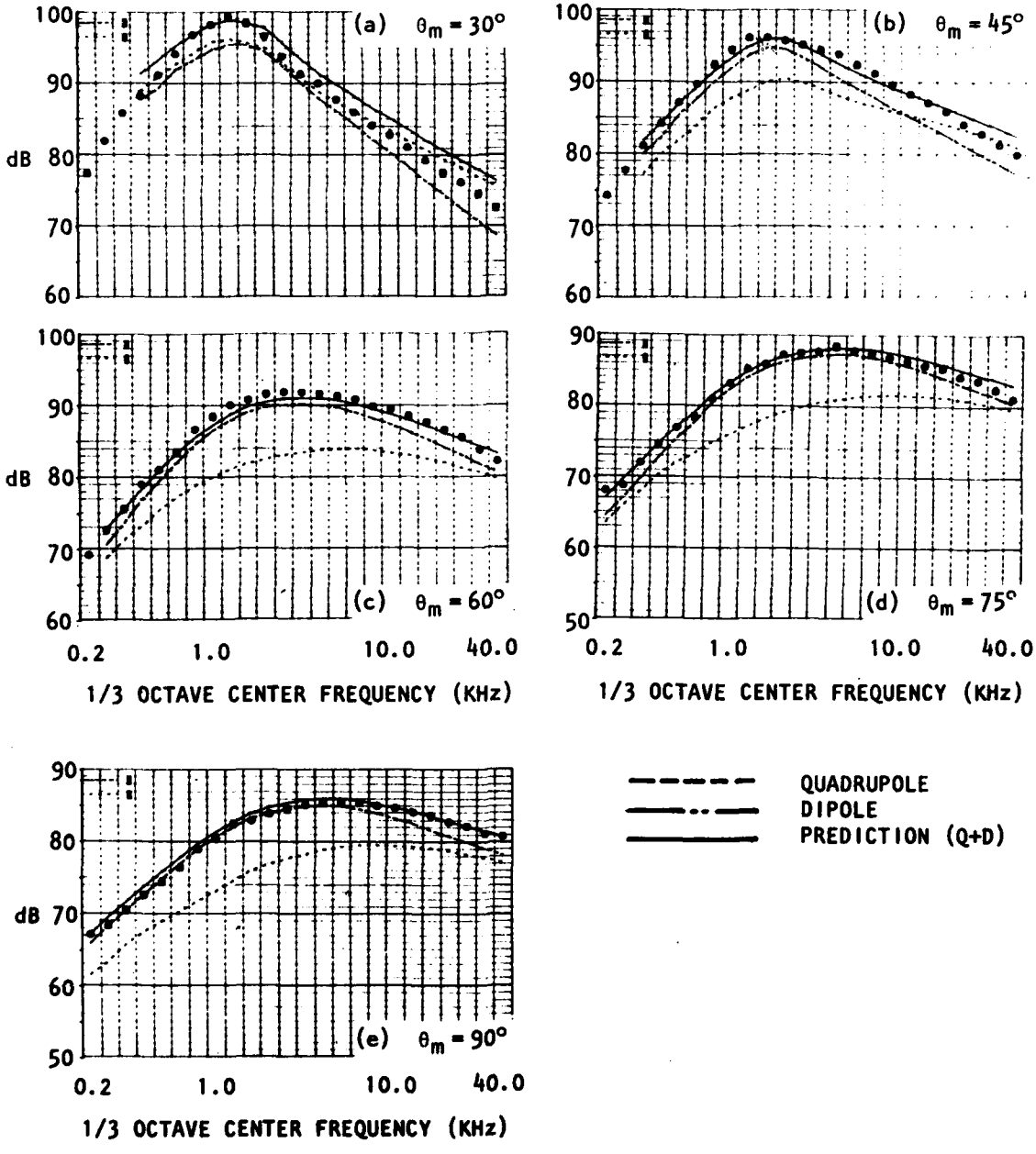

Figure 2.67
Comparison of Measured Mixing Noise Spectra and Predictions Based on High-Frequency Lilley Equation Solutions. Medium-Temperature Jet, TP #36. Method 2.

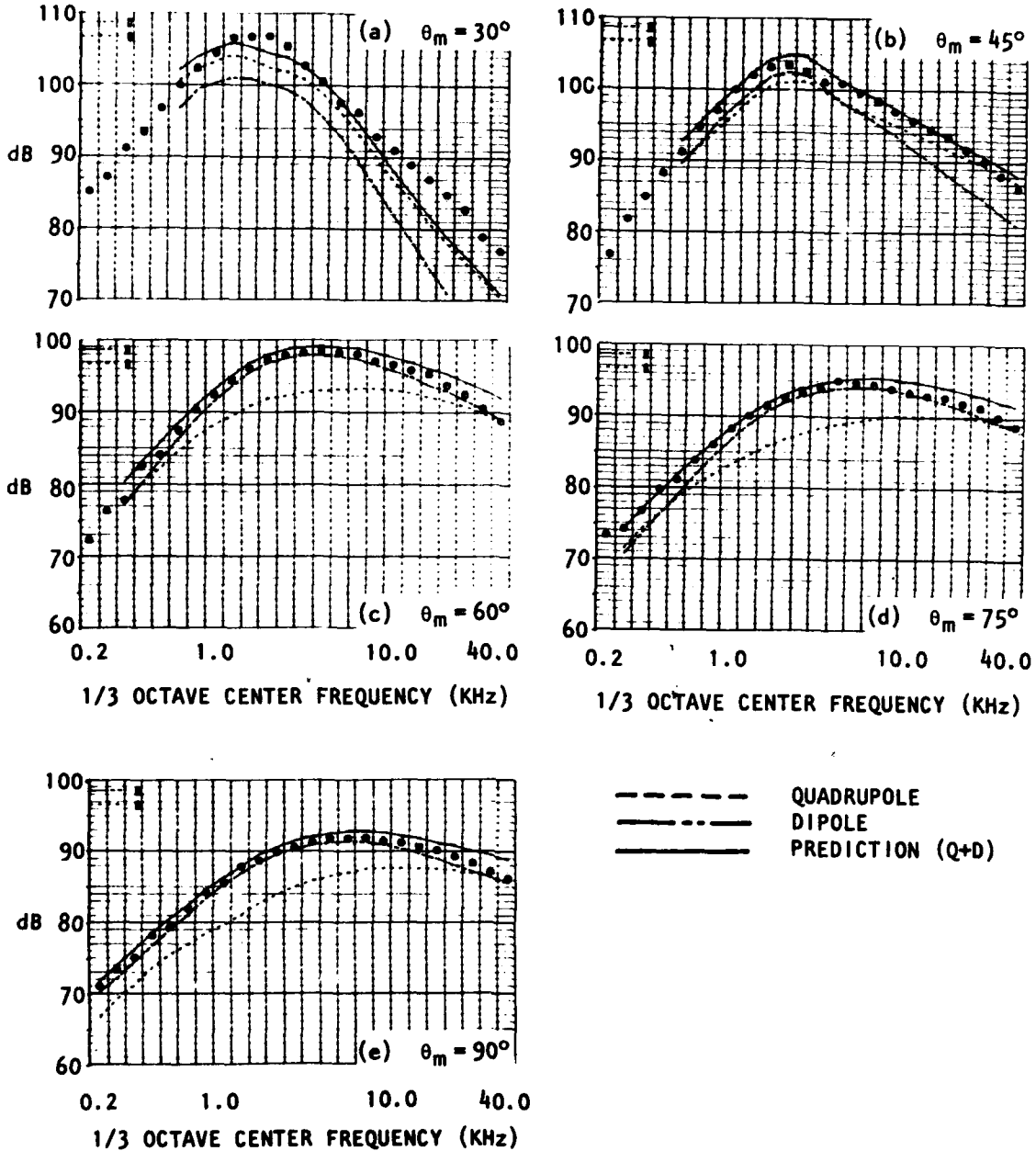

Figure 2.68
Comparison of Measured Mixing Noise Spectra and Predictions Based on High-Frequency Lilley Equation Solutions. Medium-Temperature Jet, TP #37. Method 1.

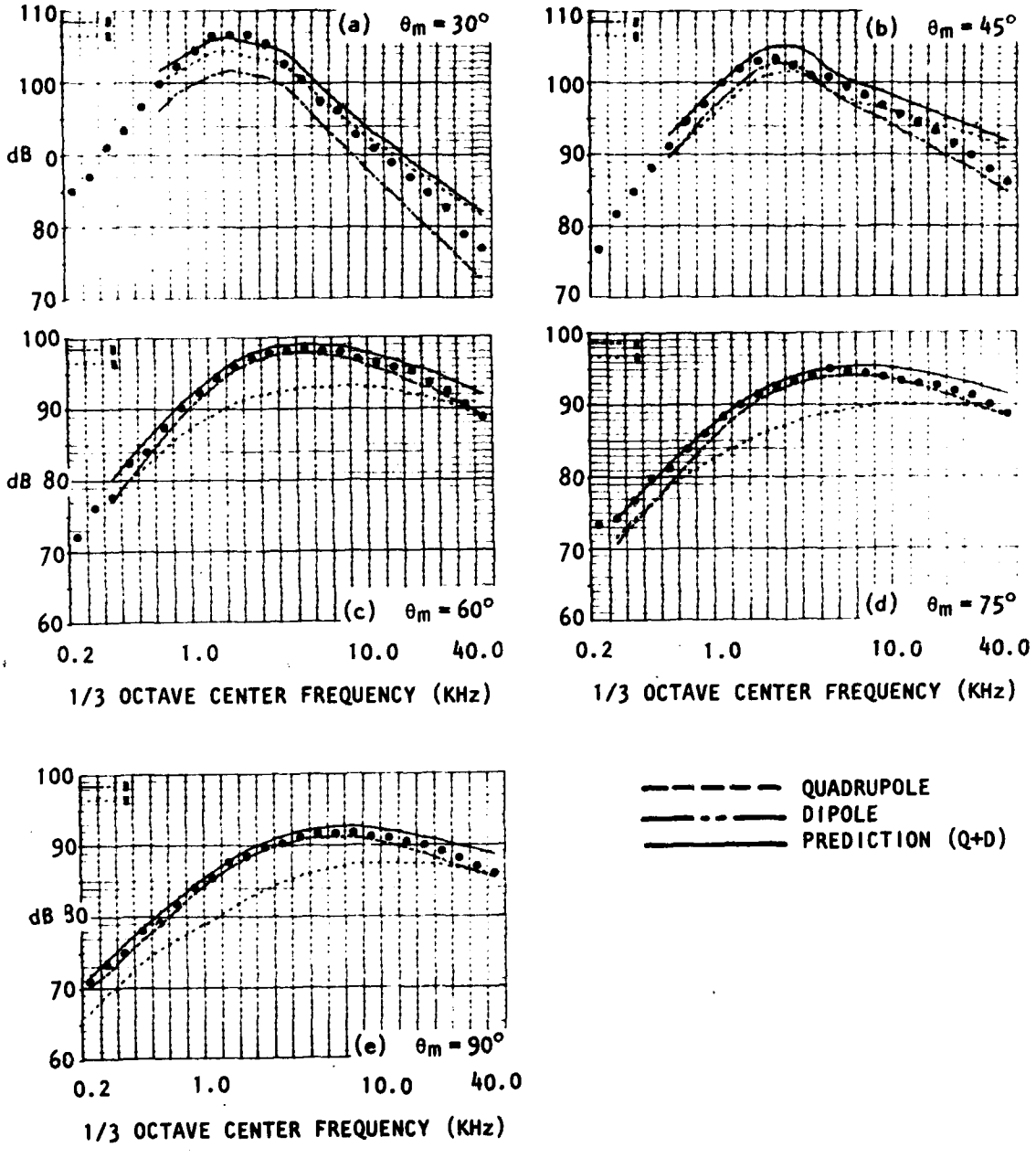

Figure 2.69
Comparison of Measured Mixing Noise Spectra and Predictions Based on High-Frequency Lilley Equation Solutions. Medium-Temperature Jet, TP #37. Method 2.

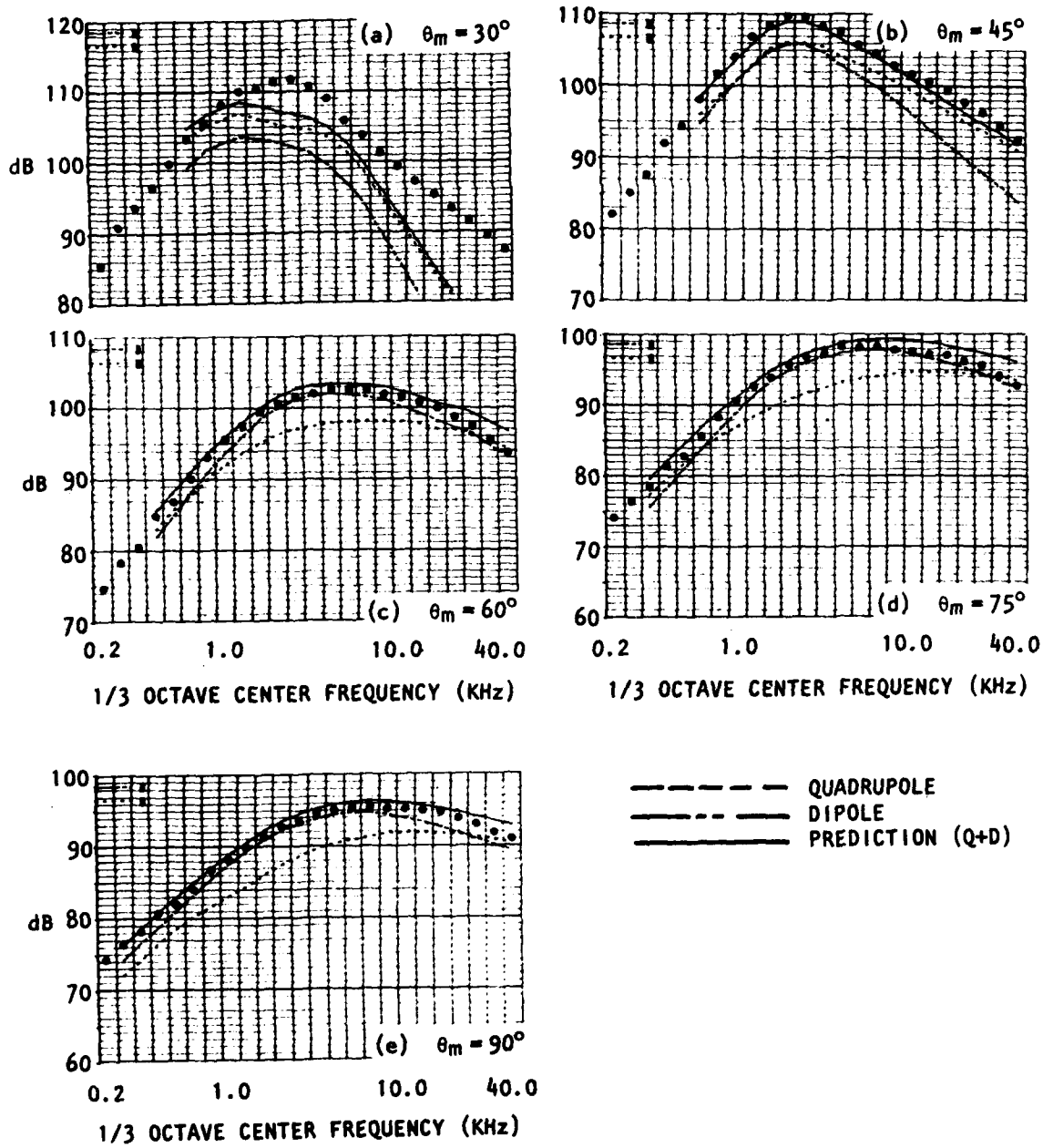

Figure 2.70
Comparison of Measured Mixing Noise Spectra and Predictions Based on High-Frequency Lilley Equation Solutions. Medium-Temperature Jet, TP #38. Method 1.

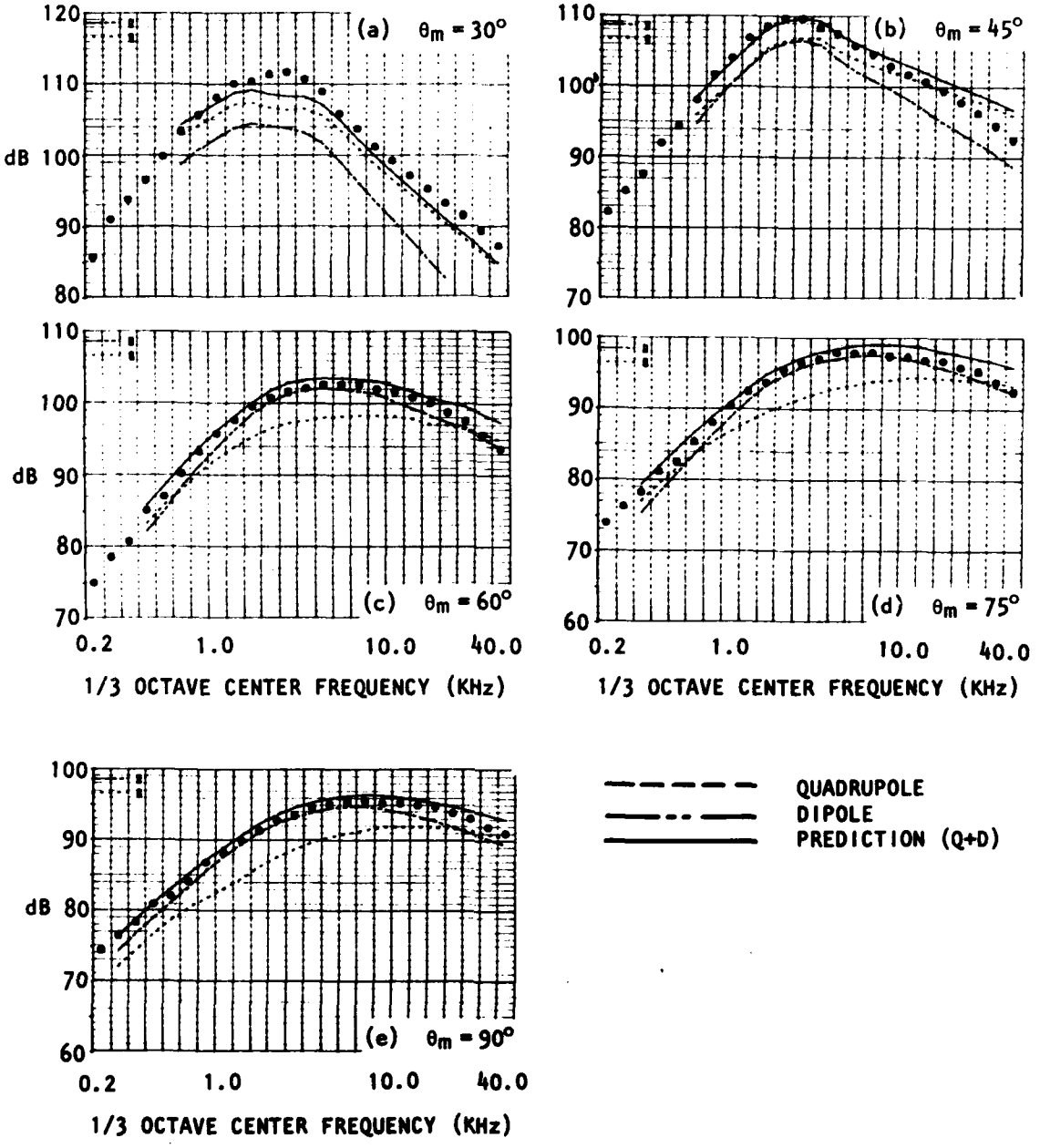

Figure 2.71
Comparison of Measured Mixing Noise Spectra and Predictions Based on High-Frequency Lilley Equation Solutions. Medium-Temperature Jet, TP #38. Method 2.

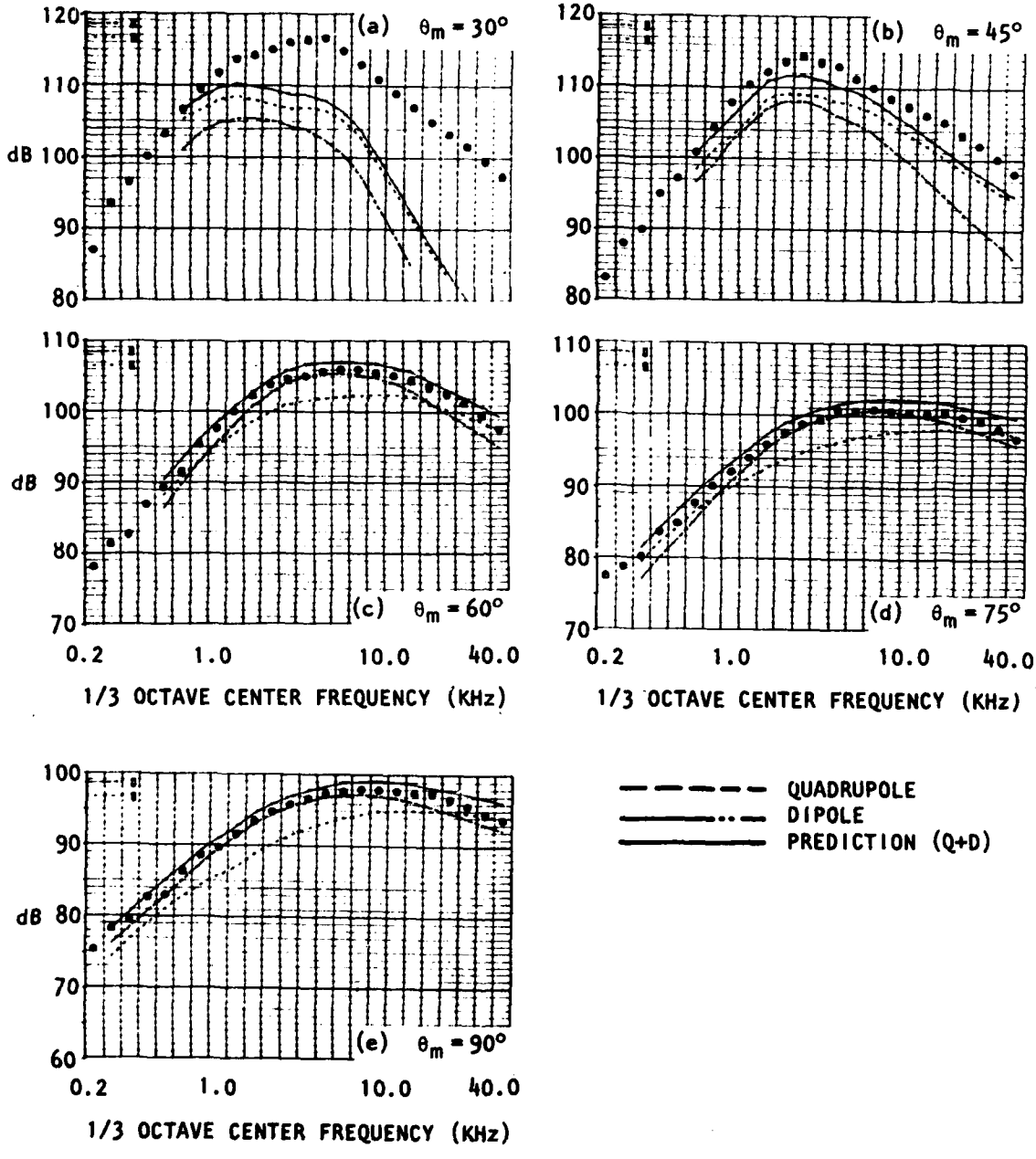

Figure 2.72
Comparison of Measured Mixing Noise Spectra and Predictions Based on High-Frequency Lilley Equation Solutions. Medium-Temperature Jet, TP #39. Method 1.

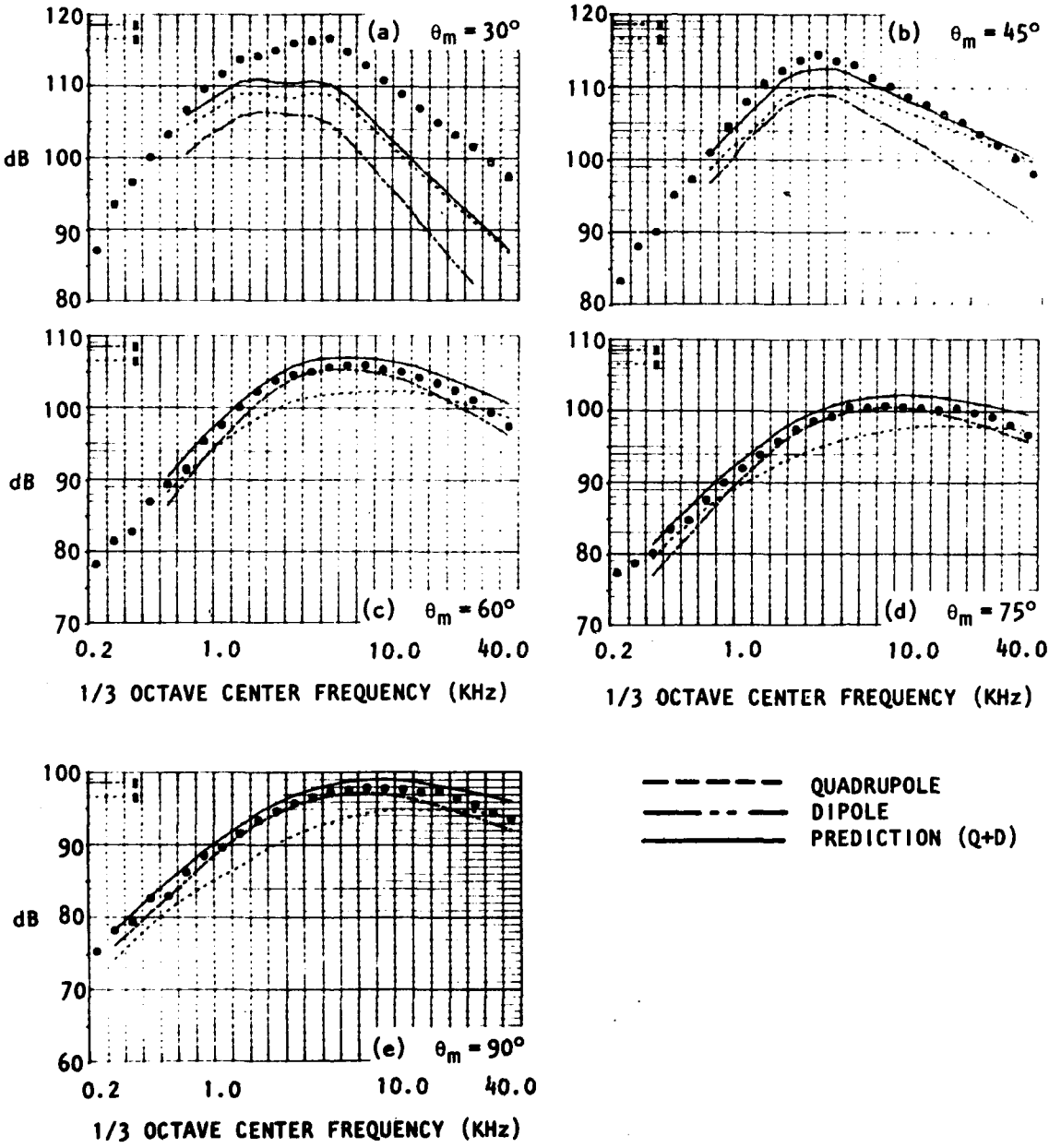

Figure 2.73
Comparison of Measured Mixing Noise Spectra and Predictions Based on High-Frequency Lilley Equation Solutions. Medium-Temperature Jet, TP #39. Method 2.

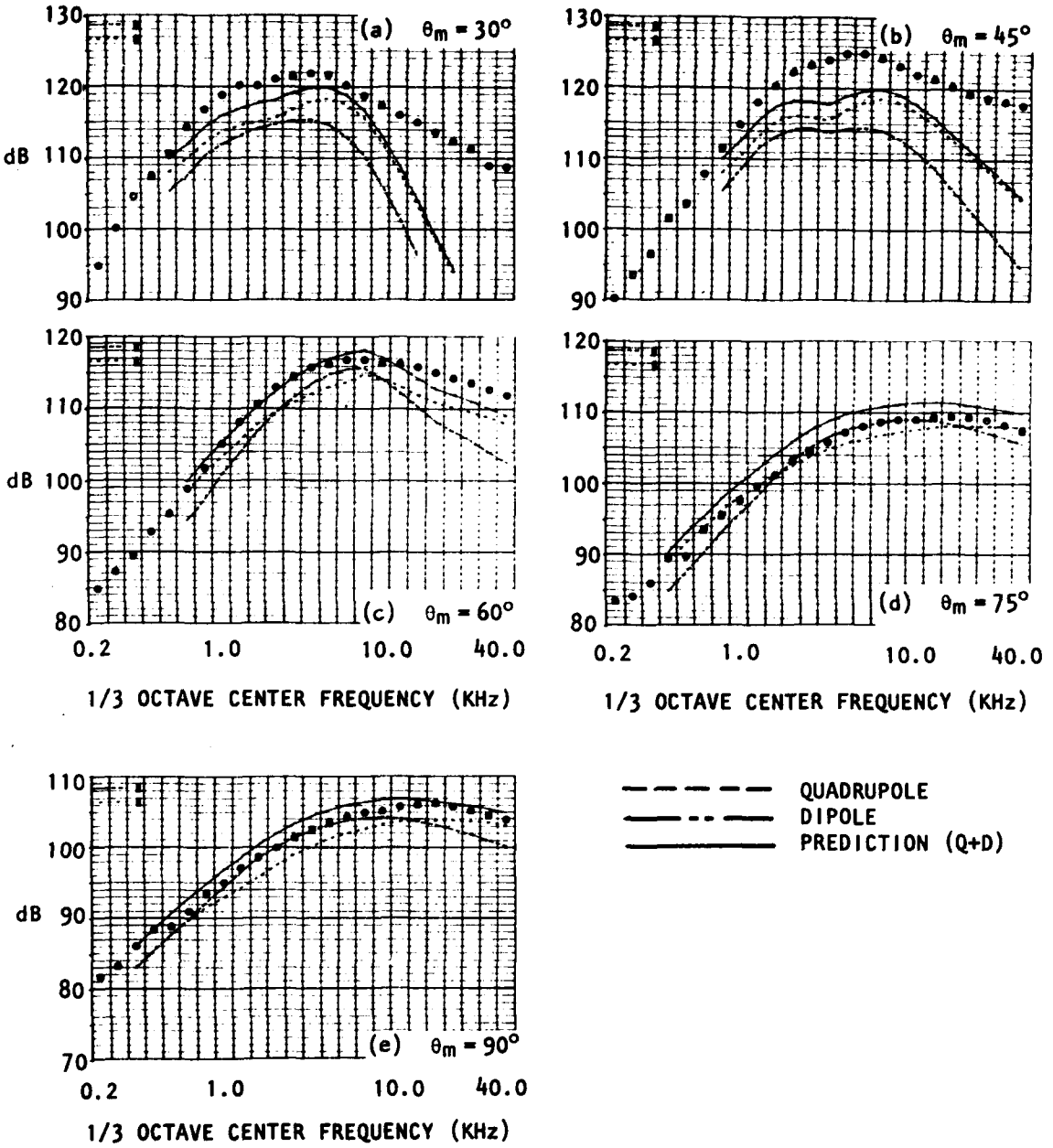

Figure 2.74
Comparison of Measured Mixing Noise Spectra and Predictions Based on High-Frequency Lilley Equation Solutions. Medium-Temperature Jet, TP #55. Method 1.

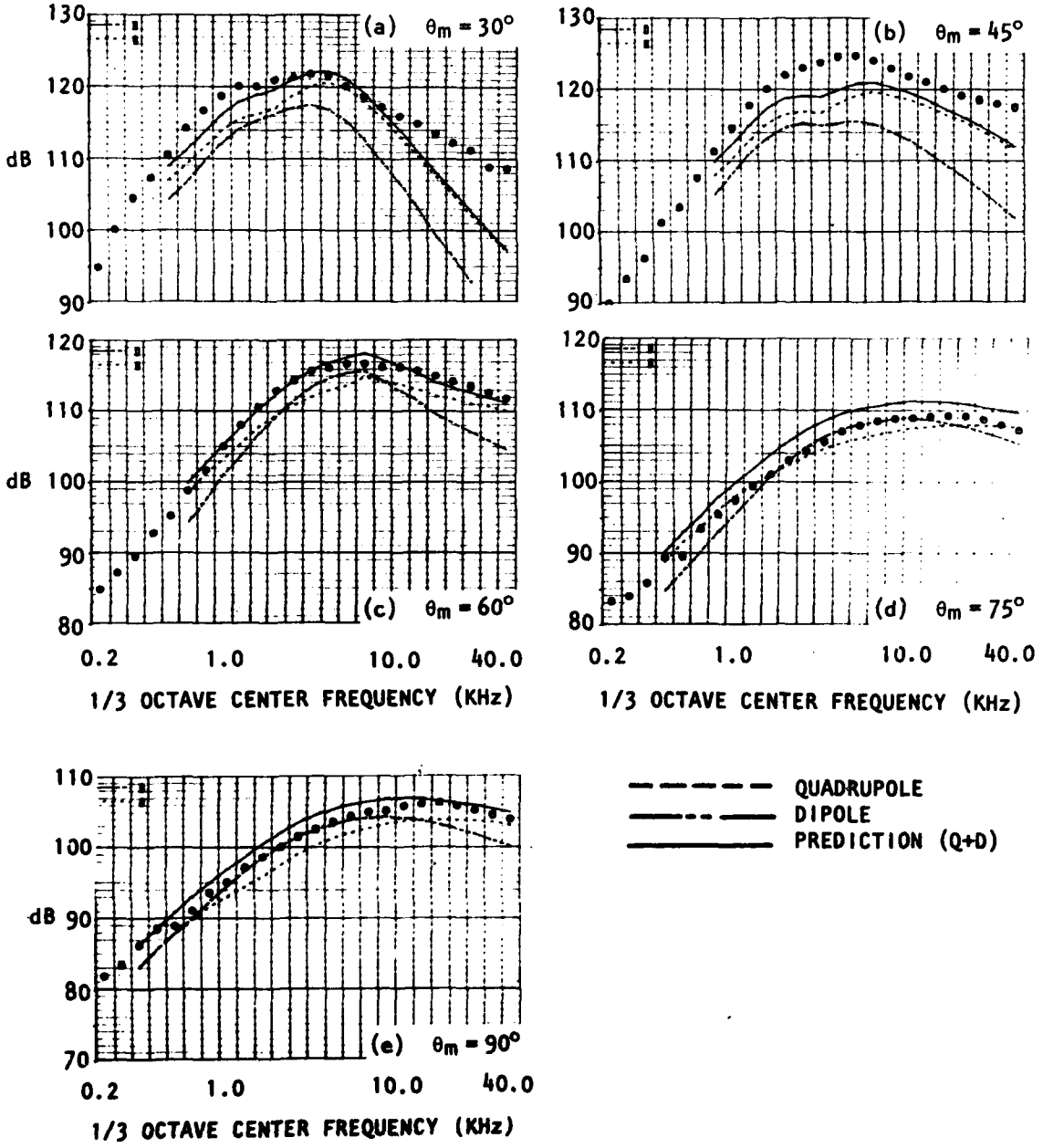

Figure 2.75
Comparison of Measured Mixing Noise Spectra and Predictions Based on High-Frequency Lilley Equation Solutions. Medium-Temperature Jet, TP #55. Method 2.

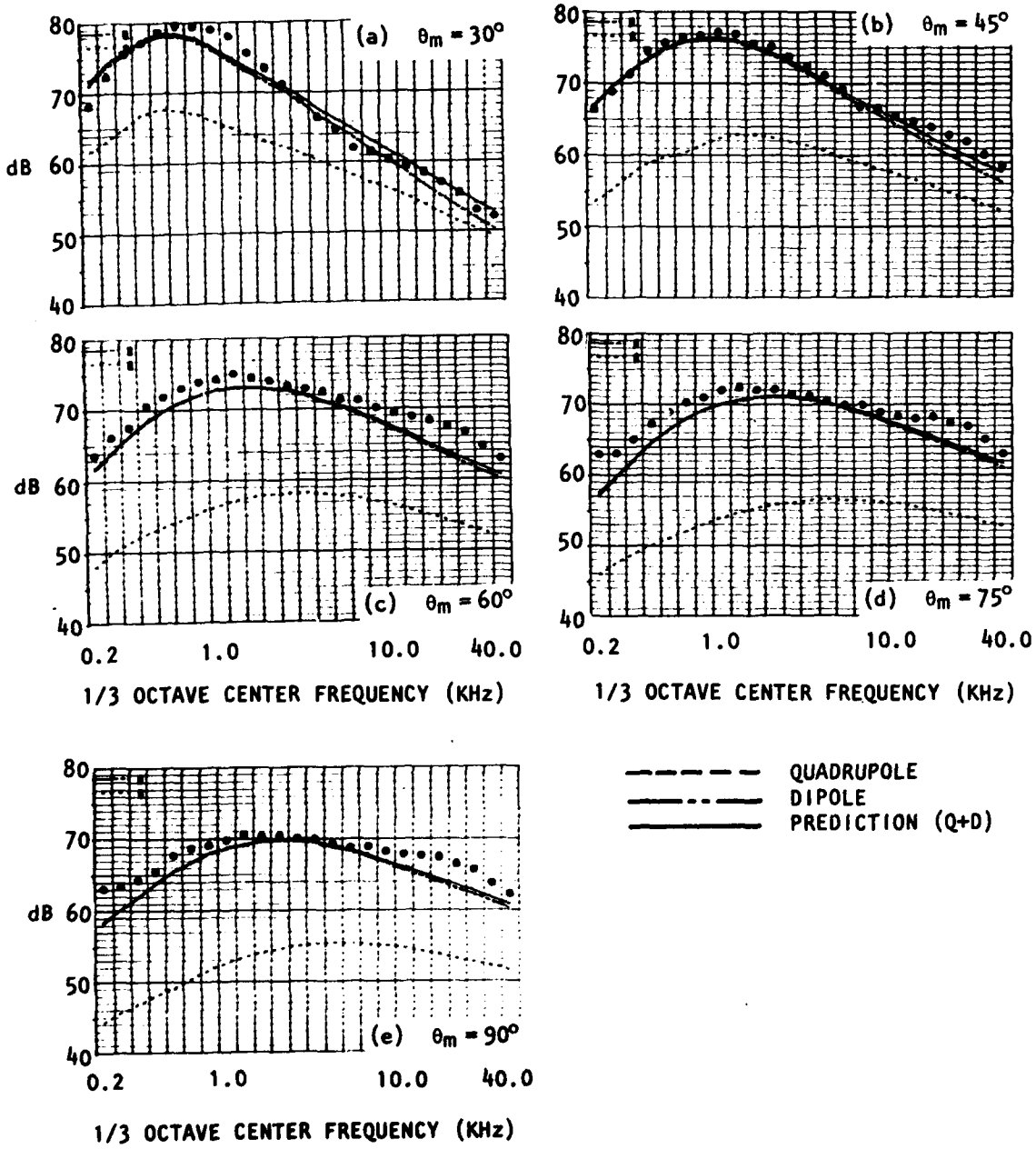

Figure 2.76
Comparison of Measured Mixing Noise Spectra and Predictions Based on High-Frequency Lilley Equation Solutions. High-Temperature Jet, TP #68. Method 1.

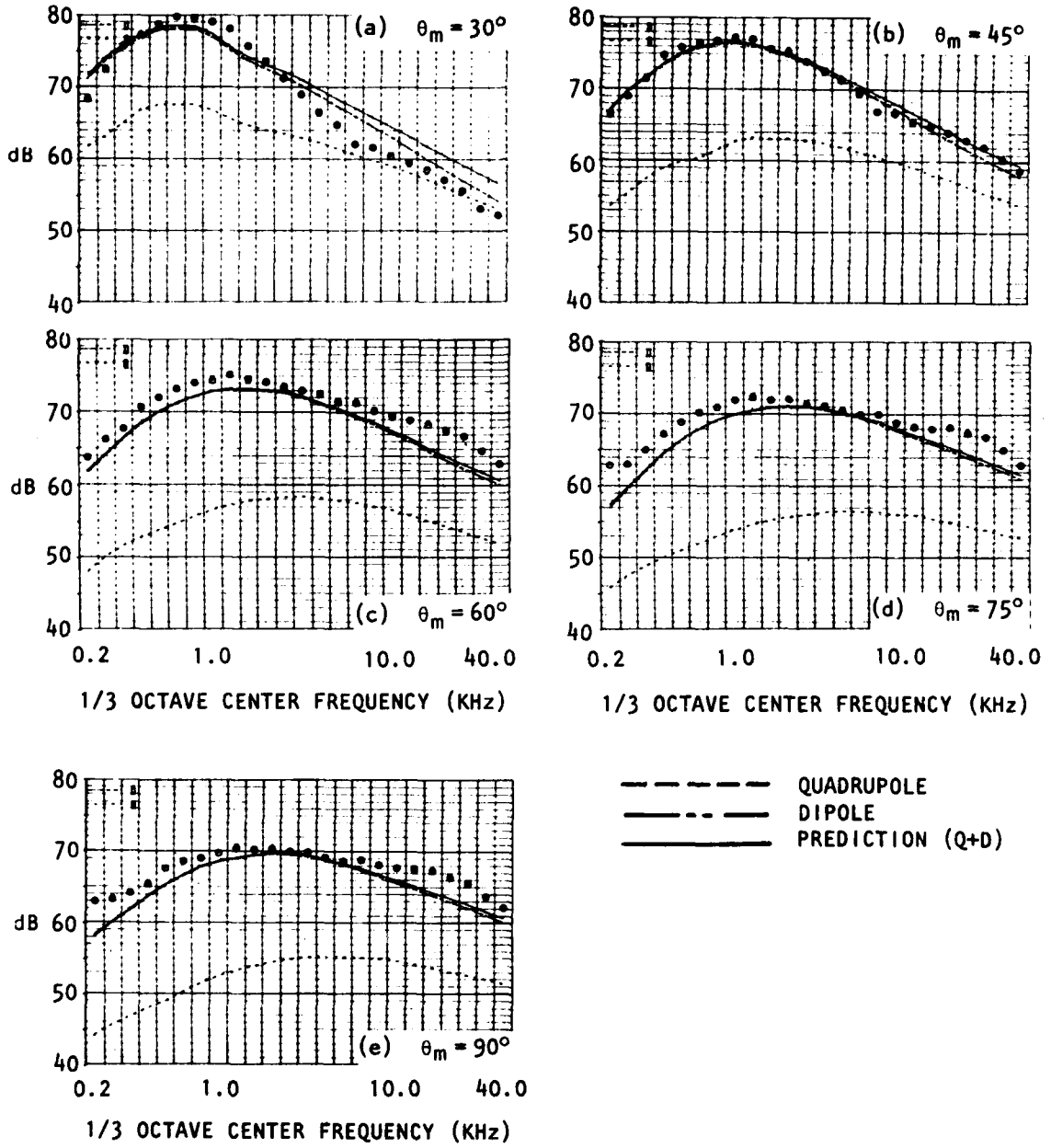

Figure 2.77
Comparison of Measured Mixing Noise Spectra and Predictions Based on High-Frequency Lilley Equation Solutions. High-Temperature Jet, TP #68. Method 2.

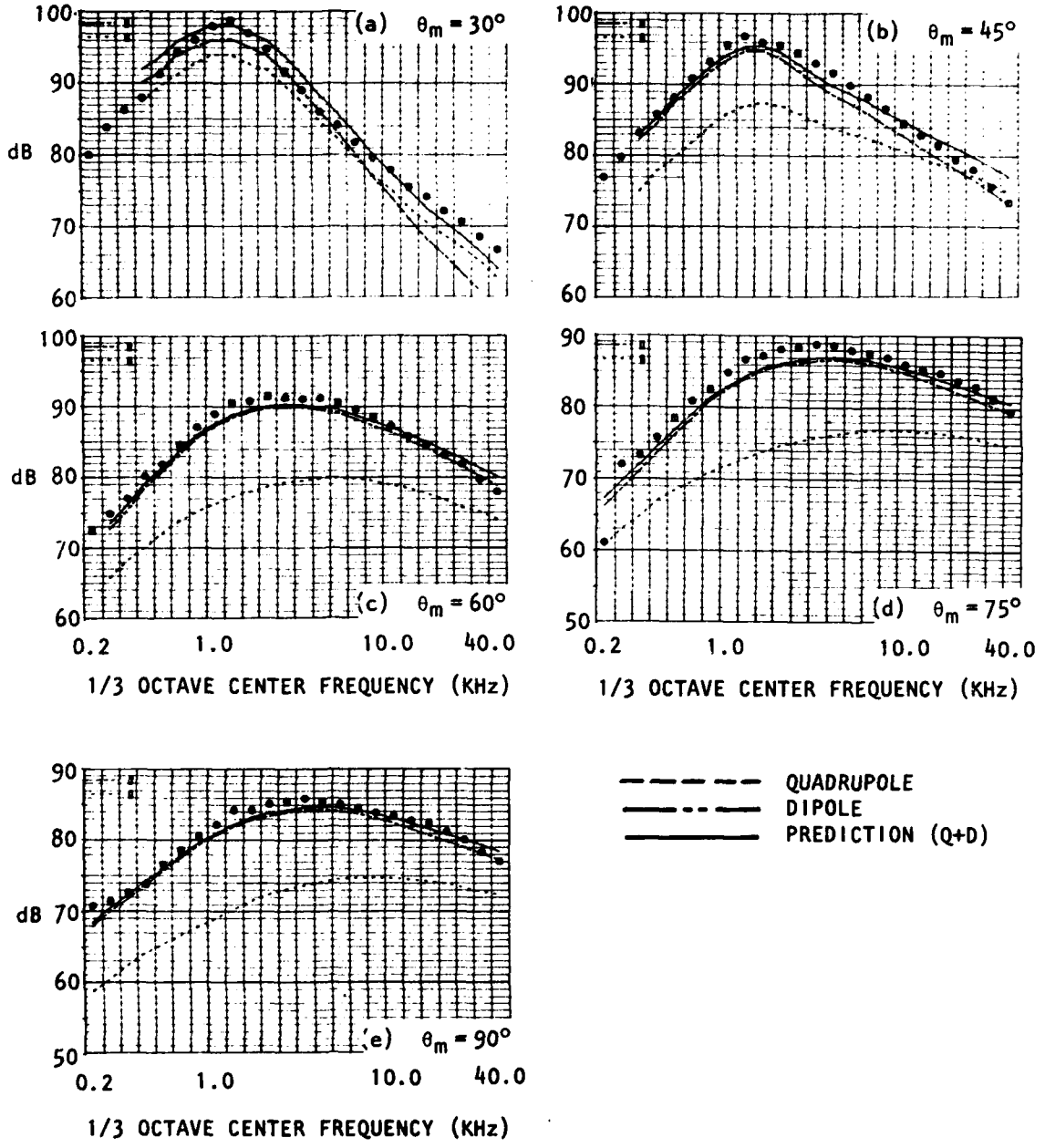

Figure 2.78
Comparison of Measured Mixing Noise Spectra and Predictions Based on High-Frequency Lilley Equation Solutions. High-Temperature Jet, TP #72. Method 1.

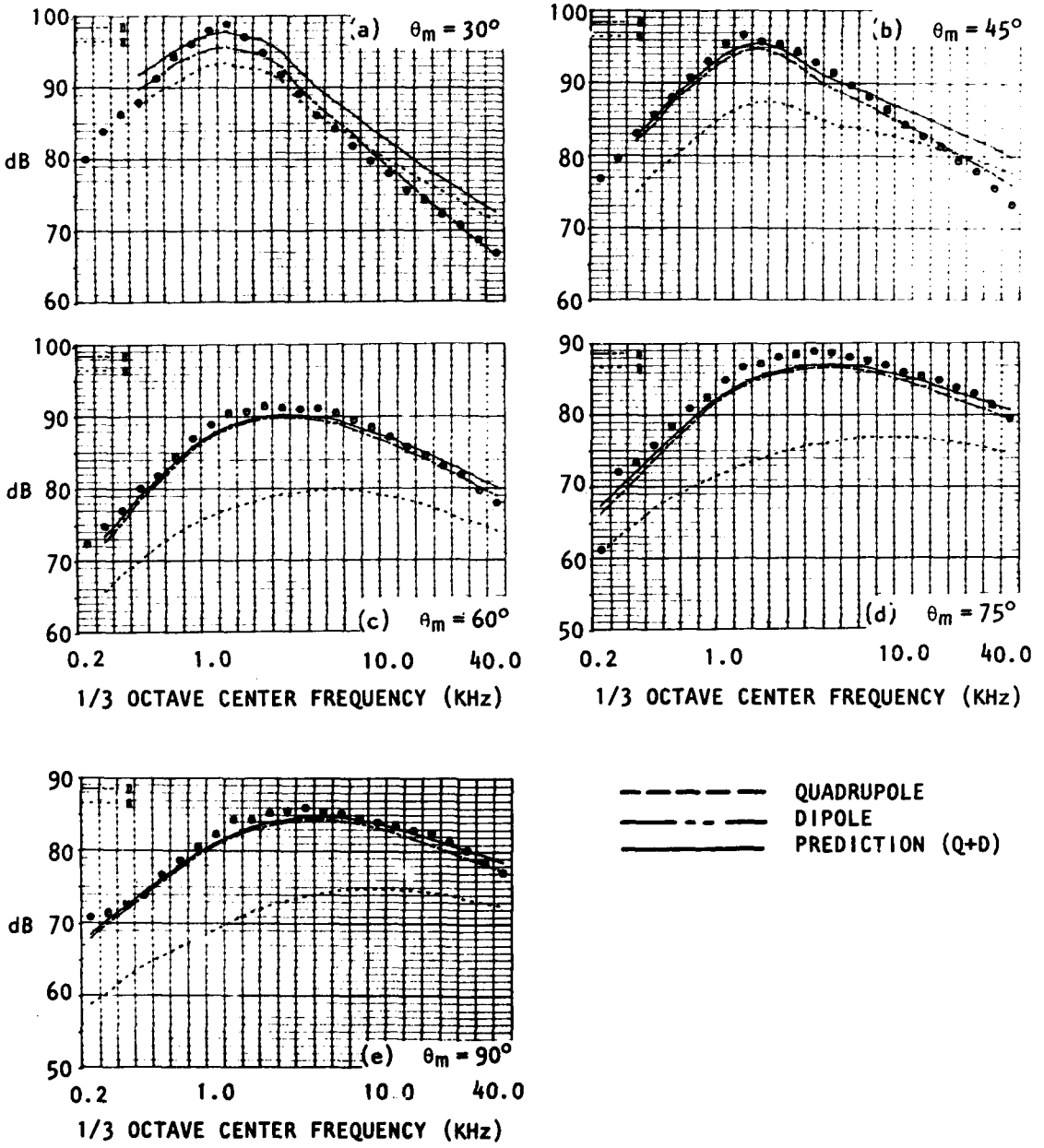

Figure 2.79
Comparison of Measured Mixing Noise Spectra and Predictions Based on High-Frequency Lilley Equation Solutions. High-Temperature Jet, TP #72. Method 2.

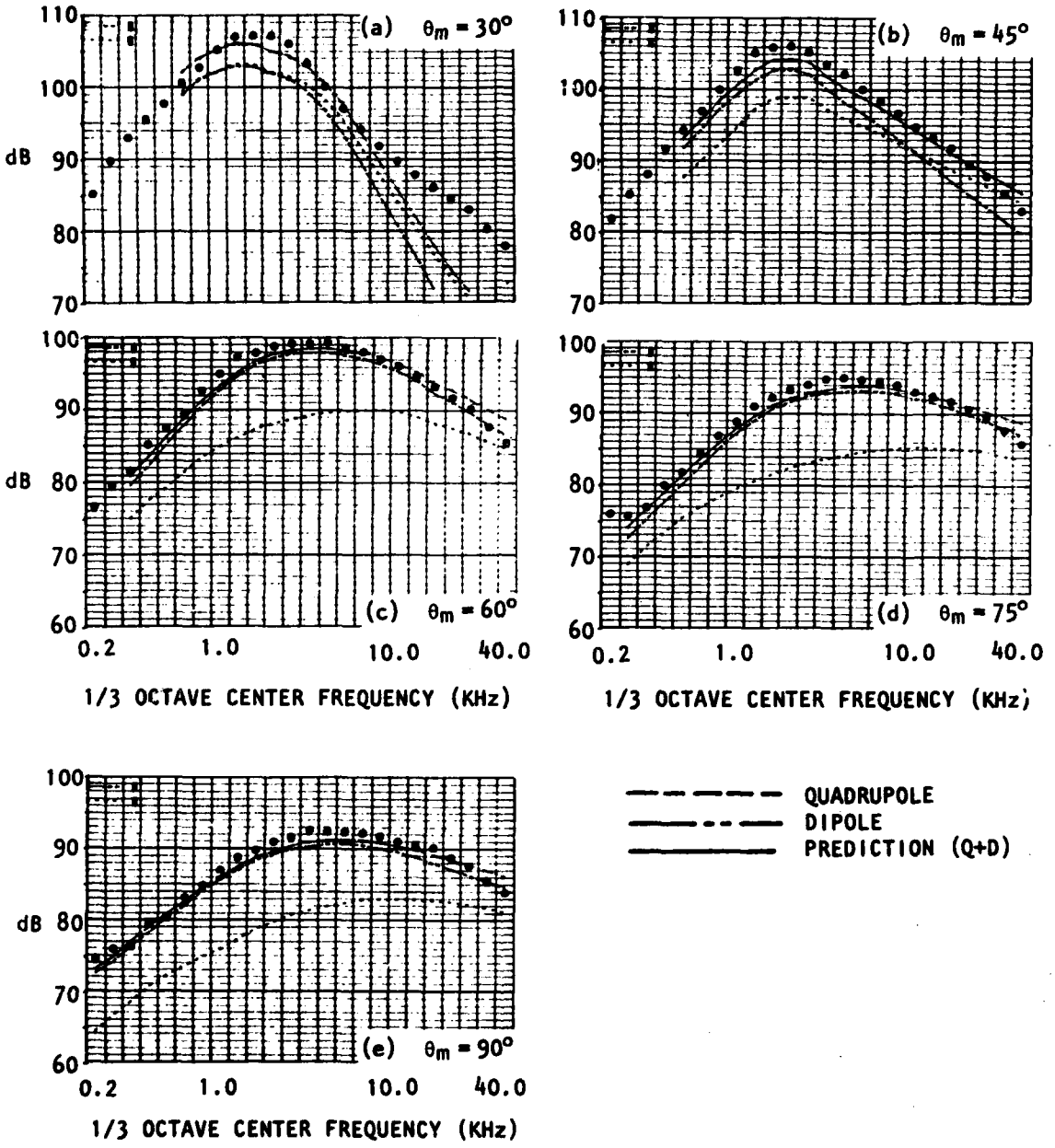

Figure 2.80
Comparison of Measured Mixing Noise Spectra and Predictions Based on High-Frequency Lilley Equation Solutions. High-Temperature Jet, TP #73. Method 1.

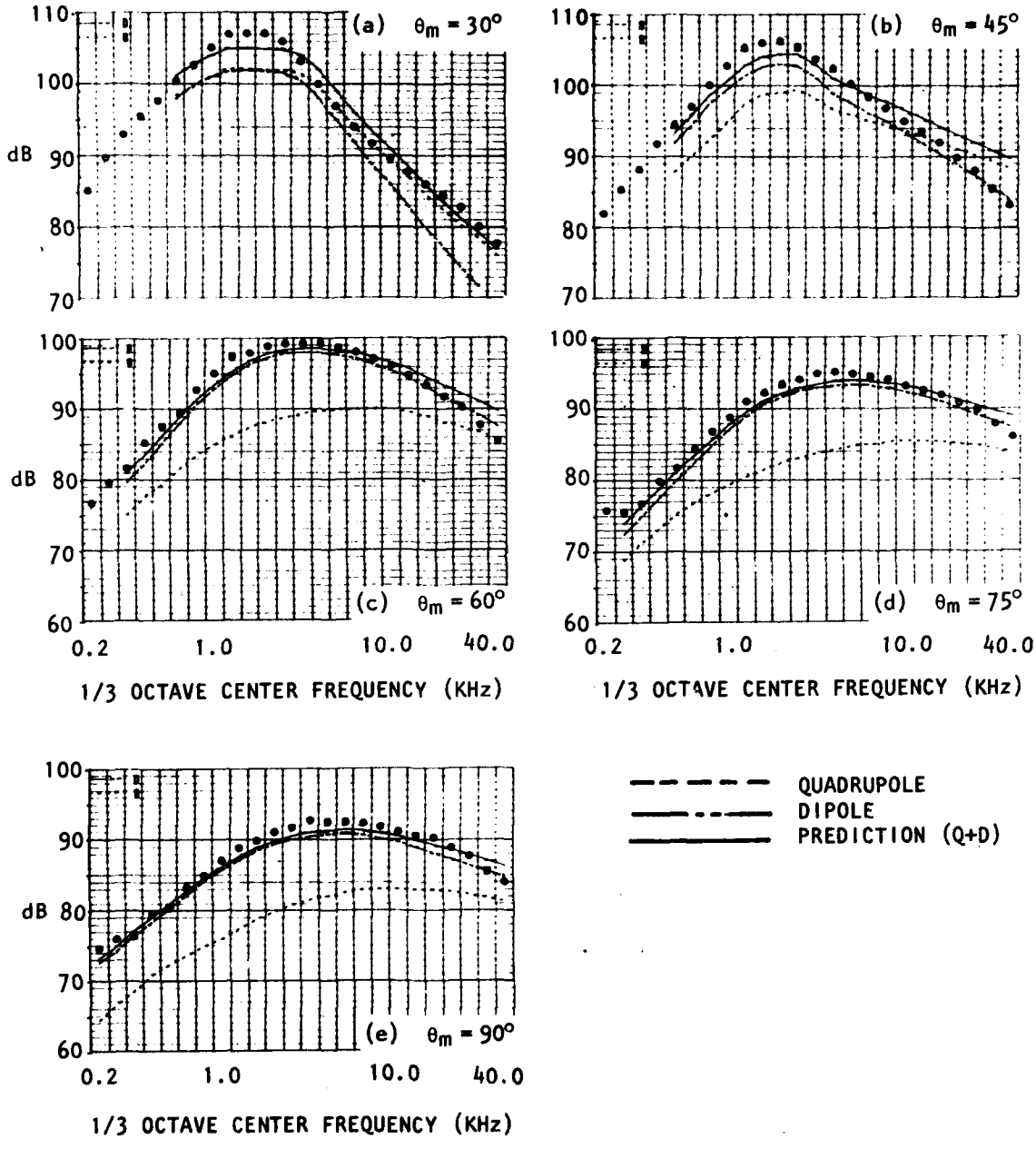

Figure 2.81
Comparison of Measured Mixing Noise Spectra and Predictions Based on High-Frequency Lilley Equation Solutions. High-Temperature Jet, TP #73. Method 2.

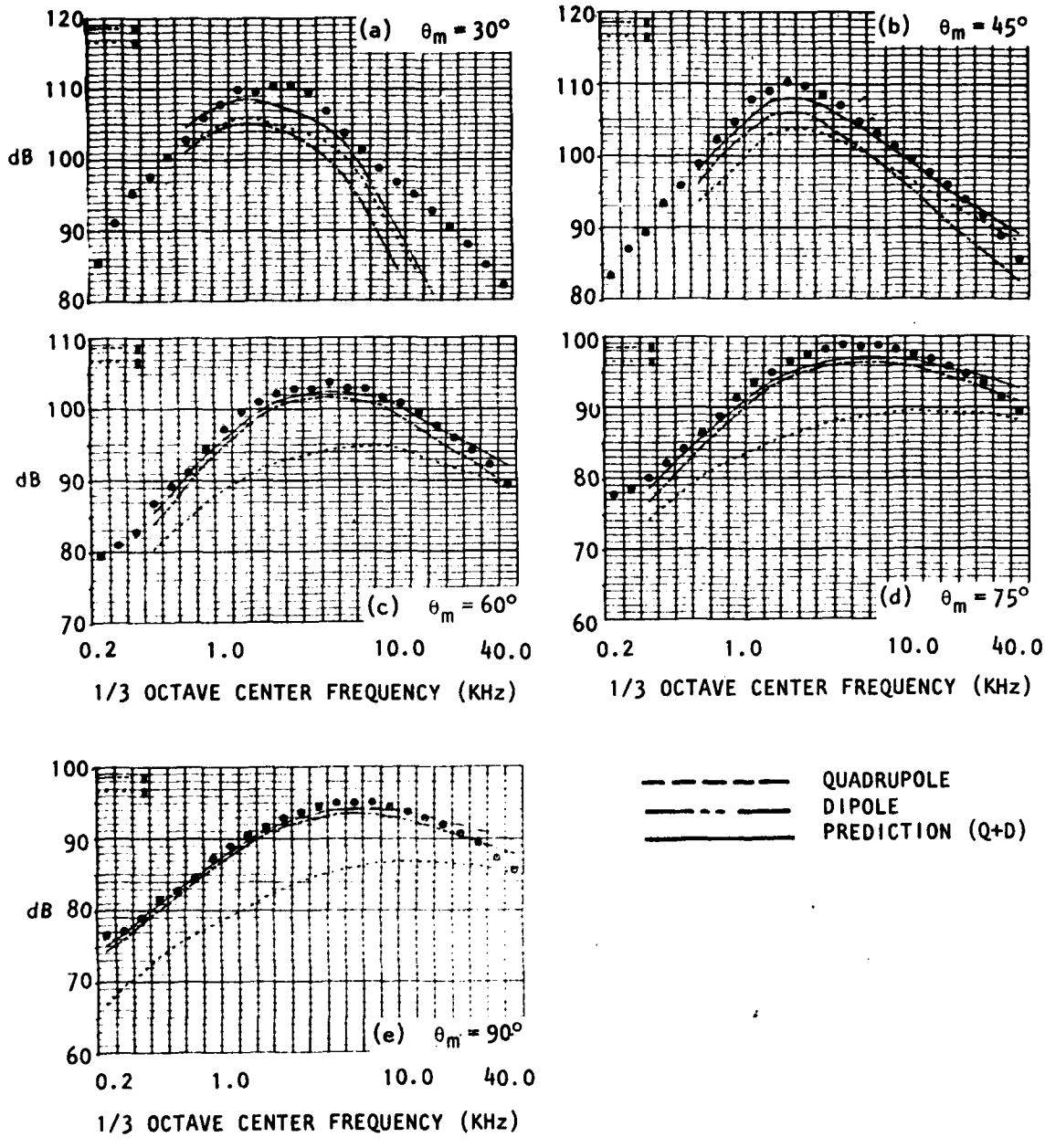

Figure 2.82
Comparison of Measured Mixing Noise Spectra and Predictions Based on High-Frequency Lilley Equation Solutions. High-Temperature Jet, TP #74. Method 1.

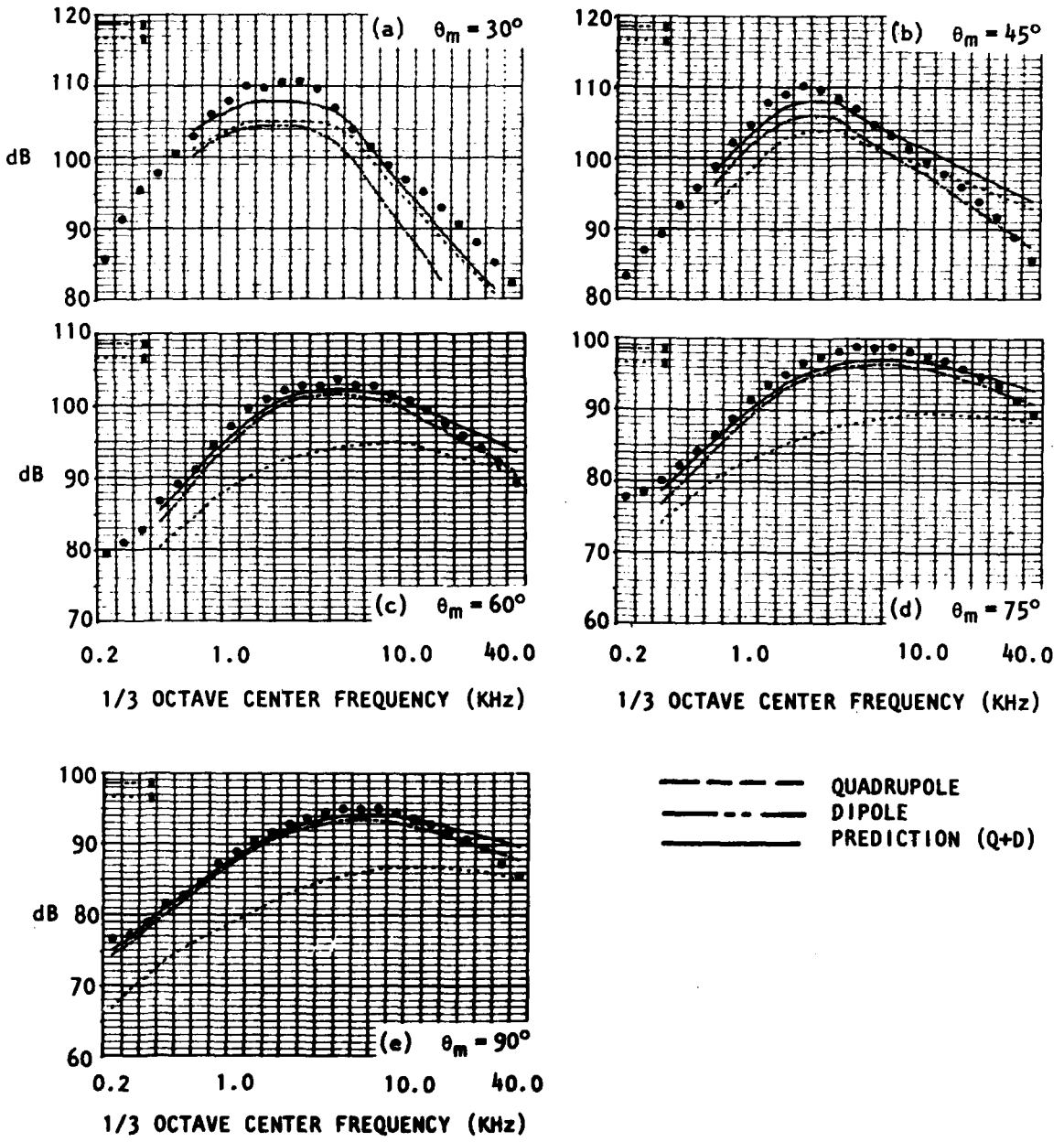

Figure 2.83
Comparison of Measured Mixing Noise Spectra and Predictions Based on High-Frequency Lilley Equation Solutions. High-Temperature Jet, TP #74. Method 2.

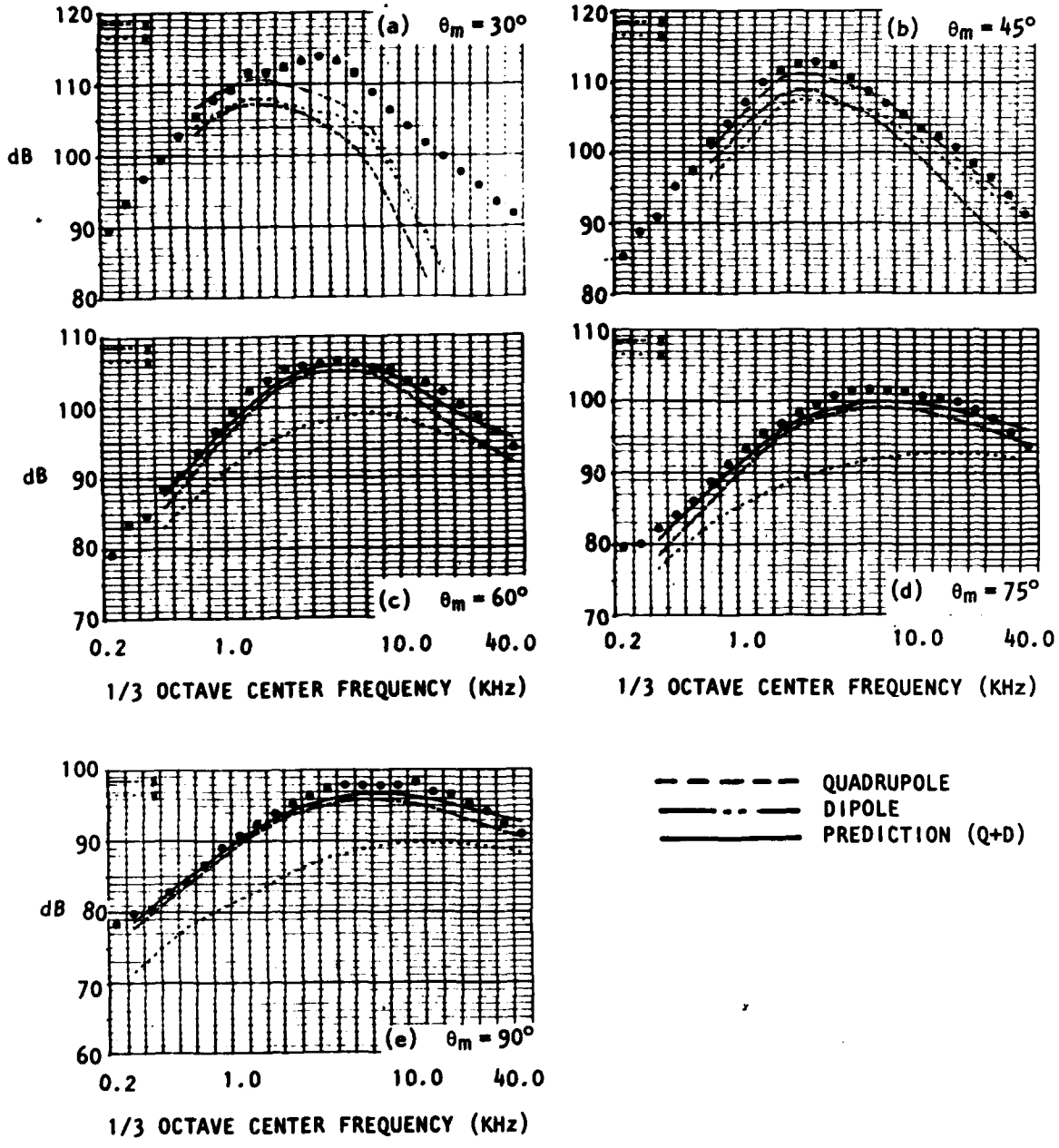

Figure 2.84
Comparison of Measured Mixing Noise Spectra and Predictions Based on High-Frequency Lilley Equation Solutions. High-Temperature Jet, TP #75. Method 1.

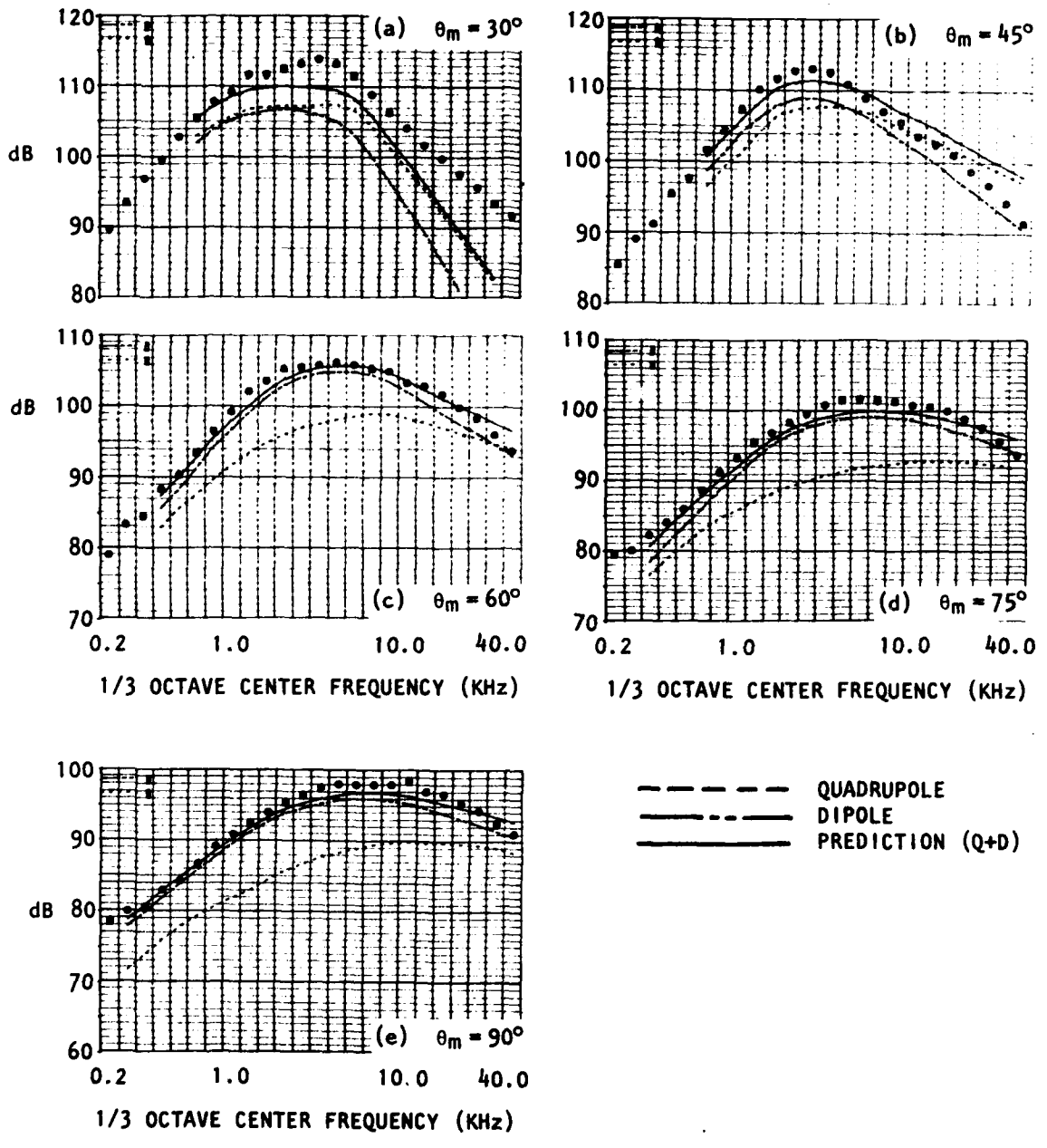

Figure 2.85
Comparison of Measured Mixing Noise Spectra and Predictions Based on High-Frequency Lilley Equation Solutions. High-Temperature Jet, TP #75. Method 2.

The alternative approach is to rely on an extra source mechanism like the large-scale turbulence structure investigated in Section 3.

The double-hump feature of some spectra, at $\theta_m = 30°$, for example, in Figures 2.58 and 2.60, is associated with supersonic conditions and the critical layer (where $D_S \equiv 1 - V_S \cos\theta_o / a_o = 0$): at *low* Strouhal numbers $D_S \sim 1$ since the source-region velocity, V_S, is small due to the centerline velocity decay, but as the frequency is increased V_S increases and (at small angles) $D_S \to 0$. The double hump is *not* a feature of the approximate, high-frequency Lilley equation solutions above but also appears in the numerical solutions as illustrated in Section 2.5.3.4.

Finally, it should be noted that these prediction methods apparently can be used to estimate noise levels quite close to the jet nozzle, according to recent work at Lockheed [2.21], as close as three diameters ($R_m = 3d$) for an observer angle of ninety degrees ($\theta_m = 90°$).

2.5.3 General Method of Jet Mixing Noise Prediction Based on *Numeric* Lilley Equation Solutions

The general prediction method is identical to the high-frequency prediction methods 1 and 2 described in Section 2.5.1 except that the factor

$$\frac{1}{\tilde{D}_S^2} \cdot \frac{N_\infty}{(T_S/T_o)} \left[\cos^4\theta_o \, (1 + C_q) + 2|\kappa_S^2|\cos^2\theta_o + |\kappa_S^2|^2\right] \qquad (2\text{-}156)$$

in Equation (2-112) for the quadrupole component is replaced by

$$F_q + F_m \, C_q \cos^4\theta_o \qquad (2\text{-}157)$$

and the factor

$$\frac{1}{\tilde{D}_S^2} \frac{N_\infty}{(T_S/T_o)} \left[\cos^2\theta_o \, (1 + C_d) + |\kappa_S^2|\right] \qquad (2\text{-}158)$$

in Equation (2-139) for the dipole component by

$$F_d + F_m \, C_d \cos^2\theta_o \qquad (2\text{-}159)$$

The quantity F_m is referred to as the monopole *flow factor* since it is unity in the absence of flow (assuming the speed of sound, density and hence temperature are uniform and equal to the ambient values, in the absence of flow) and is defined as the ratio of the far-field intensity *with flow* to its value without the jet flow, the source strength being held constant. Similarly, F_d and F_q are the *statistically isotropic* (SI) dipole and quadrupole flow factors.

It should be noted that the monopole flow factor arises in the present calculations because acoustic-mean flow interaction effects for both the axial-axial quadrupole and axial dipole are identical to that of the monopole

source; it does *not* imply that a monopole source term appears on the right-hand side of the Lilley equation. The acoustic-mean flow interaction effects are identical because the mean flow is axially uniform in the Lilley equation model.

The flow factors are calculated from numerical solutions to the Lilley equation with three different models of the radial (and azimuthal) source distribution.

2.5.3.1 *The ring source model*

The first and simplest model corresponds closely to that adopted for the high-frequency prediction method described in Section 2.5.1, in that the source region is confined to a narrow annular region (radius r_s) of vanishing radial extent such that the source region can be identified with particular values of the mean velocity and temperature. Although this implies radial compactness (and azimuthal compactness is assumed also), the effects of radial-azimuthal noncompactness in the real source distribution can and are taken into account by continuing to use the high-frequency-based modified Doppler factor. For this ring source model the flow factors are calculated according to the following formulae.†

$$F_m(\theta_o, r_s, \omega) = \sum_{n=0}^{N_{max}} \varepsilon_n |C(k_x, r_s, n, \omega)|^2 / \rho_o D^4(r_s) \qquad (2\text{-}160)$$

$$(\varepsilon_o = 1;\ \varepsilon_n = 2,\ n \neq 0)$$

$$F_d(\theta_o, r_s, \omega) = \sum_{n=0}^{N_{max}} \varepsilon_n \left| \overset{(x)}{\cos^2\theta_o} + \left| \frac{1}{C(r_s)} \cdot \overset{(r)}{\frac{dC}{d(k_o r_s)}} \right|^2 + \overset{(\phi)}{\frac{n^2}{k_o^2 r_s^2}} \right| \frac{|C(r_s)|^2}{\rho_o D^4(r_s)} \qquad (2\text{-}161)$$

$$F_q(\theta_o, r_s, \omega) =$$

$$\sum_{n=0}^{N_{max}} \varepsilon_n \left| \overset{(xx)}{\cos^4\theta_o} + \left| \kappa^2(r_s) - \frac{n^2}{k_o^2 r_s^2} + \overset{(rr)}{\left(\frac{1}{k_o r_s} - \frac{1}{\bar{\rho}(r_s)} \frac{d\bar{\rho}(r_s)}{d(k_o r_s)} \right)} \frac{1}{C(r_s)} \frac{dC(r_s)}{d(k_o r_s)} \right|^2 \right.$$

$$\left. + \left| \overset{(\phi\phi)}{\frac{1}{k_o r_s C(r_s)}} \frac{dC(r_s)}{d(k_o r_s)} - \frac{n^2}{k_o^2 r_s^2} \right|^2 \right|$$

†*In these formulae* $C(k_x, r_s, n, \omega)$ *is usually abbreviated by* $C(r_s)$; *also* $k_x = k_o \cos\theta_o$.

$$+ 2\cos^2\theta_o \left| \frac{1}{C(r_s)} \cdot \frac{dC(r_s)}{d(k_o r_s)} - \frac{\cos\theta_o}{D(r_s)} \frac{dM_o(r_s)}{d(k_o r_s)} \right|^2 \quad (x\phi) \quad + 2\cos^2\theta_o \frac{n^2}{k_o^2 r_s^2}$$

$$+ 2 \frac{n^2}{k_o^2 r_s^2} \left| \frac{1}{C(r_s)} \cdot \frac{dC(r_s)}{d(k_o r_s)} - \frac{\cos\theta_o}{D(r_s)} \frac{dM_o(r_s)}{d(k_o r_s)} - \frac{1}{k_o r_s} \right|^2 \quad (r\phi) \quad \left| \frac{|C(r_s)|^2}{\rho_o D^4(r_s)} \right| . \qquad (2\text{-}162)$$

In these series N_{max} is determined by the criterion that the value of the term $n = N_{max}$ does not change the partial sum by more than a specified relative-error tolerance. The monopole solution, C, is given by

$$C(r) = p_i(r) \left| \frac{2\bar{\rho}(r)\, D^2(r)}{j\pi r W\{p_i(r),\, p_o(r)\}} \right| \qquad (2\text{-}163)$$

where p_i is the numeric solution of

$$\frac{d}{dr} \left| \frac{r}{\bar{\rho}\omega^2 D^2} \frac{dp_i}{dr} \right| + \frac{r p_i}{\bar{\rho}\omega^2 D^2} \left| k_o^2 \kappa^2 - \frac{n^2}{r^2} \right| = 0 \qquad (2\text{-}164)$$

with the initial value

$$p_i = \rho_i^{\frac{1}{2}} J_n(k_o \kappa_i r) \qquad (2\text{-}165)$$

as $r \to 0$. Here

$$D = 1 - V(r) \cos\theta_o / a_o \qquad (2\text{-}166)$$

$$\kappa = \{a_o^2 D^2/\bar{a}^2 - \cos^2\theta_o\}^{\frac{1}{2}} \qquad (2\text{-}167)$$

and subscript i denotes conditions on the jet centerline. The outer solution $p_o(r)$ is given by

$$p_o = \rho_o^{\frac{1}{2}} H_n^{(2)} (k_o \kappa_o r) \qquad (2\text{-}168)$$

and the factor in square brackets in Equation (2-163), being independent of r, is evaluated outside the flow where $\rho D^2 \to \rho_o$.

The velocity and temperature profiles V(r), T(r) are determined from the specified shear layer thickness parameter, δ_s, and the centerline values V_{max}, T_j (see Appendix 2A). The density and speed of sound are related to the temperature by

$$\bar{\rho}(r)/\rho_o = (T(r)/T_o)^{-1} \tag{2-169}$$

and

$$\bar{a}^2(r)/a_o^2 = \gamma(r)T(r)/\gamma_o T_o \tag{2-170}$$

although in the numerical solutions γ is assumed constant and equal to the value in the source region, γ_s [as calculated by Equation (2A-17)] so that $\bar{a}^2(r)/a_o^2 = T(r)/T_o$.

The singularity in Equation (2-164) at the critical layer (D = 0) is avoided by taking the integration path into the complex plane where the mean velocity and temperature are complex variables and are calculated by a Taylor expansion about the critical point [2.13].

2.5.3.2 Radially distributed source model - high-frequency coherence noncompactness assumed

In this case the flow factors are calculated from an *integral* of the modulus of numerical solutions; for example, the quadrupole flow factor is given by†

$$F_q(\theta_o,\omega) = \frac{\sum_{n=0}^{N_{max}} \varepsilon_n \int_0^\infty r\,dr\, \frac{C_{\alpha\beta}}{\rho_o^{\frac{1}{2}} k_o^2}(k_x,r,n,\omega)\, \frac{C^*_{\alpha\beta}}{\rho_o^{\frac{1}{2}} k_o^2}(k_x,r,n,\omega)\, [\overline{v^2}(x_s,r)]^2}{\int_0^\infty r\,dr\, [\overline{v^2}(x_s,r)]^2} \tag{2-171}$$

and similarly for the monopole and dipole flow factors. The numerical solutions $|C_{\alpha\beta}(k_x,r,n,\omega)|^2/\rho_o k_o^4$ $(\alpha,\beta = x,r,\phi)$ are identical to the corresponding terms in Equation (2-162) except that the fixed ring source radius, r_s, is replaced here by r which varies over the radial extent of the source distribution. The Gaussian model of the radially distributed source is

$$\{\overline{v^2}(x_s,r)\}^{\frac{1}{2}} = \{\overline{v^2}(x_s)\}^{\frac{1}{2}}_{max} \exp[-\{0.8326\ (n - n_s)/n_{hw}\}^2] \tag{2-172}$$

$$(n = (r - r_J)/x_s)$$

†*In these formulae* $k_x = k_o \cos\theta_o$.

where

$$\{\overline{v^2}(x_s,r)\}^{\frac{1}{2}} = \{\overline{v^2}(x_s)\}^{\frac{1}{2}}_{max} \qquad \text{at} \qquad \eta = \eta_s \tag{2-173}$$

and

$$\{\overline{v^2}(x_s,r)\}^{\frac{1}{2}} = 0.5\ \{\overline{v^2}(x_s)\} \qquad \text{at} \qquad \eta = \eta_s \pm \eta_{hw} \tag{2-174}$$

The radial center of the source distribution, $\eta_s \equiv (r_s - r_J)/x_s$ is associated with the parameter $\varepsilon_s \equiv V_s/V_J$ of the ring-source model and in fact the value of ε_s (for example, a value inferred from the measured mixing noise data with the high-frequency analysis) is used to specify η_s with the appropriate velocity profile model. That is, with either

$$\varepsilon_s = 0.5\ \{1 - \text{erf}\ (\sqrt{\pi}\chi_s)\} \tag{2-175}$$

where

$$\chi_s = \frac{r_s - r_J}{\delta_s} - .1676 \tag{2-176}$$

and

$$\delta_s = 0.1313\ x_s \tag{2-177}$$

for the "initial mixing region" or with

$$\varepsilon_s = \exp\ \{-(r_s/\delta_s)^2\ (e/2)\} \tag{2-178}$$

where

$$\delta_s = 0.08233\ x_s + 0.6782\ r_J \tag{2-179}$$

for the "fully developed region." [Iteration is required to determine χ_s from ε_s with Equation (2-175).]

The half-width η_{hw} is specified directly; typically $\eta_{hw} = 0.1$ at subsonic conditions. Note that η_{hw} is related to the parameter c used in Section 2.4 by $\sqrt{c} = 0.8326/\eta_{hw}$.

The value of $\{\overline{v^2}(x_s)\}^{\frac{1}{2}}_{max}$ is not required since it is a common factor in the numerator and denominator of Equation (2-171). In Equation (2-171) the denominator is calculated with a standard integral (omitting the peak turbulence intensity factor raised to the power four):

$$\int_0^\infty \mathrm{rdr}\ [\overline{\overline{v^2}}(x_s,r)]^2 \propto \int_0^\infty \mathrm{rdr}\ \exp\left[-4\{0.8326\ (\eta - \eta_s)/\eta_{hw}\}^2\right]$$

$$= \int_0^\infty \mathrm{rdr}\ \exp\left[-4\{0.8326\ (r - r_s)/(x_s \eta_{hw})\}^2\right]$$

$$= \frac{b^2}{2}\left\{e^{-a^2/b^2} + \frac{a}{b}\ \sqrt{\pi}[1 + \mathrm{erf}\ (a/b)]\right\} \qquad (2\text{-}180)$$

where

$$a \equiv r_s \qquad (2\text{-}181a)$$

$$b = 0.5\ x_s\ \eta_{hw}/0.8326 \qquad (2\text{-}181b)$$

2.5.3.3 Radially distributed source model – no assumptions

In the high-frequency prediction methods and in the two forms of the general prediction method described above, the *coherence-noncompactness* of the source distribution in the radial and azimuthal directions is taken into account *via* the high-frequency modified Doppler factor described in Section 2.1.3. This assumption can be relaxed and coherence effects calculated with the numerical Lilley equation solutions, but for simplicity the modified Doppler factor is still retained for prediction purposes in its high-frequency form [that is, given by Equation (2-116)] since the results of Section 2.1.5 indicate that the high-frequency result is quite accurate.† Instead the coherence effects – based on numeric solutions – are incorporated into modified flow factors which are then used in conjunction with the same (high-frequency) convective amplification factors and master spectra to yield a noise level prediction at any specified frequency and angle. The radial source distribution model described in the previous section is retained and the Gaussian model described by Equation (2-39) is used to describe the source coherence distribution. The modified flow factors are in the form of double integrals; for example, the modified quadrupole flow factor is given by

†*However, the transverse noncompactness term should be modified inside the cone of silence – see Section 2.1.5.*

$$F_q(\theta_o,\omega) =$$

$$\sum_{n=0}^{N_{max}} \varepsilon_n \int_0^\infty rdr \frac{C^*_{\alpha\beta}}{\rho_o^{\frac{1}{2}} k_o^{\frac{1}{2}}} (k_x,r,n,\omega)\ \overline{v^2}(x_s,r) \int_0^\infty r'dr' \frac{C_{\alpha\beta}}{\rho_o^{\frac{1}{2}} k_o^{\frac{1}{2}}} (k_x,r',n,\omega)\overline{v^2}(x_s,r')$$

$$\frac{\exp\left[-2\pi(r^2 + r'^2)/L_t^2\right] 2\pi\ I_n(4\pi rr'/L_t^2)}{\left\{\exp\left[-k_o^2\kappa_s^2\ L_t^2/8\pi\right] \cdot \frac{L_t^2}{2} \int_0^\infty rdr[\overline{v^2}(x_s,r)]^2\right\}} \qquad (2\text{-}185)$$

and similarly for the monopole and dipole (modified) flow factors. The transverse coherence length is assumed to be given in the form

$$\frac{L_t}{r_J} = a_\ell \frac{x_s}{r_J} + b_\ell \qquad (2\text{-}183)$$

where the coefficients a_ℓ, b_ℓ are input parameters; an example of values used in Section 2.4 is $a_\ell = 0.028$, $b_\ell = 0.28$.

The numeric solutions $C_{\alpha\beta}$ correspond to terms in Equation (2-162) except that r,r' vary over the radial extent of the source distributions and the modulus squared is replaced by the product of solutions at two different radii, as the phase of the numeric solution is required as well as the amplitude. The solutions required for the quadrupole and dipole source models, $C_{\alpha\beta}$ and C_α, are defined by Equations (2-18) and (2-19) in terms of the basic monopole solution that is obtained with Equations (2-163) – (2-168). As indicated by Equation (2-160) the monopole flow factor is simply formed from the basic monopole solution and the factor D^{-4}.

2.5.3.4 Comparison of general method predictions with Lockheed measured data

When the general prediction method described above for the ring source model is evaluated with the same parameter values (e.g. V_c/V_J, C_g) as used in the high-frequency prediction method, the results are grossly different, both from the results of the latter method and from the measured data. This is illustrated by presenting in Figure 2.86 Method 1 predictions (with measurements) and in Figure 2.87 General Method predictions (also with measurements), for an observer angle of 30° at five different jet velocities (isothermal test points 8, 12, 51, 58 and 63 – see Table 2.17 for jet exit conditions). The parameter values are the same in both cases. Clearly, these parameter values are completely incompatible with the General Method in the low-to-medium Strouhal number range. This result is to be expected, however, when considering the unrealistically large convection velocities ($V_c = V_J$) and anisotropy

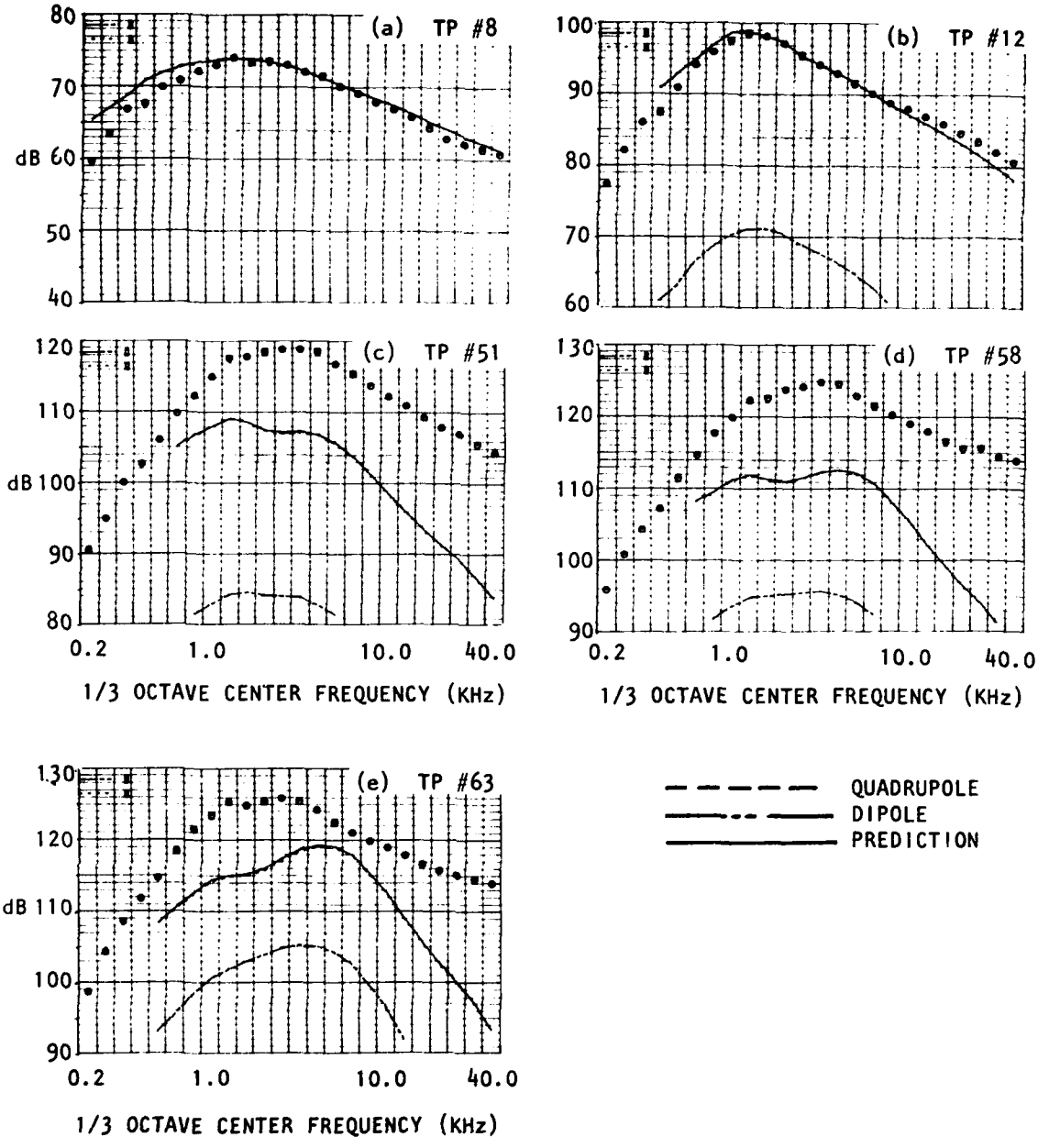

Figure 2.86
Comparison of Measured Mixing Noise Spectra and Predictions Based on *High-Frequency* Lilley Equation Solutions. Isothermal Jet, $\theta_m = 30°$. Method 1 Parameters.

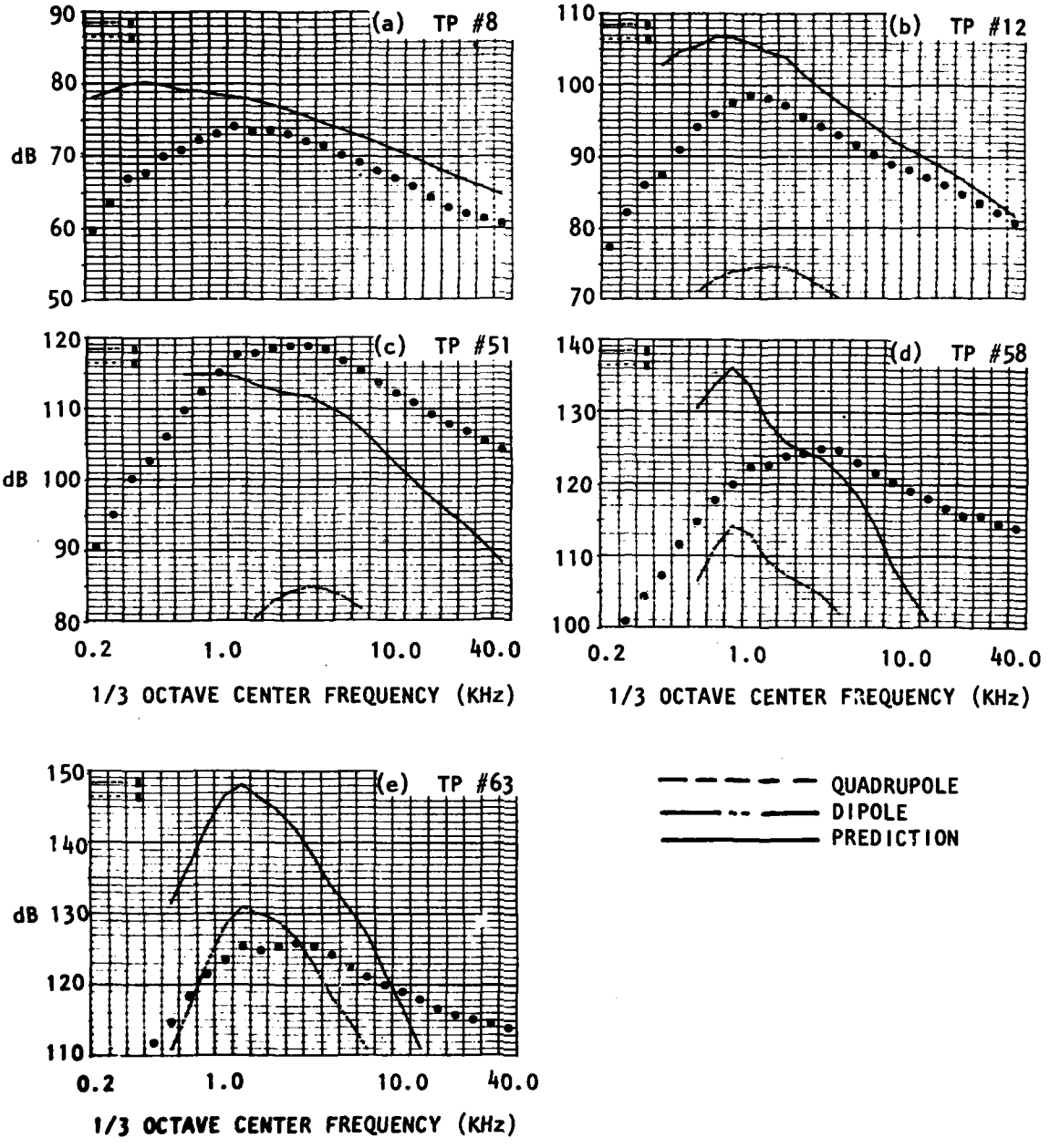

Figure 2.87
Comparison of Measured Mixing Noise Spectra and Predictions Based on Numeric Lilley Equation Solutions. Isothermal Jet, $\theta_m = 30°$. Method 1 Parameters.

coefficients ($C_q > 4$) at low Strouhal numbers, as well as the (probably) unrealistic shear layer thickness values below $S_m \doteq 0.5$ (see Table 2.15 and Figure 2.52).

As a first step towards "improving" the parameter values, the General Method is re-evaluated in Figure 2.88 with $V_c = 0.6\ V_J$ at all modified Strouhal numbers, the anisotropy coefficients, C_q, set to less than or equal to four† and with the δ_s/r_J *versus* S_m dependence replaced by that obtained from far-field source location data (given in Table 2.15 and plotted in Figure 2.52a). The improvement exhibited in Figure 2.88a is quite dramatic at the lowest jet velocity (TP #8) and in all cases the spectrum *slope* at low frequencies agrees well with that in the measured data. The double-hump feature is now clearly seen in these results but the second hump is more accentuated and this leads to an overprediction at the highest jet exit velocity in Figure 2.88e.

Conversely, when these more realistic parameter values are used in the high-frequency method, the predictions are modified substantially as shown in Figure 2.89 (which is to be compared with Figure 2.86). Although these changes are not so dramatic as those shown above for the General Method (comparing Figures 2.87, 2.88), it can be clearly seen, particularly for for TP #12, that the high-frequency prediction method is quite sensitive to the empirical parameters, and these cannot be changed at will to more realistic values without seriously degrading its accuracy. The General Method, however, gives consistently better results if the empirical parameters are modified in accordance with trends in measured turbulence and source location data.

Results from the General Method at other angles – with the modified parameter values – are shown in Figure 2.90; comparing these with the Method 1 predictions in Figures 2.56, it can be seen that the latter method *is* more accurate but again it is emphasized the General Method is largely independent of unrealistic "adjustable constants" and in certain applications (e.g. extensions to more complex flows) this could be a very useful feature.

In all the above results, the ring source model is assumed in both the high-frequency and general prediction methods. The effect of including a (realistic) radially distributed source in the General Method (see Section 2.5.3.2) can be seen by comparing the predictions in Figure 2.88 with those in Figure 2.91 in which a radial half-width $\eta_{hw} = 0.1$ has been used. In general the low-frequency spectrum levels are reduced, although the asymptotic slope remains roughly in agreement with the measured slope, while the high-frequency levels are increased quite substantially, bringing the predicted levels and slopes quite close to the measured values at the three supersonic test conditions (Figure 2.91c, d, e). The penalty for this improvement is a further degradation in the prediction quality at the high-subsonic test condition (Figure 2.91b). From these and other results, there is little

†*A maximum value suggested by LV turbulence data.*

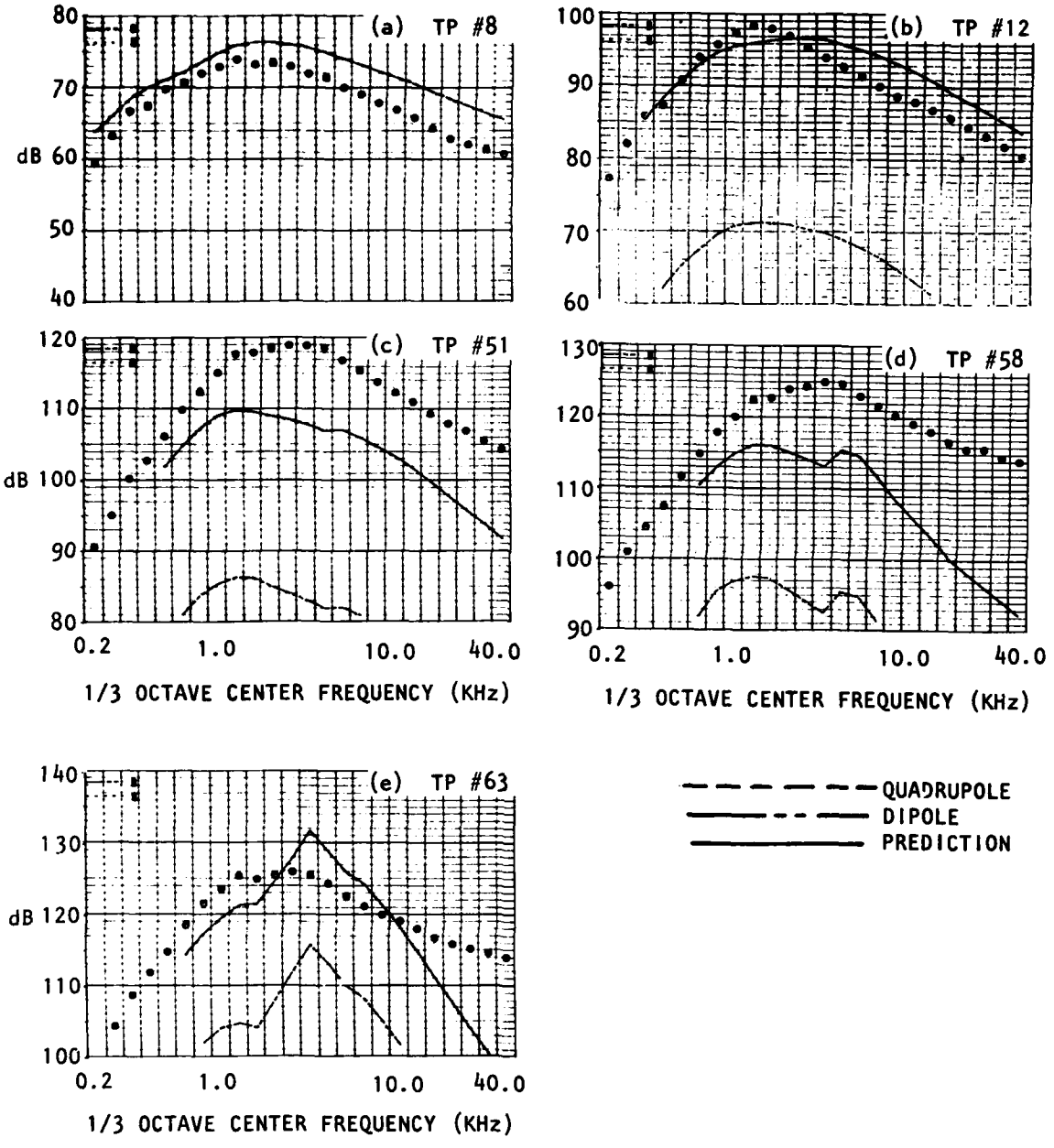

Figure 2.88
Comparison of Measured Mixing Noise Spectra and Predictions Based on *Numeric* Isothermal Jet, $\theta_m = 30°$. Modified Parameters.

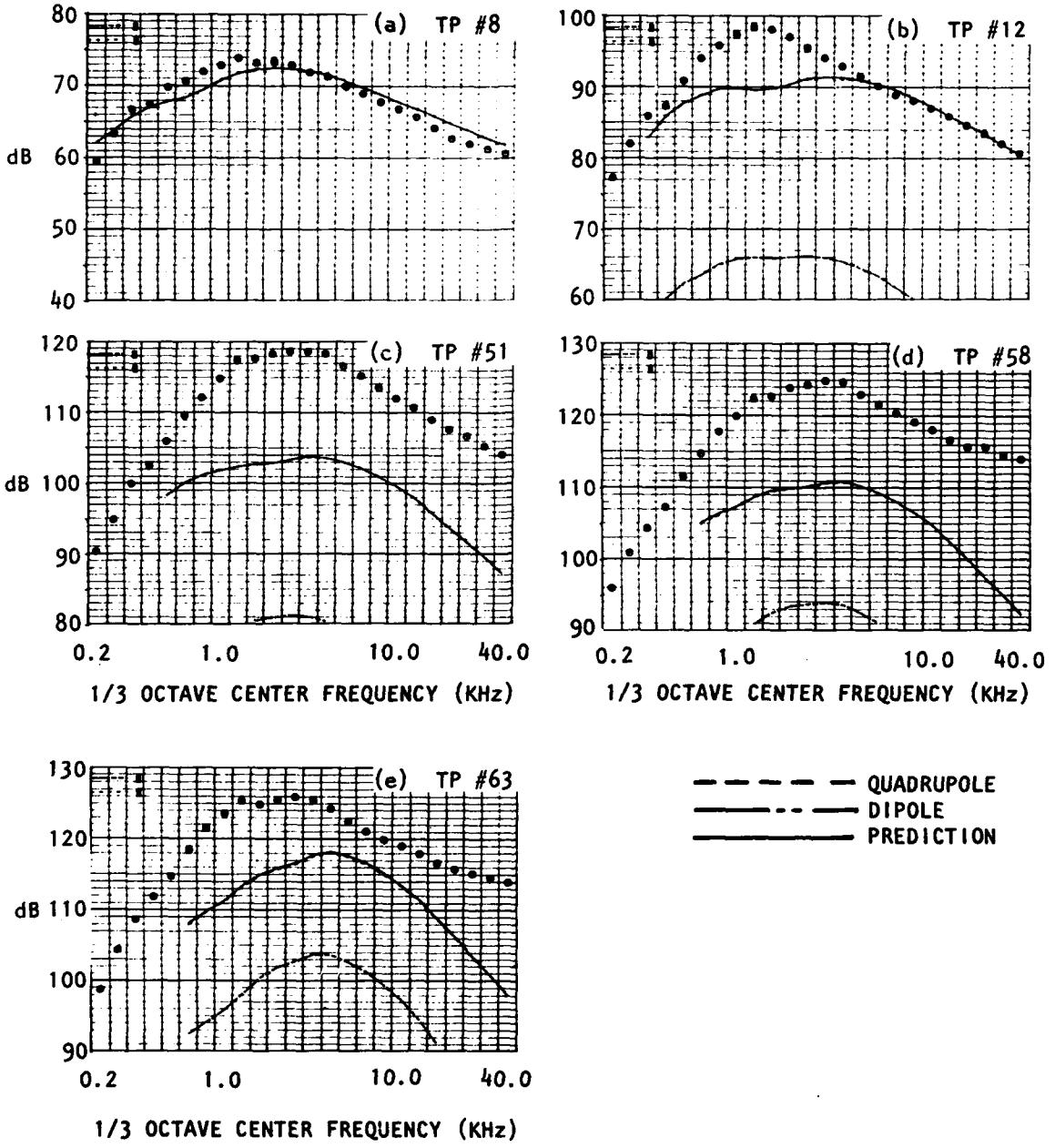

Figure 2.89
Comparison of Measured Mixing Noise Spectra and Predictions Based on *High-Frequency* Isothermal Jet, $\theta_m = 30°$. Modified Parameters.

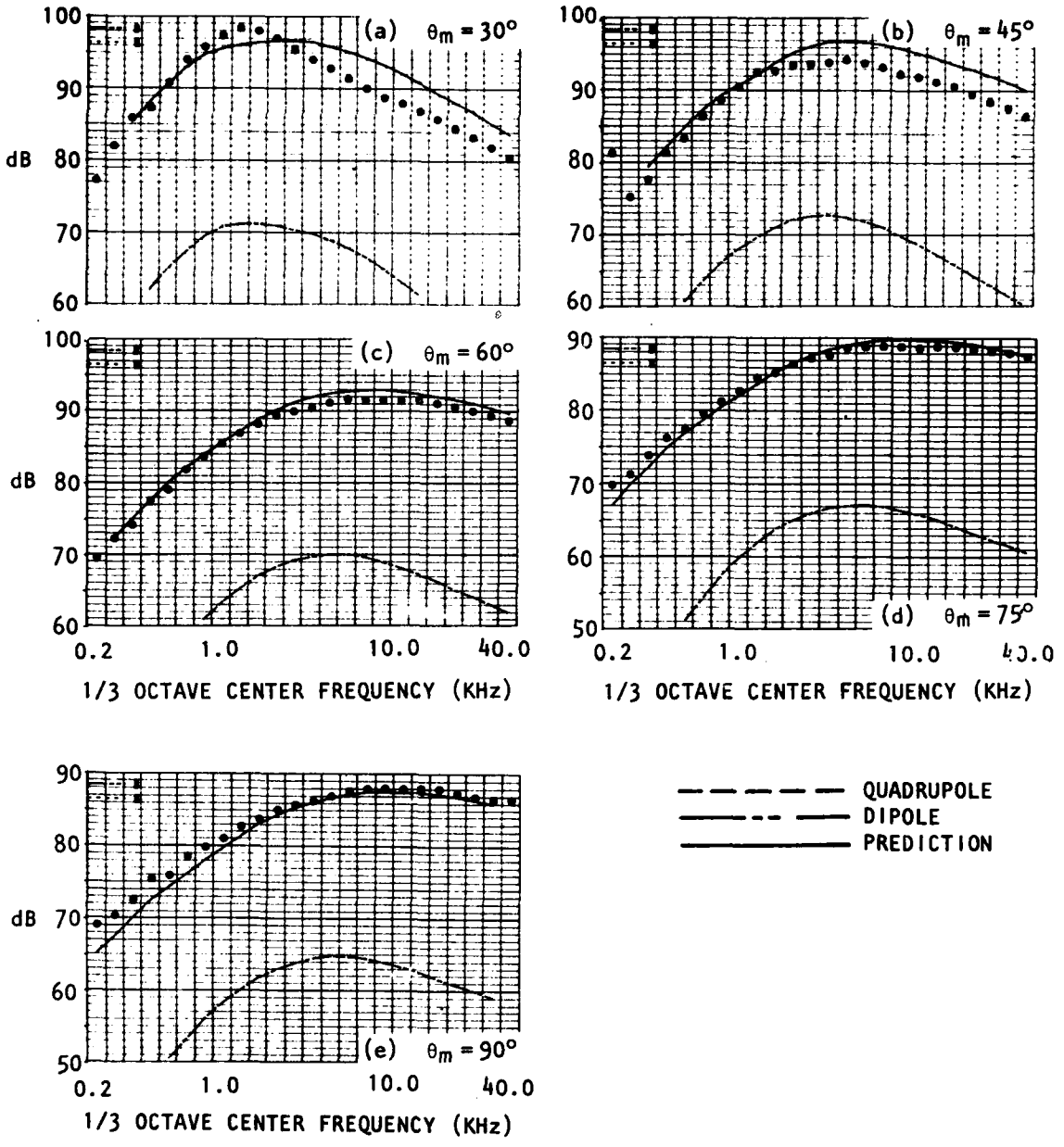

Figure 2.90
Comparison of Measured Mixing Noise Spectra and Predictions Based on *Numeric* Lilley Equation Solutions. Isothermal Jet, TP #12. Modified Parameters.

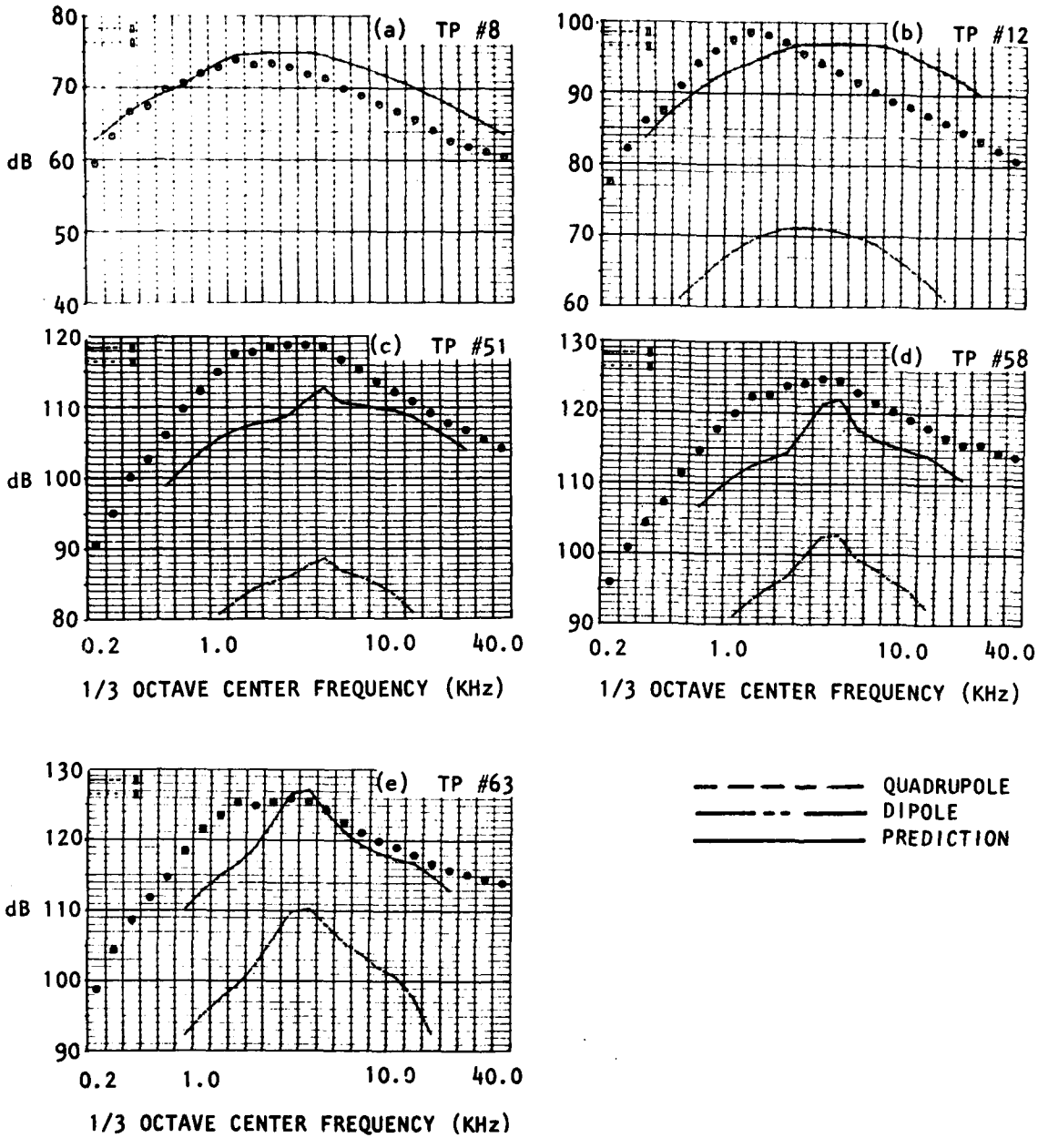

Figure 2.91
Comparison of Measured Mixing Noise Spectra and Predictions Based on *Numeric* Lilley Equation Solutions With Radially Distributed Source Model. Isothermal Jet, $\theta_m = 30°$. Modified Parameters.

doubt that the "radial source distribution effect" should be included†, but it seems unlikely that this will completely resolve the underprediction problem at high-frequencies and small angles. This conclusion is somewhat reinforced by the fact that η_{hw} apparently decreases with increasing Mach number, according to LV turbulence data, a feature utilized in the absolute spectrum level predictions of Section 2.4 (expressed there in terms of $c \equiv (0.8326/\eta_{hw})^{\frac{1}{2}}$).

Finally, one *possible* interpretation of the smaller δ_s values used by Method 2 (inferred from all the measured data) is that these actually reflect the influence of radial source distribution effects. At small angles, Method 2 yields improved predictions when $V_J/a_o > 1$ but overpredicts measured levels when $V_J/a_o < 1$ (compare Method 1 *versus* Method 2 at $\theta_m = 30°$ in Figures 2.54a–2.63a). Comparison of Figure 2.88 with Figure 2.91 for the same angle shows that a radially distributed source has a similar effect, relative to the ring-source model predictions (which is the model used to infer δ_s values from the measured data).

2.6 CONCLUSIONS

New prediction methods have been developed for the small-scale, turbulent mixing noise emitted from an unexcited, round-nozzle air-jet. The methods are based in part upon the scaling laws of Lighthill, Ribner [2.3] and Ffowcs Williams [2.7] and upon empirical constants determined from the Lockheed mixing noise data [2.14], as well as solutions to the Lilley equation, which account for acoustic-mean flow interaction effects.

The main conclusions of the analytical and numerical work are summarized below; conclusions from the experimental investigations can be found in the appropriate sections.

(1) The quadrupole and dipole displacement source terms derived earlier [2.2] for the Lilley equation have been replaced by (1) quadrupole sources which are essentially identical to those originally derived by Lilley [2.1] and (2) the dipole sources that were considered briefly in previous work [2.2]. The quadrupole source terms collectively give the correct asymptotic result for isothermal jets at low velocities (V_J^8), although some individual source terms alone do give rise to an incorrect V_J^6 law (the original reason for rejecting sources of this type).

(2) *Numerical* solutions to the Lilley equation – with the revised source terms – can now be generated as part of the calculation procedure developed for predicting jet mixing noise; these calculations are performed by the UNIJET computer program described in Section 6. With this numeric solution option, the user has to specify certain turbulence source parameters, such as the convection velocity (as a function of a modified Strouhal number).

---

†*This effect has not as yet been incorporated in the high-frequency prediction method, only in the numeric or general method.*

(3) Approximate *high-frequency* solutions to Lilley's equation have been obtained in closed form and compared with the corresponding *numeric* solutions. Except at low Strouhal numbers the differences are small and hence the high-frequency approximations have been used to represent acoustic-mean flow interactions in a general scaling law analysis of the Lockheed mixing noise data.

(4) Similarly, transverse noncompactness effects due to radial-azimuthal source coherence, which involve acoustic-mean flow interactions, have been taken into account with the aid of high-frequency Lilley equation solutions and the usual Gaussian model of the source correlation function. The result is a *modified* Doppler factor, as in the Ribner[2.3]/Ffowcs Williams[2.7] work, which determines the convective amplification for each source type. The validity of this approach has been checked with numeric (in place of approximate high-frequency) solutions and found to be sufficiently accurate for prediction purposes, and for the scaling law analysis of the mixing noise data [see (6) below]. However, the modified Doppler factor should be altered in future work for angles inside the cone of silence. There is an option in the UNIJET program which utilizes numeric Lilley equation solutions to calculate a correction to the high-frequency based predictions for these transverse noncompactness effects.

(5) The effect on acoustic-mean flow interaction calculations of replacing the basic ring source model with a more realistic radially and axially distributed source model has been investigated. The radial effect can be quite large at angles inside the cone of silence and this can be calculated with a UNIJET program option (using numeric Lilley equation solutions only). However, it is tentatively concluded that it cannot significantly improve prediction accuracy for supersonic jets at small angles and high frequencies, without degrading the prediction accuracy at subsonic conditions.

Axially distributed source models have been included in calculations performed with the now discarded displacement source terms in the Lilley equation, and this effect was found to be of little importance. Ideally, the exercise should be repeated with the present form of Lilley's equation to check that this result still applies (i.e. with the revised source terms). However, even if the axial effect is found to be significant, it is likely that it would have little impact on overall prediction accuracy as in the case of the radial effect discussed above.

(6) A general scaling-law analysis of the Lockheed mixing noise data has been conducted, utilizing the high-frequency Lilley equation solutions. The analysis has yielded "best fit" values of the turbulence source parameters which only deviate from expected trends at low Strouhal numbers. With these empirically-determined parameter values, the high-frequency solutions provide a rapid, accurate prediction method for small-scale mixing noise which deviates from experiment only in the rear arc of supersonic jets at angles less than 45°. The only disadvantage appears to be that unrealistic empirical parameters must be utilized at low Strouhal numbers, which is not the case if numeric Lilley equation solutions are used. However, the latter require a two-orders-of-magnitude increase in computer time and are recommended only in the context of an on-going research program. For prediction purposes, pure and simple, the high-frequency solution option is recommended.

(7) A limited exercise has been carried out to predict the *spectrum* levels of noise radiated by an isothermal jet in the direction normal to the axis ($\theta_o = 90°$), *directly* from turbulence measurements acquired with a laser velocimeter system (developed at Lockheed). *No scaling laws or empirical constants* inferred from acoustic data were used in this exercise, although it was necessary to assume simple forms for the turbulence cross-correlation function. Good agreement was obtained between measured and calculated far-field noise spectra. However, the calculation scheme was not incorporated into the prediction program mainly because the same type of calculations have yet to be demonstrated for the additional source that arises at non-isothermal jet exit conditions. Thus, the "90° spectrum" or "master spectrum" of each source has been determined from the acoustic data for prediction purposes.

3. NOISE FROM LARGE-SCALE TURBULENCE STRUCTURE

3.1 INTRODUCTION

In this chapter the importance of the large-scale structure of turbulence will be discussed. Firstly, some background will be given for the philosophy developed at the Lockheed-Georgia Company for the understanding of the generation and radiation of jet noise. The remaining sections of the chapter will describe the mechanism of noise generation by the large-scale structure of turbulence. A detailed mathematical derivation is provided for the case of a two-dimensional plane turbulent shear layer since the analysis is simpler for this geometry. The analysis required for the case of an axisymmetric jet is then described in less detail. Calculations of the far- and near-field sound pressure levels in a supersonic axisymmetric jet will be presented and these calculations will be compared with jet noise measurements.

3.1.1 Background

The original motivation for the work that has developed at Lockheed-Georgia in the past six years was the work by Lilley [3.1]. In this original, and exceptional, work Lilley stated that it was insufficient to view a noise-producing turbulent flow from the viewpoint of an acoustic analog theory, such as that proposed by Lighthill [3.2], if a true and accurate understanding of the noise generation and radiation process were to be fully obtained. Firstly, Lilley extended the work of Phillips [3.3] and developed a convected wave equation for the acoustic disturbances in a turbulent shear flow. In doing this he isolated, for a plane parallel shear flow, the noise generation and radiation processes. He argued that the true source of the noise was at least quadratic in the fluctuating velocity components and that in the absence of this source the behavior of pressure disturbances should be described by the linearized, inviscid, compressible equations of motion for a turbulent, sheared mean flow. The inhomogeneous equation developed by Lilley is now known as "Lilley's equation." Solutions to this equation for sources which are felt to model the random fluctuations in the turbulent jet are described in Section 2. These solutions have provided considerable insight into the effect of the mean flow on the radiation of jet noise. It should be noted at this stage that, for many critics, there appeared to be a mathematical flaw in the approach proposed by Lilley. They argued that the homogeneous form of Lilley's equation contained an unstable solution whereas previous formulations, such as that by Lighthill, did not. This unstable solution, which is part of the complementary solution of Lilley's equation, would grow without limit in the parallel shear flow model of Lilley. Lilley argued that the complementary function is only non-zero if the multiplying constant, which is fixed by the boundary conditions, is also non-zero. For this reason the "acoustic solution" or particular integral associated with a given source could be studied in isolation. It will be shown below that the unstable solution *does* exist, however, its amplitude does not grow without limit, and it does contribute to the noise radiation.

In Lilley [3.1] and Lilley et al. [3.4] a further proposition was made as to the nature of the noise source. The turbulent mean velocity profile in a

shear layer or jet is known to be unstable, in the inviscid limit, to small disturbances of a limited range of frequencies. Thus, it was argued that the turbulent fluctuations, at any location, in the flow would be dominated by disturbances of a relatively narrow range of frequencies which would be rapidly growing. This "wave model" for free shear flows had been developed by Morris [3.5] and for bounded flows by Landahl [3.6] and Reynolds [3.7]. It was originally proposed that this "deterministic" model of the turbulence be used as the source term in Lilley's equation. However, the radiation of noise by a subsonically travelling wave is very small even if the wave amplitude and velocity are varying and is zero for a constant amplitude wave. It was clear that the random characteristics of the turbulence would control the properties of the noise radiation especially at low speeds. Models of these characteristics have led to predictions of so-called "jet mixing noise" given in Section 2.

The equation that describes the propagation of a linear pressure wave in a turbulent shear flow is the compressible form of the inviscid, incompressible stability or Rayleigh equation. The inviscid approximation is valid where the mean flow is unstable in that limit. This homogeneous equation permits unstable eigensolutions for various wave frequencies. The range of frequencies varies as the mean flow profile varies. This homogeneous compressible stability equation is, in fact, the homogeneous form of Lilley's equation. So the naturally occurring instabilities in the turbulent free shear flows are part of the complementary function associated with the solution of Lilley's equation. However, there exists a fundamental difference between the mechanism of noise generation by the random components of the turbulence and by the flow instabilities, which justifies their separate treatment. The random fluctuations in the flow lead to a noise source which is very localized. Thus, the assumption of locally parallel flow made in the Lilley formulation is likely to be valid. However, with such an assumption the unstable solution of Lilley's equation grows without bound. Physically this flow instability, as is argued below, corresponds to the observed large-scale structure of the turbulence which can extend coherently for many jet diameters. Clearly, the assumption of parallel flow is not valid for the instability since the mean flow properties may change dramatically in a few jet diameters. Thus, a physically correct treatment of the instability in Lilley's equation requires that axial variations in the mean flow be taken into account. The method for doing this will be described in subsequent sections. Thus, the Lockheed philosophy has been to treat the noise radiation by the random fluctuations in the turbulence and the flow instabilities separately. This corresponds to making those mathematical assumptions in the noise models which are the simplest valid assumptions for each mechanism: locally parallel flow for the mixing-noise and a diverging mean flow model for the flow instabilities or large-scale structure.

Once it was recognized that this separation of mixing and large-scale noise was valid, a number of separate stages were pursued in determining the large-scale structure noise alone. Morris [3.8] provided a model for the large-scale structure of a subsonic round jet. The analysis was based on an integral energy analysis where, at each axial location, the large-scale structure was described in terms of the locally most unstable wave. This work provided the basis of all the subsequent approaches to the problem and highlighted the difficulties involved. The stability calculations were made for a viscous instability and the interesting properties of the viscous

instabilities of axisymmetric jets were reported by Morris [3.9]. The difficult problem of modeling the large-scale structure in a compressible round jet was then tackled. The results were reported in Plumblee [3.10] and Morris [3.11]. In the former report an attempt was made to predict the far-field noise radiation associated with the large-scale instabilities. The pressure and normal velocity fluctuations were calculated on a cylindrical surface surrounding the jet. With the fluctuations known, the far-field noise could then be readily calculated. However, although some corrections were performed to take account of the assumption of locally parallel flow that had been made, the location of the hypothetical cylinder remained somewhat arbitrary and the effect of flow divergence was not explicitly identified.

The work presented in this report seeks to overcome these difficulties and provides a uniformly valid solution, for the sound pressure associated with the large-scale instabilities, from the flow field to the acoustic far field. The method for calculating the noise radiation will first be presented in detail for the case of a two-dimensional shear layer since the analysis is more straightforward for this geometry than it is for the axisymmetric situation. The noise radiation from a supersonic round jet will then be calculated using the same method.

3.2 THE RADIATION OF SOUND BY THE INSTABILITY WAVES OF A COMPRESSIBLE PLANE TURBULENT SHEAR LAYER*

3.2.1 Introduction

This section concerns the radiation of sound associated with an artificially excited spatially growing wave of a fixed frequency, in a plane turbulent shear layer. During the past few years a number of investigators, e.g. Sedel'nikov [3.13], Tam [3.14, 3.15, 3.16], Bishop, Ffowcs Williams and Smith [3.17], Morris [3.8, 3.18] and Liu [3.19] have suggested that flow instabilities could play a very important role in supersonic jet noise generation. This idea was confirmed in a series of experiments by McLaughlin, Morrison and Troutt [3.20, 3.21] using supersonic jets with low to moderately high Reynolds numbers. To facilitate experimental measurements of the relative phase of the instability waves at different locations in the jet, the jet was gently excited by the glow discharge at the nozzle exit at certain selected frequencies. Hot-wire and microphone measurements indicated the presence of spatially growing flow instability waves together with strong noise radiation at the forced frequencies. The experimental situation just described is quite similar to the model problem being considered in this section. For cold subsonic jets no direct experimental evidence is available at this time to show whether the same mechanism is important in producing noise. For a heated subsonic jet with exit Mach number 0.7 and exit temperature 900°K, Dahan and Elias [3.22] showed that noise was radiated from large-scale motions of the jet which had the local characteristics of wave-like instabilities of the jet. Chan [3.23, 3.24, 3.25] and Moore [3.26] have demonstrated that it is possible to excite

*The analysis and results contained in Section 3.2 are also to be found in Tam and Morris [3.12].

instability waves in the shear layer of a turbulent subsonic jet. Further, when the amplitude of the excited waves was small, they found that most of their characteristics agreed quite well with the predictions of classical, linear, inviscid, hydrodynamic instability theory. In recent years, a number of workers have examined the jet flow or free shear layer instability problem. Some of the more recent works, such as those by Morris [3.8, 3.11, 3.18], Liu [3.19], Tam [3.16], Chan [3.27], Merkine and Liu [3.28], and others emphasized the slight nonlinear aspects of the problem. On the other hand, a number of papers such as those by Bouthier [3.29, 3.30], Gaster [3.31], Saric and Nayfeh [3.32] and Crighton and Gaster [3.33] discuss the modification to classical instability theory due to slight flow divergence which is inevitable in unbounded shear flows. In all these works, with the exception of Tam [3.16] and Morris [3.18], no attempt was made to calculate the sound waves generated by the flow instabilities. Tam [3.16] used physical reasoning to model the noise generation processes of supersonic jets and estimated the noise emitted. Unlike most of the works cited above, the sound radiation is the main problem to be addressed here. In this section the instability wave solution, which is valid in the shear layer and a near-field region, is constructed in terms of an asymptotic expansion using the method of multiple scales. This solution accounts for the effects of the slightly divergent mean flow. The instability wave amplitude is assumed to be small so that nonlinear effects are ignored. In fact, even if its amplitude is not small, the nonlinear effects are only important inside the shear layer. In this case the present method still applies if the instability wave solution in the shear layer is appropriately modified. Classical hydrodynamic instability theory (see Lees and Lin [3.34], Lin [3.35], Gropengieser [3.36], Blumen [3.37, 3.38]) of a compressible plane mixing layer does not predict acoustic radiation. A closer examination of this solution (see Section 3.2.2.3) reveals that it is a local solution and is valid only up to a limited region outside the shear layer. The solution developed in this report, however, has uniform validity up to the acoustic far-field region.

In classical hydrodynamic instability theory of compressible flows such as boundary layers or free-shear layers, the parallel flow approximation is invariably used. Because of this, the instability wave solution so obtained is valid only over a localized region. To determine the sound radiation associated with an instability wave, a global solution of the total wave propagation phenomenon is necessary. In a two-dimensional shear layer, because of entrainment, the mean flow diverges in the downstream direction. As a result the instability characteristics of the shear layer vary continuously from point to point in the streamwise direction. When an instability wave is initiated at a certain location in the flow by a periodic external excitation, it will first undergo a rapid spatial growth. As the shear layer thickens, the growth rate decreases until finally the wave will reach a region where the shear layer is too thick to support an unstable wave at the forced frequency. Downstream of this region the wave will be damped. Its amplitude decreases as it continues to propagate until it is vanishingly small. Except in the case of very high-speed flow, the phase velocity of the instability wave is usually subsonic relative to the stationary ambient gas. A subsonic wave with constant amplitude generates no sound. However, if the wave amplitude grows and decays spatially, then some wave components would actually be moving with supersonic phase velocities which, as is well known, would lead immediately to acoustic radiation. Thus, for the problem under consideration, the classical instability theory must be modified to allow for the phenomenon

of mean flow divergence and provide a description of the growth and decay of the excited instability wave.

Following the above reasoning, a solution is first found for the instability wave in the shear layer. This solution is constructed using the method of multiple scales. The procedure adopted is very similar to the method of Saric and Nayfeh [3.32]. Here, necessary modifications to deal with the singular behavior of the damped inviscid eigenfunctions by contour deformation in the complex plane are made. (The damped inviscid eigensolutions are shown in Section 3.2.4.2 to be a valid approximation to the damped viscous solutions at high Reynolds number.) A fast and slow spatial variable are introduced in the analysis. The slow variable is used to take into account the gradual divergence of the mean flow. The fast variable is the same one as used in the hydrodynamic instability theory. The higher order terms in the multiple scales expansion are obtained using the method of variation of parameters. Examination of these terms reveals that the multiple scales asymptotic expansion is not uniformly valid far from the shear layer. It is thus argued that the present perturbation problem is singular. An extended solution which is a uniformly valid asymptotic expansion for large distances from the shear layer is constructed by showing that a model boundary value problem, for which a uniformly valid expansion exists, is the continuation of the instability wave solution. The solution of this problem, which provides the pressure fluctuations associated with the instability wave in the far-field, is obtained by the method of Fourier transforms. The noise radiation is then readily calculated.

In Section 3.2 of this report the method outlined above is applied to the acoustic radiation problem associated with an instability wave in a plane turbulent shear layer. Experimental measurements show that the mean velocity profile of the flow can be approximated by a complementary error function. Numerical results for the inviscid instability characteristics of the shear layer including local growth rate and wavenumber with or without divergent flow corrections are presented at several Mach numbers. Directivity patterns of acoustic radiation at subsonic and supersonic flow Mach numbers are also presented in this section. Because of flow similarity (there is a lack of intrinsic length and time scales in this free shear layer problem), the directivity pattern is not sensitive to the frequency of the wave except in the extremely high frequency range. For supersonic flows the noise radiation peaks around 20 degrees to the axis of the shear layer in the ambient medium. This is qualitatively consistent with the experimental observations of Dosanjh and Yu [3.39] for a turbulent supersonic jet. The analysis and calculations for the axisymmetric jet are given in Section 3.3 of this report.

3.2.2 The Multiple Scales Instability Wave Solution

The behavior of small wave-like disturbances propagating in a pre-existing plane turbulent shear layer will be considered. These disturbances are assumed to be induced by a localized external periodic excitation of frequency ω^*. The basic flow is sketched in Figure 3.1. The turbulent mixing layer has a small initial thickness, δ_o^* at $x^* = x_o^*$ which takes account of the boundary layer on the splitter plate. The mixing layer has a constant rate of spread which will be assumed to be a known function of the freestream Mach number, M. The static pressure and temperature will be assumed constant throughout the

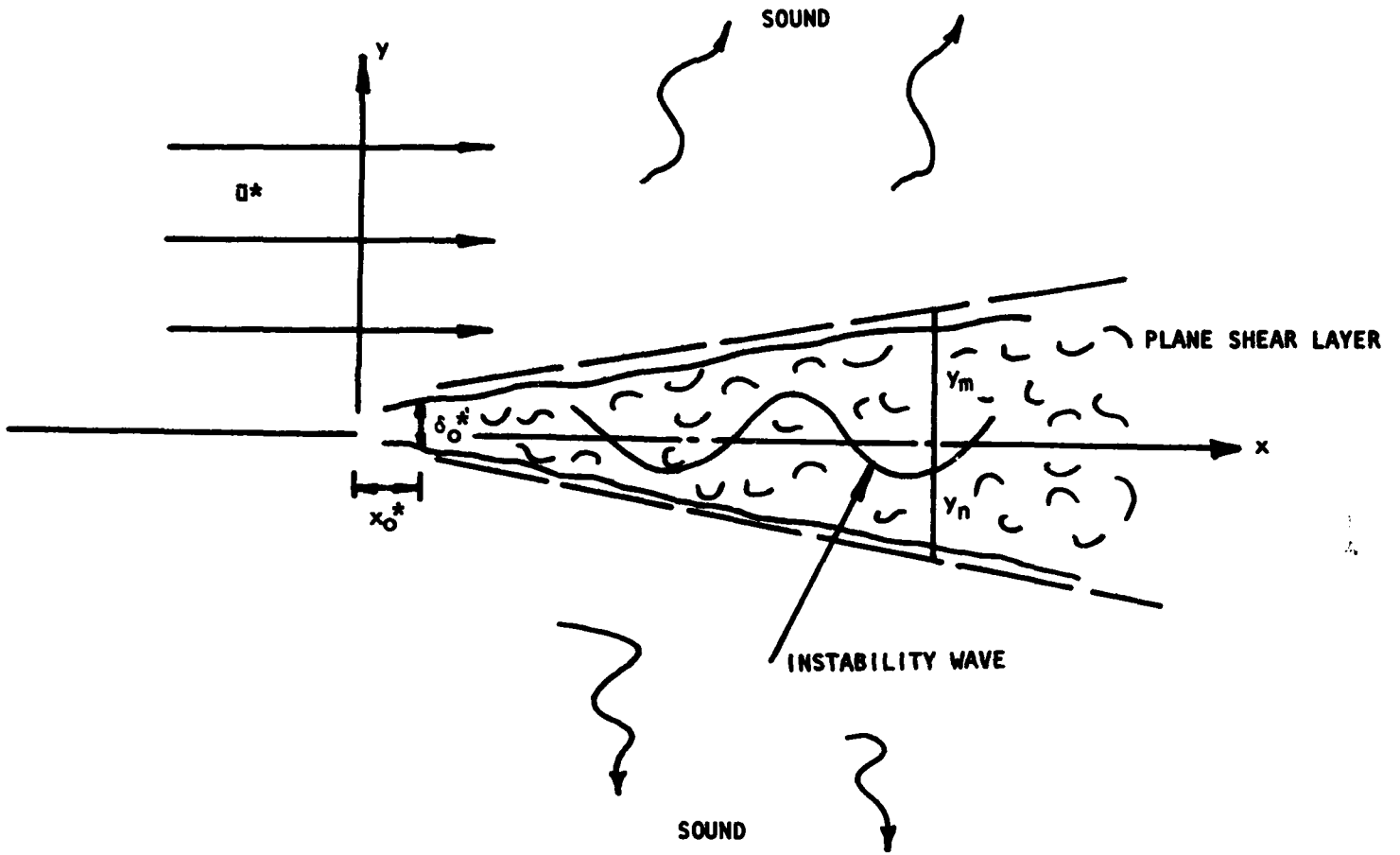

Figure 3.1 Plane Shear Layer Flow

the flow. This condition, which is physically realistic for an appropriately heated uniform stream up to Mach numbers of close to two, may easily be relaxed. The calculations for the axisymmetric jet do not make this assumption. Since the mean velocity profile has characteristics which lead to dynamic instabilities of small perturbations, even in the absence of viscosity, the wave-like disturbances will be assumed to satisfy the linearized, inviscid, compressible equations of motion. To properly describe the behavior of the excited periodic disturbances in the shear layer, it is important to take account of the divergence of the mean flow. Since the spreading rate of the mixing layer is small, especially at high freestream Mach numbers, the method of multiple scales will be used to describe the disturbance behavior. The governing equations are the linearized continuity, momentum and energy equations together with the equation of state.

All the physical variables are nondimensionalized with respect to the corresponding freestream quantities, such as the freestream velocity, $\bar{u}^*$, density, $\bar{\rho}^*$, pressure, $\bar{p}^*$, and the initial thickness of the mixing layer, δ_o^*. The appropriate time scale is $\delta_o^*/\bar{u}^*$. The governing linearized equations of motion can readily be reduced to

$$\frac{\partial p'}{\partial t} + \bar{u}_j \frac{\partial p'}{\partial x_j} + \gamma \frac{\partial u_j'}{\partial x_j} = 0 \tag{3.1}$$

and

$$\gamma M^2 \left| \frac{\partial u_i'}{\partial t} + \bar{u}_j \frac{\partial u_i'}{\partial x_j} + u_j' \frac{\partial \bar{u}_i}{\partial x_j} \right| = - \frac{\partial p'}{\partial x_i} , \tag{3.2}$$

where primes denote fluctuating quantities and γ is the ratio of specific heats. The two-dimensional turbulent mean flow is a function of the transverse coordinate, y, and a slowly varying function of axial distance, x. Measured mean flow profiles will be used. From the measurements of Liepmann and Laufer [3.40] the mean velocity vector may be written as,

$$\bar{u} = [U(y/s),\ \varepsilon V(y/s),\ 0] \tag{3.3a}$$

where

$$\left.\begin{aligned} U &= 0 \qquad y \le -y_n \\ U &= 1 \\ V &= 0 \end{aligned}\right\} \ y \ge y_m \tag{3.3b}$$

In Equations (3.3), $s = \varepsilon x$, where the small parameter ε is a measure of the rate of spread of the shear layer. Typically ε is less than 0.1. The mean velocity in the x-direction is effectively zero below the mixing layer and the flow is uniform for $y \ge y_m$ as shown in Figure 3.1. A solution will be sought to Equations (3.1) and (3.2) in the form of a slowly varying wave,

$$p'(x,y,t) = \left| \sum_{n=0}^{\infty} \varepsilon^n \beta_n(y,s) \right| e^{\,i\theta(x) - i\omega t} \tag{3.4a}$$

$$u'(x,y,t) = \left| \sum_{n=0}^{\infty} \varepsilon^n \hat{u}_n(y,s) \right| e^{i\theta(x) - i\omega t} \tag{3.4b}$$

and

$$v'(x,y,t) = \left| \sum_{n=0}^{\infty} \varepsilon^n \hat{v}_n(y,s) \right| e^{i\theta(x) - i\omega t} \tag{3.4c}$$

where ω is the forced frequency of the wave and the fast phase function, θ, is such that

$$\frac{d\theta}{dx} = \alpha(s) \tag{3.5}$$

This form of multiple scales asymptotic expansion has been used previously by Saric and Nayfeh [3.32] in their investigation of the nonparallel stability of boundary layers. Substitution of Equations (3.4) into Equations (3.1) and (3.2) and ordering the equations in the powers of ε gives, to order unity,

$$-i\hat{\omega}\,\hat{p}_o + \gamma\left(i\alpha\hat{u} + \frac{\partial \hat{v}_o}{\partial y}\right) = 0 \tag{3.6a}$$

$$\gamma M^2 \left| \hat{v}_o \frac{\partial U}{\partial y} - i\hat{\omega}\hat{u}_o \right| = -i\alpha\,\hat{p}_o \tag{3.6b}$$

and

$$i\gamma M^2\,\hat{\omega}\hat{v}_o = \frac{\partial \hat{p}_o}{\partial y}\,, \tag{3.6c}$$

where $\hat{\omega} = \omega - \alpha U$.

These equations readily reduce to a single equation for $\hat{p}_o$ of the form,

$$\frac{\partial^2 \hat{p}_o}{\partial y^2} + \frac{2\alpha}{\hat{\omega}} \frac{\partial U}{\partial y} \frac{\partial \hat{p}_o}{\partial y} - [\alpha^2 - M^2\,\hat{\omega}^2]\;\hat{p}_o = 0 \tag{3.7a}$$

which will be written as

$$L_y\,[\hat{p}_o] = 0 \tag{3.7b}$$

To order ε a set of inhomogeneous equations for the fluctuations $\hat{p}_1$, $\hat{u}_1$, and $\hat{v}_1$ are obtained where the right-hand sides are functions of the zero order fluctuations. These equations may be reduced to a single inhomogeneous equation for $\hat{p}_1$ of the form,

$$L_y[\hat{p}_1] = -2i\,(M^2U\hat{\omega} + \alpha)\,\frac{\partial \hat{p}_o}{\partial s} + \frac{2i\omega}{\hat{\omega}^2}\frac{\partial U}{\partial y}\frac{\partial^2 \hat{p}_o}{\partial y \partial s}$$

$$+ i\left|M^2U^2\hat{p}_o - \hat{p}_o + \frac{2\omega U}{\hat{\omega}^3}\frac{\partial U}{\partial y}\frac{\partial \hat{p}_o}{\partial y}\right|\frac{d\alpha}{ds}$$

$$+ i\left|\frac{2\alpha^3 V}{\hat{\omega}^2}\frac{\partial U}{\partial y} + \frac{4\alpha^2}{\hat{\omega}}\frac{\partial V}{\partial y} - \alpha M^2\left|U\frac{\partial V}{\partial y} + V\frac{\partial U}{\partial y}\right| - 2M^2\hat{\omega}\frac{\partial V}{\partial y}\right|\hat{p}_o$$

$$- i\left|2M^2V\hat{\omega} - 2\alpha\frac{(\hat{\omega}+\omega)}{\hat{\omega}^3}\frac{\partial U}{\partial y}\frac{\partial V}{\partial y} - \frac{2\alpha^2 V}{\hat{\omega}^3}\left(\frac{\partial U}{\partial y}\right)^2\right|\frac{\partial \hat{p}_o}{\partial y} \equiv \chi_1 \qquad (3.8)$$

Similarly, the higher order equations lead to inhomogeneous equations for $\hat{p}_n$ of the form,

$$L_y(\hat{p}_n) = \chi_n\,(y,s), \qquad n = 1, 2, 3, \ldots\ldots \qquad (3.9)$$

The inhomogeneous term χ_n contains fluctuation quantities of lower order. For $y \geq y_m$ the mean flow is uniform and χ_n takes a simple form. In this region of uniform flow the value of χ_n will be denoted by $\bar{\chi}_n$ which is given by

$$\bar{\chi}_n(p_{n-1}, p_{n-2}) = -2i\,(M^2\hat{\omega} + \alpha)\,\frac{\partial \hat{p}_{n-1}}{\partial s} - i\,(1-M^2)\,\frac{d\alpha}{ds}\,\hat{p}_{n-1}$$

$$- (1-M^2)\,\frac{\partial^2 \hat{p}_{n-2}}{\partial s^2}\,. \qquad (3.10)$$

(Note that in Equation (3.10), $\hat{p}_{-2} = \hat{p}_{-1} = 0$).

3.2.2.1 The eigenvalue problem

The amplitude and phase functions of the multiple scales asymptotic expansion, Equation (3.4) are given by the solution to Equations (3.7), (3.8), and (3.9). The appropriate boundary conditions for $\hat{p}_n$ are,

$$\hat{p}_n \text{ is bounded as } y \to \pm\infty\,. \qquad (3.11)$$

For convenience a new similarity coordinate is introduced given by $\eta = y/s$, and the mean velocity field is taken to be a function of η only. If a local wavenumber and frequency are defined in the form, $k_o = \alpha s$ and $\beta = \omega s$, then the pressure fluctuation may be written in terms of η and β as,

$$\hat{p}_o(\eta,\beta) = A_o(\beta)\;\hat{\zeta}(\eta,\beta) \qquad (3.12)$$

and from Equation (3.7) $\hat{\zeta}(\eta,\beta)$ satisfies the equation,

$$L_\eta[\hat{\zeta}] = 0 \qquad (3.13a)$$

and $$L_\eta[\ ] \equiv \left[\frac{\partial^2}{\partial\eta^2} + \frac{2k_o}{\hat{\beta}}\frac{dU}{d\eta}\frac{\partial}{\partial\eta} - (k_o^2 - M^2\hat{\beta}^2)\right] \tag{3.13b}$$

and $$\hat{\beta} = \beta - k_o U\ . \tag{3.13c}$$

The boundary conditions for $\hat{\zeta}$ from Equation (3.11) are

$$\hat{\zeta} \to 0 \quad \text{or bounded as} \quad \eta \to \pm\infty\ . \tag{3.14}$$

Equation (3.13) and boundary condition (3.14) form an eigenvalue problem. This is the identical problem that would have been obtained if the locally parallel flow approximation of classical hydrodynamic stability theory had been made. The eigenvalue is k_o. For $y \geq y_m$, Equation (3.13) reduces to

$$\frac{\partial^2\hat{\zeta}}{\partial\eta^2} - [k_o^2 - M^2\ (\beta - k_o)^2]\hat{\zeta} = 0. \tag{3.15}$$

The solution of Equation (3.15) which satisfies the boundedness condition is

$$\hat{\zeta} = \exp\ [-\sqrt{k_o^2 - M^2(\beta - k_o)^2}\ \eta] = \exp[-\lambda y]$$

where $$\lambda = \sqrt{\alpha^2 - M^2(\omega - \alpha)^2} \quad \text{and} \quad \mathrm{Re}\{\lambda\} > 0. \tag{3.16}$$

A normalization convention will be adopted for the eigenfunctions $\hat{\zeta}$ by choosing the arbitrary multiplication constant in front of the exponential function of Equation (3.16) to be unity. Equations (3.4), (3.12), and (3.16) lead to

$$p'(x,y,t) = A_o(s)\ \exp\ [i\theta(x) - \lambda y - i\omega t] + O(\varepsilon) \qquad y \geq y_m \tag{3.17}$$

Equation (3.8) may also be written in terms of the similarity coordinate. In order that a solution exists for the resulting equation, it must satisfy the solvability condition; that is the integral of the scalar product of its right-hand side and the solution to the adjoint homogeneous problem over all η [with appropriate contour deformation in the η-plane for damped waves (see Section 3.2.4)] must equal zero. That is,

$$\int_{-\infty}^{\infty} \psi X_1\ d\eta = 0, \tag{3.18}$$

where $\psi(\eta,\beta)$ is the solution to the adjoint homogeneous equation. It is readily verified that $\psi = \hat{\zeta}/\hat{\beta}^2$ so that Equation (3.18) becomes

$$\int_{-\infty}^{\infty} \frac{\hat{\zeta}X_1}{\hat{\beta}^2}\,d\eta = \int_{-\infty}^{\infty} \frac{\hat{\zeta}X_1}{\hat{w}^2}\,dy = 0. \tag{3.19}$$

This solvability condition leads to an ordinary differential equation for $A_o(\beta)$ in the form,

$$I_3 \frac{dA_o}{d\beta} + (I_4 + I_5) A_o = 0 \tag{3.20}$$

where

$$I_3 = \int_{-\infty}^{\infty} \left[B_1 \hat{\zeta} + B_2 \frac{\partial \hat{\zeta}}{\partial \eta} \right] \psi d\eta \tag{3.21a}$$

$$I_4 = \int_{-\infty}^{\infty} \left[B_1 \frac{\partial \hat{\zeta}}{\partial \beta} + B_2 \frac{\partial^2 \hat{\zeta}}{\partial \eta \partial \beta} \right] \psi d\eta \tag{3.21b}$$

$$I_5 = \int_{-\infty}^{\infty} \left| \left[B_3 \hat{\zeta} + B_4 \frac{\partial \hat{\zeta}}{\partial \eta} \right] \frac{dk}{d\beta} + B_5 \hat{\zeta} + B_6 \frac{\partial \hat{\zeta}}{\partial \eta} \right| \psi d\eta \tag{3.21c}$$

where the coefficients B_i are given in Appendix 3A. Now with $\hat{\zeta}(\eta,s)$ to be obtained from the eigenvalue problem of Equations (3.13) and (3.14) and $A_o(s)$ to be found by integrating Equation (3.20), the slowly varying wave solution in the form,

$$p'(x,y,t) = A_o(s)\, \hat{\zeta}(\eta,s) \exp [i\theta(x) - i\omega t] + O(\varepsilon), \tag{3.22}$$

is completely defined to order unity.

In evaluating the integrals of Equation (3.21) the values of $dk_o/d\beta$ and $\partial\hat{\zeta}/\partial\beta$ may be obtained using a finite difference calculation based on the values of k_o and $\hat{\zeta}$ at successive values of β. However, they may also be evaluated locally using the technique employed by Bouthier [3.29, 3.30] and Saric and Nayfeh [3.32]. Differentiating Equation (3.13) with respect to β gives an inhomogeneous equation for $\partial\hat{\zeta}/\partial\beta$ of the form,

$$L_\eta [\partial\hat{\zeta}/\partial\beta] = h_1\, dk_o/d\beta + h_2, \tag{3.23}$$

where h_1 and h_2 are given in Appendix 3A. Application of the solvability condition to Equation (3.23) leads to an equation for $dk_o/d\beta$ and the inhomogeneous equation for $\partial\hat{\zeta}/\partial\beta$ may then be solved directly.

3.2.2.2 Higher-order terms of the multiple scales asymptotic expansion

The higher-order terms of the multiple scales asymptotic expansion (3.4) are given by the solution of the inhomogeneous Equations (3.9). Since the corresponding homogeneous equation has an eigensolution, $\hat{\zeta}$, each solution for β_n can be regarded as consisting of the sum of a particular solution and a complementary solution of the form $A_n(s)\, \hat{\zeta}(y/s,s)$ where A_n is an unknown amplitude. This unknown amplitude may be determined in a similar manner to A_o from the solvability condition applied to χ_{n+1} in Equation (3.9)

$$\int_{-\infty}^{\infty} \frac{\hat{\zeta}(y,s)\chi_{n+1}}{\hat{\omega}^2}\, dy = 0, \qquad n=0,\ 1,\ 2\ \ldots\ . \tag{3.24}$$

The above solvability condition leads to an ordinary differential equation for A_n. This equation can be integrated, at least numerically, so that the complementary solution is determined completely. The appropriate particular solutions may be obtained by the method of variation of parameters. For $y \geq y_m$, the eigenfunction, $\hat{\zeta}$, is given by Equation (3.16). Another linearly independent solution of Equation (3.15) is

$$\hat{\xi} = \exp\left[\sqrt{k_o^2 - M^2(\beta - k_o)^2}\,\eta\right] = \exp[\lambda y] \tag{3.25}$$

Now let $\hat{\xi}$ be the solution of Equation (3.7) which takes the form given by Equation (3.25) for $y > y_m$. Then $\hat{\zeta}(y)$ and $\hat{\xi}(y)$ are two linearly independent solutions of the corresponding homogeneous equation of (3.9). It may be shown that the Wronskian, $W(\hat{\zeta},\hat{\xi})$, is given by

$$W(\hat{\zeta},\hat{\xi}) = 2\lambda\hat{\omega}^2/(\omega-\alpha)^2\ . \tag{3.26}$$

Applying the method of variation of parameters (see Boyce and DiPrima [3.41], Chap. 3) to Equation (3.9) using $\hat{\zeta}$ and $\hat{\xi}$ as the fundamental set of solutions, the complete solution is found to be

$$\hat{p}_n = A_n\hat{\zeta}(y,s) - \hat{\zeta}(y,s)\int_{\infty}^{y} \frac{\hat{\xi}(t,s)\chi_n(t,s)\,dt}{W(\hat{\zeta},\hat{\xi})} + \hat{\xi}(y,s)\int_{-\infty}^{y} \frac{\hat{\zeta}(t,s)\,\chi_n(t,s)\,dt}{W(\hat{\zeta},\hat{\xi})}\ . \tag{3.27}$$

Using the explicit form of the Wronskian given in Equation (3.26), Equation (3.27) may be rewritten as

$$\hat{p}_n = A_n\hat{\zeta}(y,s) + \frac{(\omega-\alpha)^2}{2\lambda}\left[-\hat{\zeta}(y,s)\int_{-\infty}^{y} \frac{\hat{\xi}(t,s)\,\chi_n(t,s)dt}{\hat{\omega}^2} + \hat{\xi}(t,s)\int_{-\infty}^{y} \frac{\hat{\zeta}(t,s)\,\chi_n(t,s)dt}{\hat{\omega}^2}\right]. \tag{3.28}$$

$\hat{p}_n(y,s)$ as given by Equation (3.28) clearly satisfies the boundedness condition as $y \to -\infty$. That the solution is bounded as $y \to +\infty$ is guaranteed by the solvability condition, Equation (3.24). The last term in Equation (3.28) may be written a more useful form using this solvability condition, that is,

$$\hat{p}_n = A_n\hat{\zeta}(y,s) - \frac{(\omega-\alpha)^2}{2\lambda}\left[\hat{\zeta}(y,s)\int_{-\infty}^{y}\frac{\hat{\xi}(t,s)\,\chi_n(t,s)dt}{\hat{\omega}^2}\right.$$

$$\left. + \hat{\xi}(t,s)\int_{y}^{\infty}\frac{\hat{\zeta}(t,s)\,\chi_n(t,s)dt}{\hat{\omega}^2}\right]. \qquad (3.29)$$

Equation (3.29) and the solvability condition (3.24) provide the complete solution of the amplitude functions of the slowly varying wave solution (3.4) to any order of the expansion parameter ε. Unfortunately, as will be shown below, this multiple scales asymptotic expansion has only a limited range of validity.

3.2.2.3 The singular perturbation problem

In this section it will be shown that the multiple scales asymptotic expansion (3.4) is not uniformly valid for large y. The region $y \geq y_m$, where the mean flow is uniform (i.e. $U=1$, $V=0$), will be examined. In this region the inhomogeneous terms of Equation (3.9) are given explicitly by Equation (3.10). The functions $\hat{\zeta}$ and $\hat{\xi}$ of Equation (3.29) take the following simple form,

$$y > y_m \qquad \hat{\zeta} = e^{-\lambda y}, \qquad \hat{\xi} = e^{\lambda y}, \qquad (3.30)$$

so that the general expression for $\hat{p}_n$ becomes,

$$\hat{p}_n(y,s) = D_n e^{-\lambda y} - \frac{e^{-\lambda y}}{2\lambda}\int^{y} e^{\lambda t}\,\bar{\chi}_n(t,s)dt - \frac{e^{\lambda y}}{2\lambda}\int_{y}^{\infty} e^{-\lambda t}\,\chi_n dt \qquad (3.31a)$$

$y > y_m$

where

$$D_n = A_n - \frac{1}{2\lambda}\left[(\omega-\alpha)^2\int_{-\infty}^{y_m}\frac{\hat{\xi}(t,s)\chi_n dt}{\hat{\omega}^2} + \int_{y_m} e^{\lambda t}\,\bar{\chi}_n(t,s)dt\right] \qquad (3.31b)$$

Equation (3.31) gives the dependence of $\hat{p}_n$ on y for $y > y_m$. It holds for all values of n provided χ_o is taken to be zero.

With $\hat{p}_o = A_o\hat{\zeta} = A_o \exp[-\lambda y]$ for $y > y_m$ the inhomogeneous term $\bar{\chi}_1$ may be computed from Equation (3.10). This gives

$$\bar{\chi}_1 = (C_1 + C_{2y})e^{-\lambda y} \qquad (3.32)$$

where

$$C_1 = -2i\,[M^2(\omega-\alpha)+\alpha]\frac{dA_0}{ds} - i(1-M^2)\,A_0\frac{d\alpha}{ds}$$

and

$$C_2 = 2i[M^2(\omega-\alpha)+\alpha]^2\frac{A_0}{\lambda}\frac{d\alpha}{ds}\,.$$

Substitution of Equation (3.32) into Equation (3.31a) and evaluating the various integrals it is found for $y > y_m$,

$$\hat{p}_1 = (B_{10} + B_{11}y + B_{12}y^2)e^{-\lambda y} \tag{3.33}$$

where

$$B_{10} = D_1 - \frac{1}{4\lambda^2}\left(C_1 + \frac{C_2}{2\lambda}\right)$$

$$B_{11} = -\frac{1}{2\lambda}\left(C_1 + \frac{C_2}{2\lambda}\right)$$

and

$$B_{12} = -\frac{C_2}{4\lambda}\,.$$

Now that $\hat{p}_0$ and $\hat{p}_1$ are determined, it is possible to find $\hat{p}_2$ in the same manner. After some computation it may be shown that,

$$\hat{p}_2 = [B_{20} + B_{21}y + B_{22}y^2 + B_{23}y^3 + B_{24}y^4]e^{-\lambda y} \tag{3.34}$$

The expressions for the coefficients B_{2i} are rather complicated and will not be written out. Only the dependence of the solution on y is of interest. By continuing this process or by mathematical induction it may be shown that,

$$\hat{p}_n \underset{y\to\infty}{\sim} B_{2,2n}y^{2n}\,e^{-\lambda y} \tag{3.35}$$

Thus, for large y the multiple scales asymptotic expansion (3.4) behaves like

$$p'(x,y,t) \underset{y\to\infty}{\sim} \sum_{n=0}^{\infty} K_n\varepsilon^n\, y^{2n}\, e^{-\lambda y + i\theta(x) - i\omega t} \tag{3.36}$$

where K_n are functions of x alone. Due to the appearance of $\varepsilon^n y^{2n}\exp[-\lambda y]$ in the higher order terms, the asymptotic expansion does not hold for $y \gg \varepsilon^{-\frac{1}{2}}$. In other words the multiple scales expansion is nonuniformly valid. As far as is known, no single asymptotic expansion which is uniformly valid for all y can be constructed for the present problem. Van Dyke [3.42] states on page 33 of his book that *"a singular perturbation problem is best defined as one in which no single asymptotic expansion is uniformly valid throughout the field of interest."* Thus, the present perturbation problem is unfortunately singular.

3.2.3 Continuation of the Instability Wave Solution into the Region $y > y_m$

It is now necessary to construct an extension of the multiple scales asymptotic expansion which is uniformly valid for $y > y_m$ in the upper half plane. To do this, it will be first determined what this extended solution ought to satisfy. The disturbances associated with the instability wave are governed by the linearized continuity, momentum and energy equations and the equation of state, namely, Equations (3.1) and (3.2). These are, of course, the same equations used to determine the multiple scales slowly varying wave solution. However, in the region $y > y_m$, U is unity and V is zero so that these equations simplify to

$$y > y_m \qquad \frac{\partial p_e}{\partial t} + \frac{\partial p_e}{\partial x} + \gamma\left(\frac{\partial u_e}{\partial x} + \frac{\partial v_e}{\partial y}\right) = 0 \tag{3.37a}$$

$$\gamma M^2\left(\frac{\partial u_e}{\partial t} + \frac{\partial u_e}{\partial x}\right) = -\frac{\partial p_e}{\partial x} \tag{3.37b}$$

and

$$\gamma M^2\left(\frac{\partial v_e}{\partial t} + \frac{\partial v_e}{\partial x}\right) = -\frac{\partial p_e}{\partial y} \tag{3.37c}$$

The subscript e indicates that the variables are the extended solution in the region $y > y_m$. Eliminating u_e and v_e from Equation (3.37), the governing equation for p_e is found to be

$$M^2\left(\frac{\partial}{\partial t} + \frac{\partial}{\partial x}\right)^2 p_e - \left(\frac{\partial^2}{\partial x^2} + \frac{\partial^2}{\partial y^2}\right) p_e = 0 \tag{3.38}$$

The appropriate boundary condition for p_e at large y is the radiation or boundedness condition,

$$y \to \infty, \quad p_e \text{ is bounded or behaves like outgoing waves.} \tag{3.39}$$

At this stage an inner boundary condition is needed for p_e in the region y slightly greater than y_m. For the case $\varepsilon = 0$ the multiple scales asymptotic expansion (3.4) truncates (only one term is needed for a truly parallel mean flow) so that the expansion converges for all values of y. It will be assumed that the expansion also converges for some value of y slightly greater than $y = y_m$ even when ε has a small but finite value. If this convergence is realized then, by appealing to the concept of analytic continuation, the natural inner boundary condition for the extended solution p_e is that it must be identically equal to the convergent asymptotic expansion. Under these circumstances p_e is the analytic continuation of p'. This leads to the inner boundary condition

$$p_e = \left| \sum_{n=0}^{\infty} \varepsilon^n \hat{p}_n(y,s) \right| e^{i\theta(x) - i\omega t} \tag{3.40}$$

(for y slightly greater than y_m)

where $\hat{p}_n(y,s)$; $n = 0, 1, 2 \ldots$ are given by Equation (3.31).

Summarizing, the extended solution p_e must satisfy Equation (3.38), the radiation and inner boundary conditions (3.39) and (3.40) and be uniformly valid for all $y > y_m$.

3.2.3.1 The extended problem

It will now be shown that the extended solution, p_e, as defined by Equations (3.38), (3.39), and (3.40) is identical to the solution ϕ of the following boundary value problem,

$$y \geq 0 \qquad M^2 \left(\frac{\partial}{\partial t} + \frac{\partial}{\partial x}\right)^2 \phi - \left(\frac{\partial^2}{\partial x^2} + \frac{\partial^2}{\partial y^2}\right) \phi = 0 \tag{3.41}$$

$$y \to \infty: \quad \phi \text{ satisfies the radiation or boundedness condition} \tag{3.42}$$

$$y = 0: \quad \phi = \left| \sum_{n=0}^{\infty} \varepsilon^n g_n(\varepsilon x) \right| e^{i\theta(x) - i\omega t}, \tag{3.43}$$

where $g_n(s)$, $s = \varepsilon x$, will be related to the multiple scales expansion (3.4) below. Equations (3.41), (3.42), and (3.43) constitute a well-defined boundary value problem whose solution is *unique*. Since Equations (3.41) and (3.42) are identical to Equations (3.38) and (3.39), the hypothesis that $\phi = p_e$ for $y > y_m$ could be proved if it could be shown that ϕ possesses an asymptotic expansion which is identical to the right-hand side of Equation (3.40) for y slightly greater than y_m. To show this the above boundary value problem will be solved for ϕ explicitly in the form of a multiple scales asymptotic expansion. Let ϕ be given by

$$\phi(x,y,t) = \left| \sum_{n=0}^{\infty} \varepsilon^n \phi_n(y,s) \right| e^{i\theta(x) - i\omega t} \tag{3.44}$$

Substitution of Equation (3.44) into Equation (3.41) and partitioning terms by powers of ε leads to the following set of equations,

$$\frac{\partial^2 \phi_n}{\partial y^2} - [\alpha^2 - M^2(\omega - \alpha)^2]\phi_n = \bar{\chi}_n(\phi_{n-1}, \phi_{n-2}) \qquad n = 0, 1, 2 \ldots \tag{3.45}$$

where $\phi_{-2} = \phi_{-1} = 0$ and the functional form of $\bar{\chi}_n(\phi_{n-1}, \phi_{n-2})$ is given by Equation (3.10). The boundary conditions on ϕ_n are found in Equations (3.42) and (3.43), namely

$$y \to \infty, \quad \phi_n \text{ is bounded} \tag{3.46}$$

$$y = 0, \quad \phi_n = g_n(s). \tag{3.47}$$

Two linearly independent solutions of the corresponding homogeneous equation of Equation (3.45) are $\exp[-\lambda y]$ and $\exp[\lambda y]$ where λ is given by Equation (3.16). For $n=o$ $\bar{\chi}_n = 0$ in Equation (3.45) so that the solution ϕ_o which satisfies boundary conditions (3.46) and (3.47) may easily be shown to be

$$\phi_o = g_o(s)e^{-\lambda y} \tag{3.48}$$

For $n \geq 1$, the solution of the inhomogeneous Equation (3.45) and boundary conditions (3.46) and (3.47) may again be determined by the method of variation of parameters. It is readily shown that

$$\phi_n = \left[g_n(s) + \frac{1}{2\lambda} \left| \int_o^\infty e^{-\lambda t}\ \bar{\chi}_n dt - \int_o^\infty e^{\lambda t}\ \bar{\chi}_n dt \right| \right] e^{-\lambda y}$$

$$- \frac{e^{-\lambda y}}{2\lambda} \int^y e^{\lambda t}\ \bar{\chi}_n dt - \frac{e^{\lambda y}}{2\lambda} \int_y^\infty e^{-\lambda t}\ \bar{\chi}_n dt \tag{3.49}$$

Now setting $g_o(s) = A_o(s)$, (3.50a)

and for $n \geq 1$

$$g_n(s) = A_n(s) - \frac{1}{2\lambda} \left[(\omega - \alpha)^2 \int_{-\infty}^{y_m} \frac{\hat{\xi}(t,s)\ \chi_n(t,s)\ dt}{\hat{\omega}^2} \right.$$

$$\left. - \int_o^{y_m} e^{\lambda t}\ \bar{\chi}_n dt + \int_o^\infty e^{-\lambda t}\ \bar{\chi}_n dt \right| \tag{3.50b}$$

the two expressions on the right-hand sides of Equations (3.31) and (3.49) are identical. Thus, $\phi_n = \hat{p}_n$ in the region y slightly greater than y_m. That is, ϕ satisfies the inner boundary condition (3.40). Thus, the extended solution p_e is equal to the solution ϕ $(y \geq y_m)$ of the boundary value problem defined by Equations (3.41), (3.42), and (3.43).

3.2.3.2 Uniformly valid asymptotic expansion of the extended problem

Having shown that the extended solution, p_e, is given by the solution of the boundary value problem defined by Equations (3.41), (3.42), and (3.43) a uniformly valid expansion of the extended solution for $y > y_m$ will be constructed. The solution of the boundary value problem (3.41) to (4.43) is unique. However, different methods of solution would yield solutions of different forms which may or may not be uniformly valid for $y > y_m$. At large distances from the mixing layer the disturbances mainly consist of acoustic waves. Unlike waves in the mixing layer whose amplitude changes slowly in the x direction as compared to its y variation, the acoustic waves have no such distinction. Thus, to seek a solution valid for large y the slow

variable $s = \varepsilon x$ must not be used, rather x and y must be treated on an equal footing. Thus, a solution will be sought by the method of Fourier transforms.

The Fourier transform and its inverse are defined by

$$\bar{f}(k) = \frac{1}{2\pi} \int_{-\infty}^{\infty} f(x) e^{-ikx} dx; \qquad f(x) = \int_{-\infty}^{\infty} \bar{f}(k) e^{ikx} dk. \tag{3.51}$$

Applying the Fourier transform to Equations (3.41) to (3.43) and setting $\phi = \hat{\phi}(x,y) \exp[-i\omega t]$, it is easy to show that the Fourier transform of $\hat{\phi}$, $\bar{\phi}$, is given by the solution of

$$\frac{d^2\bar{\phi}}{dy^2} + [M^2(\omega - k)^2 - k^2]\bar{\phi} = 0 \tag{3.52}$$

and at $y = 0$,

$$\bar{\phi} = \sum_{n=0}^{\infty} \varepsilon^n \bar{g}_n(k) \tag{3.53}$$

where

$$\bar{g}_n(k) = \frac{1}{g\pi} \int_{-\infty}^{\infty} g_n(\varepsilon x) e^{i\theta(x) - ikx} dx \tag{3.54}$$

The solution of (3.52) and (3.53) which also satisfies the radiation condition is,

$$\bar{\phi} = \sum_{n=0}^{\infty} \varepsilon^n \bar{g}_n(k) \exp\left[iM\omega \sqrt{\left(1 - \frac{k}{\omega}\right)^2 - \left(\frac{k}{M\omega}\right)^2}\, y \right] \tag{3.55a}$$

where

$$\mathrm{Re}\left\{ \sqrt{\left(1 - \frac{k}{\omega}\right)^2 - \left(\frac{k}{M\omega}\right)^2} \right\} > 0 . \tag{3.55b}$$

If $\mathrm{Re}\left\{ \sqrt{\left(1 - \frac{k}{\omega}\right)^2 - \left(\frac{k}{M\omega}\right)^2} \right\} = 0$, use the branch $\mathrm{Im}\left\{ \sqrt{\left(1 - \frac{k}{\omega}\right)^2 - \left(\frac{k}{M\omega}\right)^2} \right\} > 0$.

Performing the inverse Fourier transform leads to

$$\phi(x,y,t) = \sum_{n=0}^{\infty} \varepsilon^n \int_{-\infty}^{\infty} \bar{g}_n(k) \exp\left[iM\omega \sqrt{\left(1 - \frac{k}{\omega}\right)^2 - \left(\frac{k}{M\omega}\right)^2}\, y + ikx - i\omega t \right] dk. \quad (3.56)$$

Clearly Equation (3.56) is uniformly valid for all y [see also Equation (3.58) below]. Therefore, it provides the proper continuation of the mixing layer slowly varying instability wave solution to the region $y > y_m$ in the upper half plane.

3.2.3.3 Acoustic far-field solution

The sound radiation associated with the instability wave can be found by evaluating the integrals of Equation (3.56). In evaluating the far-field solution polar coordinates (r,θ) will be used as shown in Figure 3.2, where $x = r\cos\theta$, $y = r\sin\theta$. Equation (3.56) may be rewritten as (noting that ϕ is the fluctuating pressure which will be written as p)

$$p(r,\theta,t) = \sum_{n=0}^{\infty} \varepsilon^n \int_{-\infty}^{\infty} \bar{g}_n(k) \exp\left[i \left(\sqrt{M^2(\omega - k)^2 - k^2}\sin\theta - k\cos\theta \right) r - i\omega t \right] dk . \quad (3\text{-}57)$$

In the limit $r \to \infty$, the integral can be evaluated by the method of stationary phase. This gives,

$$p(r,\theta,t) \underset{r\to\infty}{\sim} \sqrt{\frac{2\pi M\omega}{r}} \frac{\sin\theta}{(1 - M^2\sin^2\theta)^{3/4}} \left| \sum_{n=0}^{\infty} \varepsilon^n \bar{g}_n(k_s) \right| \exp\left[i\omega\left(M\sqrt{1 - M^2\sin^2\theta} + M^2\cos^2\theta \right) r \right] \cdot \exp\left[-i\omega t - i\pi/4 \right] \quad (3\text{-}53)$$

where

$$k_s = \frac{M\omega}{(1 - M^2)} \left\{ \frac{\cos\theta}{\sqrt{1 - M^2\sin^2\theta}} - M \right\},$$

from which the directivity of acoustic radiation, $D(\theta)$, can be calculated.

$$D(\theta) = \lim_{r\to\infty} \frac{r}{2} |p|^2 = \frac{\pi M\omega}{(1 - M^2\sin^2\theta)^{3/2}} \left| \sum_{n=0}^{\infty} \varepsilon^n \bar{g}_n(k_s) \right|^2 \sin^2\theta . \quad (3.59)$$

Since ε is small, for practical purposes only the first term of the sum in Equation (3.59) matters. From Equations (3.50) and (3.51),

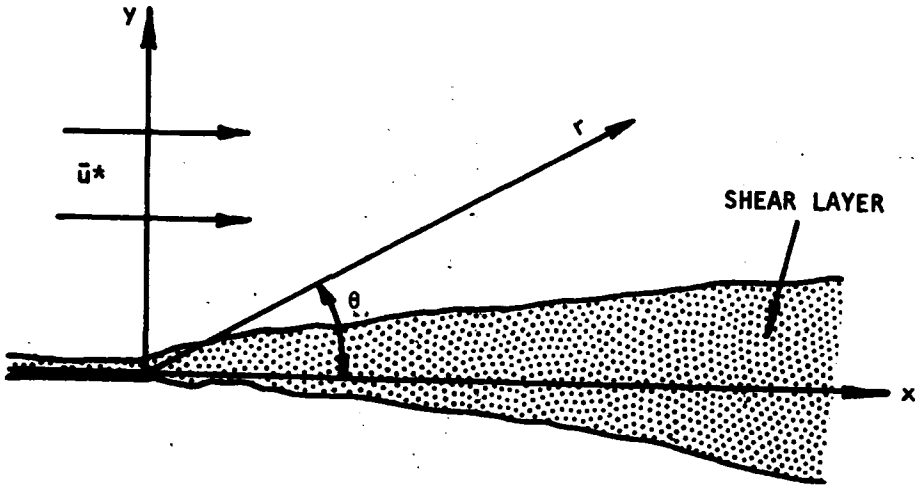

Figure 3.2 Coordinates for Acoustic Far-Field Solution

$$g_o(\varepsilon x) = A_o(\varepsilon x), \qquad \bar{g}_o(k) = \frac{1}{2\pi} \int_{-\infty}^{\infty} A_o(\varepsilon x) e^{i\theta(x) - ikx}\, dx. \tag{3.60}$$

This finally leads to

$$D(\theta) \approx \frac{\pi M\omega}{(1 - M^2\sin^2\theta)^{3/2}} \left|g_o(k_s)\right|^2 \sin^2\theta \tag{3.61}$$

for $0 \le \theta \le \pi$, if $M < 1$; $0 \le \theta \le \sin^{-1}[M^{-1}]$ if $M > 1$. Similarly, it is straightforward to show that the directivity pattern of acoustic radiation in the lower half plane or stationary medium, to the zeroth order, is

$$D(\theta) \approx \pi M\omega \left|\bar{g}_o(\omega M\cos\theta)\right|^2 \sin^2\theta, \tag{3.62}$$

for $-\pi < \theta \le 0$.

3.2.4 Numerical Results

In this section the results for the instability wave characteristics and the far-field noise radiation are presented. The mean velocity and the numerical procedure for calculating the disturbance growth by the method of multiple scales are described. The properties of damped inviscid waves are also discussed. Calculations are presented for both subsonic and supersonic freestream Mach numbers.

3.2.4.1 The instability wave solution

The mean velocity. The description of the mean velocity is based on experimental measurements in turbulent shear layers. The axial and transverse mean velocities are given by

$$U = \begin{cases} 0 & ; \quad \eta - \eta_o \le -6.0 \\ 0.5\left[1 + \text{erf}\ (\eta - \eta_o)\right] & ; \quad -6.0 < (\eta - \eta_o) \le 6.0 \\ 1 & ; \quad (\eta - \eta_o) > 6.0 \end{cases} \tag{3.63}$$

$$\text{and} \quad V = \begin{cases} 0.5\,\eta_o\,[\text{erf}(\eta-\eta_o) - 1] - \exp[-(\eta-\eta_o)^2]/2\sqrt{\pi}; & (\eta-\eta_o) \le 6.0 \\ 0 & ; \quad (\eta-\eta_o) > 6.0 \end{cases} \tag{3.64}$$

The complementary error function profile (3.63) was found to provide a good fit to the axial velocity distribution for a wide range of Mach numbers in the initial mixing region of a round jet by Lau et al. [3.43]. The value of η_o, which gives the location of the dividing streamline, is taken from Patel [3.44] to be -0.3. The rate of spread of an isothermal mixing layer is a function of the freestream Mach number. Since the perturbation parameter, ε, in the

present problem represents the rate of spread it will be a function of Mach number. The variation of ε with M is taken from Lau et al. [3.43] and is given by

$$\varepsilon = (0.165 - 0.045\ M^2)/\sqrt{\pi} \tag{3.65}$$

Numerical calculation procedure. With the mean velocity profiles defined the amplitude of the pressure fluctuation associated with the instability wave may be calcuiated above and below the layer. Firstly, the "parallel flow approximation" given by Equation (3.13) is solved subject to the boundary conditions (3.14). The form of solution in the uniform and stationary fluid above and below the layer, respectively, are easily obtained:

$$\hat{\zeta} \sim e^{-\lambda_+ \eta} \qquad \text{as} \quad \eta \to +\infty \tag{3.66a}$$

and

$$\hat{\zeta} \sim e^{\lambda_- \eta} \qquad \text{as} \quad \eta \to -\infty$$

where

$$\lambda_+ = \sqrt{k_o^2 - M^2(\beta - k_o)^2}, \tag{3.66c}$$

$$\lambda_- = \sqrt{k_o^2 - M^2\beta^2}, \tag{3.66d}$$

with $R_e\{\lambda\pm\} > 0$.

The numerical integration is started above the layer and proceeds across the layer to $Re(\eta) = 0$. A second integration is started below the shear layer and continues to $Re(\eta) = 0$, where the two solutions are matched. The matching of the two solutions leads to a determinant which must be equal to zero to obtain the eigensolution. In practice this is done by minimizing the absolute value of the determinant. The contour of integration must always be below the critical point, η_c, where $U = \beta/k_o$, for the mean velocity profile, Equation (3.63), so that the damped inviscid solutions are correctly obtained. The indentation of the integration contour in the complex η-plane lies on three straight lines joining the points, $(Re[\eta_c] - 1.,\ 0.)$, $(Re[\eta_c] - 1.,\ Im[\eta_c] - 1.)$, $(Re[\eta_c] + 1.,\ Im[\eta_c] - 1.)$, and $(Re[\eta_c] + 1.,\ 0.)$. The indentation of the contour into the complex η-plane occurs whenever $Im[\eta_c] < +1$. Further discussion of the damped inviscid solutions is given in Section 3.2.4.2. An inverse Lagrangian interpolation is used to minimize the determinant in the eigenvalue search. Once the eigenvalue is found the eigenfunction, $\hat{\zeta}$, and hence, the adjoint solution, ψ, is readily obtained since $\psi = \hat{\zeta}/\hat{\beta}^2$. The eigenfunction is normalized such that $\hat{\zeta} = \exp[-\lambda_+ \eta]$ above the layer. The terms h_1 and h_2 of Equation (3.23) are then calculated and $dk_o/d\beta$ is given by

$$\frac{dk_o}{d\beta} = -\int_{-\infty}^{\infty} h_2 \psi d\eta \Big/ \int_{-\infty}^{\infty} h_1 \psi d\eta = -I_2/I_1\ . \tag{3.67}$$

The solution of the inhomogeneous equation for $\partial\tilde{\zeta}/\partial\beta$, Equation (3.23), is then calculated using the same integration contour and the integrals in Equation (3.21) may also be found. Equation (3.20) may then be used to calculate $A^{-1}dA/d\beta$.

Above the layer the solution for the fluctuating pressure may be written

$$p'(\eta,\beta) = A(\beta)e^{-\lambda_+\eta}\ e^{i\theta(x) - i\omega t}, \tag{3.68a}$$

and below the layer the solution is

$$p'(\eta,\beta) = C(\beta)\ A(\beta)e^{\lambda_-\eta}\ e^{i\theta(x) - i\omega t} \tag{3.68b}$$

Thus the corresponding equivalent rates of change of the pressure are given by

$$\left|\frac{1}{p'}\frac{\partial p'}{\partial x}\right|_{\text{above}} = i\alpha + \frac{\varepsilon\omega}{A}\frac{dA}{d\beta} - \frac{\varepsilon\gamma}{\lambda_+}[\alpha + M^2(\omega - \alpha)]\left|\omega\frac{dk_o}{d\beta} - \alpha\right| \tag{3.69a}$$

and

$$\left|\frac{1}{p'}\frac{\partial p'}{\partial x}\right|_{\text{below}} = i\alpha + \varepsilon\omega\left|\frac{1}{A}\frac{dA}{d\beta} + \frac{1}{C}\frac{dC}{d\beta}\right| + \frac{\varepsilon\alpha\gamma}{\lambda_-}\left|\omega\frac{dk_o}{d\beta} - \alpha\right| \tag{3.69b}$$

The growth rates of the pressure fluctuations are clearly functions of distance from the layer, y. This functional dependence is due to the changing shape of the eigenfunctions with downstream distance. However, the effect of the last term in Equation (3.69) is negligible if regions close to the edge of the layer are considered. The growth rate and wavenumber of the slightly divergent flow are then given respectively by the real and imaginary parts of the remaining terms of the right-hand side of Equation (3.69), that is

$$i\alpha_+ \simeq i\alpha + \frac{\varepsilon\omega}{A}\frac{dA}{d\beta} \tag{3.70a}$$

and

$$i\alpha_- \simeq i\alpha_+ + \frac{\varepsilon\omega}{C}\frac{dC}{d\beta}\ .$$

Numerical accuracy. As a first check on the numerical accuracy of the calculation method the numerical results were compared with a known exact solution. For a mean velocity profile of the form

$$U = 0.5\ [1 + \tanh\ (\eta - \eta_o)], \tag{3.71}$$

the eigensolution, using the normalization employed above, is

$$k = 1.0, \qquad \beta = 0.5, \qquad M = 0.0$$

$$\hat{\zeta} = 0.5 \text{ sech } (\eta - \eta_o)$$

$$\psi = 2 \text{ sech } (\eta - \eta_o)/\tanh^2 \ (\eta - \eta_o) \ .$$

The integrals in Equation (3.67) may then be evaluated analytically. The comparison of the numerical and analytical solutions are shown in Table 3-I.

	Exact Solution	Numerical Solution
k_o	1.0	$(1.0000 + 1.5377 \times 10^{-5} i)$
I_1	$-(4 + 2\pi i)$	$-(4.0003 + 6.2832i)$
I_2	$4\pi i$	$(0.54219 \times 10^{-3} + 12.566i)$
$dk_o/d\beta$	$\frac{2\pi(\pi + 2i)}{(4 + \pi 2)}$	$(1.4232 + 0.90600i)$

Table 3-I Comparison of Exact and Numerical Solutions, $\beta = 0.5$.

Numerical calculations of the instability wave solution have been performed for the incompressible case, $M = 0$, and for $M = 0.75$, 1.25, and 1.75. The "parallel flow approximation" to the local growth rate, given by $-I_m[k_o]$ is shown in Figure 3.3 as a function of the freestream Mach number. It should be noted that in the parallel flow approximation the growth rate is independent of the transverse location in the shear layer. As the freestream Mach number increases, the local growth rate decreases. This was also noted by Gropengieser [3.36] and Michalke [3.45]. The variation of the parallel flow approximation wavenumber is shown in Figure 3.4. At lower frequencies, increasing the Mach number increases the local wavenumber which results in a decrease in the phase velocity. The reverse occurs at higher local frequencies though in this region the waves are decaying. The local growth rates determined from Equation (3.10) are shown in Figure 3.5. The divergence of the flow is seen, by comparison with Figure 3.3, to increase the growth rate. The maximum growth rate for the pressure below the layer for $M = 0$, is 50 percent higher than the maximum growth rate obtained using the locally parallel flow approximation. The growth rates above and below the layer are shown for the $M = 0$ case only. The pressure wave above the layer is seen to grow for a broader range of local frequencies (thicknesses) though the maximum growth rate is greatest below the shear layer. The "diverging flow" wavenumbers are shown as a function of local frequency in Figure 3.6. At high frequencies the flow divergence increases the wavenumber and hence reduces the phase velocity. At low frequencies there is a reduction in the local wavenumber which results in the occurrence of very high phase velocities. There is an indication that at sufficiently low local frequencies and Mach numbers upstream wave propagation may occur.

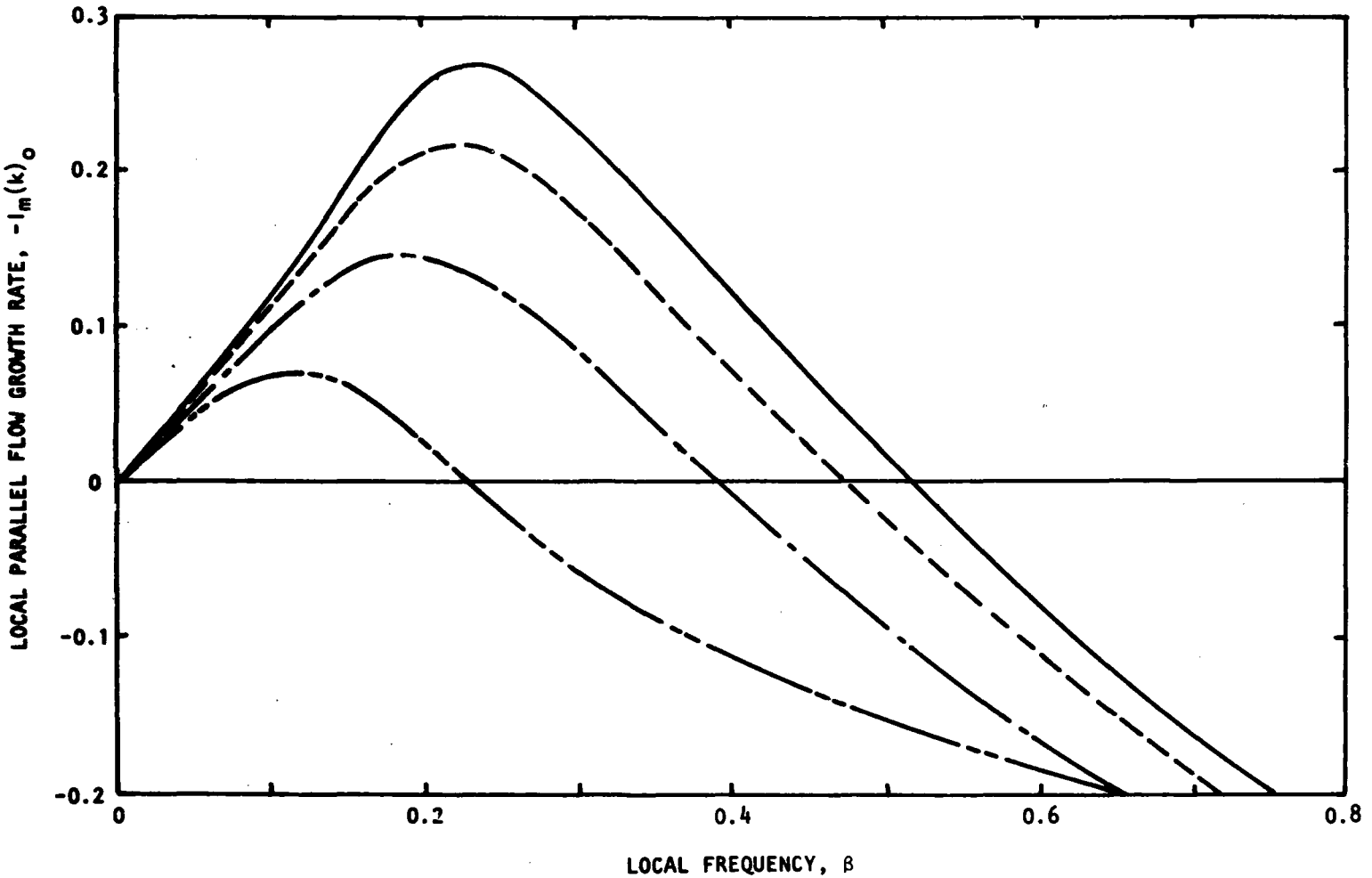

Figure 3.3 Variation of Local Parallel Flow Growth Rate With Local Frequency

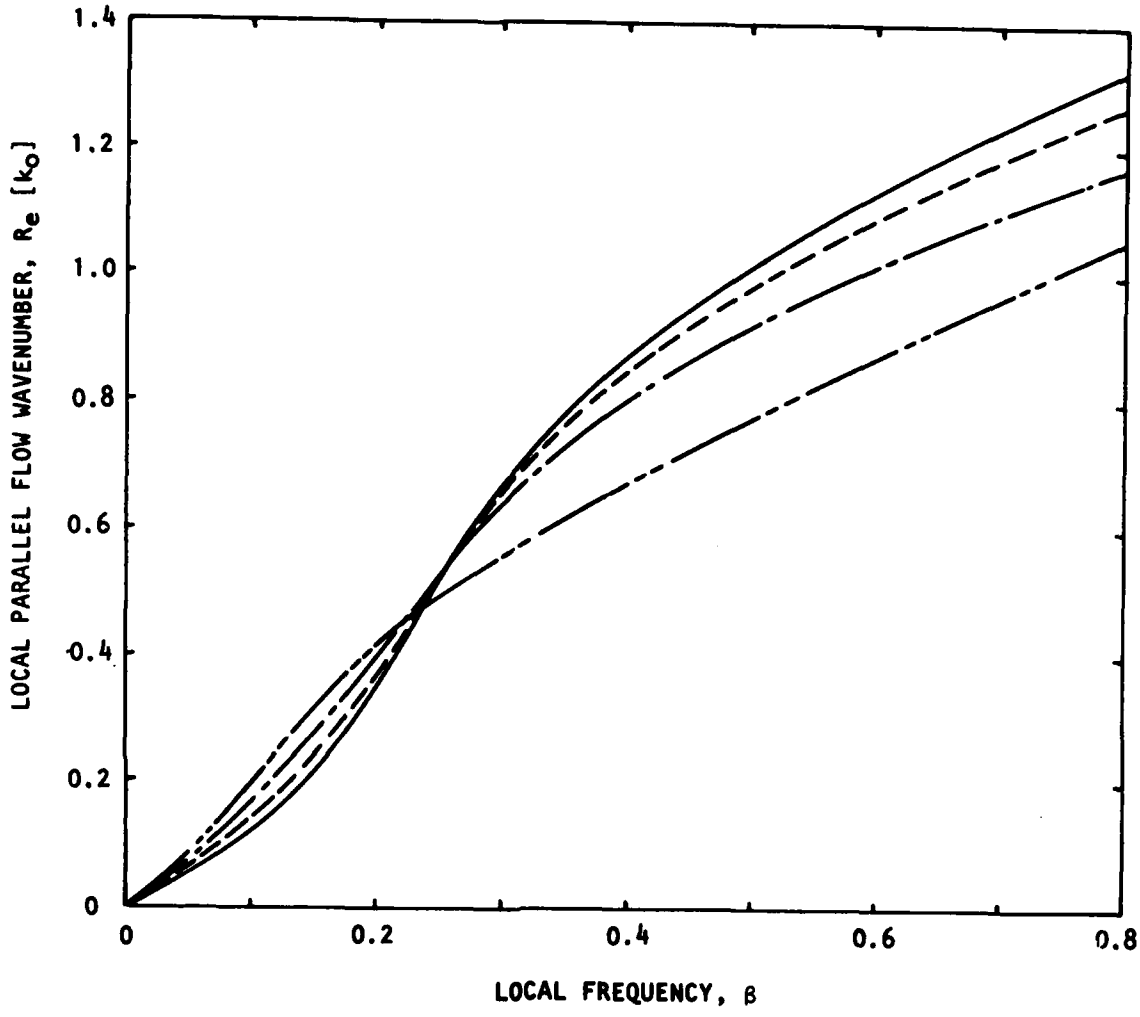

Figure 3.4 Variation of Local Parallel Flow Wavenumber With Local Frequency

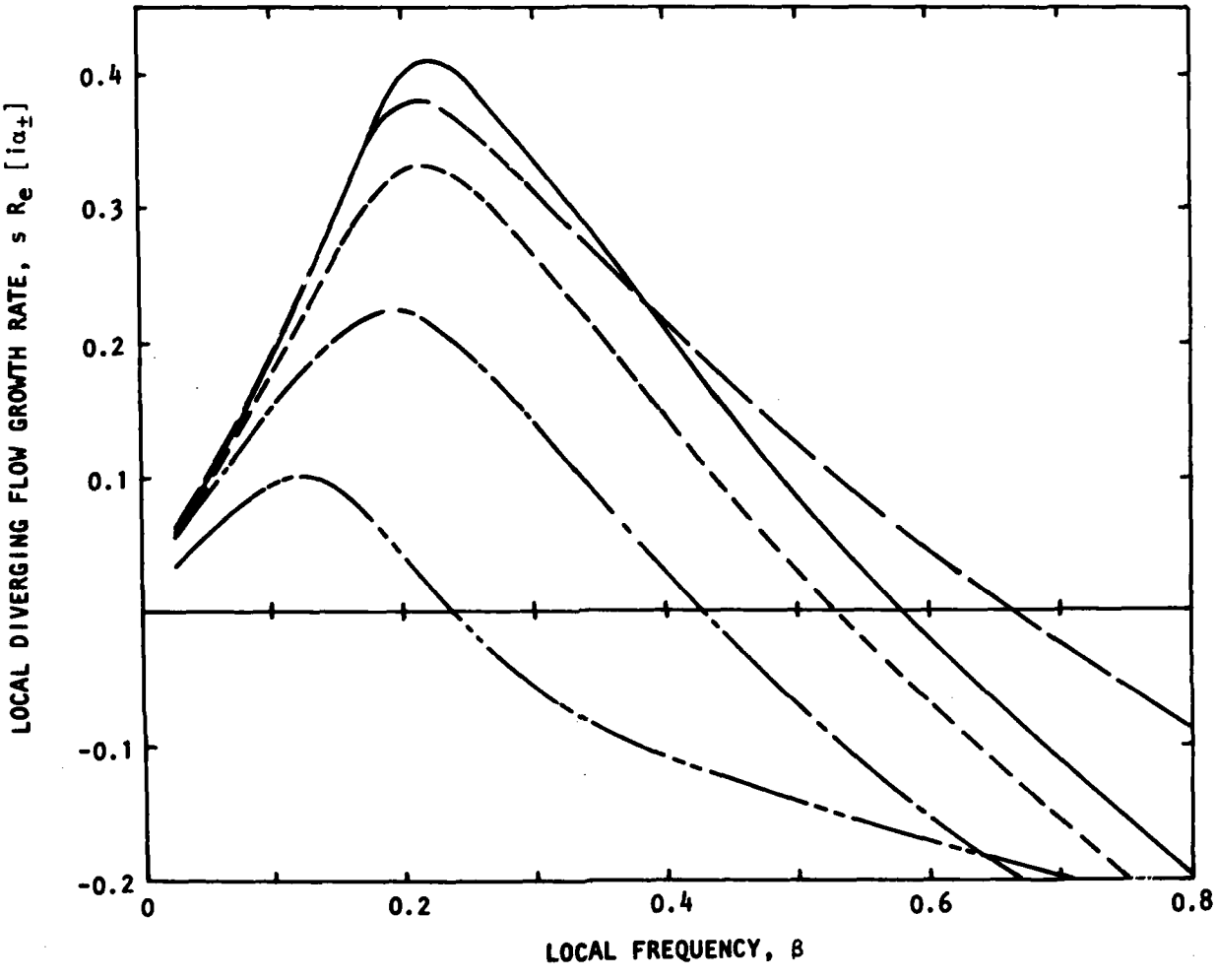

Figure 3.5 Variation of Local Diverging Flow Growth Rate With Local Frequency

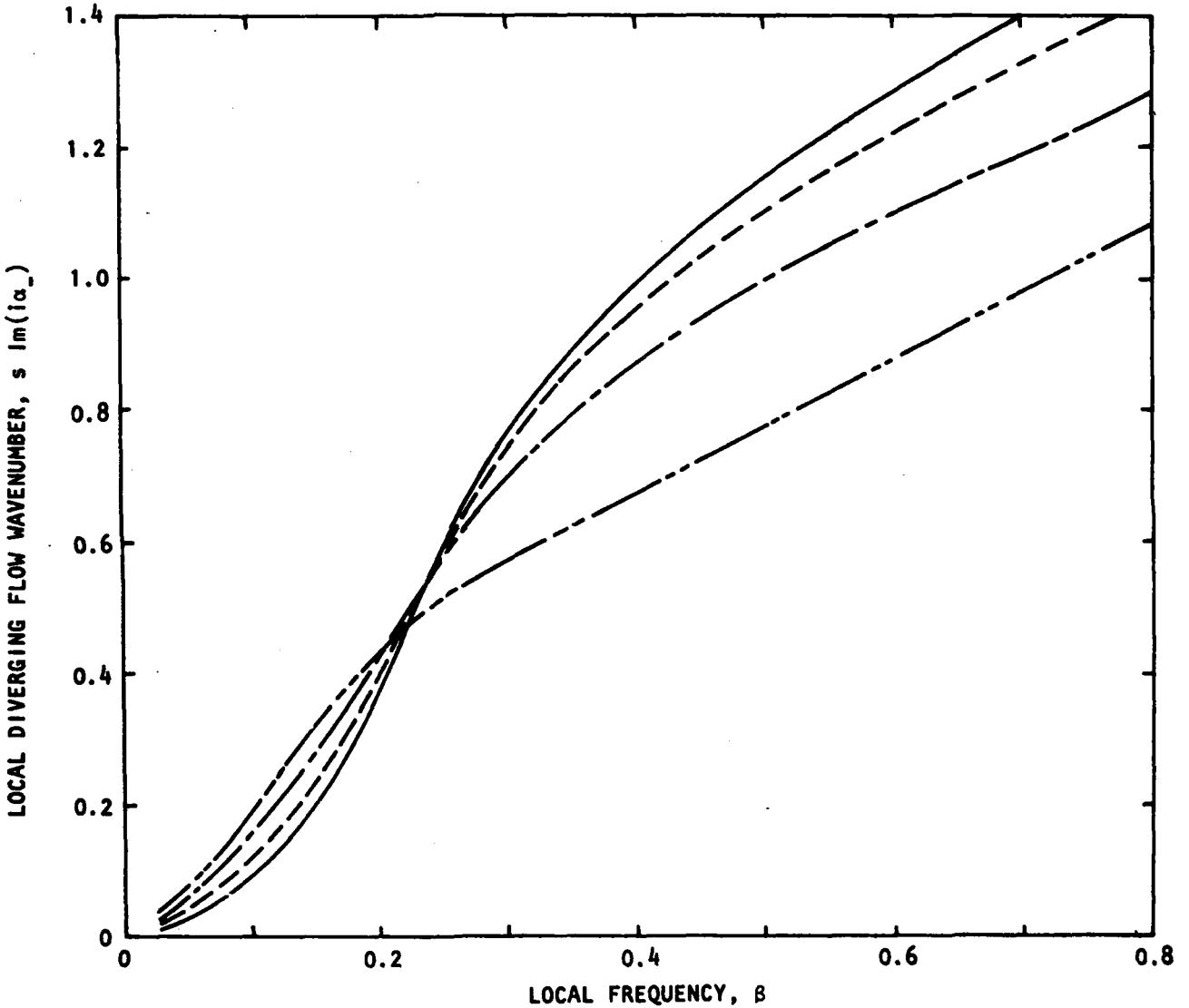

Figure 3.6 Variation of Local Diverging Flow Wavenumber With Frequency Below the Shear Layer

3.2.4.2 Inviscid damped wave solution

It has been suggested that in a slowly varying inviscid flow only the growth of waves can be followed and that for decaying modes there may not exist any continuous solution to the inviscid equations of parallel flow (Betchov and Criminale [3.46], p. 80). In order to demonstrate that the damped inviscid solutions obtained by analytic continuation in the complex plane as described above is valid for this problem, the corresponding viscous flow analysis will be performed for the incompressible, $M = 0$, case. It will be shown that the viscous solutions tend to the inviscid solution as the Reynolds number increases for damped viscous and inviscid waves.

The linearized viscous equations corresponding to the inviscid Equations (3.6) for the zero order fluctuations (or the parallel flow approximations) for incompressible flow are,

$$ik_o\hat{u}_o + \hat{v}_o' = 0 \tag{3.72a}$$

$$-i\hat{\beta}u_o + \frac{dU}{d\eta}\hat{v}_o + ik_o\hat{p}_o = \frac{1}{R}[\hat{u}_o'' - k_o^2\hat{u}_o] \tag{3.72b}$$

and

$$-i\hat{\beta}\hat{v}_o + \hat{p}_o' = \frac{1}{R}[\hat{v}_o'' - k_o^2\hat{v}_o] \tag{3.72c}$$

where the local Reynolds number, $R = \bar{u}^*s/\nu$ and primes denote differentiation with respect to η. This set of simultaneous equations may be solved directly for the eigenvalue k_o and the functions $\hat{u}_o$, $\hat{v}_o$, and $\hat{p}_o$. In the present analysis a single fourth order equation for $\hat{v}_o$, the Orr-Sommerfeld equation, was obtained in the form,

$$\hat{\beta}(\hat{v}_o'' - k_o^2\hat{v}_o) + k_o\frac{d^2U}{d\eta^2}\hat{v}_o = \frac{1}{iR}\{\hat{v}_o^{iv} - 2k_o^2\hat{v}_o'' + k_o^4\hat{v}_o\}. \tag{3.73}$$

Equation (3.73) may be integrated numerically subject to the boundary conditions,

$$\hat{v}_o = \hat{v}_o' \to 0 \qquad \text{as} \quad \eta \to \pm\infty . \tag{3.74}$$

The eigenfunction for the pressure can be obtained in terms of v_o and its derivatives from Equation (3.72). The linear independence of the solutions is preserved using an orthonormalization procedure at a number of steps within the range of integration. The numerical procedure is the same as that used by Morris [3.9]. The calculated growth rate, $-i_m(k_o)$, is shown in Figure (3.7) for several values of Reynolds number. The corresponding variations in the real part of the wavenumber, $Re(k_o)$, are shown in Figure 3.8. As the Reynolds number increases so the eigenvalues approach the inviscid solution. This is the case for both growing and damped waves. However, in the present analysis, it is the eigenfunction that must be calculated in order to evaluate the integrals required in the multiple scales asymptotic solution. In order to compare the inviscid and viscous solutions for damped waves over the entire range of integration, the viscous solution was obtained by integrating on the same contour in the complex η-plane as used in the

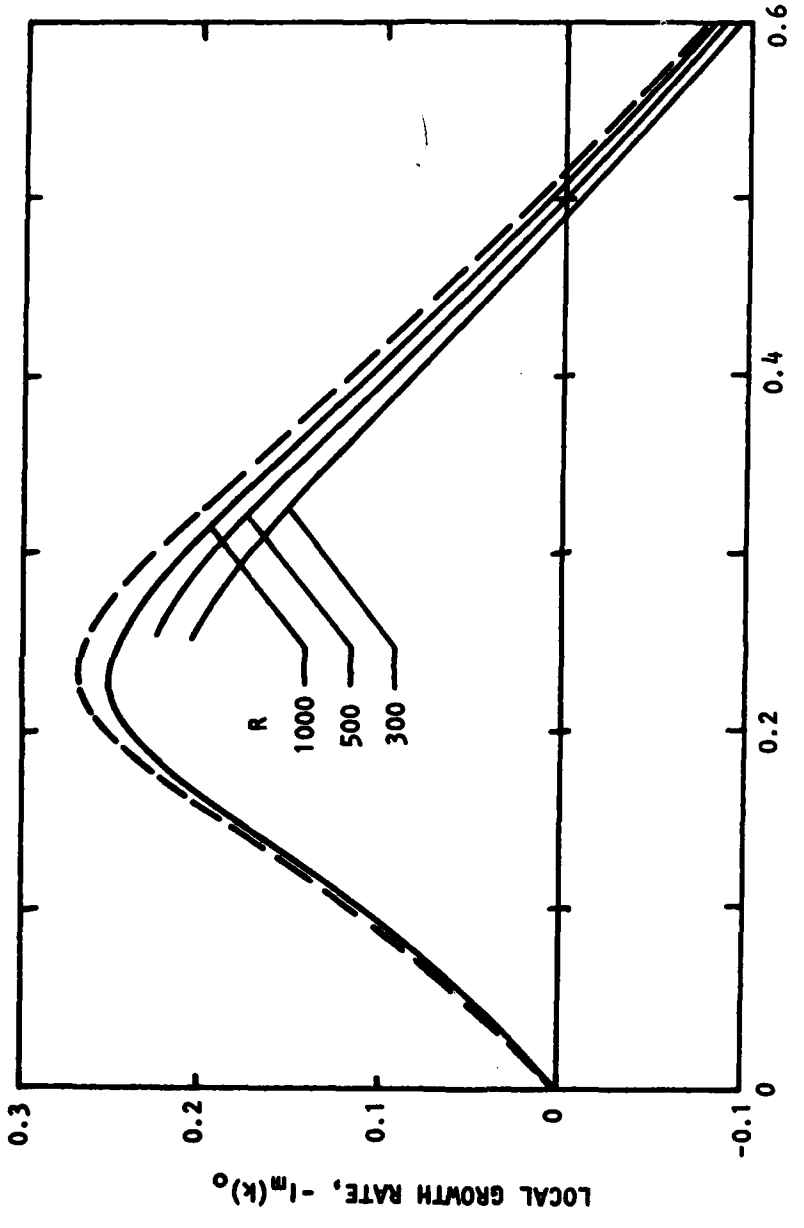

Figure 3.7 Effect of Reynolds Number on Growth Rate

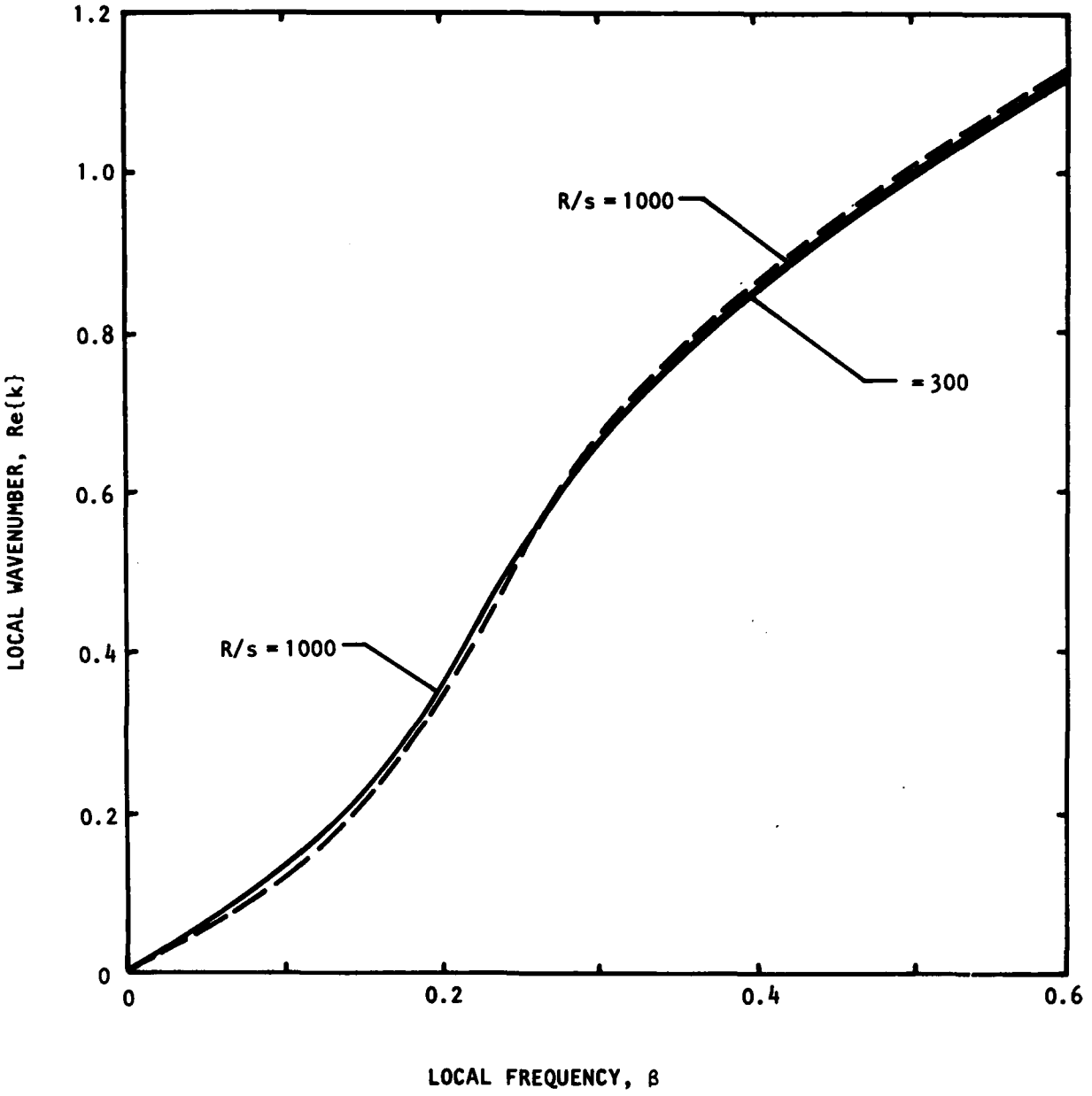

Figure 3.8 Effect of Reynolds Number on the Wavenumber.

inviscid solution. The viscous eigenfunction obtained on the complex contour was found to be identical to that obtained by integration along the real η axis where the two contours were coincident. The eigenfunction obtained for a Reynolds number, $R/\beta = 500$, and a local frequency, $\beta = 0.6$, (which corresponds to a damped wave), is compared with the corresponding inviscid solution in Figure 3.9). Parts (a) and (e) of the figure are on the real η axis and parts (b), (c), and (d) are in the complex η-plane. The eigenfunctions are both normalized such that $\hat{\zeta} = \exp[-k_o\eta]$ at $\eta = 6.0$ which is the upper limit of the numerical integration. The two solutions, viscous and inviscid, are almost identical, the difference being almost impossible to show graphically. Typical values for the two solutions are given in Table 3-II at various locations on the complex contour. Thus, we have shown that the inviscid analysis provides a valid approximation to the viscous analysis, for even moderate local Reynolds numbers, and that the validity of this approximation includes damped inviscid waves.

	$\hat{\zeta}$	
η	Inviscid	Viscous
-0.9506	(0.2904 + 0.0115i)	(0.2910 - 0.8 $\times 10^{-4}$i)
(-0.9506 - 1.0625i)	(0.1712 - 0.3673i)	(0.1737 - 0.3692i)
-1.0625i	(0.9865 - 0.0008i)	(0.9763 - 0.0071i)
(1.0494 - 1.0625i)	(0.1480 + 0.2977i)	(0.1516 + 0.2926i)
1.0494	(0.2867 - 0.0221i)	(0.2889 - 0.0259i)

Table 3-2 Comparison of Viscous and Inviscid Damped Eigenfunctions

Now that it has been shown that the inviscid wave model is valid during both the growth and decay of the wave in the present analysis, the far-field noise radiation, which is intimately connected with this growth and decay process, will be calculated in the next section.

3.2.4.3 Far-field noise radiation

In Section 3.2.3 it was shown how the multiple scales expansion for the pressure fluctuations in the shear layer may be extended into the acoustic far field. The wavenumber component spectrum of these fluctuations in the near field will now be examined and the far-field directivity patterns for both subsonic and supersonic freestream velocities will be calculated.

The far-field noise radiation, given in Equations (3.61) and (3.62), is seen to depend on the amplitude of $\bar{g}_o(k)$ evaluated at the stationary point of the integral of Equation (3.57) (for radiation into the uniform stream). $\bar{g}_o(k)$ is the Fourier transform of the quantity $A_o(\varepsilon x)\exp[i\theta(x)]$ and may be regarded as the wavenumber component spectrum associated with the axial variation, in amplitude and phase, of the pressure fluctuations. Denoting this pressure fluctuation by $G_+(x)$ and $G_-(x)$ above and below the shear layer respectively, it can be seen from Equation (3.70) that

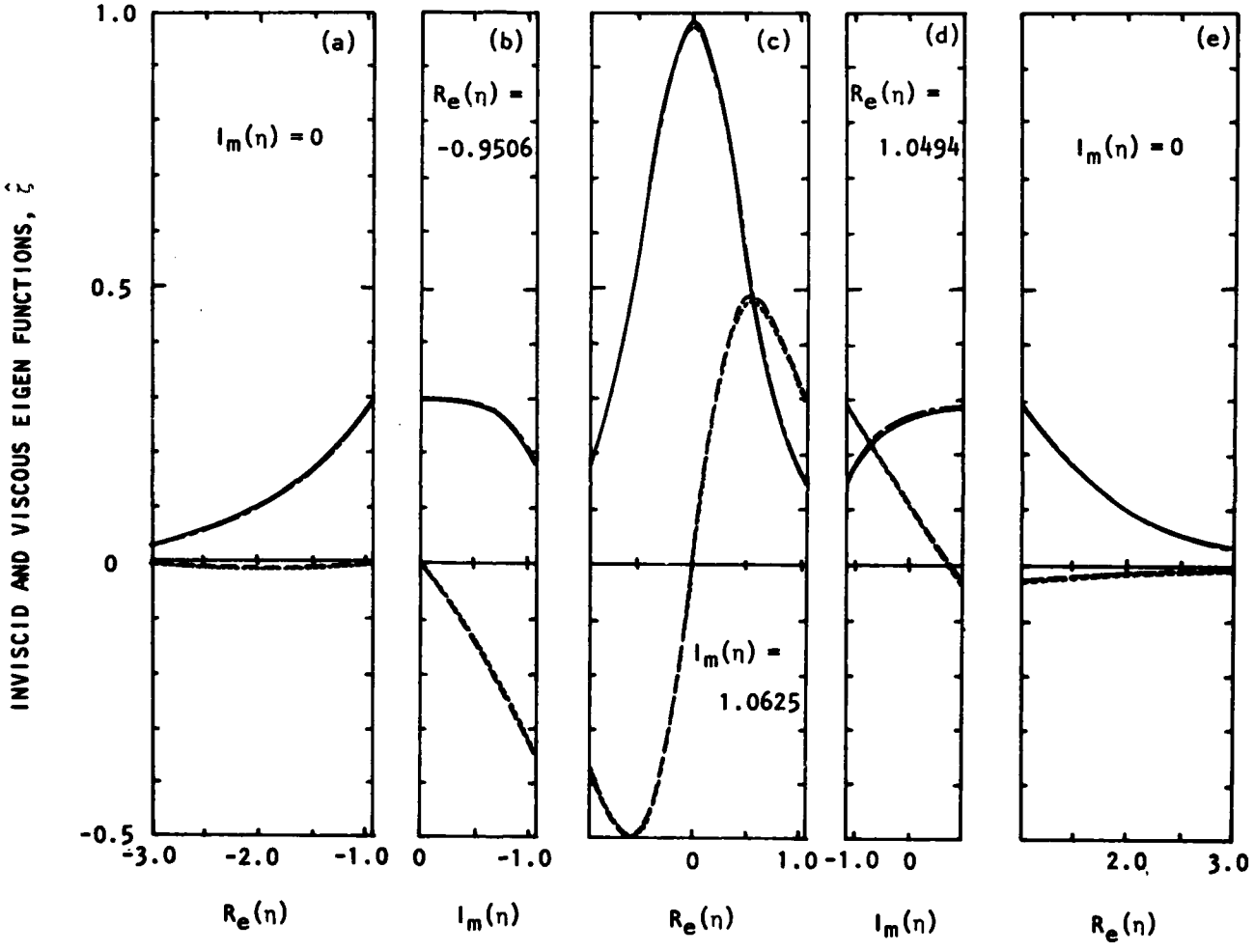

Figure 3.9 Comparison of Viscous and Inviscid Eigenfunctions, M = 0; R = 300; β = 0.6. Inviscid Solution —— Real Part, - - - - Imaginary Part; Viscous Solution —·— Real Part, ····· Imaginary Part

$$\frac{1}{G_+}\frac{dG_+}{dx} = i\alpha_+ \quad \text{and} \quad \frac{1}{G_-}\frac{dG_-}{dx} = i\alpha_- \tag{3.75}$$

These equations may be integrated numerically. The initial conditions for the integration are:

$$x_o = 1/\varepsilon \qquad G_+ = 1.0 \qquad G_- = C_o, \tag{3.76}$$

where δ_o^* is taken to be $\delta_\omega/\sqrt{\pi}$, where δ_ω is the vorticity thickness, and the value of C_o is obtained from the local eigensolution for the initial local frequency. The axial variation of $G_-(x)$ as a function of freestream Mach number for a fixed real frequency, $\omega_o = 0.05$, is shown in Figure 3.10. As the Mach number increases so the location of the peak amplitude moves further downstream. The location of the peak corresponds to the neutrally stable condition. Although the local frequency for a neutral solution decreases with Mach number, see Figure 3.5, the spread rate of the shear layer decreases with Mach number, the net effect moving the neutrally stable point further downstream. The rate of growth of the fluctuation is more rapid than its decay rate. The initial growth rate is higher for the lower Mach numbers which can also be seen in Figure 3.5. The axial variation in $G_-(x)$ as a function of frequency for a fixed Mach number of 1.75 is shown in Figure 3.11. As the frequency decreases so the location of the amplitude peak moves downstream. The peak amplitude also increases as the frequency decreases. These effects are a result of the similarity of the basic flow profile. The cycle of growth and decay of the pressure fluctuations plays a crucial role in the noise radiation mechanism. The amount of energy that radiates noise depends on the amplitude of the wavenumber component spectrum associated with the pressure fluctuations. In this paper far-field noise calculations will only be presented for radiation into the stationary medium, namely, below the layer. The wavenumber component spectrum for $G_-(x)$, given by,

$$\bar{g}_{o_-}(k) = \frac{1}{2\pi}\int_{-\infty}^{\infty} G_-(x)e^{-ikx}\,dx\,, \tag{3.77}$$

was calculated numerically using the FFT algorithm described by Bingham and Morrow [3.47]. The amplitude and phase of $\bar{g}_{o_-}(k)$, for $\omega_o = 0.05$ and $M = 1.75$, are shown in Figure 3.12. The spectrum was found to be insensitive to the number of points used in the transform and the method of truncating the value of $G_-(x)$ for $x < x_o$ and large values of x. This spectrum exhibits features which are characteristic of all the calculated spectra. The dominant peak in the spectrum occurs at a wavenumber which gives a corresponding phase velocity of approximately one half the freestream velocity.

The directivity patterns of radiated noise are readily obtained using Equation (3.26). The directivity patterns for several frequencies are shown in Figure 3.13 for $M = 1.75$. The levels are arbitrarily normalized with respect to the peak level at $\omega_o = 0.005$. The noise radiation peaks at 20 degrees to the axis of the shear layer in the ambient medium. The radiation

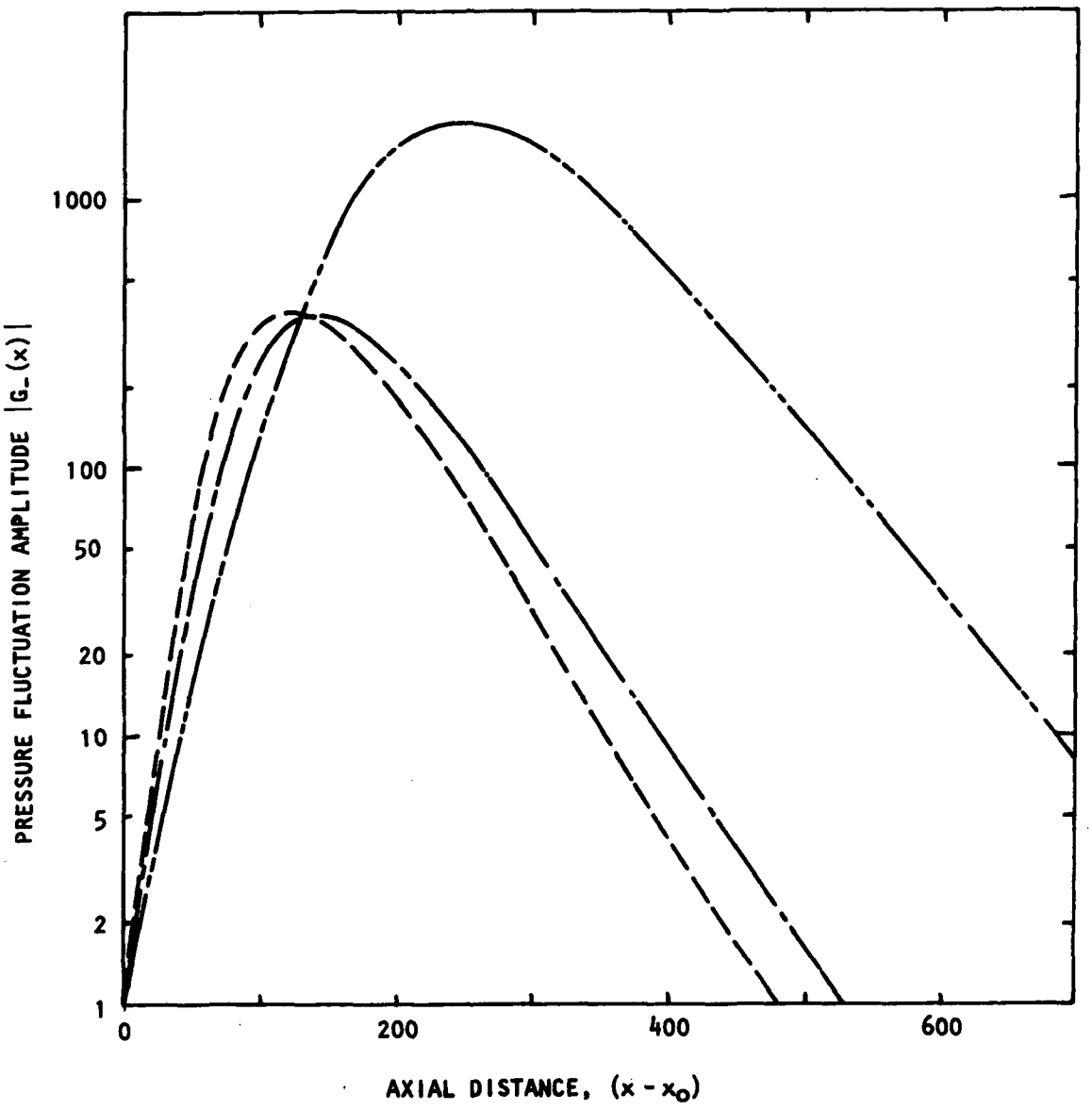

Figure 3.10 Variation of Pressure Amplitude Below the Shear Layer With Axial Distance

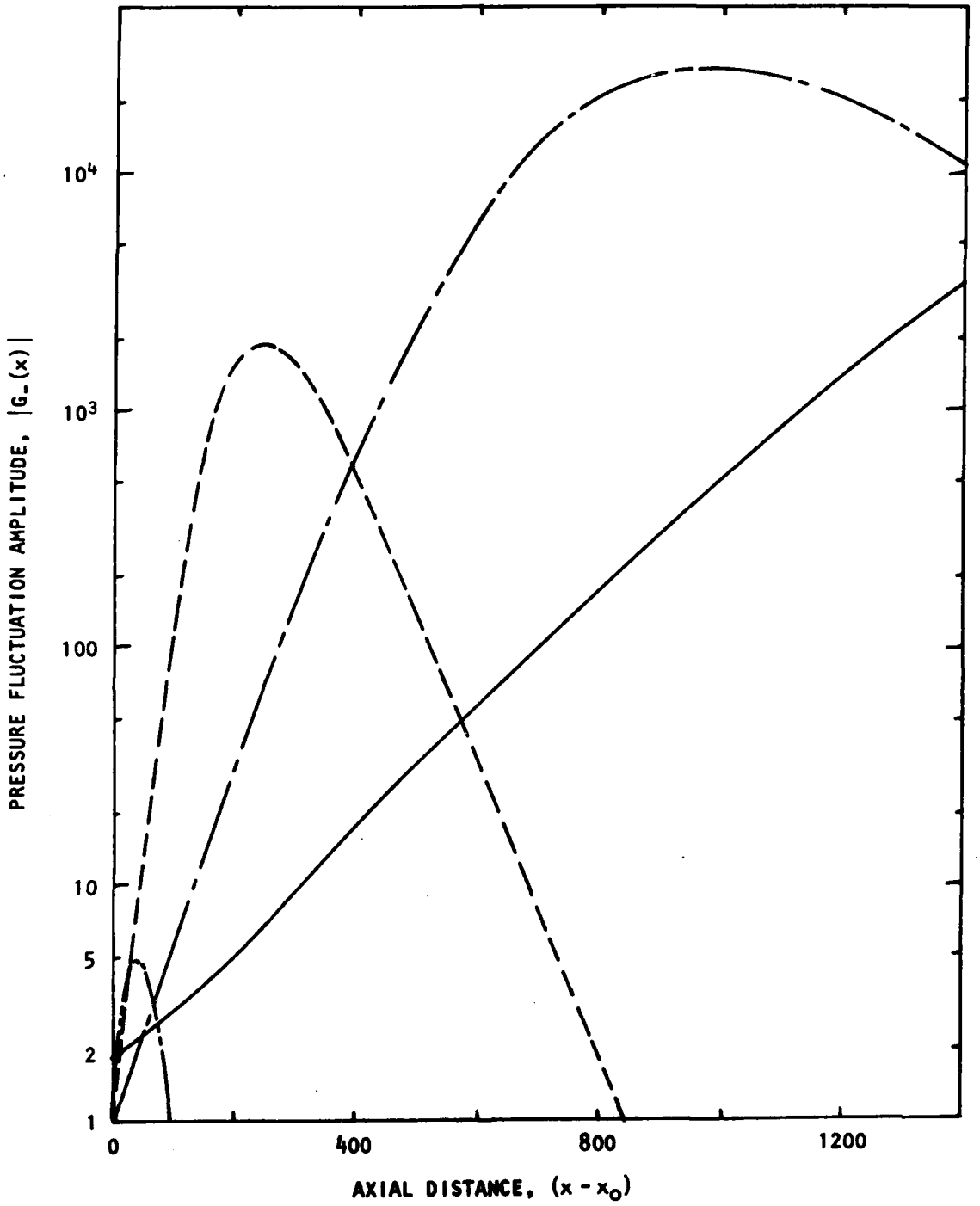

Figure 3.11 Variation of Pressure Amplitude With Axial Distance

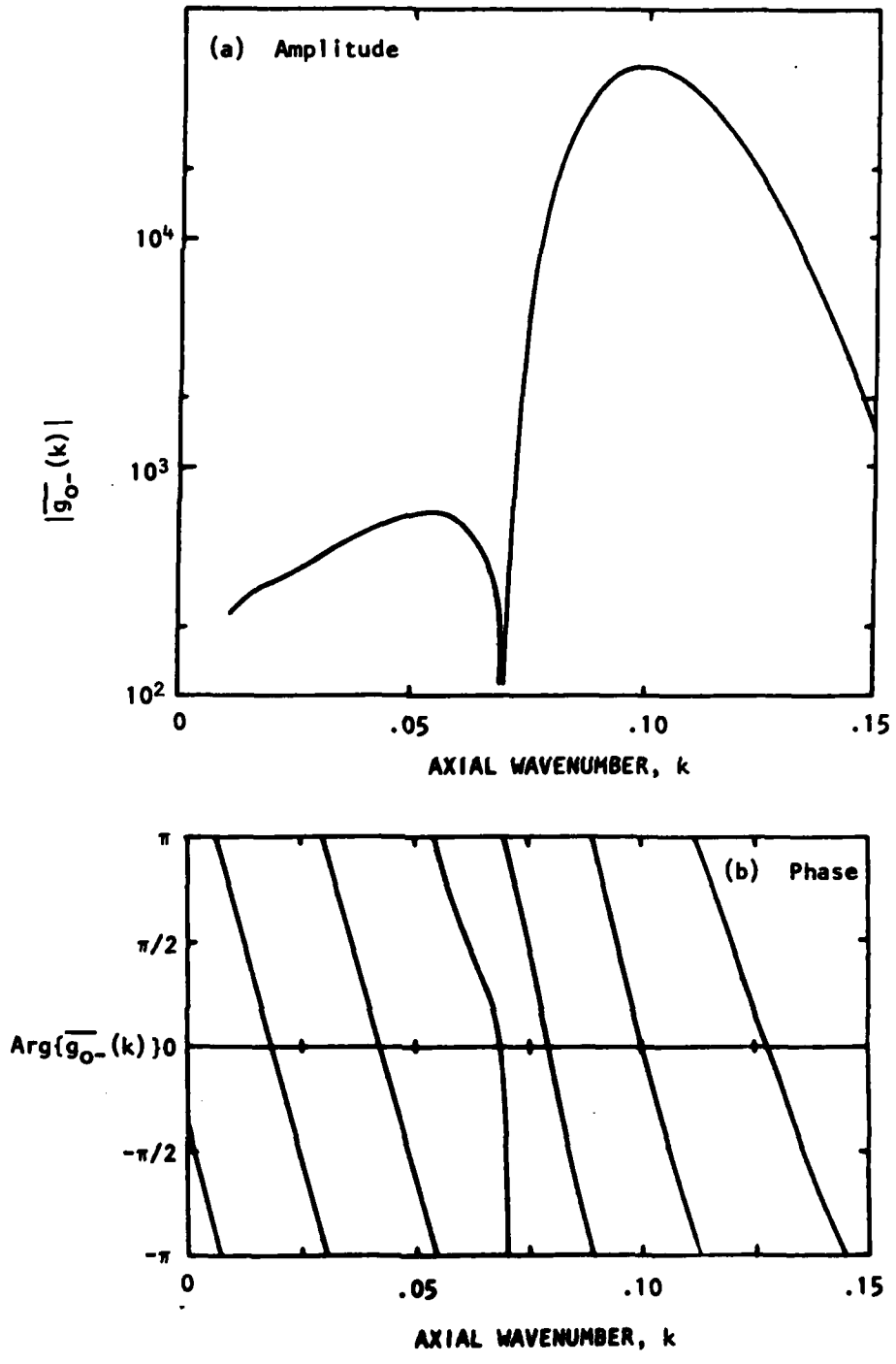

Figure 3.12 Wavenumber component spectrum, $\overline{g_{o-}}(k)$.

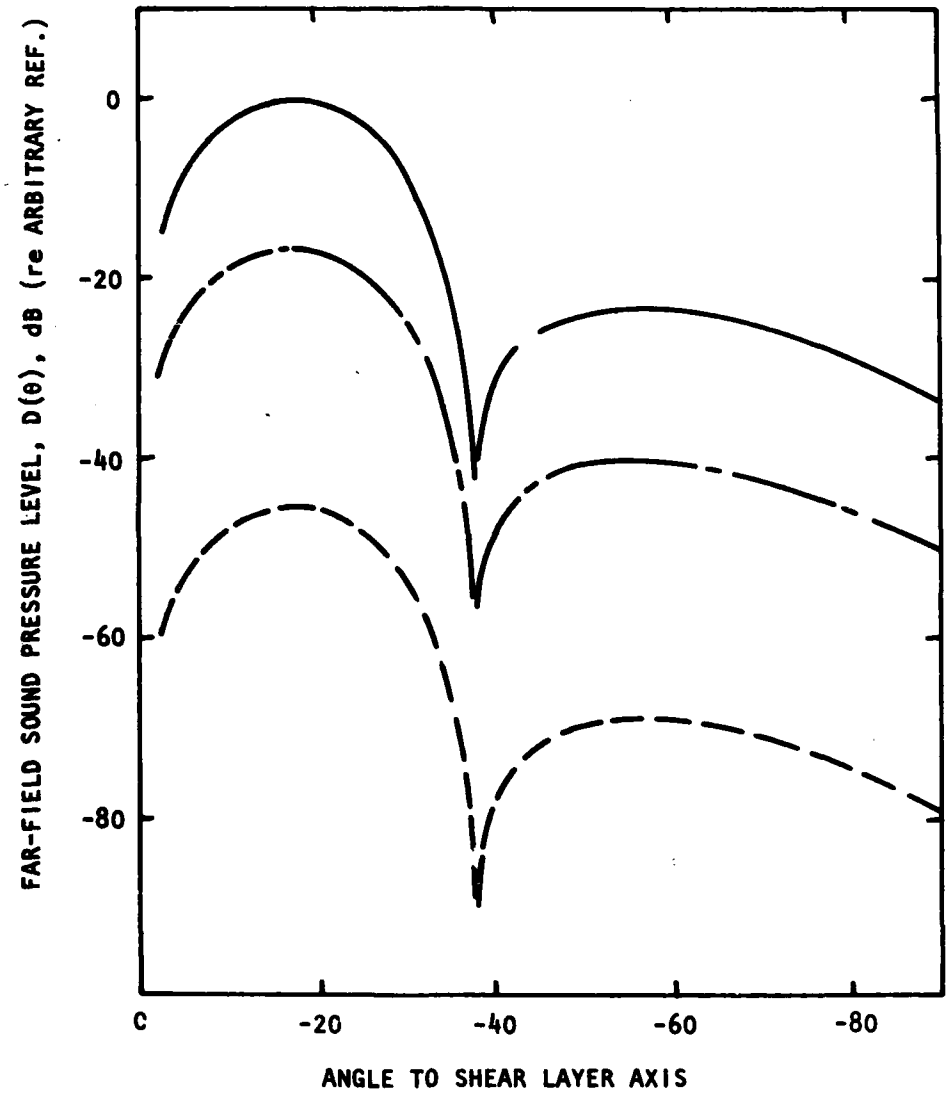

Figure 3.13 Far-Field Noise Directivity Patterns

patterns for all frequencies are similar. This reflects the basic similarity of the shear layer itself where, except at the highest frequencies which will be strongly influenced by the initial shear layer thickness, the development of each frequency wave is similar. As the frequency decreases so the relative sound pressure level in the far field increases. Since the shear layer is infinite in the downstream direction, the lower the frequency of the wave, the greater will be its peak amplitude in the near and far fields. For an experimentally generated shear layer or the mixing region of an axisymmetric jet, there will be some non-extreme frequency which will give the greatest amount of radiated noise.

The radiated noise as a function of Mach number is shown in Figure 3.14 for a frequency of $\omega_o = 0.005$. The normalization is the same as in Figure 3.13. For the $M = 1.25$ case the noise radiation peaks at 12 degrees to the shear layer axis, while there is no discernable peak for the $M = 0.75$ case. The ripples that occur for the two lowest Mach numbers reflect the limitations of the accuracy of the description of $G_-(x)$ and its Fourier transform and are discussed below. The noise radiation from the large-scale structure is seen to become increasingly efficient as the Mach number increases. As can be seen from Equation (3.62), the directivity pattern in the far field is governed by the wavenumber component spectrum amplitude as a function of wavenumber and a $\sin^2\theta$ weighting factor. For Mach numbers such that the peak energy wavenumbers do not radiate noise, that is for $M < 2$, the location of the peak radiation angle is dominated by the $\sin^2\theta$ weighting factor. For higher Mach numbers, the peak angle will depend more on the peak amplitude wavenumber of the wavenumber component spectrum, i.e., $\theta_{peak} \simeq \cos^{-1}(2/M)$: $M > 2$, though $\sin^2\theta$ will prevent the peak angle from occurring at less than 20 degrees.

Returning to the ripples on the directivity patterns for $M = 1.25$ and 0.75 in Figure 3.14, it should be recalled that only those wavenumber components of the pressure fluctuations at the edge of the flow which have a sonic phase velocity to some location in the far field can radiate noise. The lower the freestream Mach number, the smaller is the wavenumber bandwidth that can radiate noise and the further these wavenumbers will be from the peak amplitude wavenumber. The amplitudes of the wavenumber component spectra for $\omega = 0.05$ and various Mach numbers is shown in Figure 3.15. The arrows indicate the range of wavenumber components that contribute to the noise radiation. For the highest Mach number a significant portion of the near-field energy is radiated. However, the region that radiates noise in the subsonic case is far from the peak amplitude wavenumber. The amplitude of components that do radiate at $M = 0.75$ are a factor of 10^3 below the peak level at that frequency and are thus very sensitive to the exact description of the pressure fluctuations in the near field. Thus, though the mechanism by which the large-scale fluctuations in the subsonic shear layer radiate noise has been demonstrated, the calculated radiated noise level should be regarded with caution. The calculated directivity patterns for the supersonic shear layers, however, do have quantitative significance.

Having introduced the analysis in the preceding sections to enable the noise radiation by supersonic shear layers to be calculated the radiation of noise by axisymmetric jets will be considered in the following sections.

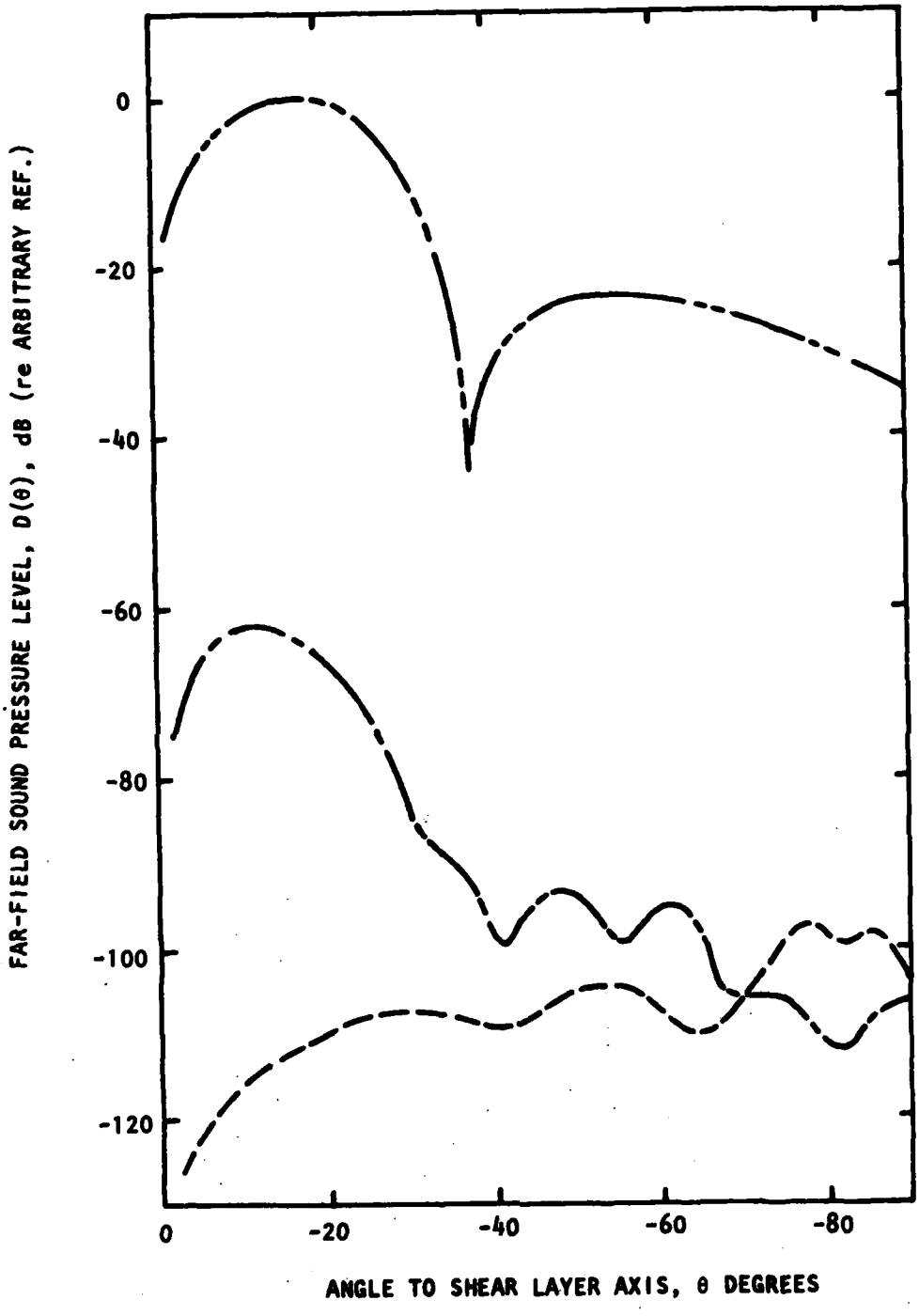

Figure 3.14 Far-Field Noise Directivity Patterns

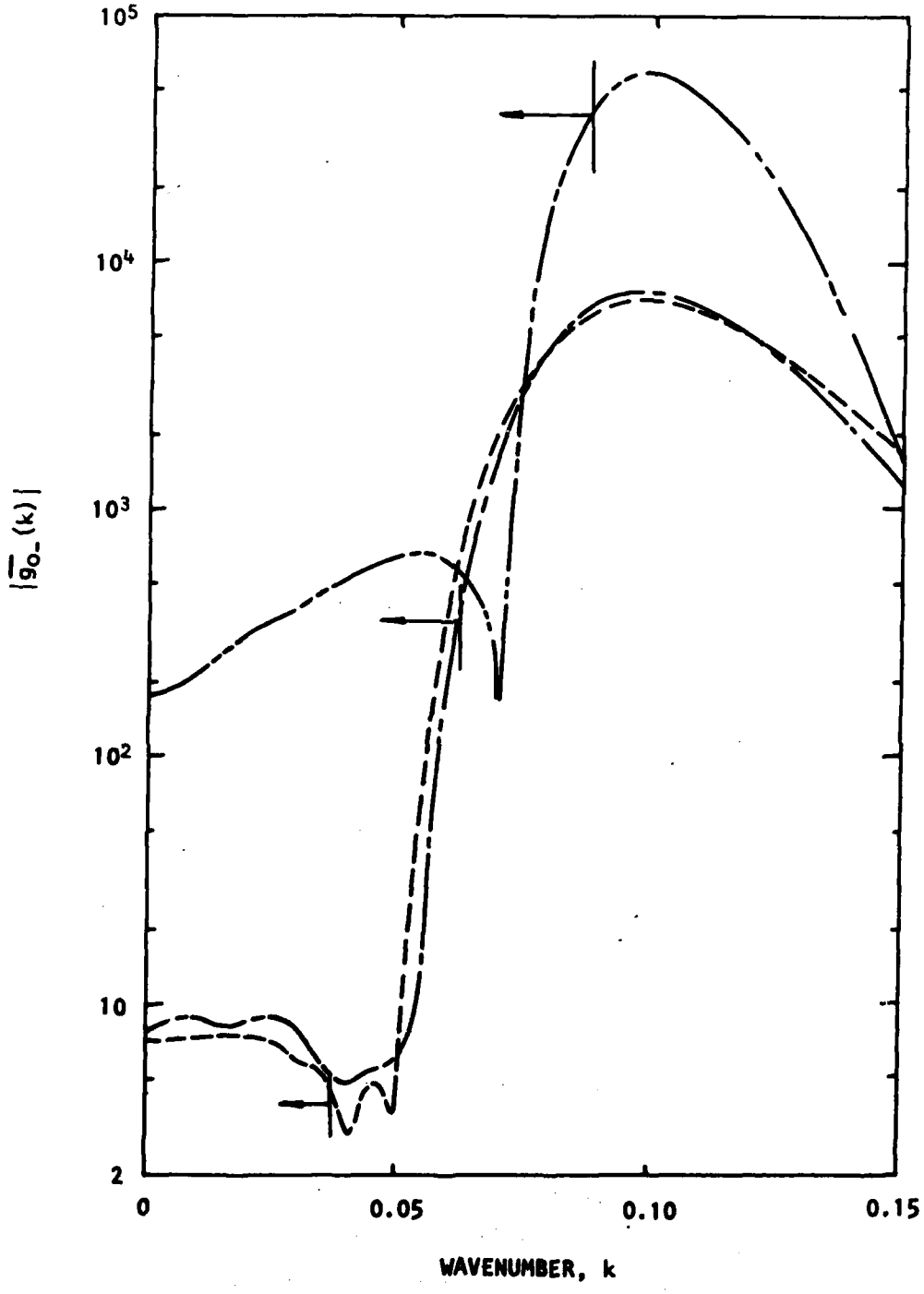

Figure 3.15 Amplitude of Wavenumber Component Spectrum, $|\overline{g_{o_-}}(k)|$

3.3 THE RADIATION OF SOUND BY THE INSTABILITY WAVES OF AXISYMMETRIC JETS

3.3.1 Introduction

In this section the noise radiation by the large-scale structure of supersonic axisymmetric jets will be described. This work forms the foundation for the prediction method for large-scale structure noise described in Section 3.4. The analysis will be presented in a simpler form than that for the plane shear layer, Section 3.2, since the cylindrical geometry increases the complexity of the algebra though it does not effect the basic approach. The experimental data which has been obtained to substantiate the existence of noise radiation by the large-scale structure; for example, McLaughlin, Morrison and Troutt [3.20, 3.21] and Dahan and Elias [3.22], has dealt exclusively with axisymmetric jets. Since these experiments, and their relationship to the present noise generation model were discussed in some detail in Section 3.2.1, they will not be discussed further here. The added feature for the numerical results, which was not presented for the plane shear layer, is a prediction of the near-field pressure fluctuations of the turbulent flow.

In keeping with the order of analysis performed in Section 3.2, the instability wave solution for the axisymmetric jet will be obtained using the method of multiple scales. This solution will be shown to be invalid for large distances from the jet. A uniformly valid solution will be obtained by showing that a model boundary value problem, which has a uniformly valid expansion far from the jet, is the extension of the multiple scales solution for the instability wave.

3.3.2 The Multiple Scales Instability Wave Solution

The behavior of small wave-like disturbances propagating in a turbulent axisymmetric flow will be considered. These disturbances are assumed to be excited by some external disturbance of frequency ω^*. The radius of the jet exit, R_J, the jet exit velocity, u_J, and the ratio R_J/u_J will be the length, velocity and time scales for the problem. In dimensionless form the linearized continuity, momentum, and energy equations and equations of state are,

$$\frac{\partial p'}{\partial t} + \bar{u}_j \frac{\partial p'}{\partial x_j} + \gamma \frac{\partial u_j'}{\partial x_j} + \gamma \frac{\partial \bar{u}_j}{\partial x_j} p' = 0 \tag{3-78}$$

$$\gamma M^2 \left[\frac{\partial u_i'}{\partial t} + \bar{u}_j \frac{\partial u_i'}{\partial x_j} + u_j' \frac{\partial \bar{u}_i}{\partial x_j} \right] = - \frac{\partial p'}{\partial x_i}, \tag{3-79}$$

$$p' = \bar{\rho} T' + \rho' \bar{T}, \tag{3-80}$$

where primes denote fluctuating quantities and bars denote mean flow quantities. M is the ratio of the jet exit velocity to the ambient speed of sound. γ is the ratio of specific heats of the gas. The thermodynamic variables ρ, p, and T, the density, pressure and temperature, respectively, are nondimensionalized with respect to their ambient values. In deriving the

above equations the mean pressure has been assumed to be constant throughout the jet. With respect to a cylindrical coordinate system (r,ϕ,x), the x-axis of which coincides with the axis of the jet and which is centered at the nozzle exit, the mean flow, on the basis of experimental observations, is a function of the radial coordinate r and a slowly varying function of the axial distance x. The mean velocity vector will be written as,

$$\underset{\sim}{\bar{u}} = [U(r,s), \quad \varepsilon V(r,s), \quad 0] \tag{3-81}$$

where

$$\left.\begin{aligned} U &= 0 \\ V &= V_1 \end{aligned}\right\} \quad r \geq r_m \tag{3-82}$$

In Equations (3-81) and (3-82), $s = \varepsilon x$, where the small parameter ε is a measure of the rate of spread of the jet. Typically, ε is numerically less than 0.1. A solution will be sought to Equations (3-78) to (3-80) in the form of a slowly-varying wave,

$$\left[u',v',w'\right](r,\phi,x,t) = \left| \sum_{n=0}^{\infty} \varepsilon^n \left[\hat{u}_n,\hat{v}_n,\hat{w}_n\right](r,s) \right| e^{\,i(\theta(x) + m\phi - \omega t)} \tag{3-83a}$$

$$p'(r,\phi,x,t) = \left| \sum_{n=0}^{\infty} \varepsilon^n \hat{p}_n(r,s) \right| e^{\,i(\theta(x) + m\phi - \omega t)} \tag{3-83b}$$

$$T'(r,\phi,x,t) = \left| \sum_{n=0}^{\infty} \varepsilon^n \hat{T}_n(r,s) \right| e^{\,i(\theta(x) + m\phi - \omega t)} \tag{3-83c}$$

$$\rho'(r,\phi,x,t) = \left| \sum_{n=0}^{\infty} \varepsilon^n \hat{\rho}_n(r,s) \right| e^{\,i(\theta(x) + m\phi - \omega t)}, \tag{3-83d}$$

where $m = 0, 1, 2, \ldots$ is the azimuthal mode number and ω is the forced frequency of the wave. The fast phase function $\theta(x)$ is such that,

$$\frac{d\theta}{dx} = \alpha(s) \, . \tag{3-84}$$

Substituting Equations (3-83) into Equations (3-78) to (3-80) and ordering equations in powers of ε gives, to order unity,

$$-i\gamma M^2 \Omega \hat{v}_o + \frac{1}{R_o} \frac{\partial \hat{p}_o}{\partial r} = 0 \tag{3-85a}$$

$$-i\gamma M^2 \Omega \hat{w}_o + \frac{im}{R_o r} \hat{p}_o = 0 \tag{3-85b}$$

$$\gamma M^2 \left[-i\Omega\hat{u}_o + \hat{v}_o \frac{\partial U}{\partial r} \right] + i \frac{\alpha}{R_o} \hat{p}_o = 0 \qquad (3\text{-}85c)$$

and

$$- i \frac{\Omega}{\gamma} \hat{p}_o + \frac{1}{r} \frac{\partial}{\partial r} (\hat{v}_o r) + \frac{im}{r} \hat{w}_o + i\alpha\hat{u}_o = 0, \qquad (3\text{-}85d)$$

where $\Omega = \omega - U\alpha$ and $\bar{\rho} = R_o(r,s)$ the mean density. These equations readily reduce to a single equation for $\hat{p}_o$ of the form,

$$\frac{\partial^2 \hat{p}_o}{\partial r^2} + \left[\frac{1}{r} - \frac{1}{R_o} \frac{\partial R_o}{\partial r} + \frac{2\alpha}{\Omega} \frac{\partial U}{\partial r} \right] \frac{\partial \hat{p}_o}{\partial r} + \left[M^2\Omega^2 R_o - \alpha^2 - \frac{m^2}{r^2} \right] \hat{p}_o = 0 \qquad (3\text{-}86a)$$

which will be written as,

$$L\,[\hat{p}_o] = 0\,. \qquad (3\text{-}86b)$$

To order ε a set of inhomogeneous equations for the fluctuations $\hat{p}_1$, $\hat{\rho}_1$, etc. are obtained where the right-hand sides are functions of the zero order fluctuations. These equations may also be reduced to a single inhomogeneous equation of the form,

$$L\,[\hat{p}_1] = F\left[\hat{p}_o, \frac{\partial p_o}{\partial s}, \frac{\partial \hat{p}_o}{\partial r}, \frac{\partial^2 p_o}{\partial r \partial s} \right] \equiv \chi_1 \qquad (3\text{-}87)$$

The boundary conditions to be imposed on $\hat{p}_o$, $\hat{p}_1$, ... are that these functions be bounded as $r \to 0$ and $r \to \infty$. Equation (3-86) and the above boundary conditions form an eigenvalue problem. The eigenvalue is α. The corresponding eigenfunction $\hat{p}_o$ has an arbitrary amplitude. We will exhibit this by writing

$$\hat{p}_o(r,s) = A_o(s)\ \hat{\zeta}(r,s)\,. \qquad (3\text{-}88)$$

The function $\hat{\zeta}(r,s)$ satisfies the equation

$$L[\hat{\zeta}] = 0 \qquad (3\text{-}89)$$

and the boundary conditions,

$$\hat{\zeta}(r,s) \quad \text{is bounded as} \quad r \to 0 \ \text{ or } \infty. \qquad (3\text{-}90)$$

For $r \geq r_m$ Equation (3-89) reduces to

$$\frac{\partial^2 \hat{\zeta}}{\partial r^2} + \frac{1}{r} \frac{\partial \hat{\zeta}}{\partial r} + \left[M^2\omega^2 - \alpha^2 - \frac{m^2}{r^2} \right] \hat{\zeta} = 0. \qquad (3\text{-}91)$$

The solution of Equation (3.91) which satisfies the boundedness condition is

$$\hat{\zeta} = H_m^{(1)}\{\lambda r\} \tag{3-92a}$$

and $$\lambda = \sqrt{M^2\omega^2 - \alpha^2}, \qquad R_e\{\lambda\} \to 0, \tag{3-92b}$$

and $H_m^{(1)}\{\ \}$ is the m^{th} order Hankel function of the first kind. A normalization convention will be adopted such that the arbitrary multiplicative constant in front of the Hankel function in Equation (3-92) is unity. Equations (3-83), (3-91), and (3-92) lead to

$$p'(r,\phi,x,t) = A_o(s)\, H_m^{(1)}\{\lambda r\} \exp[i\theta(x) + im\phi - i\omega t] + O(\varepsilon) \tag{3-93}$$
$$r \geq r_m$$

In order that a solution exists to Equation (3-87), it must satisfy the solvability condition: that is the integral of the scalar product of its right-hand side and the solution to the adjoint homogeneous problem over all r must equal zero. It is readily shown that the solution to the adjoint homogeneous problem, $\psi(r,s)$, is given by $\psi = \hat{\zeta} r/R_o\Omega^2$, so that the solvability condition may be written

$$\int_0^\infty \frac{\hat{\zeta}\chi_1}{R_o\Omega^2}\, r\,dr = 0\,. \tag{3-94}$$

The solvability condition leads to an ordinary differential equation for $A_o(s)$ of the form,

$$I_1 \frac{dA_o}{ds} + I_2 A_o = 0\,, \tag{3-95}$$

where the integrals I_1 and I_2 are given in Appendix 3B. Now with $\hat{\zeta}(r,s)$ to be obtained from the eigenvalue problem of Equations (3-89) and (3-90) and $A_o(s)$ to be found by integrating Equation (3-95), the slowly varying wave solution in the form,

$$p'(r,\phi,x,t) = A_o(s)\, \hat{\zeta}(r,s) \exp[i\theta(x) + im\phi - i\omega t] + O(\varepsilon) \tag{3-96}$$

is completely determined to order unity.

3.3.2.1 Higher-order terms of the multiple scales asymptotic expansion

In Section 3.2.2.2 above we considered all the higher-order terms for the multiple scales asymptotic expansion for the plane shear layer case. In this section only the first-order term will be considered. This is in light of the unnecessary algebra introduced by considering all the higher-order terms and to avoid any confusion generated by having to consider higher-order

terms in the mean flow description. These factors will not effect the conclusions drawn about the validity of the multiple scales expansion or the noise radiation since the latter will only be determined to zeroth order.

The first order term in the multiple scales asymptotic expansion is given by the solution to the inhomogeneous Equation (3-87). Since the corresponding homogeneous equation has an eigensolution, $\hat{\zeta}$, the solution for $\hat{p}_1$ can be regarded as consisting of the sum of a particular solution and a complementary solution of the form $A_1(s)\,\hat{\zeta}(r,s)$ where $A_1(s)$ is an unknown amplitude. This unknown amplitude may be determined in a similar manner to $A_o(s)$ from the solvability condition,

$$\int_0^\infty \frac{\hat{\zeta}\chi_2}{R_o\Omega^2}\, r\, dr = 0, \tag{3-97}$$

where χ_2 are the inhomogeneous terms of the equation for $\hat{p}_2$. Equation (3-97) leads to an ordinary differential equation for $A_1(s)$ which may be integrated and hence the complementary solution is completely determined. The appropriate particular solutions may be obtained by the method of variation of parameters. For $r \geq r_m$ the eigenfunction $\hat{\zeta}$ is given by Equation (3-92). Another linearly independent solution of Equation (3-91) is

$$\hat{\xi}(r,s) = H_m^{(2)}\{\lambda r\}. \tag{3-98}$$

Now let $\hat{\xi}(r,s)$ be the solution of Equation (3-9) which takes the form (3-98) for $r > r_m$. Then $\hat{\zeta}(r,s)$ and $\hat{\xi}(r,s)$ are two linearly independent solutions of the corresponding homogeneous equation of (3-87). It may be readily shown that the Wronskian $W(\hat{\zeta},\hat{\xi})$ is given by

$$W(\hat{\zeta},\hat{\xi}) = -\frac{4i}{\pi}\frac{R_o\Omega^2}{r\omega^2}, \tag{3-99}$$

where the relationship,

$$H_m^{(1)}(z)\, H_m^{(2)'}(z) - H_m^{(1)'}(z)\, H_m^{(2)}(z) = -(4i/\pi z), \tag{3-100}$$

has been used in determining the free constant in the Wronskian. Using the method of variation of parameters, it can be shown that

$$\hat{p}_1 = A_n\hat{\zeta}(r,s) - \hat{\zeta}(r,s)\int_0^r \frac{\hat{\xi}(t,s)\chi_1(t,s)}{W(\hat{\zeta},\hat{\xi})}\, dt$$

$$+ \hat{\xi}(r,s)\int_0^r \frac{\hat{\zeta}(t,s)\chi_1(t,s)}{W(\hat{\zeta},\hat{\xi})}\, dt \tag{3-101}$$

Using the explicit form for the Wronskian given by Equation (3-99), we obtain,

$$\hat{p}_1 = A_1\hat{\zeta}(r,s) + \frac{i\pi\omega^2}{4}\left[-\hat{\zeta}(r,s)\int_0^r \frac{\hat{\xi}(t,s)\chi_1(t,s)}{R_o\Omega^2}\,t\,dt\right.$$

$$\left. + \hat{\xi}(r,s)\int_0^r \frac{\hat{\zeta}(t,s)\chi_1(t,s)}{R_o\Omega^2}\,t\,dt\right] \qquad (3\text{-}102)$$

$\hat{p}_1(r,s)$ as given by Equation (3.102) clearly satisfies the boundedness condition at $r=0$. The solvability condition (3-94) guarantees that the solution be bounded as $r\to\infty$. The last term in Equation (3-102) may be written in a more useful form using this solvability condition, that is,

$$\hat{p}_1 = A_1\hat{\zeta}(r,s) - \frac{i\pi\omega^2}{4}\left[\hat{\zeta}(r,s)\int_0^r \frac{\hat{\xi}(t,s)\chi_1(t,s)}{R_o\Omega^2}\,t\,dt\right.$$

$$\left. + \hat{\xi}(r,s)\int_r^\infty \frac{\hat{\zeta}(t,s)\chi_1(t,s)}{R_o\Omega^2}\,t\,dt\right] \qquad (3\text{-}103)$$

Equation (3-103) and the solvability condition (3-97) provide the complete solution of the amplitude functions for the slowly varying wave solution to order unity. Higher-order terms may be obtained in a similar fashion. However, it will now be shown that this asymptotic expansion has only a limited range of applicability.

3.3.2.2 The singular perturbation problem

In the region $r > r_m$, to *first* order, the mean flow is given by $U=0$, $V=V_1$. In this region the inhomogeneous terms of Equation (3-87) may be written out in a simple form,

$$L(\hat{p}_1) = -2i\alpha\frac{\partial\hat{p}_o}{\partial s} - i\frac{d\alpha}{ds}\hat{p}_o + i\left[\frac{V_1}{\omega r^2} - 2M^2V_1\omega\right]\frac{\partial\hat{p}_o}{\partial r}$$

$$- i\left[\frac{2V_1}{\omega}\frac{m^2}{r^3} + \gamma M^2\frac{V_1\omega}{r}\right]\hat{p}_o\,. \qquad (3\text{-}104)$$

The functions $\hat{\zeta}$ and $\hat{\xi}$ of Equation (3-103) take the form,

$$r > r_m \qquad \hat{\zeta} = H_m^{(1)}(\lambda r) \qquad \xi = H_m^{(2)}(\lambda r) \qquad (3\text{-}105)$$

so that the general expression for $\hat{p}_1$ becomes,

$$\hat{p}_1(r,s) = D_1 H_m^{(1)}(\lambda r) - \frac{i\pi}{4} H_m^{(1)}(\lambda r) \int_r^{r} H_m^{(2)}(\lambda t)\, \bar{\chi}_1(t,s)\, t\, dt$$
$$r > r_m$$

$$- \frac{i\pi}{4} H_m^{(2)}(\lambda r) \int_r^{\infty} H_m^{(1)}(\lambda t)\, \chi_1(t,s)\, t\, dt \qquad (3\text{-}106a)$$

where

$$D_1 = A_1 - \frac{i\pi}{4}\left[\omega^2 \int_0^{r_m} \frac{\hat{\xi}(t,s)\chi_1(t,s)t\,dt}{R_o\Omega^2} + \int_{r_m} H_m^{(2)}(\lambda t)\bar{\chi}_1(t,s)\, t\, dt\right]. \qquad (3\text{-}106b)$$

Equation (3-106) gives the dependence of $\hat{p}_1$ or r for $r > r_m$.

With $\hat{p}_o = A_o\hat{\zeta} = A_o(s)\, H_m^{(1)}(\lambda r)$ for $r > r_m$, the inhomogeneous term $\bar{\chi}_1$ may be computed from Equation (3-104). This gives

$$\bar{\chi}_1 = \left[C_1 + \frac{C_2}{r} + \frac{C_3}{r^3}\right] H_m^{(1)}(\lambda r) + \left[C_4 r + C_5 + \frac{C_6}{r^2}\right] H_m^{(1)\prime}(\lambda r) \qquad (3.107)$$

where

$$C_1 = -i\left[2\alpha \frac{dA_o}{ds} + A_o \frac{d\alpha}{ds}\right],$$

$$C_2 = -i\gamma M^2 V_1 \omega A_o,$$

$$C_3 = -2i\, V_1 m^2 A_o/\alpha,$$

$$C_4 = 2i \frac{\alpha^2}{\lambda} \frac{d\alpha}{ds} A_o,$$

$$C_5 = -2iM^2 V_1 \omega\lambda A_o,$$

and $$C_6 = iV_1\lambda A_o/\omega.$$

The form of $\hat{p}_1$ for $r > r_m$ may be found by substituting Equation (3-107) into Equation (3-106a) and evaluating the integrals. Unfortunately, the integrals may not be evaluated in a simple form since the integrands involve products of Bessel functions and powers of r for which no integrals exist. However, the purpose in evaluating the higher-order terms is to demonstrate that the multiple scales asymptotic expansion is not valid for all values of r. Thus, the integrals have been evaluated assuming that the Hankel functions

and their derivatives may be replaced by their asymptotic form for large arguments. The tedious integration is performed in Appendix 3C. It is found that

$$\hat{p}_1(r,s) \sim K_1 r^2 H_m^{(1)}(\lambda r) . \tag{3-108}$$

Thus, for large r the multiple scales asymptotic expansion behaves like

$$p'(r,\phi,x,t) \sim [K_0 + K_1 \varepsilon r^2] H_m^{(1)}(\lambda r) e^{i\theta(x) + im\phi - i\omega t} + O(\varepsilon^2) \tag{3-109}$$

where the K_l are functions of x alone. Due to the appearance of $\varepsilon r^2 H_m^{(1)}(\lambda r)$ in the higher order term the asymptotic expansion does not hold for $r \gg \varepsilon^{\frac{1}{2}}$. Thus, in the same sense as the plane turbulent shear layer problem the present perturbation problem is also singular.

3.3.3 Continuation of the Instability Wave Solution into the Region $r > r_m$

An extension of the multiple scales asymptotic expansion will now be constructed which is uniformly valid for $r > r_m$. The analysis follows closely that of Section 3.2.3. In the region $r > r_m$, U is zero and V is a constant so the governing equations reduce to

$$\frac{\partial p_e}{\partial t} + V \frac{\partial p_e}{\partial r} + \gamma \left| \frac{1}{r} \frac{\partial v_e}{\partial r} + \frac{1}{r} \frac{\partial w_e}{\partial \phi} + \frac{\partial u_e}{\partial x} \right| + \gamma V_1 \frac{p_e}{r} = 0 \tag{3-110a}$$

$$\gamma M^2 \left| \frac{\partial v_e}{\partial t} + V \frac{\partial v_e}{\partial r} \right| = - \frac{\partial p_e}{\partial r} \tag{3-110b}$$

$$\gamma M^2 \left| \frac{\partial w_e}{\partial t} + V \frac{\partial w_e}{\partial r} + \frac{V w_e}{r} \right| = - \frac{1}{r} \frac{\partial p_e}{\partial \phi} \tag{3-110c}$$

$$\gamma M^2 \left| \frac{\partial u_e}{\partial t} + V \frac{\partial u_e}{\partial r} \right| = - \frac{\partial p_e}{\partial x} . \tag{3-110d}$$

The appropriate boundary condition for large r is the radiation or boundedness condition,

$r \to \infty$ $\quad u_e, v_e, w_e, p_e$ are bounded or behave like outgoing waves. (3-111)

At this stage an inner boundary condition is needed for p_e in the region r slightly greater than r_m. Following the arguments of Section 3.2.3, we set the inner boundary condition as, for example,

$$(u_e, v_e, w_e, p_e) = \left| \sum_{n=0}^{\infty} \varepsilon^n (\hat{u}_n, \hat{v}_n, \hat{w}_n, \hat{p}_n)(r,s) \right| e^{i\theta(x) + im\phi - i\omega t} \tag{3-112}$$

(for r slightly greater than r_m)

where $\hat{p}_1$ is given by Equation (3-106a) and the higher order $\hat{p}_n$ are given by the solution to the corresponding inhomogeneous equations to Equation (3-87) of the form

$$L[\hat{p}_n] = \chi_n. \tag{3-113}$$

Thus, the extended problem must satisfy equations (3-110), the radiation and inner conditions (3-111) and (3-112) and be uniformly valid for $r > r_m$.

3.3.3.1 The extended problem

It will now be shown that the extended solutions, u_e, v_e, w_e and p_e, as defined in Equations (3-110), (3-111), and (3-112) are identical to the solutions ϕ_u, ϕ_v, ϕ_w, ϕ_p of the following boundary value problem,

$$\frac{\partial \phi_p}{\partial t} + V \frac{\partial \phi_p}{\partial r} + \gamma\left|\frac{1}{r}\frac{\partial \phi_v r}{\partial r} + \frac{1}{r}\frac{\partial \phi_w}{\partial \phi} + \frac{\partial \phi_u}{\partial x}\right| + \frac{\gamma V \phi_p}{r} = 0 \tag{3-114a}$$

$$\gamma M^2 \left|\frac{\partial \phi_v}{\partial t} + V \frac{\partial \phi_v}{\partial r}\right| = -\frac{\partial \phi_p}{\partial r}, \tag{3-114b}$$

$$\gamma M^2 \left|\frac{\partial \phi_w}{\partial t} + V \frac{\partial \phi_w}{\partial r} + \frac{V\phi_w}{r}\right| = -\frac{1}{r}\frac{\partial \phi_p}{\partial \phi}, \tag{3-114c}$$

and

$$\gamma M^2 \left|\frac{\partial \phi_u}{\partial t} + V \frac{\partial \phi_u}{\partial r}\right| = -\frac{\partial \phi_p}{\partial x}, \tag{3-114d}$$

$r \to \infty$ ϕ_p satisfies the radiation or boundedness condition, (3-115)

and, as $r \to 0$, ϕ_p has the following singular behavior

$$\phi_p = \begin{cases} \sum_{n=0}^{\infty} \varepsilon^n \frac{2i}{\pi} \ell n\,(r)\, g_{no}(\varepsilon x) \exp[i\theta(x) - i\omega t], & m = 0 \\ -\sum_{n=0}^{\infty} \varepsilon^n \frac{i(m-1)!}{\pi} \left[\frac{2}{\sqrt{M^2\omega^2 - \alpha^2}\, r}\right]^m g_{nm}(\varepsilon x) \exp[i\theta(x) + im\phi - i\omega t], & \end{cases}$$

$$m = 1, 2 \ldots. \tag{3-116}$$

where $g_{nm}(\varepsilon x)$, $s = \varepsilon x$, will be related to the multiple scales expansion below. The solution to equations (3-114), (3-115) and (3-116) constitute a well-defined boundary value problem. Since Equations (3-114) and (3-115) are identical to Equations (3-110) and (3-111), the hypothesis that $\phi_p = p_e$, etc. for $r > r_m$ could be proved if it could be shown that ϕ_p, etc. possesses asymptotic expansions which are identical to the right-hand sides of equation (3-112) for r slightly greater than r_m. To show this the above boundary value problem will be solved for ϕ_p etc. in the form of a multiple scales asymptotic expansion. Let the ϕ be given by

$$\phi_p(r,\phi,x,t) = \sum_{n=0}^{\infty} \varepsilon^n \phi_{n,p}(r,s) e^{i\theta(x) + im\phi - i\omega t} \tag{3-117}$$

Substitution of Equation (3-117) into Equation (3-114), partitioning the equations in powers of ε and writing the equations in terms of $\phi_{n,p}$ leads to to order of unity,

$$\left[\frac{\partial^2}{\partial r^2} + \frac{1}{r}\frac{\partial}{\partial r} - \left[\alpha^2 - M^2\omega^2 + \frac{m^2}{r^2}\right]\right]\phi_{o,p} \equiv L_1[\phi_{o,p}] = 0, \tag{3-118a}$$

and to order ε,

$$L_1[\phi_{1,p}] = \left[-2i\alpha\frac{\partial}{\partial s} - i\frac{d\alpha}{ds} + i\left[\frac{V_1}{\omega r^2} - 2M^2 V_1\omega\right]\frac{\partial}{\partial r}\right.$$

$$\left. - i\left[\frac{2V_1}{\omega}\frac{m^2}{r^3} + \gamma M^2\frac{V_1\omega}{r}\right]\right]\phi_{o,p} = \bar{X}_1 \tag{3-118b}$$

The boundary conditions on ϕ_p are found in Equations (3-115) and (3-116), namely

$$r \to \infty \qquad \phi_{n,p} \quad \text{is bounded} \tag{3-119}$$

and at $r = 0$

$$\phi_{n,p} = \begin{cases} \frac{2i}{\pi}\ln(r)\, g_{no}(\varepsilon x), & m = 0 \\ -\frac{i(m-1)!}{\pi}\left\{\frac{2}{\sqrt{M^2\omega^2 - \alpha^2}\, r}\right\}^m g_{nm}(\varepsilon x), & m = 1,2, \ldots \end{cases} \tag{3-120}$$

Two linearly independent solutions of the homogeneous equation, $L_1[\phi_{n,p}] = 0$, are the form $H_m^{(1)}(\lambda r)$ and $H_m^{(2)}(\lambda r)$ where λ is given by Equation (3-92b). The solution to Equation (3-118a) which satisfies the boundary conditions (3-119) and (3-120) may readily be shown to be

$$\phi_{o,p} = g_{om}(\varepsilon x)\, H_m^{(1)}(\lambda r). \tag{3-121}$$

To order ε the solution to the inhomogeneous problem (3-118b) and boundary conditions (3-119) and (3-120) may again be determined by the method of variation of parameters. It can be shown that

$$\phi_{1,p} = \left\{ g_{1m}(s) + \frac{i\pi}{4} \left[\int_0^{\infty} H_m^{(2)}(\lambda t)\bar{\chi}_1(t,s)tdt - \int_0^{\infty} H_m^{(1)}(\lambda t)\bar{\chi}_1(t,s)tdt \right] \right\} H_m^{(1)}(\lambda r)$$

$$- \frac{i\pi}{4} H_m^{(1)}(\lambda r) \int_0^{r} H_m^{(2)}(\lambda t)\bar{\chi}_1(t,s)tdt - \frac{i\pi}{4} H_m^{(2)}(\lambda r) \int_r^{\infty} H_m^{(1)}(\lambda t)\bar{\chi}_1(t,s)tdt \tag{3-122}$$

Now setting

$$g_{om} = A_o(s) \tag{3-123a}$$

and

$$g_{1m} = A_1(s) - \frac{i\pi}{4} \left\{ \omega^2 \int_0^{r_m} \frac{\hat{\xi}(t,s)\chi_1(t,s)tdt}{R_o r\Omega^2} \right.$$

$$\left. - \int_0^{r_m} H_m^{(2)}(\lambda t)\bar{\chi}_1(t,s)tdt + \int_0^{\infty} H_m^{(1)}(\lambda t)\bar{\chi}_1(t,s)tdt \right], \tag{3-123b}$$

the two expressions on the right-hand sides of Equations (3-106) and (3-122) are identical. Thus, $\phi_{o,p} = \hat{p}_o$ and $\phi_{1,p} = \hat{p}_1$ in the region slightly greater than r_m. Thus, the extended solution p_e is equal to, to at least order ε, the solution ϕ_p (for $r \geq r_m$), of the boundary value problem defined by Equations (3-114), (3-115), and (3-116).

3.3.3.2 Uniformly valid asymptotic expansion of the extended problem

Now that it has been shown that the extended solution, p_e, is given by the solution to the boundary value problem defined by Equations (3-114), (3-115), and (3-116), a uniformly valid expansion of the extended problem for $r > r_m$ will be constructed. As in the case of the plane shear layer, Section 3.2.3.2, the method of Fourier transforms will be used.

The Fourier transform and its inverse are defined by

$$\bar{f}(k) = \frac{1}{2\pi} \int_{-\infty}^{\infty} f(x)e^{-ikx}dx; \qquad f(x) = \int_{-\infty}^{\infty} \bar{f}(k)e^{ikx}dk. \tag{3-124}$$

Since only the zero order solution will utlimately be used, the Fourier transform will be applied to this order. (That is, radiation is considered into a medium where $U = 0$ and $V = 0$). So that by setting $\phi_p = \hat{\phi}_p \exp[-i\omega t + im\phi]$ and denoting the Fourier transform of $\hat{\phi}_p$ by $\bar{\phi}$, the equation for $\bar{\phi}$ is readily shown to be

$$\frac{d^2\bar{\phi}}{dr^2} + \frac{1}{r}\frac{d\bar{\phi}}{dr} - \left[M^2\omega^2 - k^2 + \frac{m^2}{r^2} \right] \bar{\phi} = 0 \qquad (3\text{-}125)$$

It is then straightforward to show that the solution for $\bar{\phi}$, satisfying the transformed boundary conditions, is

$$\bar{\phi} = B_m(k)\ H_m^{(1)}\ (\sqrt{M^2\omega^2 - k^2}\, r) \qquad (3\text{-}126a)$$

where
$$B_o(k) = \frac{1}{2\pi} \int_{-\infty}^{\infty} g_{oo}(\epsilon x) e^{i\theta(x) - ikx}\, dx \qquad (3\text{-}126b)$$

and
$$B_m(k) = \frac{(M^2\omega^2 - k^2)^{m/2}}{2\pi} \int_{-\infty}^{\infty} \frac{g_{om}(\epsilon x)}{(M^2\omega^2 - \alpha^2)^{m/2}} e^{i\theta(x) - ikx}\, dx, \qquad (3\text{-}126c)$$

Performing the inverse transform leads to an expression for ϕ_p of the form

$$\phi_p = \int_{-\infty}^{\infty} B_m(k) H_m^{(1)}\ (\sqrt{M^2\omega^2 - k^2}\, r)\ \exp\ [i(kx - \omega t\ + m\phi)]\, dk \qquad (3\text{-}127)$$

Equation (3-127) represents the proper continuation of the zeroth order slowly varying wave solution in the region $r > r_m$.

3.3.3.3 *The acoustic far-field solution*

The sound radiation associated with the instability wave can be found by evaluating the integrals of Equation (3-127). In this evaluation of the far-field polar coordinates (R,θ) will be used where $r = R\sin\theta$ and $x = R\cos\theta$. Equation (3-127) may be rewritten as (noting that ϕ_p is the fluctuating pressure which will be written as p),

$$p(R,\theta,\phi,t) \underset{R \to \infty}{=} \sqrt{\frac{2}{\pi R \sin\theta}} \int_{-\infty}^{\infty} \frac{B_m(k)}{(M^2\omega^2 - k^2)^{\frac{1}{4}}}\ \exp[i(\sqrt{M^2\omega^2 - k^2}\ \sin\theta\ + k\cos\theta)R]$$

$$\exp\left[i(m\phi - \omega t) - i\left(\frac{\pi}{4} + \frac{m\pi}{2}\right)\right] dk + O(\epsilon) \qquad (3\text{-}128)$$

In deriving Equation (3-128), the following asymptotic form of the Hankel function has been used,

$$H_m^{(1)}(z) \underset{z \to \infty}{\sim} \sqrt{\frac{2}{(\pi z)}} \exp\left[i\left(z - \frac{\pi}{4} - \frac{m\pi}{2}\right)\right]. \qquad (3\text{-}129)$$

For large R the integral of Equation (3-128) may be evaluated by the method of stationary phase. This gives

$$p(R,\theta,\phi,t) \underset{R \to \infty}{\sim} \frac{2}{R} B_m(M\omega\cos\theta) \exp\left[i\left(M\omega R + m\phi - \omega t\right) - \frac{i\pi}{2}(m+1)\right]. \qquad (3\text{-}130)$$

The far-field directivity pattern of acoustic radiation $D(\theta)$, due to the instability wave can easily be found as

$$D(\theta) = \lim_{R \to \infty} \frac{|p|^2 R^2}{2} = 2|B_m(M\omega\cos\theta)|^2. \qquad (3\text{-}131)$$

It should also be noted that the solution for the pressure for $r \to r_m$ given by Equation (3-127) represents the pressure associated with the instability wave in both the near and far fields of the jet. This equation will be used below in evaluating near-field pressure contours.

3.3.4 Numerical Results

3.3.4.1 The instability wave solution

Mean Velocity and Density Profiles. Before numerical calculations can be performed, it is necessary to describe the mean velocity and density profiles in the jet. The mean velocity profiles are taken from experimental measurements. A shape function is used to describe the mean velocity. In the annular mixing region of the jet, the mean velocity is given by

$$U(r,s) = \begin{cases} \bar{U}(\eta) & r > h \\ 1. & r < h \end{cases} \qquad (3\text{-}132)$$

where

$$\eta = (r - h)/b. \qquad (3\text{-}133)$$

h is the potential core radius and b is the velocity half-width of the annular mixing region, that is, the radial distance from the edge of the potential core to the half-velocity point. Downstream of the end of the potential core, the mean velocity is given by

$$U(r,s) = u_c \bar{U}(\xi), \qquad (3\text{-}134)$$

where

$$\xi = r/b. \qquad (3\text{-}135)$$

u_c is the jet centerline velocity. The coordinate systems used to describe the mean velocity are shown in Figure 3.16. The shape functions $\bar{U}(\eta)$ and $\bar{U}(\xi)$ are approximated by Gaussian profiles and have the same form in both the annular mixing region and downstream of the end of the potential core. Thus, we have, for example,

$$\bar{U}(\eta) = \exp\left[-0.693147\eta^2\right] . \tag{3-136}$$

The radial mean velocity is found by integrating the mean continuity equation. The density is related to the mean axial velocity using a Crocco relationship, such that

$$R_o(r,s) = \{1 + (T_J - 1)U + \frac{(\gamma - 1)}{2} M^2 U(1 - U)\}^{-1} . \tag{3-137}$$

The axial development of the mean flow is computed using the integrated mean momentum and mechanical energy equations. The momentum integral equation can be approximated by (ignoring second order products of fluctuating quantities),

$$\int_0^\infty \bar{\rho}\bar{u}^2 \, r dr = \text{constant} = 1/2 \, T_J , \tag{3-138}$$

assuming constant jet exit conditions. T_J is the static jet exit temperature. On substituting for $\bar{\rho}$ and $\bar{u}$ from Equations (3-134), (3-136), and (3-137) into Equation (3-138), an algebraic relationship can be found between h and b in the annular mixing region and u_c and b downstream of the end of the potential core. Thus, the jet development can be determined entirely by the axial variation of the jet half width, b.

In the annular mixing region the jet width is assumed to vary linearly with axial distance in accordance with experimental observations. Downstream of the potential core the variation of the half-width is found from the integral mean mechanical energy equation. To the same approximation as the momentum integral equation (3-138), the mean mechanical energy equation may be written,

$$\frac{d}{dx} \int_0^\infty \bar{\rho}\bar{u}^3 \, r dr = -2 \int_0^\infty \tau \left(\frac{\partial \bar{u}}{\partial r}\right) \, r dr . \tag{3-139}$$

The turbulent shear stress, τ, is related to the mean velocity gradient by

$$\tau = \bar{\rho} \, \bar{\varepsilon} \, \frac{\partial \bar{u}}{\partial r} , \tag{3-140}$$

where $\bar{\varepsilon}$ is an eddy viscosity coefficient. The eddy viscosity coefficient is defined in terms of a dimensionless quantity $\bar{K}$ where $\bar{K}$ is such that

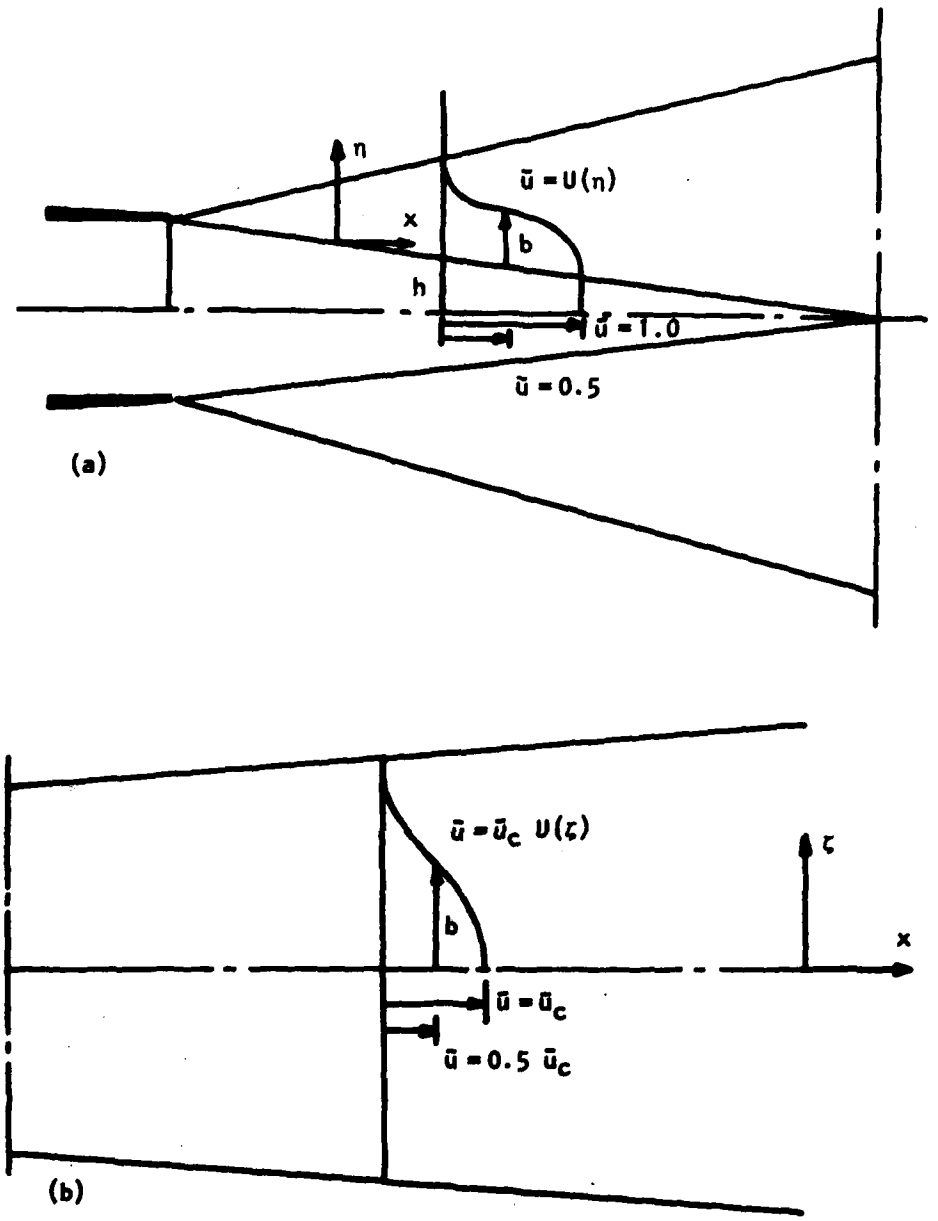

Figure 3.16 Coordinate Systems. (a) Annular Mixing Region; (b) Developed Jet Region.

$$\bar{\rho}\ \bar{\varepsilon} = \frac{\bar{K}}{2}\, b\bar{\rho}_{.5}\, u_c\ , \tag{3.141}$$

where $\bar{\rho}_{.5}$ is the mean density at the half-velocity point (see Eggers, [3-48]). Substitution of Equations (3-140) and (1-141) into Equation (3-139) and the introduction of the coordinate system and shape function downstream of the end of the potential core leads to an equation relating du_c/dx to db/dx. Differentiating the momentum integral equation with respect to x leads to a second relationship between du_c/dx and db/dx. Elimination of du_c/dx between the two expressions provides the value of db/dx. The equations for du_c/dx and db/dx are given in Appendix 3D.

Since db/dx, due to the mean velocity and coordinate definitions, is not continuous through the end of the potential core, the value of $\bar{K}$ is allowed to vary through the transition region into the fully developed jet. This variation minimizes the discontinuity in $dr_{.5}/dx$ where $r_{.5}$ is the radial distance to the half velocity point. In the annular mixing region, $r_{.5} = h + b$. The form for the variation of $\bar{K}$ with x is taken to be

$$\bar{K} = 0.04\left[1 - \frac{A}{b(x)}\right], \tag{3-142}$$

where the value of A varies with jet exit conditions. For the test case of $M = 1.2457$ and $T_J = .6897$, to be examined below, $A = 0.7464$.

The perturbation parameter, ε, which is a measure of the rate of spread of the mean flow is taken to be the value of db/dx in the annular mixing region. Since the rate of spread of the mixing layer is a function of the jet operating conditions, the value of ε for each specific test condition will vary. One measure of the rate of spread of the mixing layer is the parameter σ which defines a similarity variable for two-dimensional mixing layers. The variation of σ as a function of M_J, where M_J is the jet exit Mach number, u_J/a_J, has been tabulated by Birch and Eggers [3.49]. This data is shown in Figure 3.17. The data may be fitted by two empirical functions also shown in the figure. These correlations are given by

$$\sigma = 10.7/(1.0 - 0.1163\ M_J^2); \qquad M_J < 2.0 \tag{3-143a}$$

$$\sigma = 19.4\ \sqrt{M_J - 0.9418}; \qquad M_J > 2.0 \tag{3-143b}$$

It can be readily shown that the vorticity thickness, δ_ω, may be related to σ by $d\delta_\omega/dx = \sqrt{\pi}/\sigma$. The vorticity thickness is defined as the ratio of the velocity difference across the mixing layer to the maximum mean shear. For the Gaussian mean velocity profile

$$\delta_\omega = 1.4003b\ , \tag{3-144}$$

so that in the annular mixing region,

$$\frac{db}{dx} \equiv \varepsilon = \frac{1.2658}{\sigma} \tag{3.145}$$

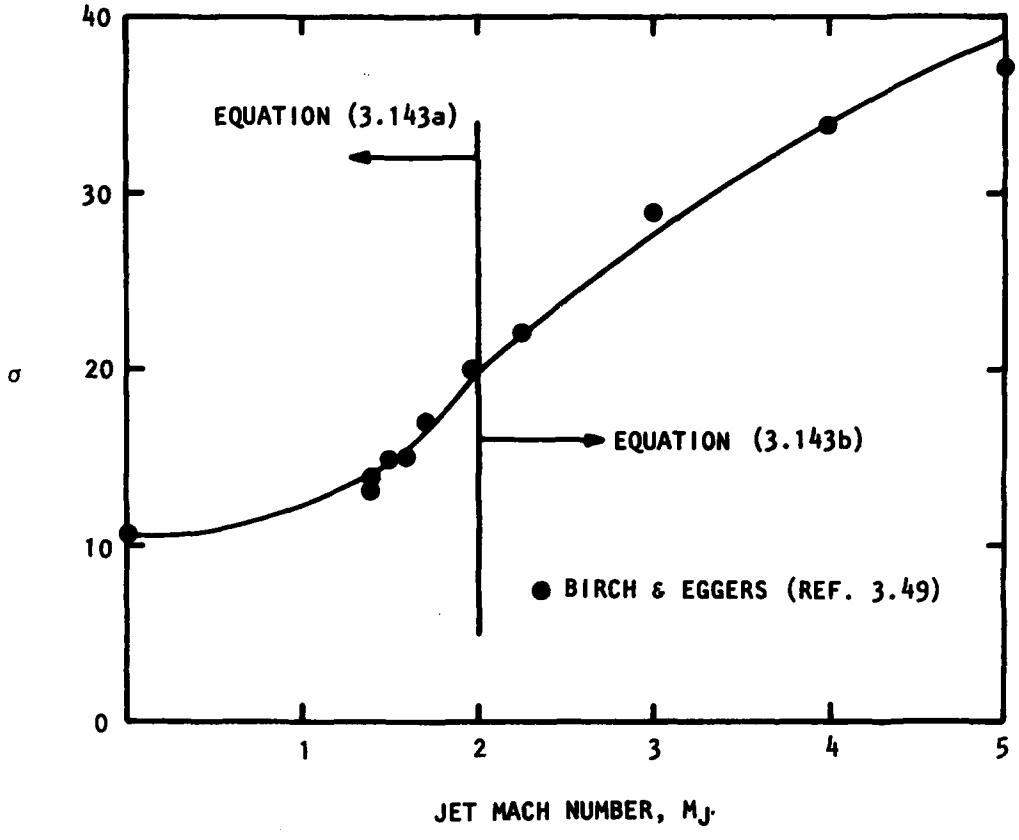

Figure 3.17 Variation of Spreading Parameter, σ, With Jet Mach Number.

The axial development of the jet is now completely defined since db/dx is calculated from Equation (3-145) in the annular mixing region and from the mean mechanical energy integral equation downstream of the end of the potential core. The operating conditions for which calculations of the flow and noise fields in this section are those used in the experiments of Yu and Dosanjh [3.50], i.e. a cold ideally expanded supersonic jet with $M_J = 1.5$. These experiments were chosen since they document the mean flow development as well as the near and far-field noise fields. The prediction for the jet centerline velocity in this case, calculated in the manner described above, is compared with the measured data in Figure 3.18. The corresponding calculated variation of jet half-width, b, and $r_{.5}$ with axial distance is shown in Figure 3.19. The mean flow prediction method clearly provides an adequate prediction of the jet flow development.

Numerical Procedure. The numerical calculation procedure is the same as that described in Section 3.2.4 and will only be summarized here.

Firstly, the "parallel flow approximation" given by Equation (3-89) is solved subject to boundary conditions (3-90). The solution for $\hat{\zeta}(r,s)$ which satisfies the boundary condition as $r \to \infty$ is given by Equation (3-92). Inside the potential core, Equation (3-89) reduces to

$$\frac{\partial^2 \hat{\zeta}}{\partial r^2} + \frac{1}{r}\frac{\partial \hat{\zeta}}{\partial r} + \left[\frac{M^2(\omega - \alpha)^2}{T_J} - \alpha^2 - \frac{m^2}{r^2} \right] \hat{\zeta} = 0 . \qquad (3\text{-}146)$$

The solution of this equation which satisfies the boundary condition as $r \to 0$ is

$$\hat{\zeta}(r,s) = C(s)\, I_m \left(\sqrt{\alpha^2 - M^2(\omega - \alpha)^2/T_J}\; r \right) . \qquad (3\text{-}147)$$

$I_m(\ )$ is the modified Bessel function of order m. The solution for small r, downstream of the end of the potential core, is obtained from a series solution to the complete equation (3-89) in the form,

$$\hat{\zeta}(r,s) = C(s)\, r^n \left[1 + A_2 r^2 + A_4 r^4 + \ldots \right] . \qquad (3\text{-}148)$$

The coefficients A_2, A_4, etc. in Equation (3-148) are readily obtained and will not be given here.

The numerical integration of Equation (3-89) is started at η or $\xi = 4.0$, with $\hat{\zeta}$ given by Equation (3-92), and proceeds towards the jet axis. A second integration starts at a small value of radius, r_s, with $\hat{\zeta}$ given by Equation (3-147) or (3-148), without the multiplicative constant, and proceeds outward. An indentation is made by the integration contour in the complex r-plane to take proper account of the singularity at the critical point where $U = \omega/\alpha$. The integration contour is shown in Figure 3.20. The two solutions are matched at $Re(r - r_c) = 0$, where r_c is the location of the critical point. Matching of the two solutions gives rise to a determinant which is zero if the proper eigensolution is obtained. In practice the absolute value of the determinant is minimized. The matching also allows the constant C(s) to be calculated.

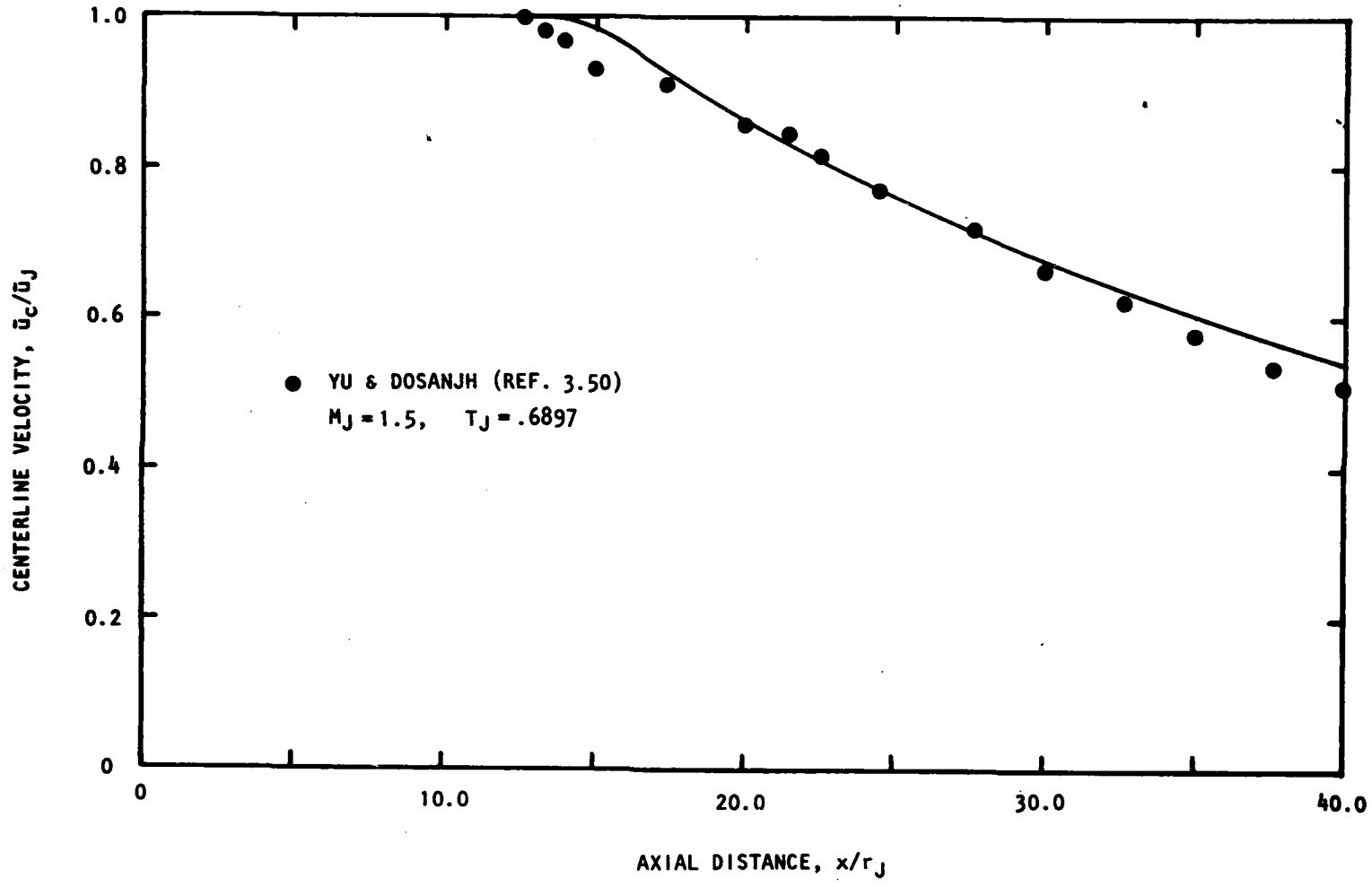

Figure 3.18 Variation of Jet Centerline Velocity With Axial Distance.

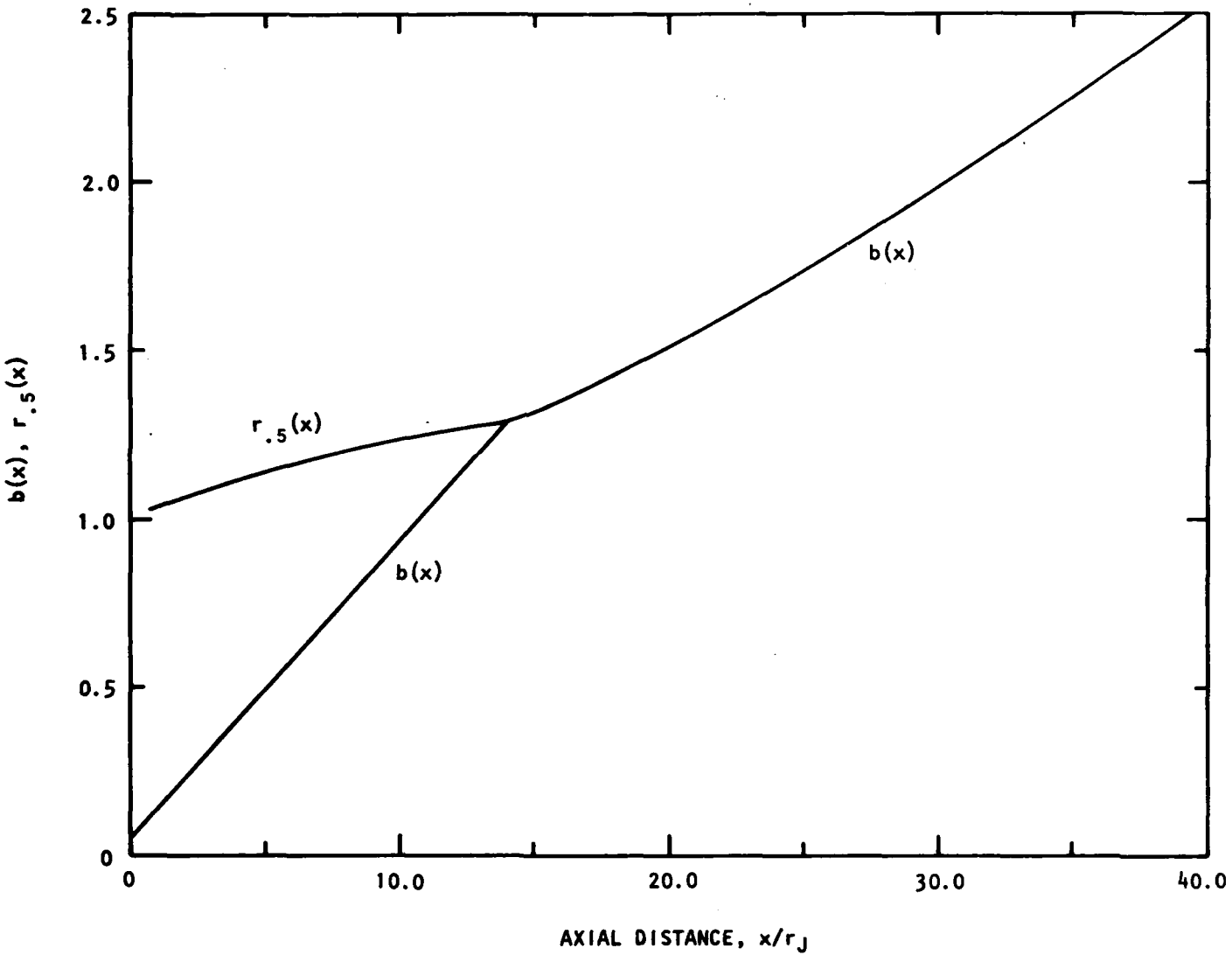

Figure 3.19 Variation of Jet Width Parameters with Axial Distance.

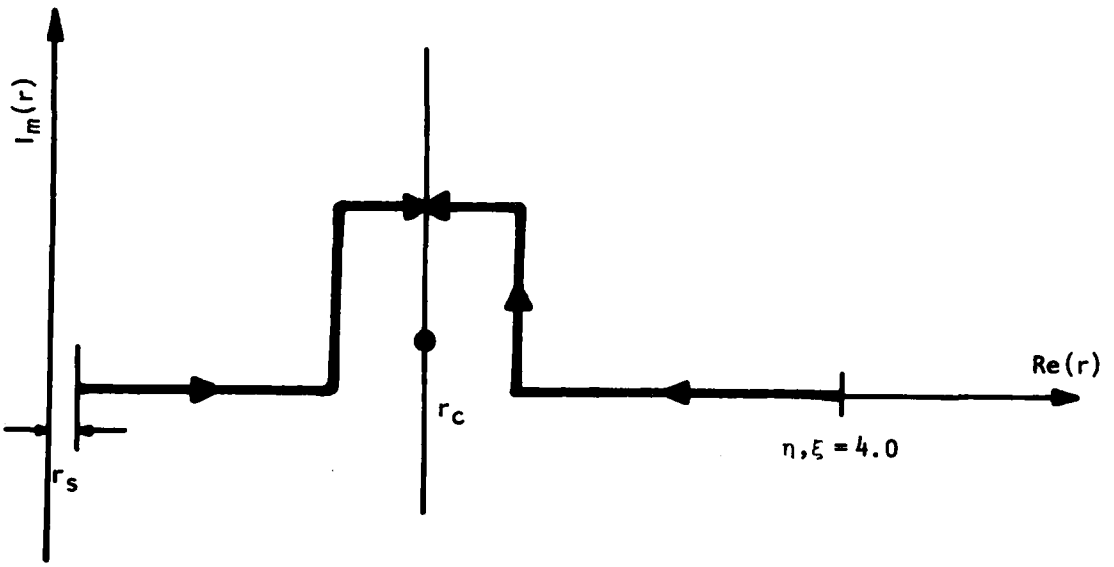

Figure 3.20 Integration Contour in Complex r-plane.

The quantity $d\alpha/ds$, which is required in the calculation of $\partial\hat{\zeta}/\partial s$, is obtained by firstly differentiating Equation (3-89) with respect to s. Applying the solvability condition to the resulting equation, we obtain

$$d\alpha/ds = - I_4/I_3. \tag{3-149}$$

I_3 and I_4 are integrals from $r = 0$ to $r = \infty$ involving the solution $\hat{\zeta}$ and mean flow gradients and are given in Appendix 3B. The solution for the inhomogeneous equation for $\partial\hat{\zeta}/\partial s$ is then calculated using the same integration contour as in the integration of Equation (3-89).

The integrals in Equation (3-95) may now be evaluated giving an equation for $A_o^{-1}dA_o/ds$. On integrating the resulting equation, the zero order multiple scales solution given by Equation (3-93) is completely defined.

As a check on the numerical calculation procedure, the values $d\alpha/ds$ and $\partial\hat{\zeta}/\partial s$ were compared with the values obtained by calculating α and $\hat{\zeta}$ at three axial locations and determining $\Delta\alpha/\Delta s$ and $\Delta\hat{\zeta}/\Delta s$ using central differences. The results from the two methods agreed at all points on the integration contour.

In the next section the effect of flow divergence on the propagation of a fixed real frequency pressure wave in the jet flow will be examined.

Numerical Results for Instability Wave Solution. Calculations have been performed for a cold ideally expanded supersonic jet with $M_J = 1.5$. A disturbance of Strouhal number 0.25 will be considered. This corresponds to a frequency of 10 kHz for the 0.4 inch model jet used by Yu and Dosanjh [3-50]. The $m = 1$ azimuthal mode will be considered since it is the least stable mode for these operating conditions.

The "parallel flow approximation" to the growth rate, given by $-Im(\alpha)$, is shown in Figure 3.21 as a function of the jet half-width. The disturbance grows very rapidly in the thin shear layer close to the jet exit. Its growth rate decreases until it reaches its maximum amplitude, according to the parallel flow approximation, at $b = 0.82$. The wave then decays with the decay rate eventually decreasing as the jet width increases. The end of the potential core occurs at a value of $b = 1.2957$. The real part of the wavenumber, $Re(\alpha)$, which is used to calculate the phase velocity of the wave, is shown in Figure 3.22 as a function of jet width. In the potential core region there is little change in the wavenumber giving an average phase velocity of $0.71\ u_J$ ($Re(\alpha) = 1.1$). Downstream of the end of the potential core the wavenumber increases. Comparison with the line, $Re(\alpha) = \omega/u_c$, shows that for large values of jet width the phase velocity of the wave is equal to the jet centerline velocity.

From Equation (3-93) it can be seen that the axial variation of the pressure, corrected for flow divergence, to order unity is given by

$$\frac{1}{\hat{\rho}_o}\frac{\partial\hat{p}_o}{\partial x} = i\alpha(s) + \frac{\varepsilon}{A_o}\frac{dA_o}{ds} + \frac{\varepsilon}{\hat{\zeta}}\frac{\partial\hat{\zeta}}{\partial s}. \tag{3-150}$$

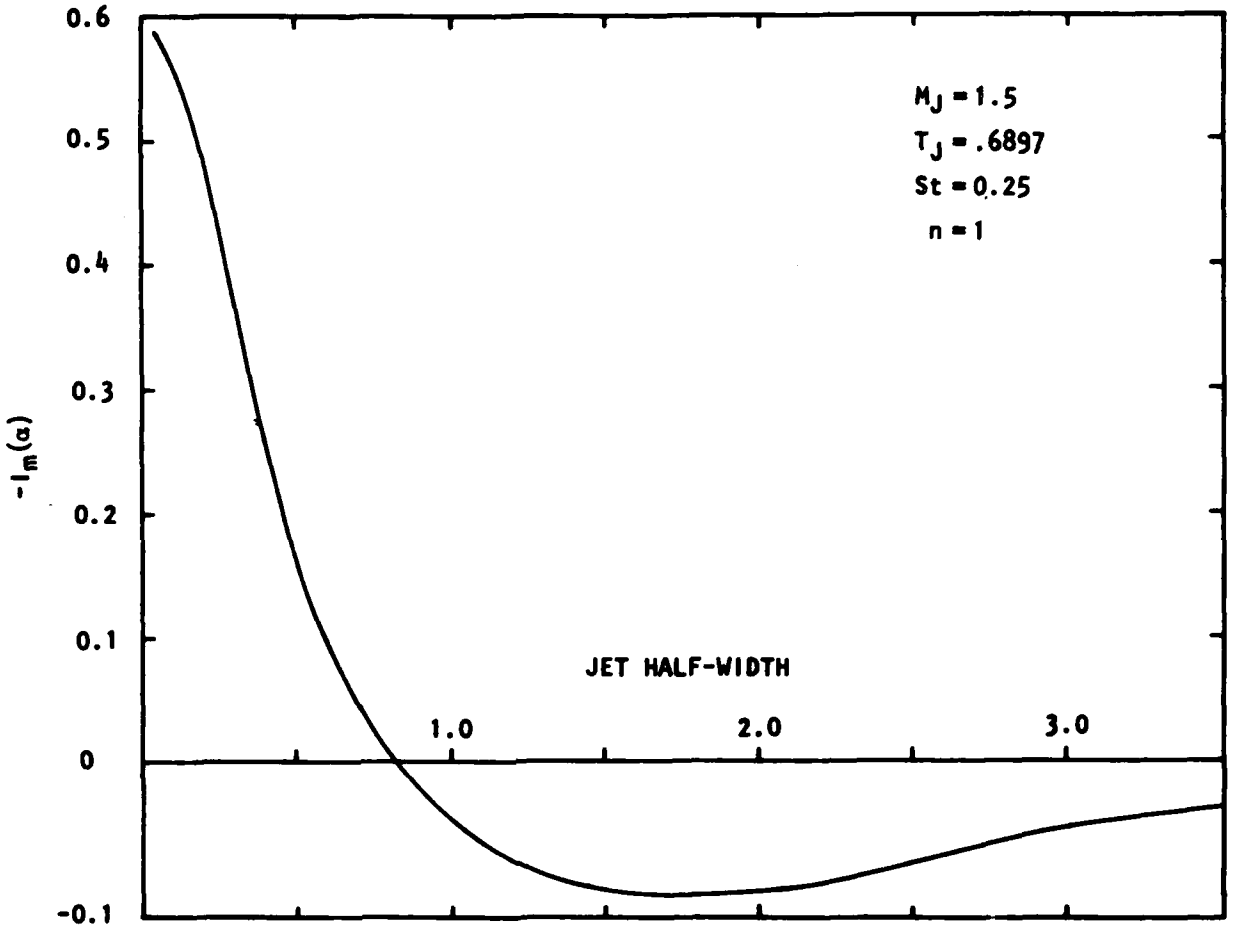

Figure 3.21 Variation of "Parallel Flow Approximation" Growth Rate With Jet Width.

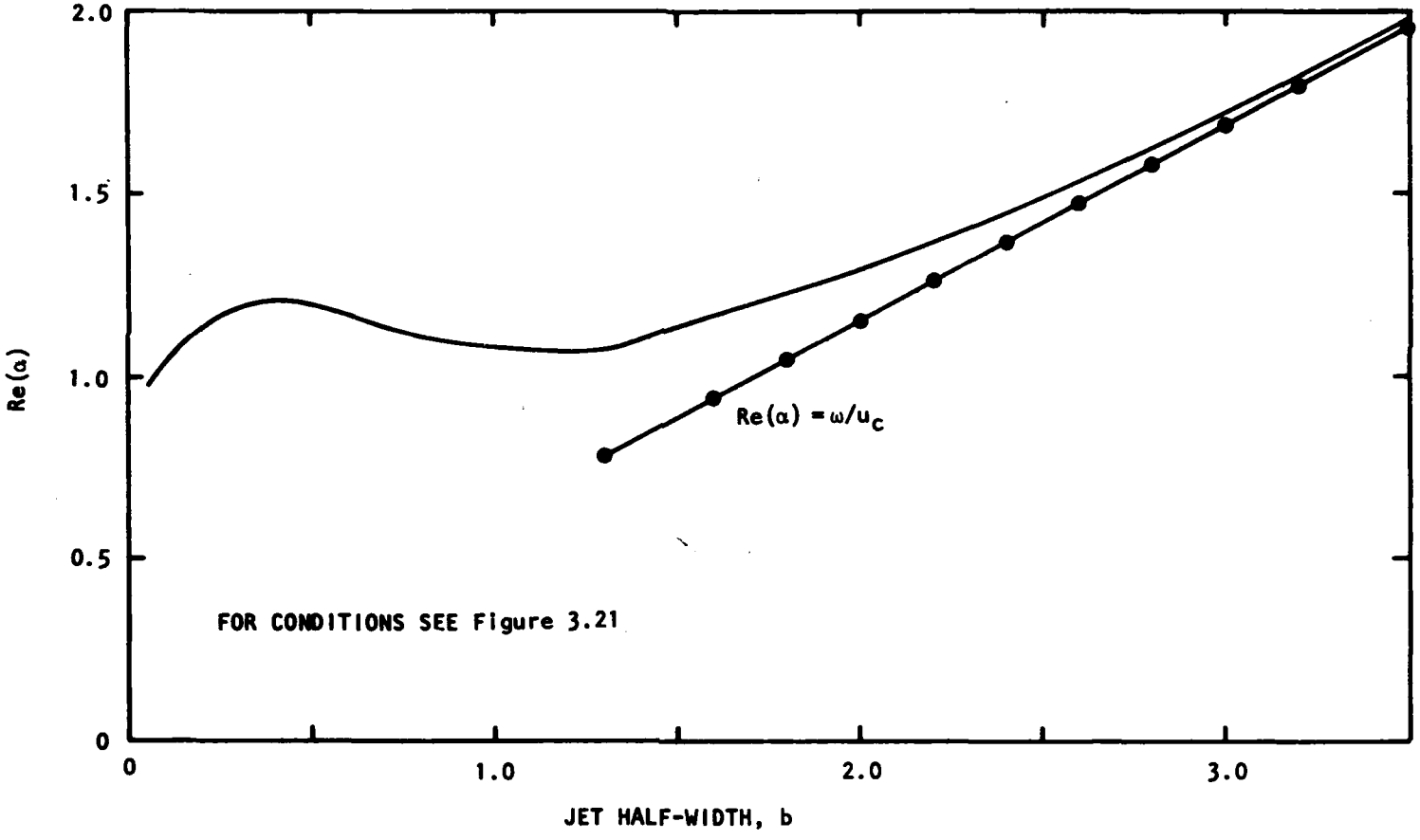

Figure 3.22 Variation of Real Part of "Parallel Flow Approximation" Wavenumber with Jet Width.

Since $\hat{\zeta}$ is a function of the radial coordinate r, $\hat{\rho}_o^{-1}\partial\hat{\rho}_o/\partial x$ is also a function of radial distance. Contours of equal axial growth rate, given by $Re(\hat{\rho}_o^{-1}\partial\hat{\rho}_o/\partial x)$, are shown in Figure 3.23 . Note that the contours are at unequal spacings of growth rate. The region within the solid lines represents that portion of the real radial axis not included on the integration contour due to the contour indentation above the critical point. However, some calculations, shown by the dotted lines, have been obtained with a smaller indentation. (This leads to a decrease in the numerical accuracy at locations near to the parallel flow neutral solution, $x = 8.9$). The line of minimum growth rate lies close to the lipline in the region of maximum pressure fluctuations. The most severe radial variations in the growth rate occur for small values of growth rate and for decaying waves. The axial variation in the phase velocity, given by $\omega/Im(\hat{\rho}_o^{-1}\partial\hat{\rho}_o/\partial x)$, is shown in Figure 3.24 at various radial locations. Though there is some radial variation in the phase velocity, it is small and confined to the initial mixing region. The parallel flow approximation for the phase velocity, $\omega/Re(\alpha)$, is shown for comparison and it represents a reasonable average of the phase velocities at the several radial locations.

From these calculations it is clear that the *gross* features of the instability wave solution are given by the locally parallel flow approximation. Moore [3.26] notes, in his extensive comparisons of measured phase velocities and amplification rates with the linear theory of Michalke [3.45], that "Although the basic behavior of the instability wave is predicted by the linear theory in the linear amplitude range, the details are not represented by the present available theory." In light of this, and since the noise radiation is likely to depend on the gross features of the instability wave rather than its details, the near- and far-field noise calculations in the sections below will make use of the parallel flow approximation to the growth and phase velocity of the wave. This simplifying assumption also provides considerable savings in computer run time. With this assumption $g_{om}(\varepsilon x)$, in Equations (3-126b) and (3-126c) for the weighted wavenumber component spectra for the pressure fluctuation, is set equal to unity.

The far-field noise radiation will now be described.

3.3.4.2 Far-field solution

Making use of the calculations described in the previous section, the integrands in Equations (3-126) may be evaluated. It is the amplitude of the wavenumber component spectrum associated with the axial variation of the quantity $e^{i\theta(x)}/(M^2\omega^2 - \alpha^2)^{m/2}$, which is the controlling factor in the far-field directivity pattern. The amplitude of this quantity as a function of axial distance is shown in Figure 3.25 for three Strouhal numbers, 0.125, 0.25, and 0.5. (These Strouhal numbers correspond to frequencies of 5 kHz, 10 kHz, and 20 kHz, respectively, in the cold $M_J = 1.5$ experiments of Yu and Dosanjh [3.50]. Calculations are presented for the axisymmetric, $m = 0$, mode since, as will be seen below, this mode appears to dominate in the near- and far-fields at these conditions. In all cases the rate of growth of the function is much faster than its rate of decay as could be inferred from the growth rate of the $m = 1$ mode shown in Figure 3.21. The location of the peak amplitude lies closer to the jet exit as the frequency increases. The location of the peak itself is not an indication of a "source location." As

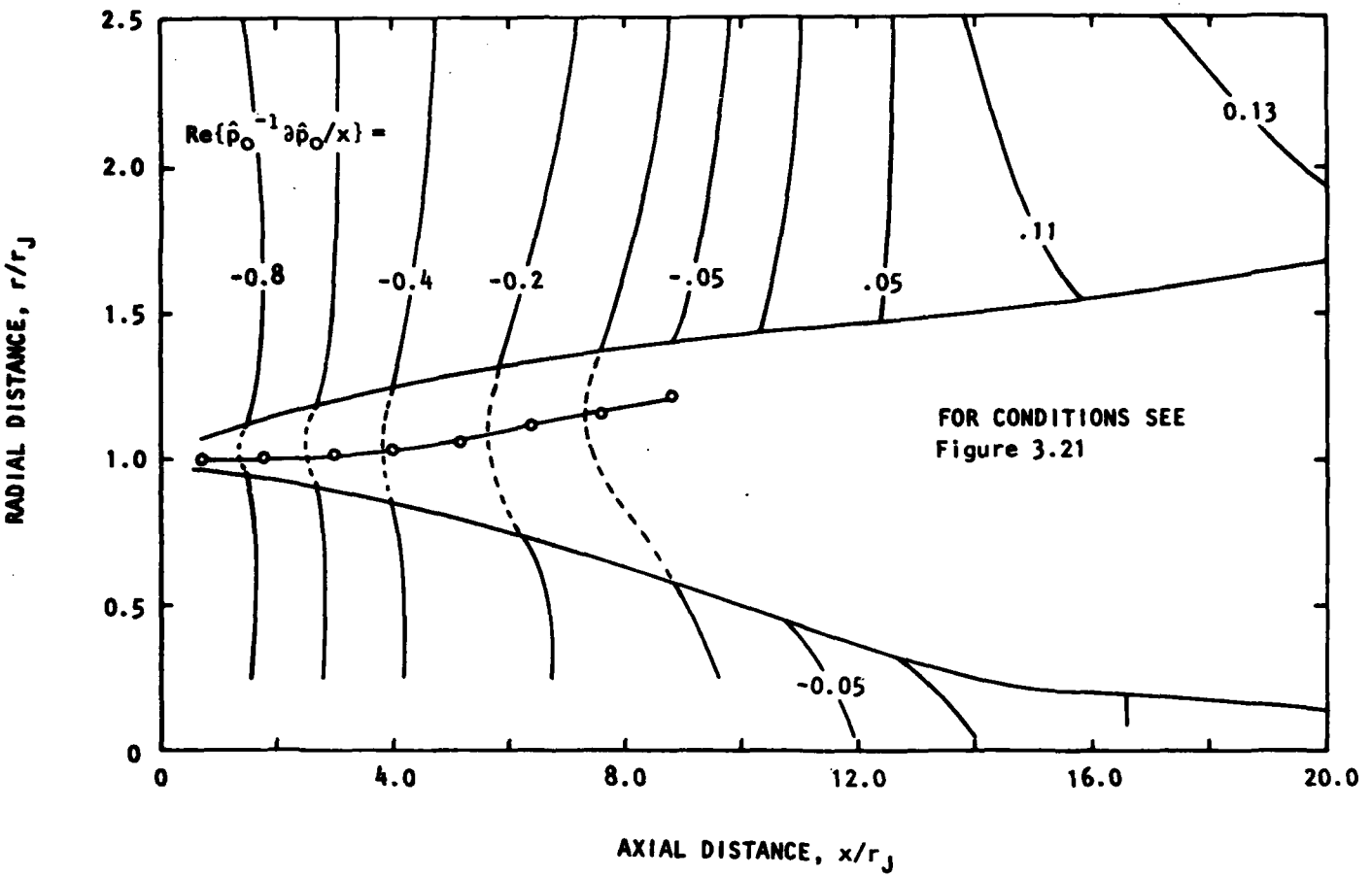

Figure 3.23 Contours of Equal Axial Growth Rate.
o—o Locus of Minimum Growth Rate.

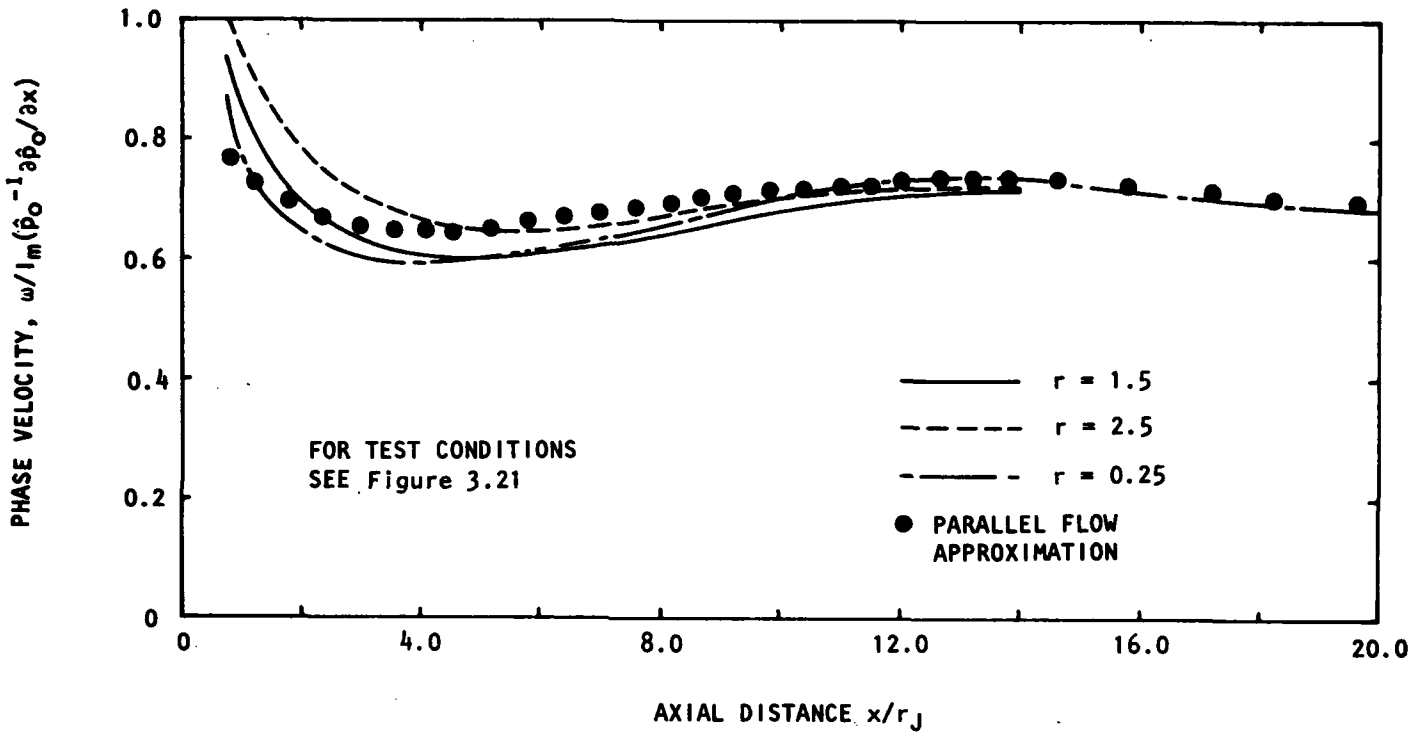

Figure 3.24 Variation of Axial Phase Velocity With Axial Distance at Several Radial Locations

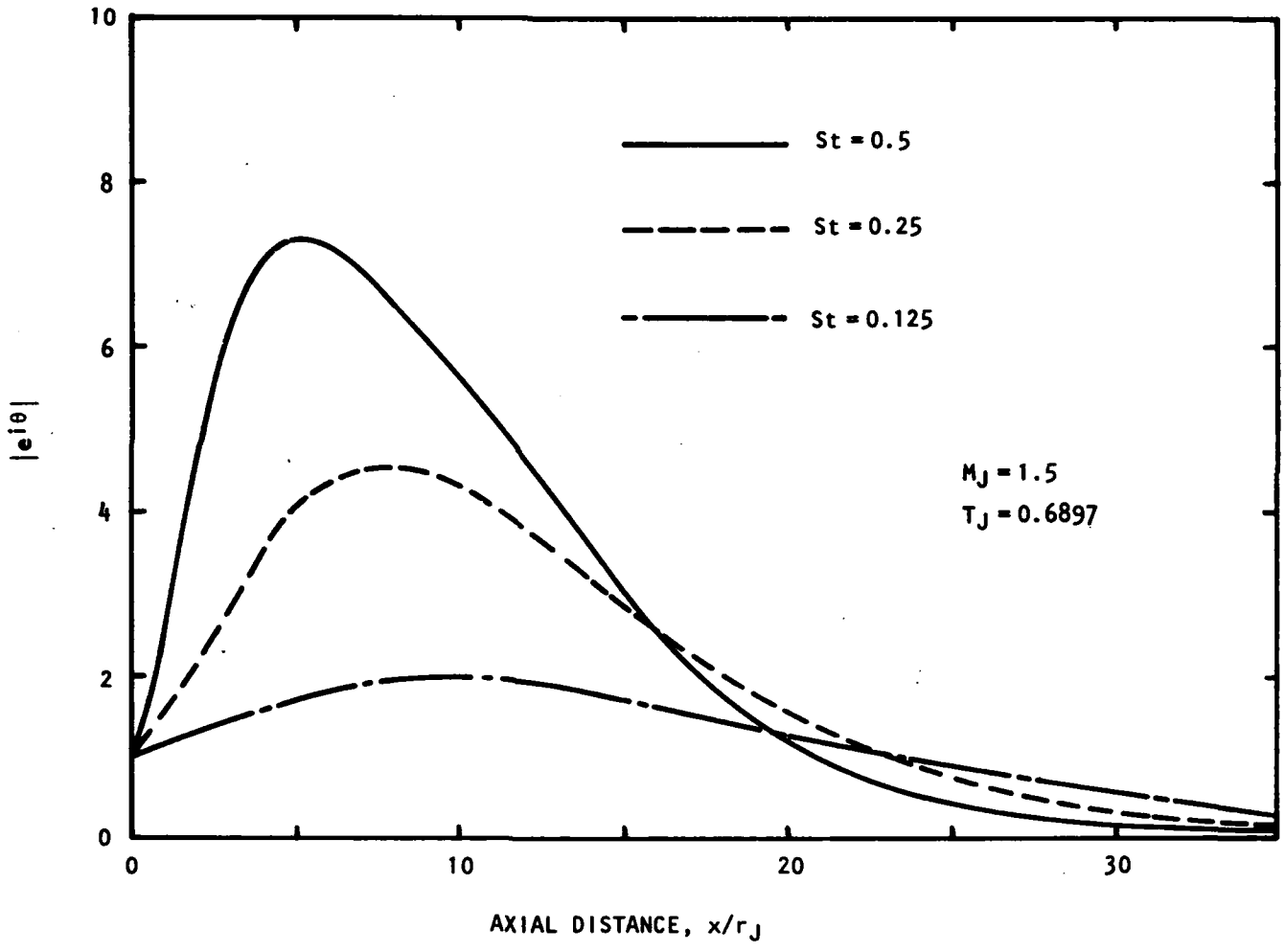

Figure 3.25 Variation of $|e^{i\theta}|$ With Axial Distance, n = 0.

can be seen from Equation (3-131) the far-field noise radiation depends on the wavenumber component spectrum for the given frequency. This spectrum depends on the entire axial variation in amplitude and phase of the wave, not simply the conditions at the location of peak amplitude.

The amplitudes of the wavenumber component spectra $B_o(k)$ for the same three frequencies are shown in Figure 3.26. The Fourier transform was performed numerically using the FFT algorithm described by Brigham and Morrow [3.47]. The peaks in the spectra correspond to phase velocities of 0.82 u_j, 0.87 u_j, and 0.91 u_j for the Strouhal numbers 0.125, 0.25, and 0.5, respectively.

The weighting of the Fourier transform of the axial pressure distribution for asymmetric modes is given by the term $(M^2\omega^2 - k^2)^{m/2}$ in Equation (3-49c). For $k < M\omega$ the term is real and modifies the amplitude of $B_m(k)$. For $k > M\omega$ the term is purely imaginary and does not effect the amplitude of $B_m(k)$. The effect of this weighting on the amplitude of the wavenumber component spectrum for $m = 1$ and $St = 0.25$ is shown in Figure 3.27. Only those wavenumber components in the range $-M\omega < k < M\omega$ radiate noise to the far field. The stationary point in the inversion of the integral for the pressure in the far-field given by equation (3-128) is $k_o = M\omega\cos\theta$. Thus, in evaluating the far-field noise the weighting factor in the wavenumber component spectrum $B_m(k)$ is $(M\omega\sin\theta)^m$. Clearly, only the $m = 0$, axisymmetric mode can radiate noise along the axis of the jet, $\theta = 0$ or π.

With the function $B_m(k)$ calculated, the far-field directivity pattern, $D(\theta)$, is readily obtained using Equation (3-131). The calculated directivity for the axisymmetric mode and Strouhal numbers of 0.125, 0.25, and 0.5 are shown in Figures 3.28, 3.29, and 3.30, respectively. The measured far-field data are one-third octave sound pressure levels with center frequencies of 5 kHz, 10 kHz, and 20 kHz ($St = 0.12$, 0.24, and 0.48). The directivity patterns have been adjusted in level to coincide with the data at the peak noise angle. This vertical adjustment of the pattern corresponds to specifying the initial amplitude of the disturbance at the jet exit. This is the only empirical constant that enters the noise calculation. In all cases the initial pressure amplitude is approximately 10^{-5} times the dynamic head at the jet exit. The agreement between the predicted directivity and the measurements is good, with the exception of the lowest frequency case, for angles less than 45° to the jet axis. It is in this region that the large-scale structure radiates noise. The correlation experiments of Dahan and Elias [3.22] showed that the noise radiated by coherent structures in the flow falls abruptly for angles greater than 45 degrees to the jet axis.

For a given initial amplitude the axisymmetric, $m = 0$, mode was found to radiate more noise (approximately 8 dB) than the helical, $m = 1$, mode, for each case with the exception of the highest frequency, $St = 0.5$, condition where both modes radiated equally efficiently. The calculated far-field directivity pattern for the $m = 1$ mode and a Strouhal number of 0.5 is shown in Figure 3.30 where it is compared with the $m = 0$ calculation at the same frequency. The amplitude of the $m = 0$ mode falls more rapidly than that of the $m = 1$ mode for larger angles. The relative weightings of the azimuthal modes is particularly important in the definition of the near field of the jet which is discussed in the next section.

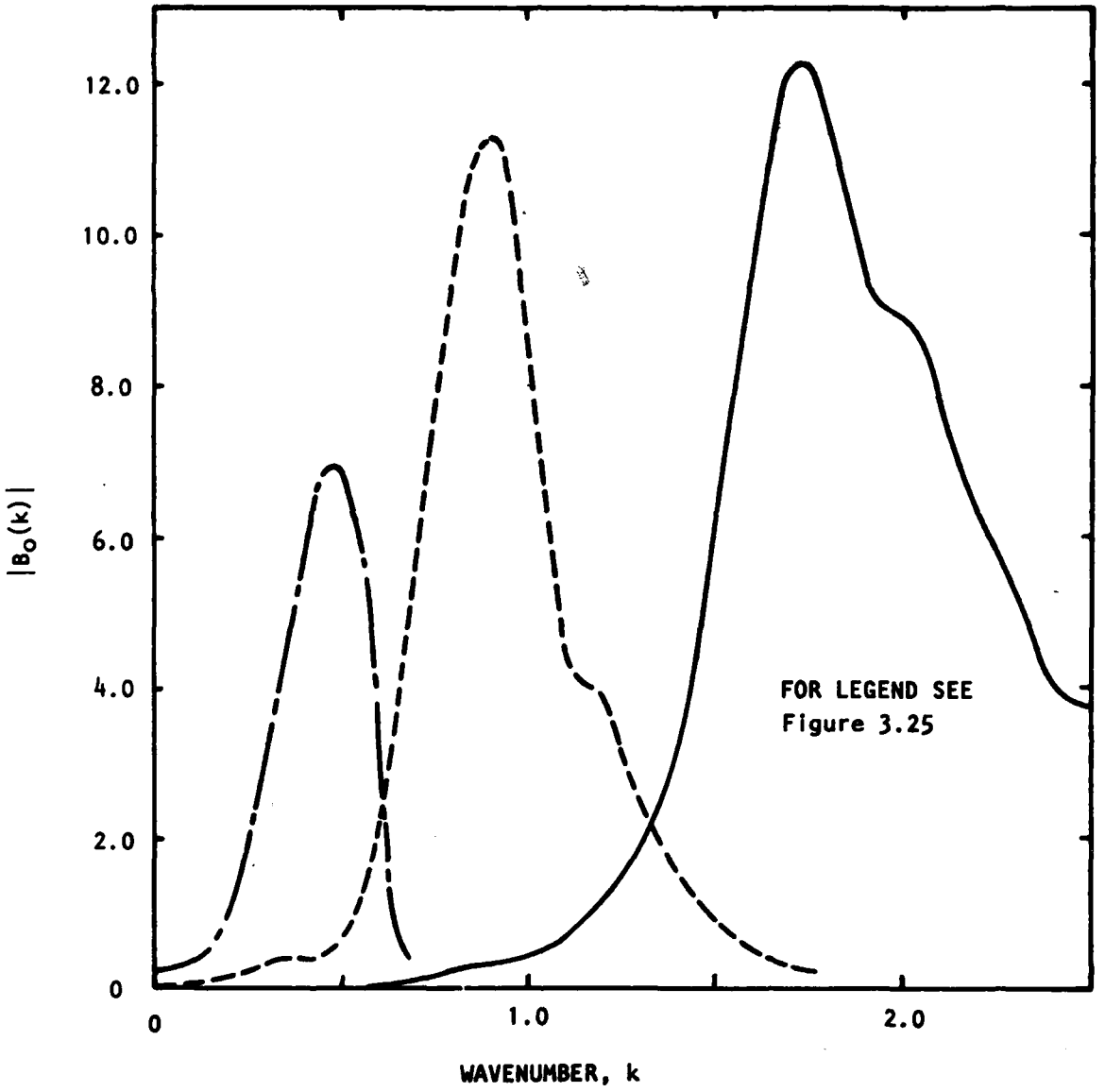

Figure 3.26 Amplitude of Wavenumber Component Spectrum, $B_o(k)$

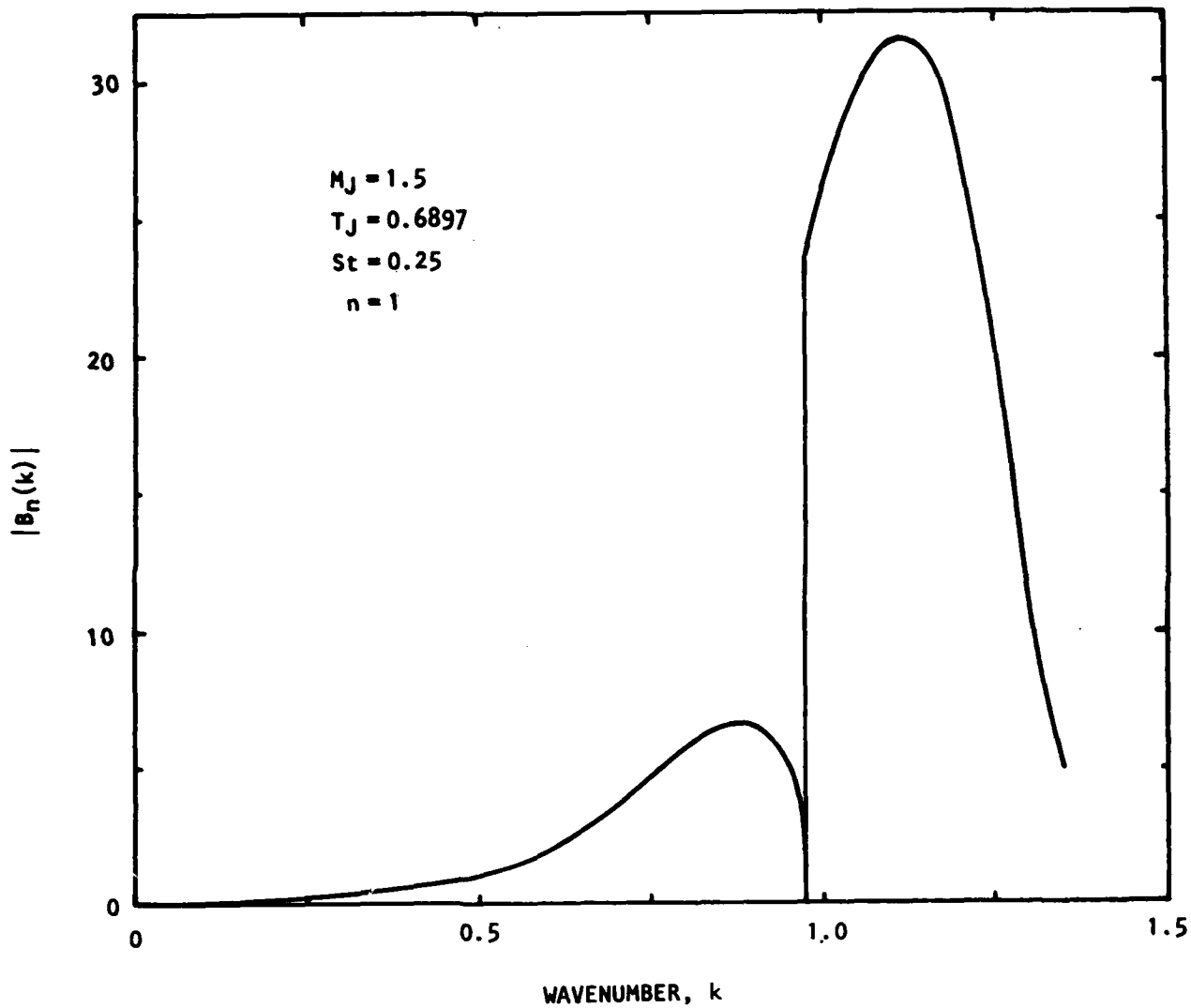

Figure 3.27 Amplitude of Weighted Wavenumber Component Spectrum I, $B_n(k)$

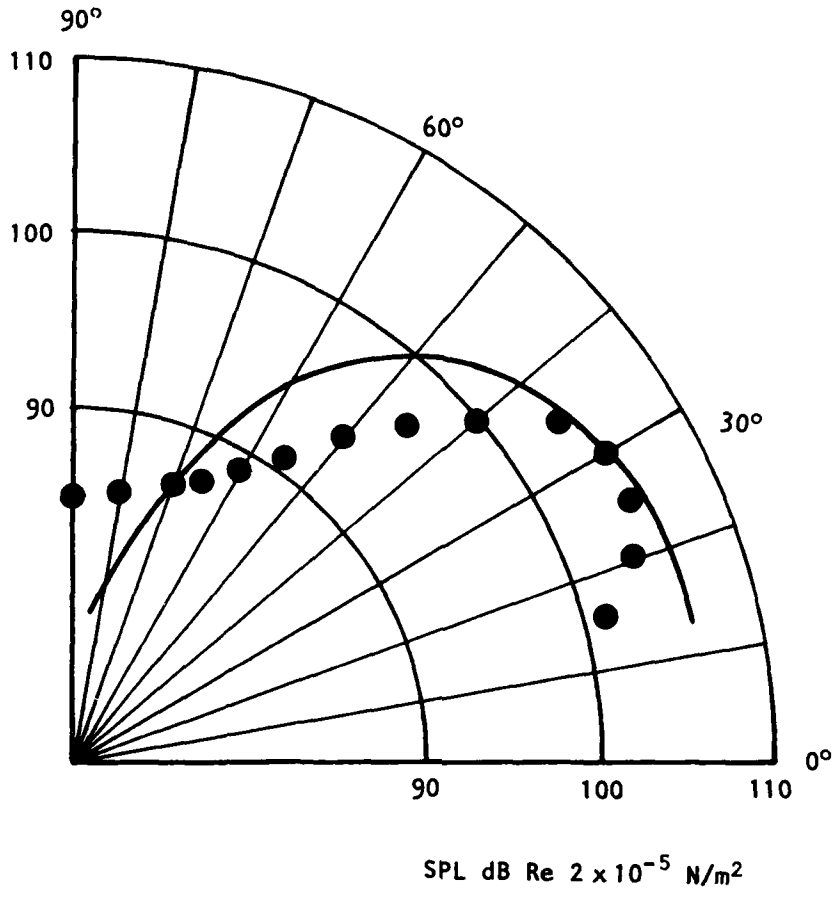

Figure 3.28 Far-Field Directivity Pattern, St = 0.125, n = 0, o Yu and Dosanjh (Ref. 3).

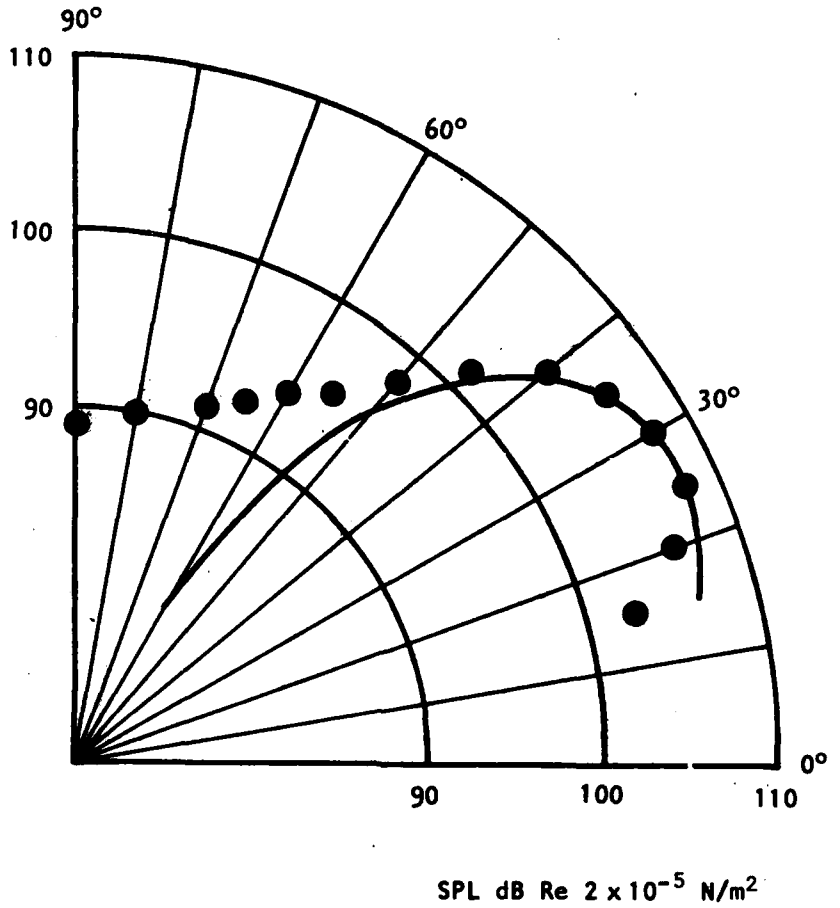

Figure 3.29 Far-Field Directivity Pattern, St = 0.25, n = 0, o Yu and Dosanjh (Ref. 3).

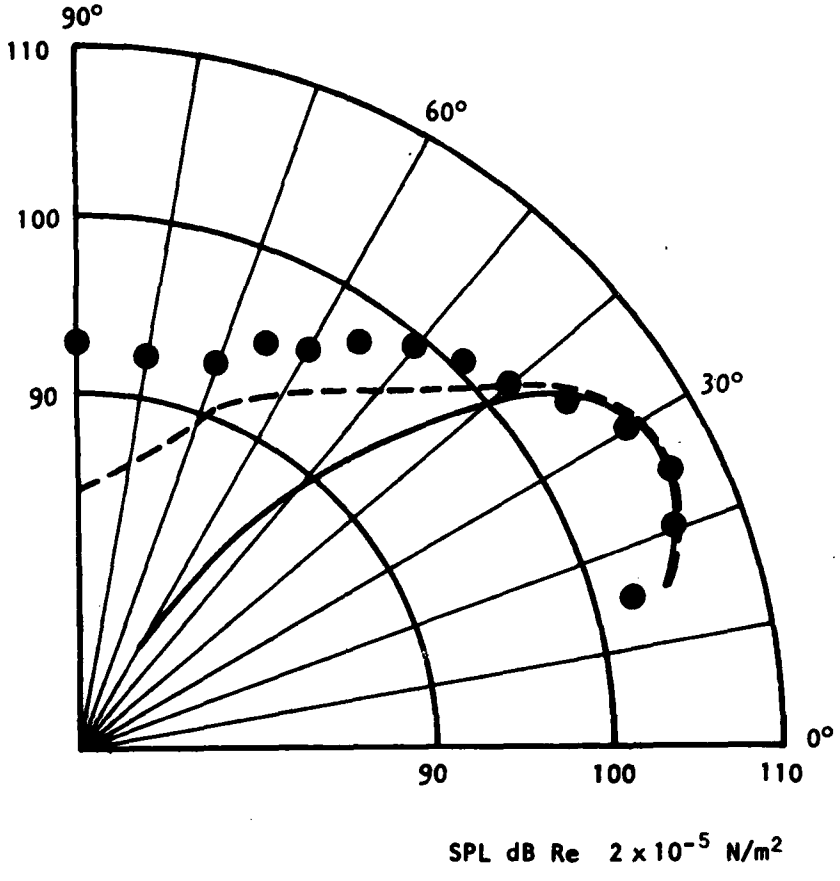

Figure 3.30 Far-Field Directivity Pattern, St = 0.50; —— n = 0; – – – n = 1. o Yu & Dosanjh (Ref. 3).

3.3.4.3 The near-field solution

In Section 3.3.3.2 above it was shown how the instability wave solution could be continued into the ambient medium surrounding the jet. This continued solution is given by Equation (3-127) and will be evaluated below.

Examining Equation (3-127) for the pressure outside the flow, it can be seen how, for increasing distance from the jet, the pressure changes from being dominated by the non-radiating components to an acoustic pressure field. The asymptotic form of the integrand in Equation (3-127) is given in Equation (3-128). For wavenumbers, k, with magnitudes greater than $M\omega$ the argument of the exponential term contains a negative real part indicating that the integrand decays exponentially for increasing radius, as well as a $1/\sqrt{r}$ dependence. For wavenumbers with magnitudes less than $M\omega$, the argument of the exponential term is purely imaginary and the Hankel function decays as $1/\sqrt{r}$ for large radius. Thus, as the radius increases, the pressure fluctuations are dominated by those components of the integrand whose wavenumbers have a magnitude less than $M\omega$. These are the components with sonic phase velocities to all directions in the far field. Thus, as the distance from the jet increases, so the far field characteristics of the pressure field become dominant. The pressure outside the jet flow, given by Equation (3-127), demonstrates this transition from the hydrodynamic to the acoustic pressure field.

Figure 3.31a shows the calculated near-field pressure contours for $M_J = 1.5$ and $St = 0.25$. The measurements of Yu and Dosanjh [3.50] are shown in Figure 3.31b for comparison. The *absolute* level of the calculations have been adjusted at one point only. The agreement between the calculations and the experiments is extremely good. Close to the jet exit, for example, the 134 dB contour, the pressure fluctuations are dominated by their non-radiating components and exhibit no preferred directivity. However, at larger distances the characteristic pattern of the acoustic field begins to emerge with a preferred noise radiation at approximately 30 degrees to the jet axis.

This lobed appearance of the contours is not found at the lowest frequency, $St = 0.125$. The calculated near-field pressure contours for the axisymmetric mode and the measured data are shown in Figures 3.32a and 3.32b, respectively. In both cases, there is no lobed contour. Calculations for the $m = 1$, helical, mode do exhibit a lobed characteristic shape. However, the far-field pressure levels associated with the $m = 1$ mode are much lower than those of the $m = 0$ mode at these conditions for equal excitation at the jet exit. The comparison of near-field pressure contours for this frequency show the dominance of the axisymmetric mode.

At the highest frequency considered, both modes are of almost equal levels in the near and far-fields for equal amplitude at the jet exit. The calculated near-field pressure contours for the $m = 0$ and $m = 1$ modes for $St = 0.5$ are shown in Figures 3.33a and 3.33b, respectively. The corresponding measured data is shown in Figure 3.33c. The amplitudes of the calculated contours have been separately matched with the measured data. The initial amplitude in each case is approximately equal. In practice the pressure field associated with each mode could be summed. The qualitative agreement between three sets of contours is good. It should be noticed that only the noise field at small angles (less than 45 degrees) to the jet axis is associated

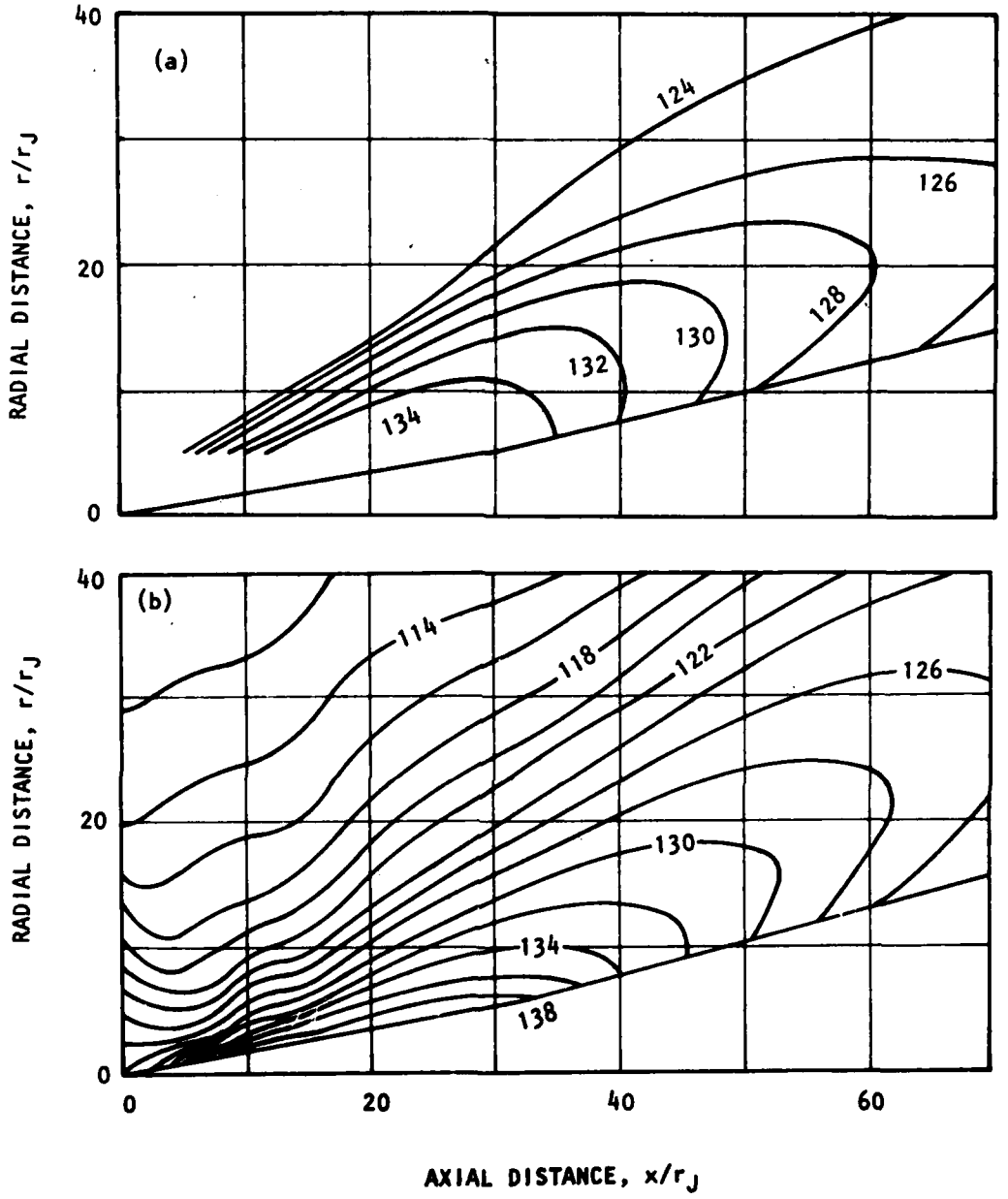

Figure 3.31 One-Third Octave Band Near-Field Sound Pressure Contours, $M_J = 1.5$, $T_J = 0.6897$, $St = 0.25$ ($f_o = 10$ kHz), $n = 0$. (a) Present calculations, (b) Measurements by Yu and Dosanjh (Ref. [3.3]).

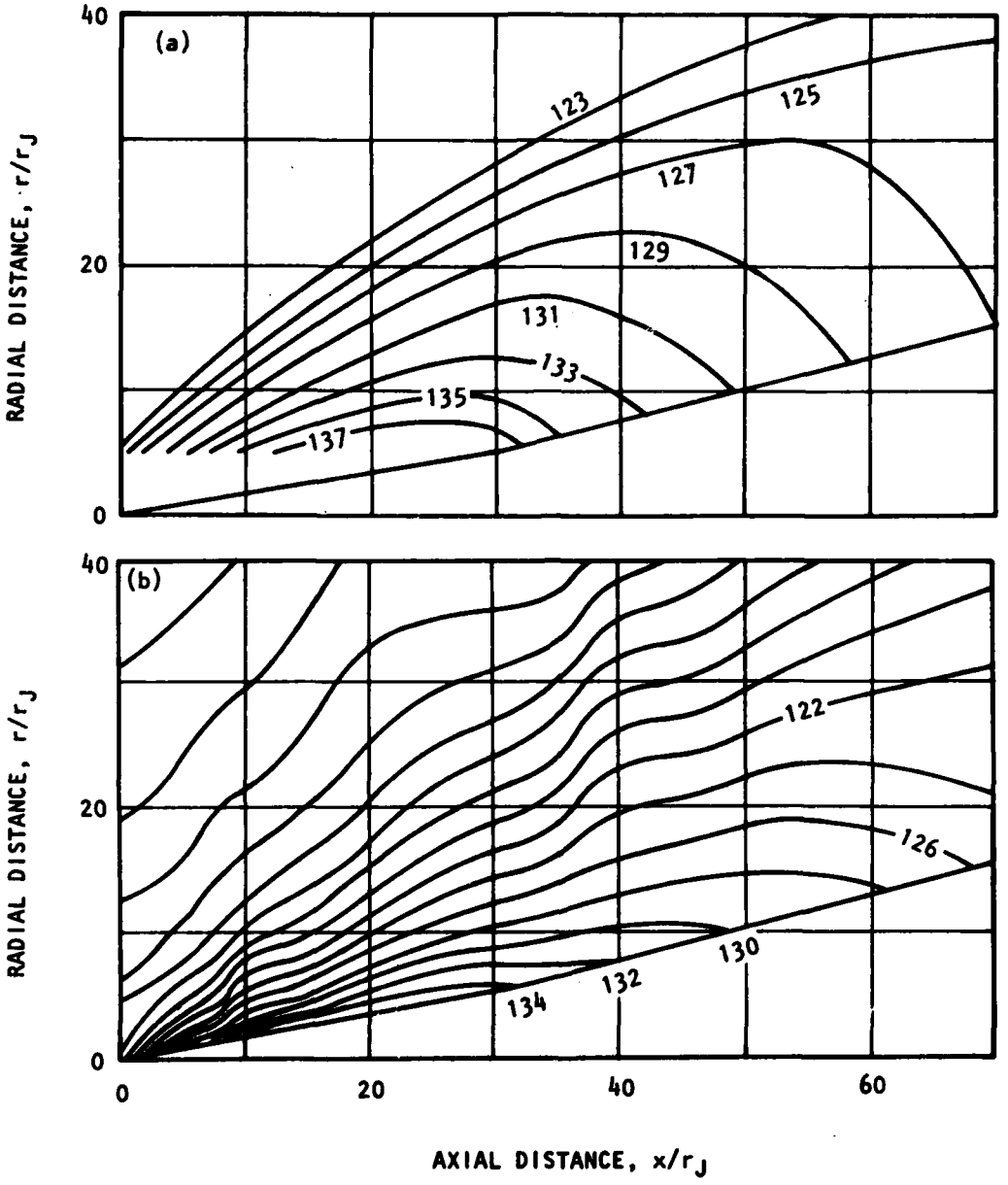

Figure 3.32 One-Third Octave Band Near-Field Sound Pressure Contours, $M_J = 1.5$, $T_J = 0.6897$, $St = 0.125$ ($f_o = 5$ kHz), $n = 0$. (a) Present Calculations, (b) Measurements by Yu (Ref. [3.3]).

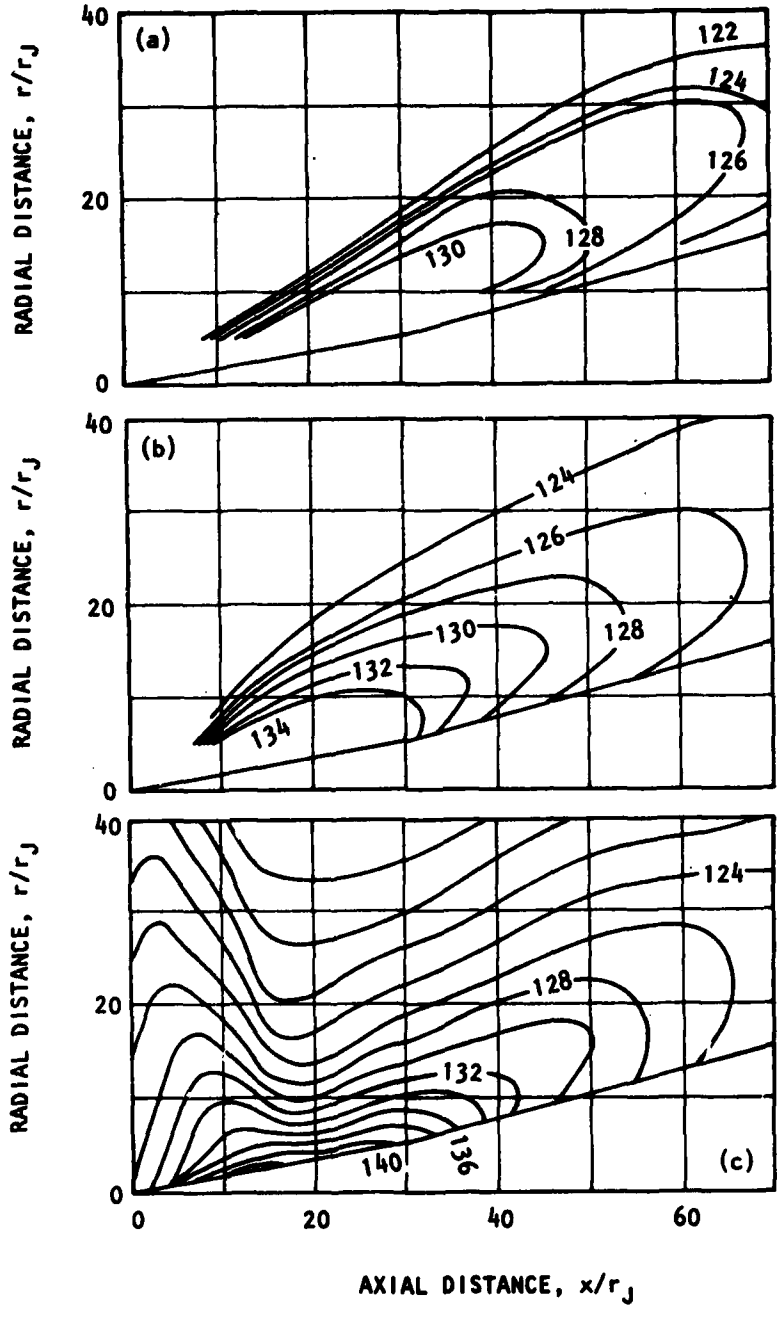

Figure 3.33 One-Third Octave Band Near-Field Sound Pressure Contours, $M_J = 1.5$, $T_J = 0.6897$, $St = 0.5$ ($f_o = 20$ kHz). (a) Present Calculations, $n = 0$, (b) Present Calculations, $n = 1$, (c) Measurements by Yu and Cosanjh (Ref. [3.3]).

with the large-scale structure. The lobes in the measured near-field contours normal to the jet axis are associated with another noise mechanism.

3.3.5 Concluding Remarks

In Section 3.3, the method of calculating the noise radiation from instability waves in a turbulent shear flow, developed for the plane shear layer, in Section 3.2, has been extended to examine the axisymmetric turbulent jet.

The instability waves were described in terms of an asymptotic expansion using the method of multiple scales to account for the slight divergence of the mean flow. It was found that the gross features of the wave were adequately described by the first-order term in the multiple scales asymptotic expansion, usually referred to as the "parallel flow approximation." The multiple scales asymptotic expansion was shown to be nonuniformly valid for large distances from the jet. A uniformly valid expansion was then constructed by showing that a model boundary value problem represented the correct continuation of the instability wave solution to large distances from the jet. This extended solution described both the near and far-field pressure characteristics associated with the instability wave. Calculations of near and far-field pressure fluctuations associated with the instability wave were made. These calculations were compared with measured data. The agreement between the calculations and the measured data was exceptionally good. The calculations predicted changes in the character of the near-field which were seen in the measurements. The ability to predict the *entire* field up to source region provides convincing evidence of the validity of the noise generation model proposed in this part of this report. It is clear that the noise radiation from supersonic jets is intimately related, in a direct manner, to the large scale instabilities of the jet flow.

In section 3.4 below, use of the analysis developed in Sections 3.2 and 3.3 will be made to develop a prediction model for the noise from supersonic jets.

3.4 PREDICTION OF NOISE RADIATION BY THE INSTABILITY WAVES OF SUPERSONIC AXISYMMETRIC JETS

In this section a method will be presented for determining the absolute level of noise radiation by the instability waves, or large-scale structure of supersonic axisymmetric jets. Before proceeding, however, it is useful to examine the extent to which the noise generation and radiation mechanism proposed above has managed to avoid resorting to empiricism. The description of the mean velocity and temperature profiles contained some approximations to facilitate simple calculations of the jet stability characteristics. The mean velocity was described in terms of a shape function which took the same form in both the annular mixing region and downstream of the end of the potential core. The development of the jet flow downstream of the end of the potential core was calculated using an eddy viscosity hypothesis. However, the mean flow itself is simply the framework within which the instability wave develops and radiates noise. Once this framework is established, the noise generation

process is free of empiricism. A disturbance of arbitrary, but small, amplitude of a given frequency is introduced at the jet exit. The development of the wave within the turbulent mean flow field and the resulting noise radiation associated with the wave are then calculated exactly. It has only to be assumed that the development of the wave is described by the linearized, compressible equations of motion. However, it would be unrealistic to assume that such a physically simple, though analytically complicated, model would describe the details of the noise generation process associated with the instability waves. In the next paragraphs, the likely limitations of this model will be discussed and these will provide a clearer perspective for the constraints and assumptions that will be made in the prediction model described below.

Firstly, let us consider the assumption that the wave satisfies an inviscid set of equations. Since the Reynolds number of the flow, based on local jet width, is high and since the mean velocity profile leads to dynamic instabilities, the role of the fluid viscosity may be reasonably ignored. However, the wave is propagating in a turbulent fluid which may be considered to increase the effective viscosity of the fluid. Some of the measurements of McLaughlin et al. [3.21] suggest that the wave breaks down more rapidly, downstream of its point of maximum amplitude, than would be expected by its behavior as a damped inviscid wave. Thus, in regions away from the peak the details of the wave behavior may not be predicted by this simple physical model of an inviscid wave. Since the directivity in the far field is controlled by the shape of the wavenumber component spectrum, describing the axial development of the wave in the flow, it is likely that only the sound pressure levels in the region of the peak noise angle will be accurately predicted. Practically, this means that predictions will be confined to angles of less than 45 degrees to the jet axis.

Secondly, let us consider the likely frequency limitations determined by physical and analytical considerations. At high frequencies of excitation, the wavelength of the instability wave is very small and its development will be especially sensitive to the initial jet conditions and mean flow description. In the low frequency limit, the wavelength of the disturbance is many jet diameters. Thus, in a single wavelength the mean flow profiles experience radical changes. This violates the basic assumption needed for the multiple scales asymptotic analysis which requires slow changes in the mean flow. Thus, the predictions will be limited to Strouhal numbers in the range 0.1 to 0.5.

Clearly a wave with any azimuthal mode number is potentially excitable and capable of radiating noise. In the calculations of Section 3.3.4, calculations were performed for the axisymmetric, $m=0$, mode and the helical, $m=1$, mode. For equal excitation at the jet exit, the axisymmetric mode was shown to be a more efficient noise radiator at lower frequencies. So far as the prediction of absolute far-field noise is concerned, two questions must be answered. Firstly, what is the level of the excited wave at the jet exit and secondly, which of the azimuthal modes will be excited. The experiments of McLaughlin et al. [3.20, 3.21] indicate that a supersonic jet exit velocities the helical, $m=1$, mode is preferentially excited. The process of the mode selection for arbitrary excitation at the jet exit remains an unanswered problem and for the purposes of noise prediction only the helical mode will be considered. These considerations lead to the following

constraints on the prediction of the noise associated with the jet large-scale structure,

$$\left.\begin{array}{l} V_J/a_o \geq 1.15 \\ 0.1 \leq fd/V_J \leq 0.5 \\ 0 < \theta < 45^\circ \\ m = 1. \end{array}\right\} \qquad (3\text{-}151)$$

The only remaining information required is to determine the level of excitation of the helical mode which occurs in the jet experiments. To this end, far-field noise calculations were performed for a fixed excitation level at the jet exit. These directivities were compared with the experimental data for the range of parameters given in Equation (3-151) and the decibel level change needed to match the predicted levels with the measured data were recorded. A typical comparison is shown in Figures 3.34 and 3.35 for $V_J/a_o = 1.48$, $T^* = 2.857$, $St = 0.5$, and $V_J/a_o = 1.83$, $T^* = 1.78$, $St = 0.3$, respectively. The levels of each prediction has been adjusted to give the best fit with the data in the region of peak radiation. This level adjustment corresponds to altering the initial excitation of the disturbance. The calculation provides the far-field levels assuming the initial amplitude equals unity. From Equation (3-31), it can be seen that

$$D(\theta) = 10 \log_{10} \{2|B_n|^2\} \quad \text{dB} \quad \text{(re an arbitrary reference)} \qquad (3\text{-}152)$$

The absolute level prediction is given by

$$SPL = 10 \log_{10} \{2A_o^{*2}|B_n|^2/p_{ref}^2\} \text{ dB rel } p_{ref} \qquad (3\text{-}153)$$

where $p_{ref} = 2 \times 10^{-5} N/m^2$ and A_o^* is the dimensional initial amplitude. Clearly the level adjustment is given by

$$\{SPL - D(\theta)\} = 20 \log_{10} \{A_o^*/p_{ref}\}. \qquad (3\text{-}154)$$

Typically, as will be seen below, $\{SPL - D(\theta)\} \sim 100$ dB, so that $A_o^* \sim p_{ref} \times 10^5 = 2\ N/m^2$. Since the dynamic head of the supersonic jets is typically 1 to $2 \times 10^5\ N/m^2$, the initial amplitude of the excitation is of the order of 10^{-5} times the dynamic head of the jet. This lies well below the limit of the linear excitation range measured by Moore [3.26].

The initial amplitude was found to be a function of velocity ratio and Strouhal number but essentially independent of jet exit temperature ratio. The variation of excitation amplitude as a function of velocity ratio V_J/a_o is shown in Figures 3.36 through 3.40 for Strouhal numbers 0.1, 0.2, 0.3, 0.4, 0.5, respectively, and various jet exit temperature ratios, T_J/T_o. At the lower Strouhal numbers the initial amplitude is essentially independent of jet velocity ratio. As the Strouhal number increases so the excitation level

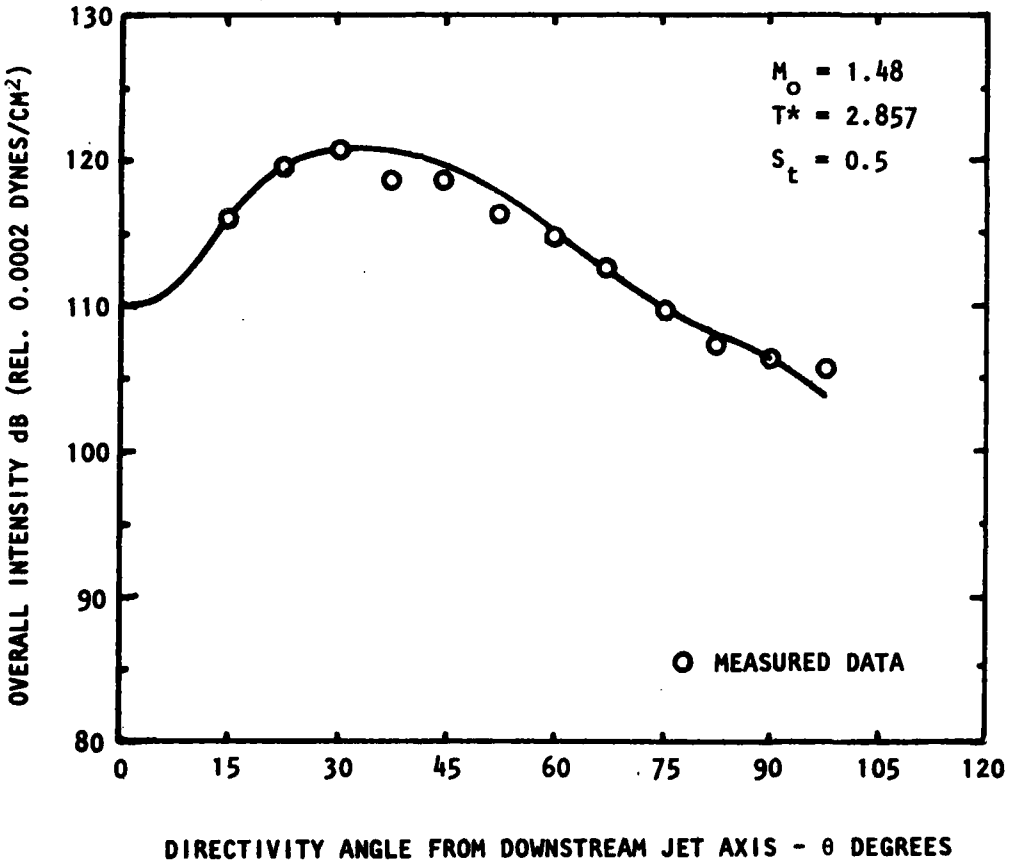

Figure 3.34 Comparison of Predicted Directivity of M=1 Mode With Measured Data

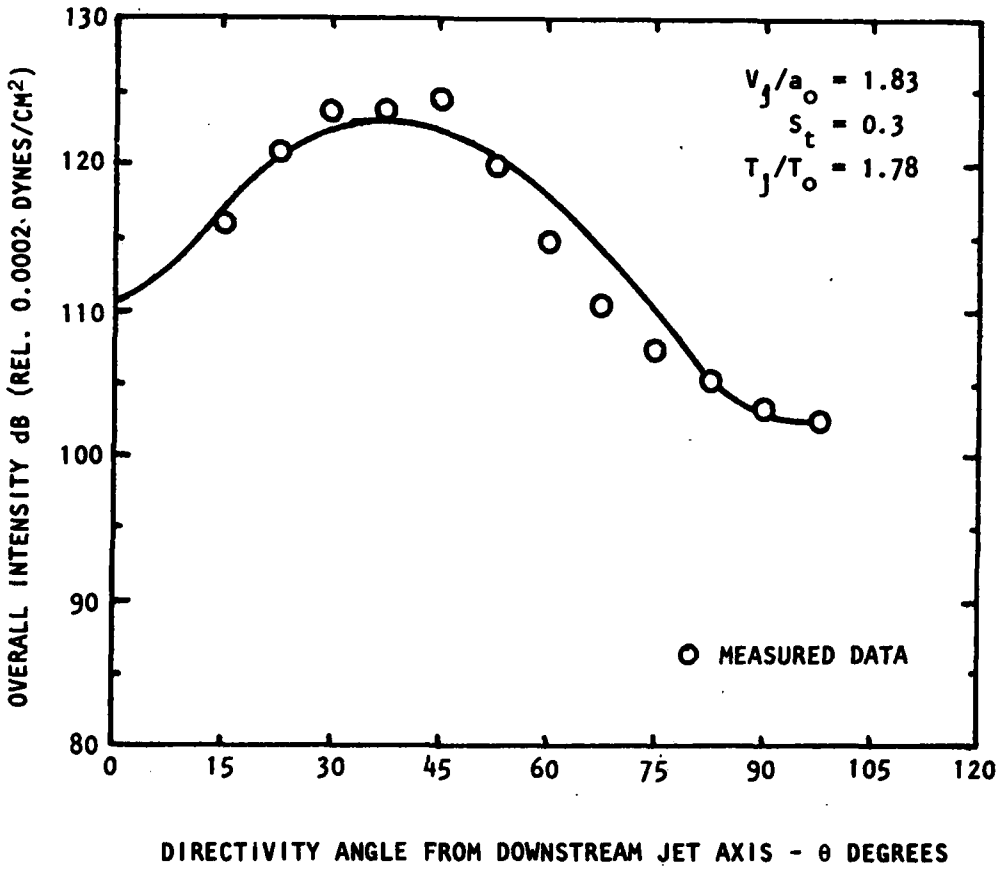

Figure 3.35 Comparison of Predicted Directivity of M=1 Mode With Measured Data

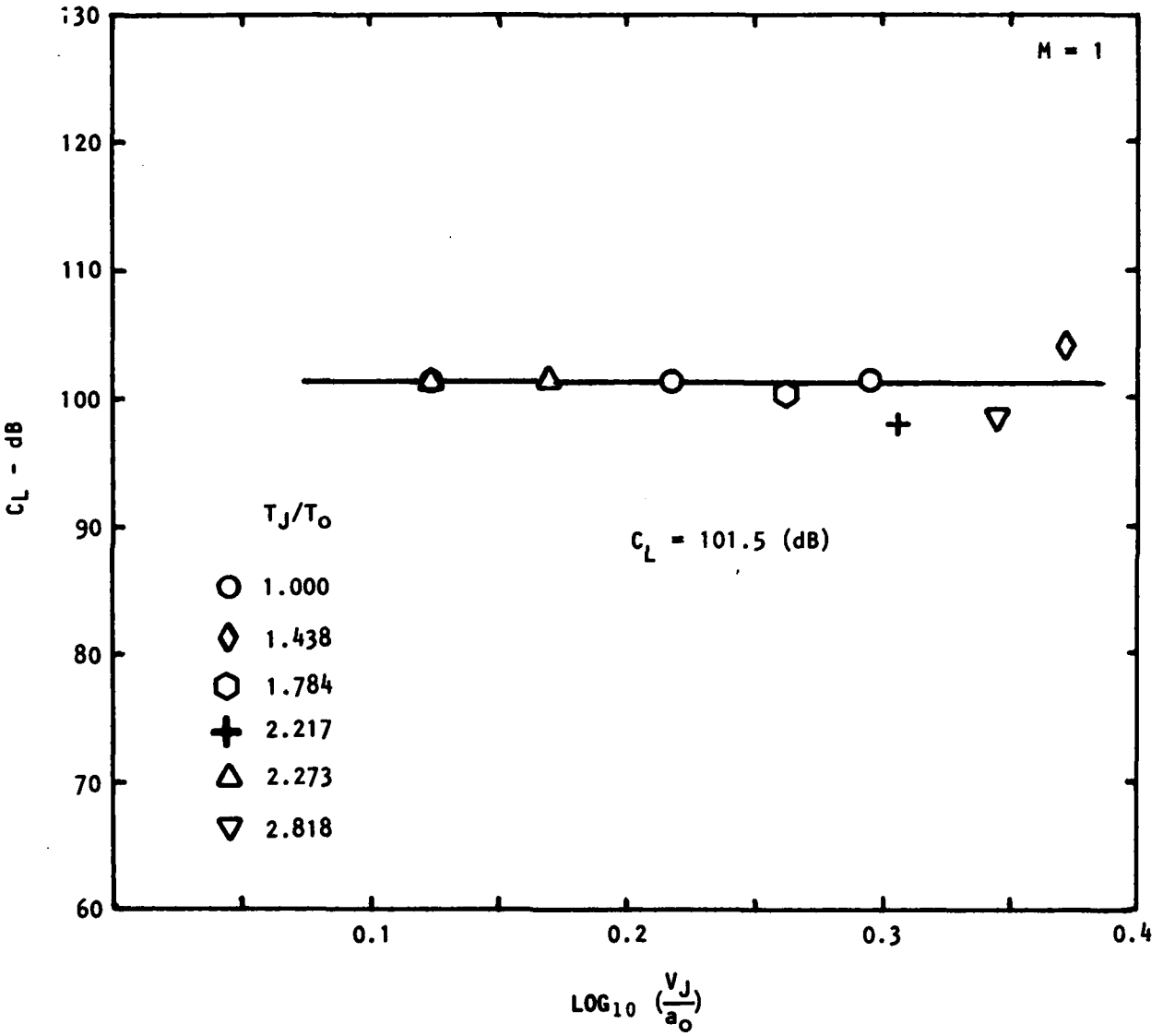

Figure 3.36 Calculation of Excitation Levels : St = 0.1

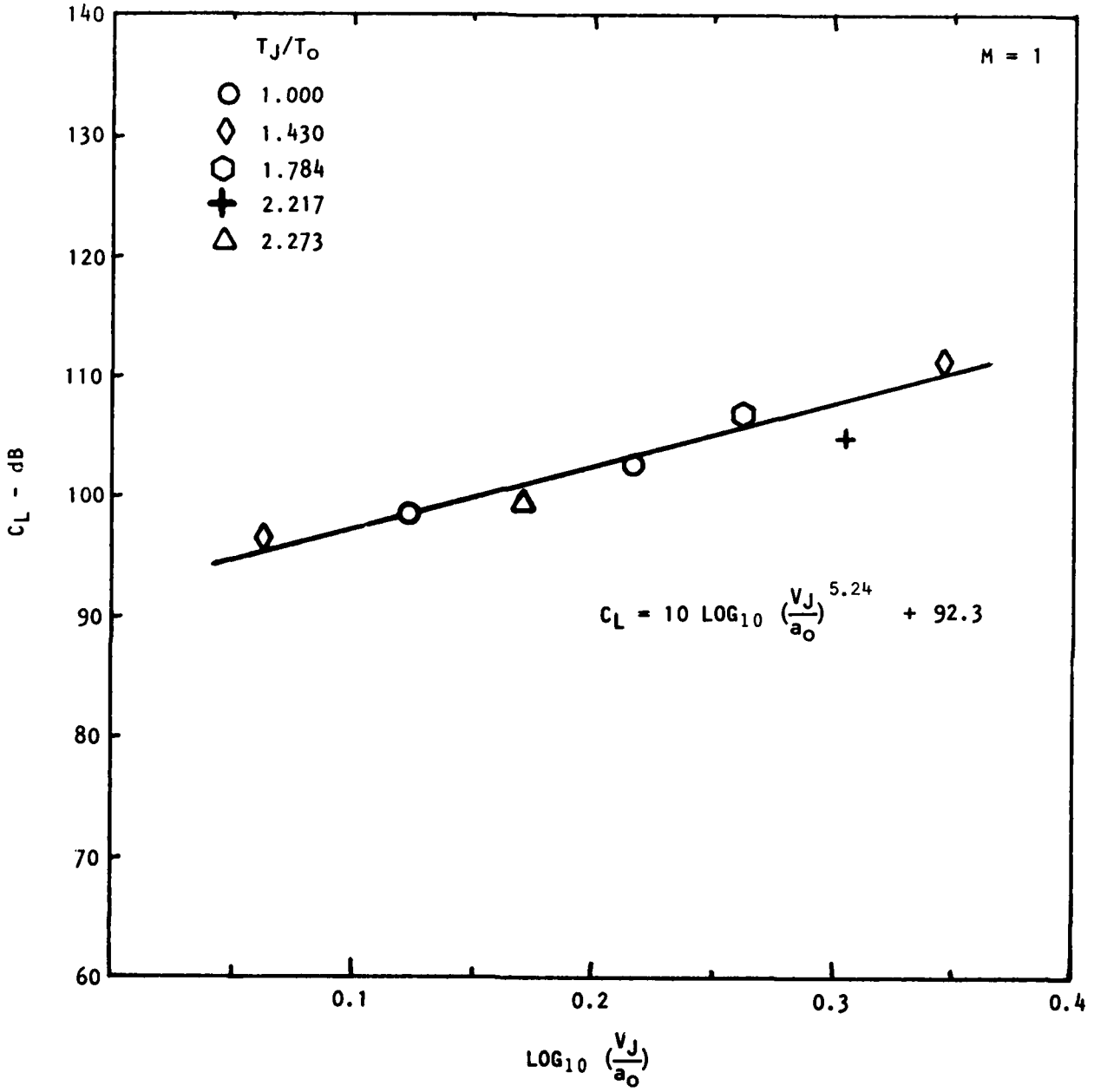

Figure 3.37 Calculation of Excitation Levels : St = 0.2

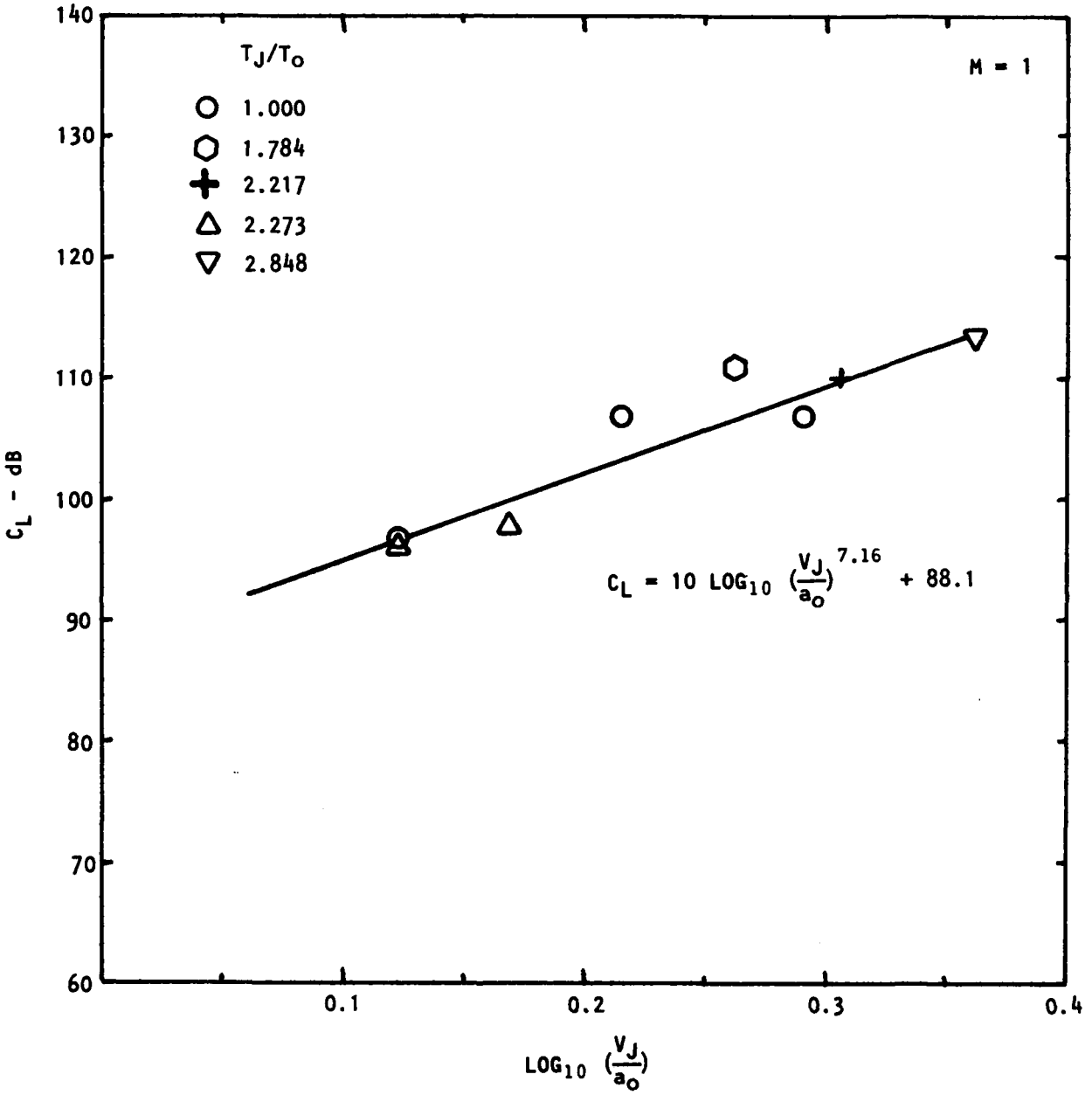

Figure 3.38 Calculation of Excitation Levels : St = 0.3

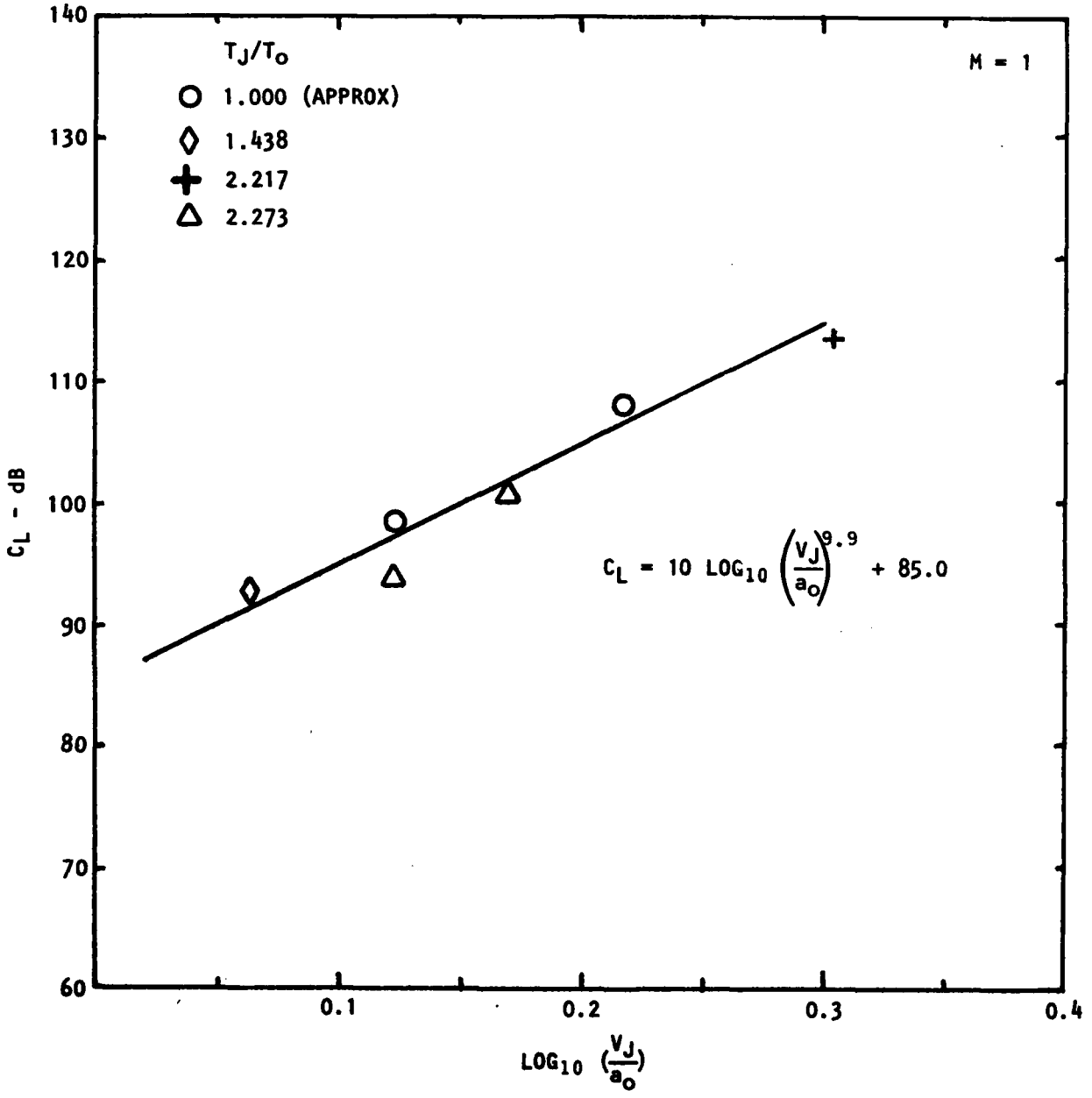

Figure 3.39 Calculation of Excitation Levels : St = 0.4

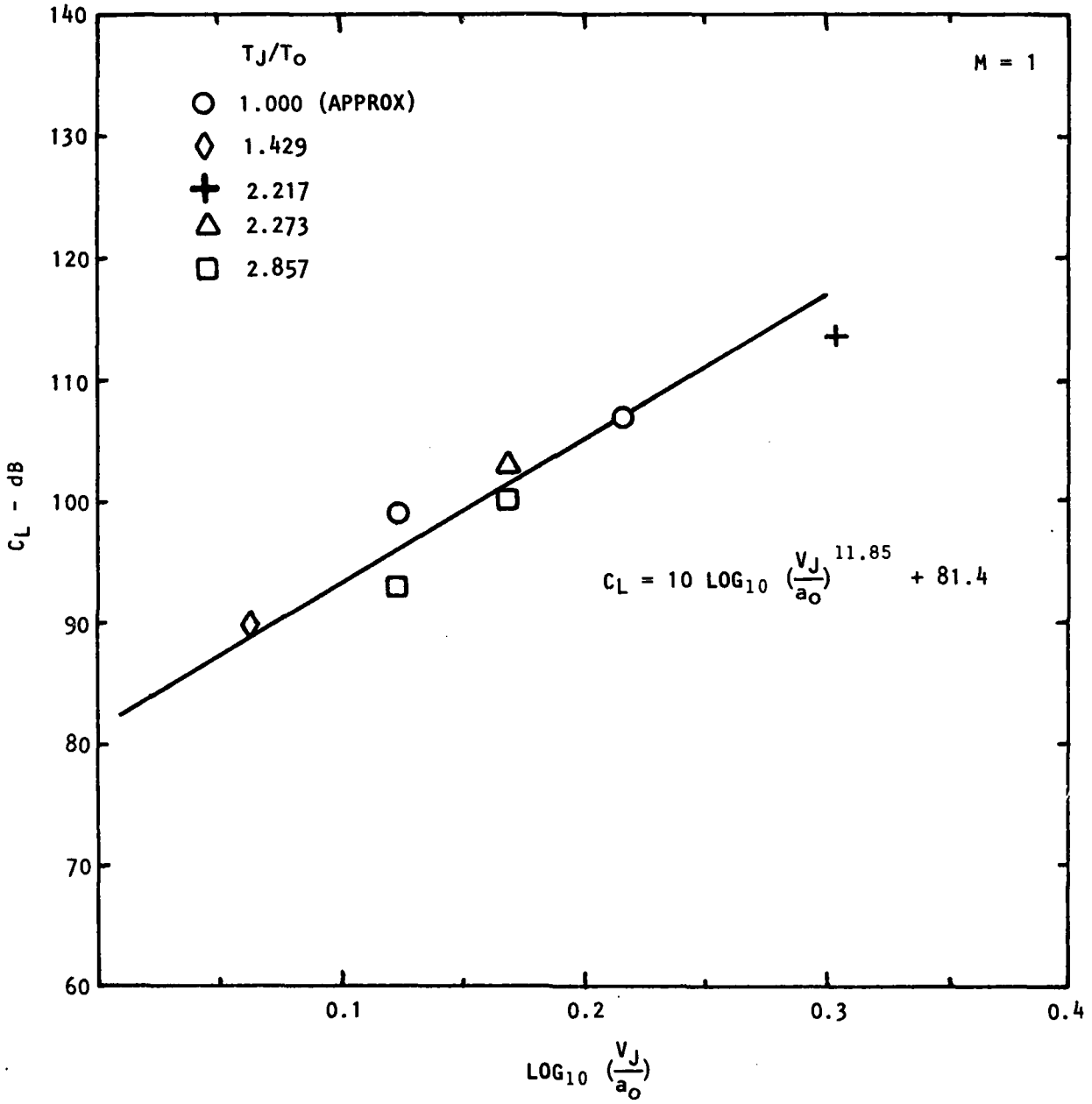

Figure 3.40 Calculation of Excitation Levels : St = 0.5

increases with increasing velocity ratio. However, all the changes are linear with V_J/a_o and may be written,

$$C_L = 10 \log_{10} (V_J/a_o)^m + c, \tag{3-155}$$

where C_L is a correction level which accounts for the initial excitation amplitude. Note that $C_L = 20 \log_{10}(A_o^*/2 \times 10^{-5})$. The coefficients m and c are functions of the Strouhal number and their variation is shown in Figures 3.41 and 3.42, respectively. The best fit to the data is given by

$$m = 17.2 \log_{10} (10\ St), \tag{3-156}$$

and

$$c = 74.13\ (St)^{-0.136} \tag{3-157}$$

Making use of Equations (3-155), (3-156), and (3-157), which describe the initial excitation amplitude, the absolute levels of the noise radiated by the large-scale structure may be calculated.

The prediction methods described in this section have been incorporated into a prediction program which is described in some detail in Section 6. Also contained in the program are predictions for the noise contributions from the small-scale mixing noise and the shock-associated noise. An example is given here which shows how the contributions from these component mechanisms may be combined to provide a total radiated noise prediction. Since the large-scale structure only makes a significant contribution for supersonic velocity ratios, $V_J/a_o > 1.15$ and small angles, $0 \leq \theta \leq 45°$, we will consider the noise prediction in the rear arc for the following jet operating conditions

$$V_J/a_o = 2.012$$

$$T_J/T_o = 2.217,$$

which corresponds to test point 55 in the experimental plan. Figure 3.43 shows the noise prediction at $\theta = 60°$, which is right at the edge of the geometric acoustics cone of silence. Since θ is greater than 45°, there is only a contribution at this location from the small-scale mixing noise which provides a good fit to the data. Figure 3.44 shows the noise prediction at $\theta = 45°$. The predicted noise radiation from the mixing noise falls well below the measured levels at all frequencies. However, at this frequency the large-scale structure contributes to noise radiation. This contribution is shown in the figure and it can be seen that the range of Strouhal numbers covered by the large-scale noise includes the peak sound pressure levels. The absolute levels predicted by the large-scale calculations could have been made to fit the measured data *exactly* at all frequencies since the excitation levels were calculated on the basis of the measurements. However, it was felt to be more valid to derive simple expressions for the absolute excitation levels, see Equation 3.155, so that trends could be easily discerned. At such time as information becomes available, either from analysis or experiment, as to the amount that the various azimuthal modes are naturally excited, such information can be readily incorporated into the prediction program.

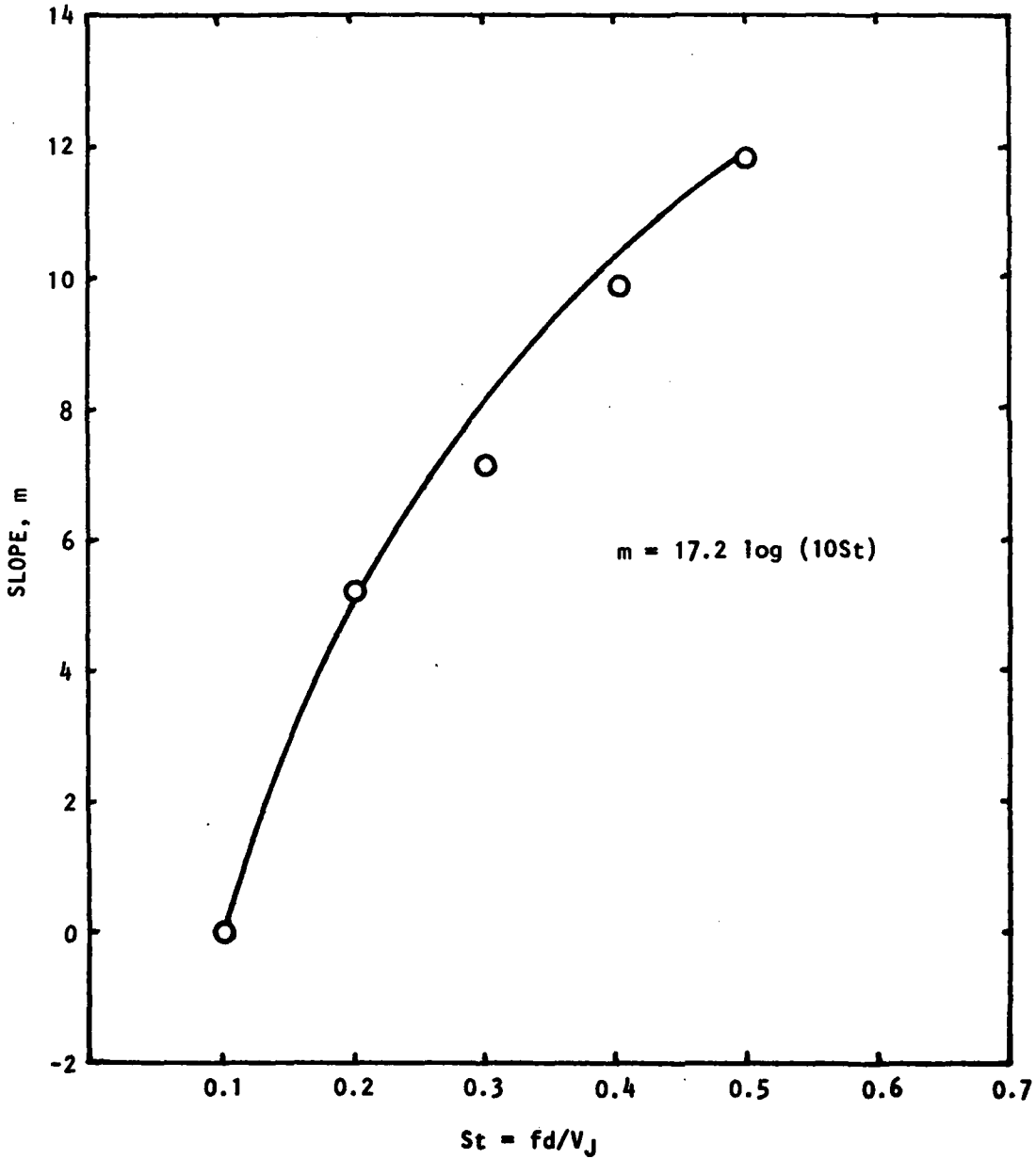

Figure 3.41 Calculation of Slope in Excitation Level Equation 3.155

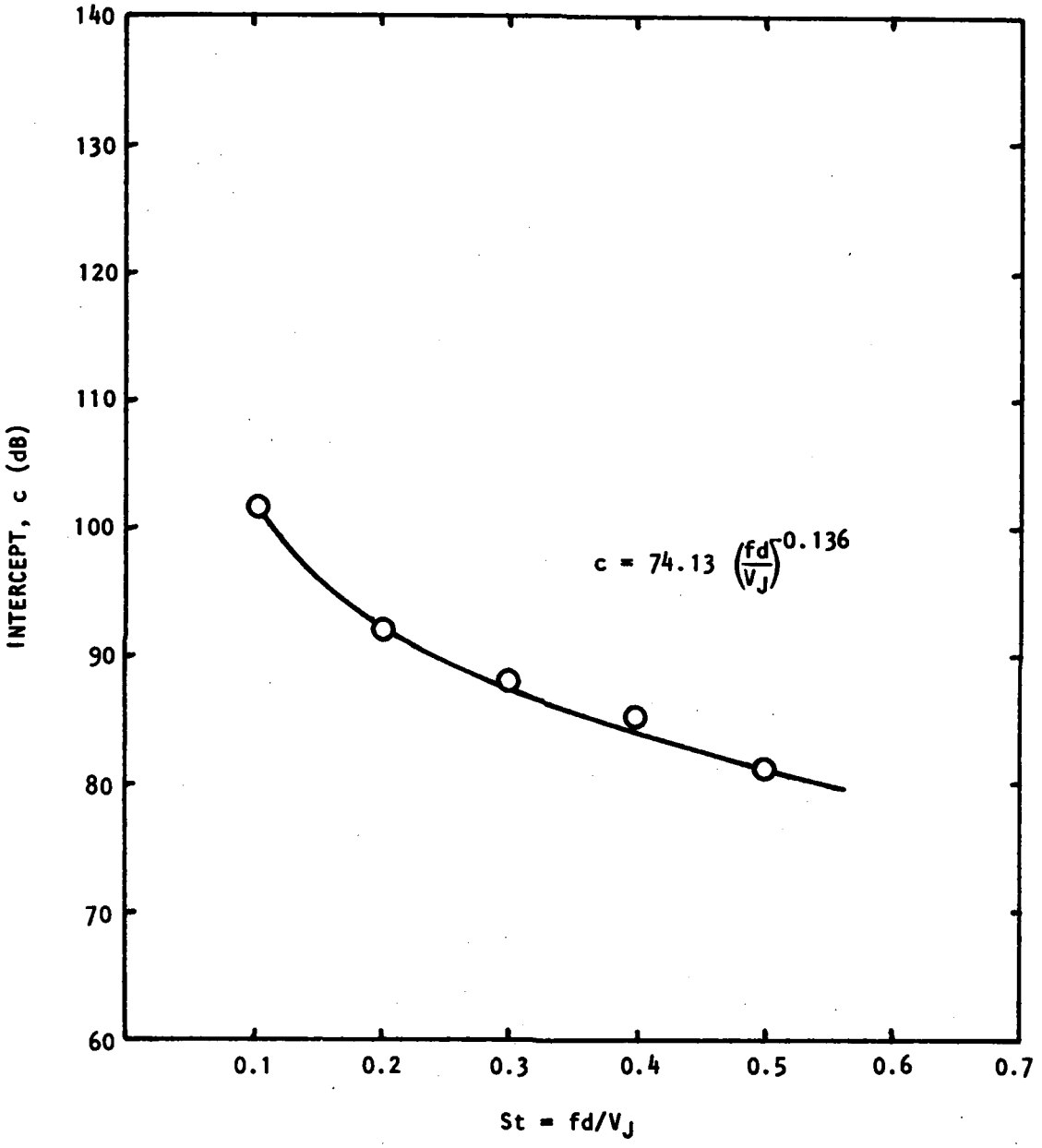

Figure 3.42 Calculation of Intercept in Excitation Level Equation 3.155

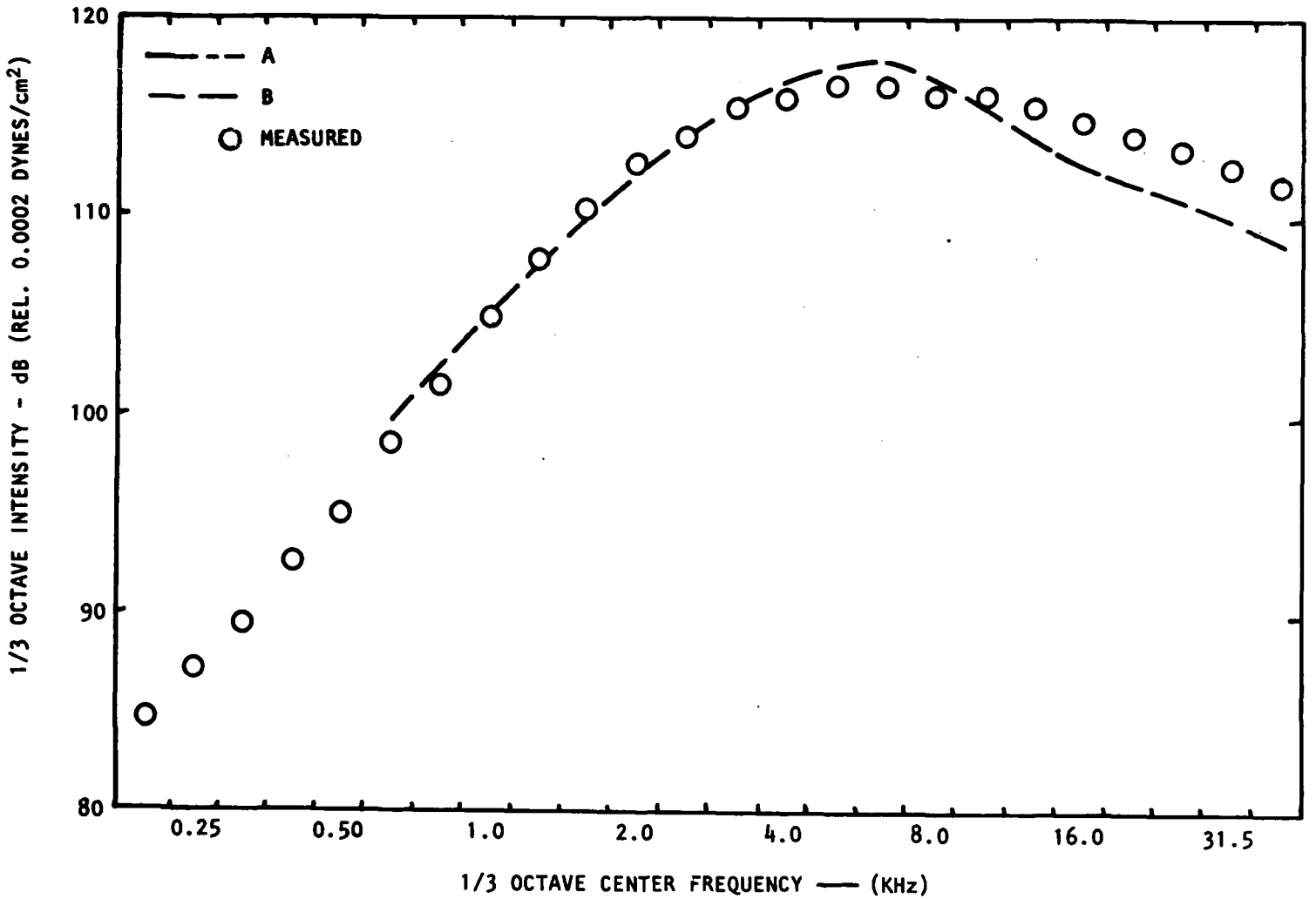

Figure 3.43 Predicted Noise Radiation from the Large-Scale Structure (A) and the Small-Scale Mixing Noise (B): $\theta = 60°$.

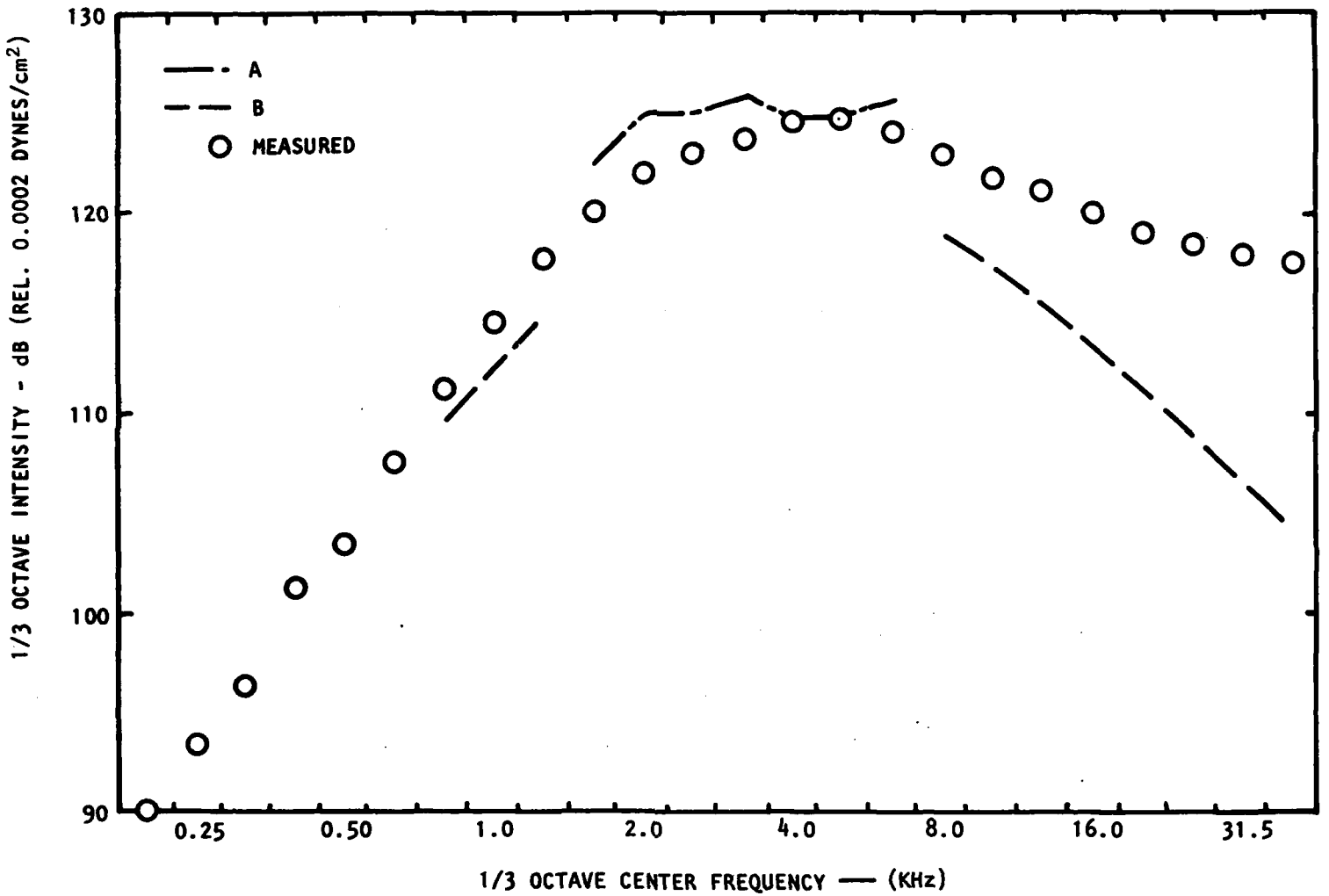

Figure 3.44 Predicted Noise Radiation from the Large-Scale Structure (A) and the Small-Scale Mixing Noise (B): $\theta = 45°$.

As an aid to the user in understanding the program, the relevant equations for calculating the noise from the jet instabilities are summarized below.

The far-field directivity pattern is given by

$$D(\theta) = 2|B_m(M\omega\cos\theta)|^2, \tag{3-158}$$

where

$$B_o(k) = \frac{1}{2\pi}\int_{-\infty}^{\infty} g_{oo}(\varepsilon x)e^{i\theta(x) - ikx}\,dx \tag{3-159}$$

and

$$B_m(k) = \frac{(M^2\omega^2 - k^2)^{m/2}}{2\pi}\int_{-\infty}^{\infty} \frac{g_{om}(\varepsilon x)}{(M^2\omega^2 - \alpha^2)^{m/2}}\, e^{i\theta(x) - ikx}\,dx, \tag{3-160}$$

$$m = 1, 2, \text{ etc.}$$

The Fourier transforms in Equation (3-159) and (3-160) are performed numerically using an FFT algorithm. In the prediction program the quantities $g_{om}(\varepsilon x)$, $m = 0,1,2$, etc., are set equal to unity. The function to be transformed in Equations (3-159) and (3-160) is given by

$$e^{i\theta(x)} \;/\; (M^2\omega^2 - \alpha^2)^{m/2} \tag{3-161}$$

where

$$\alpha = \frac{d\theta}{dx}. \tag{3-162}$$

The value of α as a function of x is obtained as the eigenvalue to the boundary value problem,

$$\left[\frac{\partial^2}{\partial r^2} + \left[\frac{1}{r} - \frac{1}{R_o}\frac{\partial R_o}{\partial r} + \frac{2\alpha}{(\omega - \alpha U)}\frac{\partial U}{\partial r}\right]\frac{\partial}{\partial r} + \left[M^2 R_o(\omega - \alpha U)^2 - \alpha^2 - \frac{m^2}{r^2}\right]\right]\hat{\zeta} = 0 \tag{3-163}$$

subject to the boundary conditions

$$\hat{\zeta}(r,s) \quad \text{is bounded as } r \to 0 \quad \text{or} \quad \infty.$$

The eigenfunction, which is obtained numerically, is related to the fluctuating pressure by the equation,

$$p'(r,\phi,x,t) = \hat{\zeta}(r,s)\,\exp[i\theta(x) + im\phi - i\omega t]. \tag{3-165}$$

Thus, the function $\theta(x)$ in Equation (3-161) is obtained by integrating Equation (3-162) having first determined $\alpha(x)$ by solving the boundary value problem, given by Equation (3-163) and (3-164) at stepped values of x. The mean velocity in the jet in the annular mixing region is given by

$$U(r,s) = \begin{cases} \bar{U}(\eta) & r > h \quad (3\text{-}166) \\ 1. & r < h \quad (3\text{-}167) \end{cases}$$

where $$\eta = (r - h)/b. \quad (3\text{-}168)$$

h is the potential core radius and b is the velocity half width of the mixing region. Downstream of the end of the potential core, the mean velocity is given by

$$U(r,s) = u_c(x)\ \bar{U}(\xi), \quad (3\text{-}169)$$

where $$\xi = r/b, \quad (3\text{-}170)$$

and $u_c(x)$ is the jet centerline velocity. The shape function $\bar{U}(\eta)$ and $\bar{U}(\xi)$ take the same form, for example,

$$\bar{U}(\eta) = \exp\ [-0.693147\ \eta^2] \quad (3\text{-}171)$$

The variation of b(x), h(x) and $u_c(x)$ is determined from the equations,

$$\int_0^\infty \bar{\rho}\bar{u}^2\ r dr = 1/2\ T_J \quad (3\text{-}172)$$

and $$\frac{d}{dx}\int_0^\infty \bar{\rho}\bar{u}^3\ r dr = -2\int_0^\infty \tau\left(\frac{\partial \bar{u}}{\partial r}\right)\ r dr \quad (3\text{-}173)$$

where it is assumed that

$$\tau = \bar{\rho}\bar{\varepsilon}\ \frac{\partial \bar{u}}{\partial r} \quad (3\text{-}174)$$

and $$\bar{\rho}\bar{\varepsilon} = \frac{\bar{K}}{2}\ b\bar{\rho}_{.5}\ u_c \quad (3\text{-}175)$$

The use of the shape function given in Equation (3-171) in Equations (3-172) through (3-175) gives equations for $u_c(b)$, db/dx and du_c/dx which are given in Appendix 3D.

The density is related to the mean velocity and the Mach number using a Crocco relationship, such that

$$R_o(r,s) = \{1 + (T_J - 1)U + \frac{(\gamma - 1)}{2}\ M^2U(1 - U)\}^{-1}. \quad (3\text{-}176)$$

The details of the numerical procedures are contained in the analysis of Section 3.3 and are given in flow chart form in Section 6.

4. SHOCK-ASSOCIATED NOISE

4.1 INTRODUCTION

The total sound field from a supersonic jet consists of contributions from three noise sources or noise components. These are (i) noise generated by small-scale turbulence structure (turbulent mixing noise), (ii) noise generated by large-scale jet flow structure (large-scale noise, for short), and (iii) noise generated by the interaction between jet turbulence and shock structure (shock-associated noise). In the present work, these three noise sources are considered independently, so that the total noise is simply the sum of the contributions from the three noise components. The contribution of any one noise source relative to the contributions from the other two noise sources depends upon the jet operating conditions, the observer angle, and the frequency. The turbulent mixing noise component and the large-scale noise component were discussed in Sections 2 and 3, respectively. The present section deals with the shock-associated noise component.

The turbulent mixing noise component is present at all jet operating conditions (subsonic and supersonic), observer angles and frequencies. On the other hand, the large-scale noise is important only at supersonic jet velocities and the shock noise is present only at supercritical pressure ratios. Furthermore, while the contribution from large-scale noise is significant at low frequencies (or low Strouhal numbers) and small angles to the jet exhaust, the shock noise contribution is significant at high frequencies and large angles to the jet exhaust (as will be discussed later). Thus, in the present section dealing with shock noise, the contribution from large-scale noise to the total noise is not considered further in order to simplify the discussion.

The broadband shock-associated noise is defined in Figure 4.1, where the spectrum from an under-expanded jet is compared with the corresponding spectrum from a fully-expanded jet at identical jet operating conditions. When a convergent nozzle is operated at subcritical pressure ratio, or when a convergent-divergent nozzle is operated at design pressure ratio, the acoustic spectrum is broad and smooth, and consists of pure turbulent mixing noise. On the other hand, when a convergent nozzle is operated at supercritical pressure ratio (under-expanded), or when a convergent-divergent nozzle is operated at off-design Mach number (under-expanded or over-expanded), the resulting acoustic spectrum contains an extra noise contribution, due to the presence of shock structure in the jet flow, in addition to the basic turbulent mixing noise. The shock-related noise can be divided into two distinct types, each having its own characteristic properties. The first component is discrete in nature, usually with several harmonics, and is often referred to as the "screech" component. The second component is broadband in nature with a well-defined peak frequency. It is this broadband component that is of real significance for full-scale aircraft engines. In the present work, where the broadband shock-associated noise is studied using model-scale jets, the contribution from the screech component to the total sound field is suppressed, as described in the final report for the previous contract [4.1].

In considering the total noise from a supersonic jet, it is worthwhile to summarize the roles played by shock-associated noise and turbulent mixing

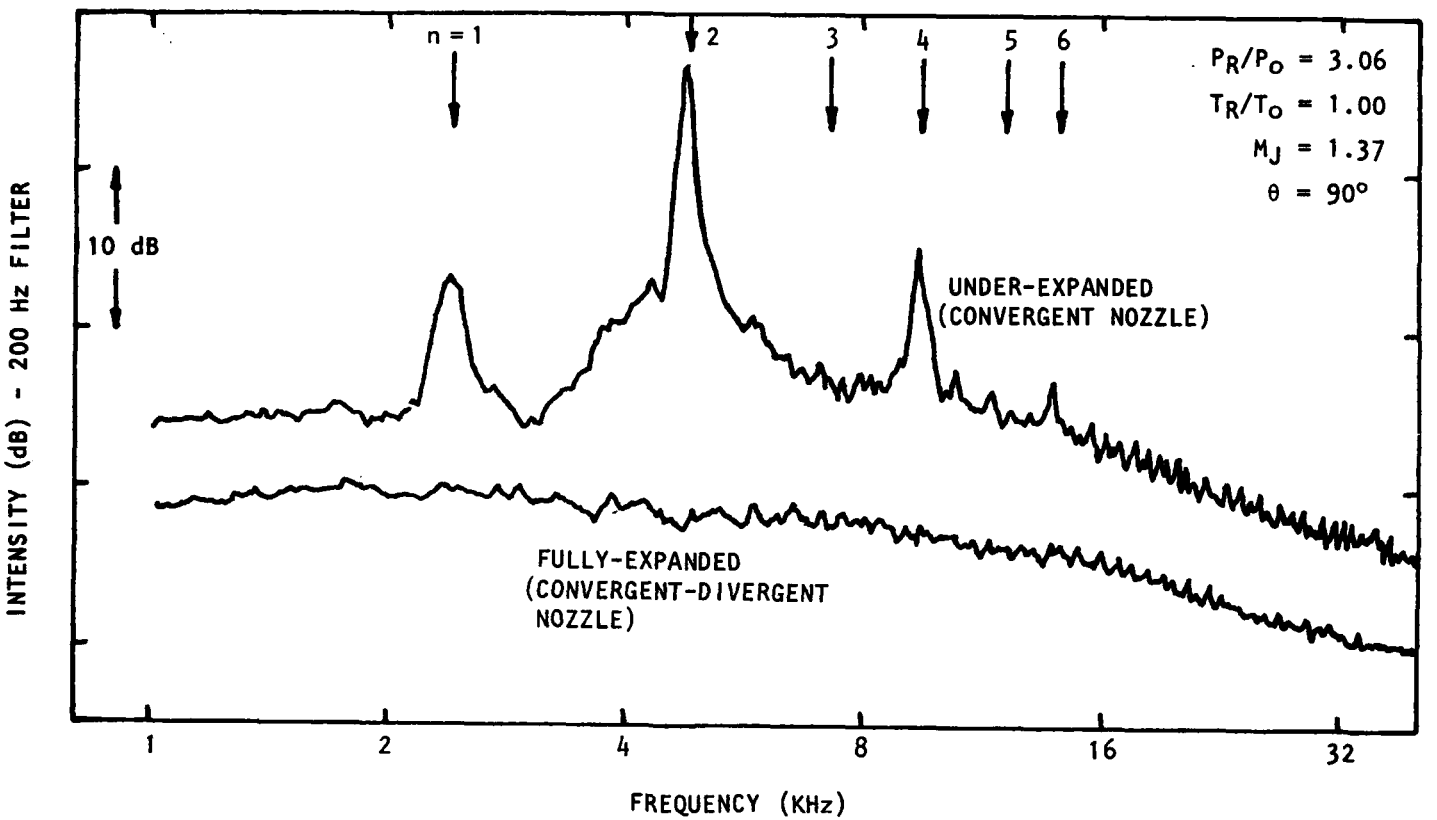

Figure 4.1 Comparison of Spectra from Fully-Expanded and Under-Expanded Jets

noise. If the sound field from a jet exhaust is characterized by three basic parameters, namely the pressure ratio P_R/P_O, the temperature ratio T_R/T_O, and the observer angle θ relative to jet exhaust, then the variations of these two noise contributions with the three parameters can be illustrated in a qualitative manner as shown in Figure 4.2. Also shown in this figure are the regimes of P_R/P_O, T_R/T_O, and θ over which the shock-associated noise dominates the turbulent mixing noise. For fixed T_R/T_O and θ (top part of Figure 4.2), the turbulent mixing noise increases as P_R/P_O increases; the shock-associated noise is generated at supercritical pressure ratios only, and its magnitude also increases as P_R/P_O increases; at supercritical pressure ratios, the shock noise contribution normally dominates over the mixing noise contribution. For fixed supercritical P_R/P_O and θ (middle part of Figure 4.2), the magnitude of shock-associated noise remains nominally independent of T_R/T_O; in contrast, as T_R/T_O is increased, the turbulent mixing noise increases due to the increase in jet velocity with heating; the net result is that at low temperatures, the shock noise dominates over the mixing noise, and as the jet temperature in increased, the *increasing* contribution from mixing noise eventually becomes larger than the shock noise contribution. Finally, for fixed supercritical P_R/P_O and T_R/T_O, the bottom part of Figure 4.2 indicates the variations of noise levels with observer angle θ. For emission angles beyond the peak radiation angle θ_p, the shock-associated noise contribution is essentially uniform, whereas the turbulent mixing noise level decreases as the observer moves from the peak angle into the forward arc; hence, in this region, shock noise becomes increasingly significant, especially at large values of θ (relative to jet exhaust) in the forward arc.

In summary, therefore, if one combines the trends discussed above, it becomes evident that the contribution of shock-associated noise to the total noise is significant (i) at supercritical pressure ratios, (ii) at low temperatures, and (iii) at large angles to the downstream jet axis.

A summary of the shock-associated noise experimental program and the main results obtained in the previous contract [4.1] is given in Section 4.2. Following this, the work conducted during the present contract is described in Sections 4.3 through 4.8. Finally, the prediction of shock-associated noise and comparisons with measured data are presented in Section 4.9.

4.2 SUMMARY OF PREVIOUS WORK

The characteristics of the sound field of shock-containing under-expanded jets were studied in the previous contract by measuring the noise from a two-inch diameter convergent nozzle operated at supercritical pressure ratios (up to 7.4) over the range of stagnation temperature ratios from unity to 3.7. The measurements were conducted in the Lockheed anechoic facility. The jet operating conditions were chosen carefully to be compatible with the turbulent mixing noise experiments so that, whenever possible, the results from under-expanded (shock-containing) jets can be compared directly with the corresponding results from fully-expanded (shock-free) jets.

The results, both overall and spectral, were analyzed in detail. It was confirmed that the OASPL trends for shock-associated noise, obtained previously

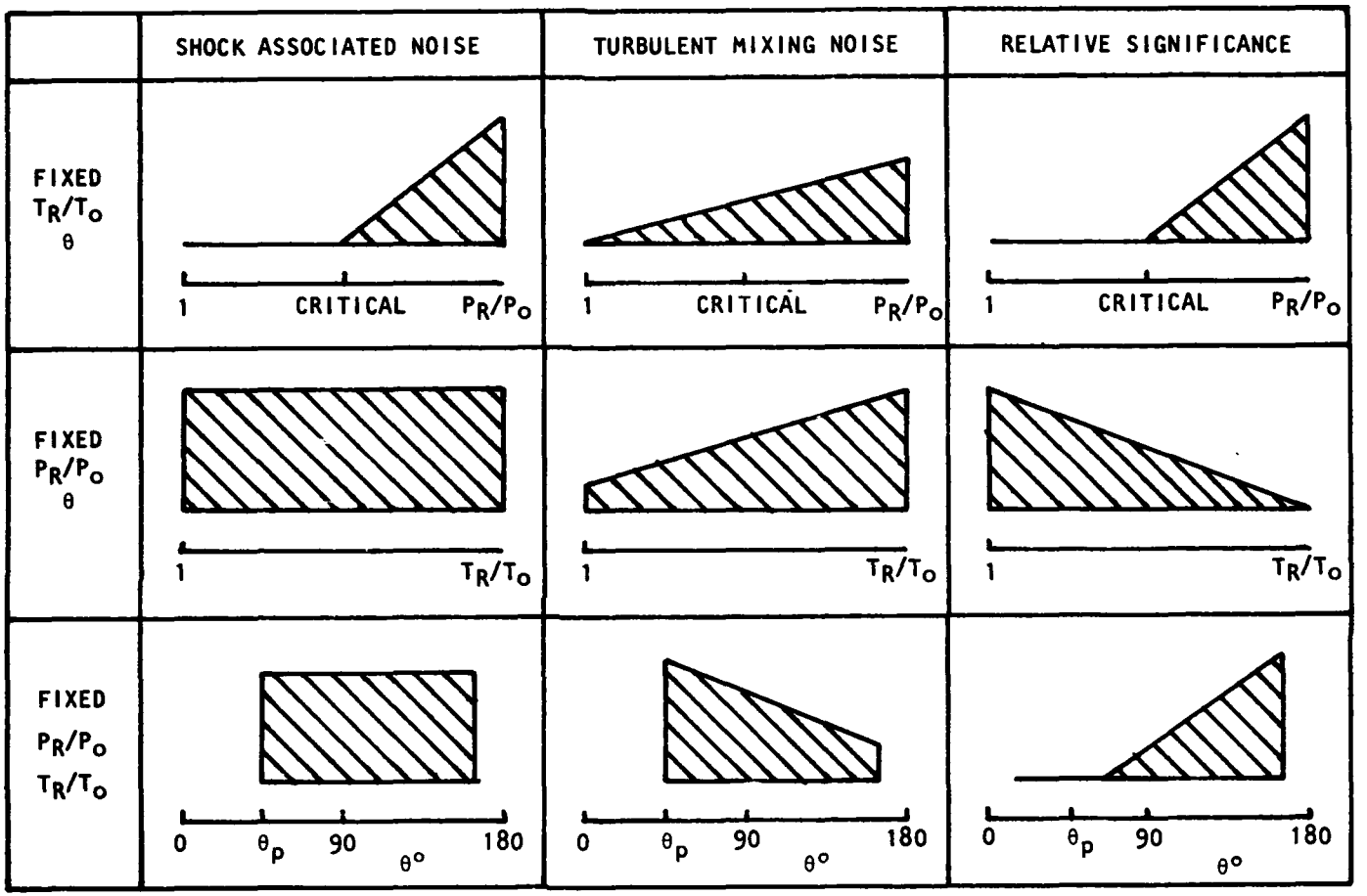

Figure 4.2 Overall Qualitative Significance of Shock-Associated Noise

(The height of the shaded area represents the noise level in a qualitative manner.)

by Harper-Bourne, and Fisher [4.2] from a limited amount of measurements mainly from unheated jets), are valid over an extensive envelope of supercritical jet operating conditions. The overall intensity of shock-associated noise is essentially independent of both the jet efflux temperature and observer angle; it is primarily a function of jet pressure ratio only, and scales according to

$$I \propto \beta^4 \qquad \text{where} \qquad \beta = (M_J^2 - 1)^{\frac{1}{2}}$$

for $\beta \leq 1.0$.

The spectral results were examined first by studying the variation of peak frequency of shock-associated noise, f_p, with observer angle θ, pressure ratio parameter β, and jet static temperature ratio T_J/T_o. At all jet operating conditions (i.e., combinations of β and T_J/T_o), the peak frequency decreases as the observer angle (relative to jet exhaust) increases, thus exhibiting a Doppler shift phenomenon. The variation of f_p with β and T_J/T_o at a fixed value of θ is also worth noting. For constant jet exit temperature, the peak frequency decreases with increasing pressure ratio parameter β; on the other hand, at a fixed pressure ratio, the peak frequency increases as the jet efflux temperature is raised. These observations are found to be in good qualitative agreement with the scaling formulae for f_p obtained by Harper-Bourne and Fisher [4.2] in their semi-empirical model for shock-associated noise. In this model, the end of each shock cell is taken as a compact source of sound and the relative phasing between the sources is determined by the convection of turbulent eddies between them. The model therefore consists of an array of shock-turbulence interaction sources in line with the nozzle lip and almost equally spaced with separation L. It is assumed that the convection of a turbulent eddy along this line of sources causes each to emit sound at the time of arrival of the eddy.

Finally, a computer program for the prediction of shock-associated noise, based on the same semi-empirical model, was developed, and a preliminary comparison between measured and predicted spectra was found to be quite encouraging.

4.3 OBJECTIVES OF PRESENT WORK

The specific items of work that are conducted during the present contract are listed below in the form of objectives:

(1) To modify the shock-associated noise prediction scheme and computer program to obtain one-third octave band spectral predictions instead of spectral density predictions.

(2) To highlight the effects of various constants used in the prediction scheme (e.g., shock spacing constant, eddy convection velocity constant, etc.) by conducting a parametric computational study.

(3) To measure the variations in shock spacing and eddy convection velocity with jet pressure ratio and temperature ratio using a Schlieren system and the laser velocimeter.

(4) To conduct extensive comparisons between predicted and measured spectra in order to examine (i) the validity of the prediction model, and (ii) the importance of flow-acoustic interactions for shock-associated noise.

(5) To obtain improved scaling laws for shock noise if found to be necessary in the above comparisons, and to incorporate these modifications in the prediction scheme.

(6) To integrate the shock-associated noise prediction routine into the unified jet noise prediction program, and to conduct a detailed comparison between measured (i.e. total noise) and predicted (i.e. sum of turbulent mixing noise and shock noise) spectra.

4.4 MODIFICATION OF PREDICTION SCHEME FOR 1/3-OCTAVE PREDICTION

As mentioned earlier, during the preceding contract, a computer program for the prediction of broadband shock-associated noise, based on the theoretical model proposed by Harper-Bourne and Fisher, was developed, and a preliminary comparison with measured spectra was conducted. This program predicted shock-associated noise in the form of *spectral density*, i.e. intensity per unit bandwidth. From the standpoint of practical application, it was necessary to modify the computer program to give predictions in one-third octave bands, rather than in narrow frequency bands. This modification was successfully completed and its operation was verified in the earlier period of the present contract. In order to avoid duplication, the prediction scheme will be presented and described in the last subsection. The program has been written to be rather flexible, such that the effects of various jet flow parameters on the predicted spectra can be examined independently. The program can be used to predict the shock-associated noise spectra at any desired observer angle, and for any set of jet operating conditions (pressure ratio and temperature ratio).

4.5 PARAMETRIC COMPUTATIONAL STUDY

A considerable effort was subsequently spent in examining the effects and optimizing the values of several parameters relevant to the prediction scheme. The most important parameters are listed below:

(1) Strouhal number scaling (i.e $\sigma = \omega L/a_o$ or $\sigma = \omega L/V_c$).

(2) Correlation coefficient spectrum $C_1(\sigma)$.

(3) Number of shocks N.

(4) Eddy convection velocity constant C (where $V_c = CV_j$).

(5) Shock spacing constant K (where $L = K\beta D$).

In the parametric optimization procedure, each parameter was varied independently in a systematic manner, and the predicted spectra were compared with the measured spectra. The findings can be summarized as follows:

4.5.1 Strouhal Number Scaling

In the shock-associated noise study reported by Harper-Bourne and Fisher, it was found that the measured spectra collapsed with Strouhal number based on the ambient speed of sound ($\sigma = \omega L/a_o$) rather than the Strouhal number based on the eddy convection velocity ($\sigma = \omega L/V_c$). Hence, they elected to retain the Strouhal number scaling given by $\sigma = \omega L/a_o$ in the theoretical model. In the present investigation, we have examined this effect, and the result is in agreement with their finding.

This feature is clarified by the two typical comparisons between measured and predicted spectra shown in Figures 4.3 and 4.4. In the first case (Figure 4.3), the value of V_c is approximately equal to a_o. Therefore, as expected, the spectrum predicted by $\sigma = \omega L/a_o$ is nearly identical to the spectrum predicted by $\sigma = \omega L/V_c$. On the other hand, when the values of V_c and a_o are significantly different (as is the case in Figure 4.4, where $V_c/a_o = 1.45$), the spectral predictions are quite different for $\sigma = \omega L/a_o$ and $\sigma = \omega L/V_c$. In general, the prediction with $\sigma = \omega L/V_c$ tended to overpredict the levels at high frequencies. Hence, the Strouhal number scaling based on the ambient speed of sound is considered to be more appropriate.

4.5.2 Correlation Coefficient Spectrum

The influence of the correlation coefficient spectrum between fluctuations at adjacent shock locations was examined for two values of $C_1(\sigma)$. In the first case, the $C_1(\sigma)$ spectrum was taken from the work of Harper-Bourne and Fisher. In the second case, the predictions were computed using the extreme value of unity for $C_1(\sigma)$ (i.e., the shock-turbulence interactions occurring at various shock locations were assumed to be perfectly correlated). It was found that the predicted spectra were not significantly affected by the shape of the $C_1(\sigma)$ spectrum, at least in the frequency range where shock noise was dominant. (A typical example is shown Figure 4.5.) At frequencies beyond the peak frequency, f_p, the predicted spectrum levels were nearly identical. However, for $f < f_p$, the spectrum levels predicted by using $C_1(\sigma) = 1$ dropped off more rapidly. On further examination, it was found that at these lower frequencies, as expected, the interference phenomenon was stronger with $C_1(\sigma) = 1$.

The insensitivity of shock-associated noise prediction to the detailed shape of the $C_1(\sigma)$ spectrum, at least in the region of the peak frequency, implies that this parameter is not critical for prediction purposes. However, with $C_1(\sigma) = 1$, the possibility exists for the lower frequencies to be underpredicted. In order to avoid this possible underprediction, all subsequent predictions of shock-associated noise were conducted with the $C_1(\sigma)$ spectrum given originally by Harper-Bourne and Fisher, and which is presented here in the last subsection.

4.5.3 Number of Shocks

The effect of the number of shock cells in the jet flow on the predicted spectra was examined by testing four cases with N = 8, 6, 4, and 2, respectively. Again, a typical comparison between measured and predicted (N = 8, 4) spectra is shown in Figure 4.6. It was found that the value of N has no

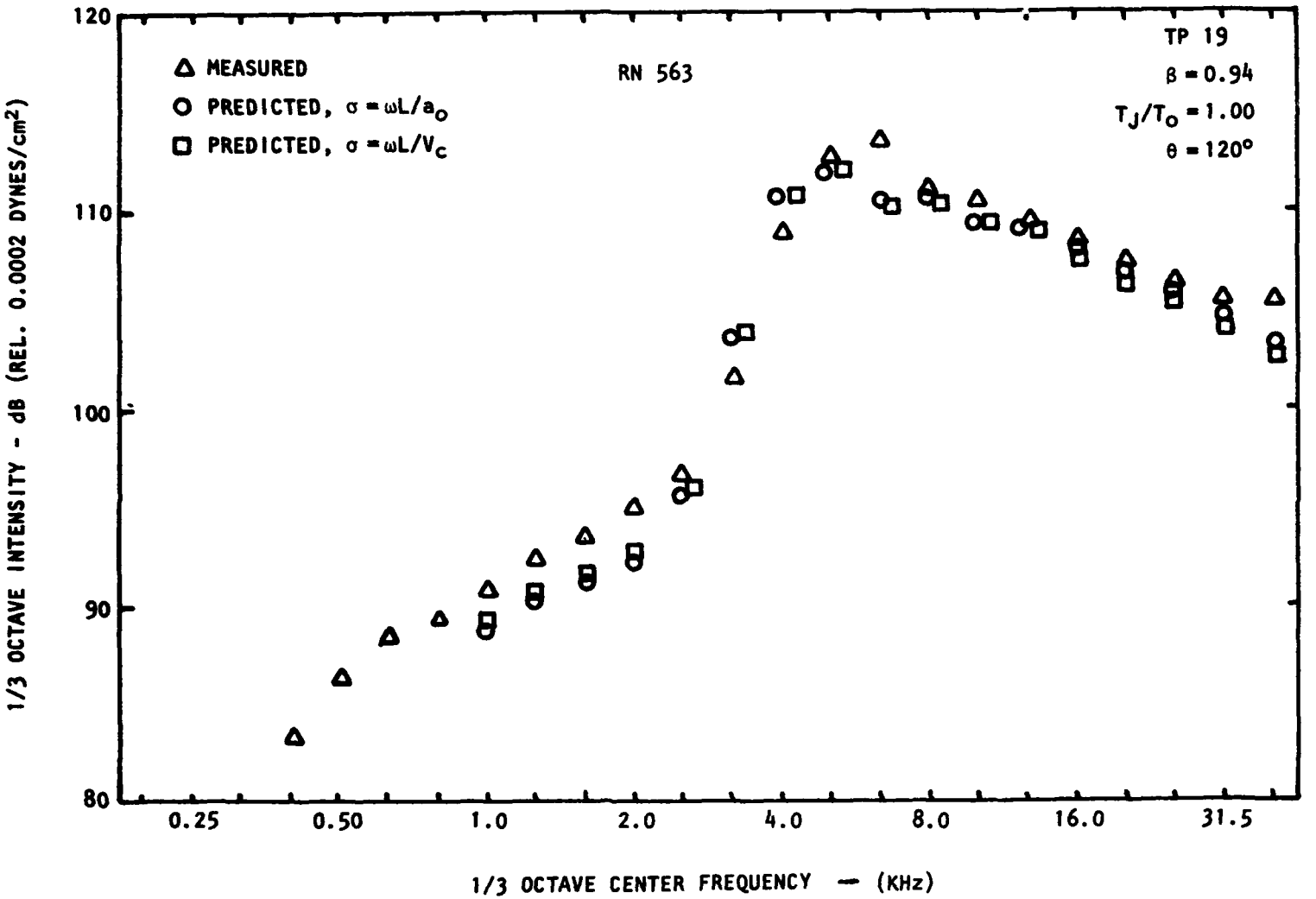

Figure 4.3 Comparison Between Measured and Predicted Spectra (With $\sigma = \omega L/a_o$ and $\sigma = \omega L/V_c$), $V_c/a_o = 0.96$.

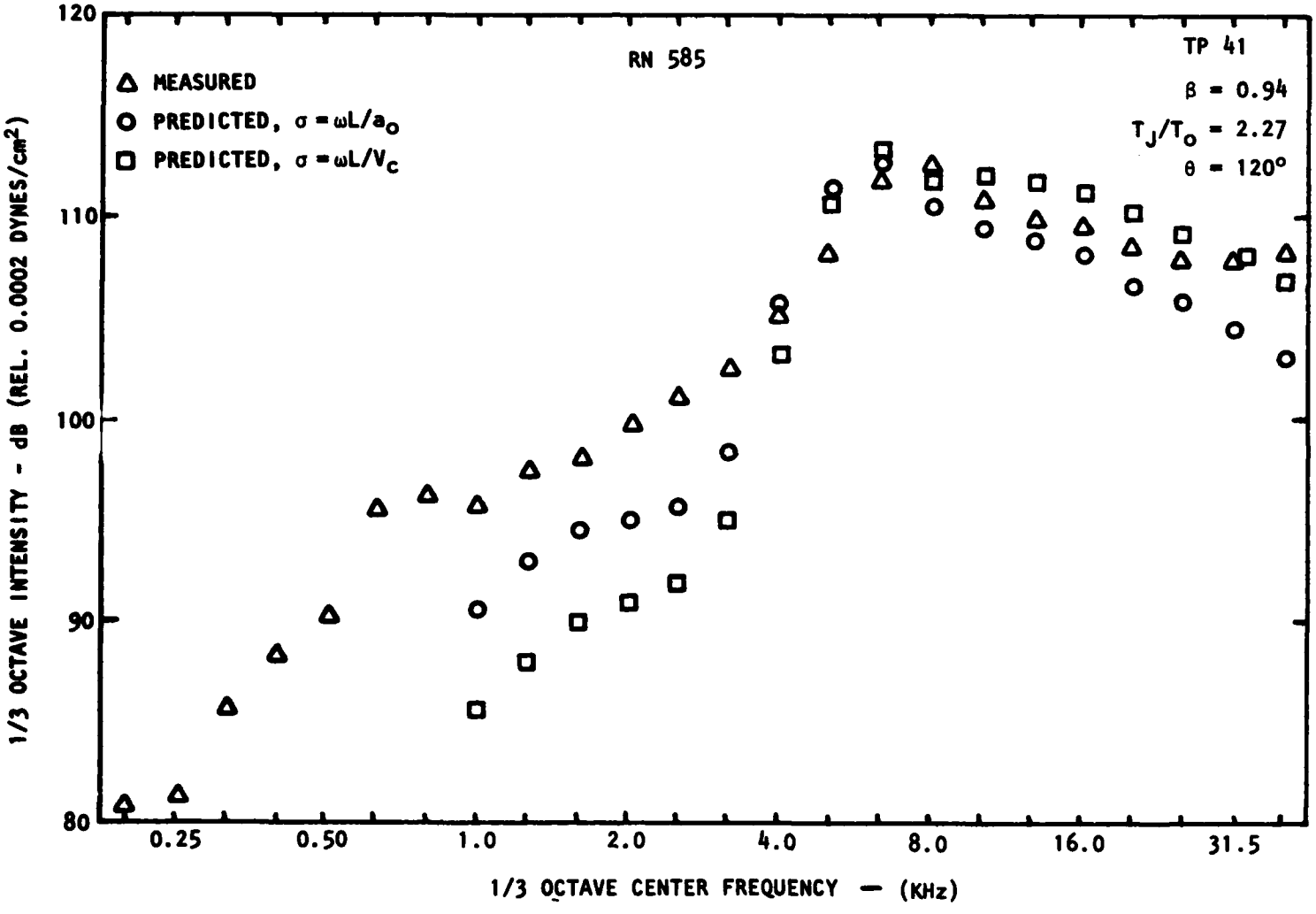

Figure 4.4 Comparison Between Measured and Predicted Spectra (with $\sigma = \omega L/a_o$ and $\sigma = \omega L/V_c$). $V_c/a_o = 1.45$.

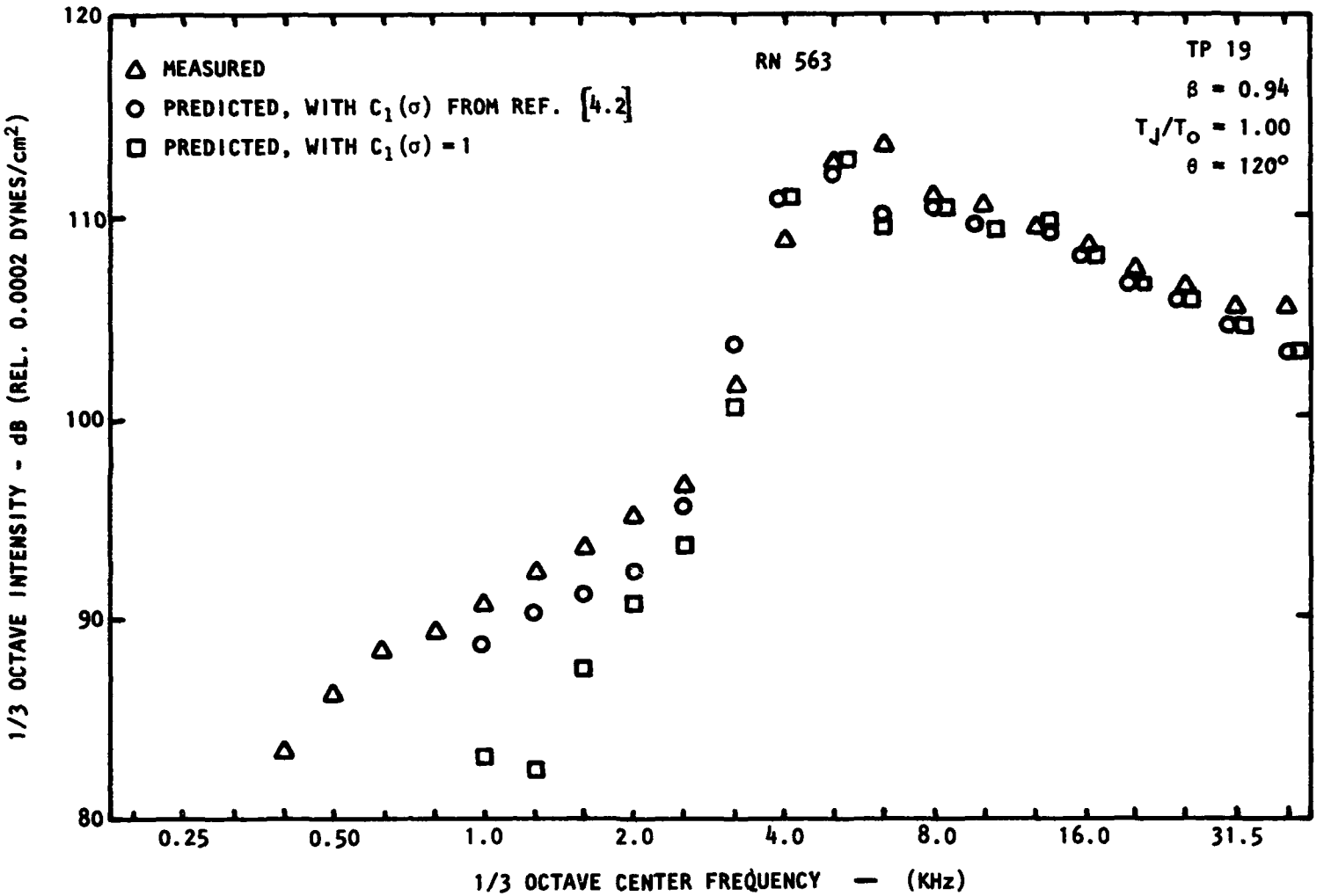

Figure 4.5 Effect of Correlation Coefficient Spectrum $C_1(\sigma)$ on Predicted Noise Spectrum.

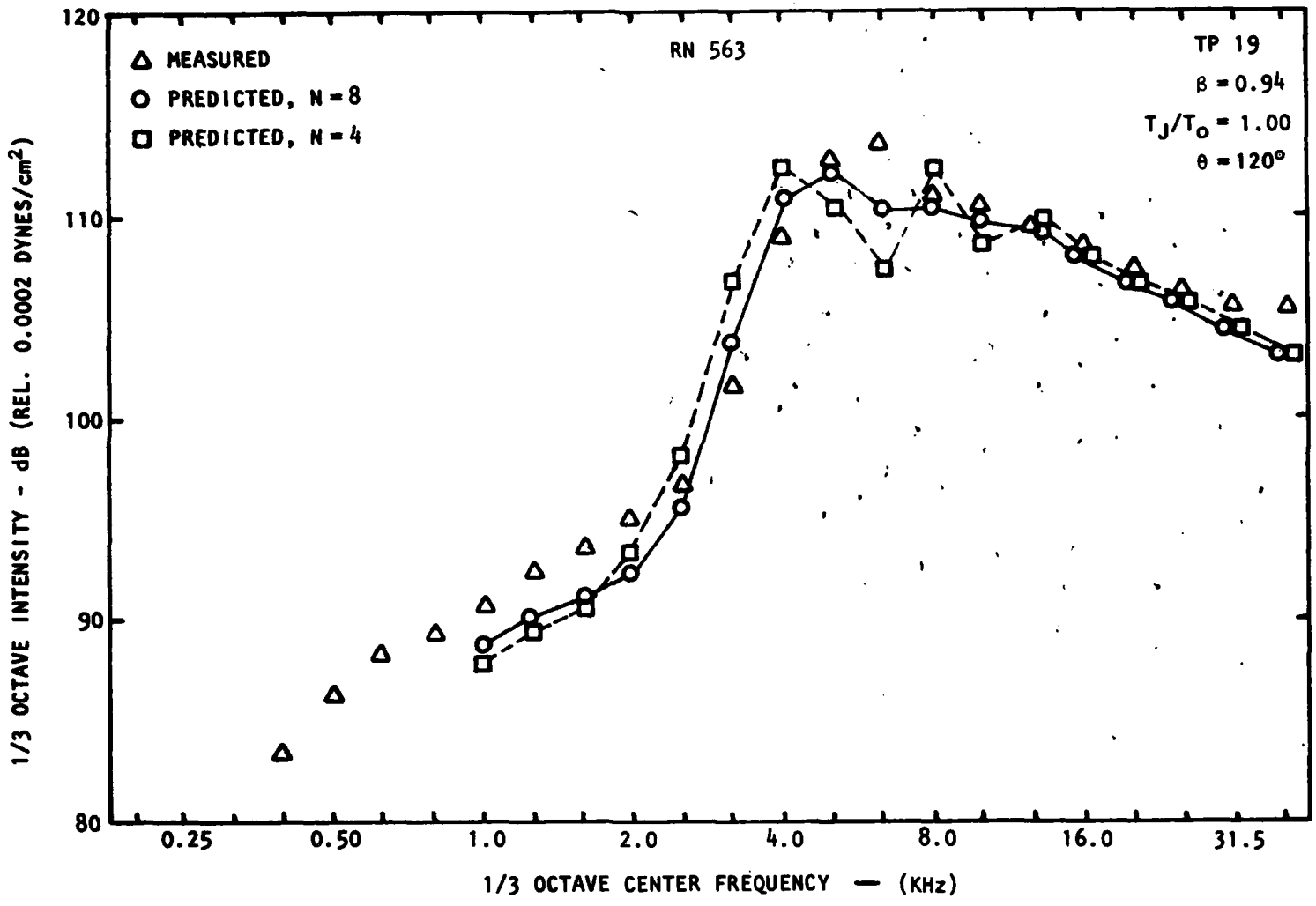

Figure 4.6 Effect of Number of Shocks (N) on Predicted Noise Spectrum.

significant effect at the higher frequencies. At low and mid-frequencies, reducing the value of N enhances the interference phenomenon. Of course, the measured spectra do not display this clear interference pattern. It was also found that as N decreases, the predicted peak frequency f_p decreases slightly and drifts away from the measured f_p. Hence, based on a large number of comparisons, it appears that the largest value of N (=8) is more appropriate.

4.5.4 Eddy Convection Velocity Constant and Shock Spacing Constant

After examining the effects of the first three parameters discussed above, several comparisons between predicted and measured spectra were conducted. For the prediction, the values of the remaining two jet flow parameters, namely the eddy convection velocity constant C and the average shock cell spacing constant K_o, were taken to be 0.7 and 1.1, respectively, as suggested by Harper-Bourne and Fisher [4.2] from their measurements in unheated shock-containing flows. It was found that the agreement between predicted and measured spectra was good although the predicted peak frequencies were in general slightly lower (of the order of one one-third octave band) than the measured peak frequencies. In order to resolve this problem, the effects of these two parameters, C and K, were examined in detail. Since the peak frequency is essentially controlled by these two parameters, it was felt that this discrepancy may have resulted from an incorrect choice of the values of these two constants.

This parametric study was conducted in two parts. In the first part, the values of K_o (average shock-cell spacing constant) and K_1 (first shock-cell spacing constant) were kept fixed at 1.10 and 1.31, respectively, and the eddy convection velocity, C, was increased from 0.70 to 0.87. In the second part, the values of K_o and C were kept unaltered (i.e., $K_o = 1.10$ and $C = 0.70$), and the first shock-cell spacing constant, K_1, was reduced from 1.31 to 1.05. It was found that in both cases, while there was some improvement in the prediction over certain areas (especially in the forward arc angles and at high frequencies), this improvement was in general accompanied by a deterioration in the prediction over other areas (especially at angles less than 90° and at lower frequencies). At that stage, it became apparent that rather than improving the prediction by introducing hypothetical values of such constants, which may not be physically realistic, it would be desirable to obtain these constants experimentally. This is discussed in the next subsection.

4.6 SHOCK-CONTAINING JET FLOW MEASUREMENTS

The aerodynamic measurements for shock-containing jets were conducted by using a two-inch diameter convergent nozzle operated over a range of temperatures for several supercritical pressure ratios. Both a Schlieren system and the laser velocimeter were used for this purpose. The measurements were mainly concentrated on obtaining the values of shock spacings and eddy convection velocities for input to the shock-associated noise prediction model.

4.6.1 Shock Positions

A typical Schlieren picture showing the shock structure in an underexpanded isothermal jet operated at a Mach number of 1.37 is given in Figure 4.7. The shock cells are clearly seen and their positions relative to the nozzle exit plane or the spacings between successive shocks may be readily determined. Shock spacings have been studied by other investigators in the past, and the results have indicated that the spacing is linearly proportional to β, which is defined as $(M_J^2 - 1)^{\frac{1}{2}}$. The locations ($x_1$, x_2, x_3, etc.) of successive shocks measured in the present work are plotted against the pressure ratio parameter β in Figure 4.8. For unheated and isothermal jet operating conditions, the shock positions do follow a linear variation with β. For unheated jets, Harper-Bourne and Fisher [4.2] suggested a relationship for the shock spacings, which is given by

$$L_n = L_1 \left(1 - (n-1) \frac{\Delta L}{L_1}\right)$$

where $L_1 = 1.31\, D\beta$ and $\Delta L/L_1 = 0.06$. Lines representing this equation are also shown superimposed on the measurement points in Figure 4.8. Within the accuracy with which the shock positions can be determined experimentally, this relationship agrees with the present measurements reasonably well.

The variation of shock spacings with jet temperature ratio T_J/T_o is shown in Figure 4.9. Heating apparently has a small effect on the shock spacings initially, but further heating reduces the shock spacings noticeably.

4.6.2 Mean Velocities and Turbulence Intensities

The mean velocities and the turbulence intensities in the axial and radial directions were measured with the laser velocimeter. For an isothermal jet operated at $M_J = 1.37$ (i.e. $\beta = 0.94$), the distribution of the axial mean velocity along the jet centerline is shown in Figure 4.10. From the nozzle exit plane to about $x/D = 6.5$ (which is the potential core length of an equivalent *shock-free* jet), the magnitude of the mean velocity oscillates. The oscillations seem to center around a mean value which is very close to the exit velocity of an equivalent shock-free jet (1530 ft/s). The positions and the extent of the shock cells observed in the corresponding Schlieren pictures are also sketched in Figure 4.10. It appears that the apex and the end of each shock cell lie close to the trough and the peak, respectively, of each cycle of the mean velocity oscillation.

The above features for measurements along the jet centerline are also observed for measurements at other radial locations. Figure 4.11 shows the distribution of the axial mean velocity along the jet lipline (i.e. $r/D = 0.5$). The oscillations and the correspondence between these oscillations and the shock cells are evident in this case also. It is observed, however, that the oscillations here extend to a greater distance downstream of the nozzle exit plane.

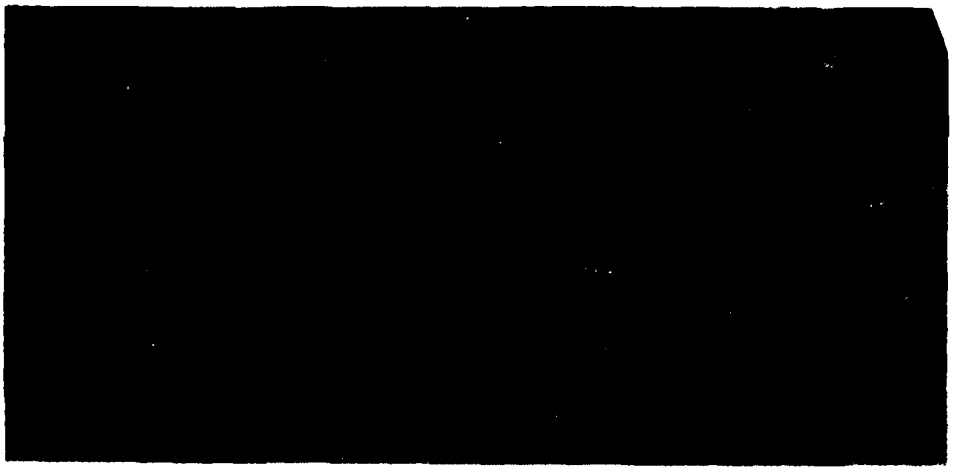

Figure 4.7 Schlieren Picture of a Shock-Containing Jet: $M_J = 1.37$, $T_J/T_o = 1.0$.

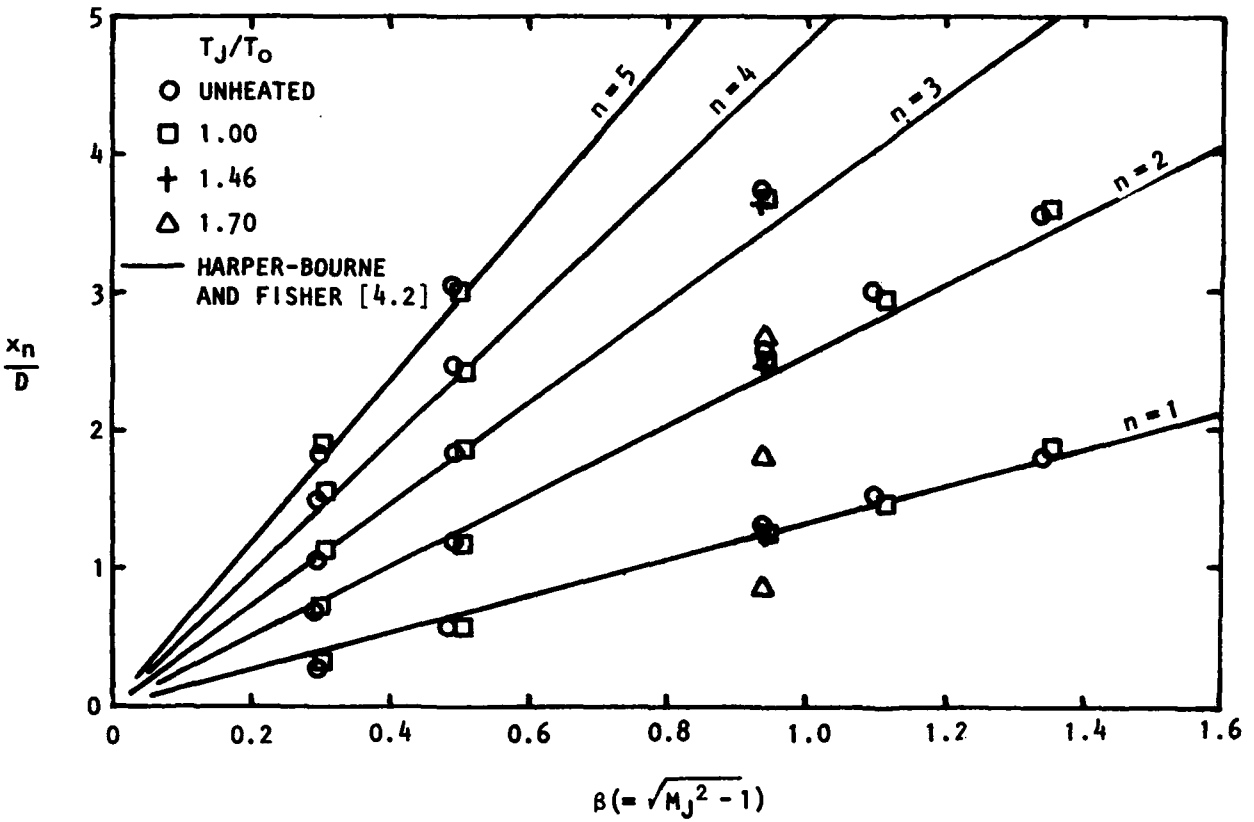

Figure 4.8 Variation of Shock Positions With Pressure Ratio Parameter β.

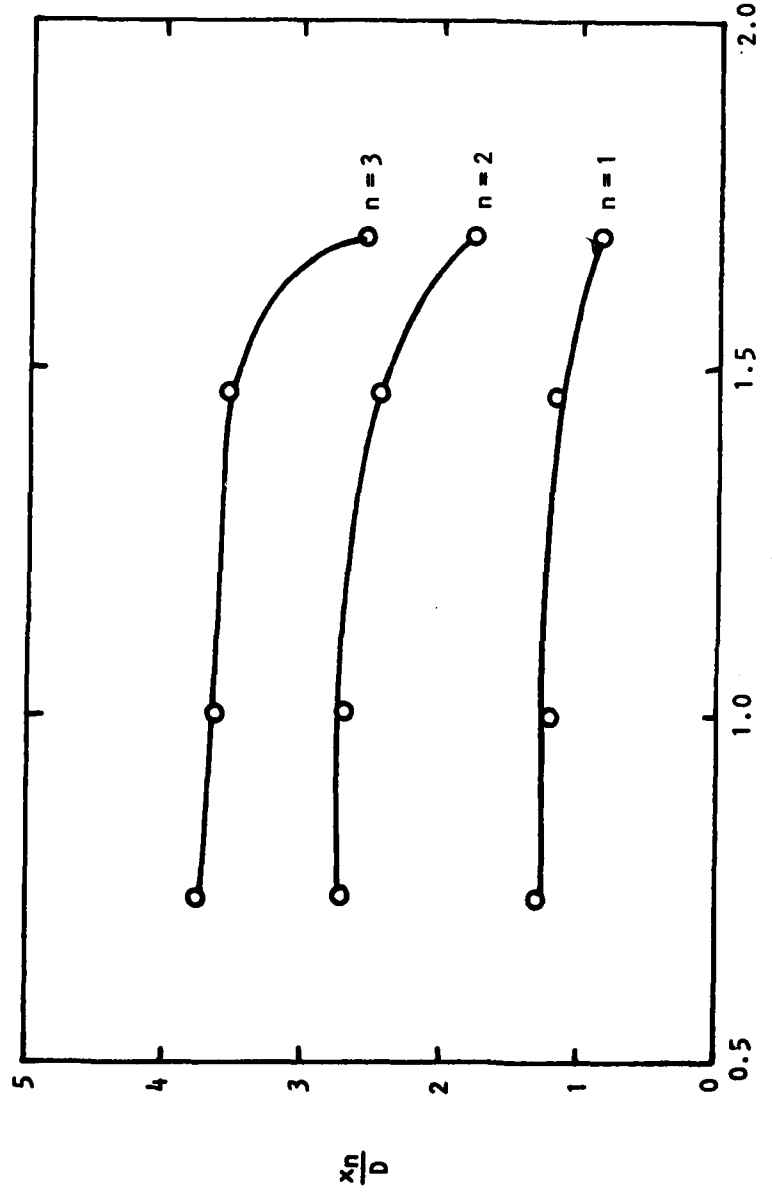

Figure 4.9 Variation of Shock Positions with Temperature Ratio T_J/T_o: $\beta = 0.94$.

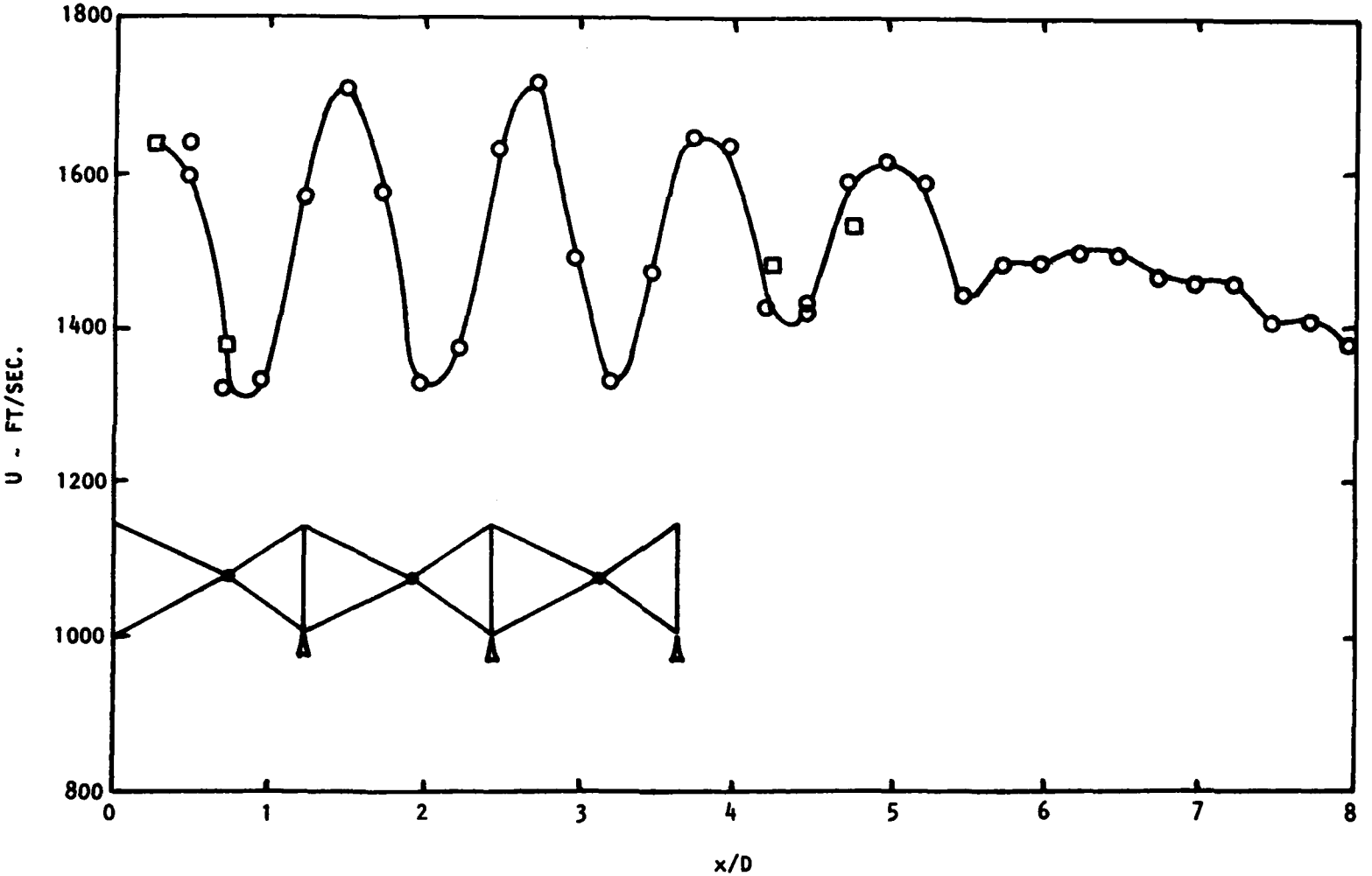

Figure 4.10 Variation of Axial Mean Velocity With x/D Along Jet Centerline: $M_J = 1.37$, $T_J/T_o = 1$.

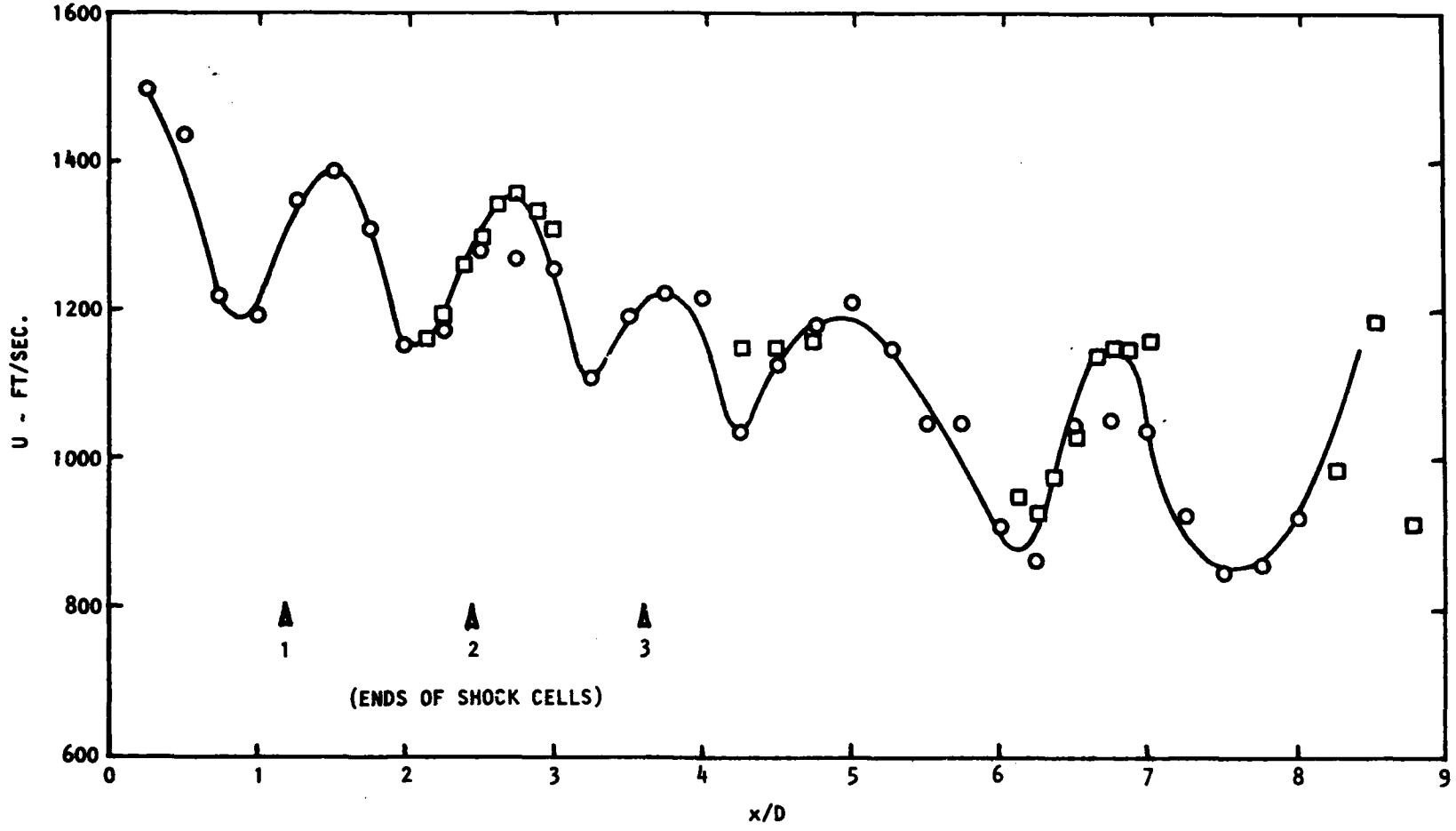

Figure 4.11 Variation of Axial Mean Velocity with x/D Along Jet Lipline: $M_J = 1.37$, $T_J/T_o = 1.$

The lipline distribution of the radial mean velocity is shown in Figure 4.12. It also displays the oscillatory behavior associated with the positions of the shock cells, as discussed above for the axial mean velocity.

The lipline distributions of the axial and radial turbulence levels for the Mach 1.37 isothermal jet are shown in Figure 4.13. In both cases, the levels rise with axial distance, but while the u' results are characterized by peaks and troughs, the v' results appear to rise in reasonably well defined steps. The peaks in the u' component and the steps in the v' component appear to coincide with the locations of the apex of the conical shock elements observed in the Schlieren pictures. A similar behavior was found to exist for turbulence data acquired on the jet centerline.

4.6.3 Eddy Convection Velocities

Some two-point LV measurements were conducted to determine the eddy convection velocities in shock-containing jets. Figure 4.14 shows the cross-correlation of u' signals detected at two points located along the lipline of a Mach 1.12 isothermal jet. The two points are separated by a fixed distance of 0.75 D, and their average distance from the nozzle exit plane is about 1.6 D. This is the closest upstream position at which meaningful results could be obtained in the present experiments. A very low peak is visible and based on the time delay of this peak, a convection velocity of 0.75 V_J is obtained, where V_J is the jet exit velocity of an equivalent shock-free jet.

The values of convection velocity measured at other downstream stations are shown in Figure 4.15. Over the limited range of x/D considered here, there is a tendency for V_C/V_J to fall with x/D. However, the fall is very gradual, and the convection velocity may be reasonably assumed to have an average value of 0.7 V_J.

At Mach 1.37, meaningful results were not obtainable at small values of x/D. In fact, the correlograms obtained as far downstream as x/D = 3.4 showed no significant peak which might allow the convection velocity to be determined. The reasons for the poor correlation in the Mach 1.37 case is not clear, but it is suspected that it may be associated with the jittering of the shock cells with time and the accompanying large fluctuations in velocity tending to swamp the velocity fluctuations due to turbulence. In the upstream region where the shock is stronger, the effect is more adverse. This seems to be borne out by the good cross-correlation results obtained at x/D = 4.8 D on the jet axis, as shown in Figure 4.16. A pronounced peak is obtained by cross-correlating the v'-signals, and the corresponding value of convection velocity is 0.69 V_J.

4.6.4 Summary

To summarize, the measurements of shock spacings and eddy convection velocities obtained by using a Schlieren system and a laser velocimeter are essentially in agreement with the values obtained previously by Harper-Bourne and Fisher [4.2], and which are used in the shock-associated noise prediction scheme.

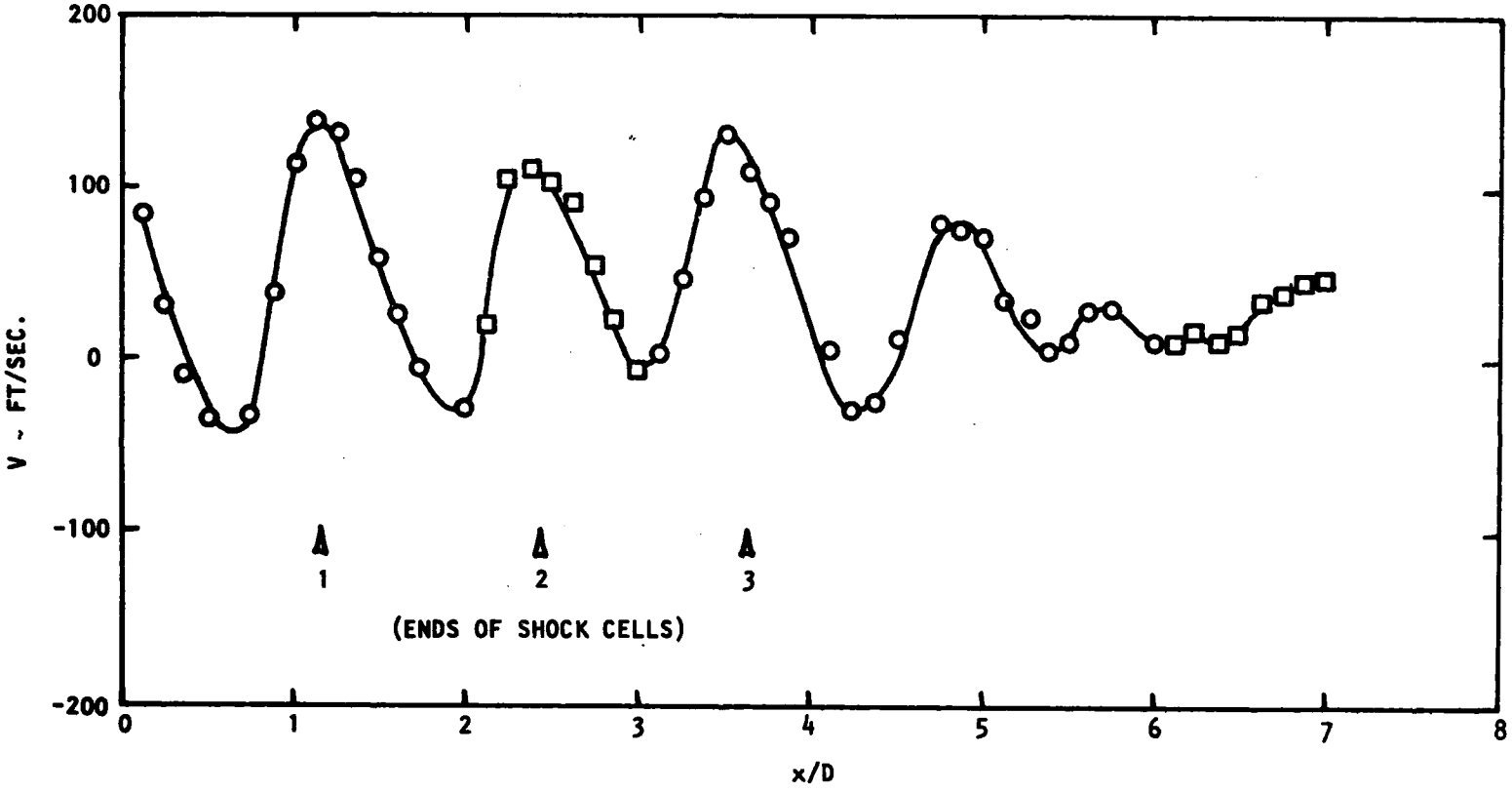

Figure 4.12 Variation of Radial Mean Velocity with x/D Along Jet Lipline: $M_J = 1.37$, $T_J/T_o = 1$.

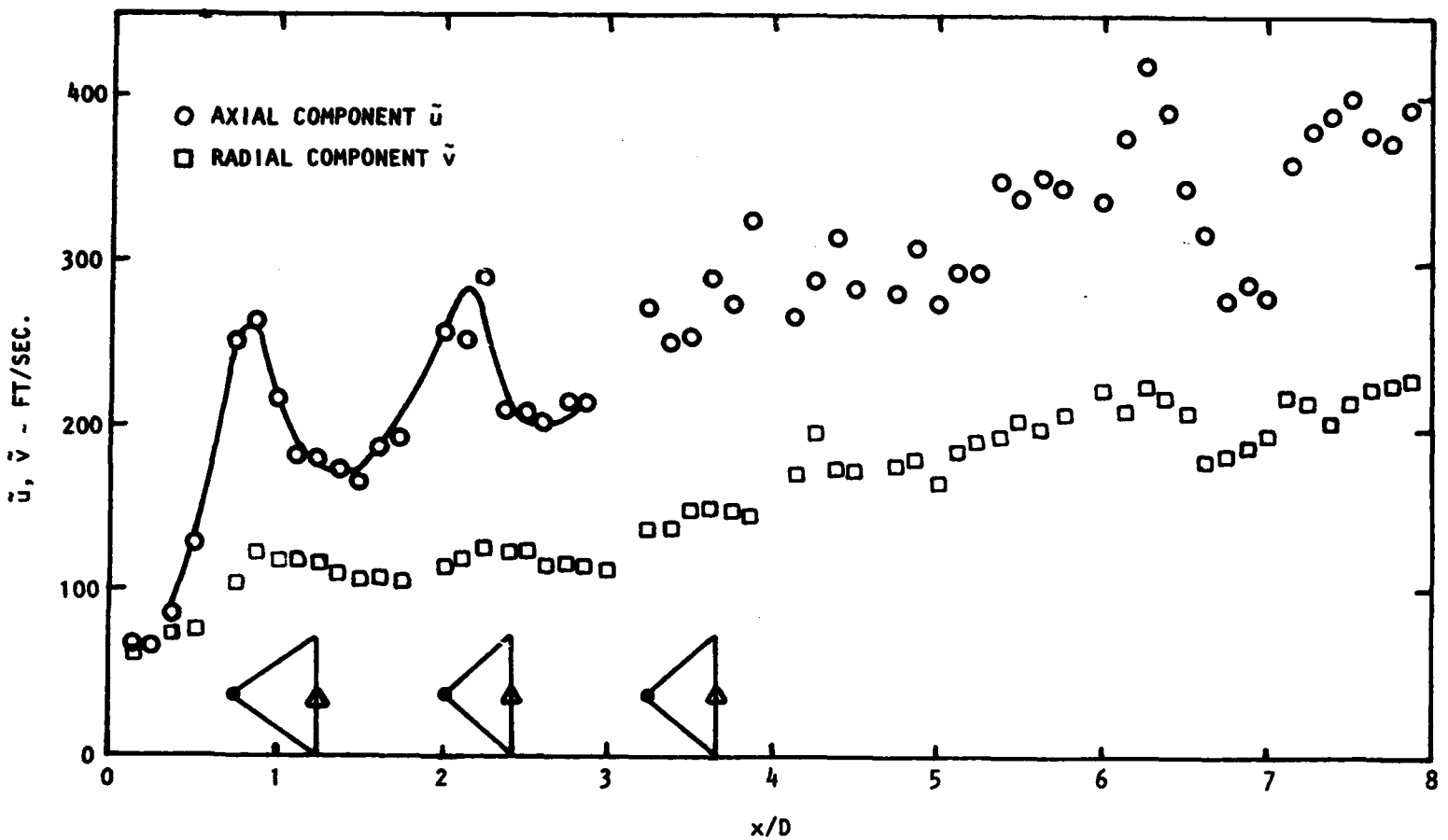

Figure 4.13 Variation of Axial and Radial Turbulence Level with x/D Along Jet Lipline: $M_J = 1.37$, $T_J/T_o = 1$.

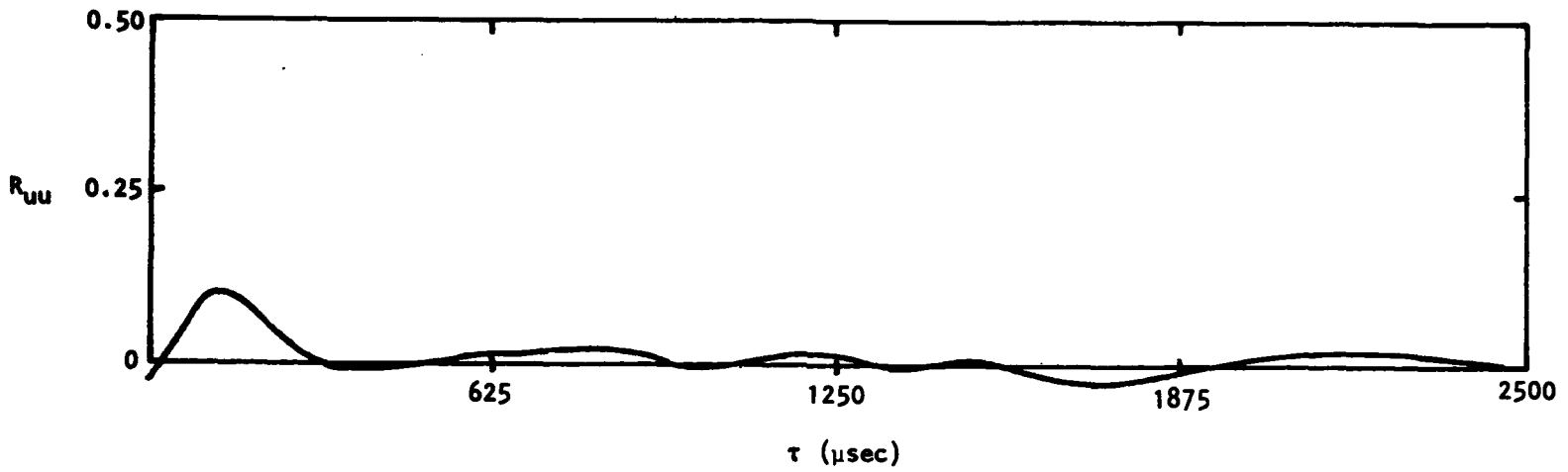

Figure 4.14 Cross-Correlation of u'-Signals at $x/D \doteq 1.6$: $\Delta x = 0.75\,D$, $r/D = 1.0$, $M_J = 1.12$, $T_J/T_o = 1$.

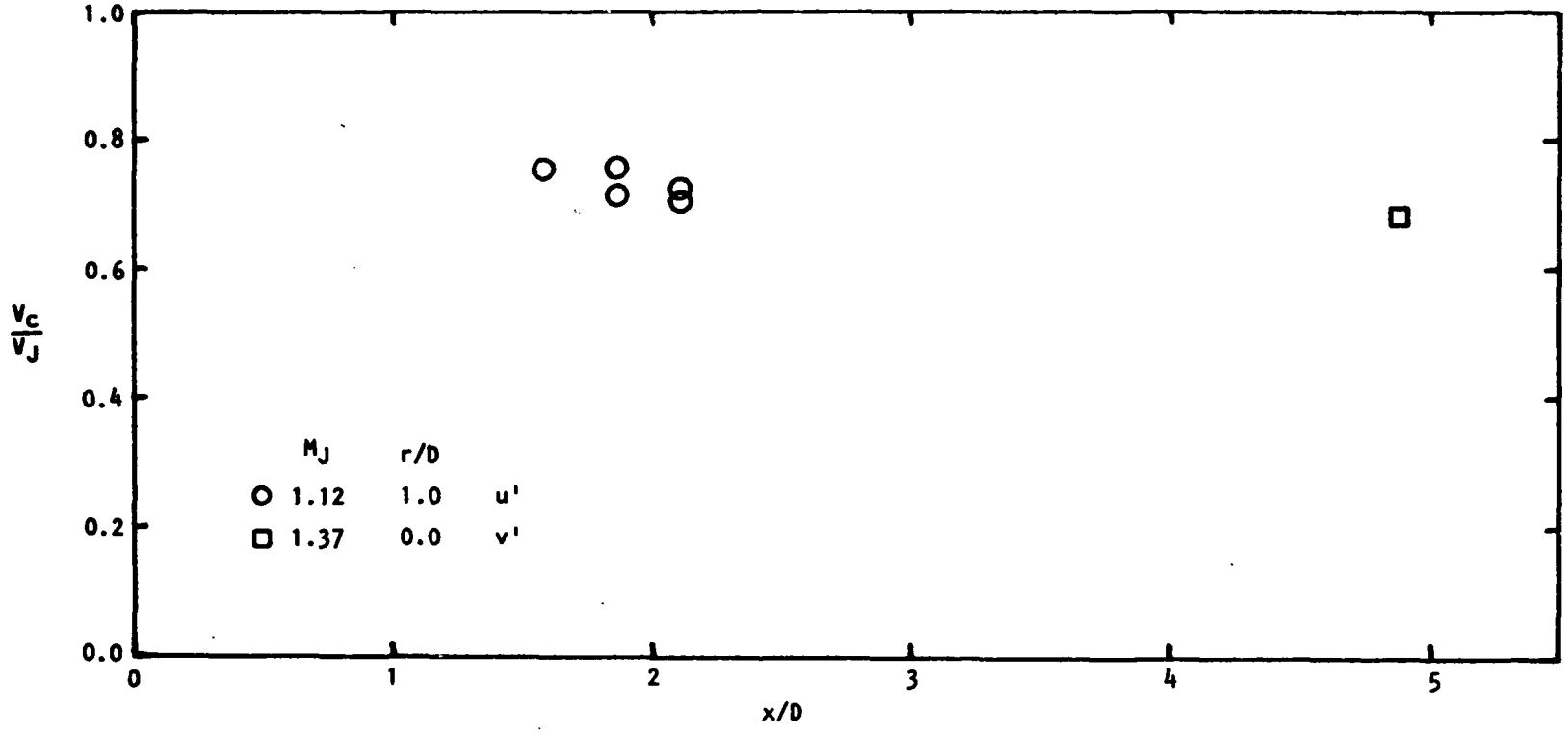

Figure 4.15 Variation of Convection Velocity V_c With x/D.

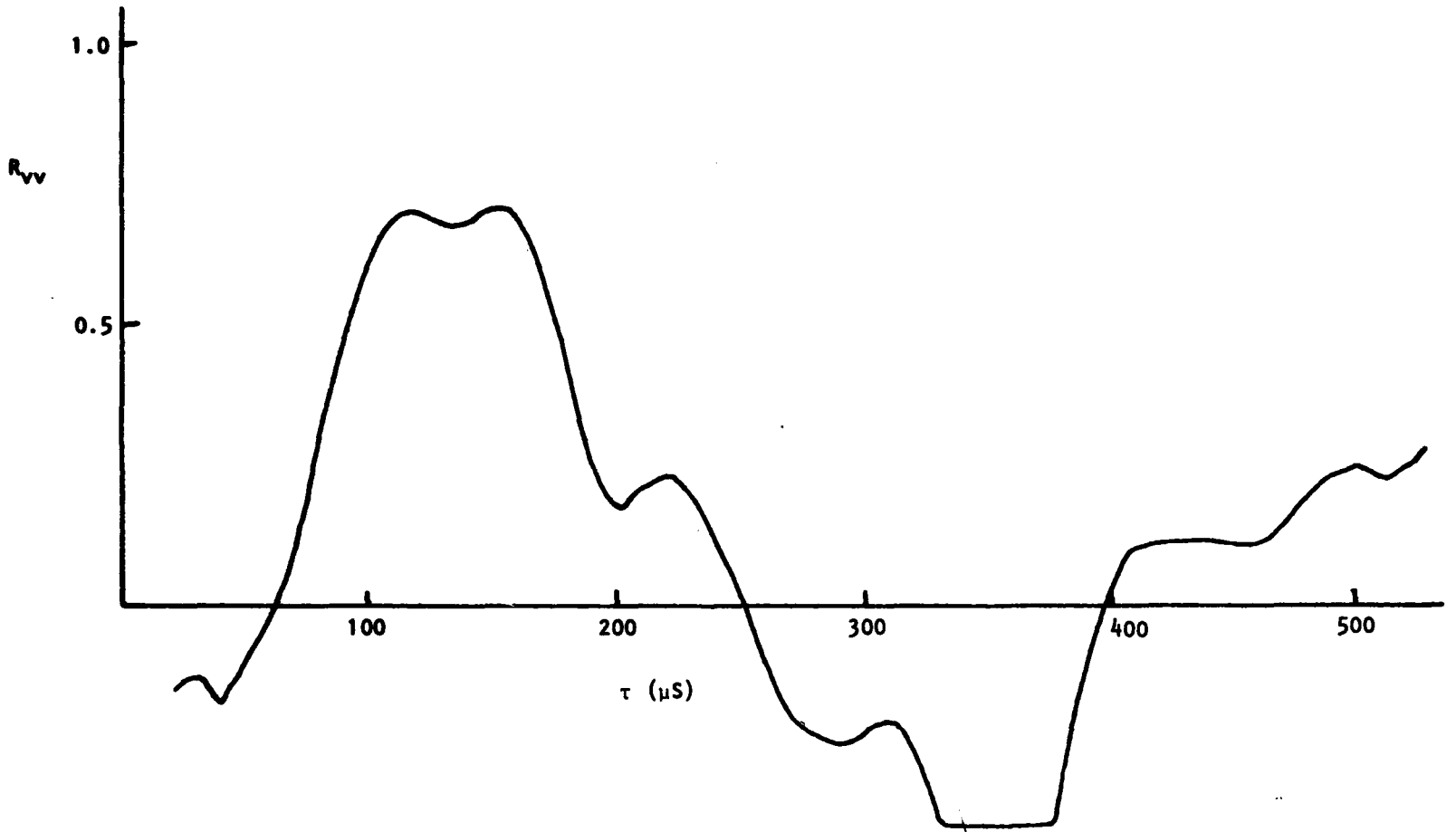

Figure 4.16 Cross-Correlation of v^1Signals at x/D = 4.8, r/D = 0: $M_J = 1.37$, $T_J/T_O = 1$.

4.7 FURTHER ASSESSMENT OF SHOCK-ASSOCIATED NOISE MODEL

In the course of the parametric evaluation study summarized in Section 4.5, although the comparisons between measured and predicted spectra evaluated the validity of the model as functions of (i) pressure ratio parameter β, (ii) jet exit temperature ratio T_J/T_o, and (iii) observer angle θ, these comparisons were rather limited, and only a few selected jet operating conditions were considered in this initial evaluation of the prediction model. It was decided, therefore, to extend the comparisons between measured and predicted spectra to cover the entire envelope of jet operating conditions for which shock-associated noise data were acquired in the previous contract [4.1]. These comparisons were conducted for the following twelve jet exhaust conditions (i.e. combinations of β and T_J/T_o):

TP	β (Nominal)	T_J/T_o (Nominal)
4	0.50	0.80 } $T_R/T_o = 1$
8	0.94	0.73 } $T_R/T_o = 1$
10	1.34	0.64 } $T_R/T_o = 1$
15	0.50	1.00
19	0.94	1.00
21	1.34	1.00
26	0.50	1.82
30	0.94	1.82
32	1.34	1.82
37	0.50	2.27
41	0.94	2.27
43	1.34	2.27

Angles: Rear Arc: $\theta = 15°, 30°, 45°, 60°, 75°, 90°$

Forward Arc: $\theta = 90°, 105°, 120°, 135°$

Thus, the measured and predicted spectra were compared for twelve TP's and ten values of θ, giving a total of 120 spectral comparisons.

The purpose of these extensive comparisons was two-fold: (1) to examine the validity of the prediction model over the entire envelope of supercritical jet operating conditions of practical interest and, hence, to detect any consistent discrepancies that may be present, and (2) to assess the influence of flow-acoustic interaction phenomena, which can be expected to yield significant overestimations in the spectral levels at small angles to the jet axis. The major inferences related to these two aspects are summarized below.

(1) The prediction model overestimates the spectrum levels over two regimes: (i) for unheated jets and (ii) for values of β greater than approximately 1.1 (corresponding to pressure ratios above approximately 3.6). The latter was perhaps to be expected since it was observed previously [4.1] in the overall SPL results, that, while the intensity was proportional to β^4 for low values of β, it tended to level off for values of β beyond approximately 1.1. Although no physical explanation of this effect is

apparent at the present time, for prediction purposes, it is felt that this behavior can be accounted for by a simple adjustment of the β dependence for shock-associated noise at values of β beyond 1.1. This will be examined further in Section 4.8, where the experimental data will also be used to correct the overpredictions for unheated jet conditions. At this point, however, it should be remembered that for application to aircraft engines, the current overestimation of shock-associated noise from *unheated* jets is of no practical significance.

(2) From our existing knowledge of flow-acoustic interaction effects in the case of turbulent mixing noise, it can be crudely concluded that in the case of shock-associated noise, these effects may play a dominant role for radiation at small angles to the jet exhaust (inside the so-called cone of silence).

The extensive comparisons discussed above show that although these effects are indeed present in the case of shock-related noise, they can be neglected when we consider the prediction aspects of the model. The reasons are quite simple. The spectral comparisons show that the overprediction due to these flow-acoustic interaction effects occurs only over a limited angular range, usually for angles less than approximately 30° to the downstream jet axis. Furthermore, at these angles, the total sound field in almost all cases is dominated either by the turbulent mixing noise contribution, or by noise from large-scale turbulence structure. Thus, it appears that even if one wanted to incorporate the flow-acoustic interaction effects, based on fundamental principles, in the shock noise prediction model, a quantitative assessment based on *measured* levels is practically impossible when the shock noise contribution at small angles is masked by other noise sources.

4.8 IMPROVEMENTS USING EXPERIMENTAL RESULTS

In the assessment of the validity of the shock noise model discussed in the preceding subsection, the predicted levels were compared with the *total* measured levels. That is, the measured levels contained the turbulent mixing noise contribution in addition to the shock noise contribution, and it was assumed that in areas where the total noise appeared to be dominated (or controlled) by shock noise, the comparison would be valid. It was subsequently felt that in order to improve the prediction scheme in the two specific areas mentioned above [i.e. to verify the overprediction (i) at values of β greater than approximately 1.1, and (ii) for unheated jets], it would be necessary to extract true shock-associated noise levels from the total noise levels. This can be achieved by subtracting "the noise levels from fully-expanded jets" from "the noise levels from under-expanded jets" at identical jet operating conditions (pressure ratio and temperature ratio).

Using the experimental results, the true OASPL's due to shock-associated noise were therefore obtained, and the scaling of OASPL with the pressure ratio parameter β was re-examined separately for the heated and the unheated conditions.

The variation of OASPL of shock-associated noise (i.e. total noise minus turbulent mixing noise) with β for all *heated* jet conditions is plotted in Figure 4.17. At each value of β, there are nine points - corresponding to three angles $\theta = 90°$, 120°, 135° for each of the three temperature ratios $T_J/T_O = 1.00$, 1.82, and 2.27. For $\beta \leq 1$, the OASPL is proportional to β^4, whereas for $\beta \geq 1$, the OASPL is proportional to β^2, as shown by the two straight lines drawn through the experimental points. At low values of β, the experimental points tend to depart from the β^4 dependence for higher values of T_J/T_O and lower values of observer angle θ. The reason for this is that at these conditions (i.e. high T_J/T_O, low θ), the turbulent mixing noise contribution to the total noise is comparable to the shock noise contribution. Hence, when mixing noise is subtracted from total noise to obtain shock noise levels, the answer is quite sensitive to the decibel levels used in the subtraction, and it cannot be relied upon. Of course, this limitation disappears at higher values of β where the shock noise component is much stronger than the mixing noise component. For the sake of completeness, however, all data points are included in the figure.

A similar plot for the variation of OASPL with β for the *unheated* jet conditions is given in Figure 4.18. In this case, the OASPL is proportional to β^4 for $\beta \leq 1$, and for values of β beyond unity, the OASPL appears to scale on β rather than on β^2 for the heated conditions shown in Figure 4.17. For small values of β (<0.4), the points depart from the β^4 dependence, and the comments made earlier apply here as well.

For prediction purposes, the results shown in Figures 4.17 and 4.18 provide the following relationships for the OASPL of shock-associated noise:

(1) Heated jets:

(a) $\beta \leq 1$: $\text{OASPL} = 157.5 - 20 \log (R/D) + 40 \log \beta$ (dB)

(b) $\beta > 1$: $\text{OASPL} = 157.5 - 20 \log (R/D) + 20 \log \beta$ (dB)

(2) Unheated jets:

(a) $\beta \leq 1$: $\text{OASPL} = 155.5 - 20 \log (R/D) + 40 \log \beta$ (dB)

(b) $\beta > 1$: $\text{OASPL} = 155.5 - 20 \log (R/D) + 10 \log \beta$ (dB)

Prior to this stage, the prediction model utilized the following relationship for OASPL,

$$\text{OASPL} = 159 - 20 \log (R/D) + 40 \log \beta \quad \text{(dB)}$$

which was derived in the previous contract by using total noise levels and assuming that these total noise levels were representative of the shock noise levels. Furthermore, this relationship or scaling formula was taken to apply to all values of β and jet temperatures.

Using the more accurate (or more realistic) relationships, obtained above by re-examining the experimental results, the prediction scheme was modified. The improved scaling laws were incorporated to correct the

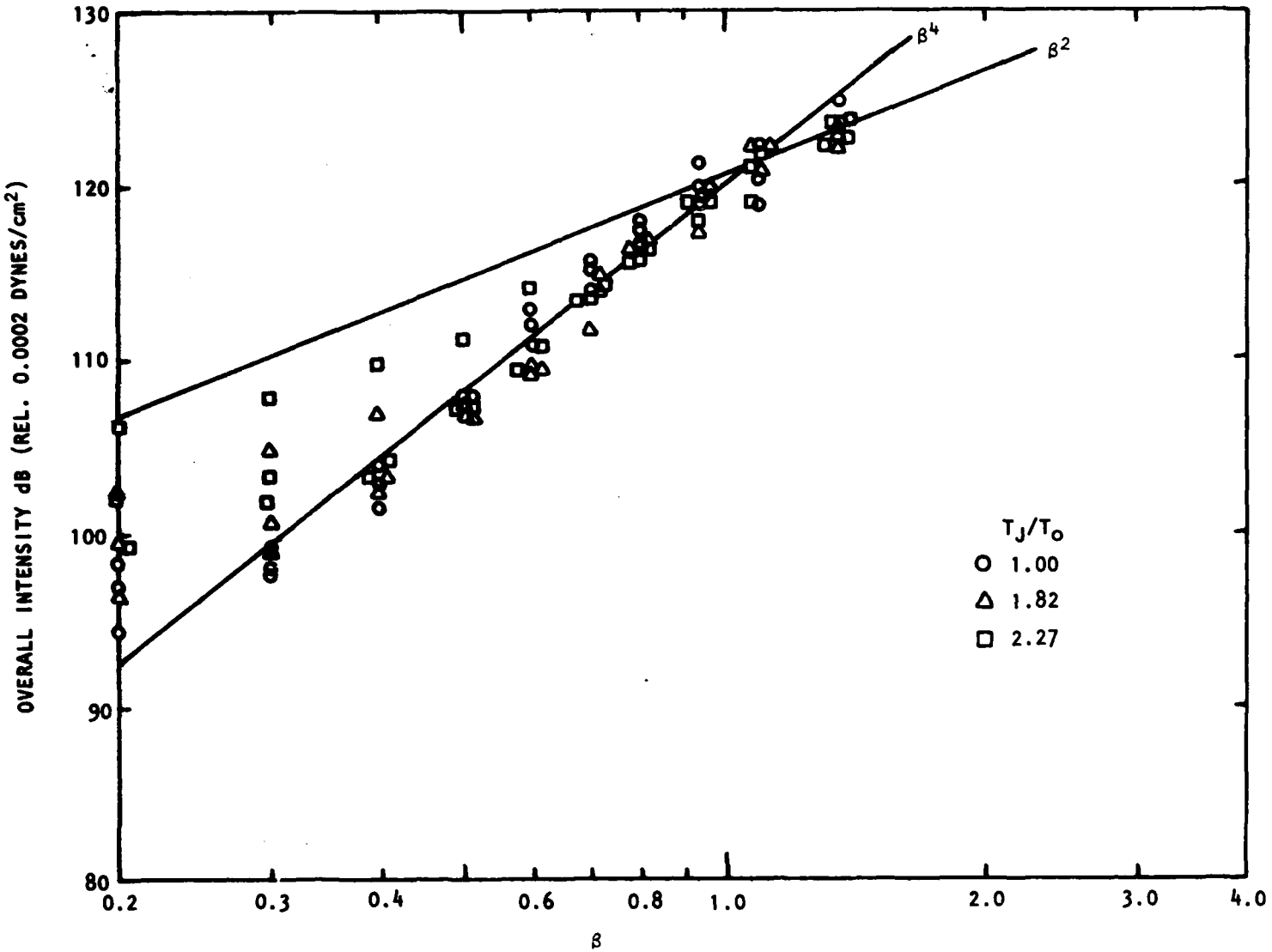

Figure 4.17 Variation of OASPL of Shock-Associated Noise (Total Noise Minus Turbulent Mixing Noise) With Pressure Ratio Parameter β for *Heated* Jets: Results at Three Angles, θ = 90°, 120°, 135°.

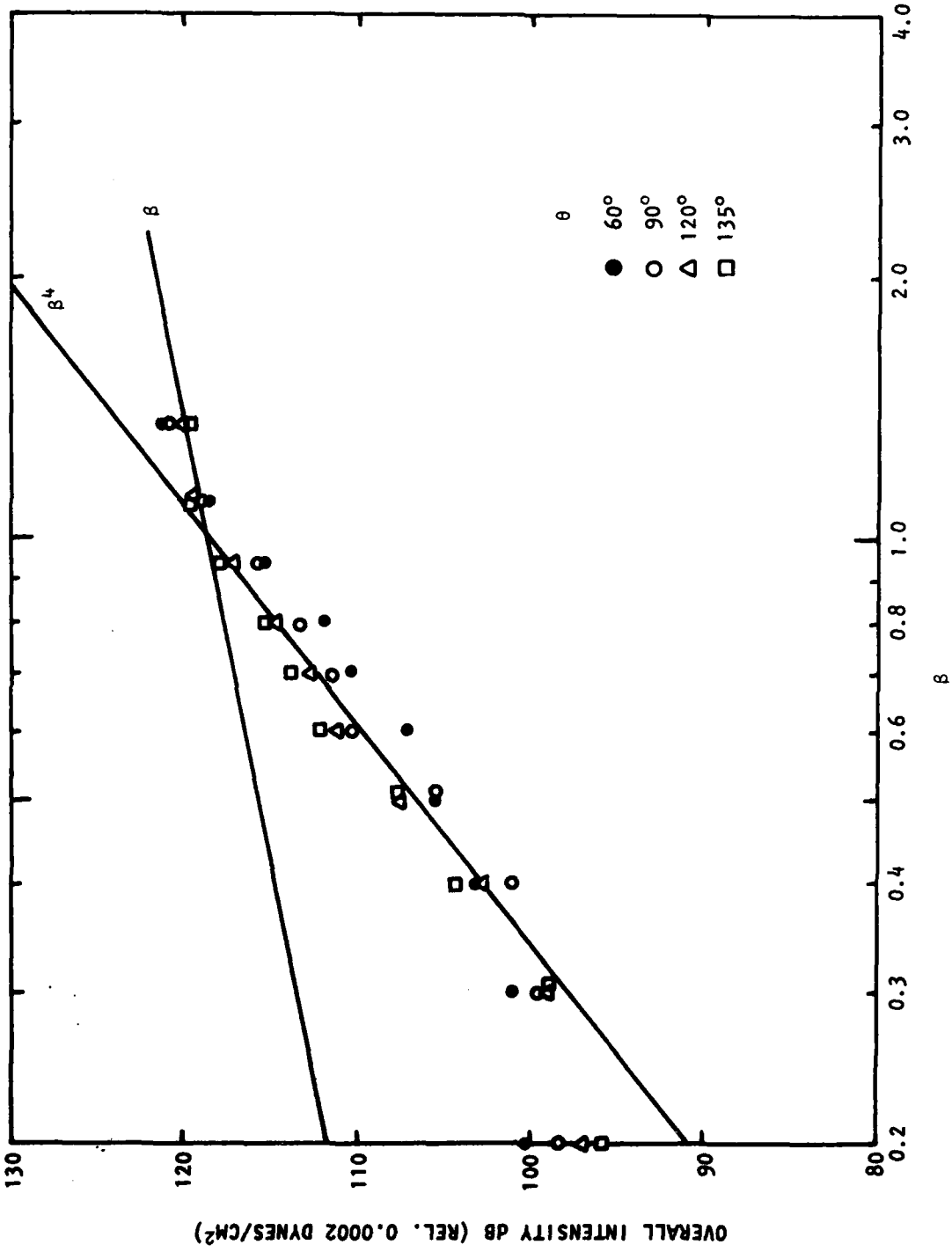

Figure 4.18 Variation of OASPL of Shock-Associated Noise (Total Noise Minus Turbulent Mixing Noise) With Pressure Ratio Parameter β for *Unheated* Jets.

overprediction at unheated conditions and for $\beta > 1$. The final version of the prediction scheme is documented formally in the next subsection.

4.9 FINAL PREDICTION SCHEME AND COMPARISON WITH EXPERIMENT

4.9.1 Prediction Scheme

A method for the prediction of broadband shock-associated noise from a (static) single convergent nozzle operated at supercritical pressure ratios is presented below. Taken together with the turbulent mixing noise prediction method discussed in Section 2, it enables the prediction of total noise from a shock-containing under-expanded jet. The total noise spectrum can be obtained by adding the individual predicted spectra for the mixing noise and the shock noise components.

The 1/3-octave SPL spectrum of shock-associated noise is given by

$$SPL(R,\theta,f_c) = 10 \log_{10}\left[1 + \frac{4}{Nb}\sum_{i=1}^{N-1}\left[C_1(\sigma)\right]^{1/2} \sum_{s=0}^{N-(i+1)} \frac{1}{q_{is}\sigma}\left[\cos(q_{is}\sigma)\,\sin(bq_{is}\sigma/2)\right]\right] + 10 \log_{10}\left[\left(\frac{D}{R}\right)^2 \beta^n\right] + 10 \log_{10}\left[\frac{b\sigma}{K_o}\right] + H_o(\sigma) \qquad (4.1)$$

where

$$q_{is} = \frac{(K_1/K_oC)\,i}{(V_J/a_o)}\left[1 - 0.06\left(s + \frac{i+1}{2}\right)\right]\left(1 - C\,\frac{V_J}{a_o}\cos\theta\right) \qquad (4.2)$$

$H_o(\sigma)$ = group source strength spectrum

$C_1(\sigma)$ = correlation coefficient spectrum

} master spectra

$$\sigma = \omega_c L/a_o \qquad (4.3)$$

$$L = K_o D\beta \qquad (4.4)$$

$$\beta = (M_J^2 - 1)^{\frac{1}{2}} \qquad (4.5)$$

$$\omega_c = 2\pi f_c \qquad (4.6)$$

R = observer distance from nozzle exit plane

D = nozzle diameter

θ = observer angle relative to jet exhaust

f_c = one-third octave band center frequency

N = number of shocks (=8)

b = proportional bandwidth constant (=0.2316 for one-third octave band spectrum)

K_o = average shock spacing constant (=1.10)

K_1 = first shock spacing constant (=1.31)

C = eddy convection velocity constant (=0.70)

a_o = ambient speed of sound

V_J = fully-expanded jet exit velocity (function of nozzle pressure ratio and total temperature ratio)

M_J = fully-expanded jet Mach number

4.9.1.1 Master spectra

Equation (4.1) requires two "master" spectra as primary input for the prediction. The first spectrum is called the "group source strength spectrum," and it represents the total "equivalent source strength" of the shock-turbulence interaction process occurring at all shock locations. The second spectrum is called the "correlation coefficient spectrum," and it defines the degree to which the fluctuations at adjacent shock locations are correlated. These two spectra are given in Figure 4.19.

The $C_1(\sigma)$ spectrum can be used for heated as well as unheated jet conditions. The $H_o(\sigma)$ spectrum shown here should be used for heated jets only. A heated jet is defined here as a jet having static temperature ratio T_J/T_o greater than 0.9. For prediction at unheated conditions ($T_J/T_o < 0.9$), the $H_o(\sigma)$ spectrum presented here should be reduced in level by 2 dB at all values of σ.

4.9.1.2 Pressure ratio dependence

The exponent n of the pressure ratio parameter β in Equation (4.1) takes the following values:

$\beta \leq 1.0$, heated and unheated jets: $n = 4$

$\beta > 1.0$, heated jet ($T_J/T_o \geq 0.9$): $n = 2$

$\beta > 1.0$, unheated jet ($T_J/T_o < 0.9$): $n = 1$

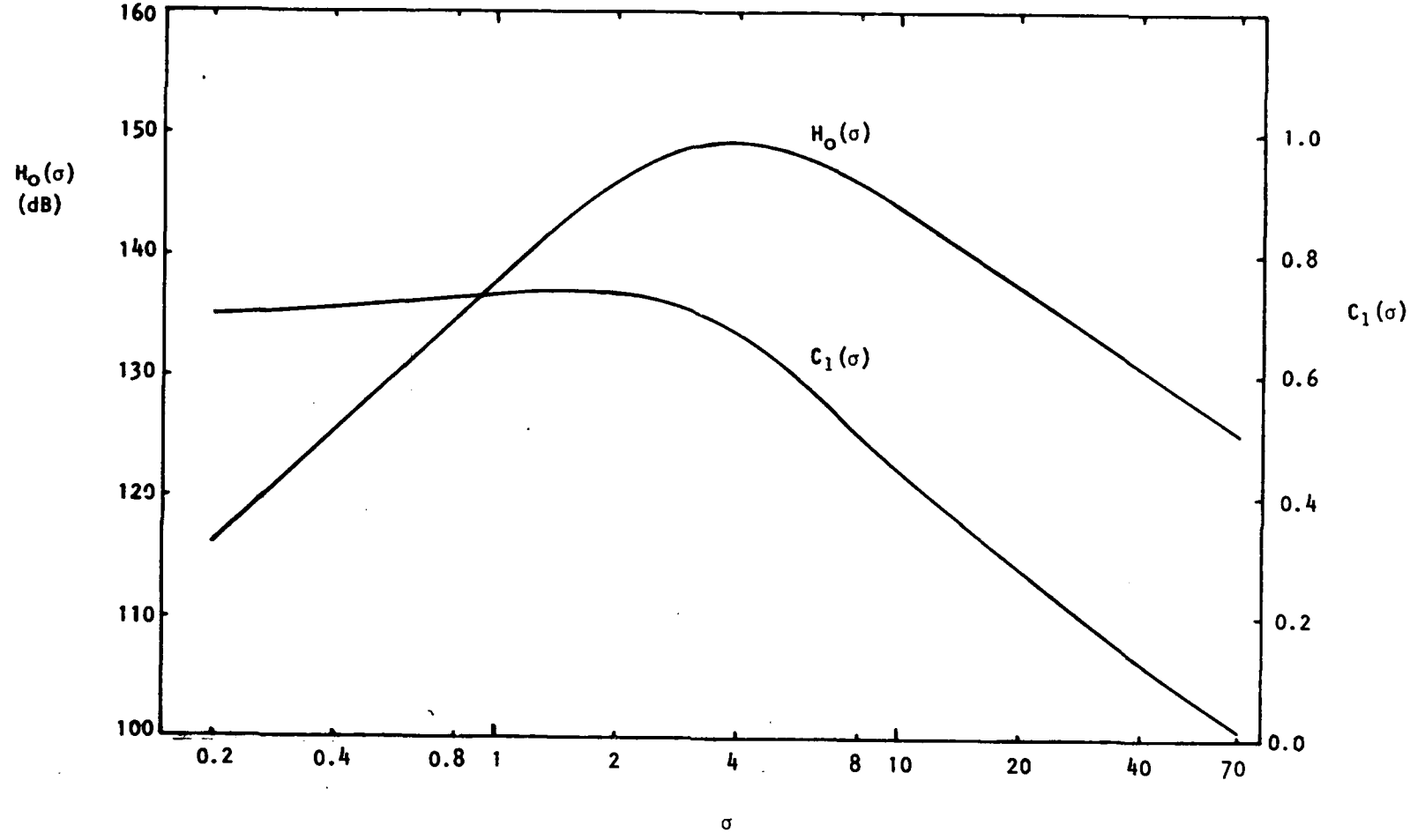

Figure 4.19 Master Spectra for Shock-Associated Noise Prediction.

4.9.1.3 Overall SPL prediction

It is recommended that the OASPL's for shock-associated noise should strictly be predicted by adding the individual 1/3-octave SPL's. However, an approximate prediction of OASPL can also be obtained by using the empirical relationships (which are independent of angle θ) given in Section 4.8.

4.9.1.4 Angular range of application

For heated jets (static temperature ratios T_J/T_O greater than approximately 0.9 or total temperature ratios T_R/T_O greater than approximately 1.1), the prediction method is applicable for $\theta \geq 30°$. For unheated jets, it is applicable for $\theta \geq 50°$. For smaller angles, the measured total spectrum is normally dominated by turbulent mixing noise and/or large-scale noise, and the shock noise contribution should be neglected for prediction purposes.

4.9.2 Comparison With Experiment

The shock-associated noise prediction scheme has been incorporated in the unified jet noise prediction program, and the purpose of this subsection is to show some typical comparisons between measured and predicted spectra from supersonic jets. Each comparison plot shown in Figures 4.20 through 4.30 contains four spectra as follows:

⊙ Measured - total noise

——— Predicted - total noise

———— Predicted - turbulent mixing noise

– – – – – Predicted - shock-associated noise

Variation with β: The comparison between measured and predicted spectra as a function of the pressure ratio parameter β is shown in Figures 4.20 through 4.22. The observer angle and the jet temperature ratio are kept fixed at $\theta = 135°$ and T_J/T_O (nominal) = 1.82, respectively.

Variation with T_J/T_O: Likewise, the comparison between measured and predicted spectra as a function of temperature ratio T_J/T_O is shown in Figures 4.23 through 4.26. In this case, the observer angle and the pressure ratio parameter are kept fixed at $\theta = 135°$ and β (nominal) = 1.34, respectively.

Variation with θ: Finally, the comparison between measured and predicted spectra as a function of the observer angle θ (relative to the jet exhaust) is shown in Figures 4.27 through 4.30 for the jet operated at $\beta = 0.94$ and $T_J/T_O = 2.26$.

It can be seen that although there are some small differences between measured and predicted results, the agreement between the two in general is very good. The shock-associated noise prediction scheme, when combined with the turbulent mixing noise prediction, is capable of predicting the majority

of noise characteristics of shock-containing under-expanded jets. In view of the fact that the measured spectrum shapes of shock-associated noise are somewhat sensitive (especially if the screech component is present) to the environment around the nozzle exit plane (for example, the nozzle lip thickness, and other reflecting surfaces in the vicinity of the nozzle exit), the small differences between measured and predicted spectra may not be serious in any practical application of the prediction model. Hence, it is felt that the prediction scheme is adequate for shock-associated noise considerations in selecting engine cycles for aircraft engines of the next generation.

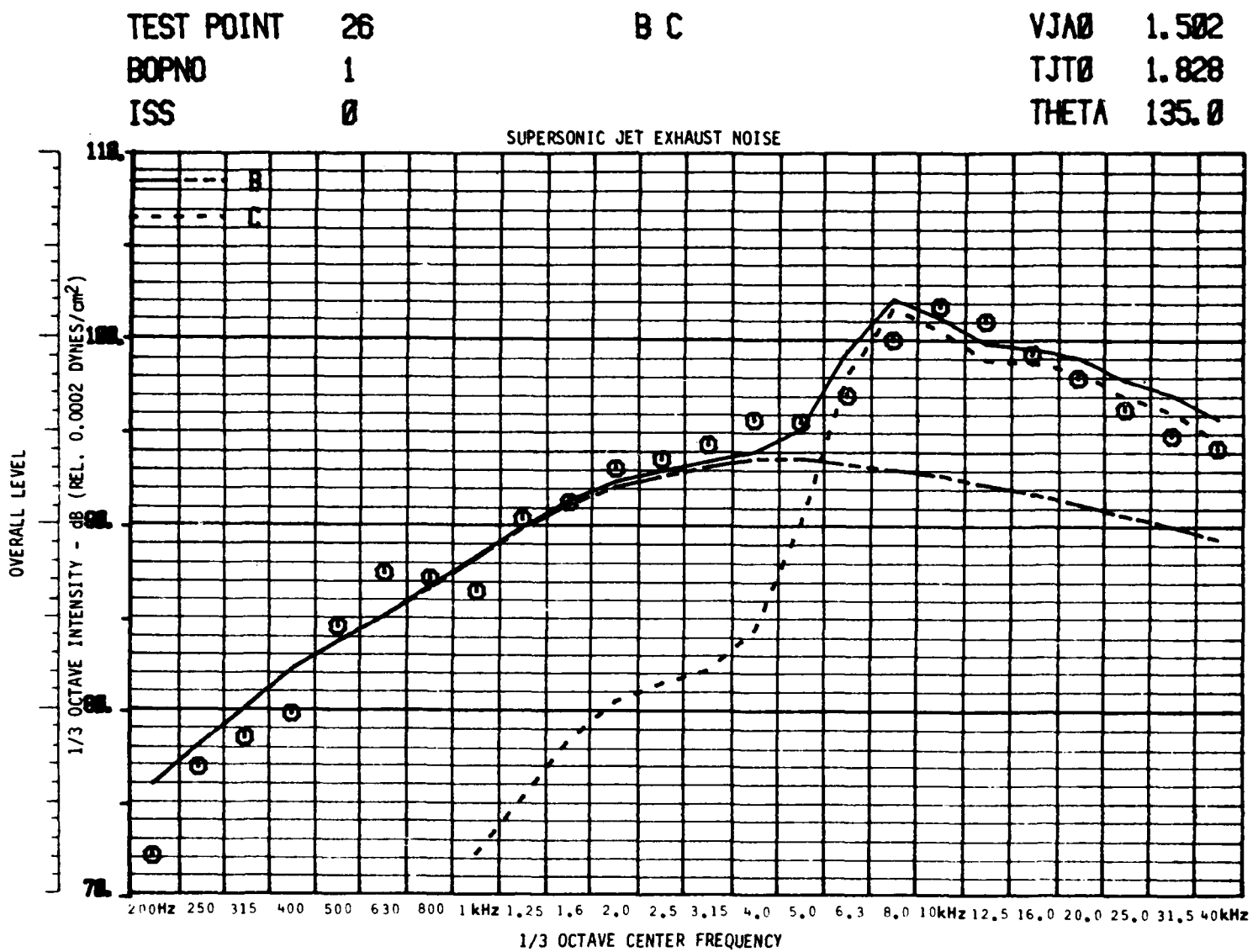

Figure 4.20 Comparison Between Measured and Predicted Spectra: $\beta = 0.50$; $\theta = 135°$, T_J/T_o (Nominal) = 1.82.

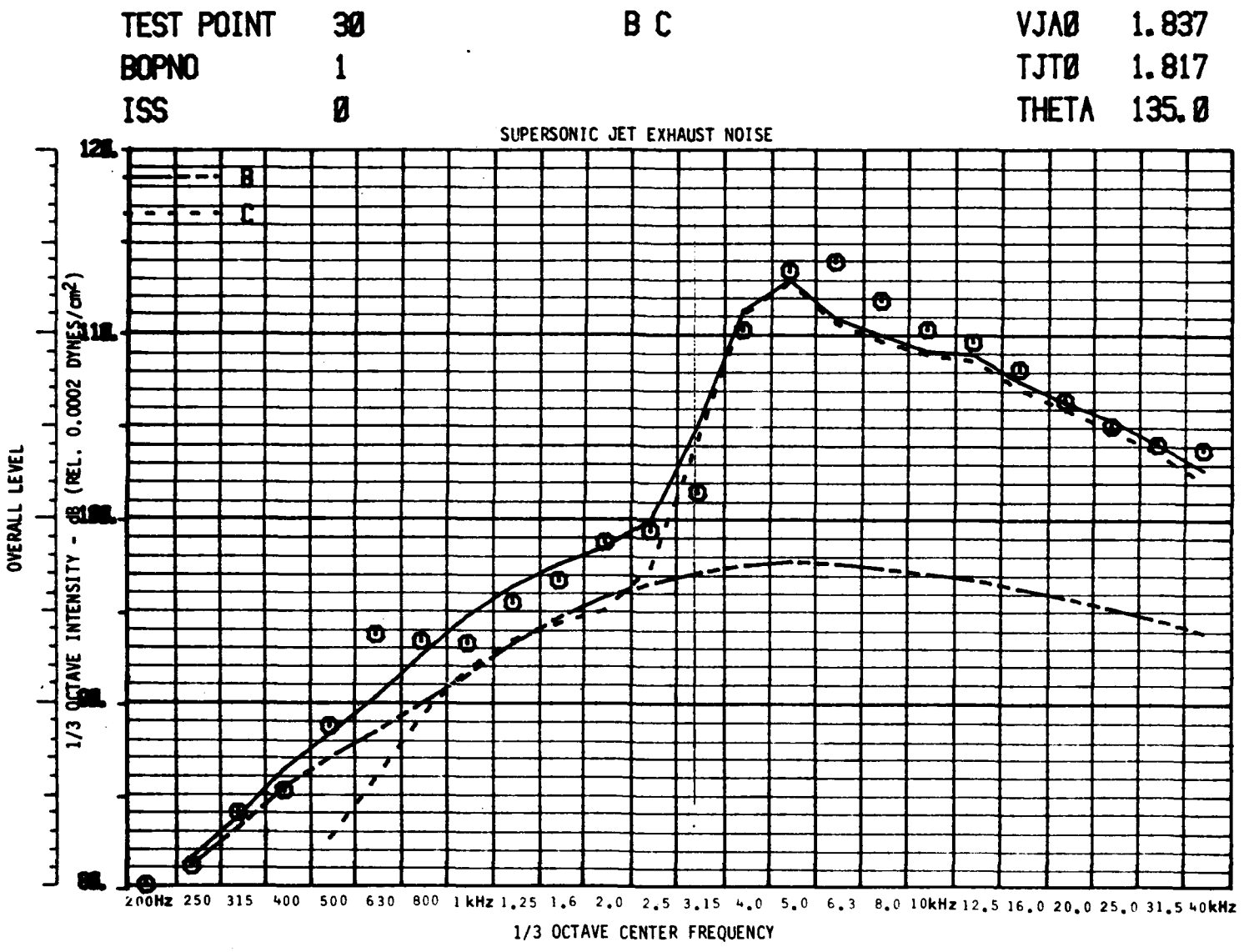

Figure 4.21 Comparison Between Measured and Predicted Spectra: $\beta = 0.94$; $\theta = 135°$, T_J/T_O (Nominal) = 1.82.

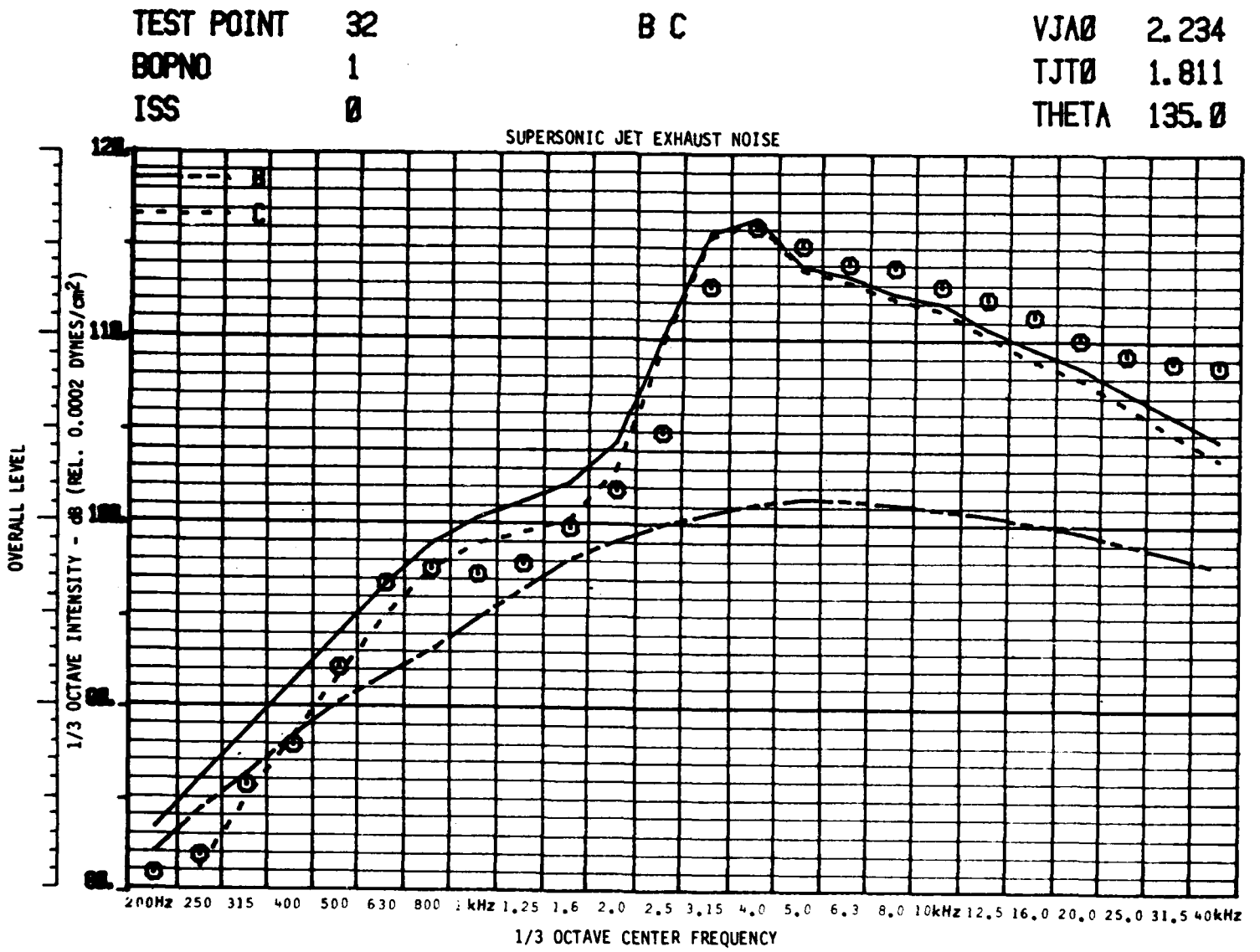

Figure 4.22 Comparison Between Measured and Predicted Spectra: $\beta = 1.34$; $\theta = 135°$, T_J/T_O (Nominal) = 1.82.

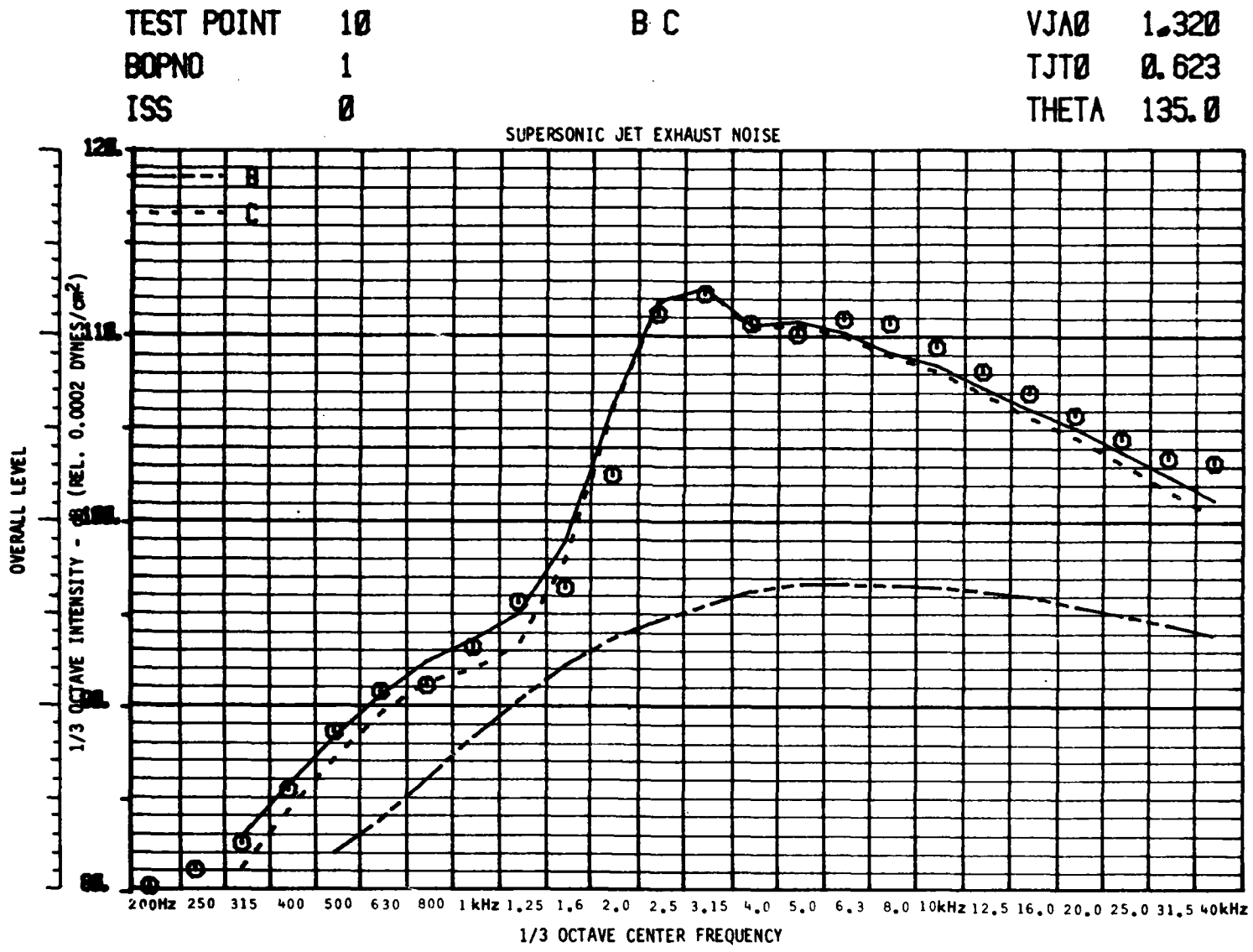

Figure 4.23 Comparison Between Measured and Predicted Spectra: $T_J/T_O = 0.623$; $\theta = 135°$, β (Nominal) = 1.34.

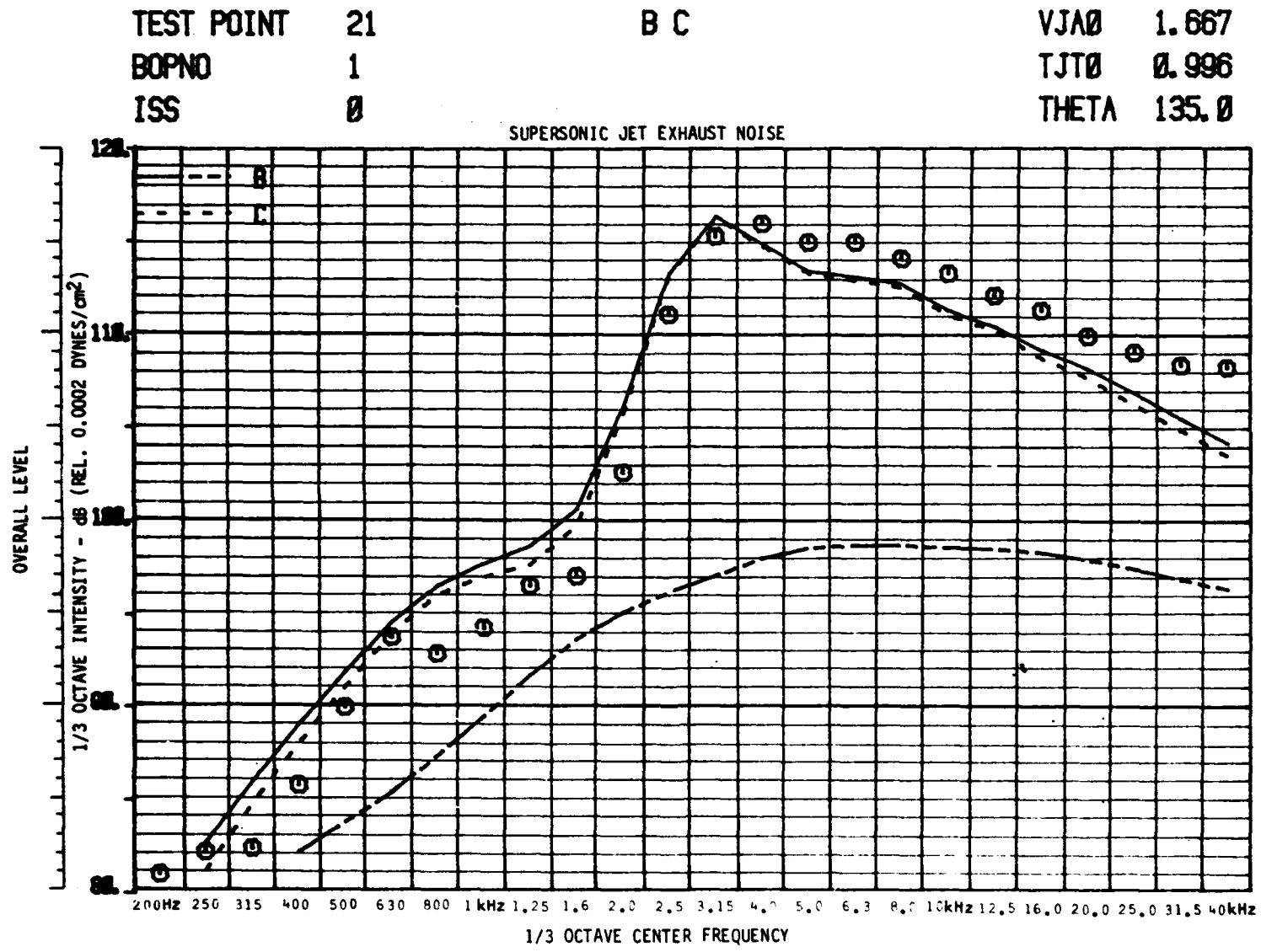

Figure 4.24 Comparison Between Measured and Predicted Spectra: $T_J/T_O = 0.996$; $\theta = 135°$, β (Nominal) = 1.34.

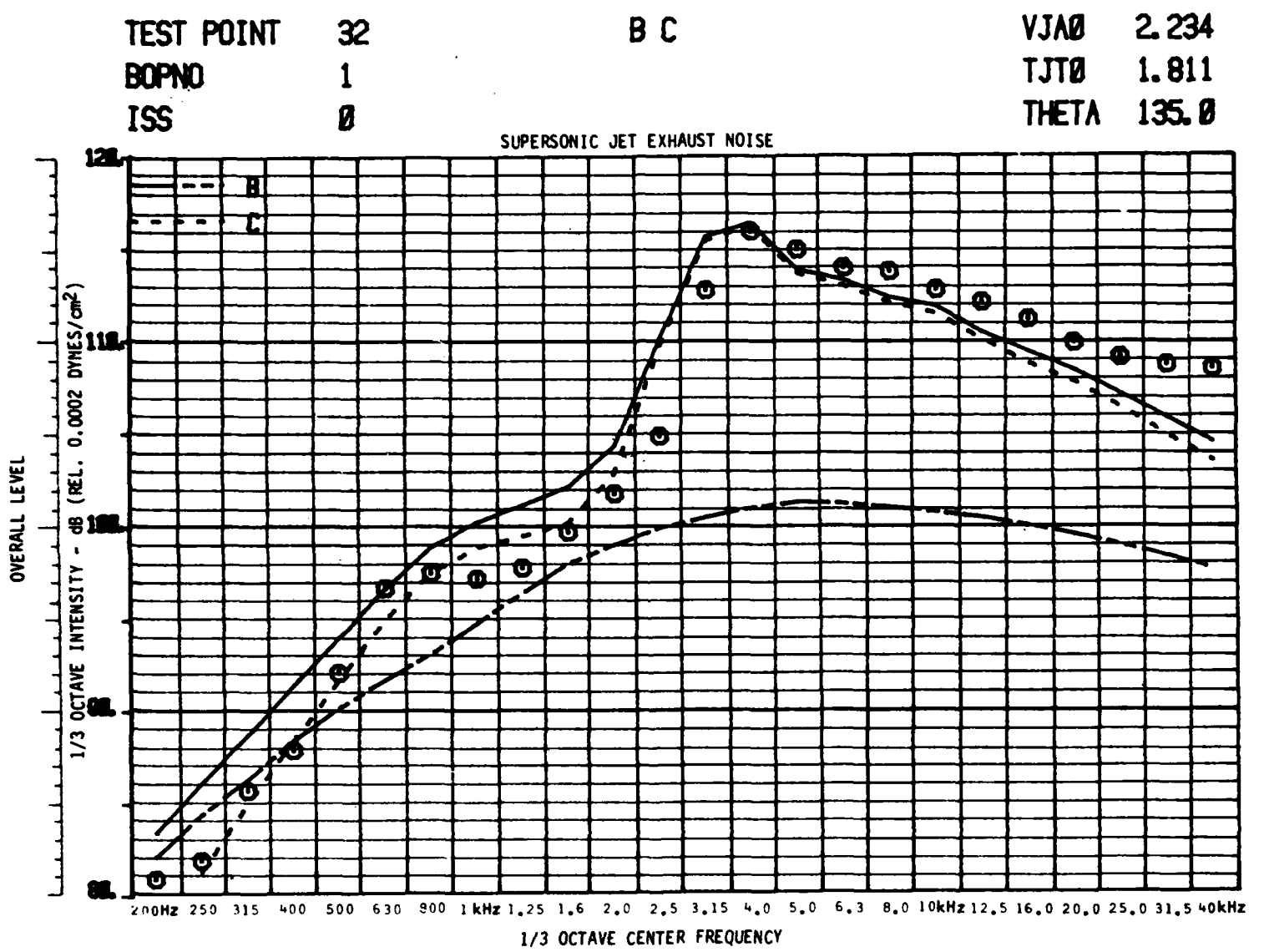

Figure 4.25 Comparison Between Measured and Predicted Spectra: $T_J/T_O = 1.811$; $\theta = 135°$, β (Nominal) = 1.34.

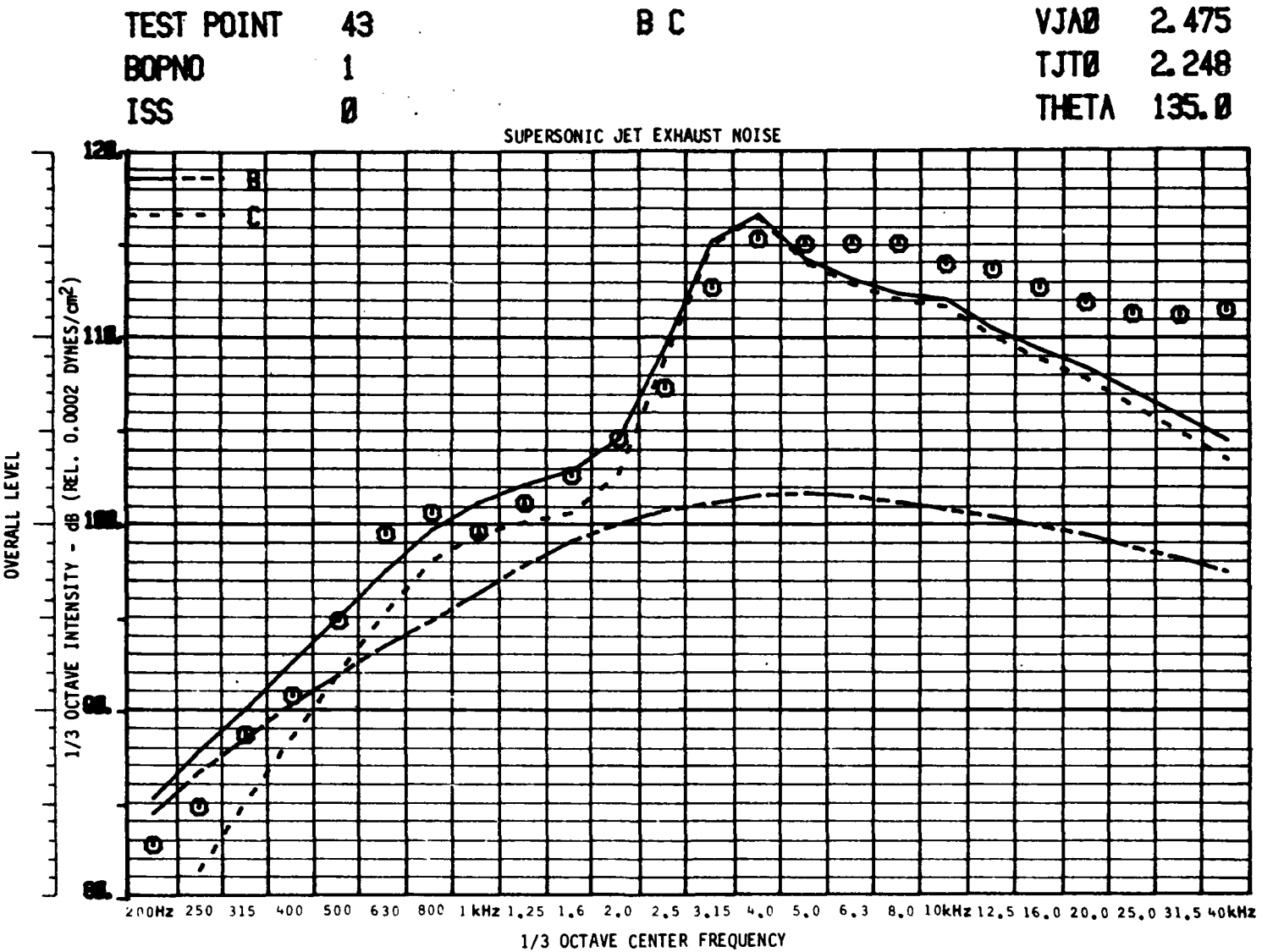

Figure 4.26 Comparison Between Measured and Predicted Spectra: $T_J/T_O = 2.248$; $\theta = 135°$, β (Nominal) = 1.34.

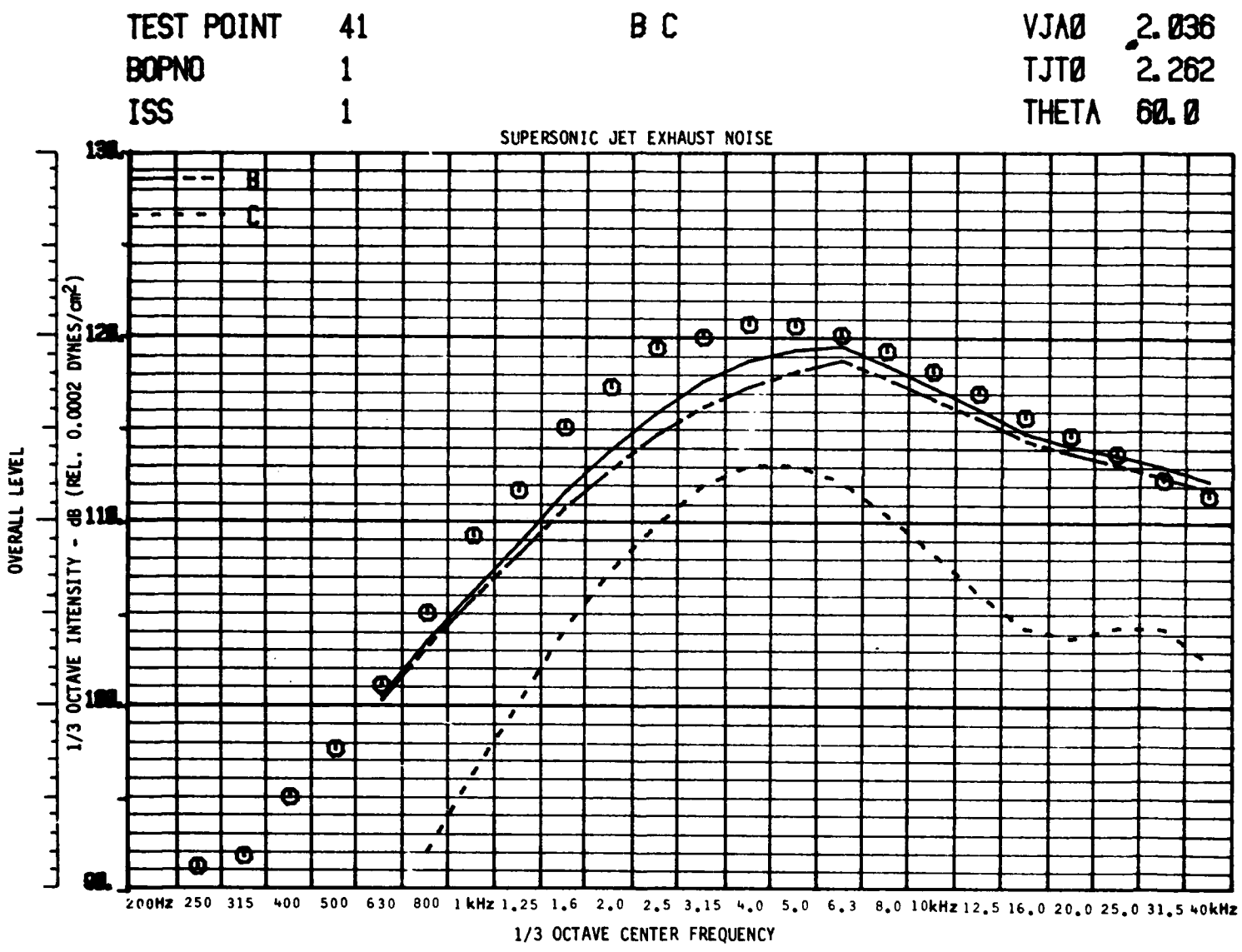

Figure 4.27 Comparison Between Measured and Predicted Spectra: $\theta = 60°$; β (Nominal) = 0.94, T_J/T_O (Nominal) = 2.26.

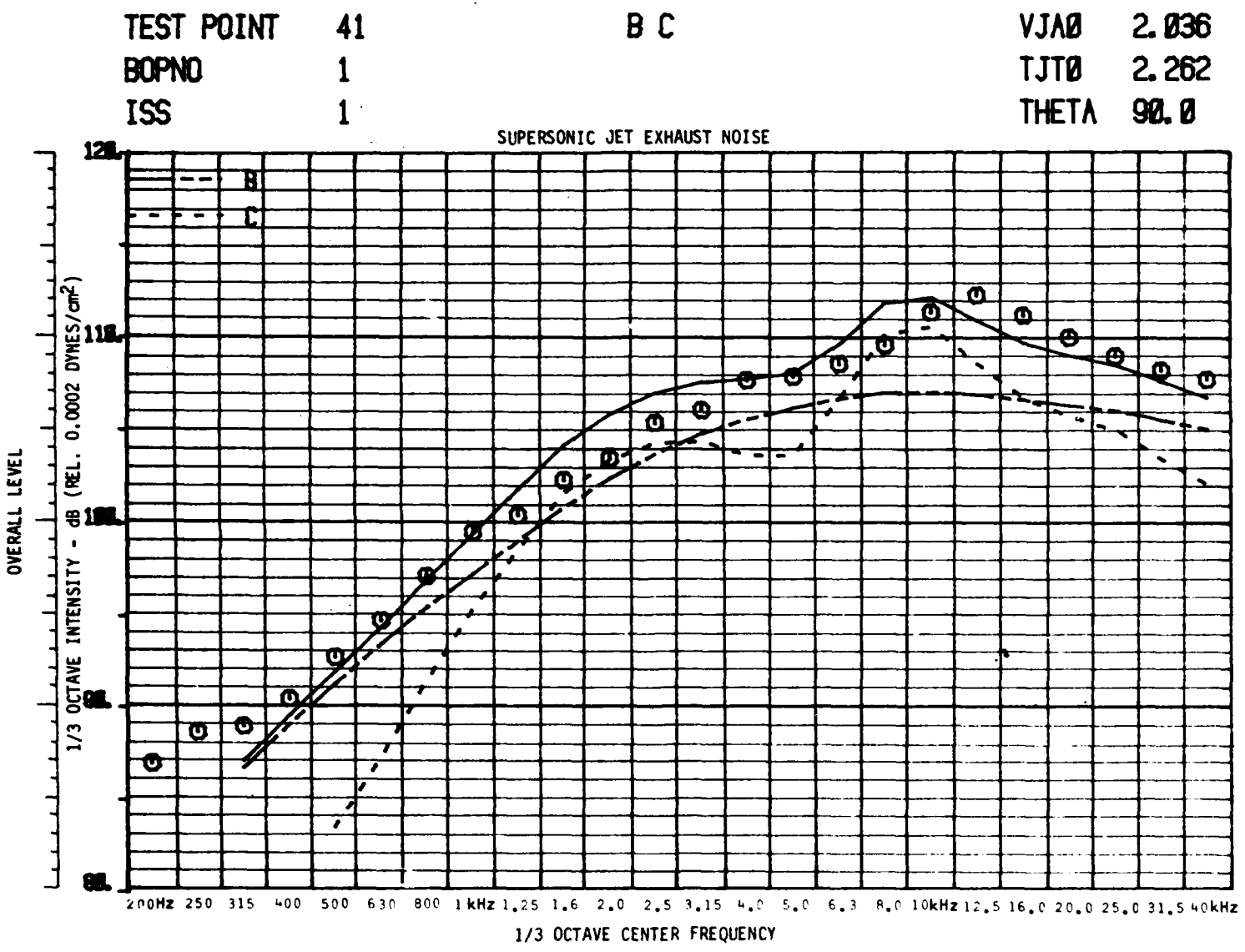

Figure 4.28 Comparison Between Measured and Predicted Spectra: $\theta = 90°$; β (Nominal) = 0.94, T_J/T_O (Nominal) = 2.26.

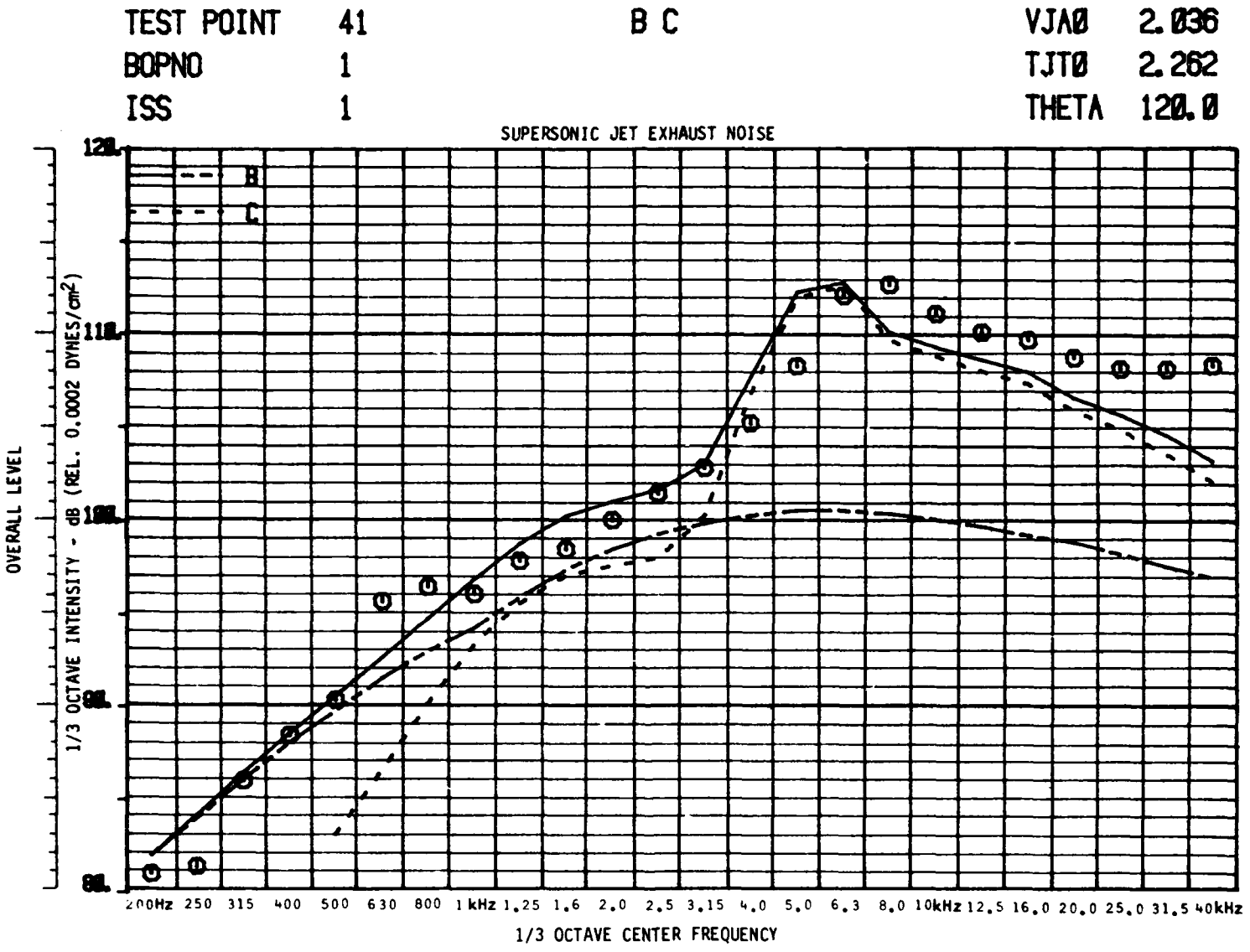

Figure 4.29 Comparison Between Measured and Predicted Spectra: $\theta = 120°$; β (Nominal) = 0.94, T_J/T_O (Nominal) = 2.26.

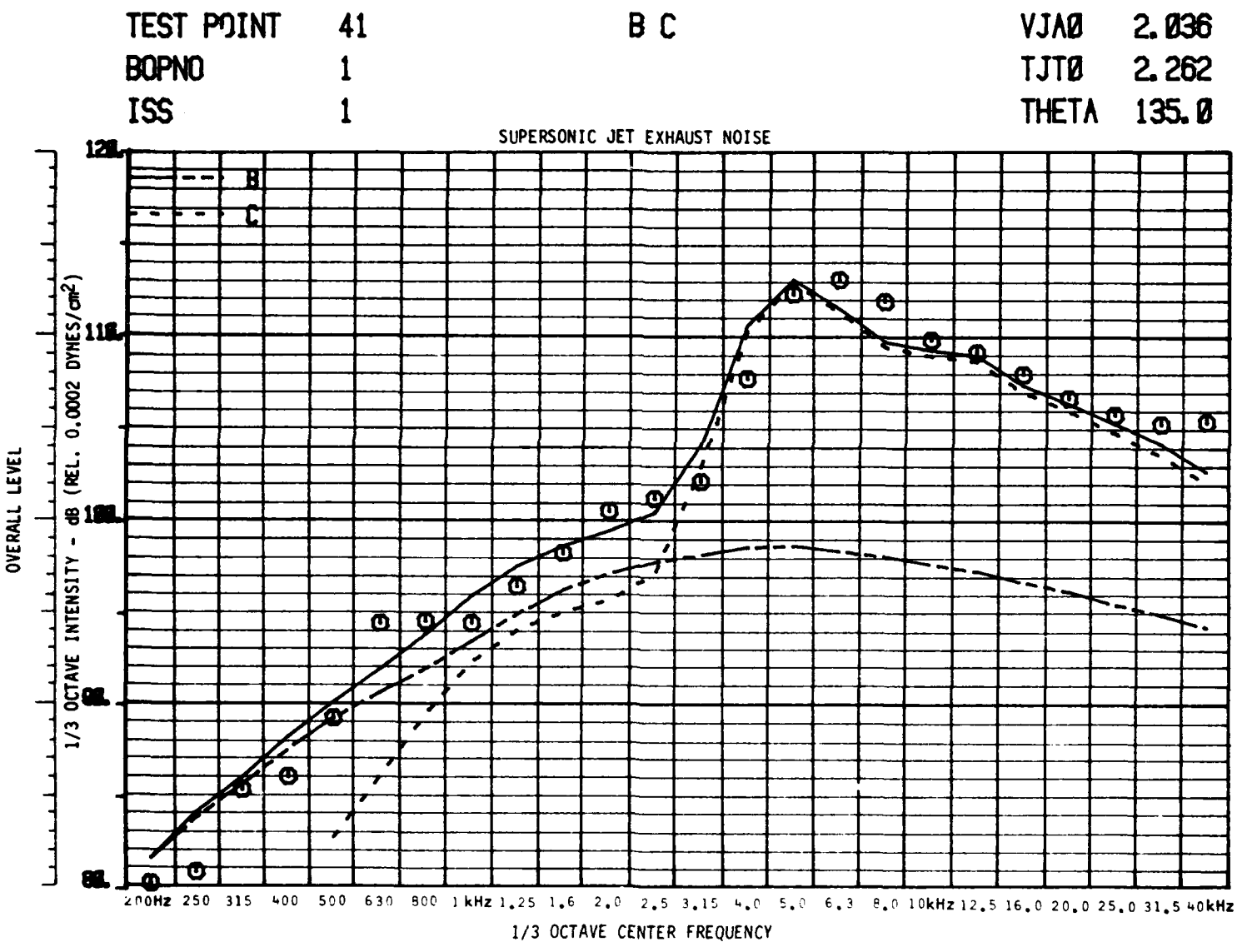

Figure 4.30 Comparison Between Measured and Predicted Spectra: $\theta = 135°$; β (Nominal) = 0.94, T_J/T_O (Nominal) = 2.26.

5. AERODYNAMIC MEASUREMENTS

5.1 INTRODUCTION

The experimental work described in this section is carried out in support of the theoretical effort presented in other chapters of this report. It consists mainly of laser velocimeter measurements of the mean flow and the various turbulence characteristics and is supplemented by corresponding temperature and Mach number measurements obtained with total head and total temperature tubes.

Many attempts have been made over the years to study the jet, and a considerable amount of data has been accumulated on the mean flow and fluctuating velocities distributed over the flow field of the round jet (e.g. Laurence [5.1]; Corrsin and Uberoi [5.2]; Davies, Fisher and Barratt [5.3]; and Wygnanski and Fiedler [5.4]). Unfortunately, they have tended to be concentrated in specific regions of the jet (e.g., most of the work is performed either in the initial mixing region or the "fully developed" region far downstream of the nozzle). Moreover, they have been confined to a limited set of varying jet conditions. Therefore, the data available to date present an inadequate view of the overall effects of jet flow conditions in the noise source region which is believed to extend from the nozzle to about eight to ten diameters downstream. Furthermore, because of the limitations of the experimental equipment at the time of those measurements, certain kinds of data could not be obtained under some flow conditions. For instance, no data on turbulence have been obtained for supersonic and heated air jets under atmospheric conditions until more recently when the laser velocimeter became available.

In the present effort an attempt is made to study the jet flow conditions within the region of the major noise sources over a wide range of jet Mach number and temperature conditions. Figure 5.1 shows the plan of the test conditions undertaken. The ordinate of the chart gives the ratio of the static jet temperature (T_J) to the ambient temperature (T_o) and the abscissa the ratio of the jet velocity (U_J) to the ambient speed of sound (a_o).

In planning this program, three aspects about the jet, discovered during the previous work [5.5] are taken into account. Firstly, the general structure of the jet changes continuously in the transition from subsonic to supersonic flow. This suggests that substantial knowledge about supersonic flows may be inferred from data on subsonic jets by observing the trends indicated as the Mach number is increased. Secondly, the spreading rate of the mixing region appears to be affected independently by the Mach number and temperature. Thus, the two effects should be studied separately. Thirdly, experience with heated and isothermal jets indicates that the spreading rate of the shear layer does not scale linearly with jet efflux velocity.

The program is therefore designed so that the changing pattern of the jet may be studied under the following constraints: (a) at constant jet Mach number, (b) at constant jet temperature, and (c) at constant jet velocity. This is indicated by the various grid lines shown in the chart of Figure 5.1.

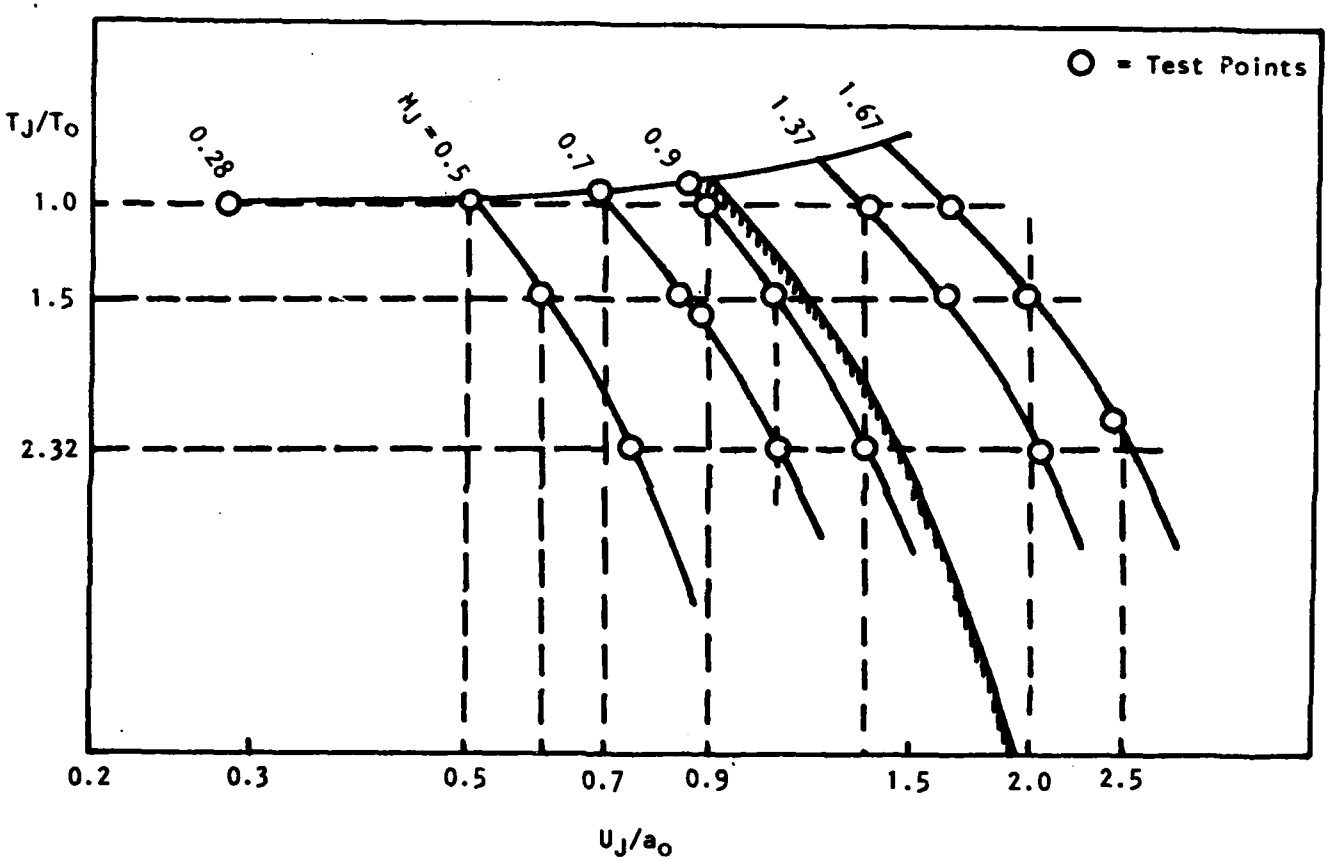

Figure 5.1 Test Plan

5.1.1 Scope of Measurements

The measurement program consists of two parts. In the first part, measurements are made at individual points in the flow. Mean velocity, turbulence intensity, covariances of orthogonal velocity fluctuations and spectra of the signals are obtained. These measurements are made for all the test conditions shown in Figure 5.1. In the second part, two-point cross-correlation measurements are obtained. Due to the limitation of time, these measurements are conducted only at four test points. Space-time cross-correlations of $(u_i')_A$ and $(u_j')_B$, and $(u_iu_j)'_A$ and $(u_ku_\ell)'_B$ are measured. From these data, various turbulence characteristics such as integral length scales and time scales in both the fixed and moving frame, and convection velocities are derived, from which the acoustic source term and source spectrum are determined.

5.2 MEAN FLOW

5.2.1 Radial Distributions

5.2.1.1 Mean velocity

Figure 5.2 shows radial distributions of the axial mean velocity for a Mach 0.5 cold jet. The velocity is normalized by the jet efflux velocity (U_J) and the radial position is denoted by the parameter $\eta^* = (r - r_{0.5})/x$ where $r_{0.5}$ is the radial position where the mean velocity is 0.5 U_J and x the axial distance from the nozzle exit plane. It was found during the previous phase of the study [5.5] that this method of reducing the results provided the best way of collapsing the data for isothermal jets ($T_J/T_O = 1.0$), and data as far as two potential core lengths downstream of the nozzle exit plane could be reduced to one curve. Moreover, this curve followed the results of two-dimensional free shear layers very faithfully. These features are demonstrated by the collapsed data in the figure. The advantage of plotting the results in this manner is that this allows the real effects resulting from changes to the jet conditions to be studied systematically and in isolation from other effects connected with the natural spreading of the jet.

Figure 5.3 shows the distributions for a jet heated to 2.32 times the ambient temperature. There is also good collapse of the data up to 8 diameters downstream. It is clear therefore that the method of plotting the results may also be used to advantage for heated jets even when the results extend beyond the potential core. Heating does not alter the distributions markedly, except that the maximum slope of the distribution for the heated jet is higher than for the unheated jet. Since the spreading rate is inversely proportional to this slope, this corresponds to a lower spreading rate for the heated jet.

Figures 5.4 and 5.5 show the distributions for a Mach 1.37 jet heated to the ambient and 2.32 times the ambient temperature, respectively. The similarity of the two sets of curves is also evident. As for the subsonic case, the results from the heated jet show a different maximum slope from those of a jet set at the ambient temperature. However, in the supersonic case, the maximum slope is *lower* for the high temperature jet than for the isothermal

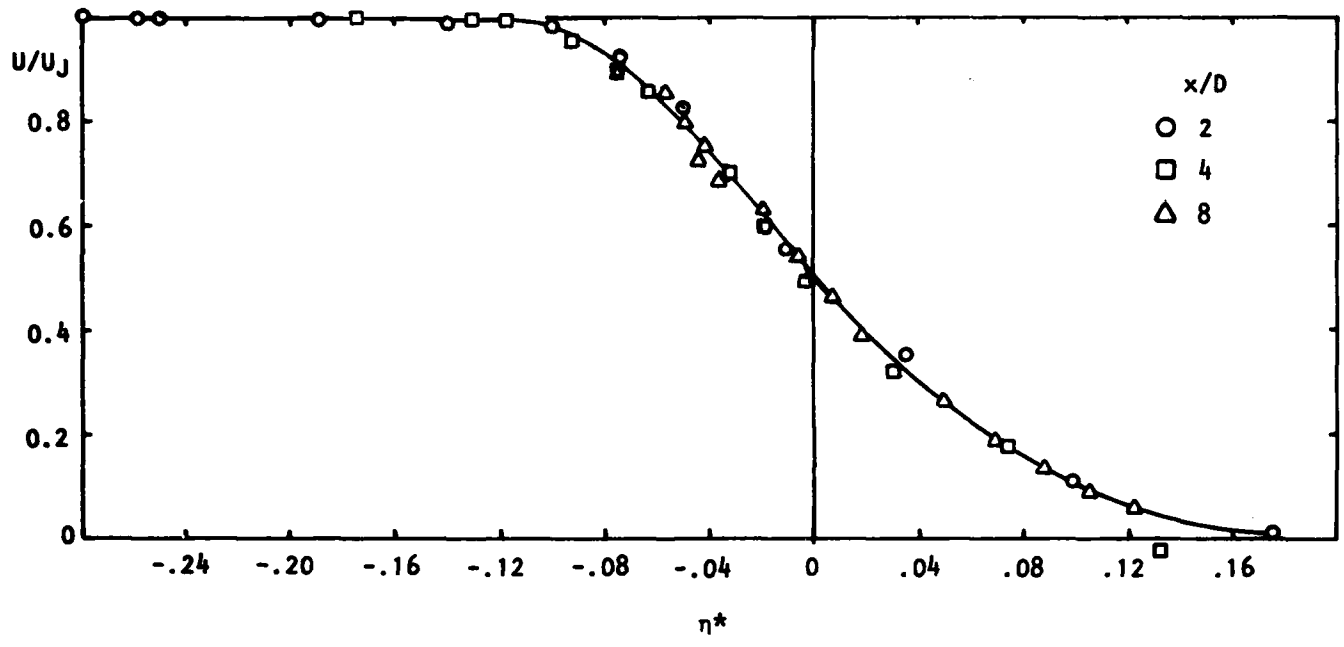

Figure 5.2 U/U_J vs η^* (M_J = 0.5, Cold)

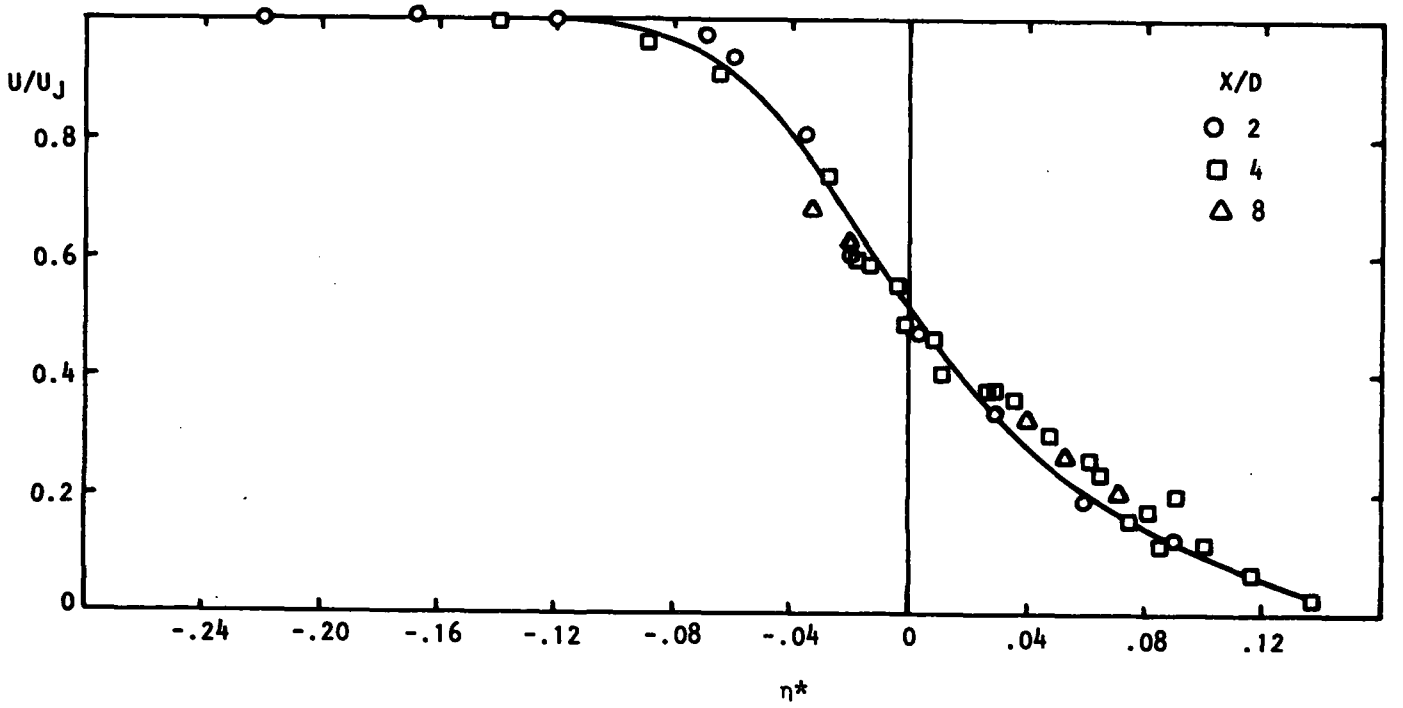

Figure 5.3 U/U_J vs η^* ($M_J = 0.5$, $T_J/T_o = 2.32$)

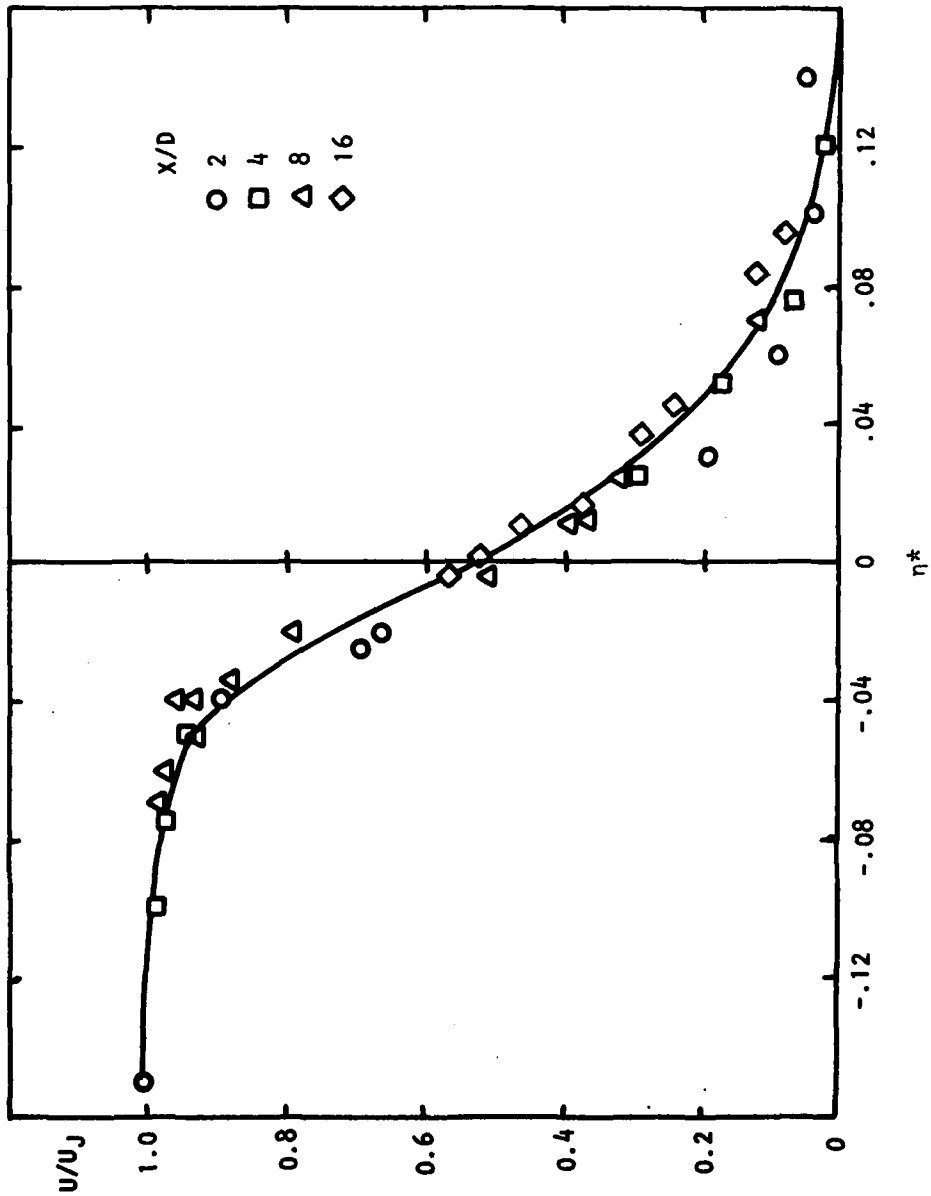

Figure 5.4 U/U_J vs η^* ($M_J = 1.37$, $T_J/T_O = 1.0$)

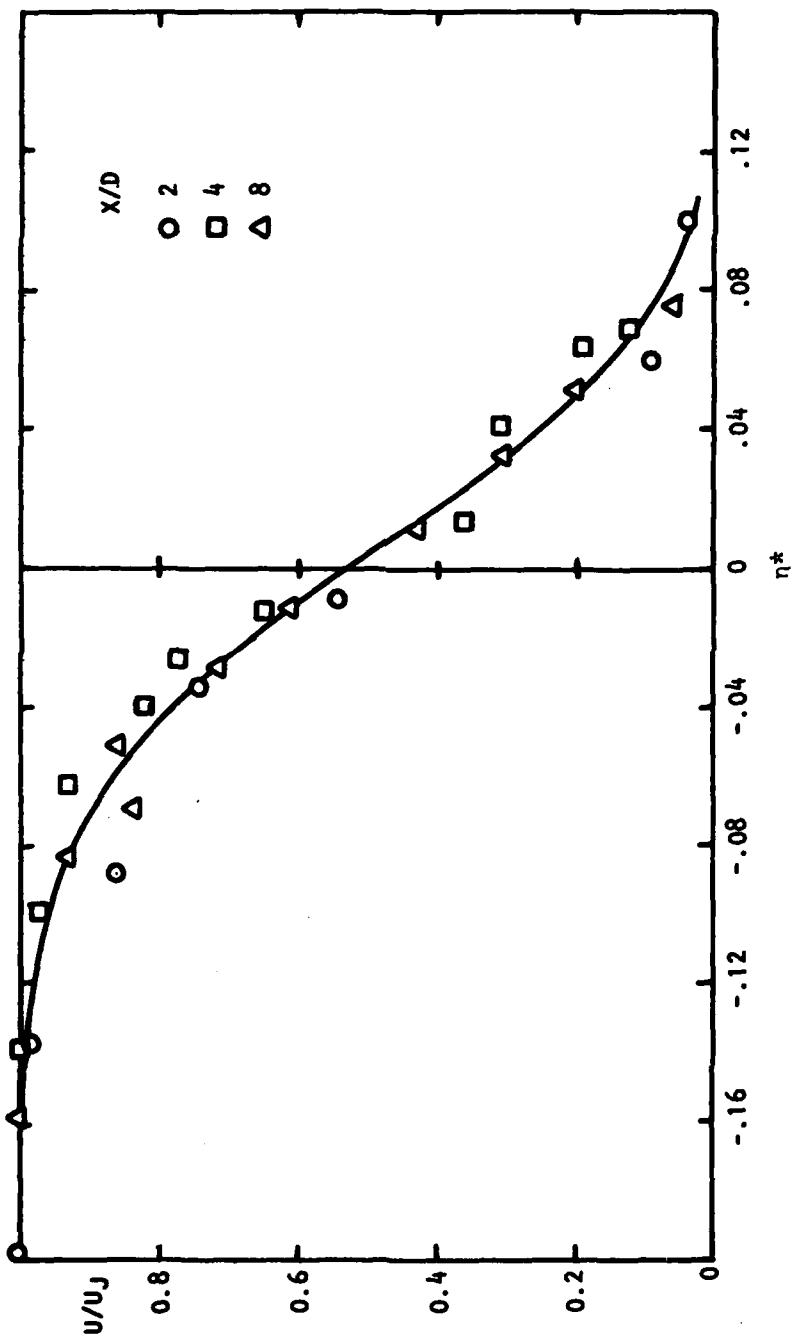

Figure 5.5 U/U_J vs η^* ($M_J = 1.37$, $T_J/T_O = 2.32$)

jet. It thus appears that subsonic and supersonic jets react differently when they are raised to a high temperature. It would be instructive therefore to study the changes in the spreading rate as Mach number and temperature are varied.

5.2.1.2 The spreading rate (δ_η)

Figure 5.6 shows the variation of the spreading rate as a function of the temperature ratio (T_J/T_o) for various jet exit Mach numbers (M_J). The spreading rate (δ_η) is defined by $\delta_\eta = U_J/x\ (dU/d\eta^*)_{max}$, and is determined from collapsed data similar to those shown in Figures 5.2 to 5.5.

The differences in subsonic and supersonic jets may clearly be seen. For subsonic jets, initial heating appears not to affect the spreading rate significantly, and from $T_J/T_o = 1.0$ to 1.5, δ_η remains essentially unchanged. From $T_J/T_o = 1.5$ to 2.32, δ_η *falls* and the results for different Mach numbers appear to converge close to $T_J/T_o = 2.4$. For supersonic jets, δ_η behaves the same as for subsonic jets with initial heating but increases as the temperature is raised further. The curve also tends to converge close to $T_J/T_o = 2.4$. It would appear that for a jet at the sonic speed, heating would have practically no effect on its spreading rate at all.

For temperature ratios of about 0.5 to 2.4, the general tendency is for δ_η to fall with increasing Mach number. This trend is illustrated more clearly by Figure 5.7 which shows the variation of δ_η with M_J. The present experimental results are shown by solid symbols.

It may be seen that for cold jets and jets at $T_J/T_o = 1.0$ and 1.5, δ_η decreases monotonically with increasing M_J between Mach 0.5 and 1.4 and there is little distinction between the results for the two temperature ratios. The results of other investigators show a similar trend [5.6]. Except for Carey's, which are measured with an interferometer, they are obtained with pitot-static tubes and are carried out in cold jets. These pitot-tube results tend to be systematically higher than Carey's or the present data. In order to ascertain if the discrepancy is due to differences in the jets or the method of measurement, pitot-static measurements are also carried out in a cold jet at Mach 0.9 and 1.37 and in an isothermal jet at 1.37. The data are shown by the flagged solid symbols and lie above the LV results. In particular, those for the cold jet lie on the curve drawn through the earlier pitot measurements. It is clear therefore that the difference observed between the present results obtained with the LV, and those obtained with pitot-static tubes, results from a difference in the measuring technique used. It is interesting that Carey's data which are obtained by an optical method follow the LV results very closely. This would seem to indicate that there is a restructuring of the jet when an external probe is inserted into the flow region.

For the isothermal jet, using the present LV results, the following relationship was established between δ_η and M_J [5.5],

$$\delta_\eta = 0.165 - .045\ M_J^2 \qquad (5\text{-}1)$$

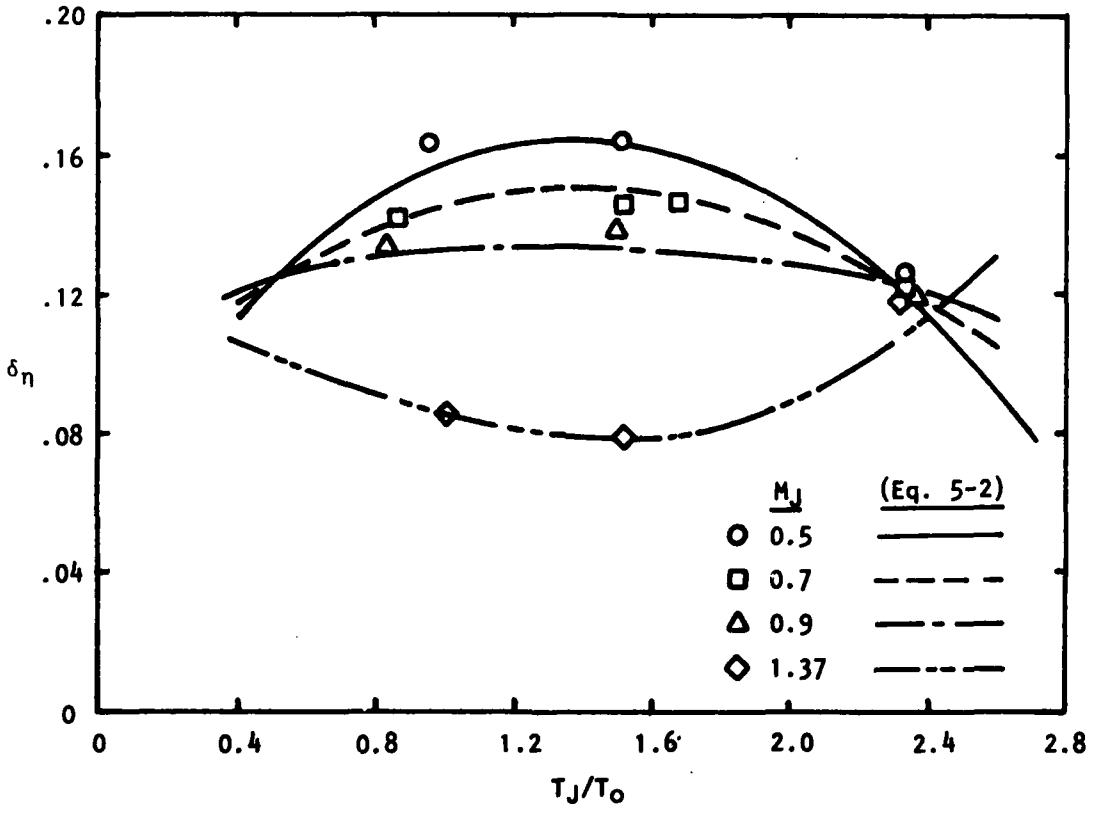

Figure 5.6 δ_η vs T_J/T_o

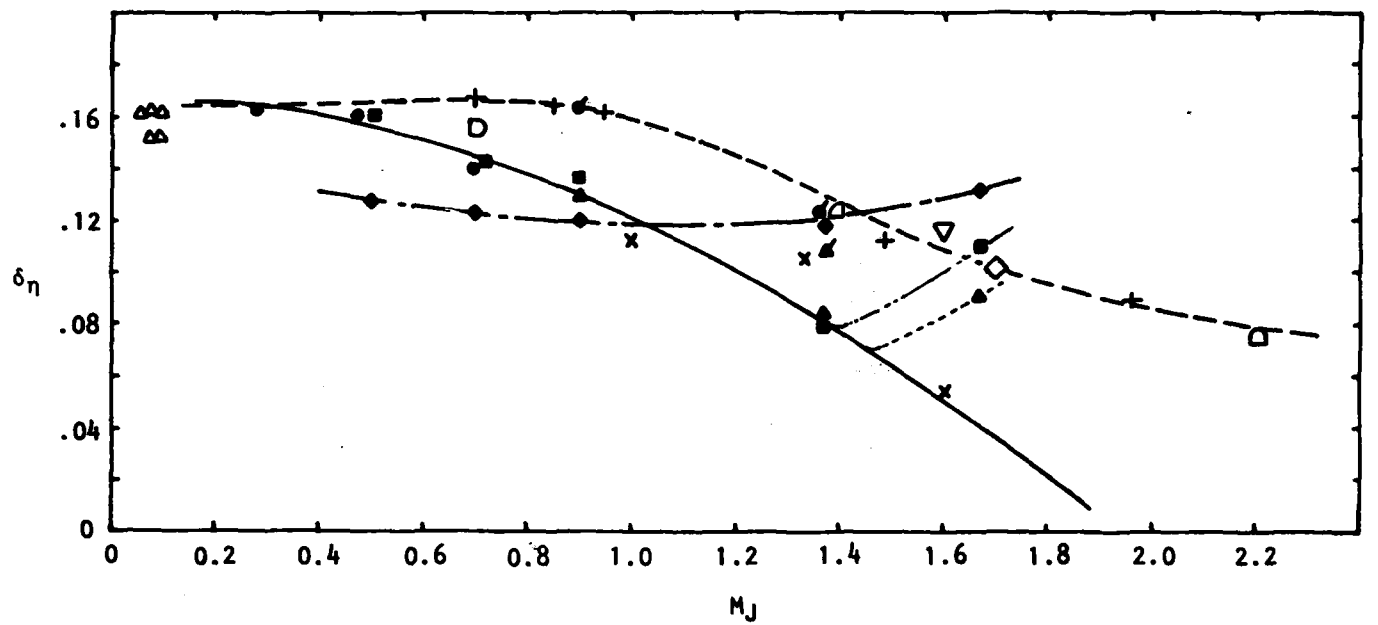

Present Results: T_J/T_o = ● cold, ▲ 1.0, ■ 1.5. ◆ 2.32;
Pitot-Tube Measurements are Flagged. (Eq. 5-1) ——

△ Tollmien 1926, Liepmann 1947, ⊿ Reichardt 1942,
▽ Gooderum et al 1949, ◇ Bershader and Pai 1950,
✕ Carey 1954, ⊐ Crane 1957, ⊿ Johannesen 1959,
+ Maydew and Reed 1963, ⊐ Eggers 1966.

Figure 5.7 δ_η vs M_J.

and it would appear that the same equation may be used for jets heated to at least 1.5 times the ambient temperature.

From about Mach 1.4, the LV results rise. This is true for jets at $T_J/T_o = 1.0$ and 1.5 and the upturn corresponds approximately with the eddy convection velocity being supersonic. The trend however is not present in the pitot-static results. It is not certain if this trend will continue at higher M_J. However, Brown and Roshko have predicted a $1/M_J$ type of variation for very high Mach numbers, and it is speculated that δ_η would probably fall again as the Mach number is increased, possibly following the pitot-static results. Unfortunately, time did not permit this to be fully explored.

The results for jets heated to 2.32 times the ambient temperature are also shown but they exhibit quite a different behavior. The values of δ_η remains essentially constant with Mach number although there appears to be a shallow trough at $M_J \doteq 1.0$. The line through the data points intersects the previous curve for the jet at $T_J/T_o = 1.0$ at about $M_J = 1.0$. It is interesting that a similar situation exists with results of the overall far-field noise intensity at 90° to the jet axis (Reference 5.5, p. 34). Lines showing the variation of noise intensity with velocity for jets at $T_J/T_o = 1.0$ and 2.3, respectively, intersect at a Mach number close to one. This might suggest the possibility of a strong connection between the noise generation mechanisms and the spreading rate (or appropriately, the maximum slope in the mean shear), which would be worth exploring more fully.

Based on the available results, an empirical equation is derived to describe the variation of δ_η with T_J/T_o and Mach number in the Mach number range 0 to 1.4. This is given by:

$$\delta_\eta = (.1765 - .052\, M_J^2)\, [1 + 0.50\, (M_J^2 - 1)\, (T_J/T_o - 1.4)^2] \qquad (5\text{-}2)$$

and the curves for the Mach 0.5, 0.7, 0.9, and 1.37 jets are shown in Figure 5.6.

5.3 Universal curve for the radial distributions

The spreading rate δ_η defined here is equal to the axial gradient of the vorticity thickness used by other investigators [5.7, 5.8, 5.9] and Korst and Chow [5.10] have shown that if the radial profile of the axial mean velocity were represented by an error function, δ_η is related to the Görtler spreading parameter (σ) by $\sigma\delta_\eta = \sqrt{\pi}$.

It was found earlier (Reference 5.5, p. 62) that the radial distributions of the axial mean velocity collapsed, for all isothermal jets between Mach 0.3 and 1.4, if the radial distance was expressed in terms of $\sigma\eta^*$. This is attempted for the heated jets also and is shown in Figure 5.8. The data do collapse and their variation is reasonably well represented by the Görtler error function profile.

$$U/U_J = 0.5\, [1 - \mathrm{erf}(\sigma\eta^*)] \qquad (5\text{-}3)$$

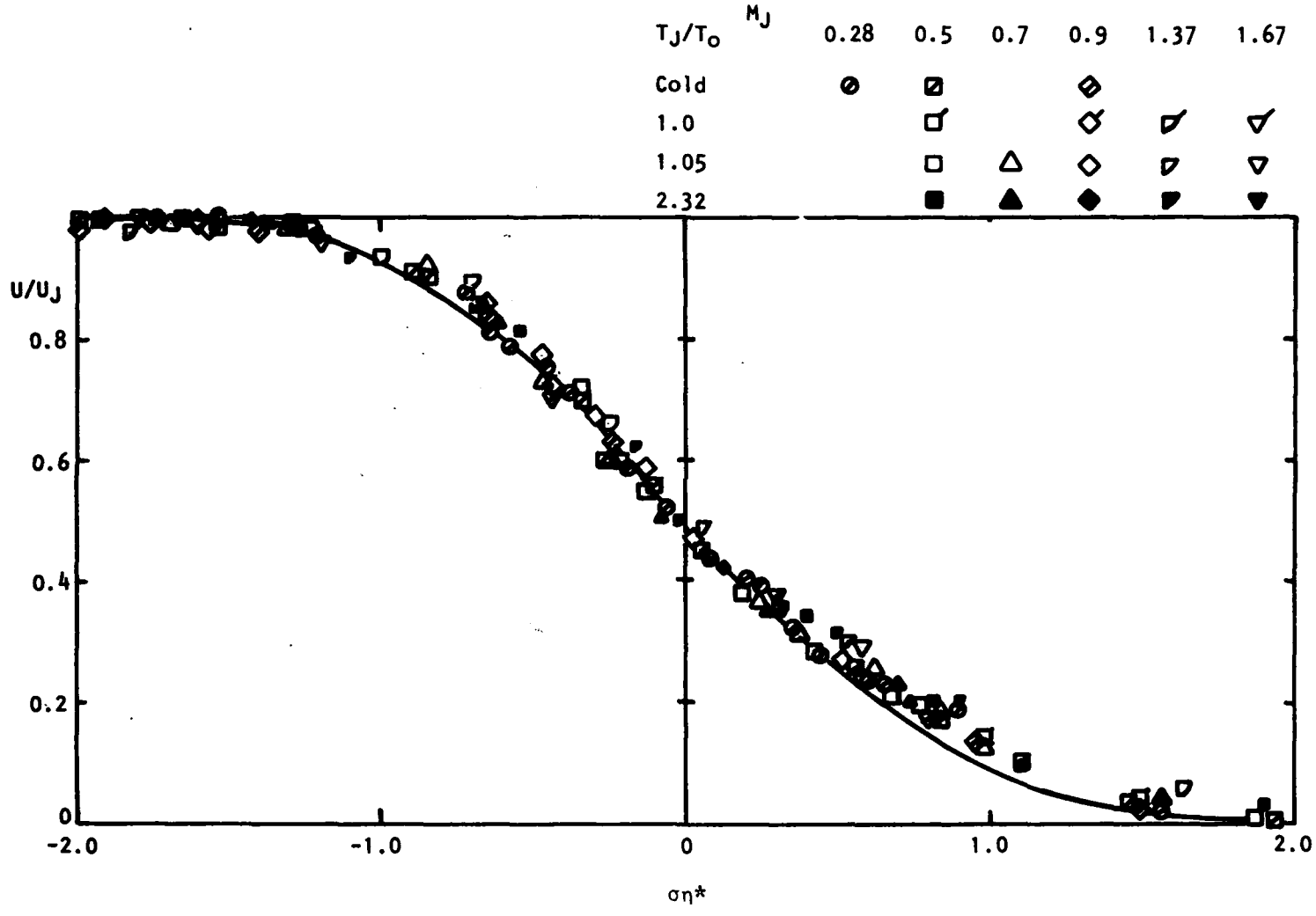

Figure 5.8 U/U_J vs $\sigma\eta^*$.

5.2.1.4 Total and static temperature

Figure 5.9 shows the radial distributions of the static temperature at Mach 0.5 and 0.7. The temperature is expressed in terms of the temperature-difference ratio $\Delta T/\Delta T_J = (T - T_o)/(T_J - T_o)$ and the radial distance in terms of η^*. The curves are obtained at two axial stations in the jet, and show strong similarity. However, they are displaced a little laterally relative to each other, and the half-temperature ratio points do not coincide with η^* being zero. This suggests that the half-temperature ratio point is outside the half-velocity point and the distance between them varies with axial distance. The same behavior is observed at other Mach numbers.

Figure 5.10 shows the temperature distribution plotted in terms of $\eta_t^* = (r - r_{0.5t})/x$, $r_{0.5t}$ being the half-temperature radius. The results at Mach 0.5 and 0.7 fall close together but closer scrutiny suggests that the maximum gradient for the Mach 0.7 jet is a little higher, similar to what was observed in the velocity distributions. Yakovlevskiy's results (reported in reference 5.11) are also shown. They were obtained in jets at Mach numbers of 0.1 to 0.4. These results compare well with the present results.

When the maximum slopes of these curves are compared with those of the velocity distributions, they are found to be significantly lower than the latter. If a spreading rate is defined for the temperature distribution ($\delta_{\eta t}$) as for the velocity distribution (δ_η), it is larger than δ_η, and the relationship between the two is given by:

$$\delta_{\eta t} = 1.94\ \delta_\eta \qquad (5\text{-}4)$$

based on LV measurements of the mean velocity distributions. The coefficient is about 1.45 based on pitot measurements which agrees with Batt's [5.12] result of 1.41. The distributions of the total temperature-difference ratio

$$(\Delta T_t/\Delta T_{tJ}) = \frac{T_t - T_o}{T_{tJ} - T_o}$$

are shown in Figure 5.11. For comparison, the static temperature-difference ratio is also shown. There is a small deviation between the two distributions, the total temperature distribution being a little steeper at its maximum slope than the static temperature distribution. The difference, however, is within the range of experimental error. This is also true of axial distributions. It would seem therefore that the two kinds of temperature distributions may be represented by the same equation as Abramovich [5.11] has suggested.

5.2.2 Axial Distributions

5.2.2.1 Mean velocity

Figure 5.12 shows the axial distributions of the mean velocity for the cold jet and jets at $T_J/T_o = 1.0$, 1.5, 2.06, and 2.32. The jet Mach number is 0.9 but the same trends prevail at other Mach numbers (subsonic and supersonic). From a cold jet ($T_J/T_o = 0.86$) to a jet at $T_J/T_o = 1.0$ and 1.5, the distributions

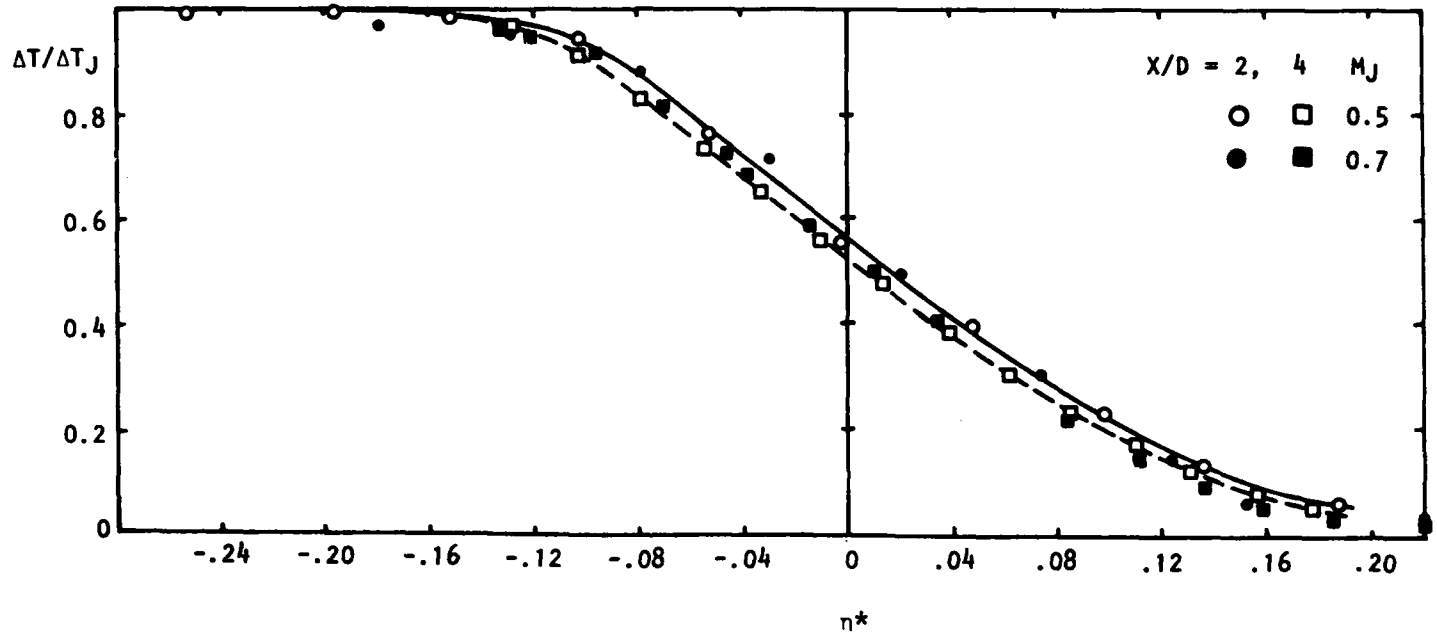

Figure 5.9 $\Delta T/\Delta T_J$ vs η^* (T_J/T_o = 2.32)

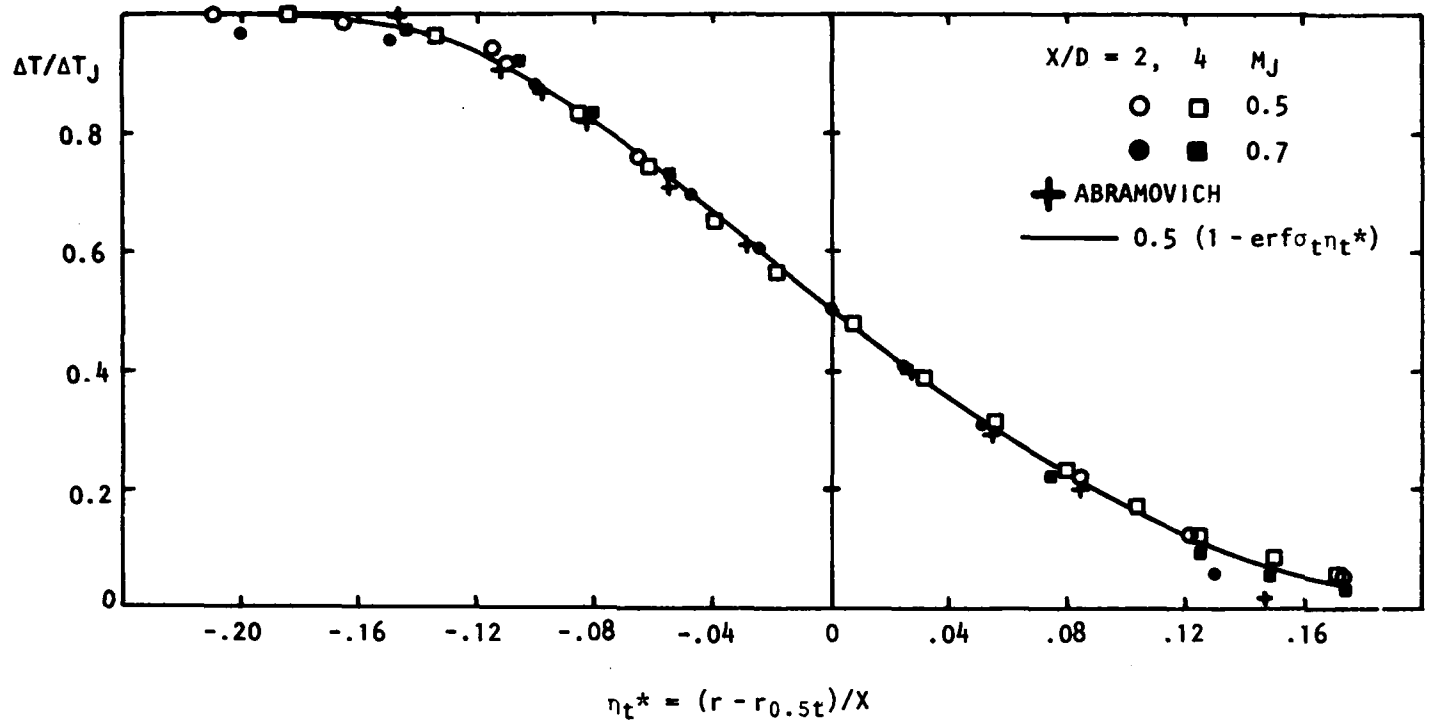

Figure 5.10 $\Delta T/\Delta T_J$ vs η_t^* $(T_J/T_o = 2.32)$

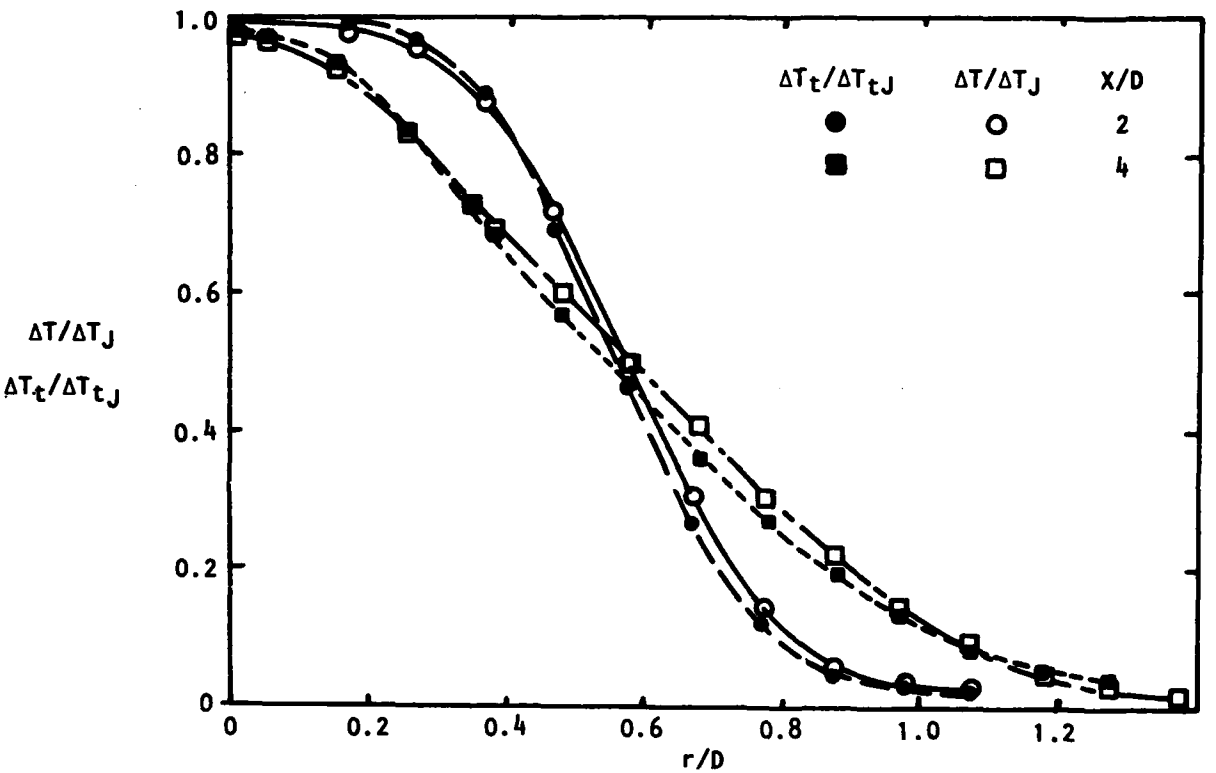

Figure 5.11 $\Delta T_t/\Delta T_{tJ}$ and $\Delta T/\Delta T_J$ vs r/D ($M_J = 0.7$, $T_J/T_o = 2.32$)

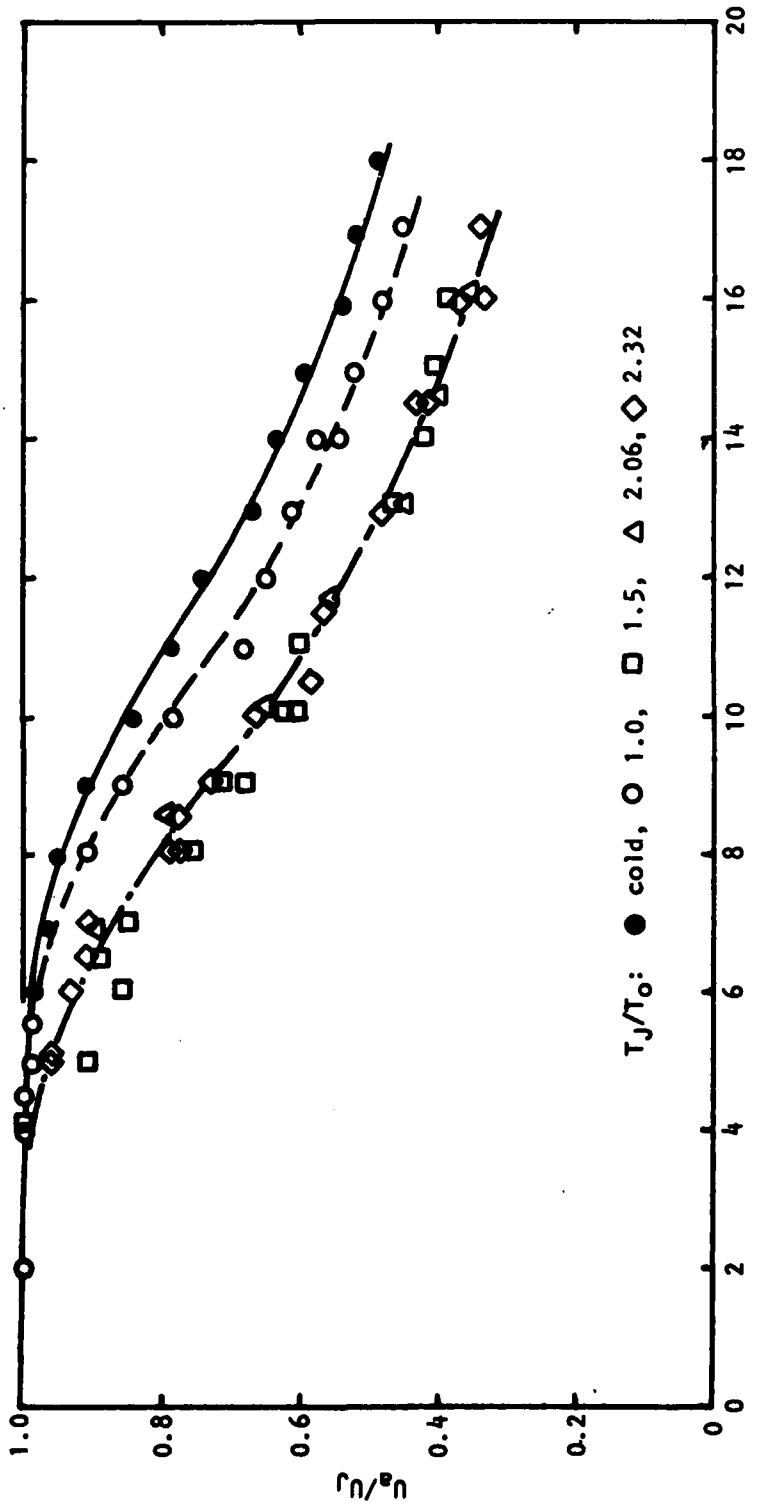

Figure 5.12 U_a/U_J vs X/D (M_J = 0.9)

move progressively upstream in almost equal increments suggesting a gradual reduction of the potential core length (x_c). However, from $T_J/T_o = 1.5$ to 2.32 there is hardly any shift in the curves. This contrasts the trends observed in the *radial* distributions where initial heating brings about minor changes to δ_η and it is only as the temperature ratio is raised above $T_J/T_o = 1.5$ that heating begins to have noticeable effect. It appears therefore that the parameters δ_η and x_c react independently of each other when the jet is heated to higher temperatures.

5.2.2.2 Universal curve for the axial distributions.

Witze [5.13] has obtained, on the basis of Kleinstein's [5.14] analytic work on turbulent axisymmetric compressible flows, an expression for the centerline decay of the mean velocity (U_a). It is given for $x > x_c$ by:

$$U_a/U_J = 1 - \exp\{\frac{1}{\chi}\} = 1 - \exp\{\alpha/(1 - x/x_c)\} \qquad (5\text{-}5)$$

where $\alpha = D/(ax_c)$ and "a" and "x_c" are parameters determined from experimental results of U_a/U_J vs. x/D. Equation (5-5) may be rewritten as $\chi = 1/\{\ell_n(1 - U_a/U_J)\} = ax_c/D - a\ x/D$. Thus, by plotting χ against x/D, the values of "a" and x_c/D may be determined explicitly. The potential core length is thus defined by the x-intercept of the straight line passing through the data points (i.e. x_c).

It was found previously (Reference 5.5, p. 60) that when the mean velocity distributions along the jet centerline were plotted in terms of x/x_c, the results for different Mach numbers of isothermal jets collapsed. Apparently, this is true of cold and heated jets also, as shown in Figure 5.13, and a curve representing Equation (5-5) may be drawn to pass through the middle of the data points. In this case, α has the same value of 1.35 as found previously for isothermal jets.

Traditionally, it has been maintained that far downstream of the potential core, where the jets have had the opportunity to become "fully developed," the velocity on the centerline would vary as 1/x. Indeed, for very large values of x, Equation (5-5) reduces to the asymptotic form of $\alpha x_c/x$. In order to determine how soon downstream the asymptotic form of the equation may begin to be used, a series of curves are drawn for varying values of α. It is found that good agreement is achieved as early as about $x = 2.5\ x_c$ provided a value of 1.4 is used for α in the asymptotic form. Wygnanski and Fiedler's results [5.4] also indicate a coefficient of 1.4 for α and good agreement is found to extend to about $x/x_c = 13.0$.

The good collapse of the data at varying M_J and T_J/T_o implies a value of α which is unaffected by jet conditions. This assumption is also implicit in the results of both Kleinstein [5.14] and Witze [5.13] who took the value of $\alpha = 1.43$. However, this appears not to be true. Figure 5.14 shows the variation of $1/\alpha(T_J/T_o)^{0.2}$ with M_J and suggests that $1/\alpha$ increases almost linearly with M_J and $(T_J/T_o)^{0.2}$. However, the effect is small enough (for Mach numbers ranging from 0 to 1.7 and temperature ratios of up to 2.4) so that the dependency may to a good approximation be overlooked.

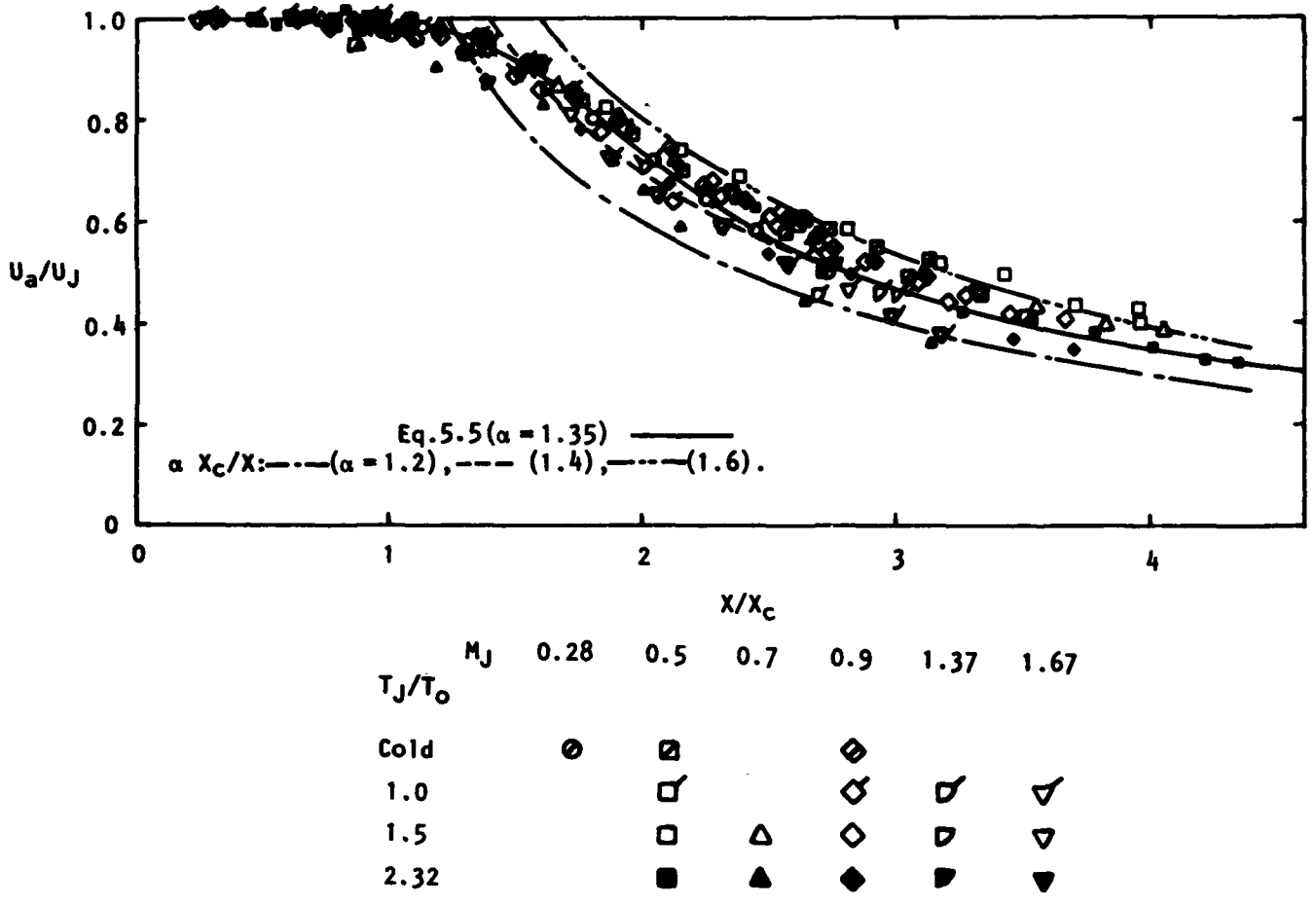

Figure 5.13 U_a/U_J vs X/X_c.

5.2.2.3 The potential core length (x_c)

It was found during the study of isothermal jets [5.5] that the potential core length varied with Mach number. Apparently other parts of the flow field also stretch as Mach number is increased. The potential core length is however a more visible indication of this stretching of the flow field and gives a measure of the extent that the flow field is stretched. Figure 5.15 shows the variation of x_c/D with M_J for cold jets and jets heated to various temperatures. It may be seen that at any given temperature ratio T_J/T_o, x_c/D increases monotonically with Mach number. The equation obtained previously for isothermal jets is given by:

$$x_c/D = 4.2 + 1.1\ M_J^2 \qquad (5\text{-}6)$$

and is shown also in the figure. The curve appears to follow the data points fairly closely until about $M_J = 1.4$ where they begin to deviate. It would seem therefore that the equation should apply to jets up to a Mach number of about 1.4 for the present. The results for jets heated to $T_J/T_o = 1.5$ and 2.32 run almost parallel to the results for the isothermal jets, and it would appear that a parallel equation may be derived for these heated jets.

Witze [5.13] made a study of the results of thirteen experimental investigations (eight subsonic hot and cold jets and five supersonic cold jets) and derived expressions for the variation of x_c/D with M_J and ρ_o/ρ_J (the density ratio) in both the subsonic and supersonic ranges. The expressions are represented by the full lines in Figure 5.15 for an isothermal jet. The curves exhibit the same Mach number trend as observed here, and in the subsonic range there is very good agreement between Witze's formula and the present results. In the supersonic range, the predicted results tend to be lower. On studying some of the original data used by Witze, it appears that the experimental results are lower also*. These results are shown in Figure 5.15. It appears therefore that a significant difference exists between results of x_c/D obtained with the LV and those of the pitot-static probes. To confirm this, pitot-static readings are made in the Mach 0.9 cold jet and they indicate a value of x_c/D of 4.7 compared with the value of 5.8 from LV measurements.

The reason for this discrepancy is still not clear. As in the case of the discrepancy in the values of δ_η, it is believed to be associated with the pitot probe being inserted into the flow region and consequently altering the flow pattern. This aspect of the result would need to be investigated further.

The effect of higher jet temperature ratio is to decrease the potential core length. Witze has suggested a linear variation of x_c/D with $(\rho_o/\rho_J)^{-0.28}$ [or $(T_J/T_o)^{-0.28}$] for subsonic flows, and $(T_J/T_o)^{-0.5}$ for supersonic flows. The present results however indicate that the same relationship may hold for

---

*It should be pointed out that this was not observed previously in Reference 5.5. The reason is that the values of x_c/D referenced in Reference 5.5 were obtained from an intermediary source and contained inherent errors due to inaccuracies in extracting data from graphs. There is perhaps also a contribution due to a different interpretation of x_c.

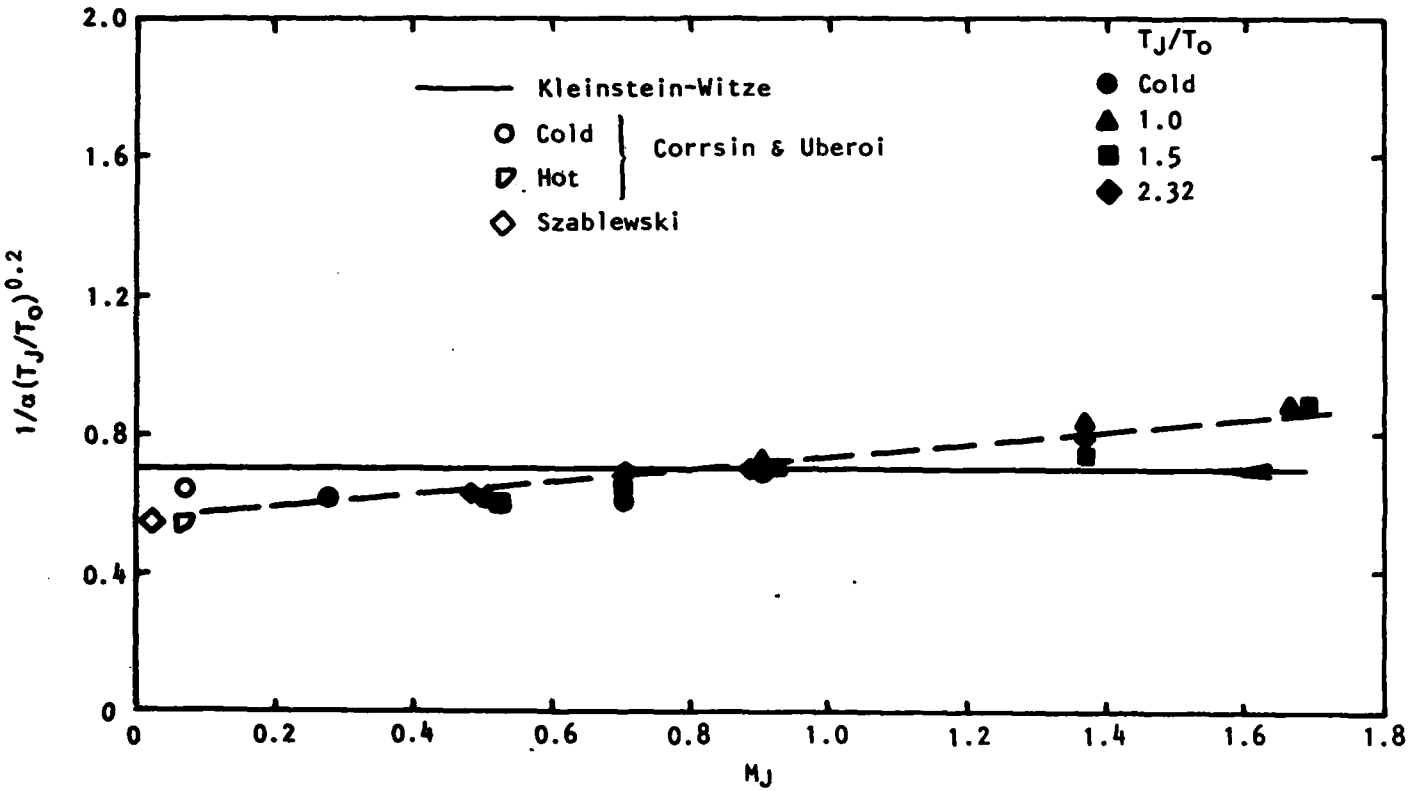

Figure 5.14 $1/\alpha(T_J/T_o)^{0.2}$ vs M_J

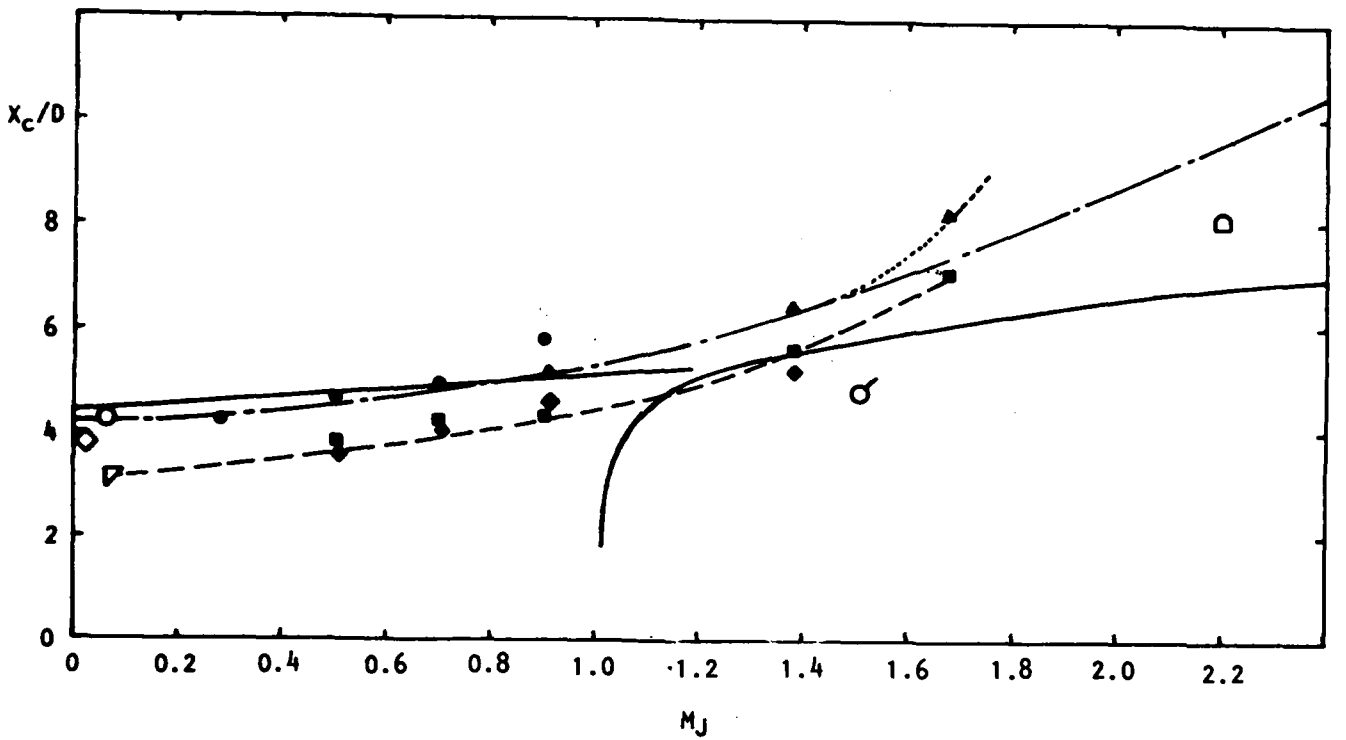

Present Results: T_J/T_o = ● cold, ▲ 1.0, ■ 1.5, ◆ 2.32, —·— Eq. 5.6. ◇ Szablewski 1950, Faris 1963; ○ (Cold) ▽ (T_J/T_o = 2.06) Corrsin and Uberoi 1950; ♂ Warren 1957; ⊓ Eggers 1966. —— Witze.

Figure 5.15 X_c/D vs M_J.

both subsonic and supersonic flows and a power of -0.2 would be more appropriate. This applies to heated jets. For the cold jet a power of -0.5 seems to give a better collapse.

5.2.2.4 Total and static temperature

Figure 5.16 shows the centerline distribution of the temperature-difference ratio for a Mach 0.5 jet. Both the static and total temperatures are shown and there is very little difference between the two. This agrees with the observation made in respect of radial distributions of static and total temperature. Data reconstructed from Wilson and Danckwert's [5.15] results for a Mach 0.29 jet are also shown and the distribution lies upstream of the present results. This is consistent with the stretching of the flow field and the centerline distributions moving downstream with increasing Mach number.

The potential core length of the thermal flow field (x_{ct}) is determined from the temperature distributions, and is found to be smaller than the corresponding value from the velocity flow field. At Mach 0.5, x_{ct} is about 0.77 x_c.

5.3 TURBULENCE INTENSITIES

5.3.1 Radial Distributions

Figures 5.17, 5.18, and 5.19 show typically the radial distributions of the axial ($\tilde{u}/U_J$) and radial ($\tilde{v}/U_J$) turbulence intensities and the covariance $\overline{u'v'}/U_J^2$, respectively. As noted before $\tilde{v}/U_J$ is about 2/3 to 3/4 of the corresponding values of $\tilde{u}/U_J$.

The variations due to the spreading of the jet are taken care of by plotting the distributions in terms of η^*. In spite of this precaution, however, the curves do not fully collapse. It is clear, therefore, that the turbulence intensity is not preserved as has been assumed. Instead, it falls with axial distance. It was suggested [5.5] that a better collapse would be achieved if the turbulence intensity at each axial station were normalized by the peak value measured at that station. This is carried out in Figures 5.20, 5.21, and 5.22, respectively, and a definite improvement is seen.

For the purpose of the noise source calculations in Section 2.4, it is necessary for the radial distributions of the turbulence to be given as explicit expressions. Now, some of the distributions have a Gaussian appearance and may reasonably be fitted with curves of the form $e^{-c\eta^{*2}}$ (e.g. Liu and Maestrello [5.16]). For the other distributions, it would seem that a more complex expression would be required (e.g. Figure 5.23, which shows a fairly sharp peak and exhibits pronounced skewness). However, as was seen earlier, the calculations for the noise source strength only involves the area under the distribution. As such, the equation does not need to follow the distribution exactly, provided that the trends are generally reproduced and the area under the curve is reasonably correct. A Gaussian-type profile would therefore be adequate in most cases.

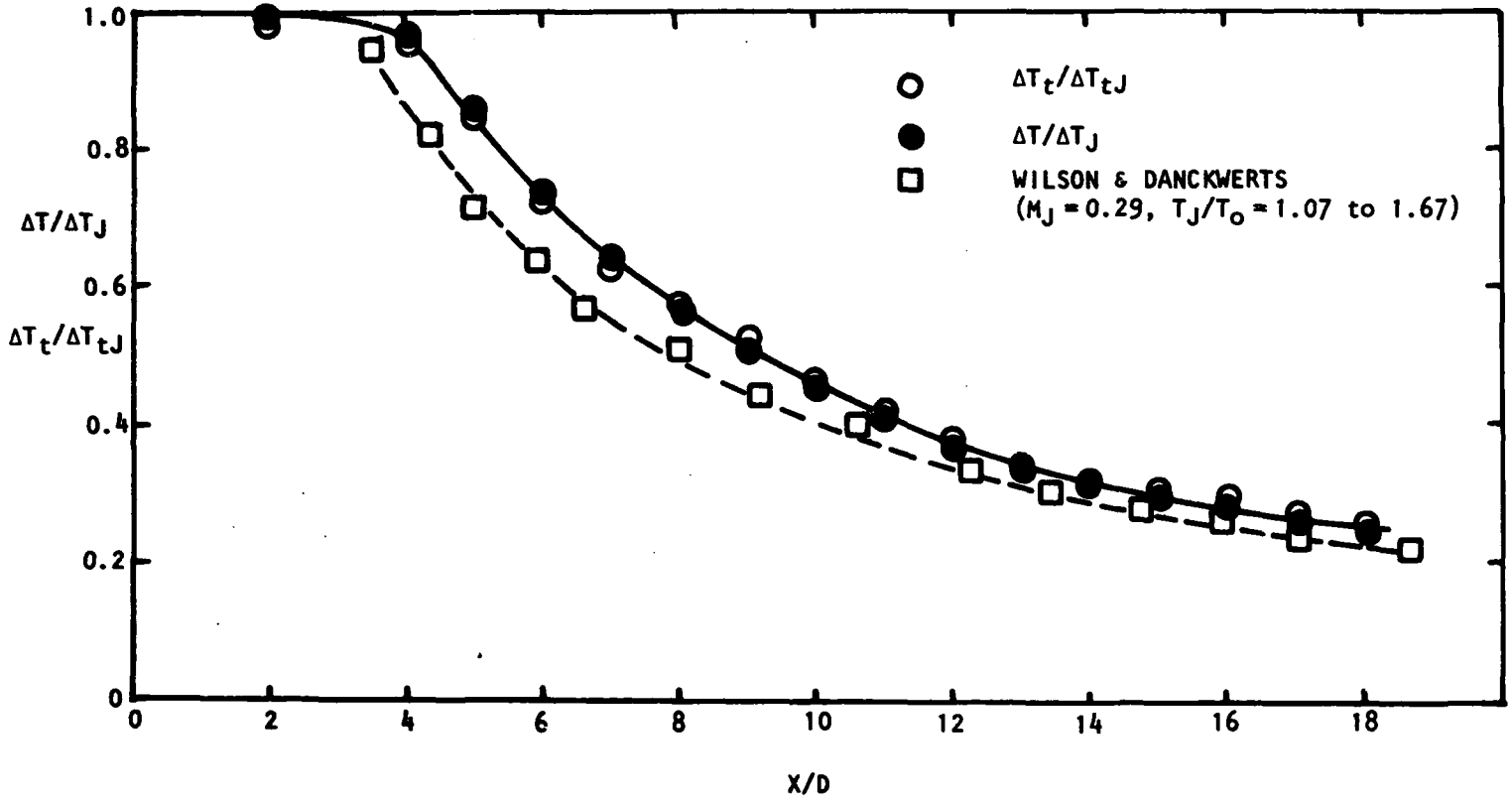

Figure 5.16 $\Delta T/\Delta T_J$ and $\Delta T_t/\Delta T_{tJ}$ vs X/D ($M_J = 0.5$, $T_J/T_o = 2.32$)

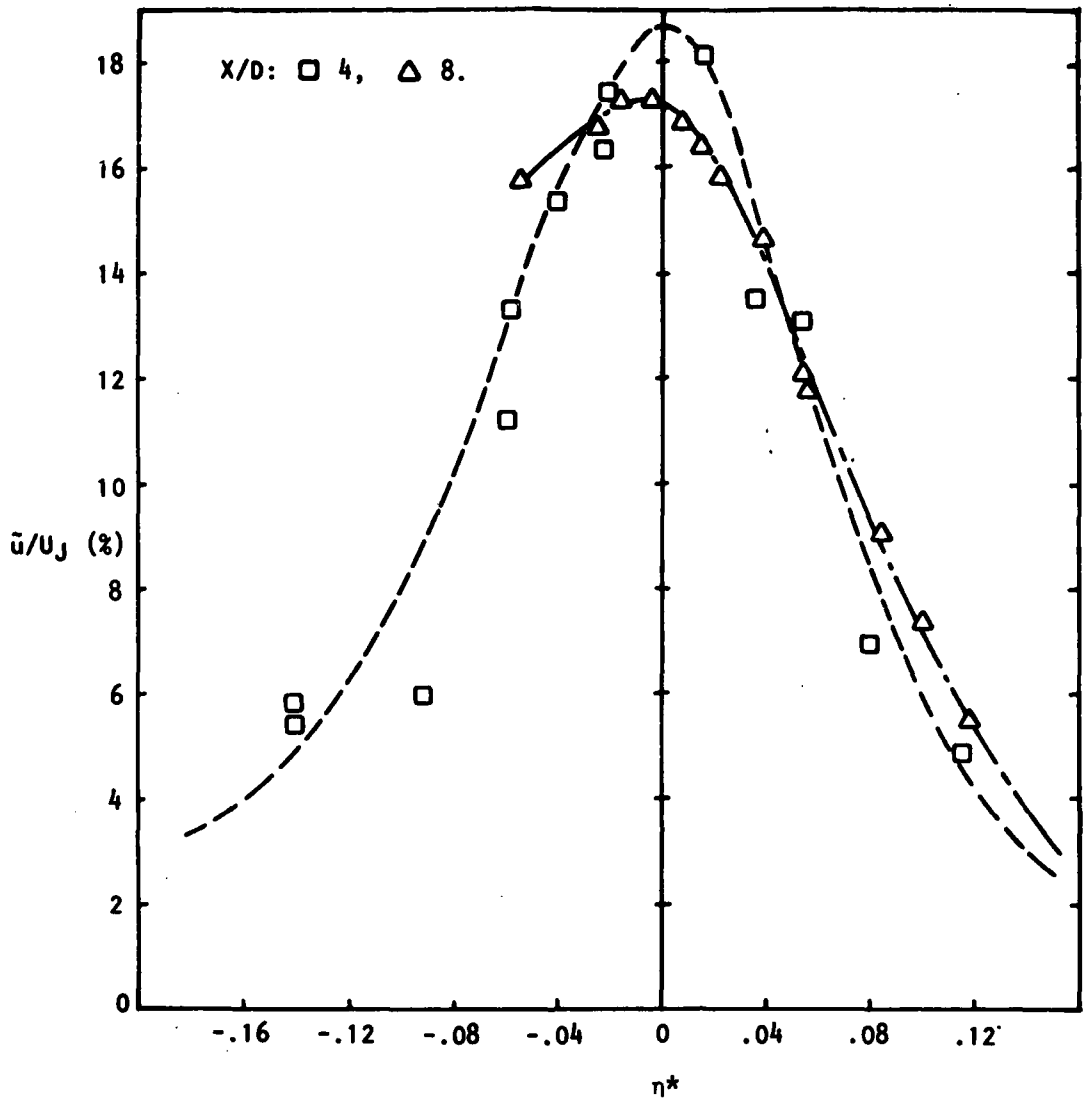

Figure 5.17 $\tilde{u}/U_J$ vs η^* ($M_J = 0.7$, $T_J/T_o = 2.32$).

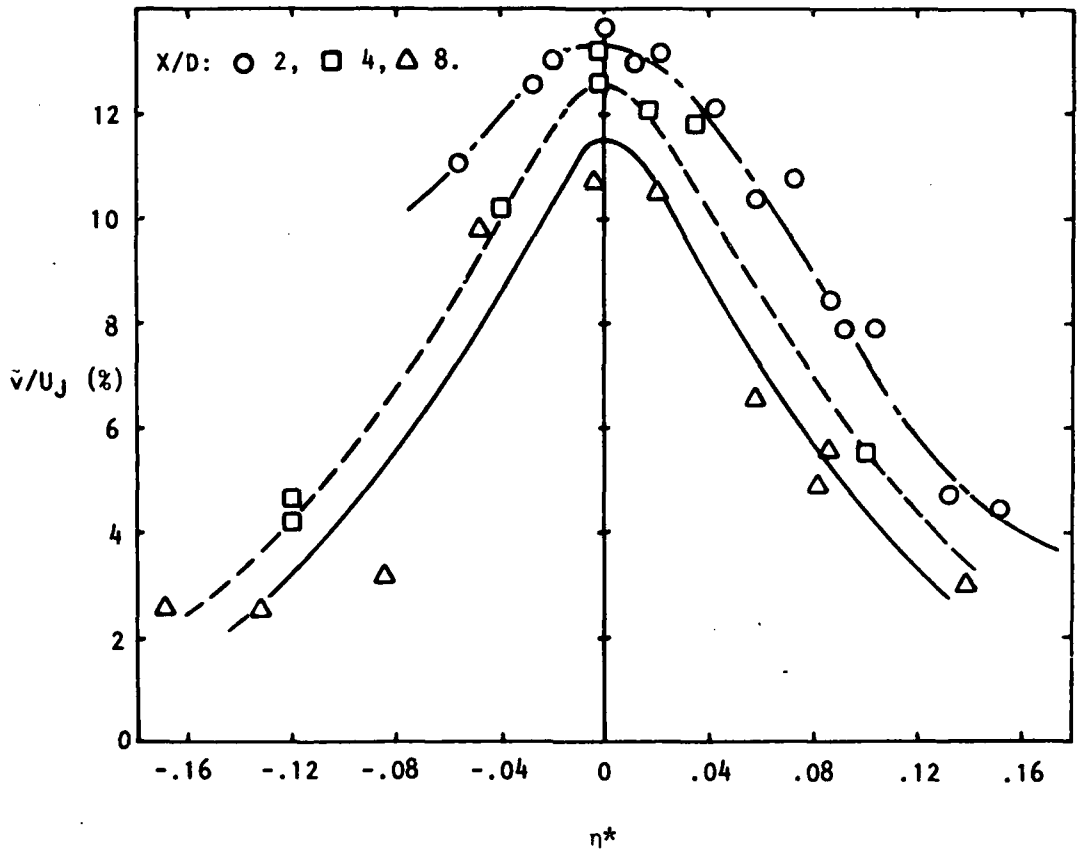

Figure 5.18 $\tilde{v}/U_J$ vs η* ($M_J = 0.7$, $T_J/T_o = 2.32$).

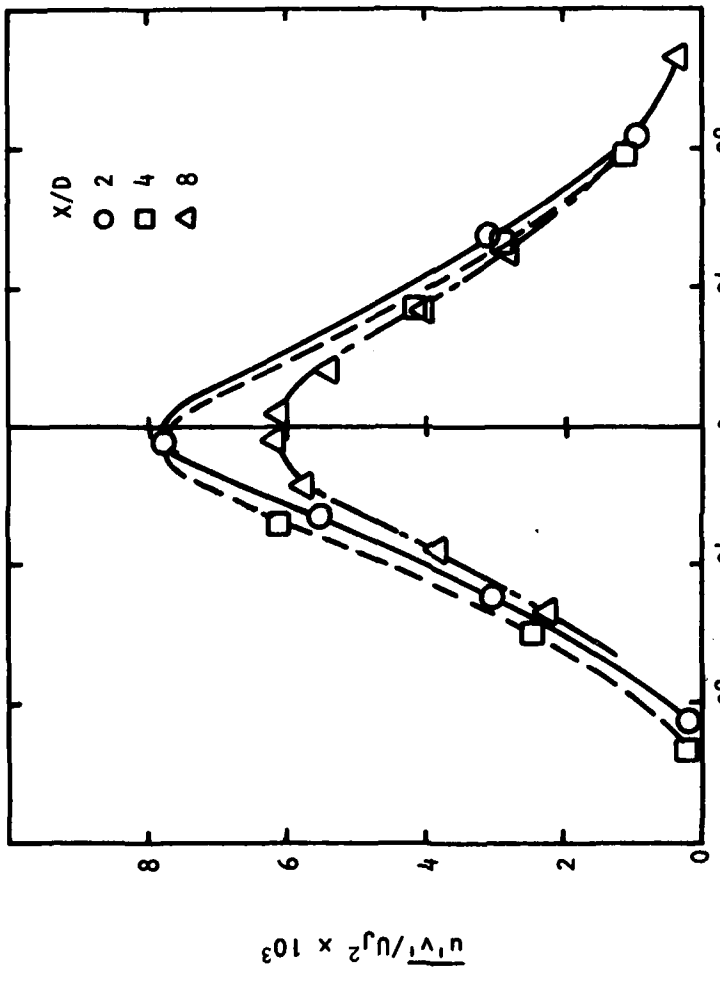

Figure 5.19 $\overline{u'v'}/U_J^2$ vs η* ($M_J = 0.7$, $T_J/T_O = 2.32$).

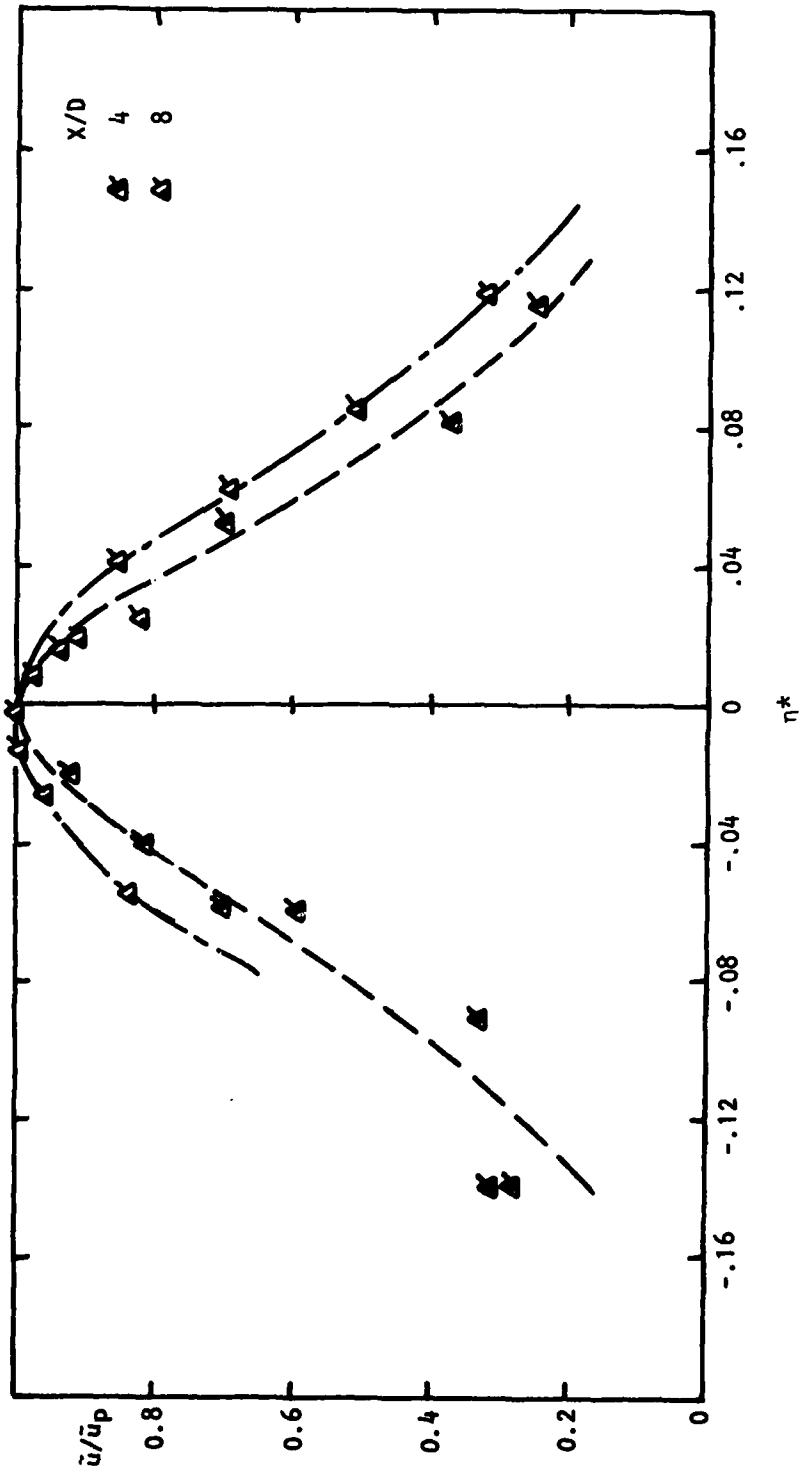

Figure 5.20 $\tilde{u}/\tilde{u}_p$ vs η^* ($M_J = 0.7$, $T_J/T_O = 2.32$).

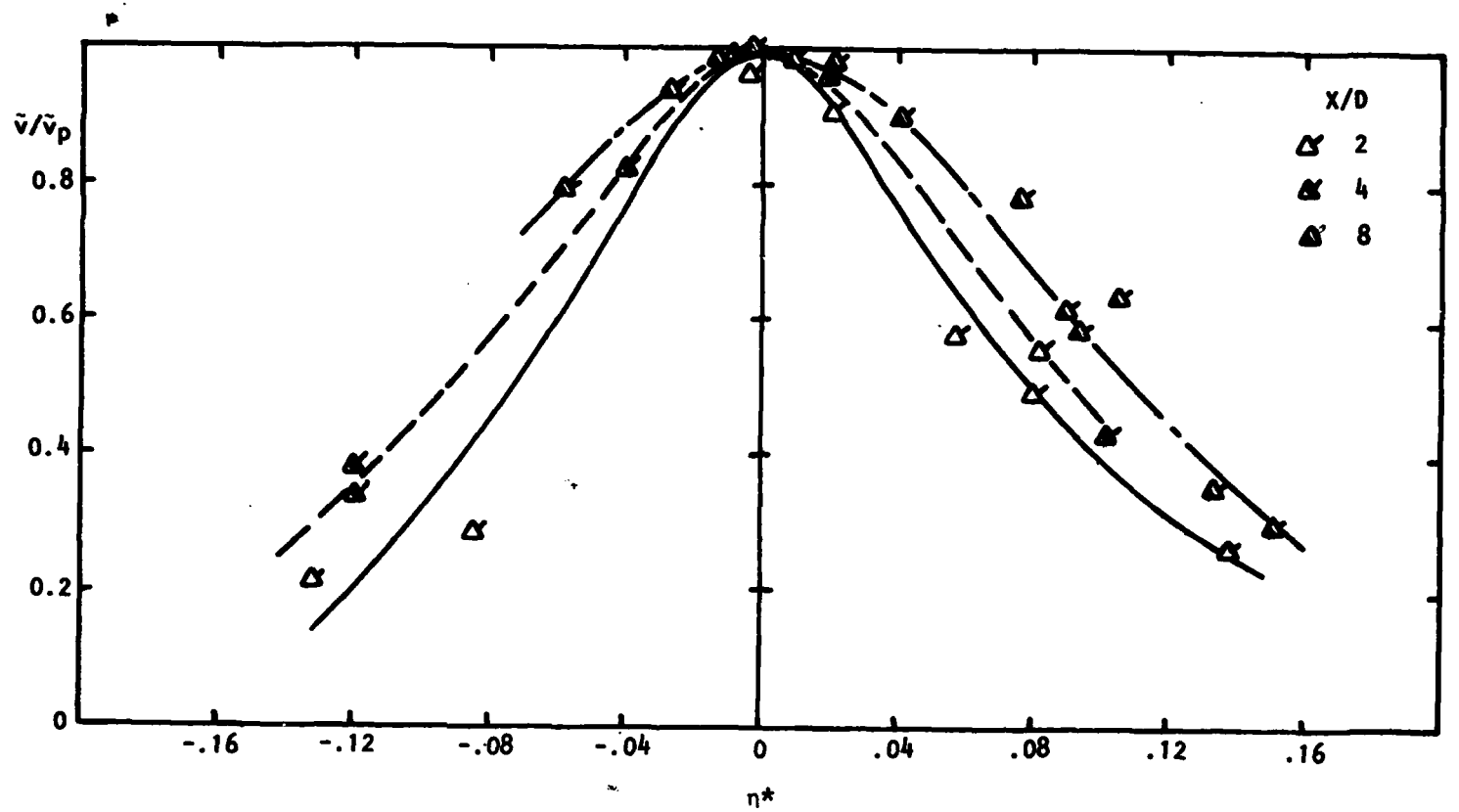

Figure 5.21 $\tilde{v}/\tilde{v}_p$ vs η^* ($M_J = 0.7$, $T_J/T_o = 2.32$)

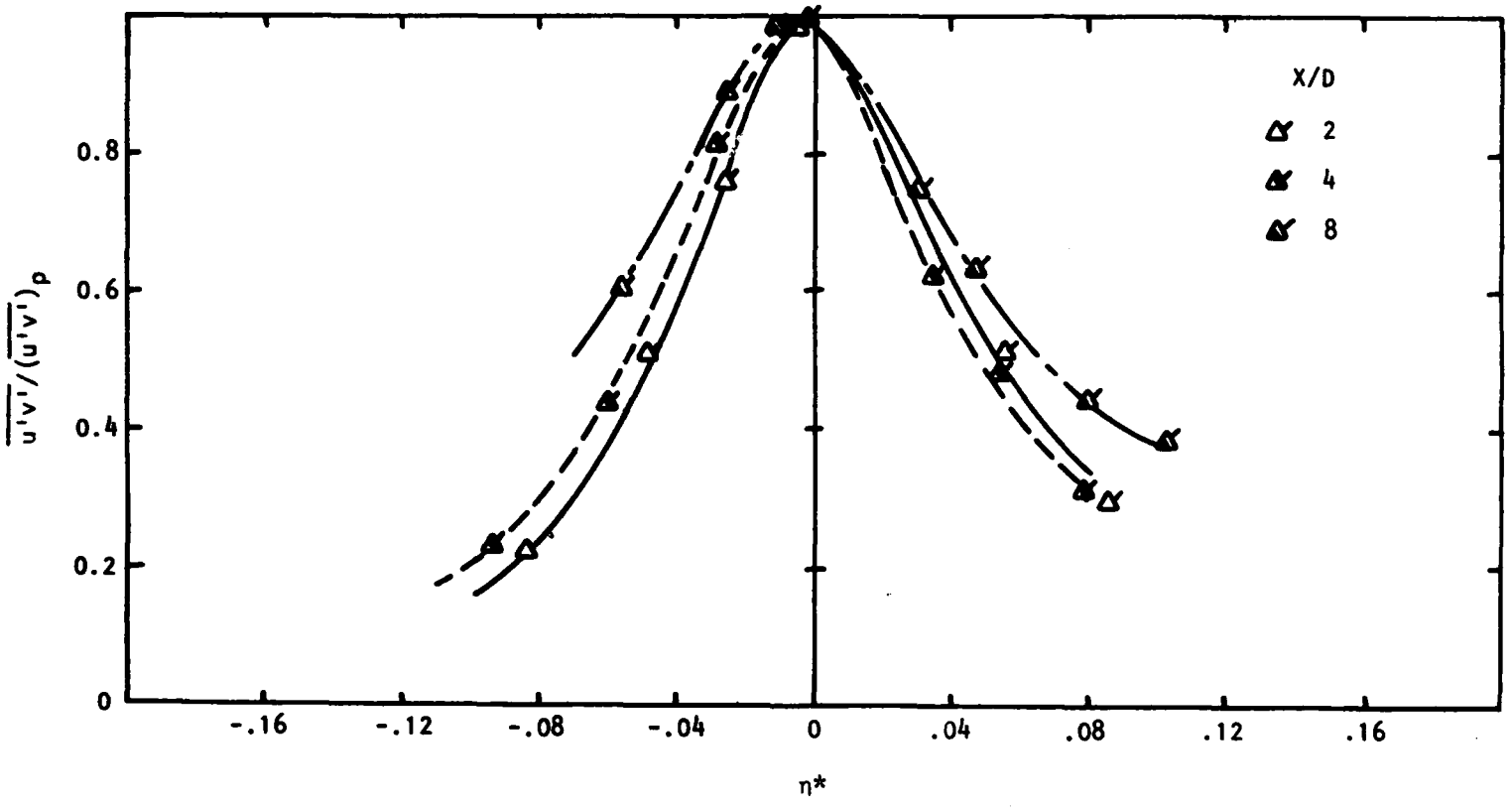

Figure 5.22 $\overline{u'v'}/(\overline{u'v'})_p$ vs η* ($M_J = 0.7$, $T_J/T_o = 2.32$)

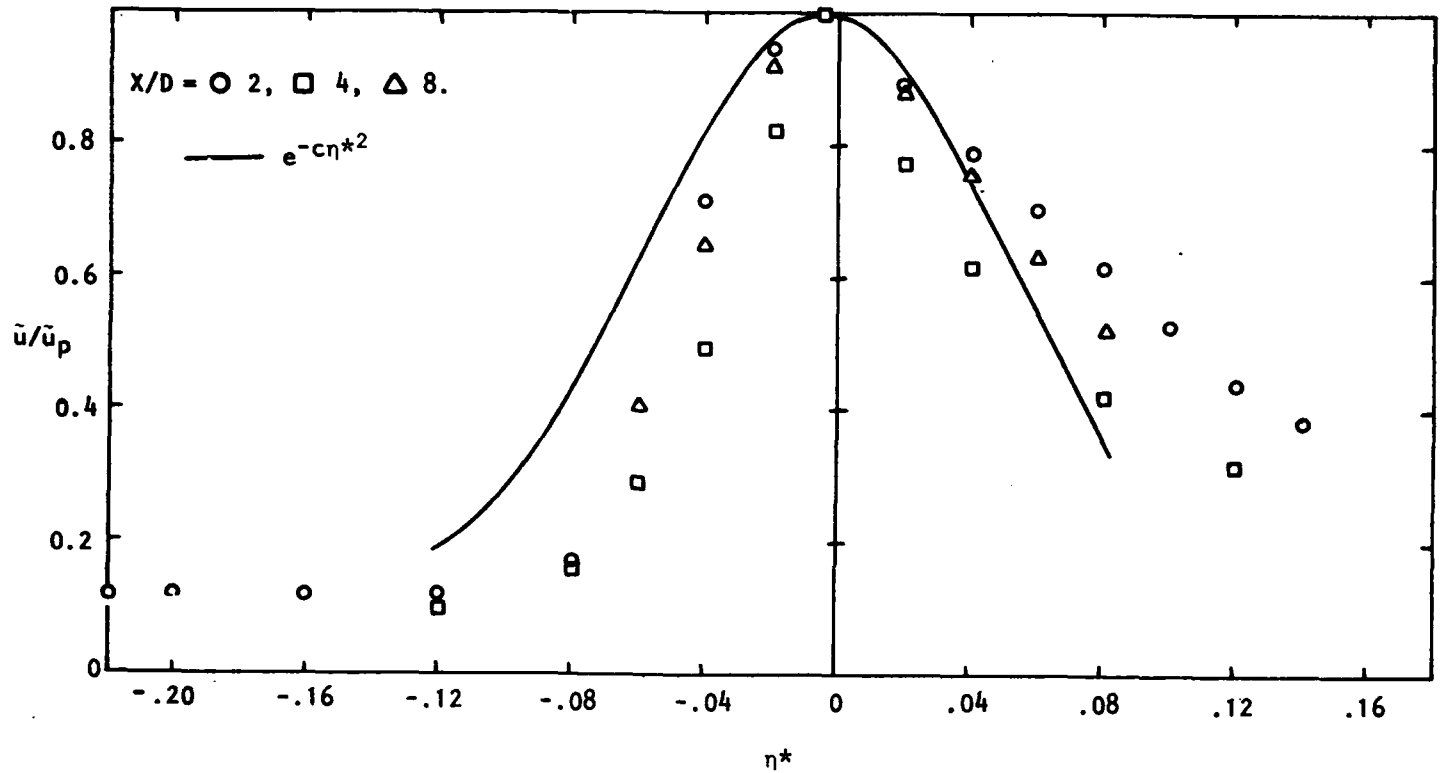

Figure 5.23 $\tilde{u}/\tilde{u}_p$ vs η^* ($M_J = 1.37$, $T_J/T_O = 1.0$).

Figure 5.24 shows a composite diagram of the normalized axial turbulence levels plotted in terms of $\sigma\eta^*$ for various Mach number and temperature ratio conditions. Although the data may not be as compact as for the mean velocity distribution, they do tend to fall in one band. The collapsed data, interestingly, has a Gaussian appearance and may be represented by a curve of the form $e^{-.56(\sigma\eta^*)^2}$. The parameter σ is given by the Korst-Chow relationship $\sigma\delta_\eta = \sqrt{\pi}$ and Equation (5-2) which expresses δ_η in terms of the jet Mach number and temperature ratio. It would seem appropriate therefore to describe the radial distributions of normalized turbulence intensity by $e^{-c\eta^{*2}}$, where $c = 0.56\sigma^2$.

In the foregoing figures, the peaks of the turbulence intensity lie at or very close to $\eta^* = 0$. This suggests that the vicinity of $r_{0.5}$ is also the position for maximum turbulence intensity. Figure 5.25 shows the variation of $r_{0.5}$ with x/D for various Mach number and temperature ratios. The magnitude of $r_{0.5}$ rises initially with x, reaches a peak and subsequently falls. The curvature of the curves increases slightly with temperature ratio. It is expected therefore that the position of the peak turbulence intensity would vary in the same manner.

The variation of the peak axial turbulence intensity ($\tilde{u}_p/U_J$) with x/D is shown in Figure 5.26 for isothermal jets of different Mach numbers. As noted above, the values of $\tilde{u}_p/U_J$ fall with increasing x/D and M_J.

At any given Mach number, the fall is very gradual at first, and for the Mach 0.3 or 0.5 jets, this may be represented by the equation

$$\tilde{u}_p/U_J = 0.193 \quad \exp\,[-.0016\ (x/D)^2] \qquad (5\text{-}7)$$

From about two potential core lengths downstream, the ratio $\tilde{u}_p/U_J$ decreases more rapidly. This is better illustrated by Figure 5.27 which shows the reciprocal of $\tilde{u}_p/U_J$ for the Mach 0.3 or 0.5 jets. Data reconstructed from Wygnanski and Fiedler [5.4] for a Mach 0.15 jet are also shown. From the jet exit to about x/D = 10, the change in $U_J/\tilde{u}_p$ is very little but between x/D = 10 and 35, $U_J/\tilde{u}_p$ rises linearly. From x/D = 45, the rise is still linear but the slope is greater. Wygnanski and Fiedler's data in the region x/D = 10 to 18 are also plotted in Figure 5.26, and may be represented by a curve given by $\tilde{u}_p/U_J = 1.6\ D/x$. The curve intersects the present data for the Mach 0.3 and 0.5 jets at about x = 10D or 2.4 x_c.

These trends are confirmed in the Mach 0.9 results which extend to greater values of x/D. It may be seen that from the jet exit to about x = 13D or 2.5 x_c, the fall is very gradual, but downstream of that, the 1/x fall is evident and the curve of 1.88 D/x passes through the data point at x/D = 16. The Mach 1.37 data show similar tendencies and on the basis of the above the large change in slope is expected to occur at about x/D = 16. The Mach 1.67 data deviate from these trends. Instead, it rises with x/D. This apparently is not an erroneous trend and seems to be supported by data obtained at other temperature ratios. It is clear therefore that for jets at $M_J < 1.4$ say, there are two zones having different rates of decay in $\tilde{u}_p/U_J$. In the first zone extending to about $x/x_c = 2.4$, the decay is very gradual but from $x/x_c = 2.4$, it varies as 1/x.

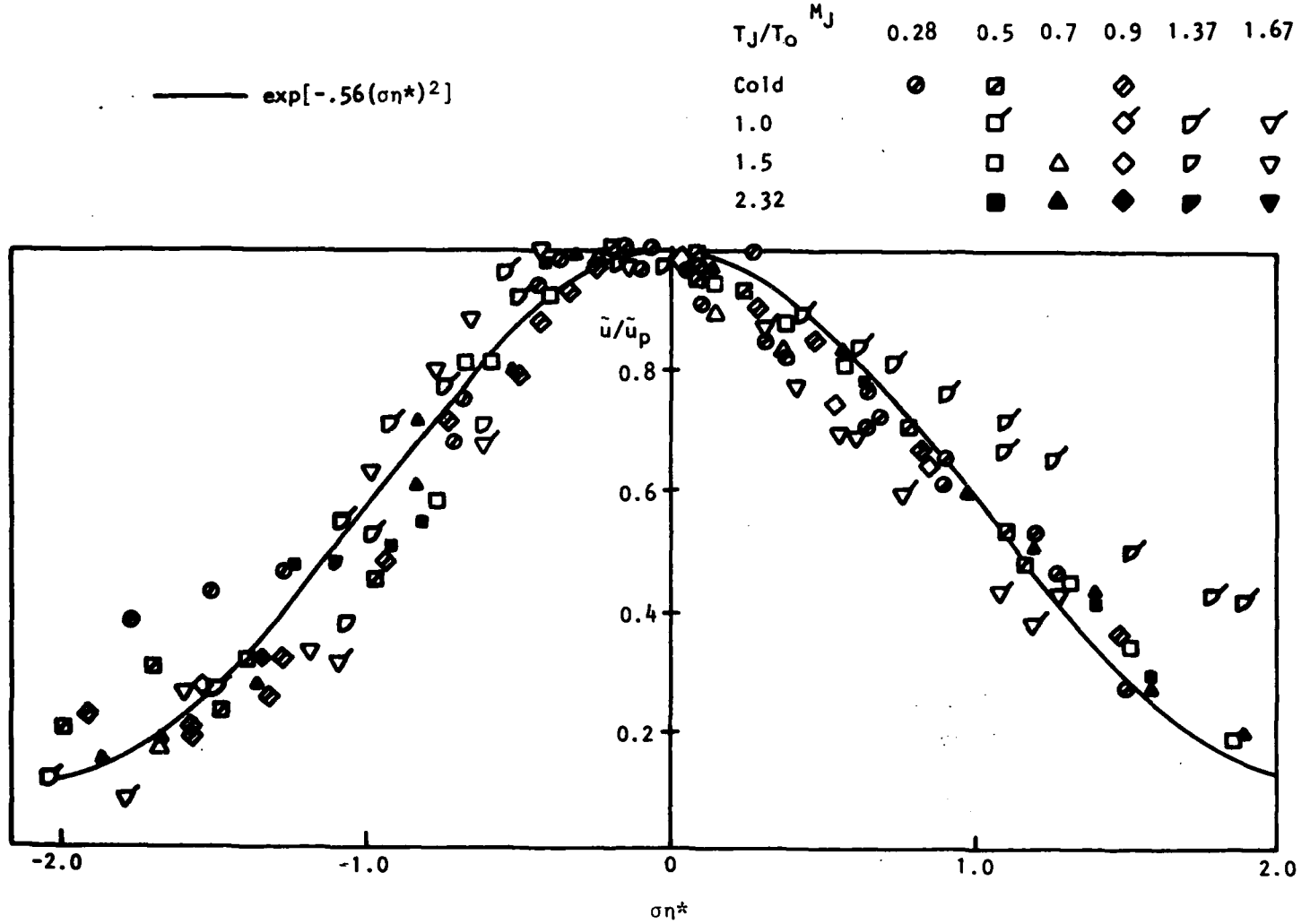

Figure 5.24 $\tilde{u}/\tilde{u}_p$ vs $\sigma\eta^*$.

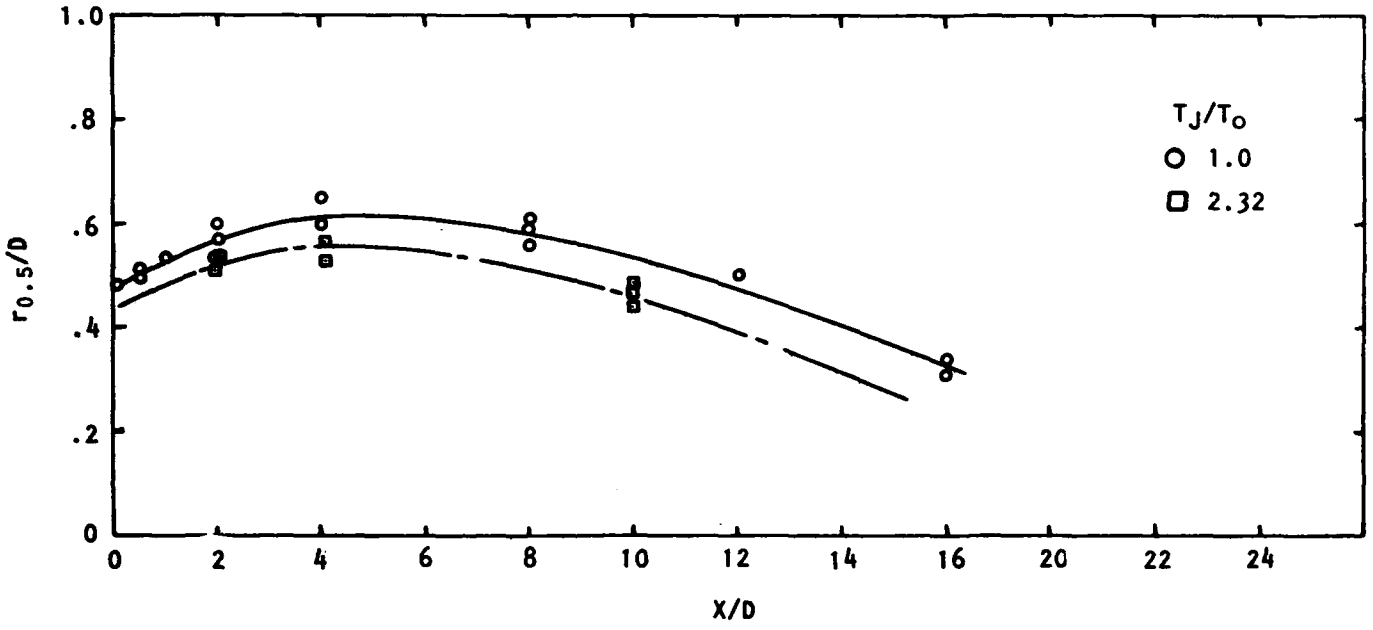

Figure 5.25 $r_{0.5}/D$ vs x/D (M_J = 0.5 to 1.67).

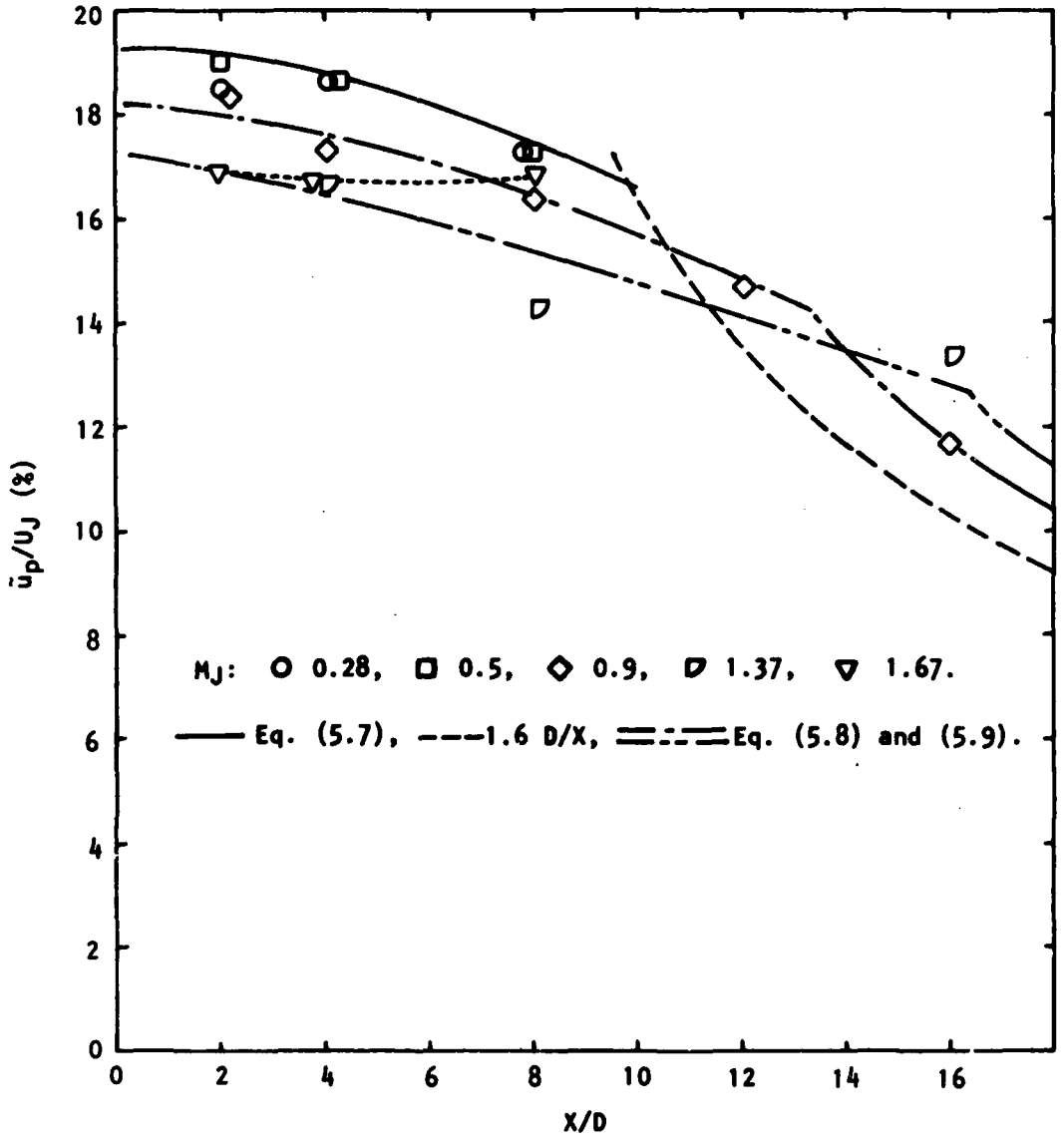

Figure 5.26 $\tilde{u}_p/U_J$ vs X/D (T_J/T_o = 1.0).

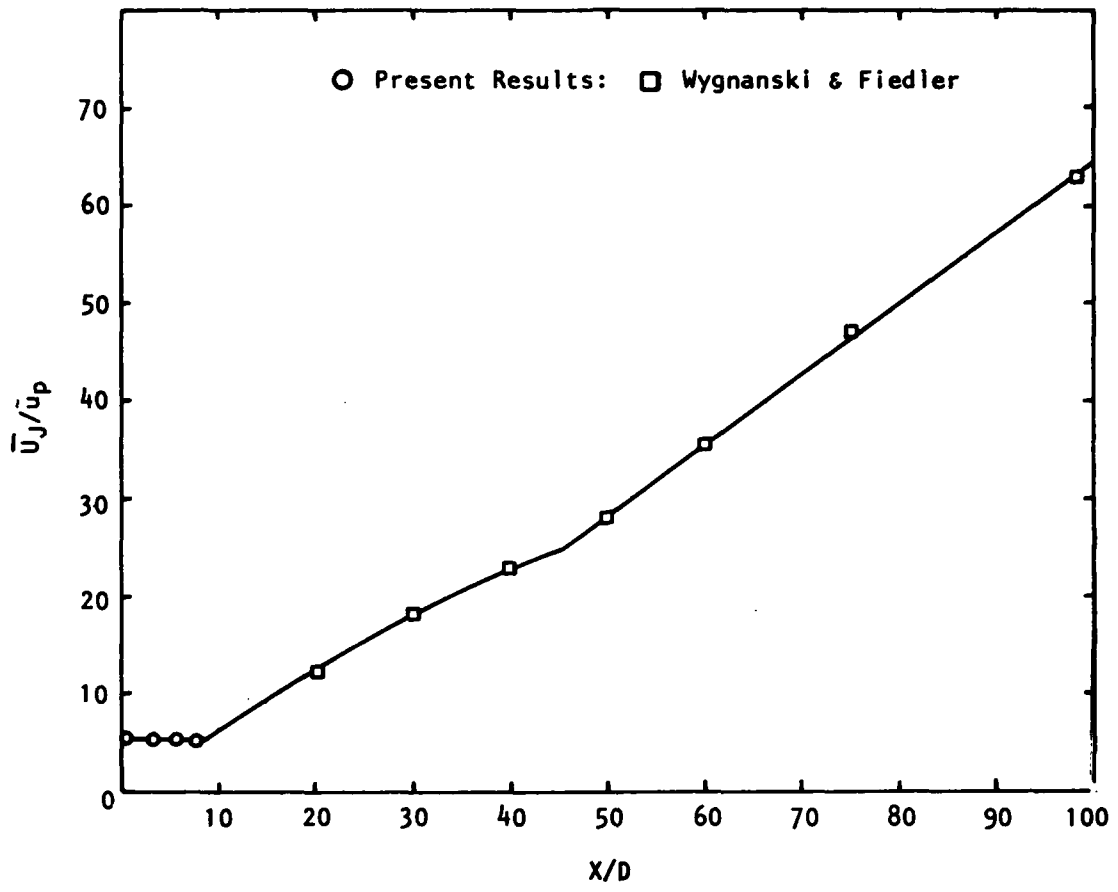

Figure 5.27 $U_J/\tilde{u}_p$ vs X/D.

The peak turbulence intensity (for $M_J \leq 1.4$) at a given point in the jet falls with increasing Mach number. On incorporating Mach number effects into equations for $\tilde{u}_p/U_J$, we obtain the following expressions:

$$\tilde{u}_p/U_J = 0.179\ M_J^{-0.1028}\ e^{-.0016\ (x/D)^2} \tag{5-8}$$

for $x < 2.4\ x_c$ and

$$\tilde{u}_p/U_J = 0.43\ M_J^{-0.128}\ \frac{x_c}{x}\ e^{-.0092\ (x_c/D)^2} \tag{5-9}$$

for $x > 2.4\ x_c$.

A Mach number change is accompanied by the stretching of the flow field. Therefore, the changes observed at a fixed point reflect to some extent also changes due to shifts in the flow field. Figure 5.28 shows the variation of the peak turbulence intensity at the station $x = x_c$. Since this station moves with the stretching of the flow field, the results would represent the real effects of Mach number more correctly. The peak turbulence intensity falls initially with increasing Mach number and there is little distinction between jets of different temperatures. As the Mach number is increased further, the peak turbulence reaches a trough and subsequently rises. This change in the trend of $\tilde{u}_p/U_J$ is similar to that observed in the variation of $\delta\eta$. The troughs also occur at about the same Mach number. It suggests that the rise in peak turbulence intensity at the higher Mach numbers may also be associated with the eddies convecting supersonically.

5.3.2 Centerline Distributions

Centerline distributions of the turbulence intensities tend to move with the stretching of the flow field. It has been found [5.5] that for isothermal jets, increasing the Mach number causes the distributions to move downstream. In particular, the peaks which appear in these distributions move to greater distances.

Figure 5.29 shows the centerline distributions of the axial turbulence intensity for a Mach 0.5 jet and varying temperature ratios. As the temperature ratio is increased, the distributions move upstream. This is in agreement with the decreasing potential core length and the upstream movement of the centerline distributions of the mean velocity. The peaks may also be seen to move upstream, and in line with previous work [5.5], they lie close to $x = 2\ x_c$. The magnitude of the peaks rises with temperature ratio. This is opposite to the trends observed in Mach number effects and is different from the trend suggested by the peak values of the radial distributions (Figure 5.28). It would seem therefore that unlike Mach number effects, there is no consistency in the trends observed in the peaks of radial and axial distributions.

Figures 5.30 and 5.31 show axial distributions of the axial and radial turbulence intensities plotted against x/x_c. The turbulence intensities are normalized by the respective peak values. The results fall in one band with the peaks located close to $x/x_c = 2.0$.

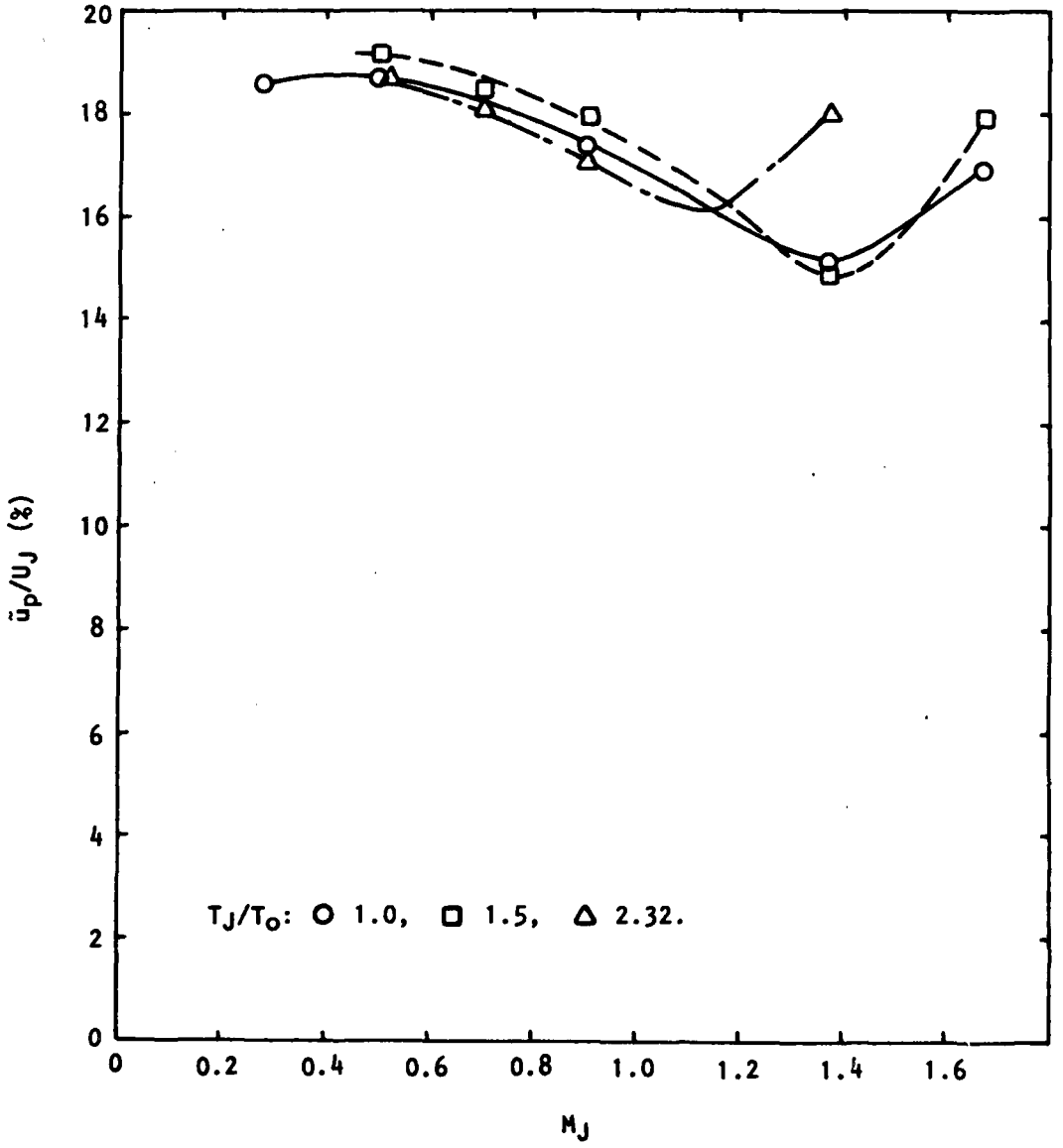

Figure 5.28 $\tilde{u}_p/U_J$ vs M_J (at $X = X_c$).

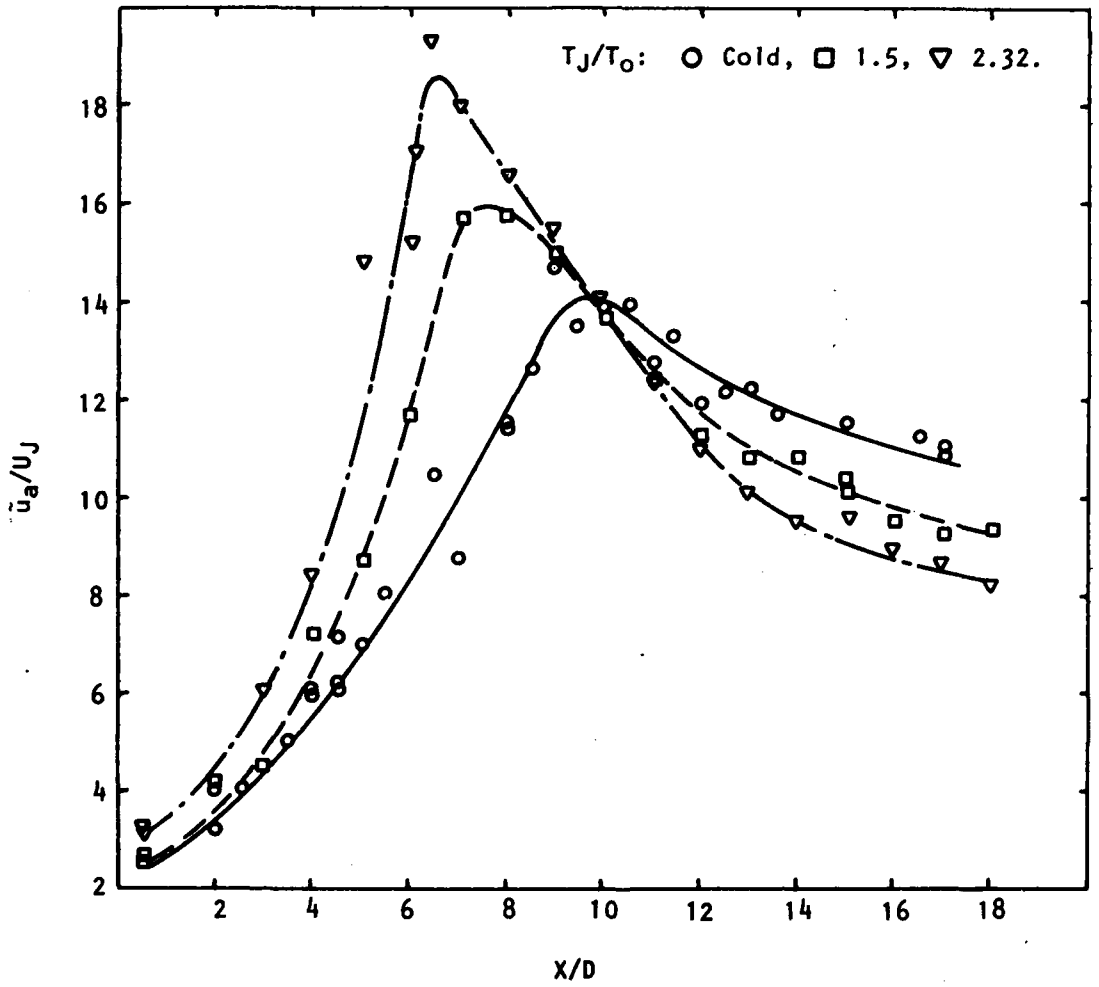

Figure 5.29 $\tilde{u}_a/U_J$ vs X/D ($M_J = 0.5$).

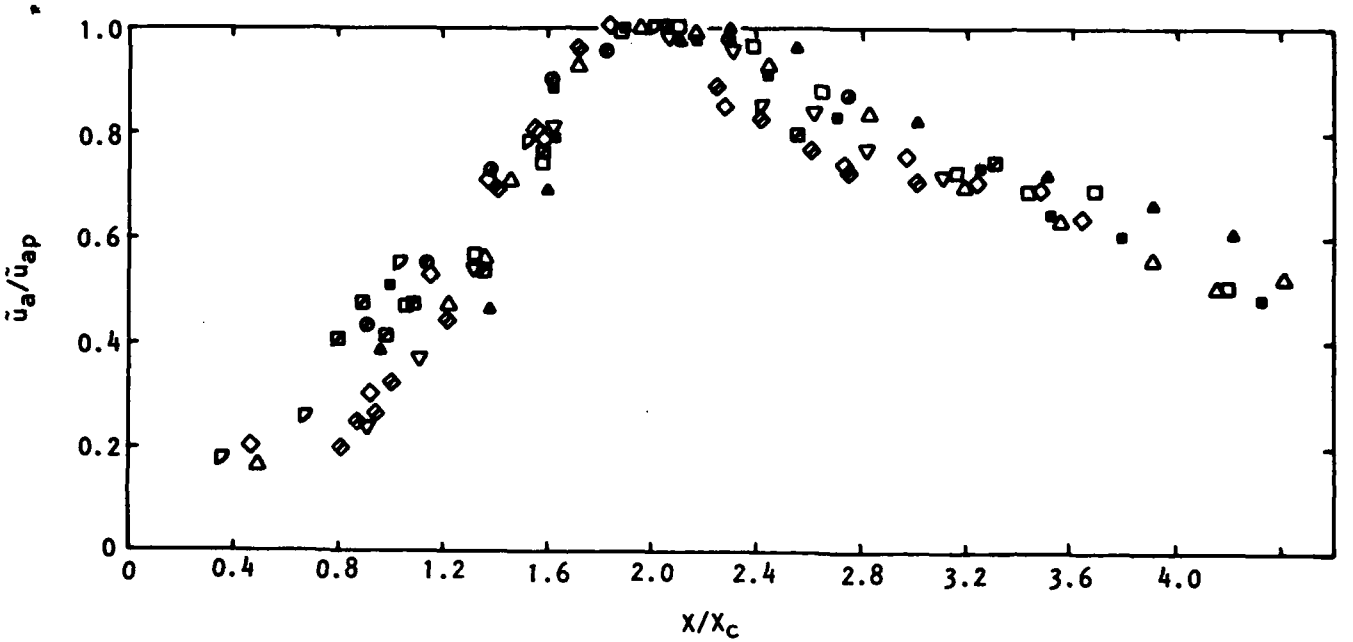

T_J/T_o \ M_J	0.28	0.5	0.7	0.9	1.37	1.67
Cold	⊘	⊡		◇		
1.0		▽		◇	▽	▽
1.5		□	△	◇	▽	▽
2.32		■	▲	◆	▼	▼

Figure 5.30 $\tilde{u}_a/\tilde{u}_{ap}$ vs X/X_c.

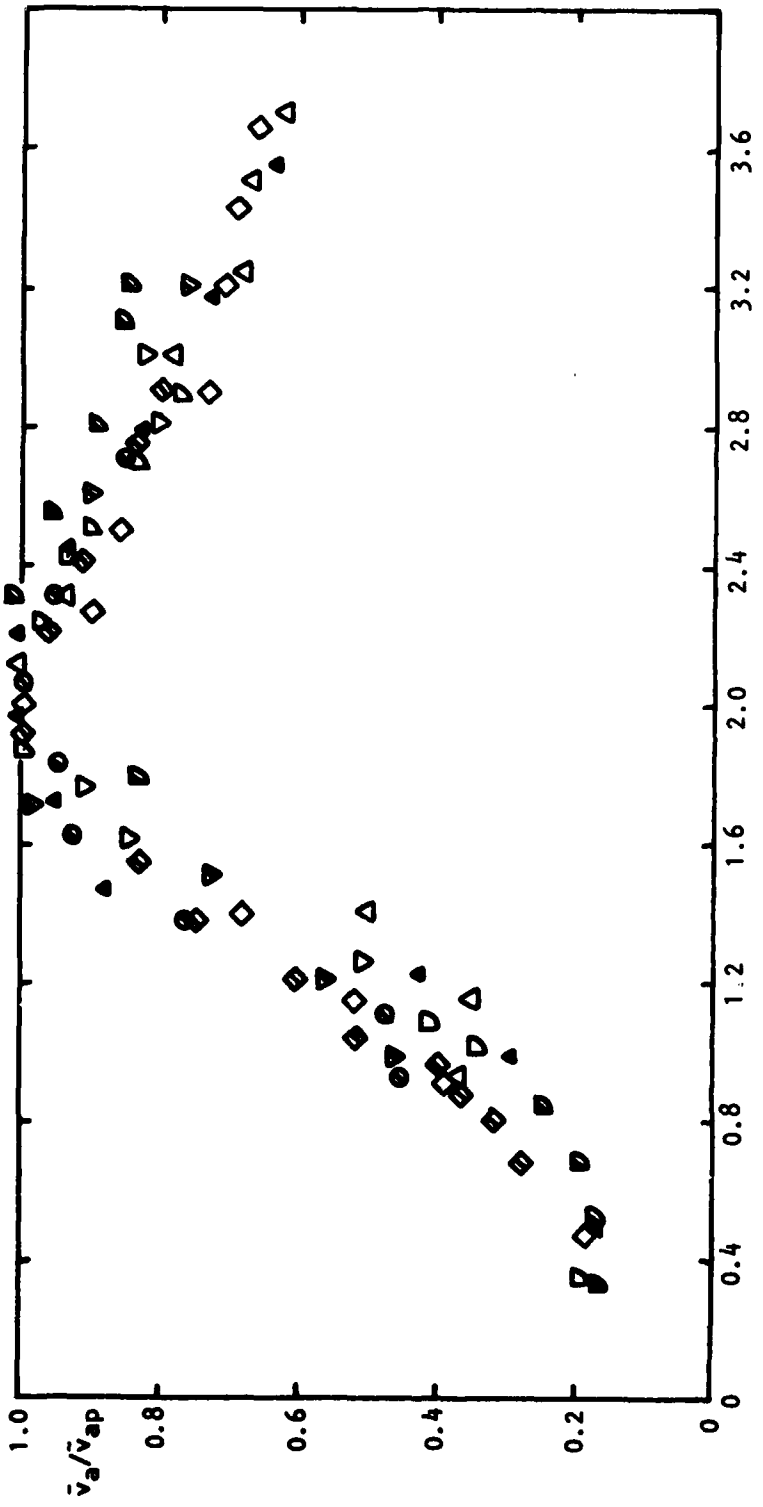

Figure 5.31 $\bar{v}_a/\bar{v}_{ap}$ vs X/X_c. (Legend in Fig. 5.30)

Figures 5.32 and 5.33 show respectively the variation of the peak values of the axial and radial turbulence intensities. The values generally fall with increasing Mach number. The gradient is higher for the heated jets and the results for $T_J/T_O = 2.32$ cut across those for $T_J/T_O = 1.0$ at around $M_J = 1.0$.

5.4 OTHER TURBULENCE CHARACTERISTICS

5.4.1 Autocorrelations and Spectra

Figure 5.34 shows the autocorrelation curve for axial velocity fluctuations on the jet centerline of a Mach 0.5 cold jet. This is obtained in the potential core of the jet at $x/D = 2.0$. The ordinate is expressed in terms of the space-time correlation coefficient which is defined in a more general form by:

$$R_{ij}(\vec{\xi},\tau) = \frac{\overline{u'_{iA}(\vec{x};t) \cdot u'_{jB}(\vec{x}+\vec{\xi};\ t+\tau)}}{\tilde{u}_{iA} \cdot \tilde{u}_{jB}} \qquad (5\text{-}10)$$

where the bar denotes a time-averaged value, and tilde the rms value. The subscripts i and j refer to the direction of the velocity component, and A and B the locations of the two measurement points. In the present case of autocorrelations, the points A and B are coincident and the separation and $\vec{\xi} = 0$. The abscissa gives the time delay τ.

The curve has a tendency to oscillate about the zero axis, which is typical of autocorrelation curves obtained in the region of the potential core, and has a period of about 700 μs. The period transforms to a frequency of over 1400 Hz which scales with the jet speed (U_J) and diameter (D) to give a Strouhal number (S) of about 0.5. This also agrees with data obtained previously with hot-wires (e.g. Davies [5.17]).

There is, however, one important detail of the curve which does not appear to be correct and deserves some mention. The autocorrelation of velocity signals detected in the potential core invariably traces a *slowly damped* cosine curve [5.17]. This is understandable because the velocity signals in the potential core are generated by the passage of a fairly regularly spaced array of vortices (Lau, Fisher and Fuchs [5.18]) and have a sinusoidal appearance. On the basis of this criterion, the present curve would be incorrect because of a very sharp spike appearing close to $\tau = 0$. It suggests that the value of the correlation coefficient measured at $\tau = 0$ is in error. The more appropriate value would be obtained by extrapolating the results at $\tau > 20$ μs back to $\tau = 0$. The correct value of correlation coefficient at other time delays should therefore be determined by normalizing with this quantity rather than the measured value.

The reasons for the spike at $\tau = 0$ are still not clear. At present the electronic switches in the LV processor require an interval of about 10 μS to reset. There is also a tolerance window built into the system to allow for possible coincidence of signals in the different channels of the LV. Together, they add up to a period of between a few microseconds to 20 μS

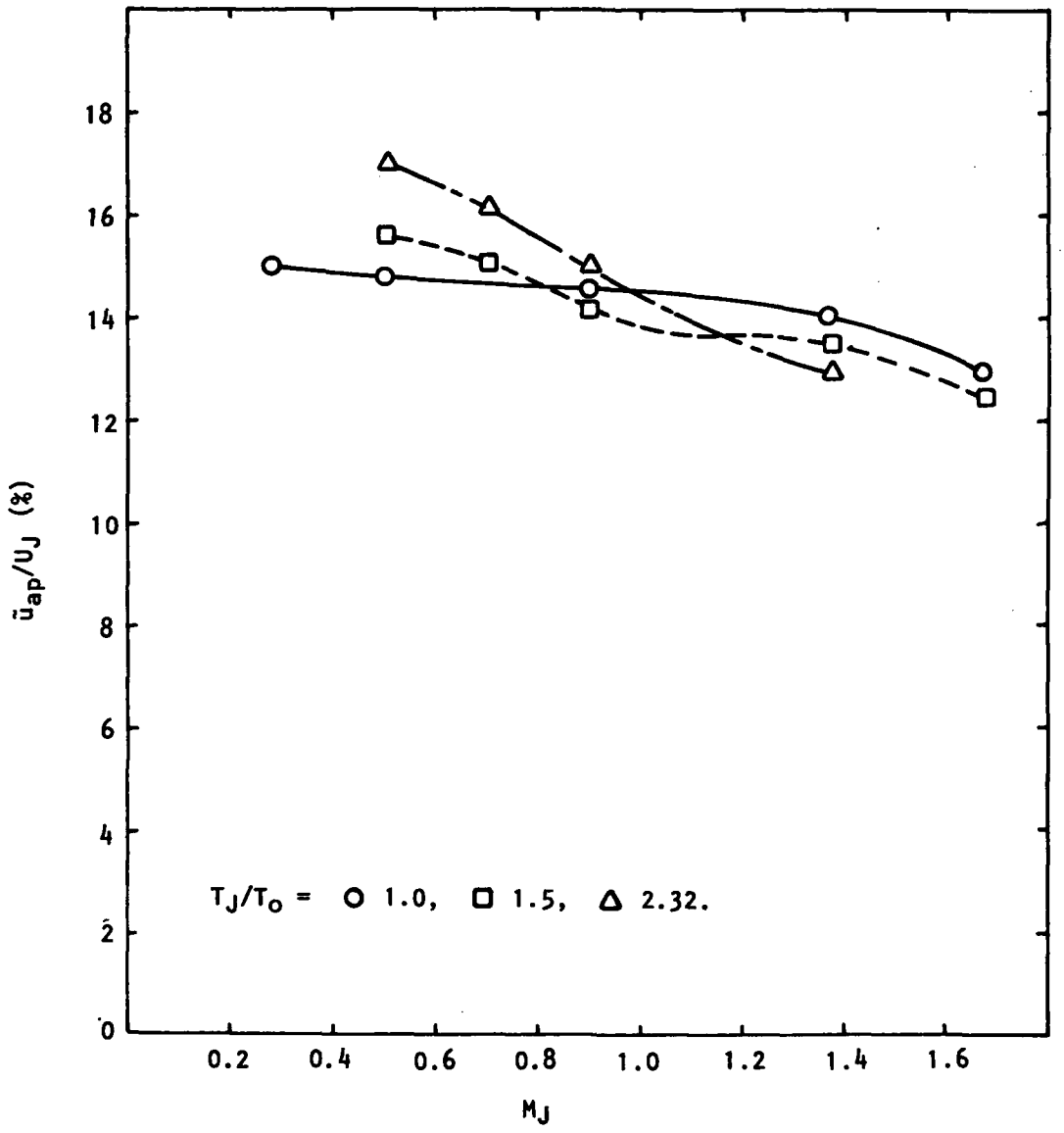

Figure 5.32 $\tilde{u}_{ap}/U_J$ vs M_J.

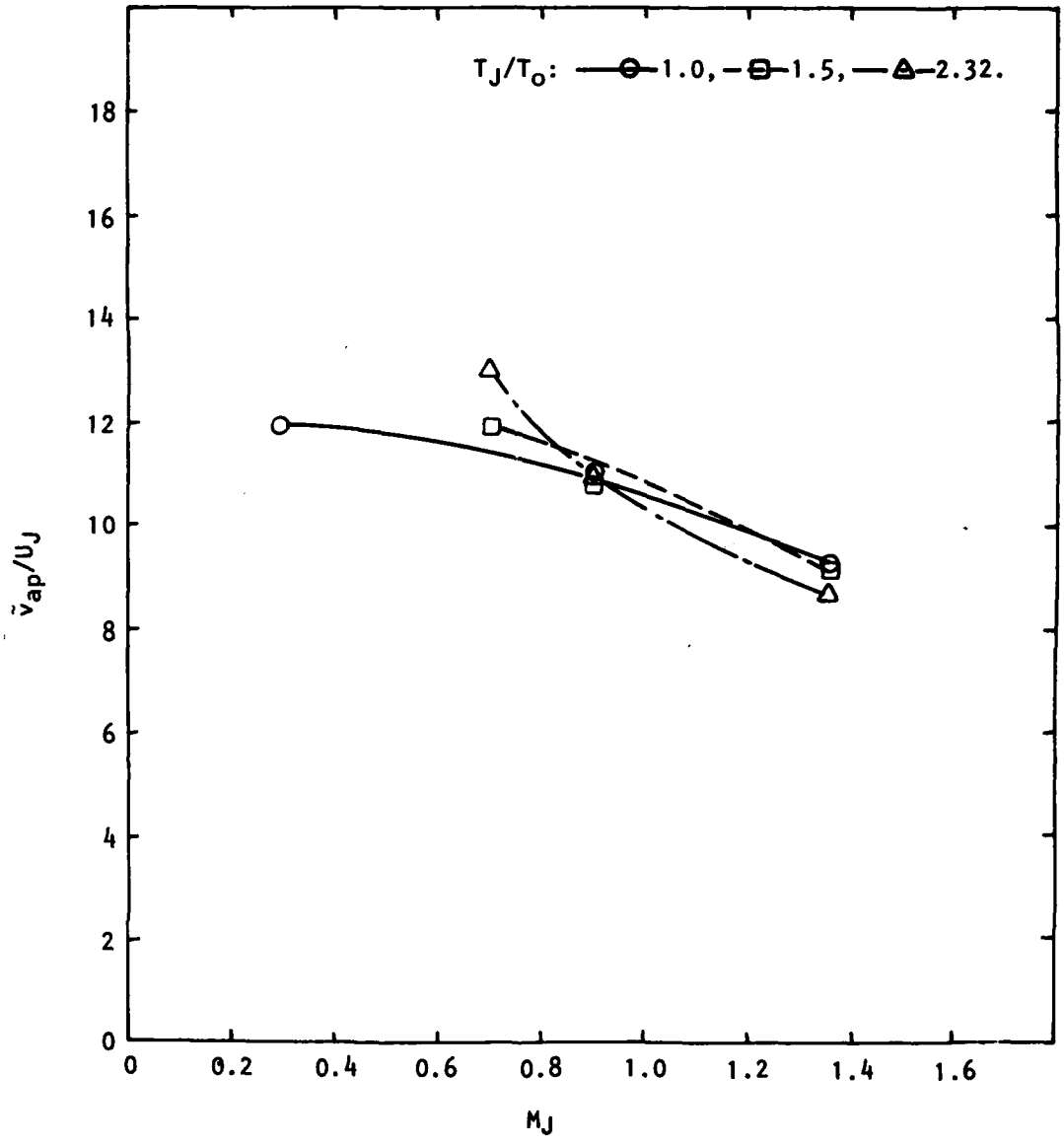

Figure 5.33 $\tilde{v}_{ap}/U_J$ vs M_J.

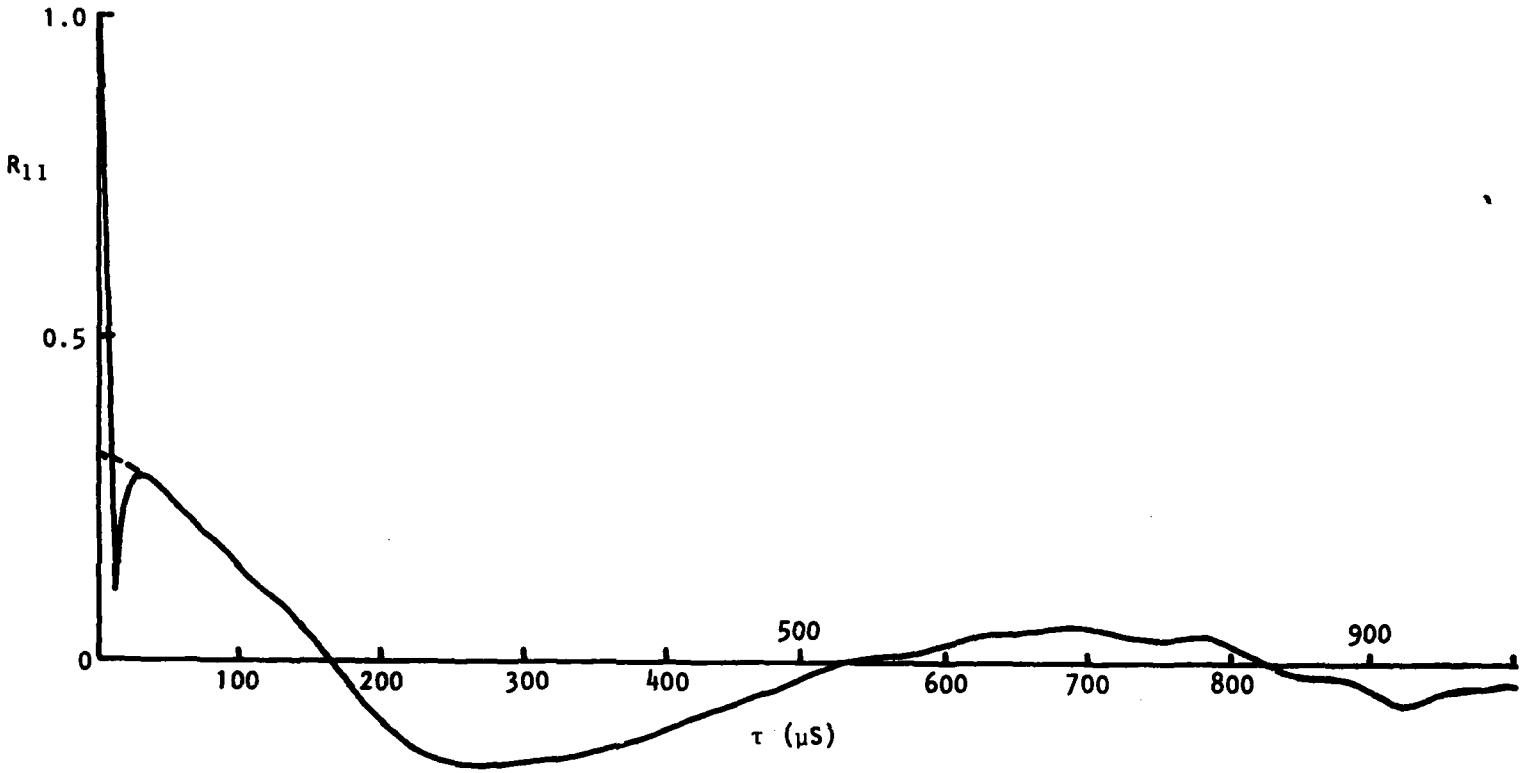

Figure 5.34 Autocorrelation Diagram ($M_J = 0.5$, $X/D = 2.0$, $r/D = 0.0$)

during which the time information is not precisely defined. As such, correlation results are not reliable within this first 20 μS period. This could contribute to the error at $\tau = 0$. Moreover, there is the possibility that electronic noise may erroneously be confirmed by the validation circuits, in which case, uncorrelated and random velocity points would appear. This would augment the correlation results at $\tau = 0$, but not at larger τ. The jitter in the zero-crossing detection is another possible contributor. Work is in progress to try to understand these phenomena, and some of the findings are reported in Reference 5.19.

Figure 5.35 shows the autocorrelation diagram for velocity signals at $x/D = 2.0$ and $r/D = 0.5$ in the same jet. A spike is also visible at $\tau = 0$, but the magnitude of the spike is significantly smaller than that on the jet centerline. In general, it is found that the size of the spike decreases with the *local* turbulence intensity and is negligible from about $r/D > 0.6$.

The Fourier transform of the autocorrelation gives the power spectral density of the velocity fluctuations. Figure 5.36 shows typical spectral results of the axial velocity fluctuations in the potential core, on the lipline ($r/D = 0.5$) and in the outer part of the mixing region. In the potential core, the spectrum shows a narrowband peak (at frequency f_p). As the mixing region is traversed, the peak becomes progressively shallower until $r/D = 0.5$, when the peak disappears [5.5]. At this point, the spectrum is flat for the low frequencies, and begins to fall only when the frequency reaches f_p. At $r/D = 0.7$, the spectrum has a similar appearance except that the spectrum begins to peel off at a lower frequency. Proceeding further outward ($r/D = 0.9$) the process reverses and the spectrum returns to the shape at $r/D = 0.5$.

The peak frequencies are extracted from these spectra and plotted in Figure 5.37 in terms of a Strouhal number ($S = f_p D/U_j$). Where a spectrum does not display a well-defined peak, the frequency at which the spectrum begins to peel off is taken as the peak frequency.* At the radial positions shown, the Strouhal number falls with increasing x/D at first and then asymptotes to a fixed value. The magnitude of the asymptote depends on the radial position. Lau's [5.20] data obtained with hot wires are also shown [Figure 5.37(a)], and agree with the present results.

Results at other Mach numbers and temperature ratios exhibit the same general behavior and are summarized in Figures 5.38 to 5.40. Figure 5.38 shows the axial distribution of the Strouhal number on the jet centerline for isothermal jets at Mach 0.5, 0.9, and 1.37. From Mach 0.5 to 0.9, the distributions of Strouhal numbers are indistinguishable from each other. At Mach 1.37, however, the Strouhal numbers are generally lower. This trend is evident also in the distributions of Strouhal number on the lipline shown in Figure 5.39. It would seem therefore that Strouhal number scaling extends continuously to Mach 0.9 at least. In the supersonic range a small modification apparently takes place.

**In a third-octave spectrum a peak would show at about this frequency.*

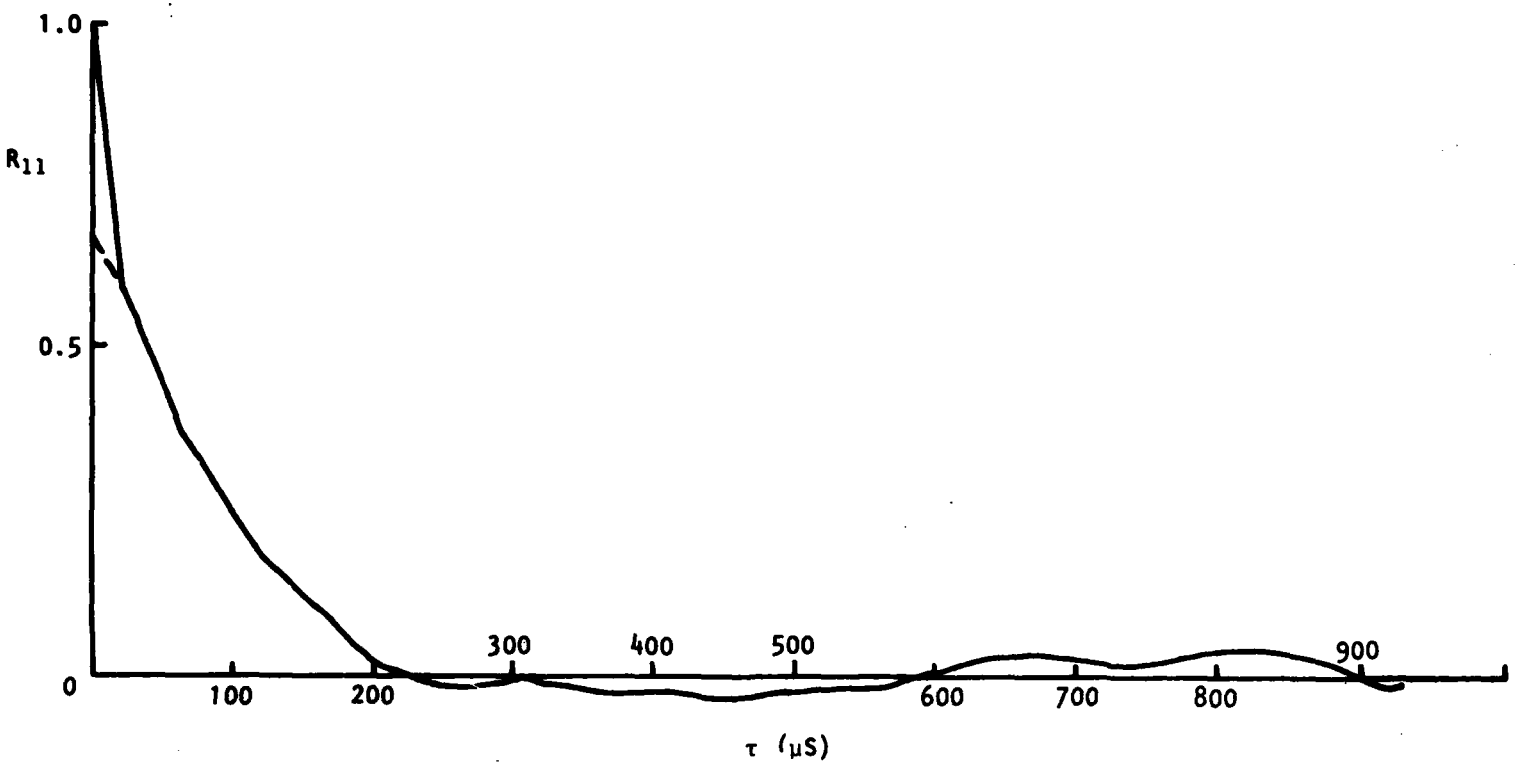

Figure 5.35 Autocorrelation Diagram ($M_J = 0.5$, $X/D = 2.0$, $r/D = 0.5$)

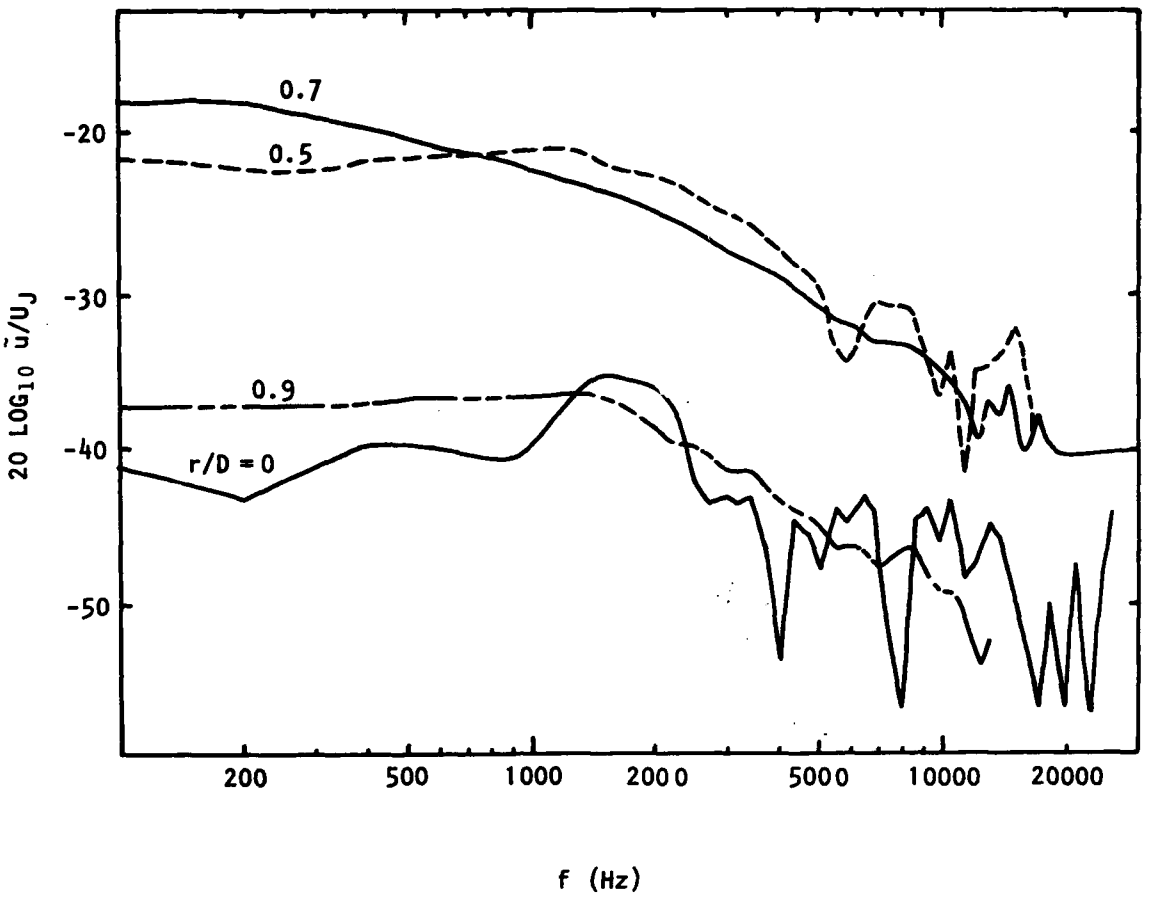

Figure 5.36 Spectra of u'-signals ($M_J = 0.5$, $X/D = 2.0$)

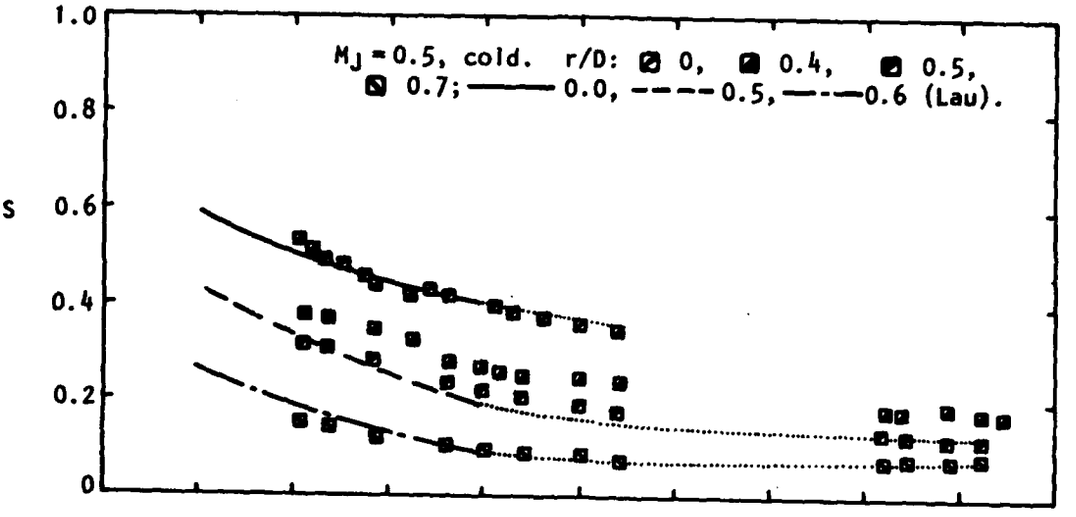

Figure 5.37(a) Strouhal Number vs. X/D (u'-signals).

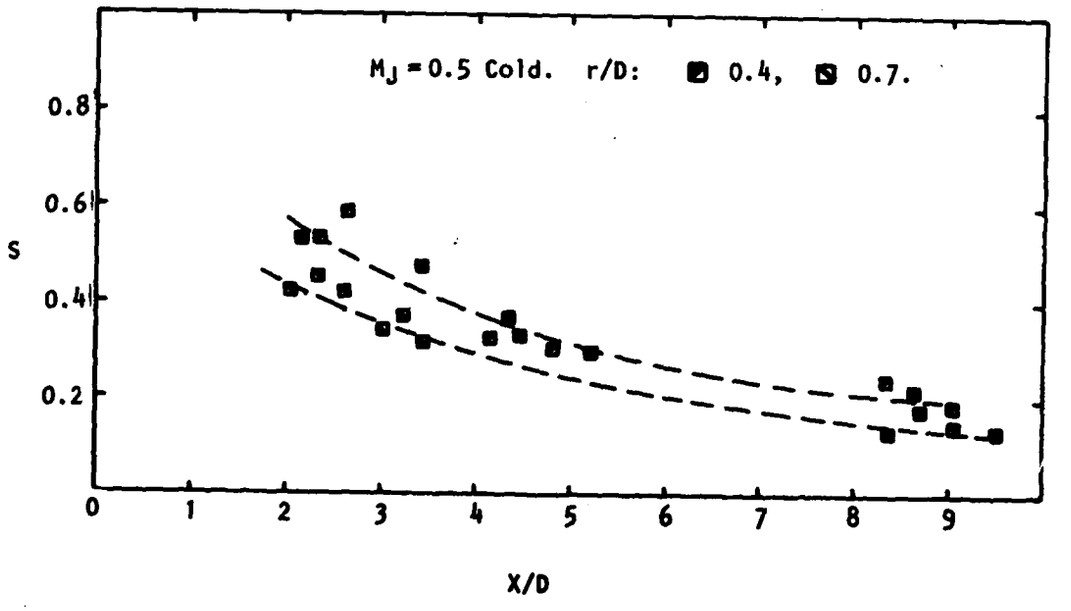

Figure 5.37(b) Strouhal Number vs X/D (v'-signals).

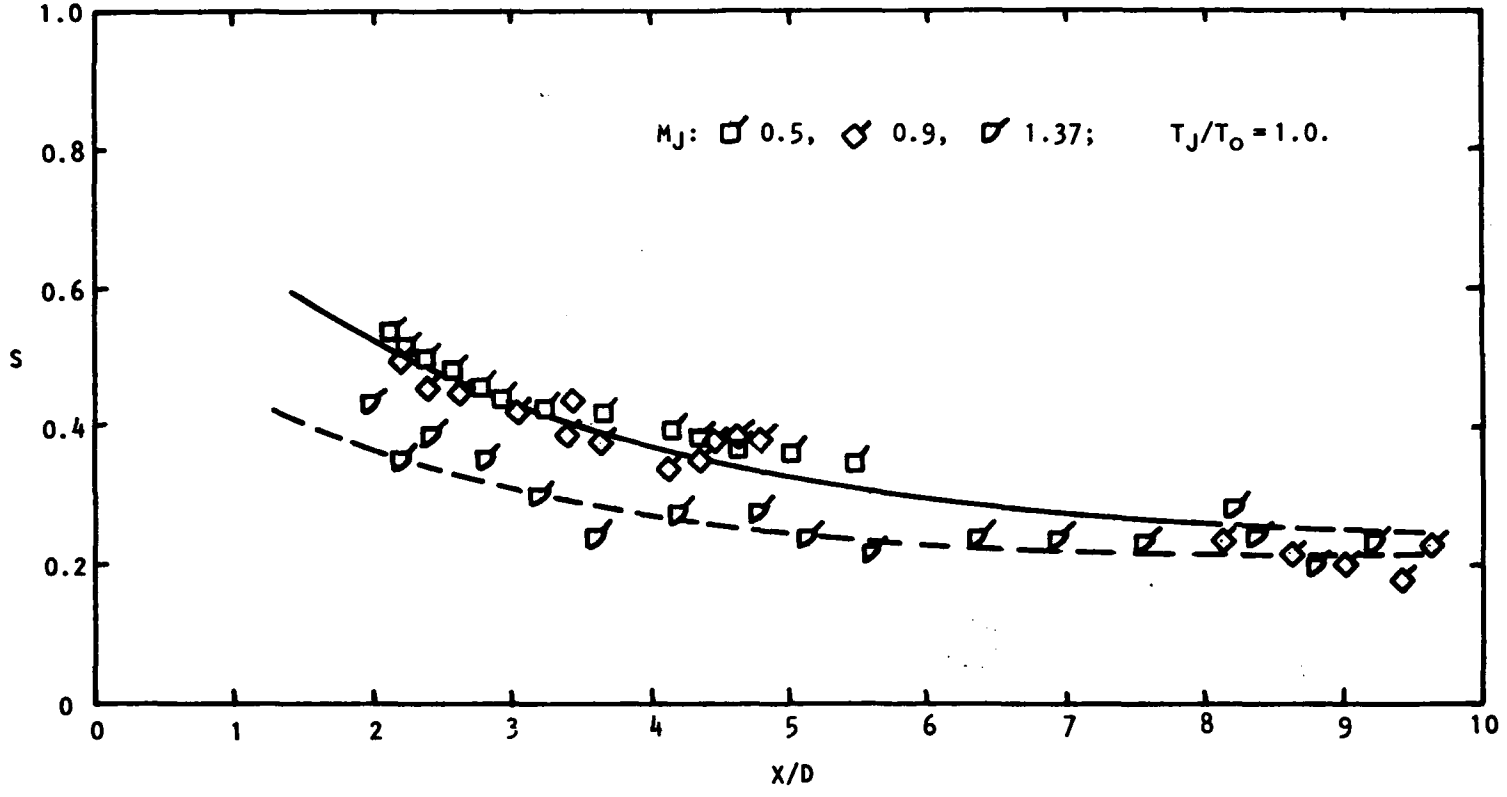

Figure 5.38 Strouhal Number vs X/D (u'-signals, r/D = 0).

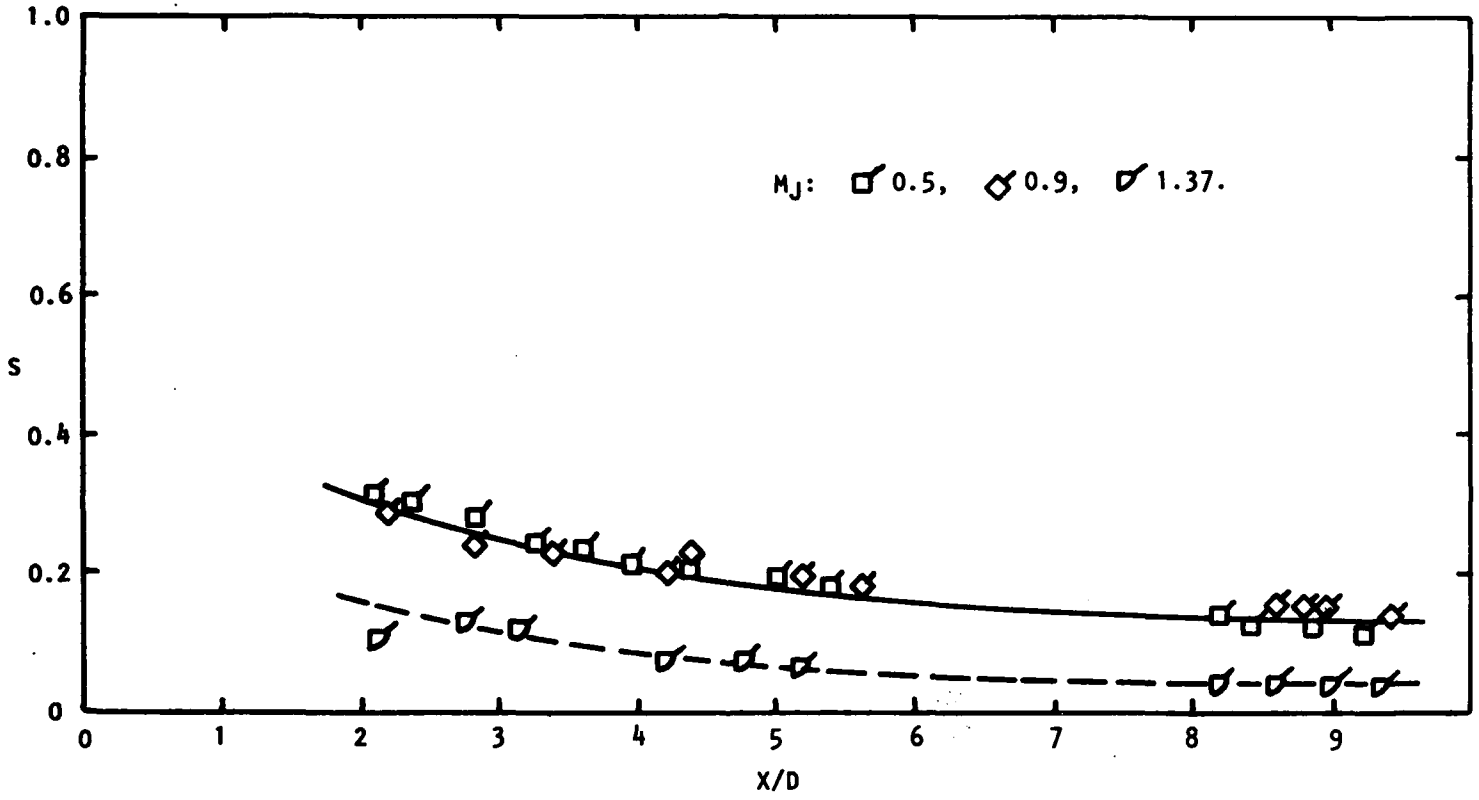

Figure 5.39 Strouhal number vs X/D (u'-signals, r/D = 0.5).

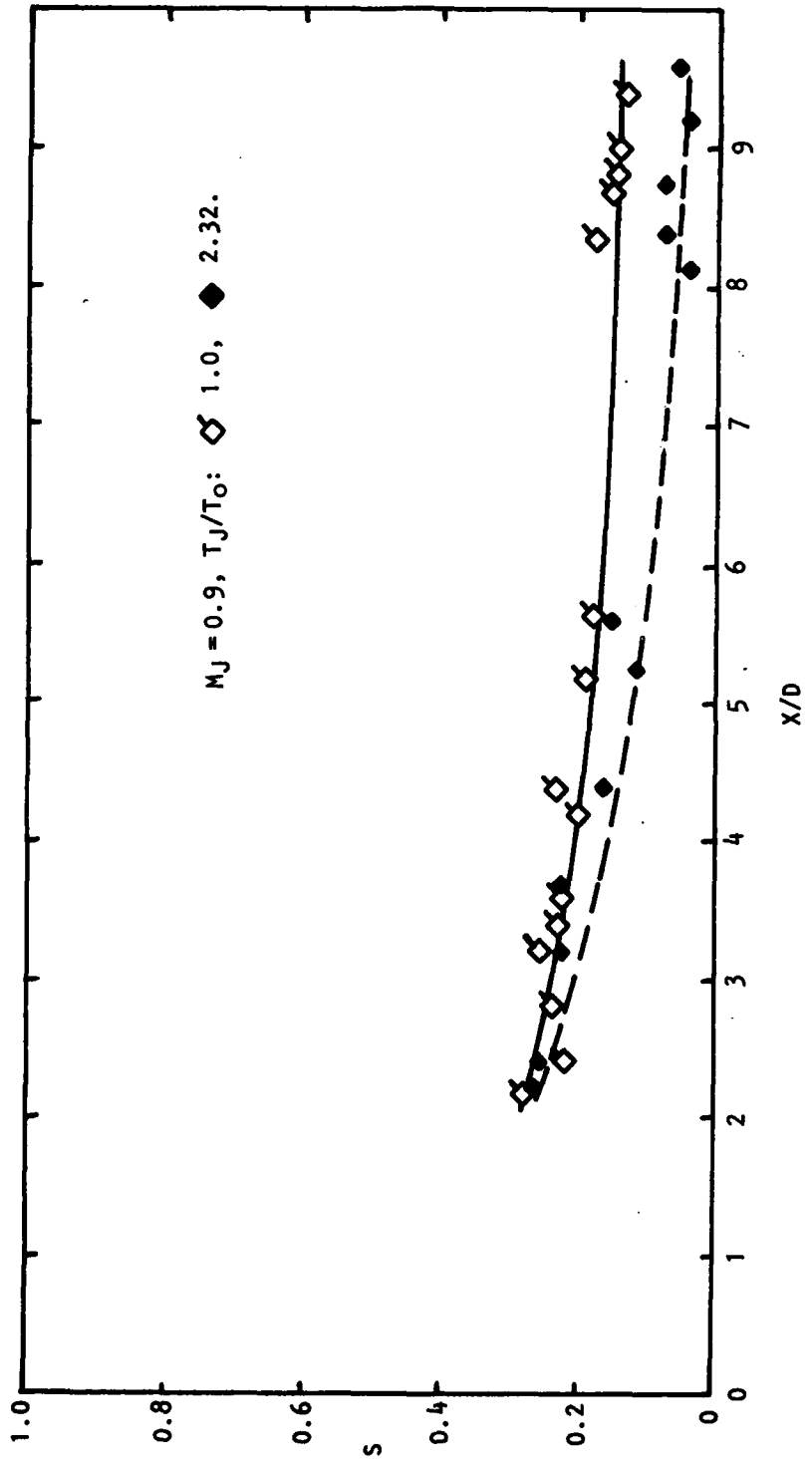

Figure 5.40 Strouhal Number vs X/D (u'-signals, r/D = 0.5).

Figure 5.40 shows the plot comparing the results of Mach 0.9 isothermal and hot ($T_J/T_o = 2.32$) jets. Close to the nozzle the isothermal and hot jets give the same Strouhal number, but as x/D is increased the values of S for the heated jet deviate from those of the isothermal jet. Therefore, in the region where the potential core exists, the heated jet scales with Strouhal number also.

5.4.2 Two-Point Space-Time Cross-Correlations

The above measurements deal with flow characteristics detected at individual points in the jet flow field. They give results in the Eulerian space frame and embody changes resulting from actual modifications to the flow structure as it convects downstream and apparent changes brought about by the passage of the flow structure past the observation point. In order to study the temporal changes of the flow structure, apart from the convective effect, it is necessary to carry out two-point correlation measurements.

Figure 5.41 shows a family of correlation curves obtained in a Mach 0.5 cold jet. The individual curves represent results obtained at different *axial* separations (Δx) of the two measurement points. As the separation distance ($\xi = \Delta x$) of the two measurement points is increased, the curves and their peaks move to higher time delays (τ). At the same time, the magnitudes of the peak correlation fall and the curves increase in their spread. The curves have a Gaussian appearance [compare Equation (2-38) and (2-41)] and may be fitted with curves of the form $A\, e^{-\beta(\tau - \Delta x/U_c)^2}$ as shown in the figure. These characteristics are typical and may be observed in the results at other jet conditions also.

An envelope curve may be drawn to touch the peaks of the correlation curves. This is interpreted as the autocorrelation in the moving frame. The fall in this correlation envelope with time delay is interpreted as representing the "decay" of the average eddy during its passage downstream, and the area under the envelope gives a measure of the average time scale involved in this decaying process.

An equation of the form $e^{-\tau/\tau_o}$ is fitted to the envelope curve and integrated to obtain the integral time scale τ_o. Figure 5.42 shows the variation of $\tau_o U_c/D$ with x/D for different isothermal jets. In the region from x/D = 0 to 4, $\tau_o U_c/D$ rises linearly with x/D for all Mach numbers, and it appears on the basis of the data at Mach 0.5 and 1.37 that the slope becomes progressively smaller as the Mach number is increased. Larson, McColgan and Packman [5.21] conducted a similar set of measurements for a Mach 0.35 jet issuing into a co-flowing stream of varying speed, and their results for a stationary outside stream are also shown. These results suggest the same trends.

From x/D = 4 both Larson et al.'s and the present results for the Mach 0.5 jet are still in agreement. They deviate from the initial straight line trend and flatten out. The Mach 1.37 results on the other hand continue in the same straight line to 8D. Intuitively, this latter behavior seems more reasonable especially since τ_o is supposed to be proportional to $1/(\partial U/\partial r)_{max}$ everywhere in the flow field (Davies, Fisher and Barrat [5.3]), and it was seen earlier that $1/(\partial U/\partial r)_{max}$ varies linearly with x for at least two potential core

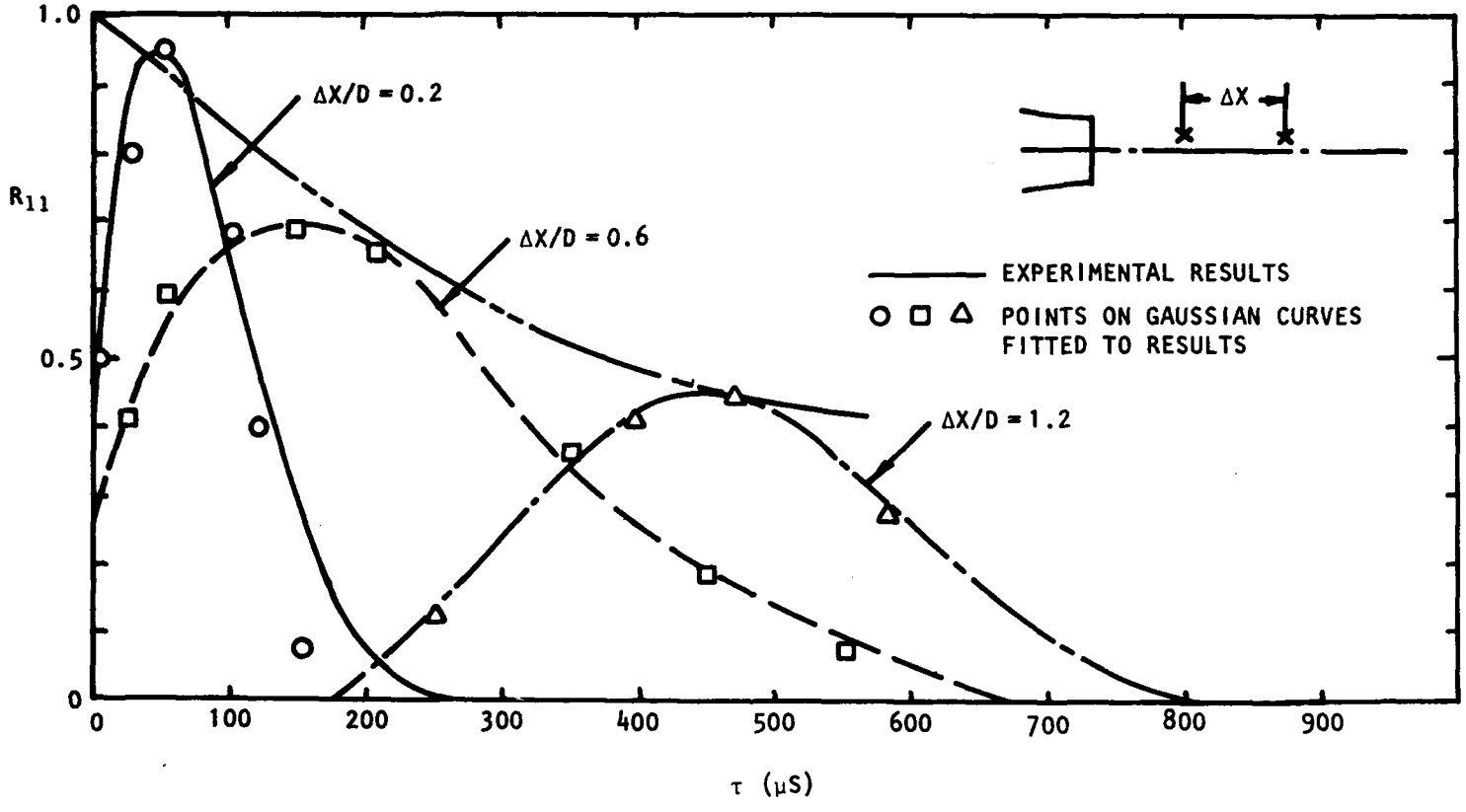

Figure 5.41 Space-Time Correlation Distributions ($M_J = 1.37$, $T_J/T_o = 1.0$, $X/D = 8$, $r/D = 0.5$).

M_J: □ 0.5, ◇ 0.9, ▽ 1.37,
+ 0.35 (Larson et al); $T_J/T_o = 1.0$.

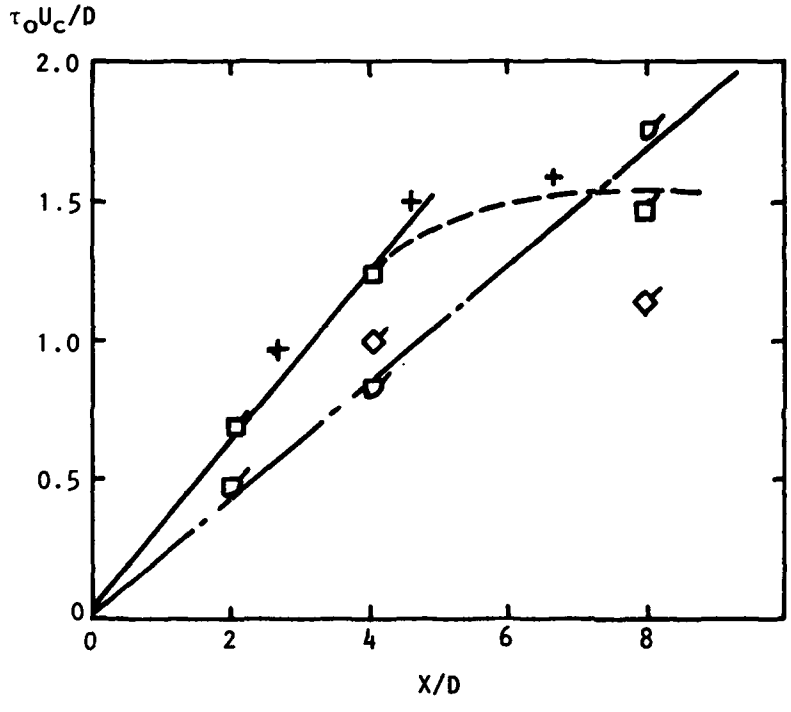

Figure 5.42 $\tau_o U_c/D$ vs X/D (at r/D = 0.5)

lengths. It would seem therefore that a more intensive set of measurements covering the region from x/D = 4 to 10 needs to be carried out to verify this difference in trends. For the purpose of the noise prediction program, however, it is assumed that for any given Mach number, $\tau_o U_c/D$ varies linearly up to x/D = 4 and flattens out downstream of that point. It is also assumed that the slopes of the straight lines fall with increasing Mach number. From the results of the Mach 0.5 and 1.37 jets, the following relationship is obtained for the integral time scale:

$$\tau_o U_c/D = x/D\ (2.2 + 1.8\ M_J) \tag{5-11}$$

With equation (5-1), this leads to

$$\tau_o \left(\frac{\partial U}{\partial r}\right)_{max} = [(2.2 + 1.8\ M_J)\ (0.165 - 0.045\ M_J^2)\ U_c/U_J]^{-1} \tag{5-12}$$

This relationship is plotted in Figure 5.43 for M_J from 0 to 1.4. It suggests a mean value of about 3.8 which would agree with Larson et al.'s value of 3.7 [5.21] for a jet issuing into still air. Davies et al.'s [5.3] results on the other hand give the value of 4.5, which is higher. The reason is that they defined the time scale as the time for the moving frame auto-correlation to fall to 1/e instead of an integral scale as is adopted here and by Larson et al.

5.4.2.1 Convection velocities

The two-point cross-correlation results permit the eddy convection velocity to be determined. Figure 5.44 shows the variation of the peak time delay with the axial separation of the two measurement points. By taking the gradient of the straight line drawn through the data, an average convection velocity of the predominating fluctuations may be determined.

The convection velocity is obtained over the flow field of a Mach 0.5 jet and is plotted as U_c/U_J in terms of x/D and r/D in Figure 5.45. Similar results obtained on another subsonic jet (Mach 0.17) using hot-wires [5.20] are also shown, and there is very good agreement between the two sets of results. They indicate that at any axial station, there is a substantial variation of the convection velocity with radial position. This is quite different from convection velocities measured with microphones which stay essentially constant across the jet [5.22]. As was pointed out, the pressure fluctuations tend to have a more global character while velocity fluctuations tend to be more localized. It is clear therefore that the LV, like the hot-wire, is detecting these highly localized fluctuations.

On the jet centerline, the convection velocity rises with axial distance and cuts across the results at r/D = 0.4 and 0.5. The results along r/D = 0.4 and 0.5, however, fall with x/D at first, but from about x/D = 4, it is essentially constant. At r/D = 0.7 it rises initially but reaches a constant at about x/D = 4 also.

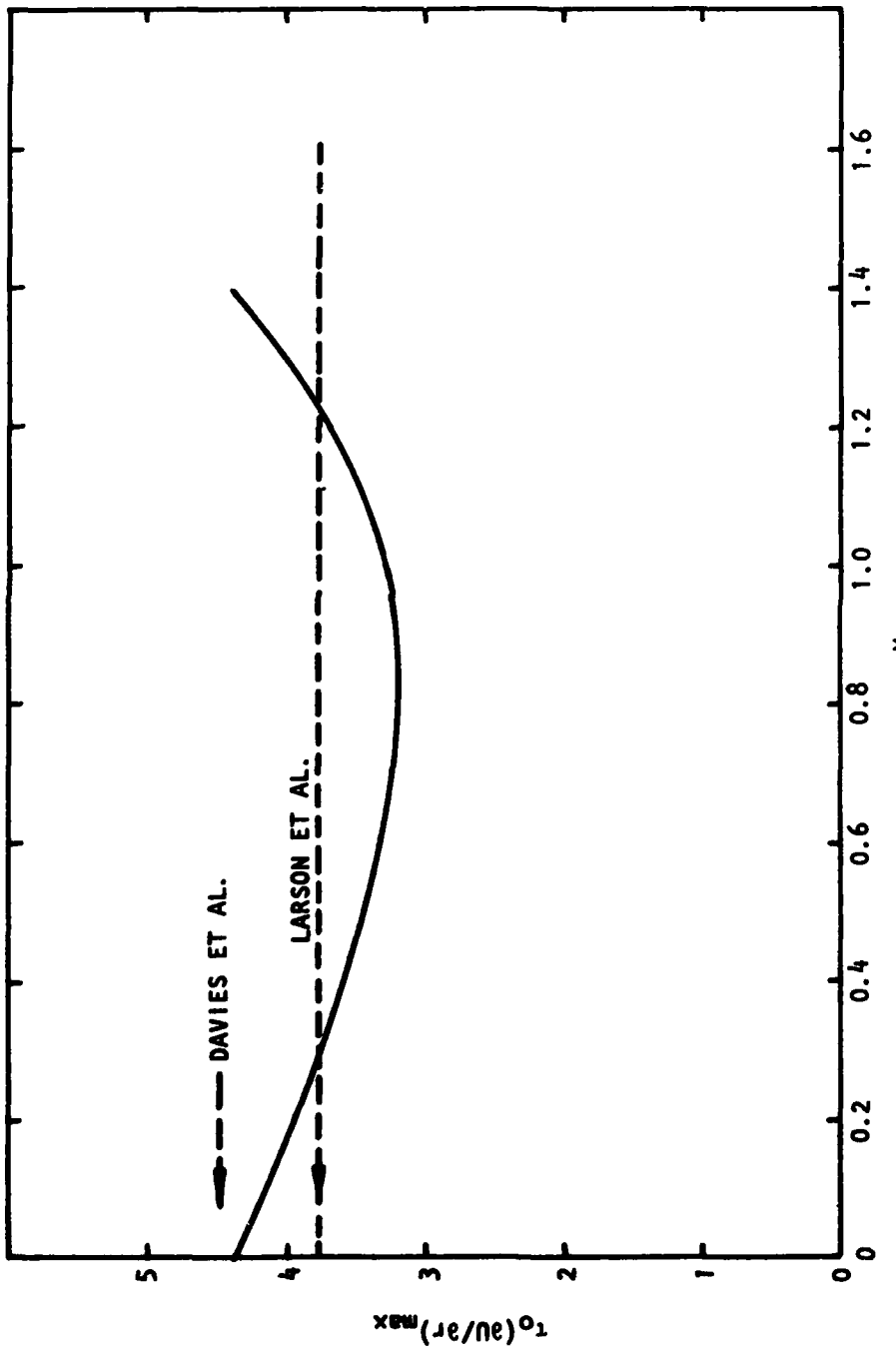

Figure 5.43 $\tau_o\ (\partial U/\partial r)_{max}$ vs M_J $(T_J/T_o = 1.0)$

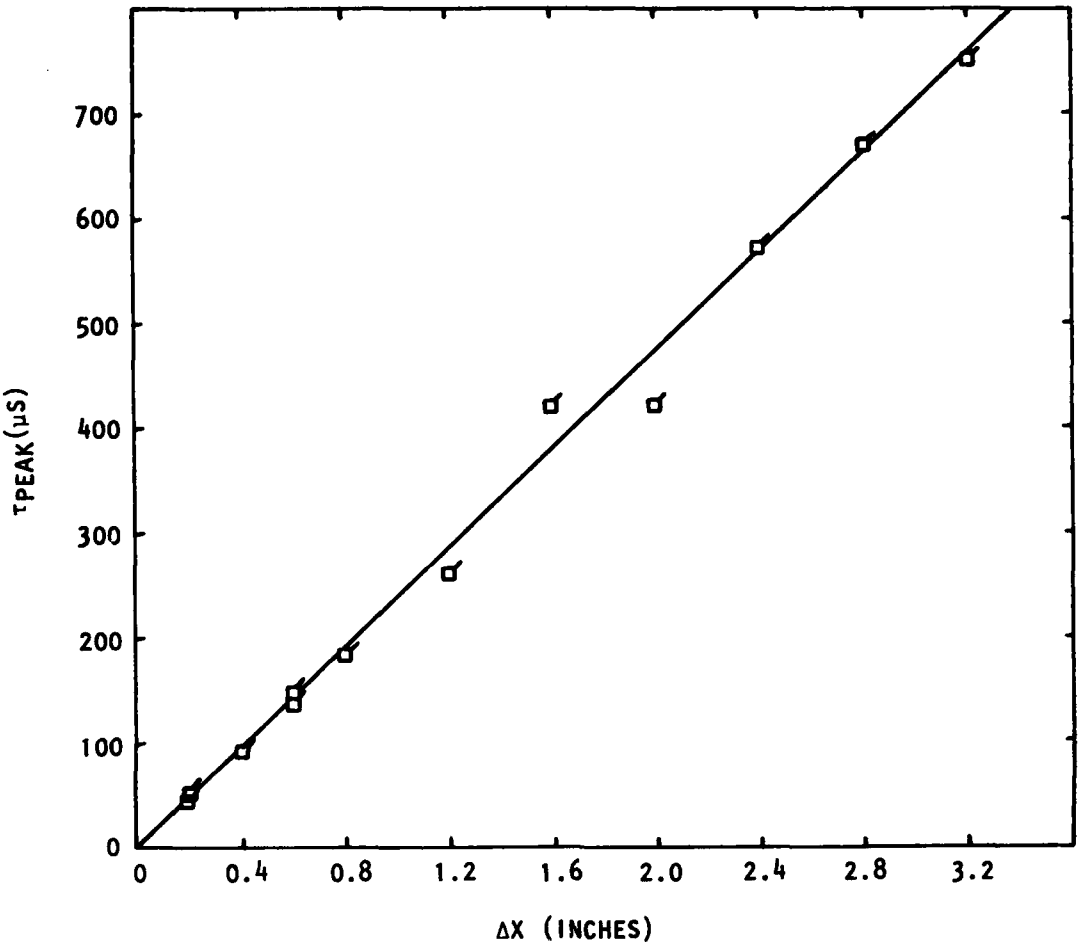

Figure 5.44 τ_{peak} vs ΔX ($M_J = 0.5$, cold)

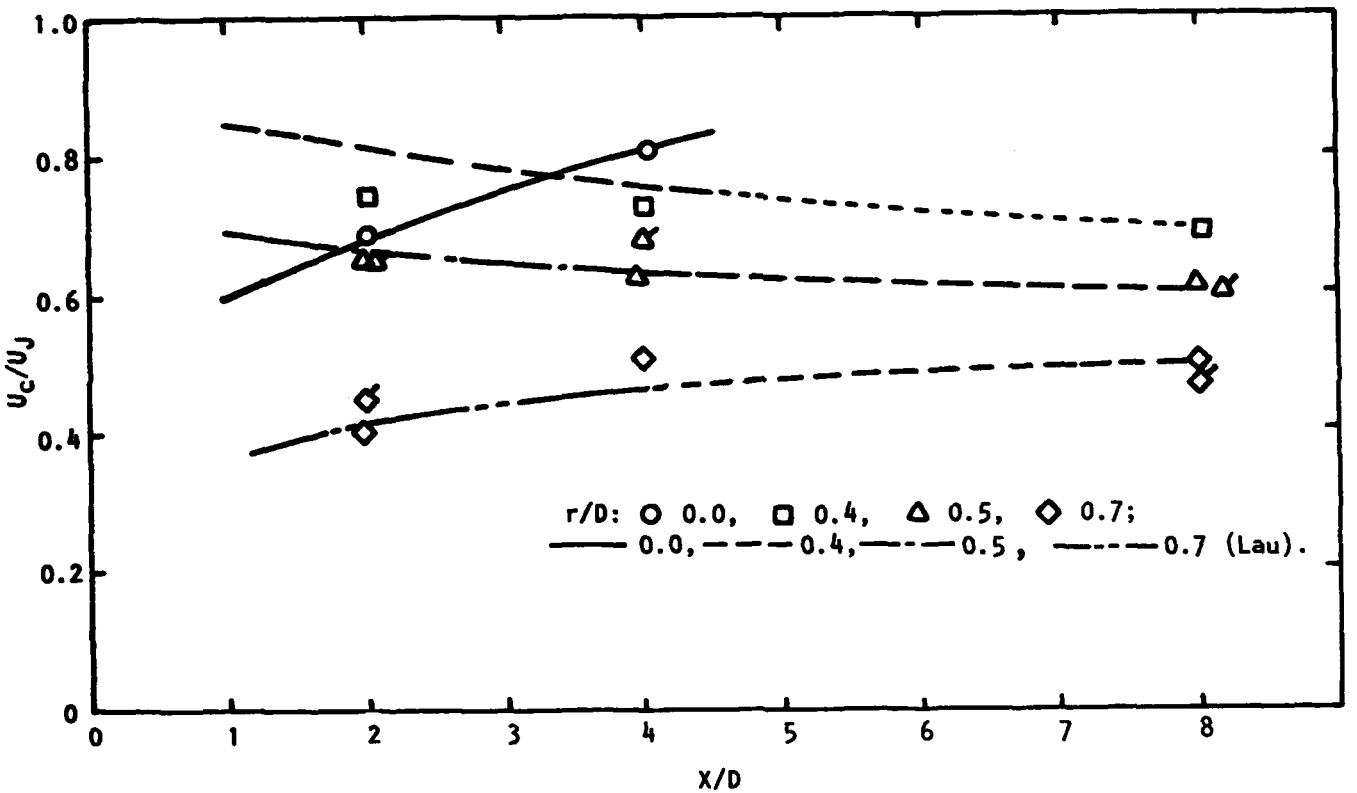

Figure 5.45 U_c/U_J vs X/D ($M_J = 0.5$, Cold).

The convection velocity of the radial velocity fluctuations is also shown and at corresponding positions its values do not differ significantly from those of the axial fluctuations.

The results along the jet centerline are plotted for varying Mach number and temperature ratio in Figure 5.46. They show no definite trend with changing Mach number. For all Mach numbers U_c/U_J rises rapidly with x/D up to x/D = 5 and subsequently falls slowly. Heating apparently affects conditions in the upstream region; and at x/D = 2.0, U_c/U_J is significantly lower than the corresponding value for an isothermal jet. Since the convection velocity along the jet axis is a measure of the velocity of the "large-scale" structure, this suggests that relative to the jet efflux velocity the structure is moving more slowly for a heated jet, and reflects the rather uneven heating of the jet whereby the potential core is heated more than the outer side. From x/D = 4, the difference between heated and isothermal jets gradually disappears.

The variation of U_c/U_J along r/D = 0.5 is shown for different Mach number jets in Figure 5.47. For the subsonic cases, U_c/U_J remains essentially constant at 0.63. For the supersonic case, however, the convection velocity rises and reaches a value of about 0.8 U_J. Heating apparently does not alter the trend significantly at this radial position.

5.4.2.2 Length scales

Figure 5.48 shows a distribution of the cross-correlation coefficient as a function of the axial separation (Δx) of the two measurement points at $\tau = 0$. Such distributions provide information on the axial extent of the coherence in a given flow structure. The curve is typical of results obtained within the potential core of the jet. It has a damped sinusoidal appearance and is reminiscent of the autocorrelation curves obtained in this region. It suggests the recurrence of a high correlation at a distance from the fixed point and reaffirms the existence of an array of fairly regularly spaced "large-scale" disturbances in the mixing region of the jet [5.18]. The average spacing (λ) of the disturbance is given by the distance between the peaks in the correlogram.

Figure 5.49 shows the variation of λ/D with x/D determined in this manner for the Mach 0.5 jet. The spacing may also be obtained by the formula $f_p\lambda = U_c$ where f_p is the peak frequency of the spectrum and U_c the convection velocity on the jet centerline. These results are shown in the figure and there is good agreement between the two sets of results as might be expected. Data obtained with hot-wires in a Mach 0.17 jet [5.20] are also provided and coincide with the present results for subsonic jets.

Figure 5.49 also shows the variation of λ/D with x/D for different Mach numbers. For the subsonic cases, changes in Mach number or heating do not affect λ/D. However, raising the Mach number to 1.37 raises λ/D.

Figure 5.50 shows typically the distribution of the cross-correlation at $\tau = 0$ obtained in the mixing region of the jet (r/D = 0.5). There is a continuous fall in the correlation coefficient with axial separation and at large separations it asymptotes to zero. For this case, an integral length scale is defined. This is given for axial separations by:

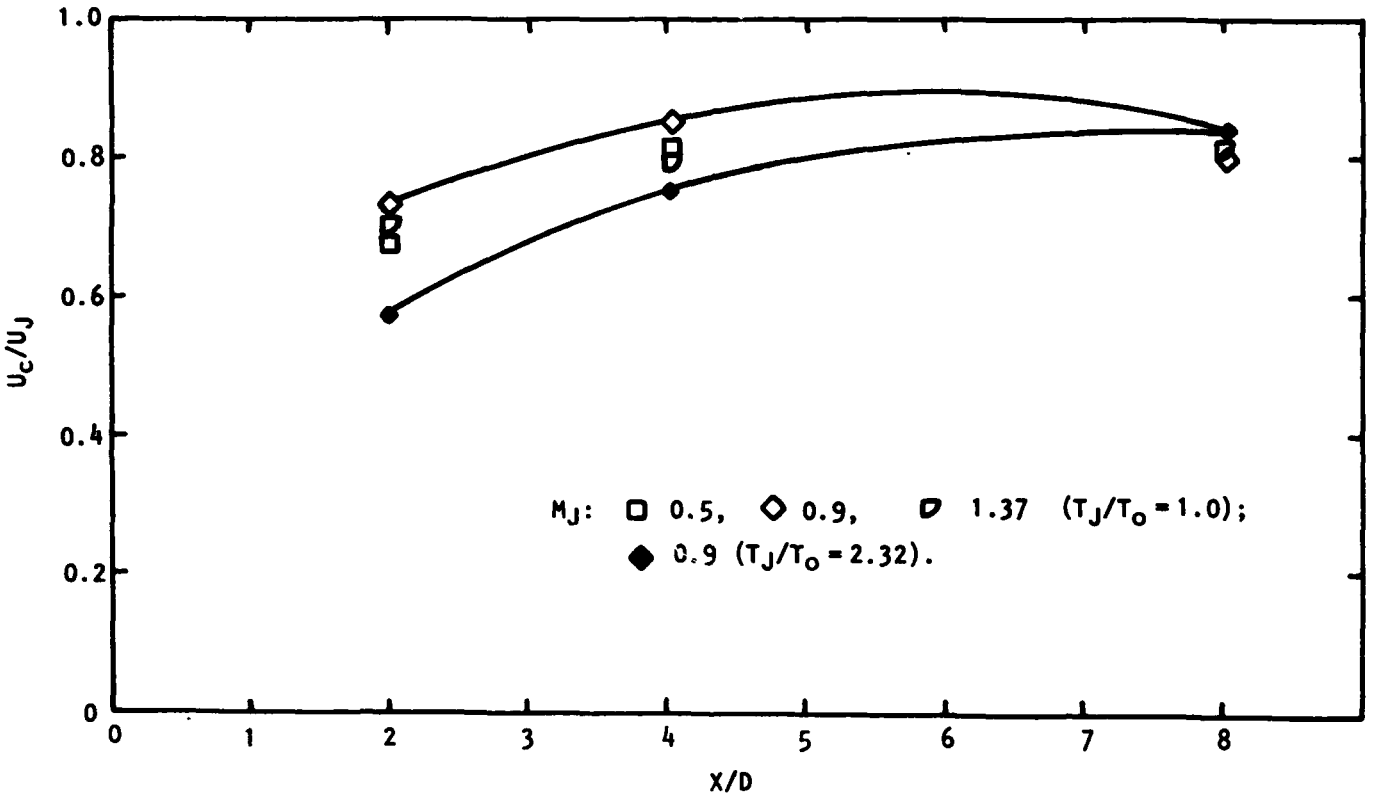

Figure 5.46 U_c/U_J vs x/D (r/D = 0.0).

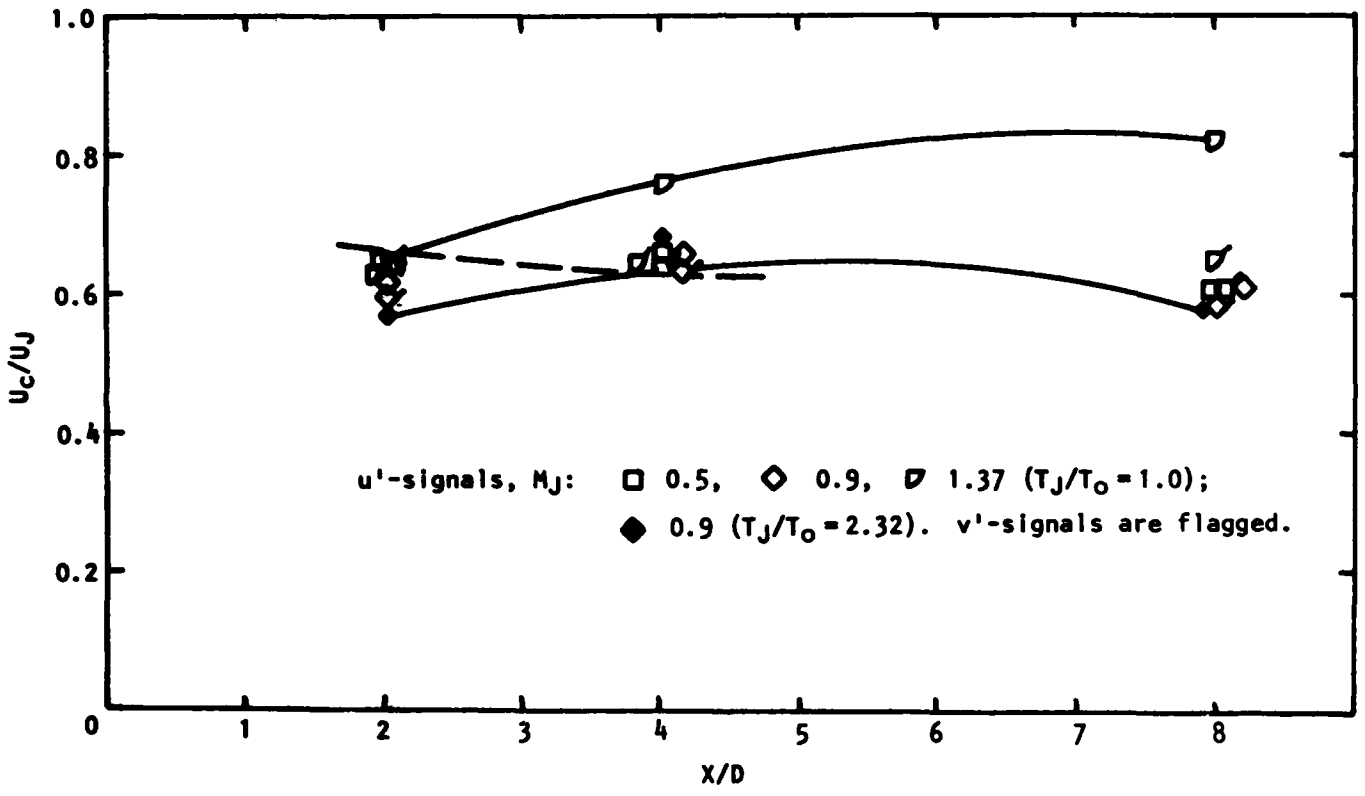

Figure 5.47 U_c/U_J vs X/D (r/D = 0.5).

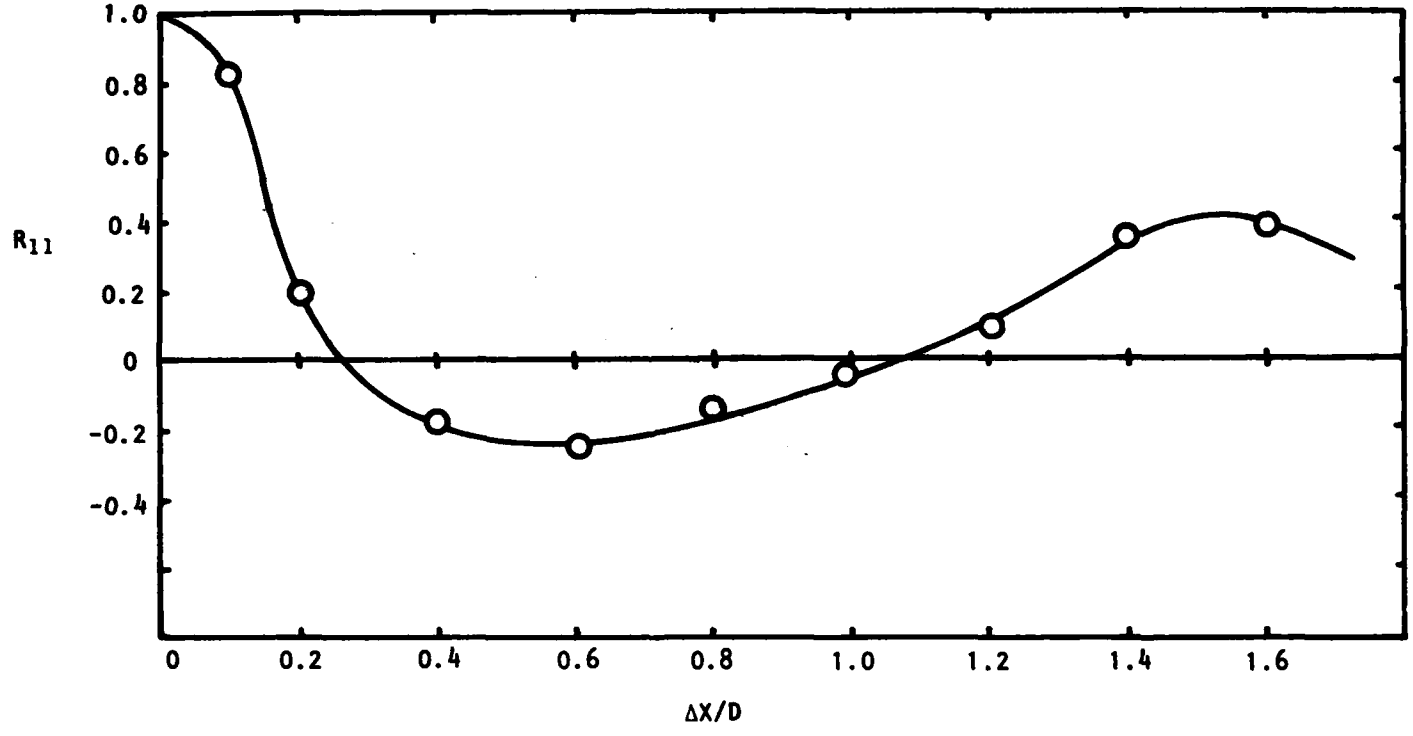

Figure 5.48 R_{11} at $\tau = 0$ vs $\Delta X/D$ ($M_J = 0.9$, $T_J/T_O = 1.0$, $X/D = 2$, $r/D = 0.0$)

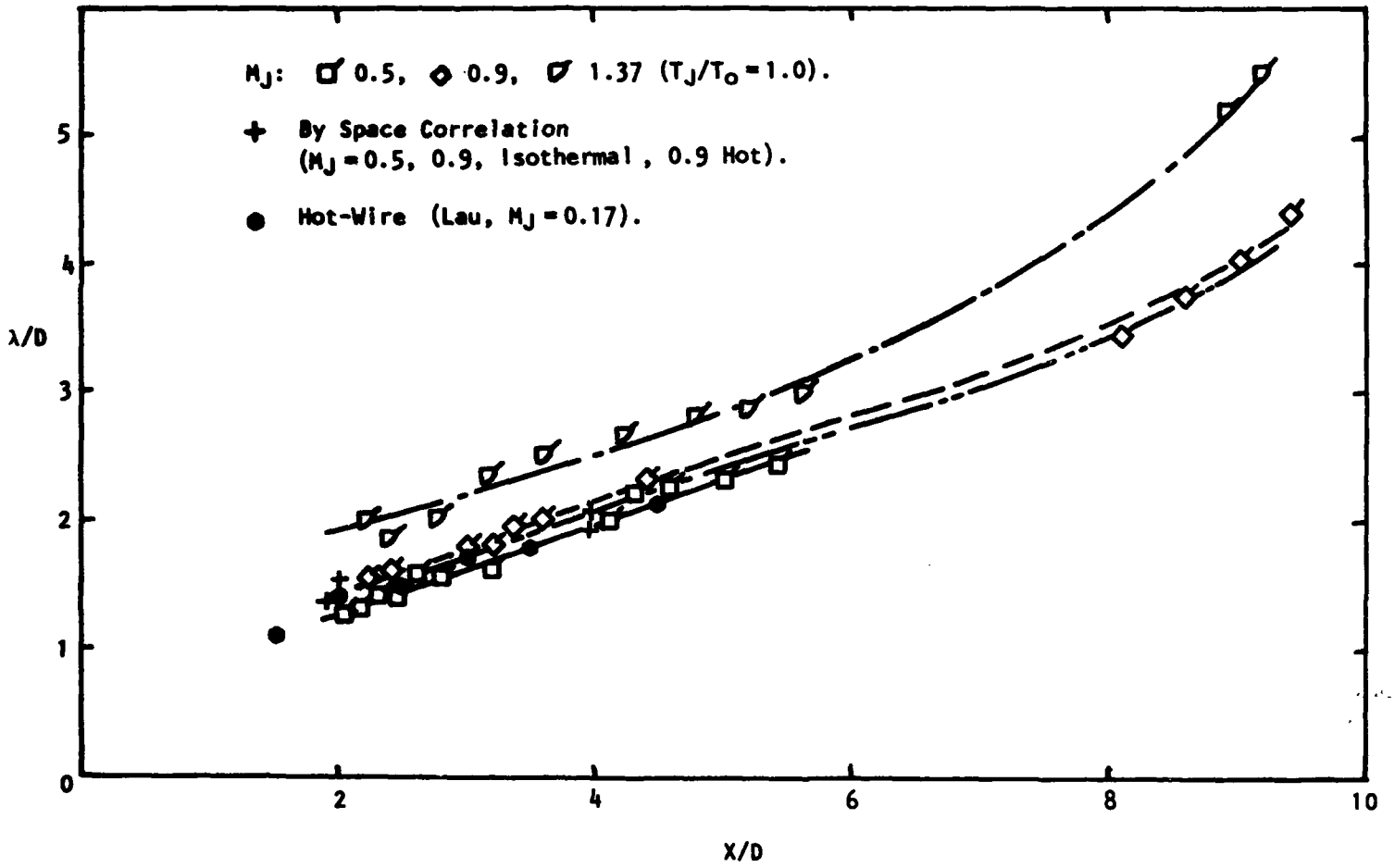

Figure 5.49 Distribution of Wavelength with X/D.

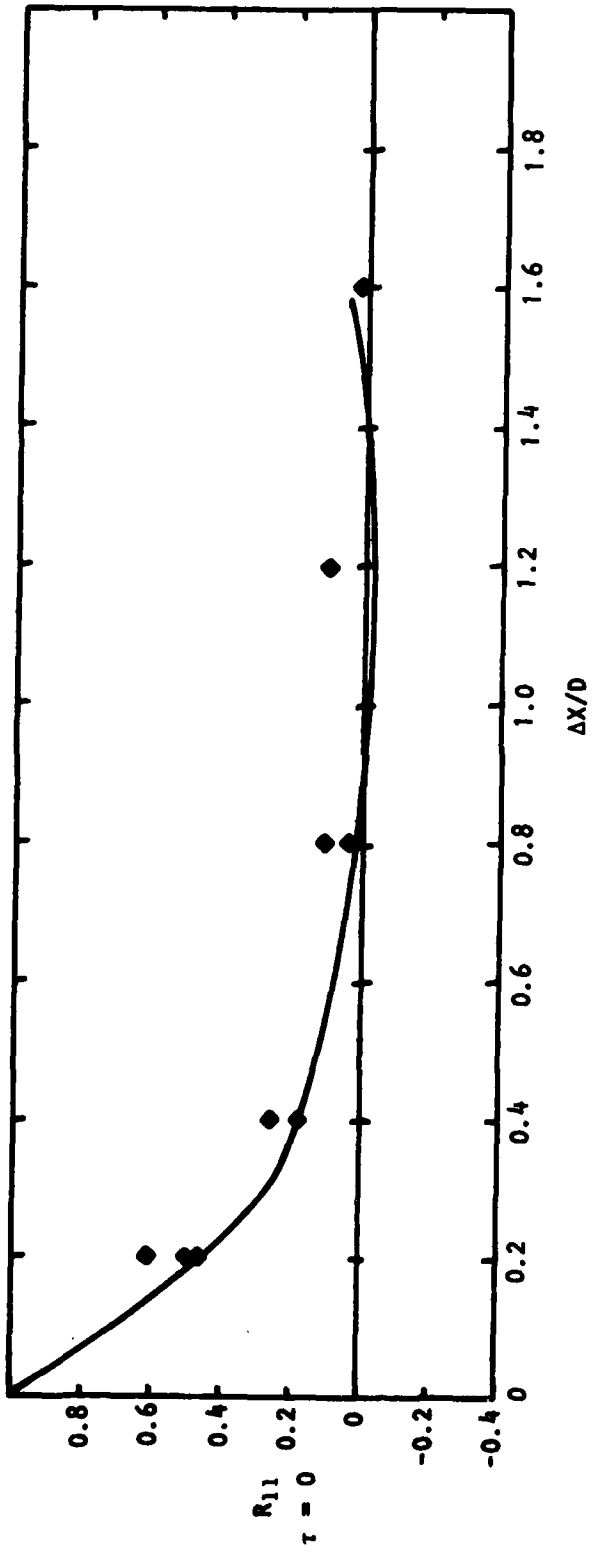

Figure 50 R_{11} at $\tau = 0$ vs $\Delta X/D$. ($M_J = 0.9$, $T_J/T_O = 2.32$, $X/D = 8$, $r/D = 0.5$)

$$L_x' = \int_0^\infty R_{11}(\Delta x;\ \tau = 0)\ d\Delta x. \qquad (5\text{-}13)$$

The variaton of L_x' and x is shown in Figure 5.51. Bradshaw et al.'s [5.23], Davies et al.'s [5.3] data and those quoted by the latter are also shown. From their quoted data, Davies et al. obtained a variation of $L_x' = .13x$. Jones [5.24] on the other hand proposed, on the basis of his measurement in a shear layer, a relationship which is half as steep ($L_x' = .068x$). The present results together with Bradshaw et al.'s and Davies et al.'s own results seem to indicate an even lower slope, with a possible intercept along the ordinate. This is consistent with the results of Larson et al. [5.21], which suggested a variation of the form $L_x' = 0.20 + .038x$. The data from v-fluctuations are shown by the flagged symbols in the figure and exhibit the same trends.

The results of the axial length scale for different Mach numbers and jet temperature ratios are summarized in Figure 5.52 and tend to form a band. No consistent trend can be detected with regards to the effects of changing Mach number or the temperature ratio, and it is felt that since the measurements are rather sparce, it may be better for the present to overlook any such effects and draw an average line through the results. This line is given by:

$$L_x' = 0.24 + .021x\ . \qquad (5\text{-}14)$$

A radial (transverse) length scale (L_t') may similarly be defined as per Equation (5-13) from cross-correlation measurements obtained with radial separations (Δr). The results are shown in Figure 5.53 and also form a band. The band of data points appears to have a constant slope throughout the whole jet and the average line through the data points may be represented by:

$$L_t' = 0.14 + .014x\ . \qquad (5\text{-}15)$$

The ratio between L_t' and L_x' is of the order of values proposed by Davies et al. [5.3] and Jones [5.24].

5.4.3 Spectral Distribution from Measured Convection Velocity and Length Scale

On the basis of the expressions for the cross-correlation given by Equations (2-38) ("Gaussian Model") and (2-41) ("Exponential-Gaussian" model), the power spectral distribution of the turbulence may be shown to be given by:

$$\Phi = 10\ \log_{10}\ [\exp\ (-\omega^2 L_x^2/8\pi U_c^2)] \qquad (5\text{-}16)$$

where L_x is the axial length scale $=2L_x'$, and U_c is the convection velocity. Since the length scales and the convection velocity are now available, it would be interesting to compare the spectral distributions determined from Equation (5-16) with those obtained experimentally. Based on the measured values of L_x and U_c, spectral distributions are computed for jets at Mach 0.5, 0.9 and 1.37, respectively, at various points in the jets. These are shown

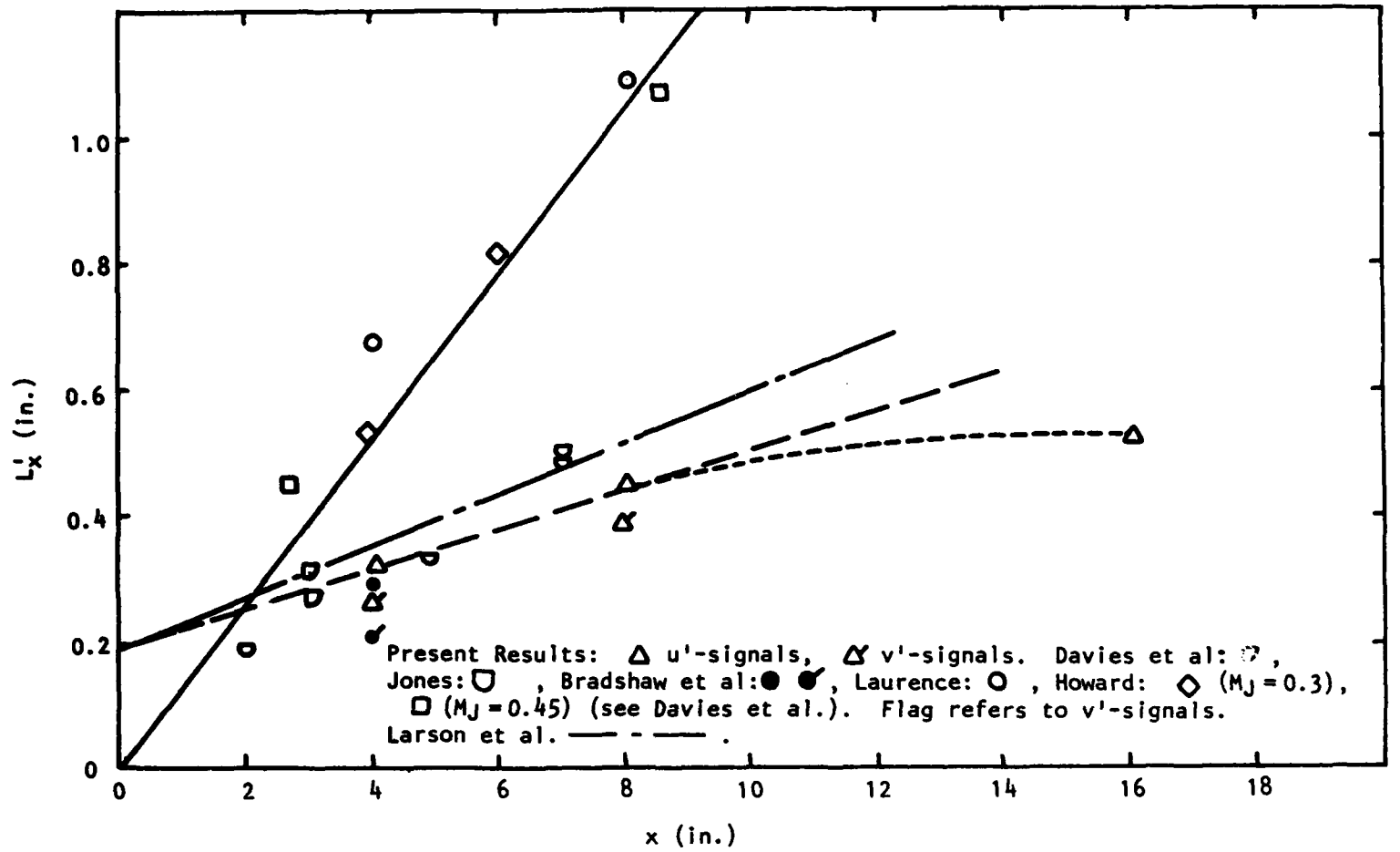

Figure 5.51 Integral Length Scale vs x ($M_J = 0.5$ cold, $r/d = 0.5$).

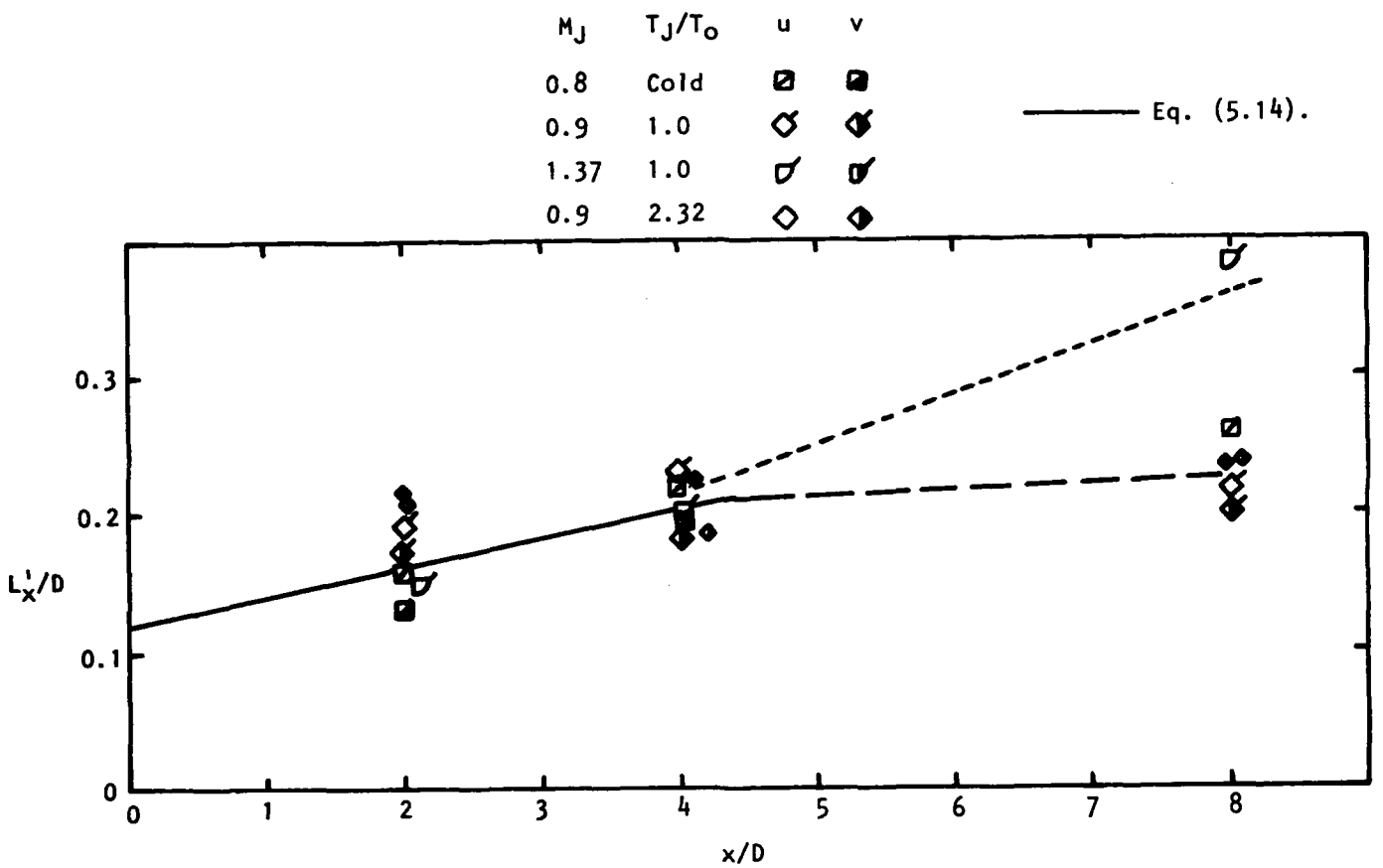

Figure 5.52 L_x'/D vs X/D (r/D = 0.5).

Legend in Figure 5.52. ——— Eq. (5.15).

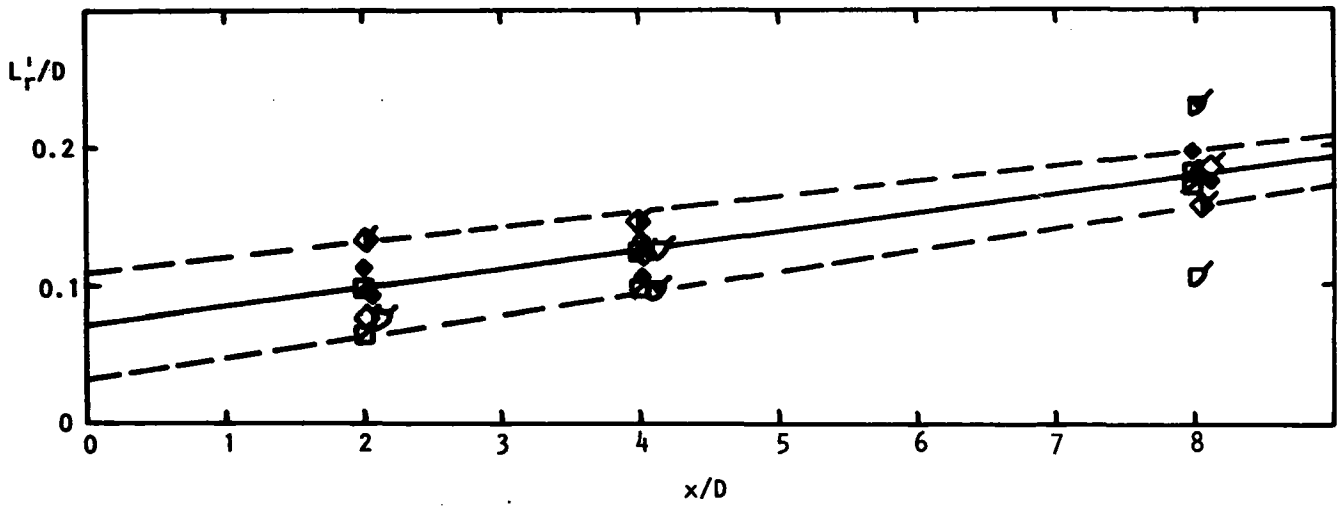

Figure 5.53 L_r'/D vs X/D (r/D = 0.5).

typically in Figures 5.54(a), (b), and (c). The corresponding measured spectral distributions are also shown, and it may be seen that the measured and computed spectra compare very well. In particular, the frequency at which the distribution begins to fall off and the initial fall is reproduced faithfully by the computed results at the various Mach numbers.

5.4.4 Fourth-Order Correlations

In the original Lighthill formulation of the sound intensity equation, a fourth-order correlation of the source fluctuations is called for. This is essentially a correlation of the fluctuating stresses and is defined in general by:

$$R_{ijkl}(\vec{\xi},\tau) = \frac{\overline{(u_iu_j)_A\ (u_ku_\ell)_B}}{(\widetilde{u_iu_j})_A\ (\widetilde{u_ku_\ell})_B} \tag{5-17}$$

where A and B refer to the two points in the flow separated by a distance $\vec{\xi}$; and the bar and tilde denote mean and rms values, respectively.

The integral length scale of the fluctuating stresses may thus be determined in a similar manner as before. For example, an axial length scale would be given by:

$$L_x'^* = \int_0^\infty R_{ijkl}\ (\Delta x,\tau)\ d(\Delta x)\ . \tag{5-18}$$

In principle, it is an extension of the second order correlation technique to the processing of signals which are products of two fluctuating velocities. Jones [5.24] conducted an extensive series of measurements of the axial and traverse length scales in the free shear layer of a jet using hot wires and showed in the region of high shear that the assumption of a joint normal probability distribution of the velocity fluctuations is fairly well borne out by the measurements: e.g. $L_x'^* = 0.55\ L_x'$, $L_t'^* \approx 0.63\ L_t'$.

Fourth-order correlations are also carried out under this program using the laser velocimeter since the four-channel LV permits measurement of velocity fluctuations in two orthogonal directions at any two given points. The cross-correlations are performed with $u^{2\prime}$, $v^{2\prime}$ and $(uv)'$ signals, respectively.

Figure 5.55 shows a cross-correlation distribution obtained in a Mach 0.9 hot jet. It is carried out with $(uv)'$-signals. It shows a well-defined peak, and the shape of the correlogram is very similar to those of second-order correlograms. However, such correlograms are rare and constitutes only about 3% of the total of over 150 correlations performed with different signals in different parts of jets having varying conditions. Most of the others have qualities which are poorer than those shown in Figure 5.56. Some of the measurements were repeated with more stringent controls of the flow conditions, but this resulted in no improvement. Therefore, only scant and sporadic data are available on the convection velocities and the situation is even worse for length scales.

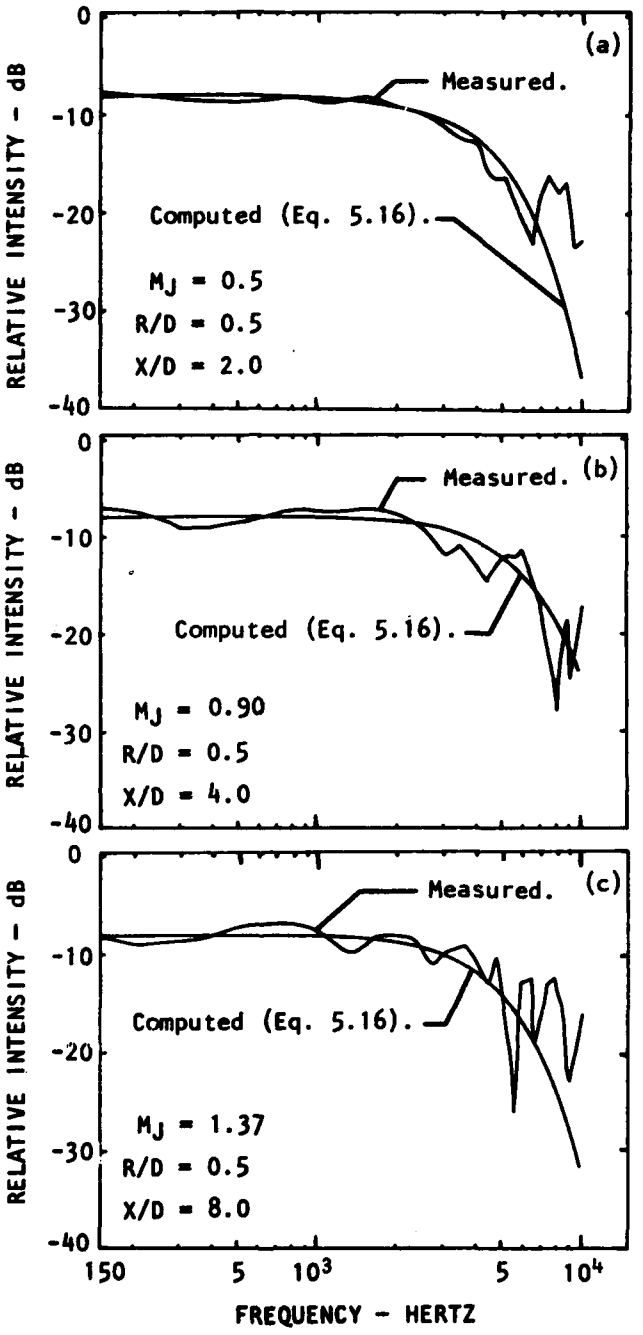

Figure 5.54 Spectral Distribution

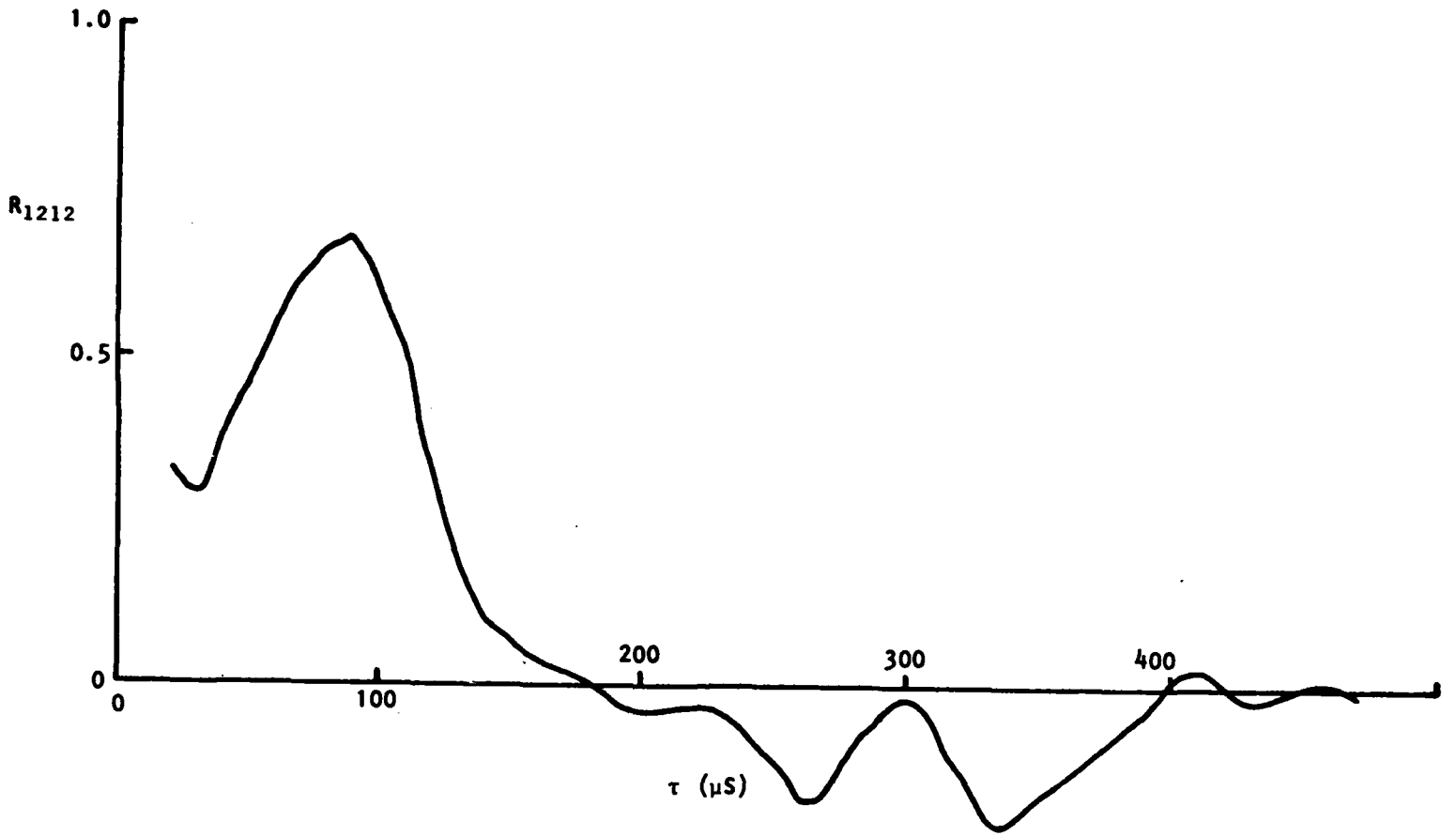

Figure 5.55 R_{1212} vs τ ($M_J = 0.9$, $T_J/T_O = 2.32$; $X/D = 4$, $r/D = 0.5$, $\Delta X/D = 0.4$).

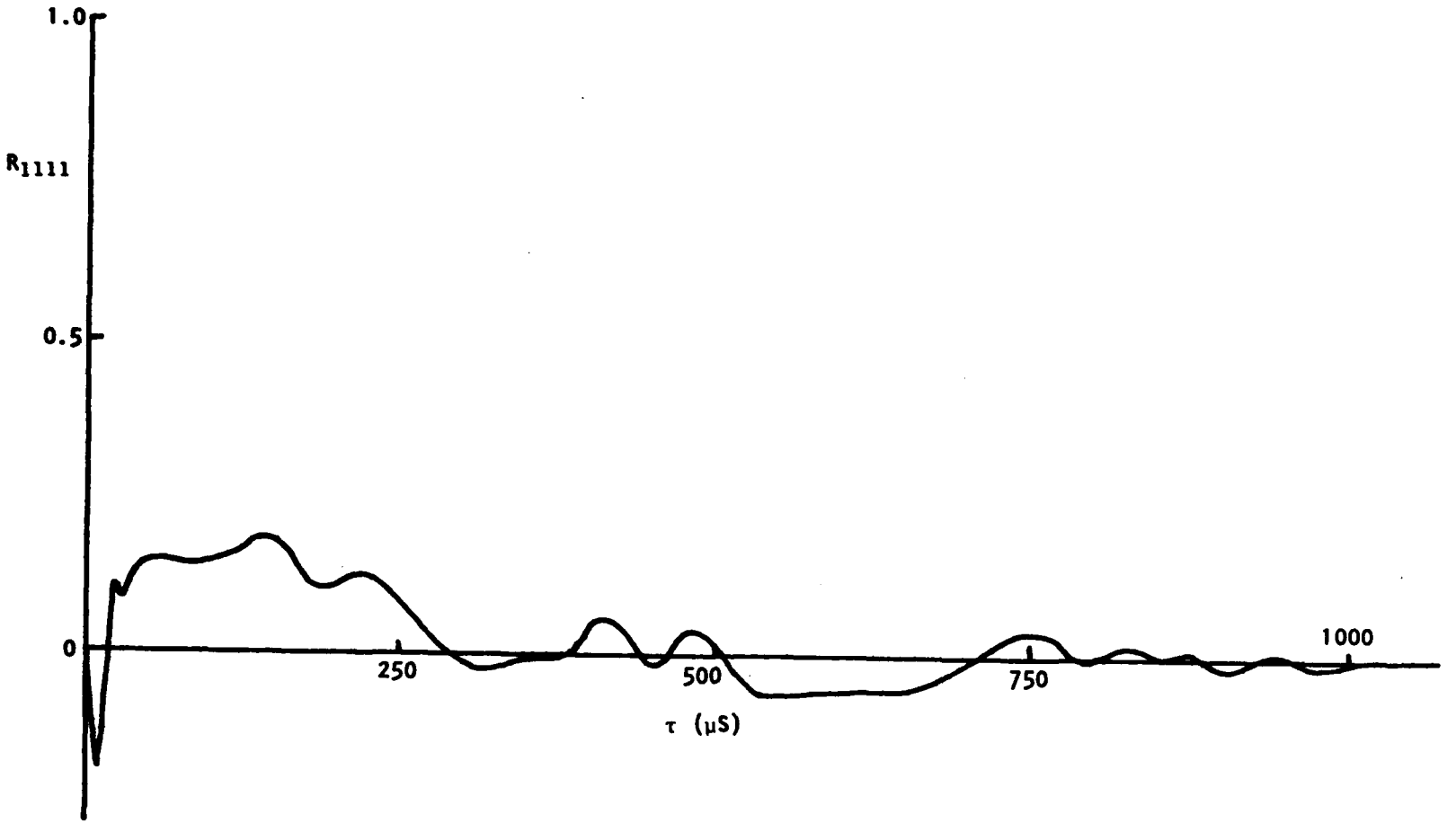

Figure 5.56 R_{1111} vs τ ($M_J = 0.5$, Cold; $X/D = 4$, $r/D = 0.5$, $\Delta X/D = 0.4$).

x/D / r/D	2			4			8		
	L'_x	L'^*_x	L'^*_x/L'_x	L'_x	L'^*_x	L'^*_x/L'_x	L'_x	L'^*_x	L'^*_x/L'_x
0.0				.49	.27	.55			
0.5				.44	.37	.83	.51	.32	.63
0.7	.31	.25	.80						

Table 5-1 Length scales of (u') and ($u^{2'}$) Fluctuations

Table 5-1 shows some of the results of L'^*_x which could be determined from the available data. They have been obtained with very crude extrapolations of the available data points and must therefore be considered to be very inaccurate. The corresponding values of L'_x are also shown for comparison.

The results of the convection velocity (U^*_c) of $u^{2'}$ and (uv)' signals are shown in Figure 5.57 for the different jet flow conditions. (It is not possible to determine U^*_c from the results of $v^{2'}$ signals.) Corresponding results from u'-signals are also shown, and they indicate that both the fluctuating velocities and the stresses are convected with essentially the same velocity.

The generally poor results from the fourth-order correlations is still not clear. Various attempts were made during the course of the experimentation to identify the cause of the trouble. For example, it was thought that the erroneous results might have been caused by a slowly varying mean velocity which would not normally be taken into account in the data analysis procedure. A subroutine was therefore incorporated into the program to determine a running mean velocity, and the new fluctuating velocities based on this running mean. However, this resulted in only a marginal change in the appearance of the correlograms. Effort is continuing to try to resolve this problem.

5.5 CONCLUSIONS

The measurement program undertaken in this phase of the study provides better insight into the jet structure. It confirms the basic suggestions derived in the earlier phase of the work regarding Mach number effects and affords new results on the effects of heating the jet.

The salient results are summarized below:

(1) Radial distributions of the mean velocity collapse when plotted in terms of U/U_j and $\eta^* = (r - r_{0.5})/x$. This applies to jets at varying Mach numbers and temperature ratios, and extends to about two potential core lengths from the nozzle, irrespective of the jet flow conditions. These distributions for varying jet conditions collapse on one curve when plotted

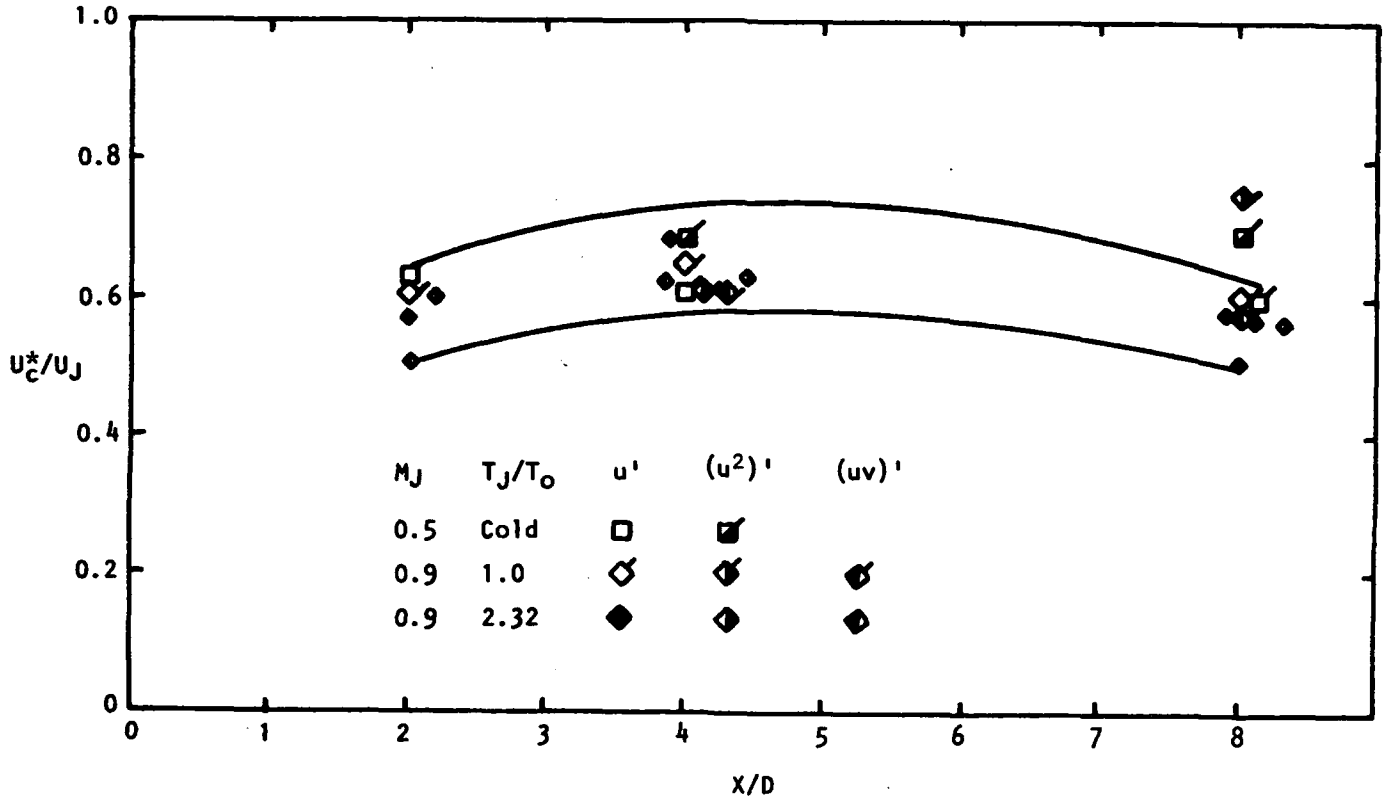

Figure 5.57 U_c^*/U_J (of $(u^2)'$, $(uv)'$-signals) vs X/D (r/D = 0.5).

in terms of U/U_J and $\sigma\eta^*$, σ being the Görtler spreading parameter which is derived from the spreading rate based on the maximum slope (Figure 5.8).

(2) The spreading rate of the mean velocity (δ_η) generally falls with increasing Mach number for jet temperature ratios of up to and probably a little above 1.5. At a Mach number which appears to be associated with the eddy convection velocity being supersonic, the spreading rate undergoes a change and rises with increasing Mach number (Figure 5.7). The spreading rate of the jet heated to a temperature ratio of 2.32 does not change substantially with Mach number and its distribution intersects those of the lower temperature jets at about Mach 1.0.

(3) The radial distributions of the temperature (Figure 5.9) also tend to collapse when plotted in terms of $\Delta T/\Delta T_J = (T - T_O)/(T_J - T_O)$ and $\eta t^* = (r - r_{0.5t})/x$, $r_{0.5t}$ being the position where $\Delta T/\Delta T_J = 0.5$. Apparently, $r_{0.5}$ and $r_{0.5t}$ are not a constant distance apart for all values of x. The spreading rate of the temperature distribution is higher than that of the mean velocity distribution.

(4) The Kleinstein-Witze formulation [Equation (5-5)] for the centerline distribution of the mean velocity appears valid for isothermal and heated jets at Mach numbers of up to 1.7 at least, a good approximation for the value of α is 1.35 (Figure 5.13). The actual variation of α with M_J and T_J/T_O is represented in Figure 5.14.

(5) The potential core length increases with Mach number, and increased heating reduces it (Figure 5.15).

(6) The peak turbulence intensity in radial distribution falls with increasing axial distance (Figure 5.26). Initially, the fall is very gradual, but at about twice the potential core length it falls as 1/x. This applies to jets at all Mach numbers and temperatures investigated. At the end of the potential core, the peak value of turbulence intensity falls with increasing Mach number at first, but rises subsequently (Figure 5.28). There is apparently no significant effect due to temperature.

(7) The peak turbulence intensity in centerline distributions also falls with increasing Mach number. Heating in this case seems to accelerate the fall (Figure 5.32).

(8) The Strouhal number falls with axial distance for all jets (Figure 5.38). Initially, the fall is significant, but downstream of about x/D = 6, it begins to level off to a constant value. For subsonic Mach numbers, increasing the Mach number of isothermal jets produces no change in the Strouhal number. However, when the Mach number becomes supersonic, the Strouhal number falls. This behavior is observed at both the jet centerline and along the lipline (Figures 5.38 and 5.39). Increased heating does not affect the Strouhal number in the upstream region but downstream of x/D = 4, the value falls.

(9) The autocorrelation of velocity fluctuations in the moving frame changes with jet position and flow conditions. The time scale in the decay of the correlation coefficient increases linearly with x, but there are

indications which might suggest that in the subsonic range, the increase may not be linear beyond x/D = 5 (Figure 5.42). This change in the slope is not evident in the supersonic case.

(10) Along the jet centerline, the ratio of the convection velocity to the jet efflux velocity (U_c/U_J) rises with axial distance until about the end of the potential core. Then, it falls very gradually (Figure 5.46). In the middle of the mixing region, it changes little for subsonic jets (Figure 5.47). It rises for the supersonic jet. There is very little distinction between u' and v' signals for isothermal jets, and the effect of Mach number and temperature is not apparent.

(11) The convection velocity for u^{2}'-fluctuations follows the same trends as for the u'-fluctuations (Figure 5.57).

(12) The rate of increase of the axial (L_x') and transverse (L_t') integral length scales with axial distance is lower than the respective values given by either Davies et al (Figure 5.51). Furthermore, the present results indicate that the appropriate equation for the length scale would have an intercept on the ordinate axis. There is no consistent variation in the values of L_x' and L_t' with Mach number and temperature (Figure 5.52). Consequently, average values for the respective rates of change of L_x' and L_t' with x are used. They are given by $L_x' = .24 + .021x$ and $L_t' = .14 + .014x$.

6. UNIFIED JET NOISE PREDICTION PROGRAM

6.1 INTRODUCTION

The purpose of this section is to present an overall description, in the form of a user's guide, of the unified supersonic jet noise prediction program (UNIJET) that has been developed by using the results and individual prediction routines generated under the previous tasks, in conjunction with the knowledge gained from the research conducted in the previous contract. In addition to the UNIJET prediction program, a separate program for isothermal jets is provided for the prediction of turbulent mixing noise at 90° to the jet axis using jet flow measurements (Section 6.6).

The UNIJET program enables the prediction of total noise from a single jet under static conditions for any desired set of jet operating conditions (i.e. velocity/temperature combination or pressure ratio/temperature ratio combination) and at angles and frequencies specified by the user. The program is designed for use on the CDC 6600 or 7600 computing systems. A complete listing of the program and a detailed flow chart are given in the Appendix volume of this report.

6.2 GENERAL FEATURES

The total noise from a supersonic jet is taken to consist of contributions from three individual or independent noise sources. These three noise sources are (i) the noise generated by large-scale jet structure, (ii) the noise generated by small-scale turbulence structure, and (iii) the noise generated by interaction between turbulence and shock structure. In the prediction program, the sound pressure levels due to these three noise components are labelled SPLA, SPLB, and SPLC, respectively, and the sources are referred to as follows:

SPLA: Large scale noise
SPLB: Turbulent mixing noise
SPLC: Shock-associated noise

6.2.1 Program Options

In order to provide maximum computational flexibility to the user, the prediction program has been carefully structured such that it can be executed in any of the following seven options:

(OPNO = Option Number)

OPNO = 1: SPLA
OPNO = 2: SPLB
OPNO = 3: SPLC
OPNO = 4: SPLA, SPLB, and SPLT = SPLA + SPLB
OPNO = 5: SPLB, SPLC, and SPLT = SPLB + SPLC
OPNO = 6: SPLA, SPLC, and SPLT = SPLA + SPLC
OPNO = 7: SPLA, SPLB, SPLC, and SPLT = SPLA + SPLB + SPLC

In addition to the seven main options listed above, SPLB can be computed using either one of the following two options:

BOPNO = 1: High-frequency analytic solution to Lilley equation
BOPNO = 2: Numerical solution to Lilley equation.

6.2.2 Limitations

(1) The prediction of large-scale noise (SPLA) is restricted to the following ranges:

Jet velocity	$V_J/a_o \geq 1.15$
Observer angle	$0° \leq \theta \leq 45°$
Strouhal number	$0.1 \leq S \leq 0.5$

Outside these ranges, SPLA is neglected.

(2) When turbulent mixing noise (SPLB) is predicted in conjunction with large-scale noise (SPLA) (i.e. when OPNO = 4 or 7), the SPLB contribution within the parameter ranges given in (1) above is neglected.

(3) The shock-associated noise contribution (SPLC) is neglected when

$\theta < 30°$ for $T_J/T_o \geq 0.9$ (i.e. heated jets),

and $\theta < 50°$ for $T_J/T_o \leq 0.9$ (i.e. unheated jets).

6.2.3 Failure Codes

In addition to the major limits given above, several failure codes have been incorporated in the program. The purpose of these failure codes is to prevent a premature termination of the program execution (a) whenever a parameter falls outside its allowable range or (b) when a numerical difficulty is encountered in the computation. In other words, when the program is not able to provide a valid prediction at some angle/frequency combination, it prints out an appropriate failure code, and proceeds to the next angle/frequency combination. For each program execution, the explanations for these failure codes will be listed on the first page of the output listing.

6.2.4 Option for Comparison With Measured Data

In the event that the user wishes to compare the predicted spectra with the corresponding measured spectra, an option has been provided to facilitate this. When this option is exercised, the program lists the difference between predicted and measured SPL at each frequency and angle, and also computes the standard deviation for the difference in spectra at each angle.

6.2.5 Computing Time and Cost

The execution of the program on the CDC 7600 computing system requires the following (nominal) computing time and cost:

(1) Large-scale noise - SPLA:

10 seconds and $12 per frequency (all θ)

(2) Turbulent mixing noise - SPLB:

(a) BOPNO = 1: 1 second and $1 per test point (i.e. spectra at all angles)

(b) BOPNO = 2: 10 seconds and $12 per spectrum at each angle.

(3) Shock-associated noise - SPLC:

1 second and $1 per test point (i.e. spectra at all angles).

6.3 INPUT REQUIREMENTS

The input parameters and their format, required to run the unified jet noise prediction program, are described below.

(1)

DIA	R
F10.0	F10.0

DIA - Nozzle diameter (D) in inches.
R - Observer distance (R) from nozzle exit plane in feet.

(2)

NANG	NFREQ	ISTART	ISTOP
I5	I5	I5	I5

NANG - Number of observer angles at which prediction is required (NANG ≤ 20).

NFREQ - Number of frequencies for which prediction is required (NFREQ ≤ 30). Put NFREQ = 0 if standard 1/3-octave band prediction is desired.

ISTART - Last 1/3-octave band number (as defined in Table 6.1) for which prediction is desired. This parameter is not required if NFREQ ≠ 0.

ISTOP - Last 1/3-octave band number (as defined in Table 6.1) for which prediction is desired. This parameter is not required if NFREQ ≠ 0.

FREQ(I), I = 1, NFREQ

(3)

F10.0	F10.0	F10.0					F10.0

FREQ - Frequencies (f) in Hz for which prediction is desired. These are not required if NFREQ = 0 (as explained above).

TM(J), J = 1, NANG

(4)

F10.0	F10.0	F10.0					F10.0

TM - Observer angles (θ_m) in degrees relative to jet exhaust at which prediction is desired.

- The following two cards, (5) and (6), are relevant to the shock-associated noise prediction:

(5)

NS
15

NS - Number of shocks (=8).

(6)

C	KO	K1	BC
F10.0	F10.0	F10.0	F10.0

C - Eddy convection velocity constant (C) (=0.70).
KO - Average shock spacing constant (K_O) (=1.10).
K1 - First shock spacing constant (K_1) (=1.31).
BC - Bandwidth constant (b) (=0.2316 for standard 1/3-octave band prediction).

(7)

OPNO	OPPER	ICODE	IFLG	BOPNO	ISS	IOPT	ILWR
15	15	15					15

OPNO - Main option number as defined in Section 6.2.1 (i.e. OPNO = 1 to 7 as desired by the user).

OPPER - Option number for jet operating conditions. If the jet operating conditions are specified in terms of P_O, T_O, V_J/a_O, and T_J/T_O, then OPPER = 0. If the jet operating conditions are specified in terms of P_O, T_O, P_R and T_R, then OPPER = 1.

ICODE - Option number to facilitate comparison with measured data.
ICODE = 0 if comparison is not desired;
ICODE = 1 for comparison with Lockheed measured data stored on Tape 2;
ICODE = 2 for comparison with user's measured data, to be provided as input.

IFLG - Option number to control the printout from large-scale noise calculations.
IFLG = 0 if intermediate printing is to be suppressed;
IFLG = 1 if detailed stability, transform, and wavenumber information is to be printed.

BOPNO - Option number for turbulent mixing noise prediction.
BOPNO = 1 uses high-frequency analytic solution to Lilley equation;
BOPNO = 2 uses numerical solution to Lilley equation.

ISS - Option for axial source distribution data in turbulent mixing noise prediction.
ISS = 0 - inferred from Lockheed *subsonic* mixing noise data;
ISS = 1 - inferred from Lockheed *subsonic and supersonic* mixing noise data (this provides the best overall prediction);
ISS = 2 - if user desires to input some or all of source data in subroutine SELECT.

IOPT - Source model indicator (used with BOPNO = 2 only).
IOPT = 1 - ring source, high frequency noncompactness assumed;
IOPT = 2 - radial source distribution, high frequency coherence noncompactness assumed;
IOPT = 3 - general noncompactness (no assumptions).

ILWR - Print option for Lilley equation solutions.
ILWR = 0 if all intermediate printing is to be suppressed;
ILWR = 1 if intermediate values interspersed in the turbulent mixing noise output (using BOPNO = 2) is to be printed.

- If ISS = 2 in the previous card, one or more of cards (8) through (16) are required by subroutine SELECT; these special input cards are described at the end of this list.

- The following input (17) through (23) should be provided for *every* test point:

(17)

TP
I5

TP - Any test point (or identification) number desired by the user to appear on output.

(18)

P0	T0F	VJA0	TJT0
F10.0	F10.0	F10.0	F10.0

P0 - Ambient pressure (P_0) in psia.
T0F - Ambient temperature (T_0) in °F.
VJA0 - Jet exit velocity ratio (V_j/a_0).
TJT0 - Jet static temperature ratio (T_j/T_0).
This card is required only if OPPER = 0.

(19)

PO	TOF	PRG	TRF
F10.0	F10.0	F10.0	F10.0

PO - Ambient pressure (P_O) in psia.
TOF - Ambient temperature (T_O) in °F.
PRG - Reservoir or total pressure (P_R) in psig.
TRF - Reservoir or total temperature (T_R) in °F.
This card is required only if OPPER = 1.

(20)

RSW
F10.0

RSW - Turbulence intensity radial half width (η_{hw}). This card is required only if IOPT = 2.

(21)

RSW	ALTB	BLTB
F10.0	F10.0	F10.0

RSW - Turbulence intensity radial half-width (η_{hw}).
ALTB, BLTB - Coefficients (a_ℓ, b_ℓ) which determine L_t, the radial-azimuthal coherence length.
This card is required only if IOPT = 3.

(22)

IVEL	IANG	INCANG
I5	I5	I5

IVEL - Number (according to Table 6.2) which specifies the test point number at a particular value of T_J/T_O for Lockheed measured data.

IANG - Angle number (from Table 6.3) which specifies the first observer angle at which comparison with measured data is to be conducted.

INCANG - Increment for advancing through measured data.
INCANG = 1 for 7.5° increments,
INCANG = 2 for 15.0° increments,
INCANG = 3 for 22.5° increments, etc.

This card is required only if ICODE = 1.

(23)

(SPLM(I,J), I = 7, 30), J = 1, NANG											
F6.1	F6.1	F6.1									F6.1

SPLM - User's measured SPL data for comparison with predictions.
This information is required only if ICODE = 2.

- At the end of the input data for the *last* test point, put a blank card. This will end the program execution.

Special Input Cards (Subroutine SELECT)

- The following input (8) through (16) is required only if ISS = 2 in card number 7:

IRD(I), I = 1, 8

(8)

I5	I5	I5					I5

IRD - Option number which specifies whether or not the user is going to input a particular turbulent mixing noise source parameter (as defined below).
IRD = 0 if the user does not desire to input a parameter;
IRD = 1 if the user does desire to input a parameter.

SPLNQ(N), N = 1, 28

(9)

F10.0	F10.0	F10.0					F10.0

SPLNQ - $10 \log_{10} (I_q)$
This information is not required if IRD(1) = 0.

CQ(N), N = 1, 28

(10)

F10.0	F10.0	F10.0					F10.0

CQ - C_q
This information is not required if IRD(2) = 0.

SPLND(N), N = 1, 28

(11)

F10.0	F10.0	F10.0					F10.0

SPLND - $10 \log_{10} (I_d)$
This information is not required if IRD(3) = 0.

CD(N), N = 1, 28

(12)

F10.0	F10.0	F10.0					F10.0

CD - C_d
This information is not required if IRD(4) = 0.

ETA(N), N = 1, 28

(13)

F10.0	F10.0	F10.0					F10.0

ETA - ε_s ($=V_S/V_J$)[†]
This information is not required if IRD(5) = 0.

XE(N), N = 1, 28

(14)

F10.0	F10.0	F10.0					F10.0

XE - ε_c ($=V_C/V_J$)
This information is not required if IRD(6) = 0.

UCLUJ(N), N = 1, 28

(15)

F10.0	F10.0	F10.0					F10.0

UCLUJ - V_{max}/V_J
This information is not required if IRD(7) = 0.

(DELRAD(N,JJ), N = 1, 28), JJ = 1,4

(16)

F10.0	F10.0	F10.0					F10.0

DELRAD - δ_s/r_J
This information is not required if IRD(8) = 0.

[†]*If BOPNO = 2 (Lilley numeric solutions), values of V_s exceeding 0.95 V_{max} in the jet transition region ($1.0 \leq \delta_s/r_J \leq 1.819$) may cause a program error. The standard parameter values in BLOCK DATA (used if ISS = 0 or 1) do not, but when V_s is specified by the user it is recommended that values should be less than or equal to 0.95 V_{max}.*

1/3 Octave Band Number	Center Frequency (Hz)	1/3 Octave Band Number	Center Frequency (Hz)
1	50	18	2500
2	63	19	3150
3	80	20	4000
4	100	21	5000
5	125	22	6300
6	160	23	8000
7	200	24	10000
8	250	25	12500
9	315	26	16000
10	400	27	20000
11	500	28	25000
12	630	29	31500
13	800	30	40000
14	1000	31	50000
15	1250	32	63000
16	1600	33	80000
17	2000		

Table 6.1 One-Third Octave Band Number and Corresponding Center Frequencies

File →	T10	T14	T18	T22	T28	T34
T_J/T_o →	1.0	1.4	1.8	2.2	2.8	3.4
IVEL Number						
1	8	13	21	30	41	67
2	9	14	22	31	42	68
3	10	15	23	32	43	70
4	11	16	24	33	44	71
5	12	17	25	34	45	72
6	51	18	26	35	46	73
7	58	19	27	36	47	74
8	63	20	28	37	48	75
9		53	29	38	49	
10		59	54	39		
11		64	60	55		

V_J/a_o ↓

Table 6.2 IVEL Numbers Corresponding to the Test Points at Each Value of T_J/T_o for Lockheed Jet Mixing Noise Data Stored on File (Rear Arc Only)

Angle Number	Angle (Degrees)
1	15.0
2	22.5
3	30.0
4	37.5
5	45.0
6	52.5
7	60.0
8	67.5
9	75.0
10	82.5
11	90.0
12	97.5

Table 6.3 Angle Number and Corresponding Angle for Lockheed Jet Mixing Noise Data Stored on File (Rear Arc Only)

6.4 FLOW CHARTS AND SUBROUTINES

The unified jet noise prediction program (UNIJET) consists of the main program, called UNIMAIN, and sixty-one subroutines. The flow chart for UNIMAIN is given in Figure 6.1. In addition, flow charts for the following *four main subroutines* are given in Figures 6.2 through 6.4:

LSNOISE/DIRECT	(Figure 6.2)	- Computation of large-scale noise
MXNOISE	(Figure 6.3)	- Computation of turbulent mixing noise
SANOISE	(Figure 6.4)	- Computation of shock-associated noise

The remaining fifty-seven subroutines are defined briefly below:

(1) CALPER - Computes all parameters that describe the jet operating conditions (e.g. total pressure ratio P_R/P_O, total temperature ratio T_R/T_O, static temperature ratio T_J/T_O, velocity ratio V_J/a_O, Mach number M_J, gamma ratio γ_J/γ_O, etc.) using the input parameters.

(2) LSMAIN - Intermediate routine between UNIMAIN and LSNOISE to handle initialization, error messages and to determine the absolute noise radiation levels.

(3) PJMRUN - Fourth-order Runge-Kutta integrator with round-off error minimization for complex step size.

(4) DERY - Evaluates the local value of the function derivatives in stability calculation.

(5) UEVAL - Calculates the mean velocity and density and their radial and axial derivatives.

(6) LAGRAN - Minimization routine using an m^{th} order inverse Lagrangian interpolation scheme.

(7) NCBRTS
(8) CBRTS
(9) BSSLS
(10) BELS
(11) BELZ
(12) HAN

- Calculates either the Bessel functions of the first and second kinds or Hankel functions of first and second kinds for complex arguments and arbitrary integer order.

(13) INTEG - Three point integration routine.

(14) RUNREL - Fourth-order Runge-Kutta integrator with round-off error minimization for real step size.

(15) DERY1 - Evaluates the local value of the function derivatives for the axial wave amplitude calculation.

(16) COEFF - Calculates local wavenumber from tabulated values of $\alpha(s)$ stored during stability calculation.

(17) FFT
(18) ISOL
(19) IMOVE
(20) IDASH
(21) IREV
- Fast Fourier transform routines.

(22) ASTART
(23) ISEQ
- Interpolation routine for starting eigenvalue guess from tabulated values as function of Strouhal number, jet exit static temperature ratio, mode number and Mach number.

(24) SIMQ - Solution of simultaneous algebraic equations.

(25) BLKLSN - Tables of initial eigenvalue guesses.

(26) SELECT - Sets up data arrays either from BLOCK DATA TMN and/or from optional inputs and calculations.

(27) DOPPLE - Calculates flow parameters in source region and Strouhal number for a given *modified* Strouhal number.

(28) GPT - Calculates the profile gradient at a specified position (by iteration) for the error function velocity profile.

(29) LILLEY - Intermediate routine between MXNOISE and SUB2 where numeric solution procedure is controlled. Calls DSETUP and SUB2.

(30) DSETUP - Sets up parameters in the form required by SUB2, checks that input parameters do not exceed certain limits.

(31) SUB2 - Controls numerical solution procedure. Calls AXIAL, SLOC, VELT, CRIT, RABC, IDERY, HPCL, TRANS, WRCAL, RADCSD, TCON, TSIGN.

(32) AXIAL - Computes profile parameters for either initial mixing or fully developed region.

(33) SLOC - Computes radii of standard ring sources (specified in terms of flow velocity/center line velocity).

(34) VELT - Computes velocity and temperature at a given radius: also velocity and temperature (transverse) gradients if required. Uses function routine ERF.

(35) ERF - Computes error function.

(36) CRIT - Computes (by iteration) radius of critical layer. Calls VELT.

(37) RABC - Computes initial values of independent solutions. Calls CBESL1, CBESL2.

(38) CBESL1 - Computes Bessel function of the first kind, of complex argument and integer order.

(39) CBESL2 - Computes Bessel function of the second kind, of complex argument and integer order.

(40) IDERY - Sets up relative error weighting vector for HPCL and profile derivative indicator for VELT.

(41) HPCL - Computes approximate solution of a linear system of first-order differential equations with given initial values by Hamming's modified predictor-corrector method.† Calls AFCT, FCT, OUTP.

(42) AFCT - Sets up coefficients of the two first-order differential equations. Calls COEF.

(43) FCT - Sets arbitrary functions in set of linear differential equation to zero.

(44) OUTP - Divides solution by Doppler factor raised to required power, including critical layer case where Doppler factor is complex. (Original purpose: to output intermediate numerical solution information generated by HPCL).

(45) COEF - Computes coefficients of the two first-order differential equations. Calls VELT.

(46) TRANS - Transfers data stored from one array to another.

(47) WRCAL - Computes Wronskian of the two independent solutions.

(48) TCON - Determines convergence of complete solution with increasing azimuthal mode order for each standard ring source radius.

(49) TSIGN - Checks that solution is greater than zero, otherwise writes error message.

(50) RADCSD - Controls processing of basic numerical solutions to yield solutions for radially distributed source models. Calls INTRAP, VELT and uses ERF.

(51) INTRAP - Controls computation of single or double integrals. Calls QTFG, BESI and uses function routine SRPSD.

---

†*IBM System/360 Scientific Subroutine, modified to incorporate relative error test.*

(52) SRPSD - Computes radial Gaussian distribution of source strength.

(53) BESI - Computes the Bessel function $I_n(x)$† multiplied by e^{-x}.

(54) QTFG - Computes integration of monotonically tabulated function by trapezoidal rule.†

(55) BLKTMN - Block data for mixing noise (B) calculations.

(56) LAGRNG - Interpolates the $H_o(\sigma)$ and $C_1(\sigma)$ master spectra for argument σ.

(57) BLKSAN - Block data segment containing the two master spectra, $H_o(\sigma)$ and $C_1(\sigma)$, for shock noise (C) calculations.

6.5 SAMPLE CASE

6.5.1 Input

The input data for a sample case with OPNO = 7 and BOPNO = 1 are shown in Figure 6.5, and a listing of the corresponding output is presented in Figure 6.6 (seven pages).

The input data can be interpreted in conjunction with the description given in Section 6.3, as follows:

(1)

DIA	R
2.0	12.0

(2)

NANG	NFREQ	ISTART	ISTOP
1	0	7	30

(3) Not required.

(4) TM(J), J=1, NANG

90.0

†*IBM System/360 Scientific Subroutine.*

(5)

NS
8

(6)

C	KO	K1	BC
0.70	1.10	1.31	0.2316

(7)

OPNO	OPPER	ICODE	IFLG	BOPNO	ISS	IOPT	ILWR
7	1	2	0	1	0	1	0

(8) - (16) Not required.

(17)

TP
41

(18) Not required.

(19)

PO	TOF	PRG	TRF
14.20	70.0	28.20	1130.0

(20) - (22) Not required.

(23) (SPLM(I,J), I = 7, 30), J = 1, NANG

86.7	88.4	88.7	90.2	92.5	94.5	96.9	99.8	100.2	102.1	103.3	105.2
105.9	107.5	107.7	108.4	109.4	111.2	112.1	111.0	109.8	108.8	108.0	107.5

Finally, a blank card to end the program execution.

6.5.2 Output

The first page of the output lists the various failure codes (for each noise source) and the corresponding explanations. These failure codes form a very important part of the prediction scheme, and they have been provided specifically to prevent premature termination of the program execution. In the absence of these failure codes, the program execution would terminate

whenever a parameter (for example, frequency, angle, etc.) falls outside its allowed range or whenever a numerical difficulty is encountered. With this failure codes provision, however, the program indicates the nature of the problem (whenever it occurs), and proceeds to the next frequency or angle until a valid computation of SPLA or SPLB or SPLC is obtained. In this manner, the program scans through all frequencies and all angles and provides the noise predictions, with correct answers where possible and failure codes where a problem is encountered.

The second page of the output lists the standard values of the turbulent mixing noise source and mean flow constants used in the program.

Following these two pages, the output consists of several pages for each test point, as follows:

The first page shows the title, the test point number, and the option number (OPNO) selected by the user. Following this, the output consists of a list of various input parameters and several computed parameters that describe the jet operating conditions. If OPNO = 3, 5, 6, or 7 is selected, the remaining output on this page consists of a list of parameters relevant to the shock-associated noise prediction.

For each value of the observer angle, the predicted spectra for each noise source are first listed on a separate page, and this is followed by a page that gives the total noise spectrum at that angle.

6.5.3 Typical Comparisons With Experiment

Typical comparisons between measured and predicted spectra using OPNO = 7 (i.e., all three noise sources) for a supersonic, high-temperature jet are shown in Figures 6.7 through 6.11, corresponding to observer angles of 30°, 60°, 90°, 120°, and 135°, respectively.

6.6 PREDICTION OF ISOTHERMAL JET MIXING NOISE AT 90° TO THE JET AXIS, BASED ON LV TURBULENCE MEASUREMENTS

This section is a user's guide to INTEG, a *separate* computer program from UNIJET which was written to evaluate a model described in Section 2.4 that predicts isothermal jet mixing noise spectrum levels at 90° to the jet axis. The model utilizes measured LV turbulence data but does *not* require any "adjustable constants"; that is, it is an absolute noise level prediction method.

The input requirements, a description of the subroutines, and the flow chart for the INTEG program are given in the following three subsections. A complete listing of the program is given in the appendix volume of this report.

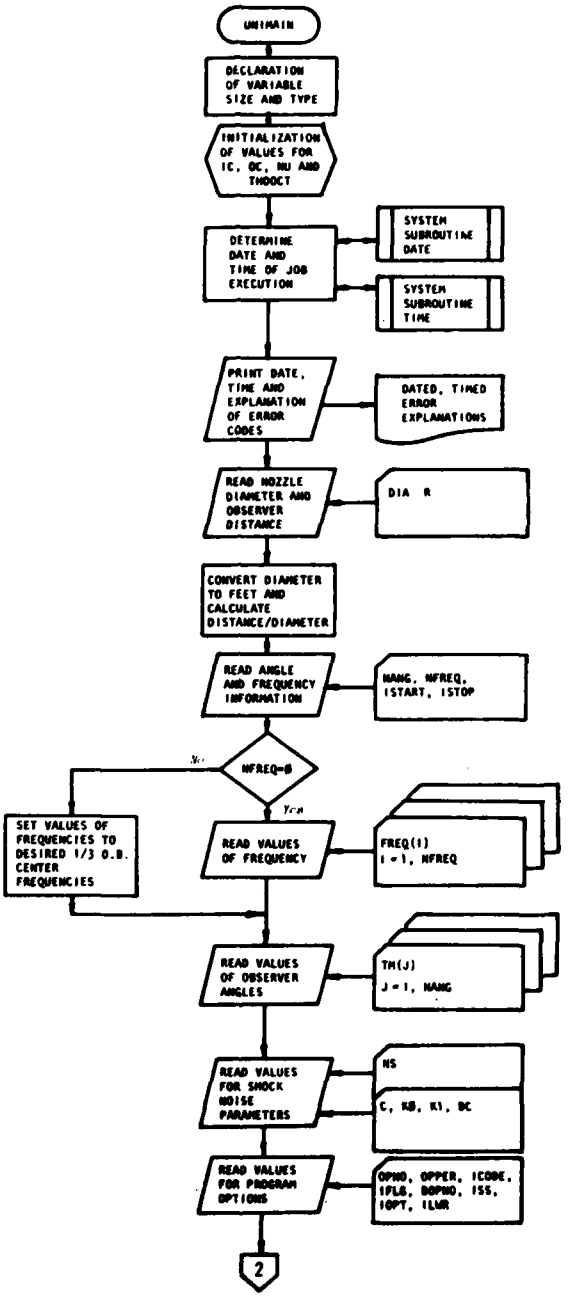

Figure 6.1 Flow Chart for Main Program UNIMAIN.

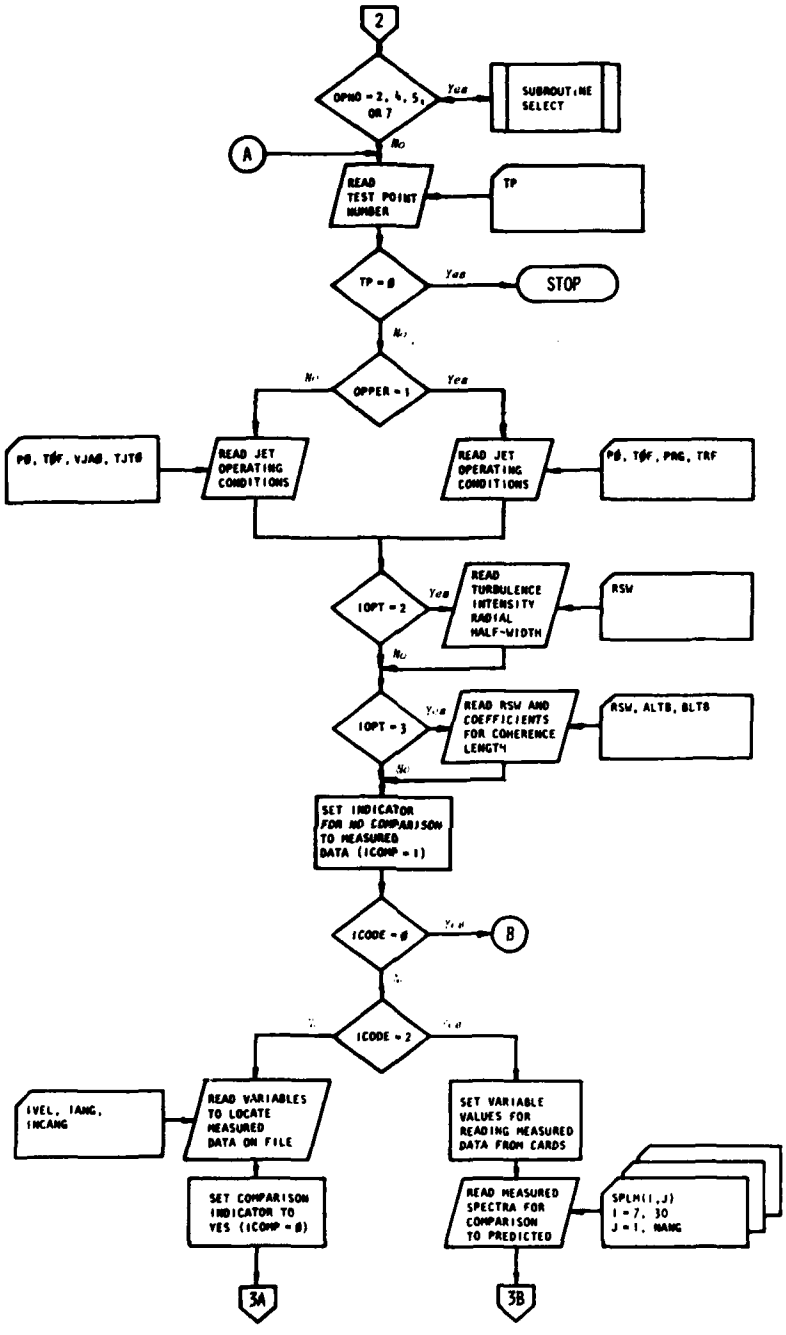

Figure 6.1 Continued.

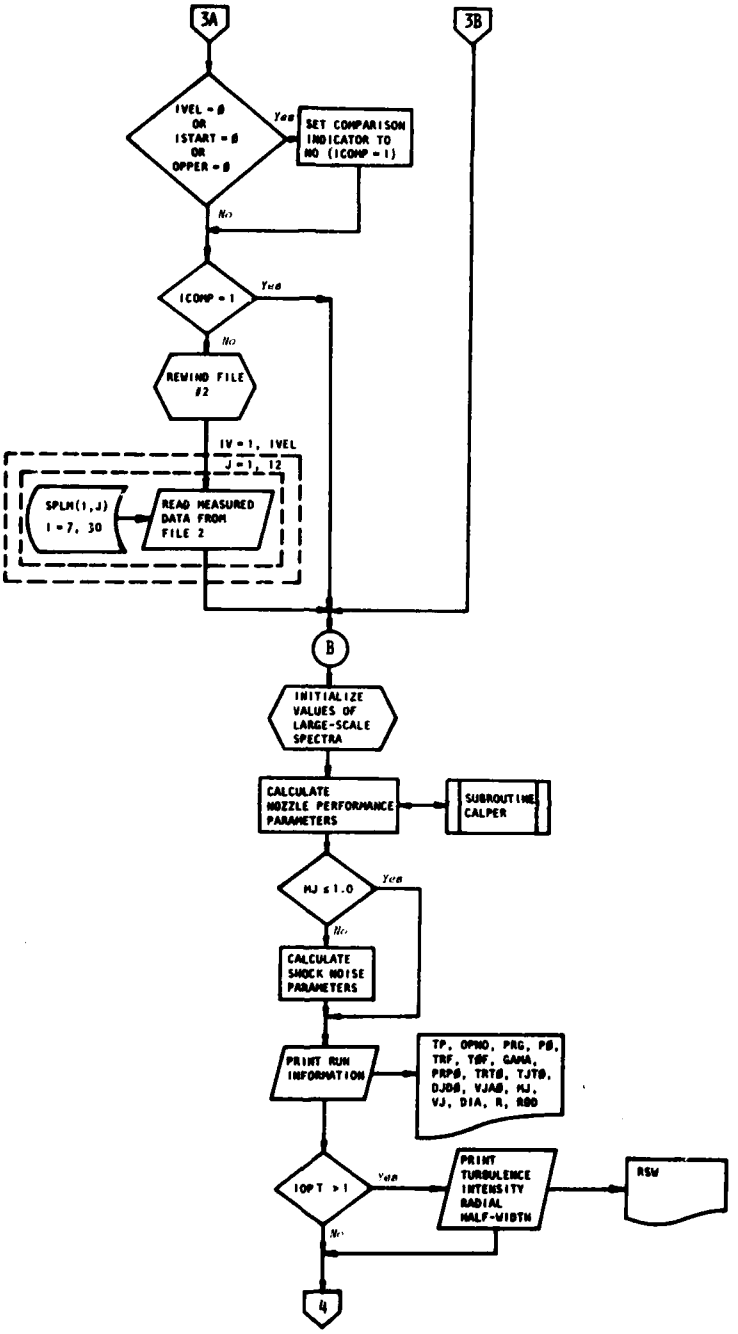

Figure 6.1 Continued.

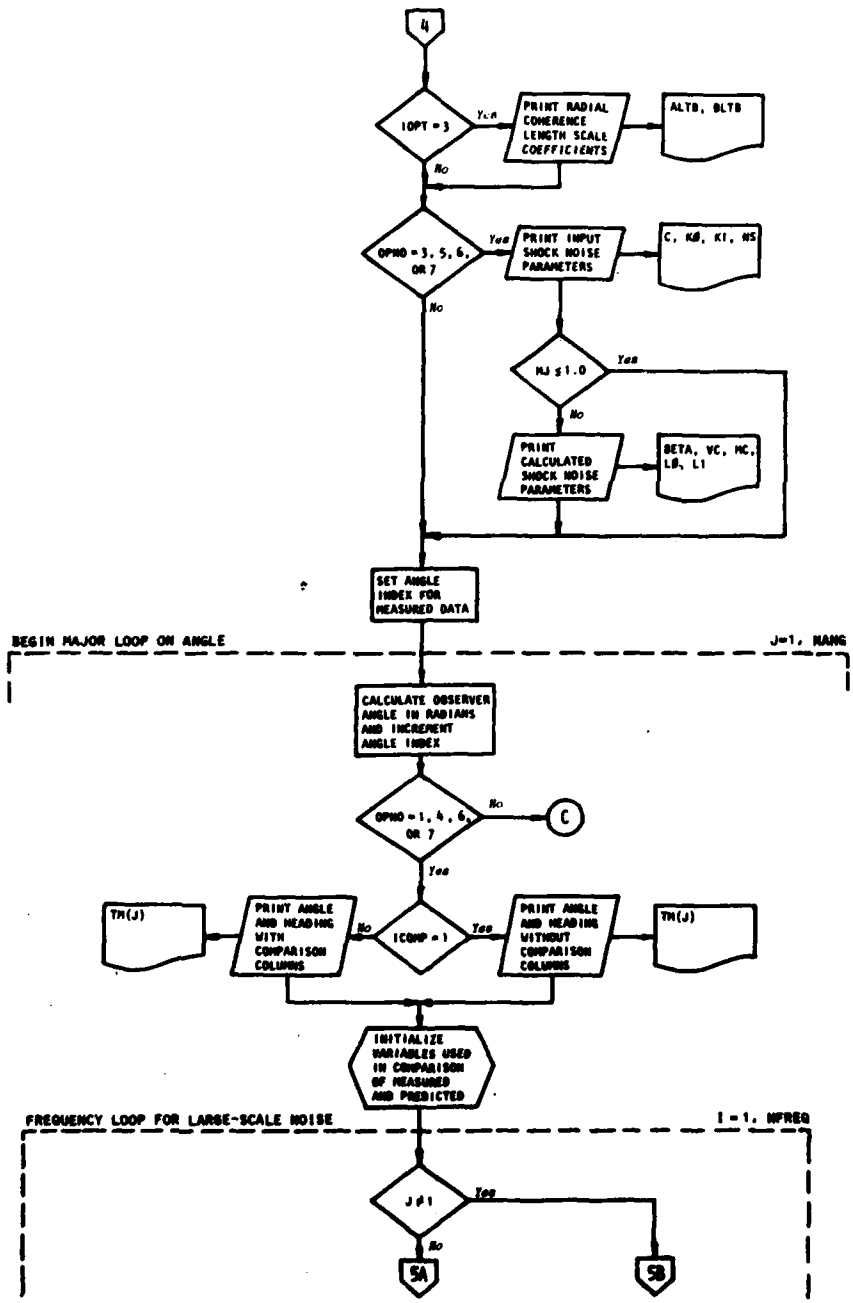

Figure 6.1 Continued.

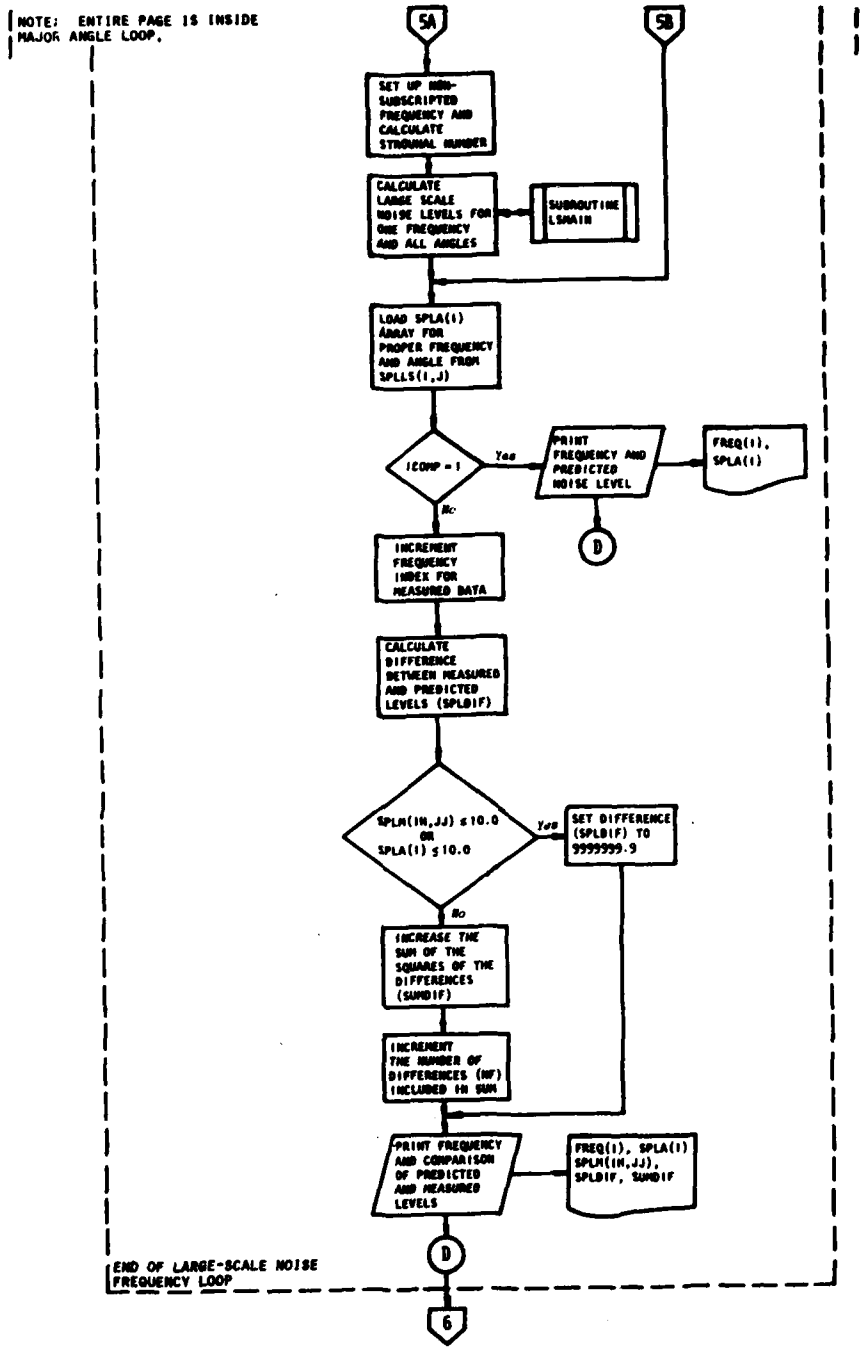

Figure 6.1 Continued.

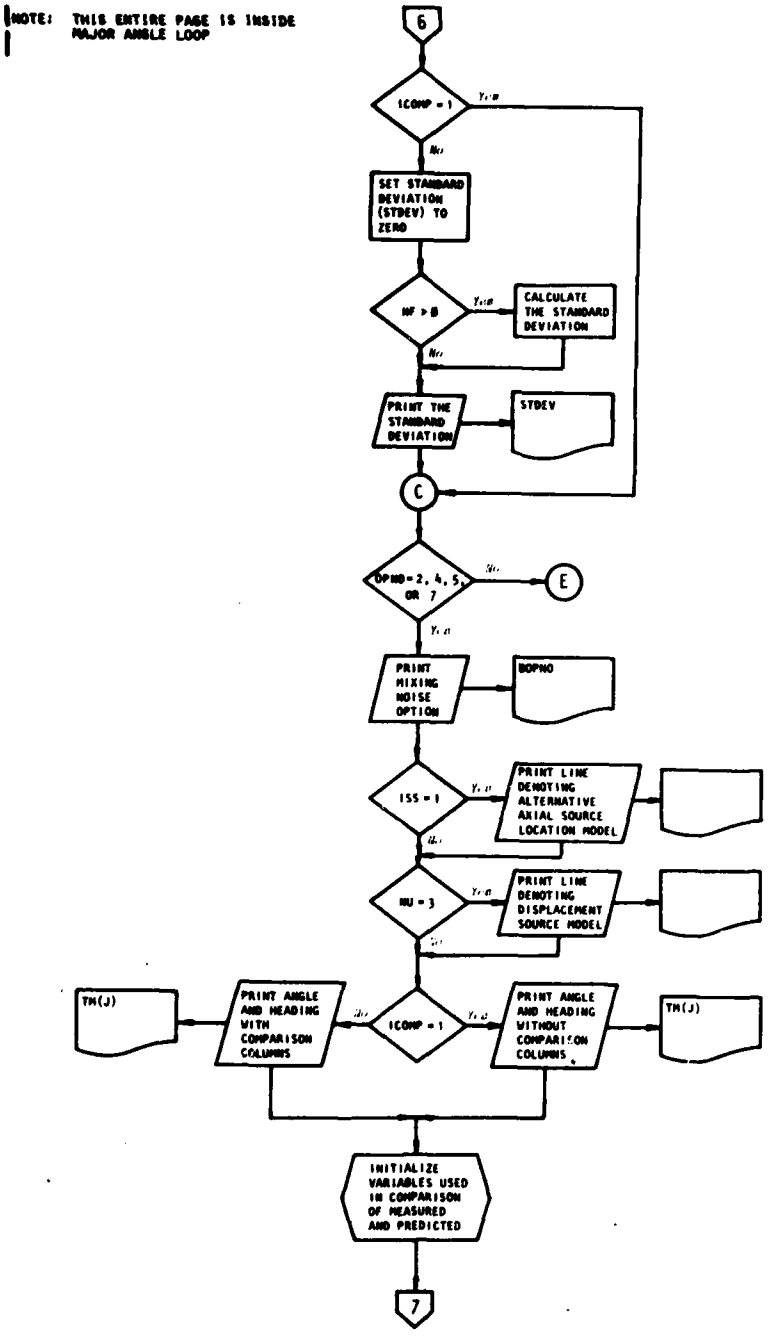

Figure 6.1 Continued.

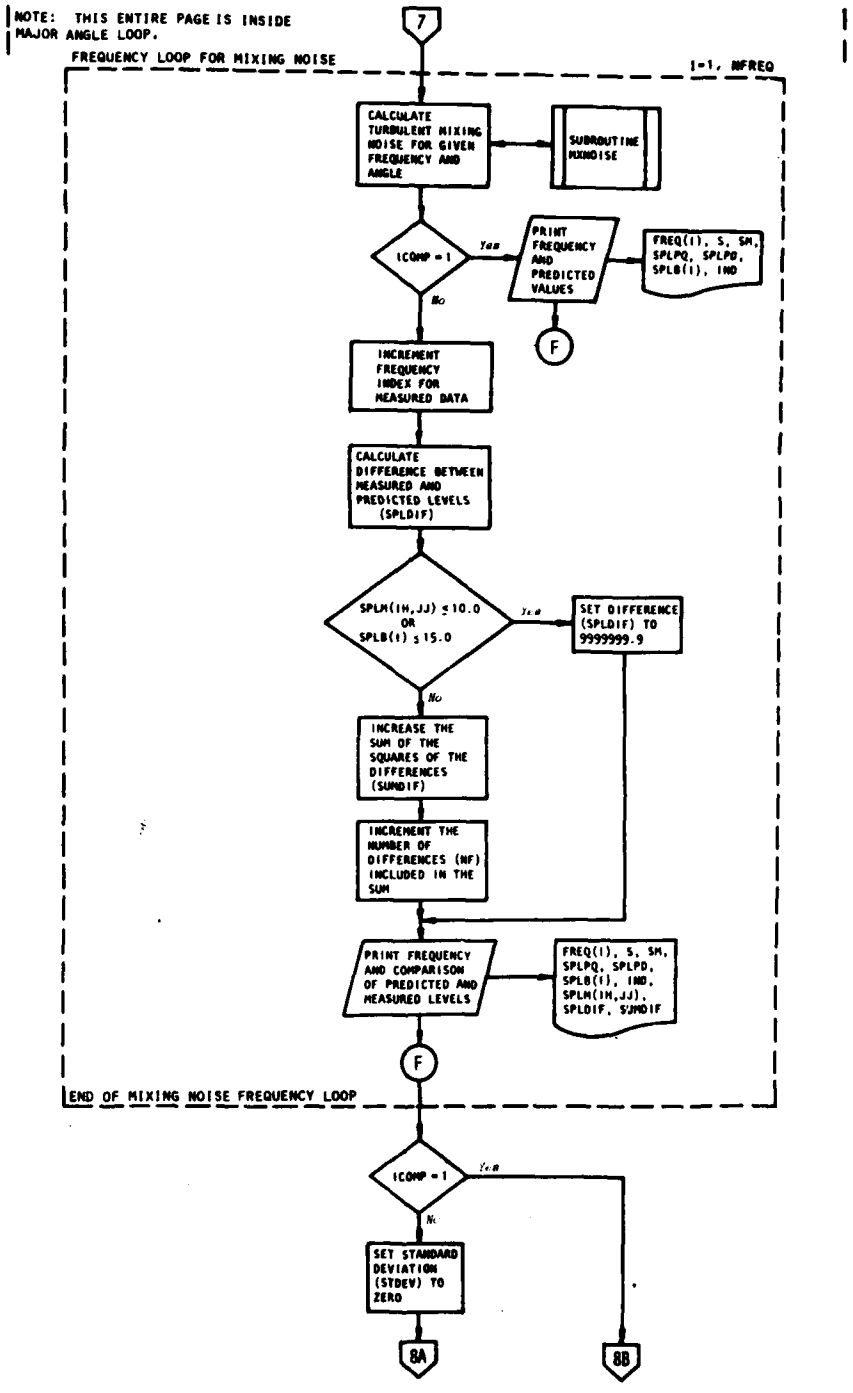

Figure 6.1 Continued.

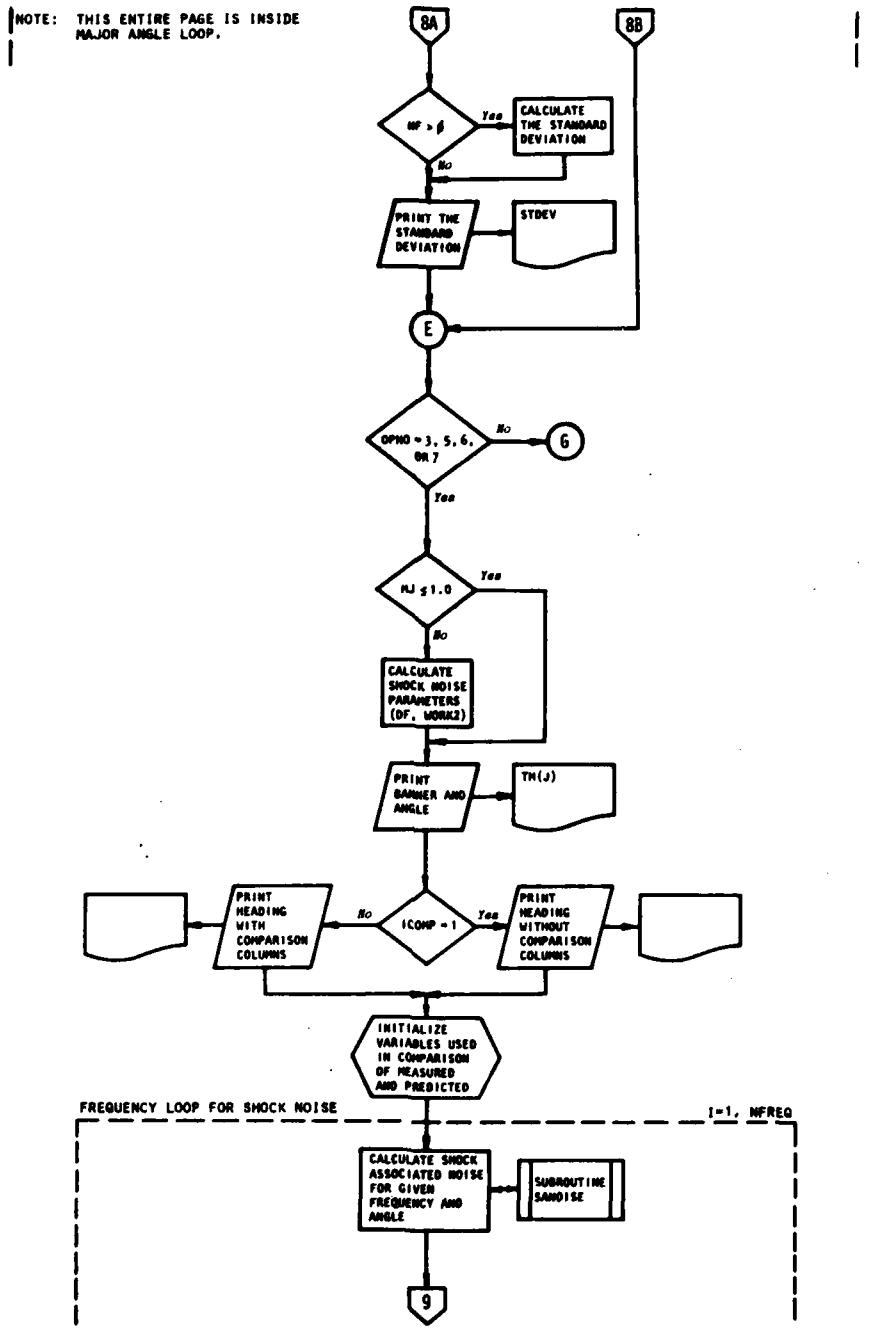

Figure 6.1 Continued.

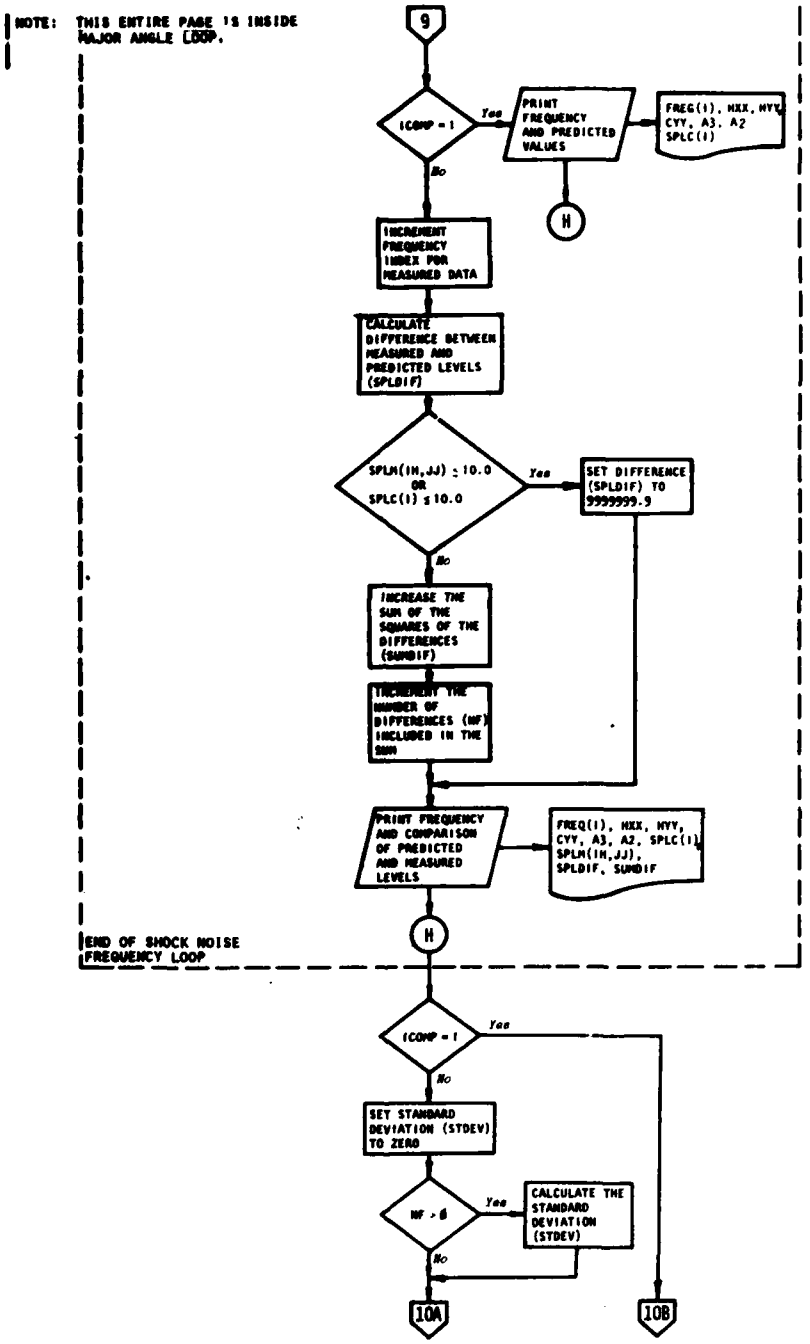

Figure 6.1 Continued.

NOTE: THIS ENTIRE PAGE IS INSIDE MAJOR ANGLE LOOP.

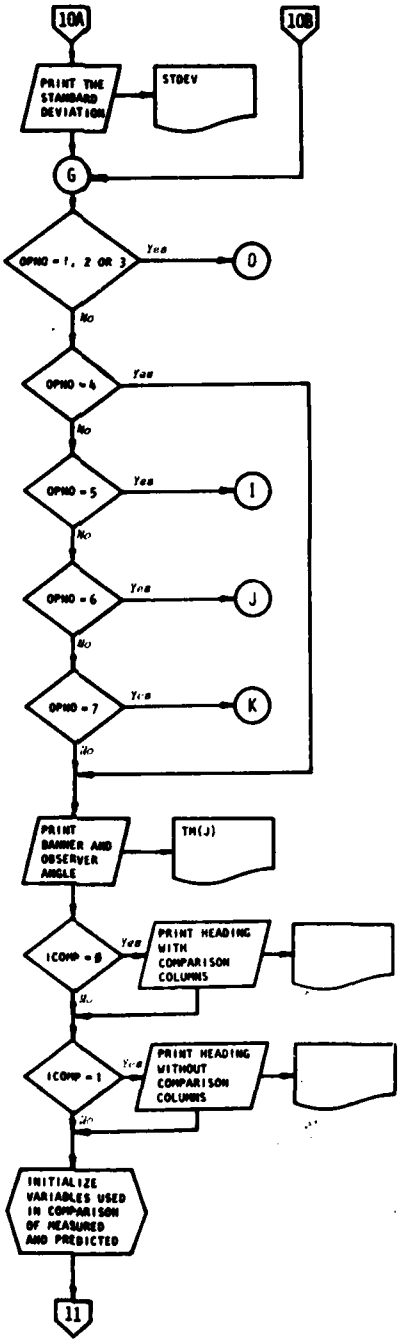

Figure 6.1 Continued.

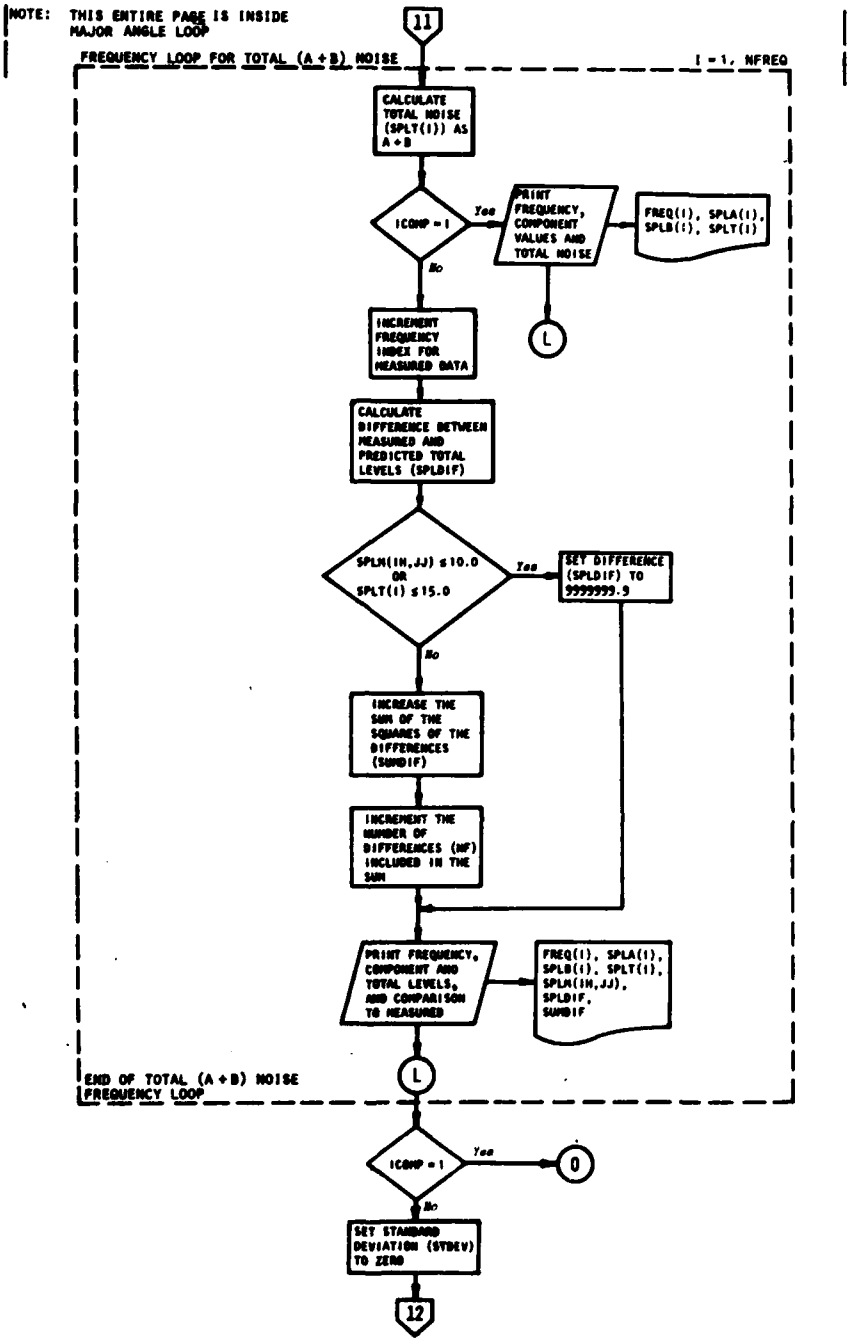

Figure 6.1 Continued.

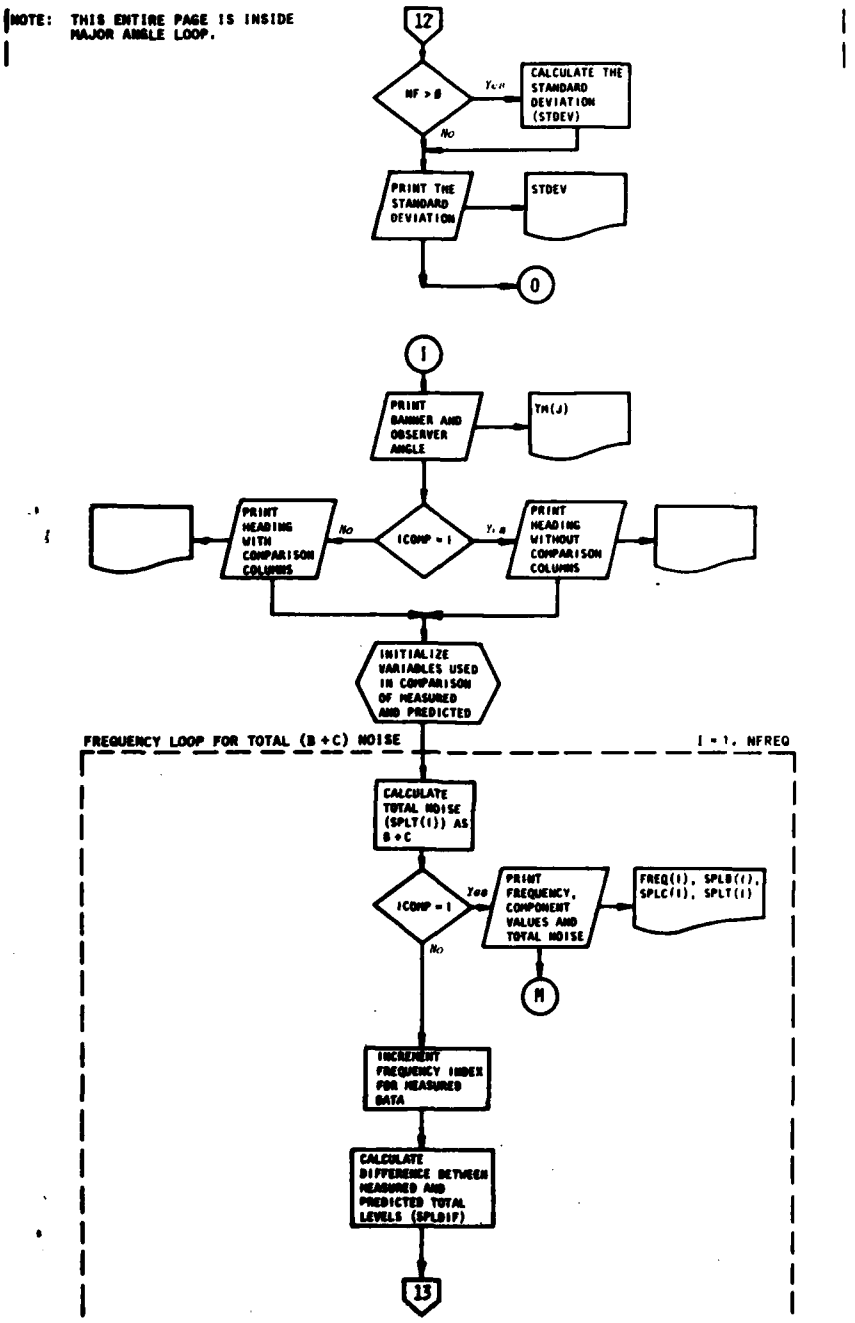

Figure 6.1 Continued.

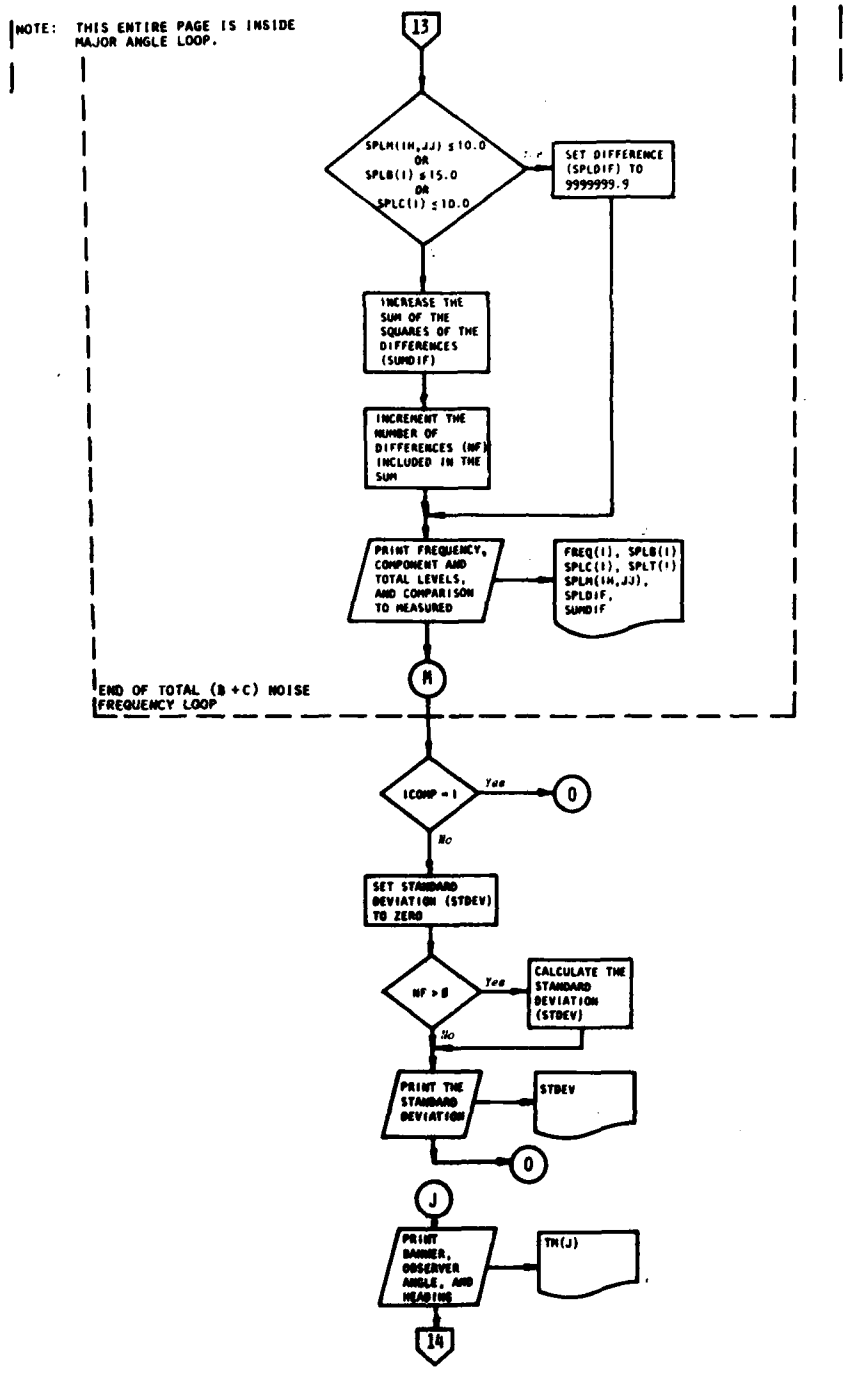

Figure 6.1 Continued.

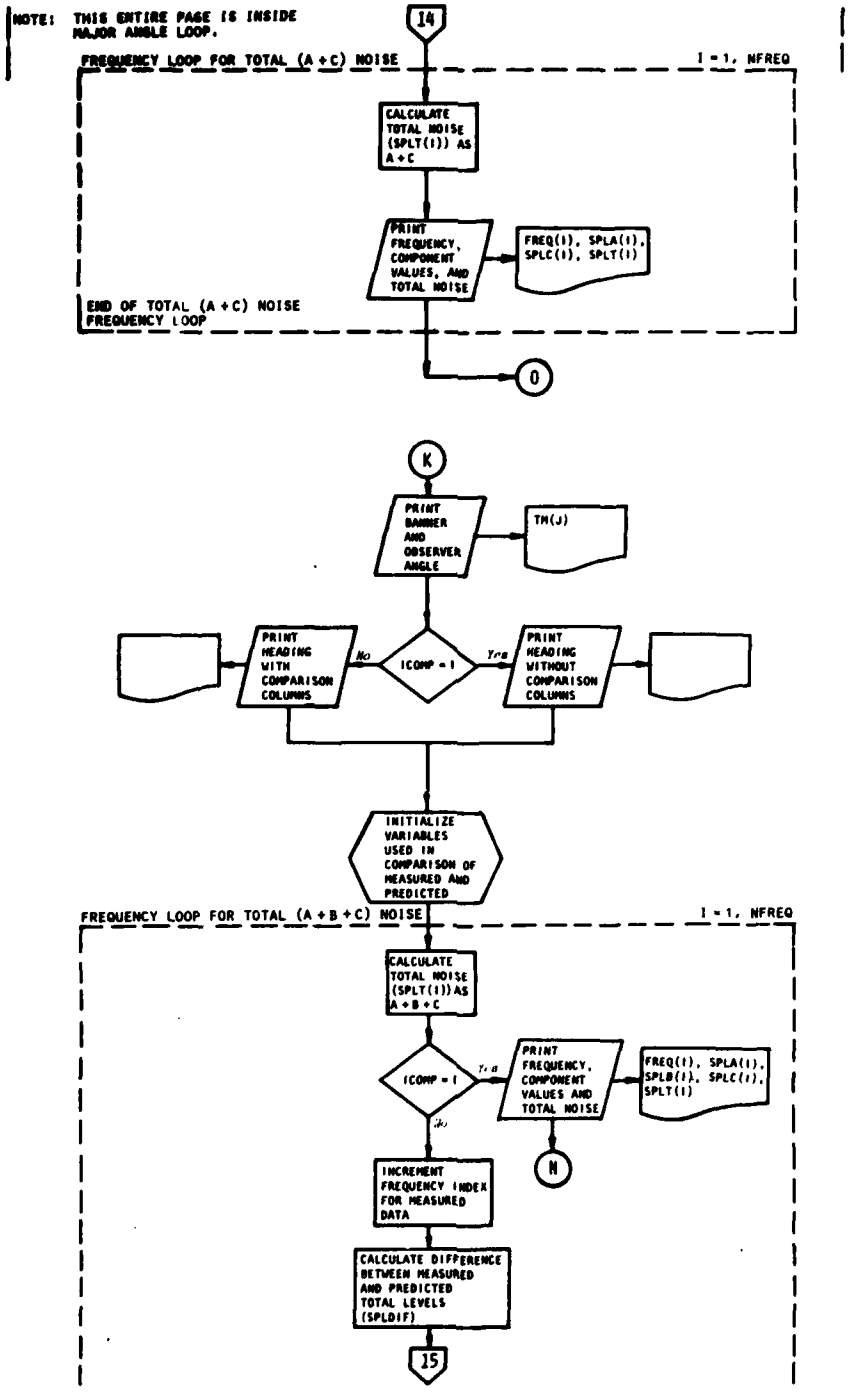

Figure 6.1 Continued.

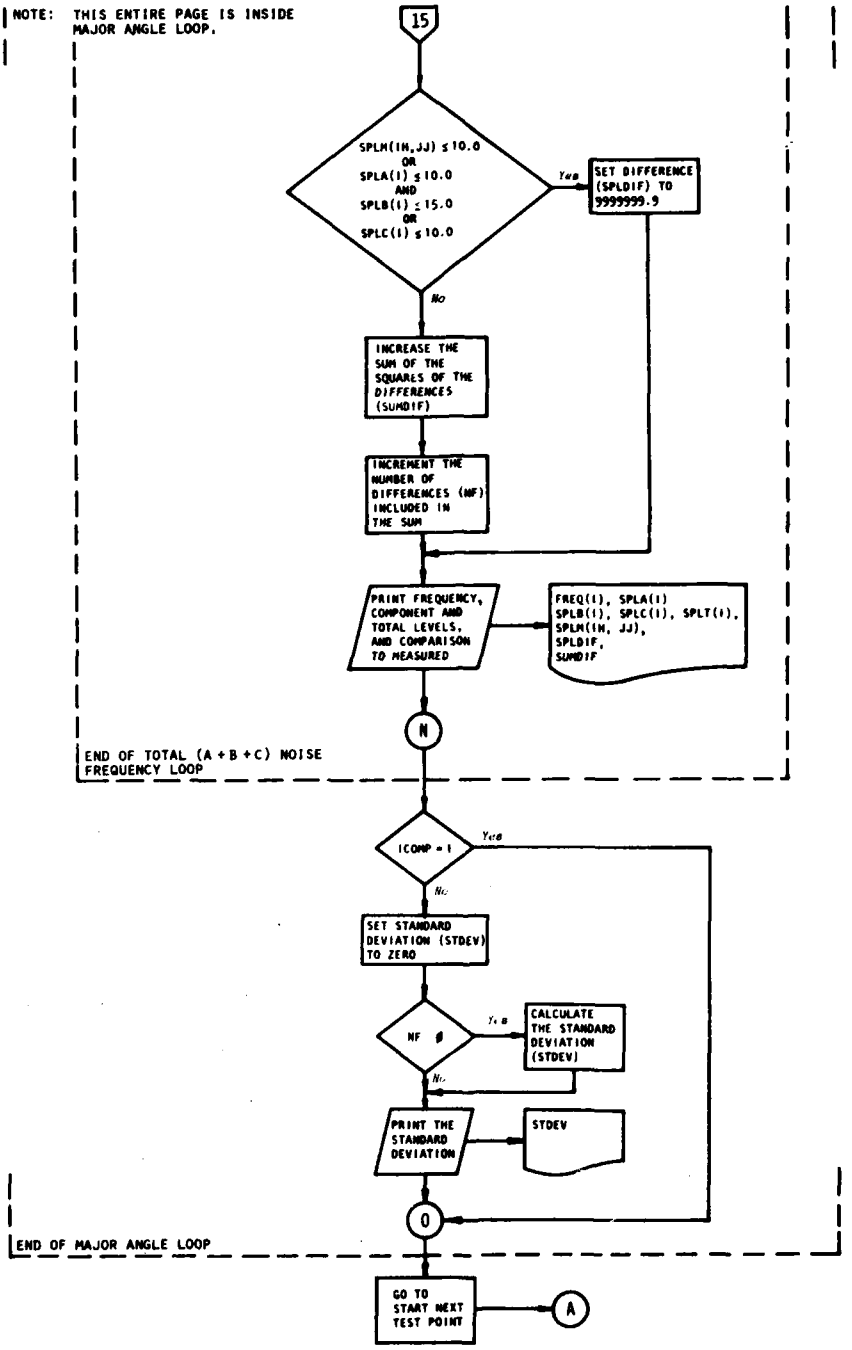

Figure 6.1 Concluded.

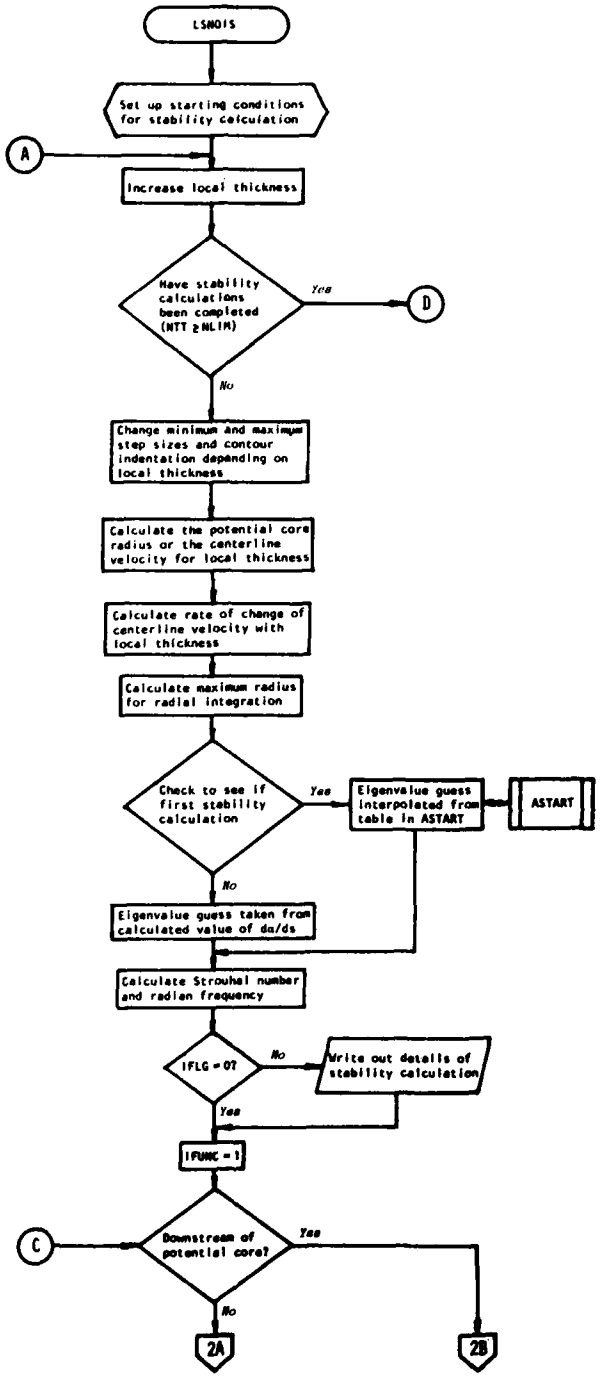

Figure 6.2 Flow Charts for Subroutines LSNOIS/DIRECT.

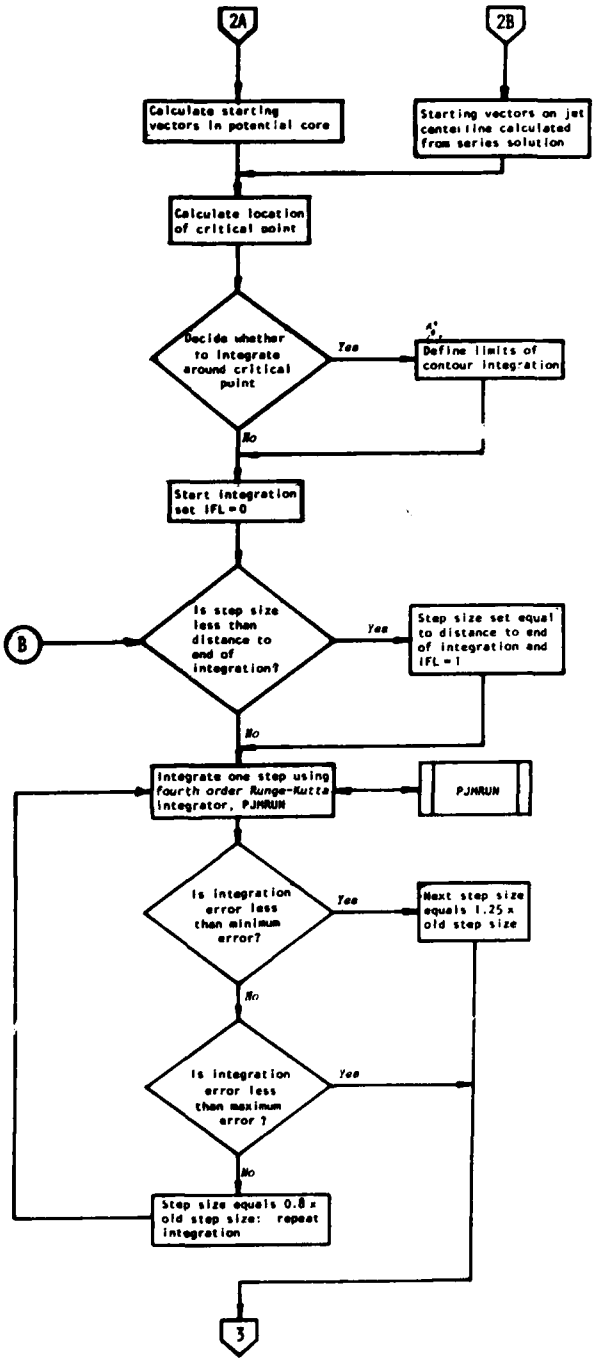

Figure 6.2 Continued.

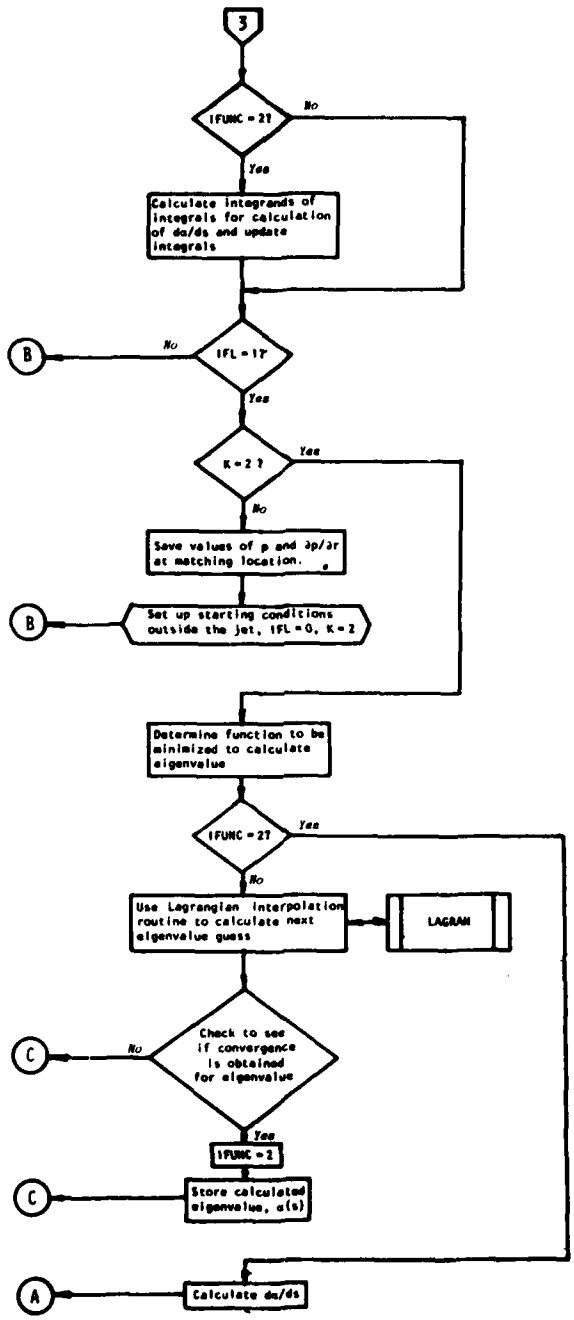

Figure 6.2 Continued.

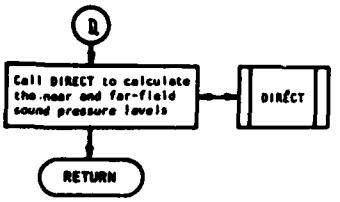

Figure 6.2 Continued.

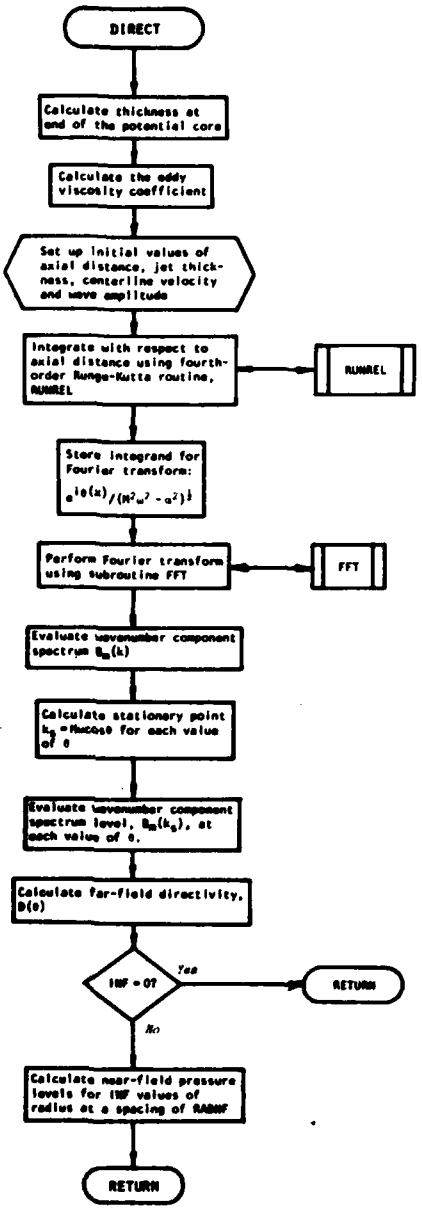

Figure 6.2 Concluded.

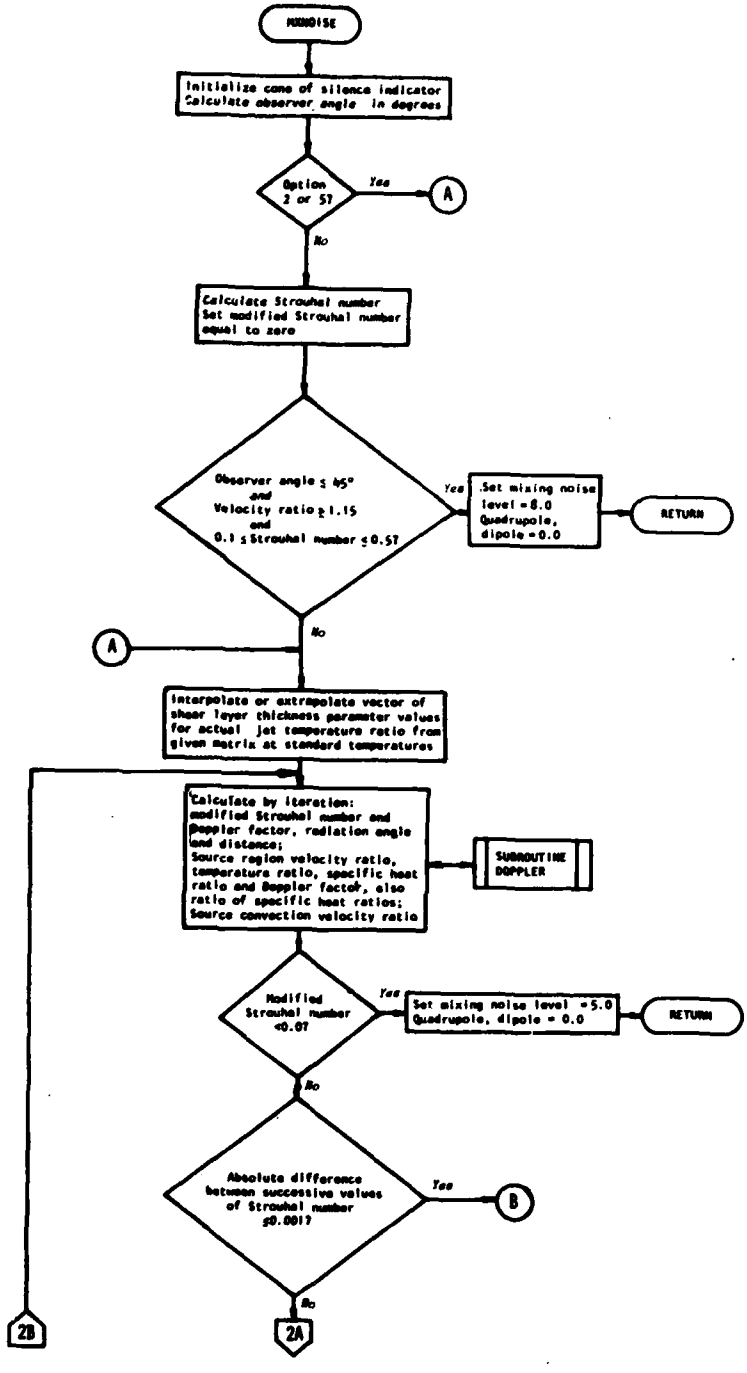

Figure 6.3 Flow Chart for Subroutine MXNOISE.

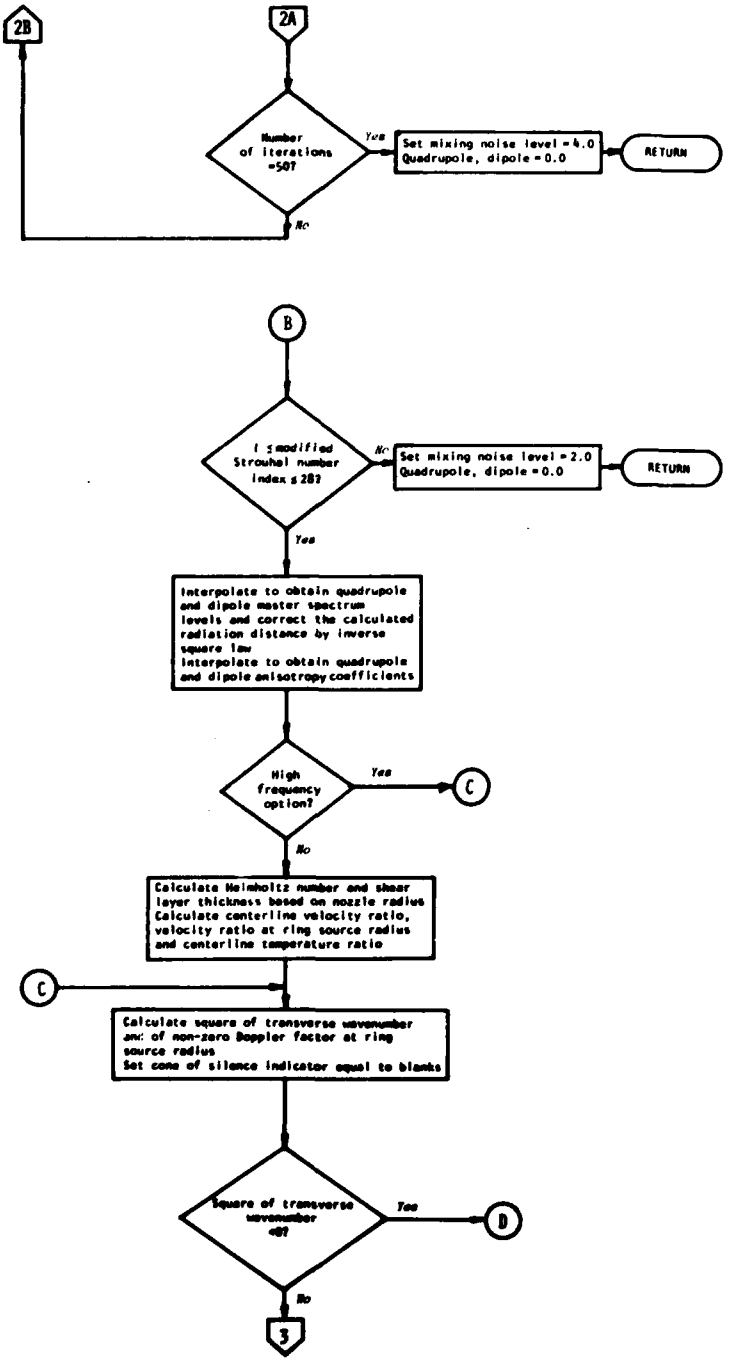

Figure 6.3 Continued.

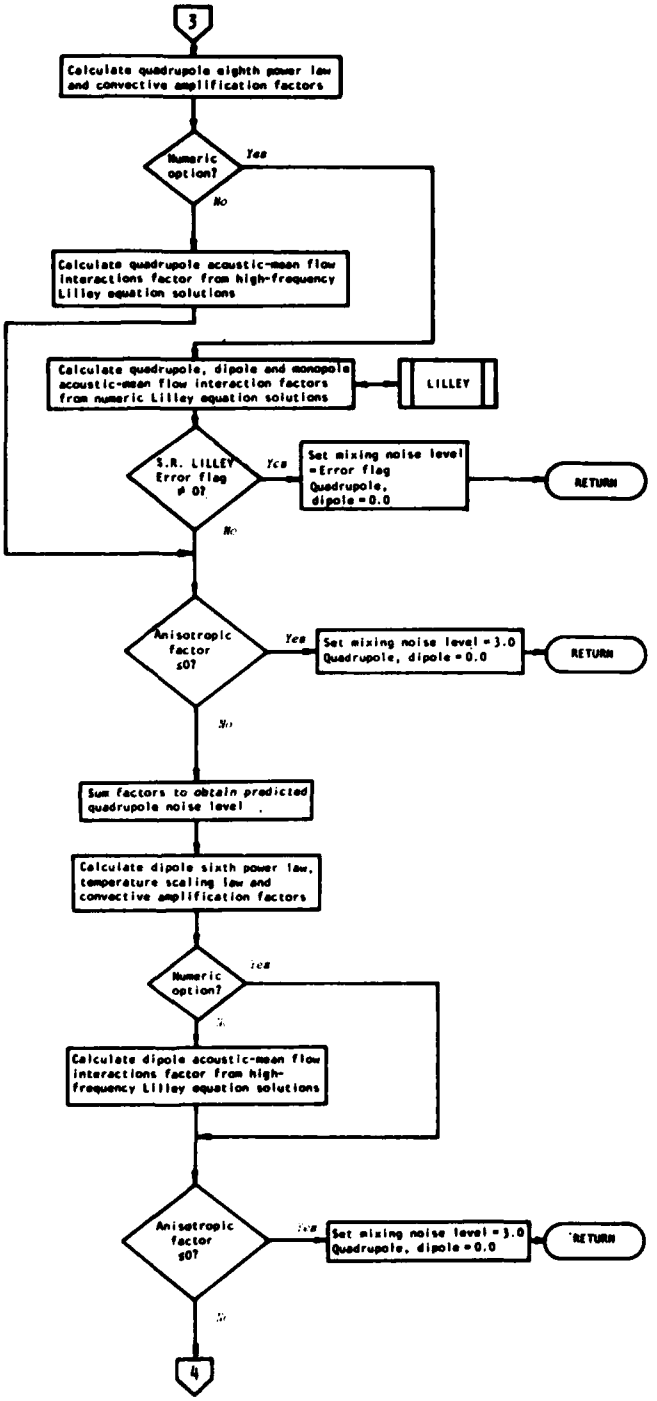

Figure 6.3 Continued.

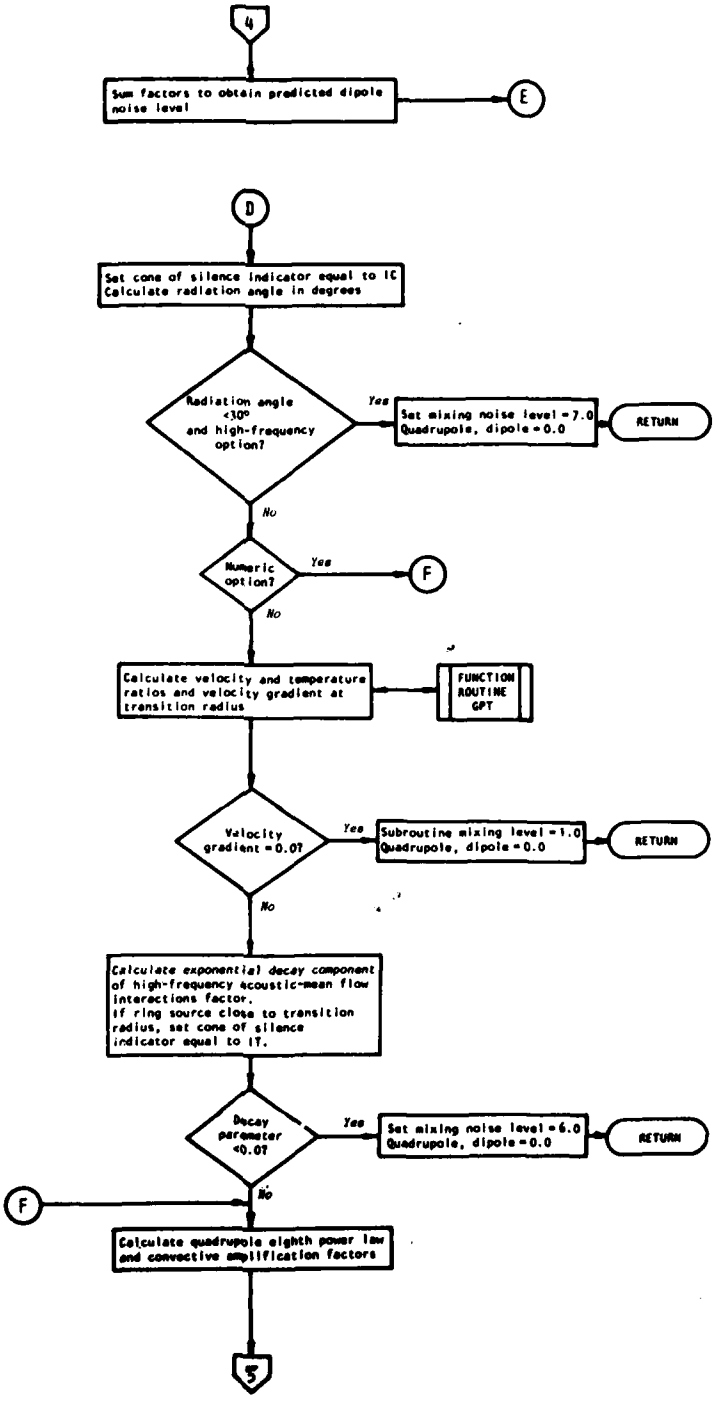

Figure 6.3 Continued.

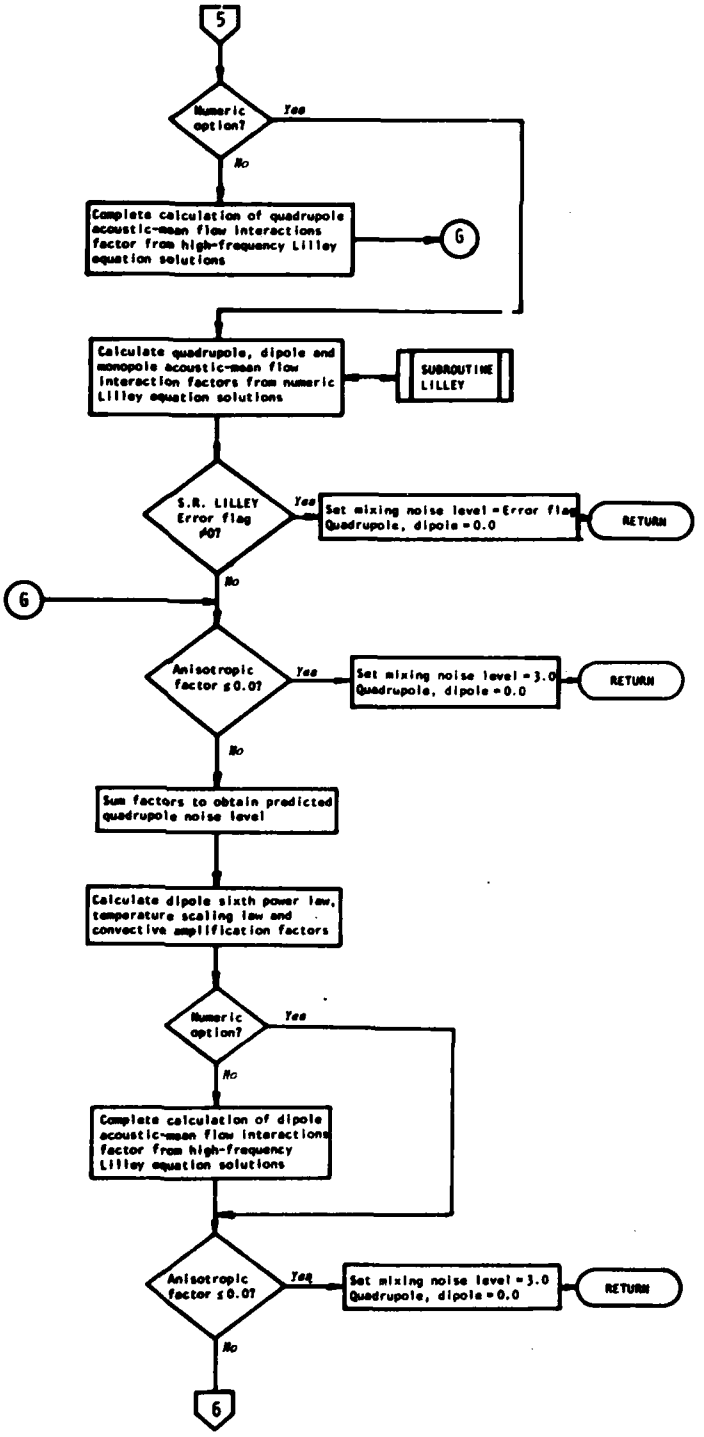

Figure 6.3 Continued.

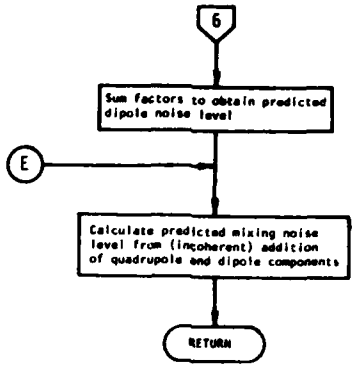

Figure 6.3 Concluded.

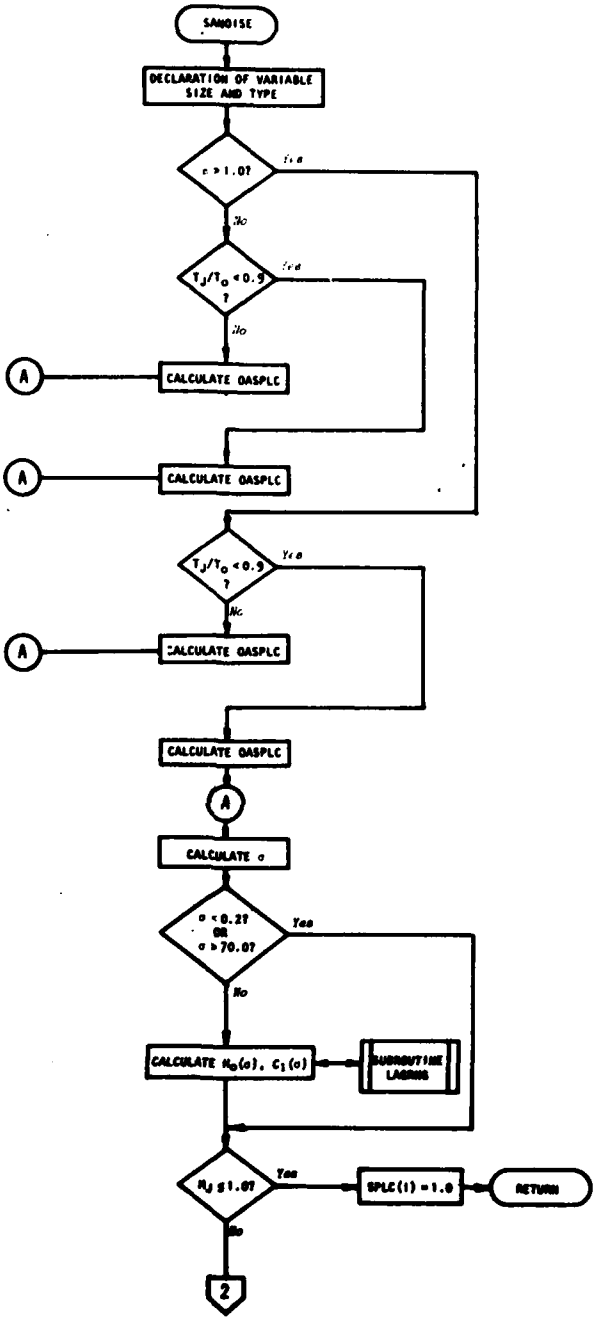

Figure 6.4 Flow Chart for Subroutine SANOISE.

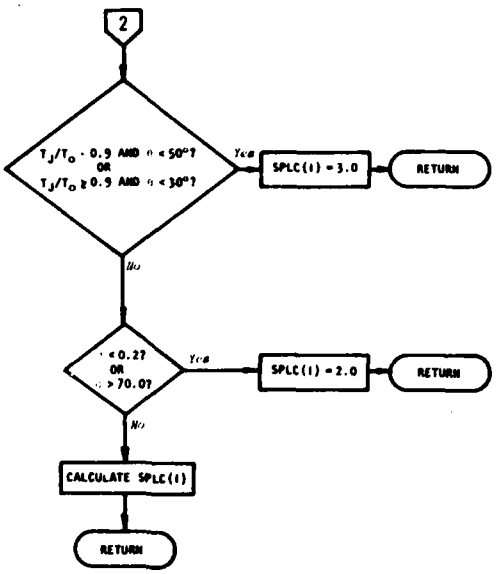

Figure 6.4 Concluded.

```
2.00        12.00
   1     0     7    30
90.0
   8
0.70        1.10        1.31        0.2316
   7     1     2     0     1     1
  41
14.20       70.0        28.20       1130.0
  86.7  88.4  88.7  90.2  92.5  94.5  96.9  99.3 100.2 102.1 103.3 105.2
 105.9 107.5 107.7 108.4 109.4 111.2 112.1 111.0 109.8 108.8 108.0 107.5
```

Figure 6.5 Input Data for Sample Case.

DATE 09/20/78 TIME 14.31.14

LARGE SCALE NOISE FAILURES ARE INDICATED BY THE FOLLOWING

SPLA=1.0 STABILITY CALCULATIONS FAILED TO CONVERGE
SPLA=2.0 LARGE SCALE NOISE AT THIS JET VELOCITY IS NEGLECTED
SPLA=3.0 LARGE SCALE NOISE AT THIS ANGLE IS NEGLECTED
SPLA=4.0 LARGE SCALE NOISE AT THIS FREQUENCY IS NEGLECTED
SPLA=5.0 SEARCH FOR STARTING VALUES GIVES SINGULAR MATRIX

TURBULENT MIXING NOISE (SOPNO 1) FAILURES ARE INDICATED BY THE FOLLOWING

SPLB=1.0 VELOCITY PROFILE GRADIENT IS NOT AVAILABLE
SPLB=2.0 S_M IS OUTSIDE THE RANGE OF SOURCE DATA
SPLB=3.0 SOURCE DIRECTIVITY EXPRESSION IS LESS THAN ZERO
SPLB=4.0 NUMBER OF ITERATIONS EXCEEDS 50
SPLB=5.0 S_M GOES NEGATIVE IN ITERATION ROUTINE
SPLB=6.0 ARGUMENT X IN DECAY FACTOR IS NEGATIVE
SPLB=7.0 RADIATION ANGLE IS LESS THAN 30.0 DEGREES
SPLB=8.0 TURBULENT MIXING NOISE AT THIS ANGLE AND JET VELOCITY IS NEGLECTED

TURBULENT MIXING NOISE (SOPNO 2) FAILURES ARE INDICATED BY THE FOLLOWING

SPLB=2.0 S_M IS OUTSIDE THE RANGE OF SOURCE DATA
SPLB=3.0 SOURCE DIRECTIVITY EXPRESSION IS LESS THAN ZERO
SPLB=4.0 NUMBER OF ITERATIONS EXCEEDS 50
SPLB=5.0 S_M GOES NEGATIVE IN ITERATION ROUTINE
SPLB=8.0 TURBULENT MIXING NOISE AT THIS ANGLE AND JET VELOCITY IS NEGLECTED
SPLB=9.0 CRITICAL LAYER RADIUS TOO SMALL
SPLB=10.0 BESSEL FUNCTION FAILURE
SPLB=11.0 SOURCE AND CRITICAL LAYER RADIUS COINCIDE

SHOCK ASSOCIATED NOISE FAILURES ARE INDICATED BY THE FOLLOWING

SPLC=1.0 M_J IS LESS THAN 1.0
SPLC=2.0 SIGMA IS OUTSIDE THE RANGE OF MASTER SPECTRA
SPLC=3.0 SHOCK NOISE CONTRIBUTION AT THIS ANGLE AND JET TEMPERATURE CAN BE (AND IS) NEGLECTED

Figure 6.6 Output from Sample Case.

MIXING NOISE SOURCE AND MEAN FLOW CONSTANTS

* STANDARD DATA VALUES USED *

SM	.032	.040	.050	.063	.080	.100	.125	.160	.200	.250	.316	.400	.500	.630
SPLO	70.50	73.50	75.50	78.00	79.90	81.50	83.10	84.60	86.20	87.70	89.00	90.00	90.70	91.30
AXWTO	7.00	5.00	4.00	3.00	3.00	2.30	1.50	1.00	1.00	1.20	1.20	1.00	.90	.70
SPLO	82.00	84.40	86.60	88.80	91.00	93.10	95.20	97.00	98.30	99.40	100.10	100.60	101.00	101.10
AXWTO	15.00	10.00	10.00	7.50	6.00	4.50	3.00	1.70	1.30	1.00	.80	.60	.30	.20
VS/VJ	.32	.36	.40	.44	.47	.50	.52	.54	.56	.57	.58	.59	.59	.60
VC/VJ	1.00	1.00	1.00	1.00	1.00	1.00	1.00	1.00	.90	.80	.73	.68	.65	.63
VMAX/VJ	.32	.36	.40	.46	.52	.58	.65	.74	.82	.90	.96	1.00	1.00	1.00
DELTA/RJ	.10	.08	.06	.05	.04	.03	.13	.26	.48	.66	.81	.84	.83	.76
DELTA/RJ	.81	.72	.70	.61	.60	.73	.81	.90	1.03	1.15	1.21	1.19	1.15	1.08
DELTA/RJ	2.01	1.75	1.59	1.41	1.23	1.24	1.35	1.39	1.51	1.59	1.61	1.55	1.43	1.29
DELTA/RJ	2.52	2.23	2.04	1.82	1.79	1.81	1.91	1.89	1.99	2.04	2.01	1.87	1.72	1.52
S	.80	1.00	1.25	1.60	2.00	2.50	3.16	4.00	5.00	6.30	8.00	10.00	12.50	16.00
SPLO	91.80	92.10	92.10	92.00	91.90	91.70	91.40	90.80	90.30	89.70	89.20	88.60	88.10	87.50
AXWTO	.60	.30	.10	0.00	-.15	-.25	-.40	-.40	-.50	-.55	-.60	-.65	-.70	-.70
SPLO	101.00	100.60	100.00	99.30	98.50	97.60	96.60	95.80	94.90	94.00	93.00	92.00	91.00	90.00
AXWTO	0.00	-.15	-.20	-.30	-.30	-.40	-.40	-.50	-.55	-.60	-.62	-.62	-.65	-.70
VS/VJ	.60	.60	.60	.60	.60	.60	.60	.60	.60	.60	.60	.60	.60	.60
VC/VJ	.60	.60	.60	.60	.60	.60	.60	.60	.60	.60	.60	.60	.60	.60
VMAX/VJ	1.00	1.00	1.00	1.00	1.00	1.00	1.00	1.00	1.00	1.00	1.00	1.00	1.00	1.00
DELTA/RJ	.70	.60	.52	.43	.37	.31	.25	.21	.17	.14	.11	.09	.08	.06
DELTA/RJ	.94	.81	.69	.58	.48	.40	.33	.27	.23	.19	.15	.12	.10	.08
DELTA/RJ	1.13	.97	.84	.70	.59	.50	.41	.34	.28	.23	.19	.15	.13	.10
DELTA/RJ	1.31	1.15	.98	.82	.68	.57	.47	.38	.32	.26	.22	.18	.14	.12

Figure 6.6 Continued.

***** UNIFIED JET NOISE PREDICTION *****

TEST POINT 41

OPTION NUMBER 7

RESERVOIR PRESSURE = 28.20 PSI, ATMOSPHERIC PRESSURE = 14.20 PSI
RESERVOIR TEMPERATURE = 1130.0 DEG.F, CHAMBER TEMPERATURE = 70.0 DEG.F
GAMMA = 1.35

PRESSURE RATIO PR/P0 = 2.986
TEMPERATURE RATIO TR/T0 = 3.000
JET STATIC TEMPERATURE RATIO TJ/T0 = 2.262
JET DENSITY RATIO DJ/D0 = .442
JET VELOCITY RATIO VJ/A0 = 2.036
JET MACH NUMBER MJ = 1.370
JET VELOCITY VJ = 2299.0 FPS

NOZZLE DIAMETER = 2.00 INCHES
MICROPHONE DISTANCE = 12.00 FEET
R/D = 72.00

SHOCK ASSOCIATED NOISE PARAMETERS

C = .70 K0 = 1.10 K1 = 1.31
NUMBER OF SHOCKS NS = 8

BETA = .936
EDDY CONVECTION VELOCITY VC = 1609.3 FPS
EDDY CONVECTION MACH NUMBER MC = 1.425
AVERAGE SHOCK CELL LENGTH L0 = 2.059 INCHES
FIRST SHOCK CELL LENGTH L1 = 2.452 INCHES

Figure 6.6 Continued.

NOISE FROM LARGE-SCALE TURBULENCE STRUCTURE

OBSERVER ANGLE = 90.00 DEGREES

FREQ(HZ)	SPLA(DB)	SPLM(DB)	DIFF	SUM
200.0	4.0	86.7	******	0.0
250.0	4.0	88.4	******	0.0
315.0	4.0	88.7	******	0.0
400.0	4.0	90.2	******	0.0
500.0	4.0	92.5	******	0.0
630.0	4.0	94.5	******	0.0
800.0	4.0	96.9	******	0.0
1000.0	4.0	99.3	******	0.0
1250.0	4.0	100.2	******	0.0
1600.0	3.0	102.1	******	0.0
2000.0	3.0	103.3	******	0.0
2500.0	3.0	105.2	******	0.0
3150.0	3.0	105.9	******	0.0
4000.0	3.0	107.5	******	0.0
5000.0	3.0	107.7	******	0.0
6300.0	3.0	108.4	******	0.0
8000.0	4.0	109.4	******	0.0
10000.0	4.0	111.2	******	0.0
12500.0	4.0	112.1	******	0.0
16000.0	4.0	111.0	******	0.0
20000.0	4.0	109.6	******	0.0
25000.0	4.0	108.8	******	0.0
31500.0	4.0	108.0	******	0.0
40000.0	4.0	107.5	******	0.0

STANDARD DEVIATION = 0.00

Figure 6.6 Continued.

TURBULENT MIXING NOISE (MOPNO = 1)

*** ALTERNATIVE AXIAL SOURCE LOCATION MODEL UTILIZED ***

OBSERVER ANGLE = 90.00 DEGREES

FREQ(HZ)	FD/V	S*	SPLPO(DB)	SPLPD(DB)	SPLR(DB)	SPLM(DB)	DIFF	SUM
200.0	.014	.024	0.0	0.0	2.0	86.7	******	0.0
250.0	.018	.031	0.0	0.0	2.0	88.4	******	0.0
315.0	.022	.039	83.3	83.5	86.4	88.7	-2.3	5.2
400.0	.029	.047	85.7	85.9	88.8	90.2	-1.4	7.2
500.0	.036	.058	87.9	88.1	91.0	92.5	-1.5	9.4
630.0	.045	.071	90.0	90.3	93.2	94.5	-1.3	11.1
800.0	.057	.088	91.7	92.6	95.2	96.9	-1.7	14.0
1000.0	.072	.108	93.1	94.7	97.0	99.3	-2.3	19.2
1250.0	.090	.133	94.5	96.8	98.5	100.2	-1.4	21.2
1600.0	.115	.167	96.0	98.8	100.6	102.1	-1.5	23.3
2000.0	.145	.204	97.5	100.3	102.2	103.3	-1.1	24.6
2500.0	.181	.249	99.0	101.7	103.5	105.2	-1.7	27.5
3150.0	.228	.304	100.2	102.6	104.6	105.9	-1.3	29.2
4000.0	.290	.384	101.2	103.3	105.4	107.5	-2.1	33.5
5000.0	.362	.475	101.9	103.9	106.0	107.7	-1.7	36.3
6300.0	.457	.597	102.5	104.2	106.5	108.4	-1.9	40.0
8000.0	.580	.743	103.1	104.3	106.8	109.4	-2.6	47.0
10000.0	.725	.922	103.5	104.1	106.8	111.2	-4.4	66.0
12500.0	.906	1.144	103.7	103.7	106.7	112.1	-5.4	95.0
16000.0	1.160	1.453	103.7	103.2	106.4	111.0	-4.6	116.0
20000.0	1.450	1.804	103.6	102.5	106.1	109.8	-3.7	129.5
25000.0	1.812	2.244	103.5	101.8	105.8	108.8	-3.0	138.8
31500.0	2.283	2.813	103.3	100.9	105.3	108.0	-2.7	146.0
40000.0	2.900	3.557	102.9	100.1	104.8	107.5	-2.7	153.6

STANDARD DEVIATION = 2.64

Figure 6.6 Continued.

SHOCK ASSOCIATED NOISE

OBSERVER ANGLE = 90.00 DEGREES

FREQ(HZ)	SIGMA	H0(DB)	C1	ANS3(DB)	ANS2(DB)	SPLC(DB)	SPLM(DB)	DIFF	SUM
200.0	.19	0.0	0.00	0.0	0.0	2.0	86.7	******	0.0
250.0	.24	118.4	.71	-13.0	4.2	71.3	88.4	-17.1	293.6
315.0	.30	121.6	.71	-12.0	4.2	75.5	88.7	-13.2	467.0
400.0	.38	124.5	.71	-10.9	4.1	79.7	90.2	-10.5	576.8
500.0	.48	127.5	.71	-10.0	4.1	83.2	92.5	-9.3	642.4
630.0	.60	130.4	.72	-9.0	3.9	87.0	94.5	-7.5	717.9
800.0	.76	133.7	.72	-7.9	3.7	91.2	96.9	-5.7	750.2
1000.0	.95	137.0	.73	-7.0	3.4	95.1	99.3	-4.2	767.8
1250.0	1.19	139.9	.74	-6.0	2.8	98.3	100.2	-1.9	771.3
1600.0	1.53	142.9	.74	-4.9	1.7	101.4	102.1	-.7	771.8
2000.0	1.91	145.2	.74	-4.0	.3	103.2	103.3	-.1	771.8
2500.0	2.39	147.0	.73	-3.0	-1.7	104.1	105.2	-1.1	773.1
3150.0	3.01	148.5	.71	-2.0	-4.0	104.2	105.9	-1.7	776.0
4000.0	3.82	149.2	.68	-.9	-6.5	103.4	107.5	-4.1	792.4
5000.0	4.77	148.9	.63	.0	-7.3	103.4	107.7	-4.3	811.3
6300.0	6.01	147.9	.58	1.0	-4.1	106.5	108.4	-1.9	815.0
8000.0	7.64	146.1	.51	2.1	.2	110.0	109.4	.6	815.4
10000.0	9.54	144.1	.46	3.0	1.6	110.4	111.2	-.8	815.9
12500.0	11.93	142.3	.41	4.0	.4	108.4	112.1	-3.7	829.4
16000.0	15.27	140.1	.35	5.1	-.4	106.5	111.0	-4.5	849.6
20000.0	19.09	137.8	.29	6.0	-.1	105.5	109.8	-4.3	868.0
25000.0	23.86	135.9	.24	7.0	.2	104.8	108.8	-4.0	884.2
31500.0	30.06	133.5	.19	8.0	-.1	103.2	108.0	-4.8	907.3
40000.0	38.19	131.0	.13	9.1	.0	101.8	107.5	-5.7	939.7

STANDARD DEVIATION = 6.39

Figure 6.6 Continued.

TOTAL NOISE

OBSERVER ANGLE = 90.00 DEGREES

FREQ(HZ)	SPLA(DB)	SPLB(DB)	SPLC(DB)	SPLT(DB)	SPLM(DB)	DIFF	SUM
200.0	4.0	2.0	2.0	7.5	86.7	******	0.0
250.0	4.0	2.0	71.3	71.3	88.4	******	0.0
315.0	4.0	86.4	75.5	86.8	88.7	-1.9	0.0
400.0	4.0	88.8	79.7	89.3	90.2	-.9	0.0
500.0	4.0	91.0	83.2	91.7	92.5	-.8	0.0
630.0	4.0	93.2	87.0	94.1	94.5	-.4	0.0
800.0	4.0	95.2	91.2	96.7	96.9	-.2	0.0
1000.0	4.0	97.0	95.1	99.2	99.3	-.1	0.0
1250.0	4.0	98.8	98.3	101.6	100.2	1.4	0.0
1600.0	3.0	100.6	101.4	104.0	102.1	1.9	0.0
2000.0	3.0	102.2	103.2	105.7	103.3	2.4	0.0
2500.0	3.0	103.5	104.1	106.8	105.2	1.6	0.0
3150.0	3.0	104.6	104.2	107.4	105.9	1.5	0.0
4000.0	3.0	105.4	103.4	107.6	107.5	.1	0.0
5000.0	3.0	106.0	103.4	107.9	107.7	.2	0.0
6300.0	3.0	106.5	106.5	109.5	108.4	1.1	0.0
8000.0	4.0	106.8	110.0	111.7	109.4	2.3	0.0
10000.0	4.0	106.8	110.4	112.0	111.2	.8	0.0
12500.0	4.0	106.7	108.4	110.7	112.1	-1.4	0.0
16000.0	4.0	106.4	106.5	109.5	111.0	-1.5	0.0
20000.0	4.0	106.1	105.5	109.8	109.8	-1.0	0.0
25000.0	4.0	105.8	104.8	108.3	108.8	-.5	0.0
31500.0	4.0	105.3	103.2	107.4	108.0	-.6	0.0
40000.0	4.0	104.8	101.8	106.5	107.5	-1.0	0.0

STANDARD DEVIATION = 1.3

Figure 6.6 Concluded.

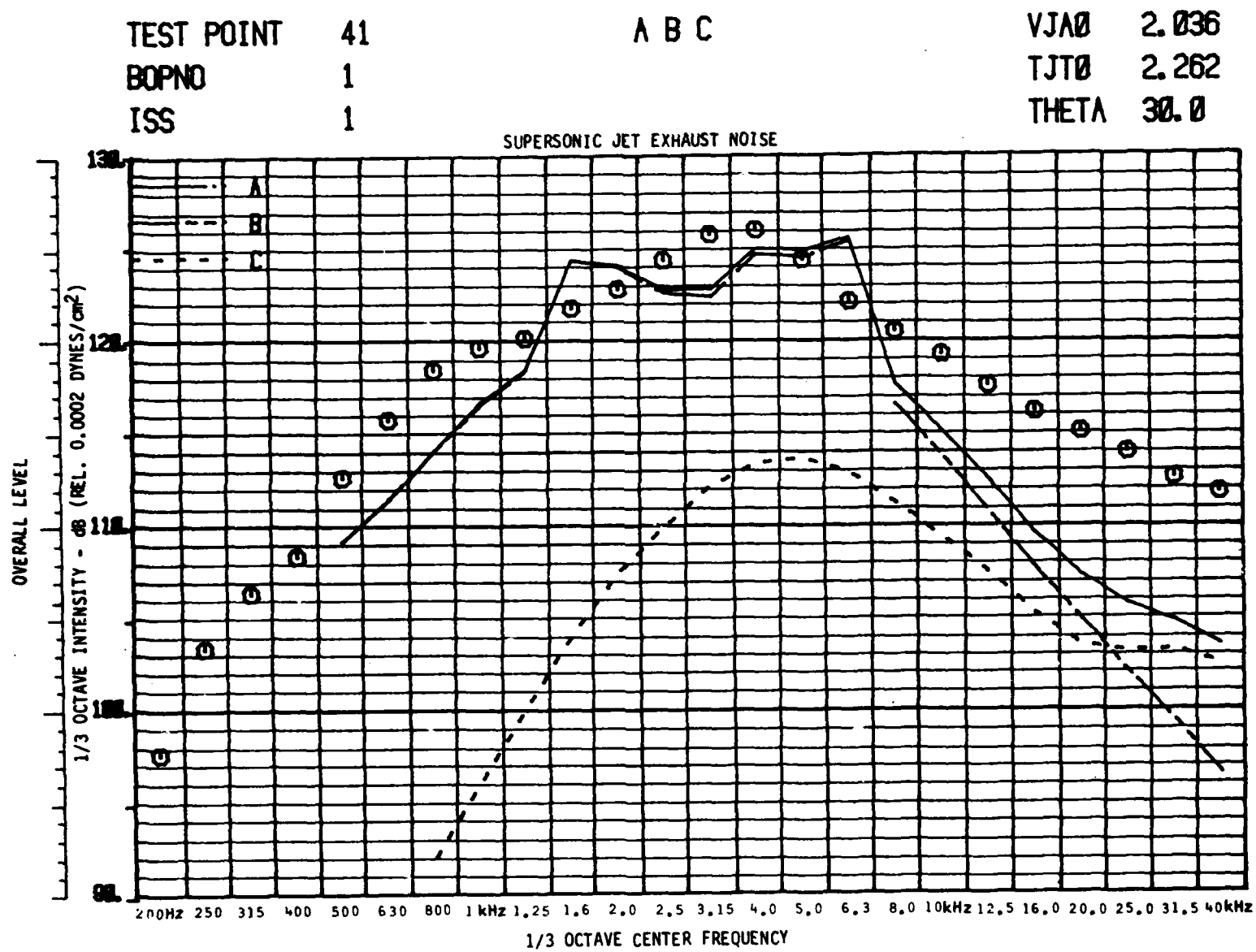

Figure 6.7 Comparison Between Measured and Predicted Spectra: $\theta = 30°$.

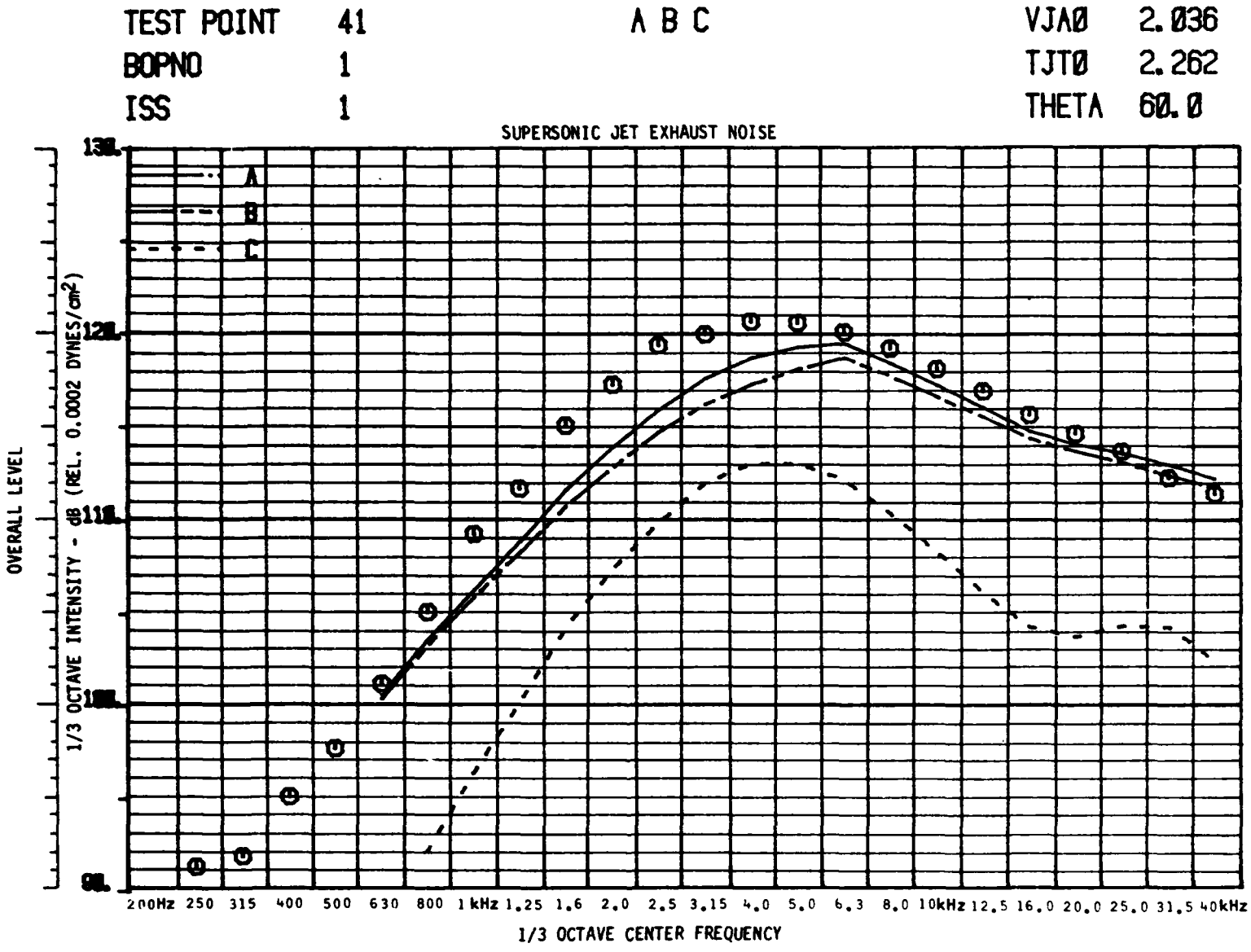

Figure 6.8 Comparison Between Measured and Predicted Spectra: $\theta = 60°$.

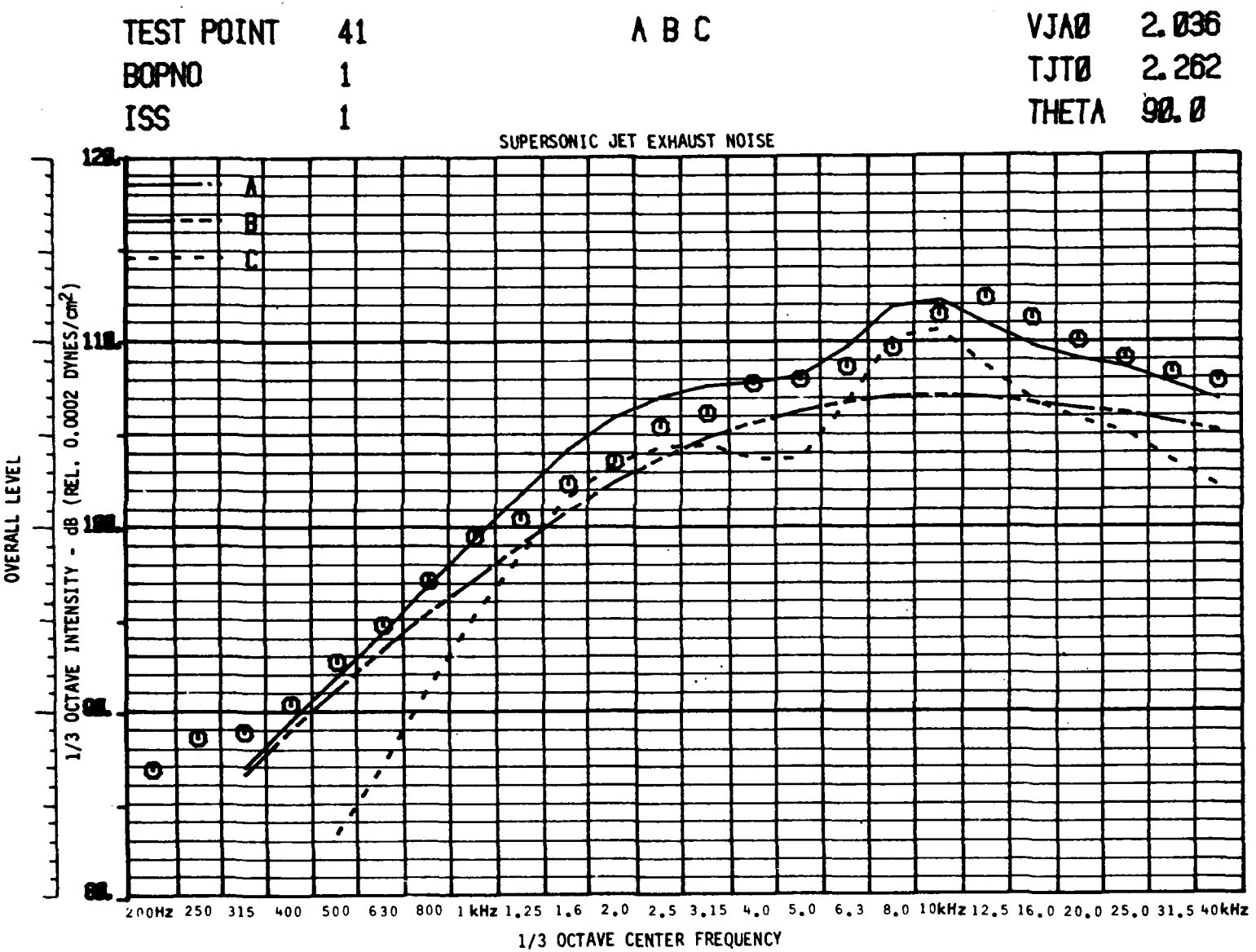

Figure 6.9 Comparison Between Measured and Predicted Spectra: $\theta = 90°$.

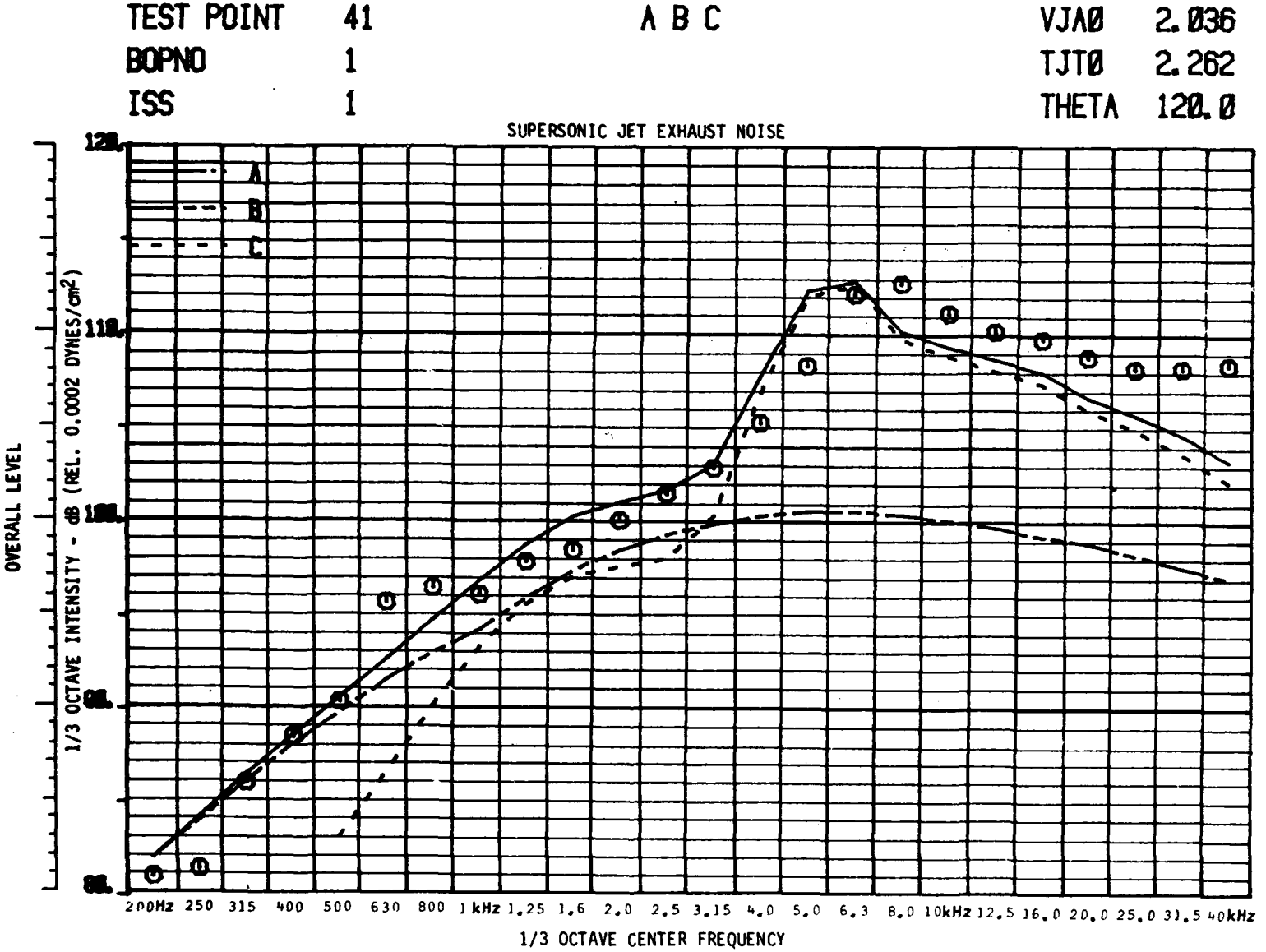

Figure 6.10 Comparison Between Measured and Predicted Spectra: $\theta = 120°$.

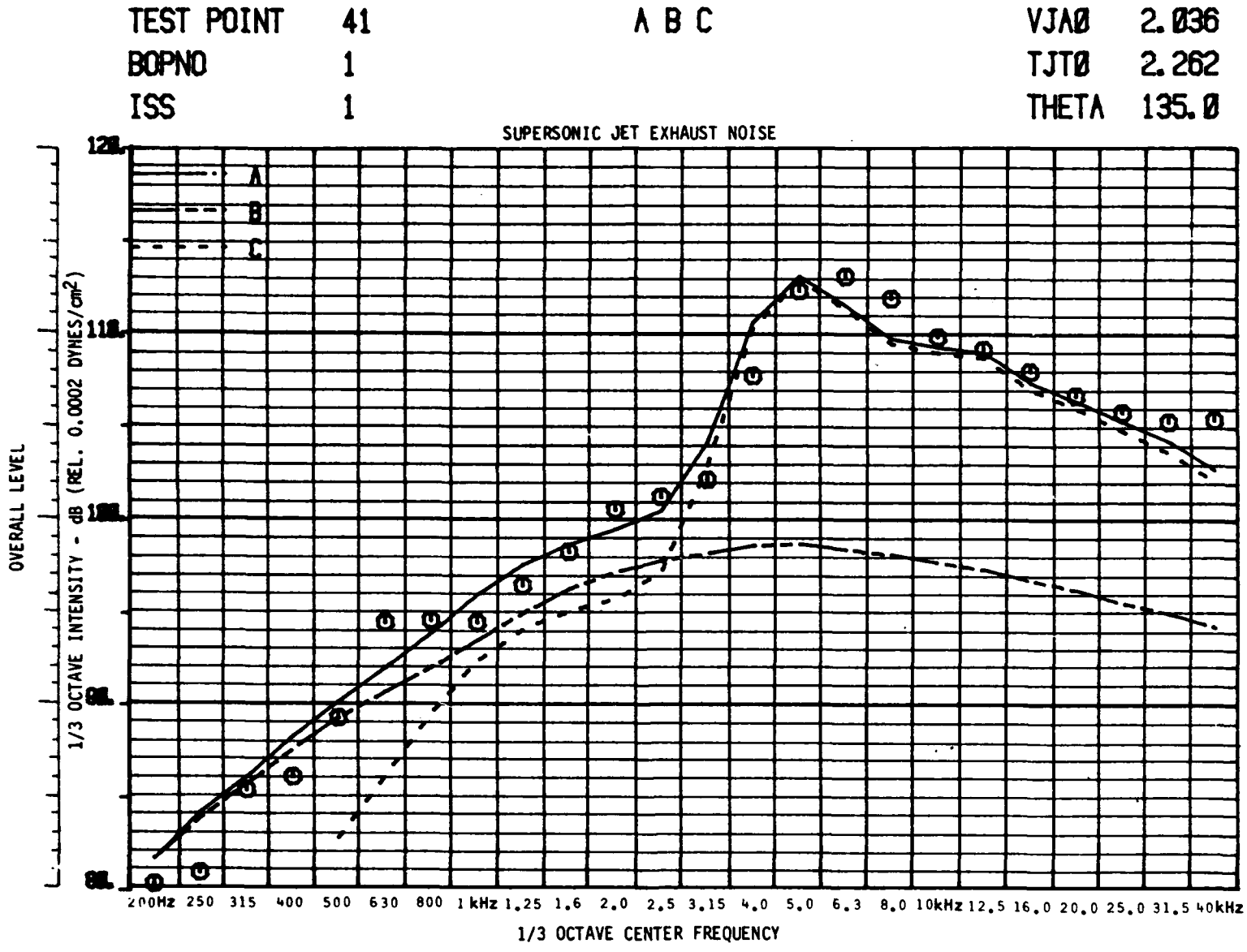

Figure 6.11 Comparison Between Measured and Predicted Spectra: $\theta = 135°$.

6.6.1 Input Requirements

The input parameters and their format, required to run the absolute jet noise level prediction program INTEG, are described below.

(1)

RUNNO
F15.1

RUNNO - Run number.

(2)

FREQ(I), I = 1, 24							
F10.1	F10.1						F10.1

FREQ - One-third octave center frequencies, 7 - 30 (see Table 6.1).

(3)

TP
F15.1

TP - Test point number (TP < 1 terminates execution).

(4)

SPLM(I), I = 1, 24											
F6.1	F6.1										F6.1

SPLM - User's measured 1/3-octave SPL data for comparison with predictions at center frequencies 7-30 (see Table 6.1). These data are not actually utilized in the program described in this report and are only required in an alternative in-house program written especially to generate comparison plots.

(5)

IOUT
I1

IOUT - Print option for integrand output.
IOUT = 0 no tabulated integrand output
≠ 0 tabulated integrand output.

(6)

INTFLG
I1

INTFLG - Indicator for source correlation function model.
INTFLG ≠ 1 Gaussian model
= 1 Exponential-Gaussian model.

MJ

(7) F15.1

MJ - Jet exit Mach number (V_J/a_J).

VJF

(8) F15.1

VJF - Jet exit velocity (V_J) in ft/sec.

XC

(9) F15.1

XC - Effective potential core length factor ($x_{c,eff}/x_c$).
(XC = 2 in calculations of Section 2.4).

TOF

(10) F15.1

TOF - Ambient temperature (T_o) in °F.

K

(11) E10.4

K - Time constant factor.
(K = 1.0 in calculations of Section 2.4.)

A1

(12) F15.1

A1 - Axial length scale coefficient (a_1) - $L_x = a_1 x + b_1$.
($x_{limit} < x \leq x_{c,eff}$)

B1

(13) F15.1

B1 - Axial length scale constant (b_1) in inches.
($x_{limit} < x \leq x_{c,eff}$)

C1

(14) F15.1

C1 - Radial integral constant (c) for upstream integral
($0 \leq x \leq x_{c,eff}$).

(15) A2 E10.4

A2 - Axial length scale coefficient (a_2) - $L_x = (a_2 x + b_2)^{d_2}$ ($x_{c,eff} \leq x \leq \infty$).

(16) B2 E10.4

B2 - Axial length scale constant (b_2) in inches ($x_{c,eff} \leq x \leq \infty$).

(17) C2 F15.1

C2 - Radial integral constant (c) for downstream integral ($x_{c,eff} \leq x \leq \infty$).

(18) D2 E10.4

D2 - Axial length scale parameter (d_2). (D2 = 1.0 in calculations of Section 2.4.) ($x_{c,eff} \leq x \leq \infty$)

(19) A3 E10.4

A3 - Transverse length scale coefficient - $L_t = a_3 x + b_3$ ($x_{limit} < x \leq \infty$).

(20) B3 E10.4

B3 - Transverse length scale constant in inches ($x_{limit} < x \leq \infty$).

(21) A4 E10.4

A4 - Axial length scale coefficient (a_4) - $L_x = a_4 x$ ("Initial Region," $0 \leq x \leq x_{limit}$).

(22) A5 E10.4

A5 - Transverse length scale coefficient (a_5) - $L_t = a_5 x$ ("Initial Region," $0 \leq x \leq x_{limit}$).

XLIMIT

(23) E10.4

XLIMIT - Axial position (x_{limit}) in inches at which $L_x = a_4x$, $L_t = a_5x$ changes to $L_x = a_1x + b_1$, $L_t = a_3x + b_3$.

RJ

(24) F15.1

RJ - Nozzle radius (r_j) in inches.

R

(25) F15.1

R - Observer distance from nozzle exit plane in inches (assumed equal to radiation distance, R_r).

PAMB

(26) E10.4

PAMB - Ambient pressure (P_o) in psia.

6.6.2 INTEG Routines

FCT - Calculates upstream integrand for either the Gaussian or the Exponential-Gaussian model.

FCD - Calculates downstream integrand for either the Gaussian or the Exponential-Gaussian model (integration variable is inverse of axial coordinate).

FQA6 - Calculates modified upstream integrand for the Gaussian model (integration variable is scaled axial coordinate).

QA6 - Six-point generalized Gaussian-Laguerre integration routine.†

DQG32 - Thirty-two point Gauss quadrature integration routine.†

†*IBM System/360 Scientific Subroutine.*

6.6.3 INTEG Flow Chart

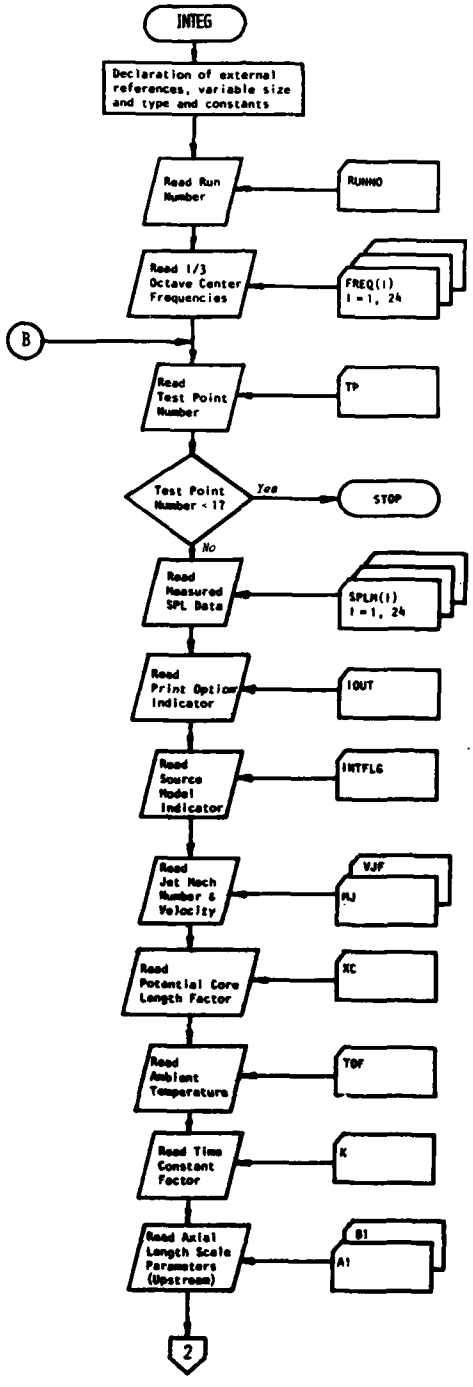

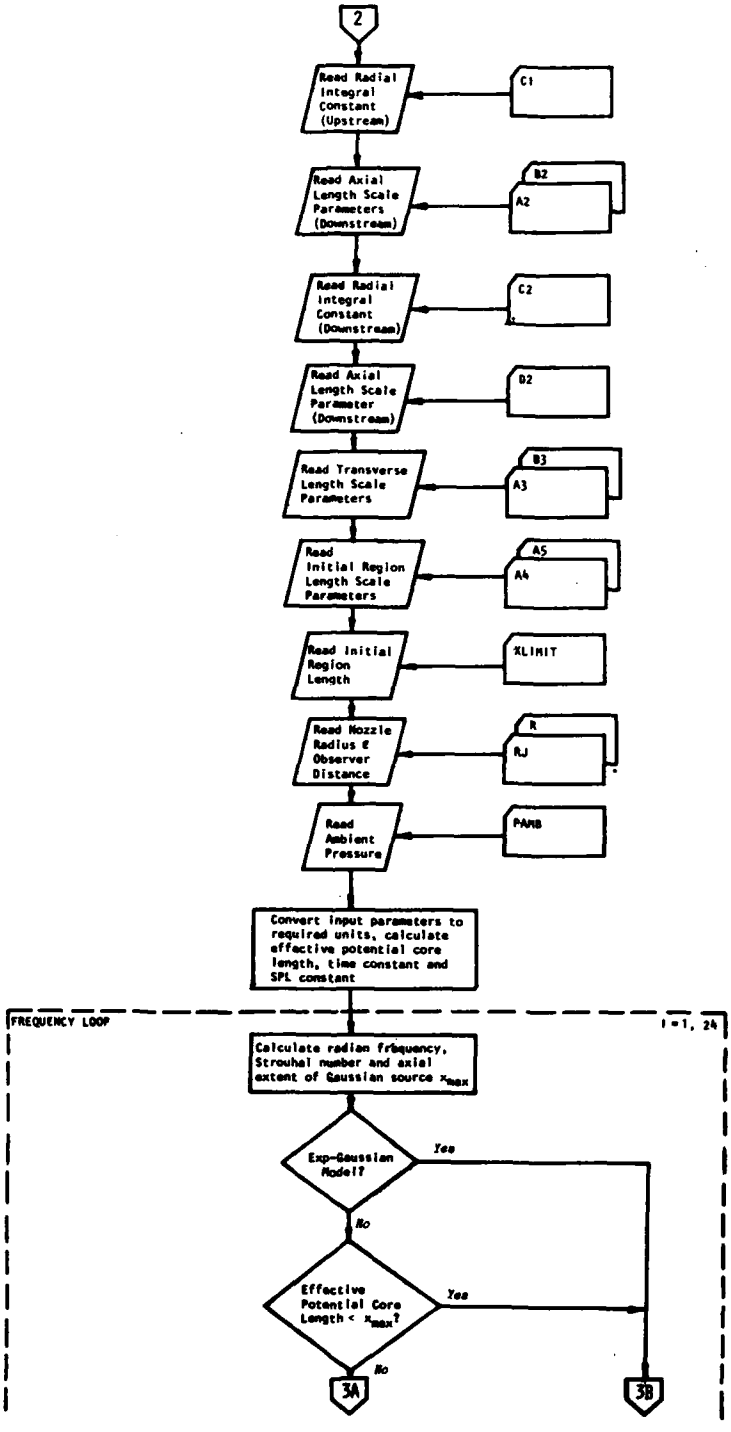
2
Read Radial Integral Constant (Upstream)
C1
Read Axial Length Scale Parameters (Downstream)
B2
A2
Read Radial Integral Constant (Downstream)
C2
Read Axial Length Scale Parameter (Downstream)
D2
Read Transverse Length Scale Parameters
B3
A3
Read Initial Region Length Scale Parameters
A5
A4
Read Initial Region Length
XLIMIT
Read Nozzle Radius & Observer Distance
R
RJ
Read Ambient Pressure
PAMB
Convert input parameters to required units, calculate effective potential core length, time constant and SPL constant
FREQUENCY LOOP
I = 1, 24
Calculate radian frequency, Strouhal number and axial extent of Gaussian source x_{max}
Exp-Gaussian Model?
Yes
No
Effective Potential Core Length < x_{max}?
Yes
No
3A
3B

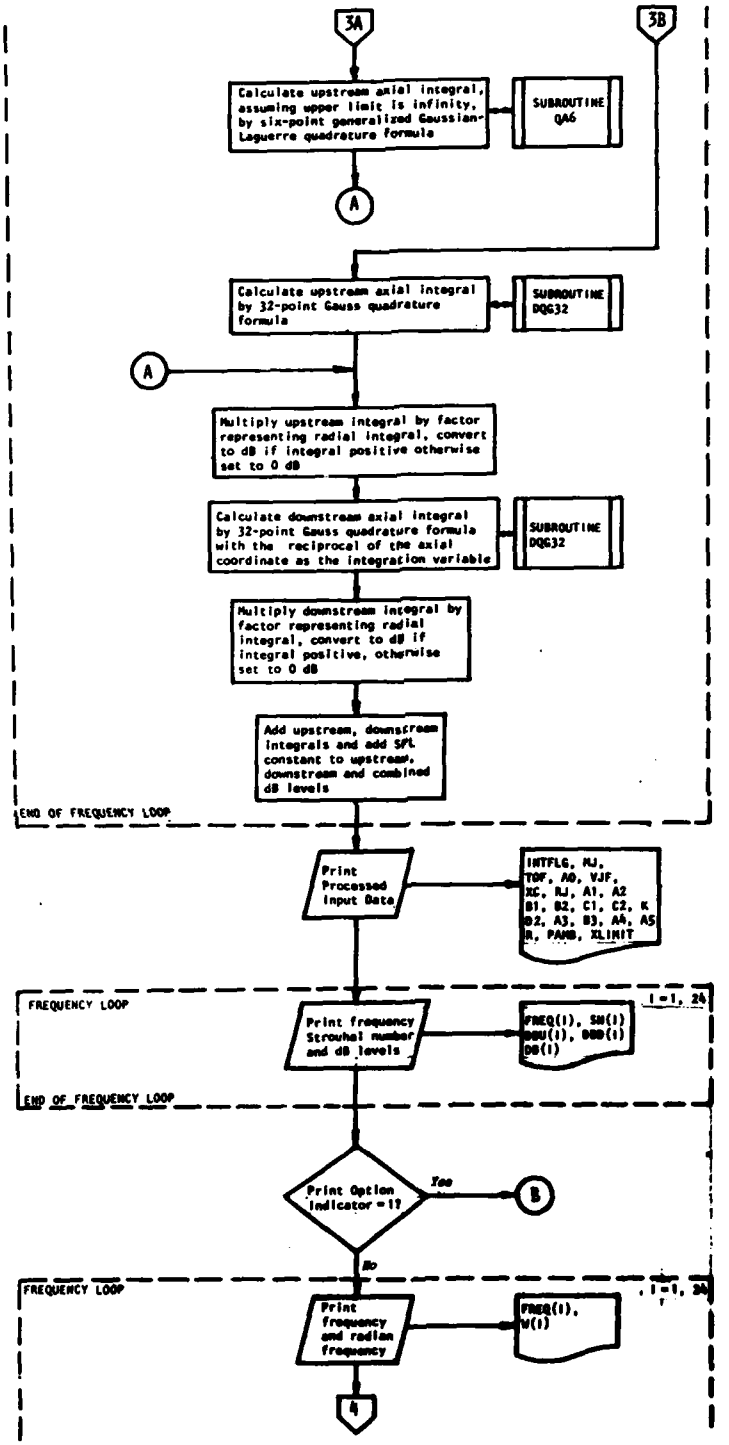
3A
3B
Calculate upstream axial integral, assuming upper limit is infinity, by six-point generalized Gaussian-Laguerre quadrature formula
SUBROUTINE QA6
A
Calculate upstream axial integral by 32-point Gauss quadrature formula
SUBROUTINE DQG32
A
Multiply upstream integral by factor representing radial integral, convert to dB if integral positive otherwise set to 0 dB
Calculate downstream axial integral by 32-point Gauss quadrature formula with the reciprocal of the axial coordinate as the integration variable
SUBROUTINE DQG32
Multiply downstream integral by factor representing radial integral, convert to dB if integral positive, otherwise set to 0 dB
Add upstream, downstream integrals and add SPL constant to upstream, downstream and combined dB levels
END OF FREQUENCY LOOP
Print Processed Input Data
INTFLG, MJ, TOF, A0, VJF, XC, RJ, A1, A2 B1, B2, C1, C2, K B2, A3, B3, AA, AS B, PAMB, XLIMIT
FREQUENCY LOOP
I=1, 24
Print frequency Strouhal number and dB levels
FREQ(I), SN(I) OSU(I), OBB(I) DB(I)
END OF FREQUENCY LOOP
Print Option Indicator = 1?
Yes
B
No
FREQUENCY LOOP
I=1, 24
Print frequency and radian frequency
FREQ(I), W(I)
4

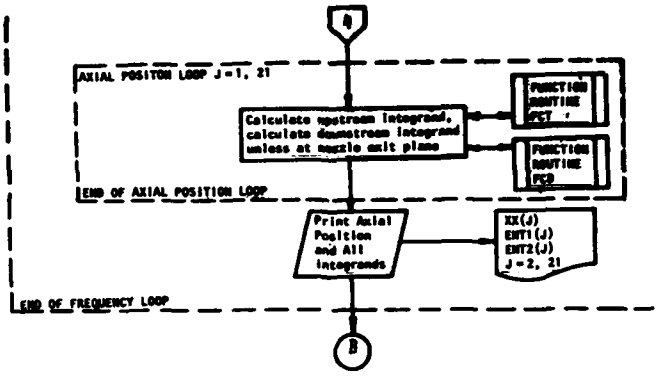
A
AXIAL POSITION LOOP J = 1, 21
Calculate upstream integrand, calculate downstream integrand unless at nozzle exit plane
FUNCTION SUBROUTINE FCT
FUNCTION SUBROUTINE FCT
END OF AXIAL POSITION LOOP
Print Axial Position and All Integrands
XX(J)
ENT1(J)
ENT2(J)
J = 2, 21
END OF FREQUENCY LOOP
B

APPENDIX 2A

MEAN FLOW PROFILES USED IN THE LILLEY EQUATION (NUMERIC AND HIGH-FREQUENCY SOLUTIONS)

Two mean velocity profile shapes are used, one for the "initial mixing" region, extending to approximately seven diameters or nearly two potential core lengths from the jet exit plane, and the other for the downstream "fully developed" region. The mean, static temperature profile is obtained directly from the velocity profile by assuming similarly between the *stagnation* temperature and velocity profiles.

These profiles are not meant to be precise descriptions of the jet mean flow field but are believed to be sufficiently realistic for the purposes of calculating acoustic-mean flow interaction effects on jet mixing noise (with Lilley equation solutions).

First, the two mean velocity profiles are given as a function of the shear layer vorticity thickness, δ, and this parameter is then related to the distance downstream from the jet exit plane, x. The static temperature profile is then given and finally assumptions concerning values assigned to the ratio of specific heats, γ, are noted and the method of calculating γ is specified.

2A.1 MEAN VELOCITY PROFILES

Initial mixing region (typically $0 \leq x/d \leq 7$)

$$\frac{V(r)}{V_J} \equiv \phi(r) = 0.5 \{1 - \text{erf } (\sqrt{\pi}\chi)\}^{\dagger} \tag{2A-1}$$

where

$$\chi = (r - r_J)/\delta - .1676 \tag{2A-2}$$

and δ lies in the range

$$0 \leq \delta/r_J \leq 1.819 \tag{2A-3}$$

Fully developed region

$$\frac{V(r)}{V_{max}} \equiv \phi(r) = \exp \{-(r/\delta)^2 (e/2)\} \tag{2A-4}$$

---

†*The error function is calculated with the rational approximation 7.1.27 of reference* [2.19].

Relations Between Shear Layer Thickness and Distance from Nozzle

In the initial mixing region the spreading rate $d\delta/dx$ is assumed constant and equal to 0.1313†, corresponding to a spreading parameter $\sigma = 13.5$ ($d\delta/dx = \sqrt{\pi}/\sigma$). Hence, where required in this section, the following relation is used between x and δ:

$$\frac{x}{d} = \frac{\sigma}{2\sqrt{\pi}} \frac{\delta}{r_J} = 3.808 \frac{\delta}{r_J} \tag{2A-7}$$

or

$$\frac{\delta}{r_J} = 0.2626 \frac{x}{d} . \tag{2A-8}$$

It follows from Equation (2A-7) and (2A-3) that the cross-over occurs at the axial position

$$\frac{x}{d} = 6.926 \tag{2A-9}$$

with the spreading rate value adopted above. This cross-over point corresponds closely to the point at which the spreading rate changes abruptly in Figure 4 of a recent paper by Morris [2.23].

In the fully developed region the spreading rate is assinged a smaller value deduced from Test Case #18 of reference 24 ($d\delta/dx = 0.08233$) which is also consistent with the results of Figure 4, reference [2.23]. The relation between shear layer thickness and axial position is therefore

$$\frac{x}{d} = 6.073 \frac{\delta}{r_J} - 4.119 \tag{2A-10}$$

or

$$\frac{\delta}{r_J} = 0.1647 \frac{x}{d} + 0.6782 . \tag{2A-11}$$

---

†*This value falls roughly in the middle of the band of measured values shown in Figure 5.6 and corresponds closely to the jet condition* $V_J/a_O = 0.9$, $T_J/T_O \doteq 1$.

where V_{max}, the centerline velocity, is given in Table 2A.1 and δ lies in the range

$$1.819 < \delta/r_J \leq \infty \qquad (2A\text{-}5)$$

Discussion

The constant in Equation (2A-2) fixes the value of ϕ on the lipline ($r = r_J$) and from previous work [2.13] this had been determined from measured data to be $\phi(r_J) = 0.6630$, thus requiring the constant to take the value -.1676. The "cross-over" from the initial mixing to fully developed profile was chosen by requiring the profiles to match at the lipline (since this is generally associated with the noise source region, or close ot it). The radius $r_{0.6630}$ at which the fully developed profile takes the value $\phi = 0.6630$ is related to the vorticity thickness by

$$r_{0.6630} = \delta/1.819 \qquad (2A\text{-}6)$$

It follows that the initial mixing profile applies if $\delta \leq 1.819\ r_J$, but the fully developed applies if $\delta > 1.819\ r_J$ as specified above by (2A-3) and (2A-5).

S_m	x_s/d	V_{max}/V_J	S_m	x_s/d	V_{max}/V_J
0.0316	23.4	0.32	0.8	4.1	1.0
0.04	20.8	0.36	1.0	3.6	↓
0.05	18.6	0.40	1.25	3.1	
0.063	16.5	0.46	1.6	2.6	
0.08	14.6	0.52	2.0	2.2	
0.1	13.0	0.58	2.5	1.9	
0.125	11.6	0.65	3.16	1.6	
0.16	10.2	0.74	4.0	1.3	
0.2	9.0	0.82	5.0	1.1	
0.25	8.0	0.90	6.3	1.0	
0.316	7.1	0.96	8.0	0.7	
0.4	6.2	1.00	10.0	0.6	
0.5	5.4	1.0	12.5	0.5	
0.63	4.8	1.0	16.0	0.4	

Table 2A.1 Centerline velocity V_{max} variation with axial position x_s, as assumed for acoustic-mean flow interaction calculations (obtained from Witze [2.22] with $\rho_J/\rho_o = 1$ and $M_J = 0.7$)

Profile Gradient

In practice it is not necessary to use the velocity profiles given above when calculating the high-frequency solutions to Lilley's equation, the one exception being the profile *gradient* $d\phi/d\chi$ (at the transition radius $r = r_T$) which follows directly from Equation (2A-1) as

$$\frac{d\phi}{d\chi} = - \exp\left[-\pi\chi^2\right] . \qquad (2A\text{-}12)$$

This radial derivative (or the corresponding derivative of the fully developed profile) is also required in the evaluation of *numerical* dipole and quadrupole solutions. In addition, higher-order derivatives are required to evaluate the mean velocity in the complex plane *via* a Taylor expansion and these are expressed as Hermite polynomials – for both types of profile – as discussed in reference [2.13] and evaluated by a simple recurrence formula.

2A.2 TEMPERATURE PROFILE (BOTH REGIONS)

The static temperature profile is calculated from

$$\frac{T(r)}{T_o} = 1 + \left(\frac{T_i}{T_o} - 1\right)\phi(r) + \frac{\gamma - 1}{2}\left(\frac{V_{max}}{a_o}\right)^2\left(\phi(r) - \phi^2(r)\right) \qquad (2A\text{-}13)$$

where T_i is the centerline (static) temperature, T_o is the ambient temperature, $\phi(r)$ is the velocity profile given by Equation (2A-1) or (2A-4), γ is the ratio of specific heats and V_{max} is the centerline velocity, so that $V_{max} = V_J$ if Equation (2A-1) applies (initial mixing region). Equation (2A-13) is based upon the assumption that the stagnation temperature and velocity profiles across the shear layer are similar.

For prediction purposes T_i is obtained indirectly from the empirical relation derived by Szewczyk [2.11] (based on measured data taken from Corrsin et al. [2.25]) which gives the "source-region" temperature T_s, associated with a particular modified Strouhal number, S_m, in terms of the *maximum* source region temperature $T_{s_{max}}$:

$$\frac{T_s}{T_o}(S_m) = 1 + \frac{(T_s/T_o)_{max} - 1}{\{0.98 + 0.073\ S_m^{-2}\}^{0.25}} \qquad (2A\text{-}14)$$

where, from Equation (2A-13) with $\phi(r) = V_s/V_J = 0.6$, $V_{max} = V_J$ and $T_i = T_J$, the maximum value is given by

$$\left(\frac{T_s}{T_o}\right)_{max} = 1 + \left(\frac{T_J}{T_o} - 1\right)\ 0.6 + \frac{\gamma - 1}{2}\left(\frac{V_J}{a_o}\right)^2 (0.6 - 0.6^2). \qquad (2A\text{-}15)$$

The *source region* temperature is all that is required by the high-frequency solutions to Lilley's equation, but in order to compute the temperature at any radius in the shear layer for the *numerical* solutions, the centerline temperature is calculated from T_s/T_o with the inverse of Equation (2A-13), viz.,

$$\frac{T_i}{T_o} = 1 - \frac{\gamma - 1}{2}\left(\frac{V_{max}}{a_o}\right)^2 + \left|\frac{T_s}{T_o} - 1 + \frac{\gamma - 1}{2}\left(\frac{V_{max}}{a_o}\right)^2\left(\frac{V_s}{V_{max}}\right)^2\right| \Big/ \left(\frac{V_s}{V_{max}}\right) \qquad (2A\text{-}16)$$

and then Equation (2A-13) is used for all temperature calculations at that (modified) Strouhal number.

In Equation (2A-15), $\gamma = 1.4$ is used but once T_s is obtained from Equation (2A-14) and when acoustic-mean flow interactions are calculated either in the high-frequency limit or numerically, the source region value, γ_s, is used, which is calculated from T_s with the empirical formula [2.11]

$$\gamma_s = 1.421 - (T_s/11800.0) + \exp\{-|T_s - 450|/200.0\}/80.0$$

$$(T_s > 290°K)$$

$$= 1.402 \quad (T_s \leq 290°K) \qquad (2A\text{-}17)$$

APPENDIX 2B
LIST OF SYMBOLS

$\bar{a}$	sound speed
a_J, a_i	sound speed in potential core, on centerline downstream
a_s, a_o	sound speed in source region, ambient medium
a_ℓ, b_ℓ	coefficients defining L_t/r_J
C	Green function coefficient
C_q, C_d	quadrupole, dipole anisotropy coefficients
c	radial integral constant $(0.8326/\eta_{hw})^2$
D	Doppler factor $1 - V\cos\theta_o/a_o$
D_c, D_s	Doppler factor value for $V = V_c$, V_s
D_m	modified Doppler factor
d	jet nozzle diameter
F	flow factor
f	frequency
f_α	components of equivalent force per unit mass
I_q, I_d	quadrupole, dipole master spectra
j	$(-1)^{\frac{1}{2}}$
k_o	acoustic wavenumber in ambient medium, ω/a_o
k_x	axial wavenumber ($k_x = k_o\cos\theta_o$ in calculations)
L	Lilley equation differential operator
L_x, L_t	axial, transverse coherence length scales
M_o	velocity ratio, $V(r)/a_o$
M_J	jet Mach number, V_J/a_J
M_c	V_c/a_o
N_∞	decay or shielding factor inside cone of silence

n	azimuthal mode number
P	power spectral density of acoustic pressure
p	pressure; transverse noncompactness temperature exponent
p_o, p_i	independent solutions of homogeneous Lilley equation
Q, Q_e	source distributions
q	axial noncompactness temperature exponent
R_r	radiation distance
R_m	observer (or measurement) distance from nozzle center
r	(cylindrical) radial coordinate
r_J	jet nozzle radius
$r_{\frac{1}{2}}$	radius of half-velocity point
S_m	modified Strouhal number, SD_m
S	Strouhal number, fd/V_J
T	static temperature (absolute); averaging time
T_J, T_j	jet exit temperature, centerline temperature
T_s, T_o	temperature in source region, ambient medium
t	time
V	axial velocity of mean flow
V_J, V_{max}	jet exit velocity, centerline velocity
V_c	convection velocity
V_s	source region flow velocity
v_j, v_α	components of velocity fluctuation
x_j	Cartesian coordinates
x	axial coordinate
x_c	potential core length
$x_{c,eff}$	effective potential core length
x_s	source location distance downstream from nozzle exit plane

α, β	transverse, axial noncompactness parameters
α_o, β_o	values of α,β under isothermal conditions ($T_s/T_o = 1$)
γ	specific heat ratio
γ_s, γ_o	specific heat ratio in source region, ambient medium
δ	shear layer vorticity thickness, $(V_J$ or $V_{max})/\lvert dV/dr\rvert_{max}$
ε_c	convection velocity ratio, V_c/V_J
ε_s	source-region flow velocity ratio, V_s/V_J
η	similarity coordinate for r.m.s. turbulence radial distribution model, $(r - r_J)/x_s$
η_s	position of r.m.s. turbulence radial peak
η_{hw}	half-width of r.m.s. turbulence radial distribution
θ_o, θ_s	polar angle of radiation (wavenormal direction) in source region, ambient medium
θ_m	observer (or measurement) polar angle
κ	dimensionless radial wavenumber
κ_J, κ_j	centerline value of κ
κ_s, κ_o	value of κ in source region, ambient medium
ρ	density of fluid
$\bar{\rho}$	mean density of fluid
ρ_J, ρ_j	mean density of fluid on centerline
ρ_s, ρ_o	mean density of fluid in source region, ambient medium
σ	shear layer spreading parameter
τ	time delay
τ_o	time scale
$\phi^{(2)}_{\alpha\beta}$	power spectrum of square of turbulent velocity cross-correlation function
ϕ, ϕ_o	(cylindrical) azimuthal coordinate in source region, far-field; mean flow profile, $V/V_{max} \equiv \phi$
χ	similarity coordinate for flow profile in initial mixing region $(r - r_{\frac{1}{2}})/\delta_s$

ω	radian frequency
ω'	convected frame frequency
ω_m	modified frequency, ωD_m

Subscripts

i,j, ...	denote Cartesian coordinate directions (i = 1, 2, 3)
i	centerline value, downstream of potential core
J	jet exit value
m, d, q	monopole, dipole, quadrupole
s	source region
T	value at transition radius, $r = r_T$
α,β, ...	denote cylindrical coordinate directions ($\alpha = x, r, \phi$)
o	ambient region

Functions

erf	error function
$H_n^{(2)}$	Hankel function of the second kind
I_n	modified Bessel function
J_n	Bessel function
$W(Z_1,Z_2)$	Wronskian $Z_1Z_2' - Z_1'Z_2$
δ	Dirac delta function

APPENDIX 3A

The coefficients, B_j, in Equations (3.21) are given by:

$$B_1 = -2i\beta[M^2 U \hat{\beta} + k] \tag{3A.1}$$

$$B_2 = \frac{2i\beta^2}{\hat{\beta}^2}\frac{dU}{d\eta} \tag{3A.2}$$

$$B_3 = i\,(M^2 U^2 - 1)\beta \tag{3A.3}$$

$$B_4 = \frac{2iU\,\beta^2}{\hat{\beta}^3}\frac{dU}{d\eta} \tag{3A.4}$$

$$B_5 = i\left|k(1 - M^2U^2) + kM_o^2\left[U\frac{dV}{d\eta} - V\frac{dU}{d\eta}\right] + \frac{2k^3V}{\hat{\beta}^2}\frac{dU}{d\eta} - \frac{2k^2(kU - \hat{\beta})}{\hat{\beta}^2}\frac{dV}{d\eta}\right| \tag{3A.5}$$

and

$$B_6 = i\left|\frac{2k^2U}{\hat{\beta}^3}\frac{dU}{d\eta}\frac{dV}{d\eta} + 2\eta[k + M^2U\hat{\beta}] - 2M^2V\hat{\beta} - \frac{2k^3V}{\hat{\beta}^3}\left(\frac{dU}{d\eta}\right)^2 - \frac{2\beta^2}{\hat{\beta}^3}\frac{dU}{d\eta}\right| \tag{3A.6}$$

The functions of h_1 and h_2 in Equation (3.23) are given by

$$h_1 = 2\{k\hat{\zeta} + M^2U\hat{\beta}\hat{\zeta} - \frac{\beta}{\hat{\beta}^2}\frac{dU}{d\eta}\frac{\partial\hat{\zeta}}{\partial\eta}\} \tag{3A.7}$$

and

$$h_2 = 2\,\{\frac{k}{\hat{\beta}^2}\frac{dU}{d\eta}\frac{\partial\hat{\zeta}}{\partial\eta} - 2M^2\,\hat{\beta}\hat{\zeta}\} \tag{3A.8}$$

APPENDIX 3B

The integrals I_1 and I_2 in Equation (3-95) may be written,

$$I_1 = \int_0^\infty \left| B_1\hat{\zeta} + B_2 \frac{\partial\hat{\zeta}}{\partial r} \right| \frac{\hat{\zeta}r}{\Omega^2 R_o} \, dr \tag{3B-1}$$

and $$I_2 = \int_0^\infty \left[B_1 \frac{\partial\hat{\zeta}}{\partial s} + B_2 \frac{\partial^2\hat{\zeta}}{\partial r \partial s} + B_3\hat{\zeta} + B_4 \frac{\partial\hat{\zeta}}{\partial r} \right] \frac{\hat{\zeta}r}{\Omega^2 R_o} \, dr \tag{3B-2}$$

where

$$B_1 = -2i\,(M^2 U R_o \Omega - \alpha) \tag{3B-3}$$

$$B_2 = \frac{2i\omega}{\Omega^2} \frac{\partial U}{\partial r} \tag{3B-4}$$

$$\begin{aligned} B_3 = i[M^2U^2R_o - 1] \frac{d\alpha}{ds} + i \Bigg| & M^2\alpha R_o \left(U \frac{\partial U}{\partial s} - V \frac{\partial U}{\partial r} \right) - 2M^2\Omega R_o \frac{\partial V}{\partial r} \\ & + \frac{2\alpha V}{\Omega^2} \frac{\partial U}{\partial r} \frac{m^2}{r^2} - \frac{2\alpha^2}{\Omega} \frac{\partial U}{\partial s} + \frac{2\alpha^3}{\Omega^2} V \frac{\partial U}{\partial r} + \frac{2\alpha^2}{\Omega} \frac{\partial V}{\partial r} - \frac{2V}{\Omega} \frac{m^2}{r^3} \\ & + \frac{2}{\Omega} \frac{\partial V}{\partial r} \frac{m^2}{r^2} + \frac{\alpha}{R_o} \frac{\partial R_o}{\partial s} - \gamma M^2 \bar{\Delta} \Omega R_o \Bigg|, \end{aligned} \tag{3B-5}$$

$$\begin{aligned} B_4 = \frac{2i\omega U}{\Omega^3} \frac{\partial U}{\partial r} \frac{d\alpha}{ds} + i \Bigg| & \frac{2\alpha(2\omega - \alpha U)}{\Omega^3} \frac{\partial U}{\partial r} \frac{\partial U}{\partial s} - 2M^2 R_o V \Omega \\ & + \frac{1}{\Omega} \frac{\partial^2 U}{\partial r \partial s} - \frac{2\alpha V}{\Omega^2} \frac{\partial U}{\partial r} \frac{1}{r} - \frac{2\alpha^2 V}{\Omega^3} \left(\frac{\partial U}{\partial r} \right)^2 - \frac{2\omega}{\Omega^2 R_o} \frac{\partial R_o}{\partial s} \frac{\partial U}{\partial r} \\ & + \frac{1}{\Omega} \left[\frac{\partial^2 V}{\partial r^2} - \frac{1}{r} \frac{\partial V}{\partial r} + \frac{V}{r^2} \right] \Bigg|, \end{aligned} \tag{3B-6}$$

$$\Omega = \omega - \alpha U, \tag{3B-7}$$

and $$\bar{\Delta} = \frac{\partial U}{\partial s} + \frac{1}{r} \frac{\partial Vr}{\partial r}. \tag{3B-8}$$

The integrals I_3 and I_4 in Equation (3-149) may be written,

$$I_3 = \int_0^\infty \left[2(\alpha + M^2\Omega R_o U)\hat{\zeta} - \frac{2\omega}{\Omega^2}\frac{\partial U}{\partial r}\frac{\partial \hat{\zeta}}{\partial r} \right] \frac{\hat{\zeta} r}{\Omega^2 R_o}\, dr, \tag{3B-9}$$

and $$I_4 = \int_0^\infty \left| \left[\frac{1}{R_o}\frac{\partial^2 R_o}{\partial r \partial s} - \frac{1}{R_o^2}\frac{\partial R_o}{\partial r}\frac{\partial R_o}{\partial s} - \frac{2}{\Omega}\frac{\partial^2 U}{\partial r \partial s} - \frac{2\alpha^2}{\Omega^2}\frac{\partial U}{\partial r}\frac{\partial U}{\partial s} \right] \frac{\partial \hat{\zeta}}{\partial r} \right.$$

$$\left. - \left[2M^2\Omega^2 \frac{\partial R_o}{\partial s} - 2M^2\alpha\Omega R_o \frac{\partial U}{\partial s} \right] \hat{\zeta} \right| \frac{\hat{\zeta} r}{\Omega^2 R_o}\, dr. \tag{3B-10}$$

APPENDIX 3C

Equation (3-107) is of the form

$$\bar{\chi}_1 = \left| C_1 + \frac{C_2}{r} + C_3 \right| H_m^{(1)}(\lambda r) + \left| C_4 r + C_5 + \frac{C_6}{r^2} \right| H_m^{(1)'}(\lambda r), \qquad (3C\text{-}1)$$

where the C_i are all independent of r. The expression for $\hat{\rho}_1(r,s)$ in the region $r > r_m$ is given by Equation (3-106a).

$$\hat{\rho}_1(r,s) = D_1 H_m^{(1)}(\lambda r) - \frac{i\pi}{4} H_m^{(1)}(\lambda r) \int^r H_m^{(2)}(\lambda t)\bar{\chi}_1(t,s)\, dt$$

$r > r_m$

$$- \frac{i\pi}{4} H_m^{(2)}(\lambda r) \int_r^\infty H_m^{(1)}(\lambda t)\chi_1(t,s)\, dt \qquad (3C\text{-}2)$$

It is necessary to evaluate the two integral terms in Equation (3C-2) in order to determine $\hat{\rho}_1(r,s)$. Substitution of Equation (3C-1) for $\bar{\chi}_1$ into Equation (3C-2) leads to twelve separate integrals. These integrals have no exact solution so it will be assumed that r_m is sufficiently large that the asymptotic forms of the Hankel functions and their derivatives may be used, i.e.

$$H_m^{(1)}(z) \simeq \sqrt{\frac{2}{\pi z}}\, e^{i\chi}, \qquad (3C\text{-}3)$$

$$H_m^{(2)}(z) \simeq \sqrt{\frac{2}{\pi z}}\, e^{-i\chi}, \qquad (3C\text{-}4)$$

$$H_m^{(1)'}(z) \simeq \sqrt{\frac{2}{\pi z}} \left| 1 - \frac{(\mu+3)}{8z} \right| e^{i\chi}, \qquad (3C\text{-}5)$$

and

$$H_m^{(2)'}(z) \simeq \sqrt{\frac{2}{\pi z}} \left| -1 - \frac{(\mu+3)}{8z} \right| e^{-i\chi}, \qquad (3C\text{-}6)$$

where

$$\chi = z - \frac{m}{2} - \frac{\pi}{4}$$

and $\mu = 4m^2$. (See Abramowitz [3.51], *Handbook of Mathematical Functions*.)

The following integrals have been evaluated:

$$\int^{r} H_m^{(2)}(\lambda t)\, H_m^{(1)}(\lambda t)\, t\,dt \simeq \frac{2r}{\pi\lambda}, \tag{3C-7}$$

$$\int^{r} H_m^{(2)}(\lambda t)\, H_m^{(1)}(\lambda t)\, dt \simeq \frac{2}{\pi\lambda}\, \ell n(r), \tag{3C-8}$$

$$\int^{r} H_m^{(2)}(\lambda t)\, H_m^{(1)}(\lambda t)\, \frac{dt}{t^2} \simeq -\frac{1}{\pi\lambda r^2}, \tag{3C-9}$$

$$\int^{r} H_m^{(2)}(\lambda t)\, H_m^{(1)\prime}(\lambda t)\, t^2 dt \simeq \frac{r}{\pi\lambda}\left| ir - \frac{(\mu+3)}{4\lambda}\right| \tag{3C-10}$$

$$\int^{r} H_m^{(2)}(\lambda t)\, H_m^{(1)\prime}(\lambda t)\, t\,dt \simeq \frac{2}{\pi\lambda^2}\left|i\lambda r - \frac{(\mu+3)}{8}\, \ell n(r)\right|, \tag{3C-11}$$

$$\int^{r} H_m^{(2)}(\lambda t)\, H_m^{(1)\prime}(\lambda t)\, \frac{dt}{t} \simeq -\frac{1}{\pi\lambda r}\left| 2i + \frac{(\mu+3)}{8\lambda r}\right|, \tag{3C-12}$$

$$\int_{r}^{\infty} [H_m^{(1)}(\lambda t)]^2\, t\,dt \simeq -\frac{i}{\pi\lambda^2}\, e^{2i\chi}, \tag{3C-13}$$

$$\int_{r}^{\infty} [H_m^{(1)}(\lambda t)]^2\, dt \simeq -\frac{2}{\pi\lambda}\, Ei\{2i\lambda r\} e^{-i\pi\,(m+\frac{1}{2})}, \tag{3C-14}$$

$$\int_{r}^{\infty} [H_m^{(1)}(\lambda t)]^2\, \frac{dt}{t^2} \simeq \frac{e^{2i\chi}}{\pi r}\left|\frac{1}{\lambda r} + 2i\right| + \frac{4\lambda}{\pi}\, Ei\{2i\lambda r\} e^{-i\pi\,(m+\frac{1}{2})}, \tag{3C-15}$$

$$\int_{r}^{\infty} H_m^{(1)}(\lambda t)\, H_m^{(1)\prime}(\lambda t)\, t^2 dt \simeq -\frac{2e^{2i\chi}}{\pi\lambda^3}\left|\frac{\chi}{2} + \frac{1}{4} + \frac{(\mu+3)i}{16} + \frac{\pi}{4}\,(m+\tfrac{1}{2})\right|, \tag{3C-16}$$

$$\int_{r}^{\infty} H_m^{(1)}(\lambda t)\, H_m^{(1)\prime}(\lambda t)\, t\,dt \simeq -\frac{e^{2i\chi}}{\pi\lambda^2} + \frac{(\mu+3)}{4\pi\lambda^2}\, Ei\{2i\lambda r\} e^{-i\pi\,(m+\frac{1}{2})}, \tag{3C-17}$$

and $\int_r^\infty H_m^{(1)}(\lambda t)\, H_m^{(1)'}(\lambda t)\, \frac{dt}{t^2} \simeq \left|\frac{2i}{\pi r}\left[\frac{1}{2\lambda r} + 1\right] - \frac{(\mu+3)}{4\pi r}\right.$

$$\left.\left[\frac{1}{3\lambda^2 r^2} + \frac{i}{3\lambda r} - \frac{2}{3}\right]\right| e^{2ix} + \frac{i\lambda}{\pi}\left[3 - \frac{\mu}{3}\right] \mathrm{Ei}\{2i\lambda r\} e^{-i\pi\,(m+\frac{1}{2})}, \qquad (3C\text{-}18)$$

where Ei{az} is the exponential integral given by

$$\mathrm{Ei}\{az\} = \int_{-\infty}^{z} \frac{e^{az}}{z}\, dz\,. \qquad (3C\text{-}19)$$

Note as $\mathrm{Re}\{az\} \to -\infty$, $\mathrm{Ei}\{az\} \to 0$.

Making use of the integrals given by Equations (3C-17) through (3C-18) and noting that as $r \to \infty$

$$\mathrm{Ei}\{2i\lambda r\} e^{-i\pi\,(m+\frac{1}{2})} \simeq -i\,\frac{e^{2ix}}{2\lambda r}, \qquad (3C\text{-}20)$$

the Equation (3C-2) for $\hat{p}_1(r,s)$ finally becomes

$$\hat{p}_1(r,s) \simeq \left| D_1 - \frac{iC_1 r}{2\lambda} - \frac{iC_2}{2\lambda}\ln(\lambda r) + \frac{iC_3}{4\lambda r^2} + C_4\left[\frac{r^2}{4\lambda} + i\,\frac{(\mu+3)r}{16\lambda^2}\right]\right.$$

$$+ C_5\left[\frac{r}{2\lambda} + i\,\frac{(\mu+3)}{16\lambda^2}\ln(\lambda r)\right] - C_6\left[\frac{1}{2\lambda r} - \frac{i(\mu+3)}{32\lambda^2 r^2}\right]$$

$$- \frac{C_1}{4\lambda^2} - \frac{C_3}{r}\left[\frac{1}{4\lambda r} - \frac{1}{2}\right] + \frac{iC_4}{2\lambda^2}\left[r + \frac{1}{4\lambda}\right] + i\,C_4\,\frac{(\mu+3)}{32\lambda^3}$$

$$+ i\,\frac{C_5}{4\lambda^2} + \frac{C_6}{2r}\left[\frac{1}{2\lambda r} + 1\right] + i\,C_6\,\frac{(\mu+3)}{16r}\left[\frac{1}{3\lambda^2 r^2} + \frac{i}{3\lambda r} - \frac{2}{3}\right]$$

$$\left. + \frac{1}{8\lambda r}\left[\frac{2C_2}{\lambda} - 4\,C_3\lambda - \frac{(\mu+3)}{4\lambda^2}C_5 - \frac{i\lambda}{\pi}C_6\left(3 - \frac{\mu}{3}\right)\right]\right|$$

$$\times \sqrt{\frac{2}{\pi\lambda r}}\, e^{ix}\,. \qquad (3C\text{-}21)$$

As $r \to \infty$ the equation behaves like

$$\hat{p}_1(r,s) \underset{r\to\infty}{\sim} K_1 r^2 H_m^{(1)}(\lambda r), \tag{3C-22}$$

where $$K_1 = \frac{C_4}{4\lambda} = \frac{i\alpha^2}{2\lambda^2}\frac{d\alpha}{ds} A ,$$

which is a function of s alone.

APPENDIX 3D

The mean flow integral equations lead to the following expressions for the variation of jet half-width, b, and centerline velocity, u_c, downstream of the potential core

(a) $M = 0$, $T_J = 1$ (incompressible, isothermal)

$$b = \sqrt{2a}/u_c, \tag{3D-1}$$

$$\frac{db}{dx} = 3aK/b, \tag{3D-2}$$

$$\frac{du_c}{dx} = -\frac{u_c}{b}\frac{db}{dx}, \tag{3D-3}$$

(b) $M = 0$, $T_J \neq 1$ (incompressible, non-isothermal)

$$b^2 = -\frac{a(1-T_J)^2}{T_J}\left|(1-T_J)u_c + \ell n\left|1-(1-T_J)u_c\right|\right|^{-1}, \tag{3D-4}$$

$$\frac{db}{dx} = \frac{aKu_c{}^3\rho^{.5}(1-T_J)}{2}\left|\frac{u_c{}^2}{2} + u_c\frac{(1-u_c)}{(1-T_J)}\right.$$

$$\left. + \frac{1-u_c(1-T_J)}{(1-T_J)^2}\ \ell n\left|1-(1-T_J)u_c\right|\right|^{-1}, \tag{3D-5}$$

$$\frac{du_c}{dx} = -\frac{2a(1-(1-T_J)u_c)}{b^3u_c\,T_J}\frac{db}{dx}, \tag{3D-6}$$

(c) $M \neq 0$ (compressible)

$$b^2 = -\frac{2aA}{T_J}\left|\ell n\left|Au_c{}^2+Bu_c-1\right| - \frac{B}{k}\ell n\left|\frac{(2Au_c+B-k)}{(2Au_c+B+k)}\frac{(B+k)}{(B-k)}\right|\right|^{-1}, \tag{3D-7}$$

$$\frac{db}{dx} = \frac{aKu_c{}^3\rho^{.5}}{2}\left|\frac{u_c}{A} - \frac{(B+Au_c)}{2A^2}\ \ell n\left|Au_c{}^2+Bu_c-1\right|\right.$$

$$\left. + \frac{(B^2+2A+ABu_c)}{2A^2k}\cdot\ell n\left|\frac{(2Au_c+B-k)}{(2Au_c+B+k)}\frac{(B+k)}{(B-k)}\right|\right|^{-1}, \tag{3D-8}$$

$$\frac{du_c}{dx} = 2a \frac{(Au_c^2 + Bu_c - 1)}{u_c b^3 T_J} \frac{db}{dx}, \tag{3D-9}$$

where

$$a = 0.693147, \tag{3D-10}$$

$$A = (\gamma - 1) M^2/2, \tag{3D-11}$$

$$B = (1 - T_J - A), \tag{3D-12}$$

and

$$k = (B^2 + 4A)^{\frac{1}{2}}. \tag{3D-13}$$

APPENDIX 3E

NEAR-FIELD AZIMUTHAL CROSS-CORRELATION EXPERIMENTS

In this Appendix a brief description is provided of a series of azimuthal cross-correlation experiments in the near field of an axisymmetric jet. The aim of the experiments was to determine which azimuthal modes dominated the near field. It was argued that the near-field fluctuations in pressure would be dominated by the large-scale turbulent motions. The arguments justifying this hypothesis are given by Liu [3.19] and Morris [3.11]. The original purpose of the experiment was to determine the absolute initial amplitudes of the pressure fluctuations associated with jet instabilities of different mode numbers. However, because of the good agreement between the entire near-field predictions and experiments, described in Section 3.3.4.3, the calibration of the absolute levels associated with the jet instabilities was based on the comparison of far-field measured and predicted sound pressure levels. This calibration process was described in Section 3.4. However, the experiments demonstrated how the near-field pressures were dominated by low azimuthal mode numbers and also indicated that the noise radiation at small angles to the jet axis differs in character to that at high angles.

The tests were conducted in the Lockheed-Georgia anechoic facility using a 2.1 inch diameter convergent nozzle. Since the time needed to perform the correlations was fairly lengthy, it was decided to operate the nozzle subsonically at a high exit temperature. This way the jet velocity ratio, V_J/a_o, was greater than unity and the jet exit velocity was subsonic. These conditions were easier to keep stable. The tests were conducted at test point 39 on the Lockheed experimental program chart: $V_J/a_o = 1.48$, $T_J/T_o = 2.27$, $M_J = 0.982$, $P_R/P_o = 1.83$. A ring of nine microphones (B&K 1/4-inch) were clamped on a circular mounting mechanism at equal radial distances. The entire ring could be moved to different axial locations and the microphones could be positioned at any radius. The microphones were spaced azimuthally at equal separations of 45 degrees. The microphone outputs were fed to a switching unit which fed in turn the signal from each microphone and the output of a reference microphone in the ring to a Hewlett-Packard 3721A correlator. The cross-correlations between each microphone and the reference were obtained and recorded on paper tape. The data were then processed on a Univac 1108 digital computer.

The cross-power spectral densities for each microphone pair were obtained by calculating the Fourier transform of the cross-correlation functions recorded on paper tape. The amplitude of the cross-power spectra were stored at three frequencies corresponding to Strouhal numbers of 0.1, 0.3, and 1.0. A Fourier series decomposition was then performed for each Strouhal number to determine the azimuthal mode number content of the pressure fluctuations.

Cross-correlations were performed at the radial and axial locations shown in Figure 3E.1. Sixty-seven test locations were used. Mode number distributions and levels were obtained for three typical Strouhal numbers - 0.1, 0.3, 1.0, corresponding to frequencies of approximately 1000 Hz, 3000 Hz,

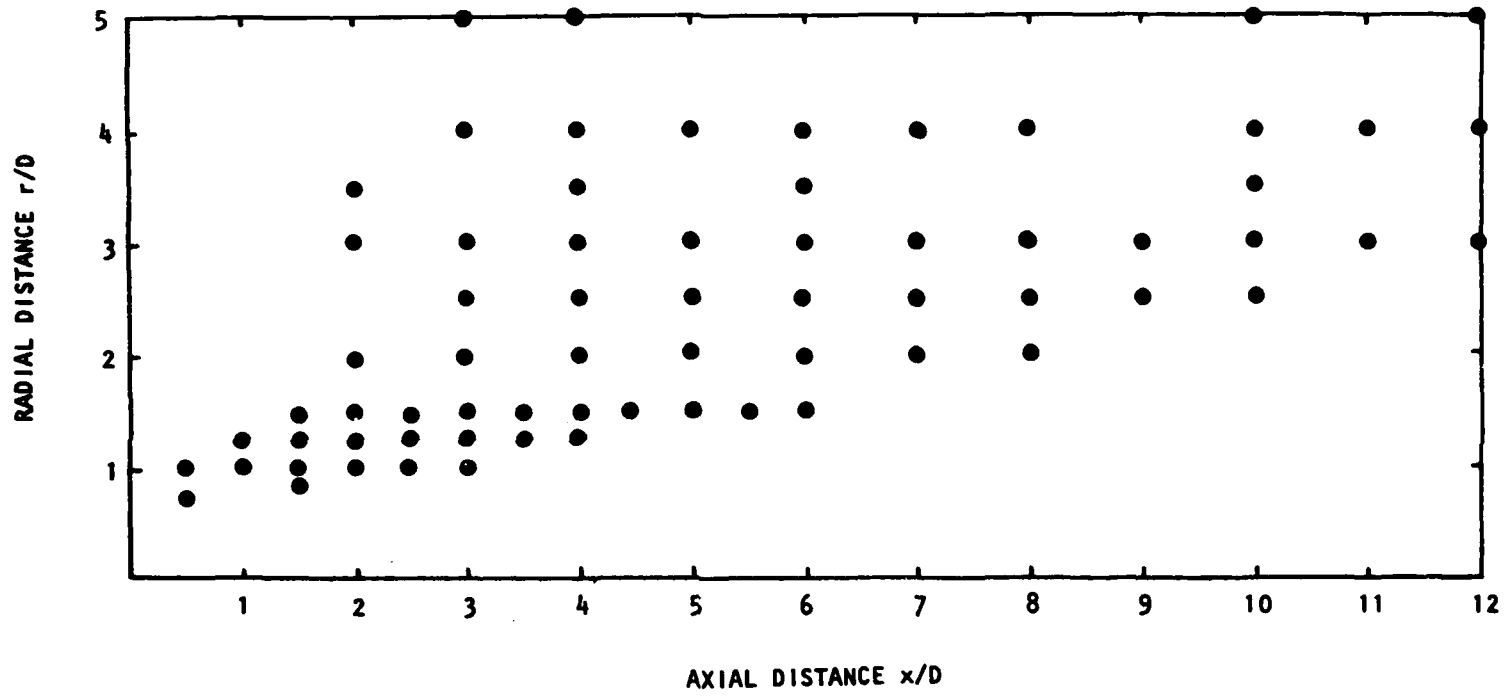

Figure 3E.1 Location of Test Points in Jet Near Field.

and 10 kHz for the jet exit velocity of 1800 ft/sec. At each location the power spectral density of the pressure at each Strouhal number were obtained for azimuthal power mode numbers up to m = 8. The power spectral density levels at several locations in the near field are shown in Figures 3E.2 through 3E.6. Several features are noticeable. The further downstream the location the lower the frequency, or Strouhal number, of the highest power spectral density levels (compare Figures 3E.2 and 3E.4). Also, as the angle to the jet axis increased (based on an origin at the jet exit) so the power spectral density levels for the higher order modes became of the same order as the lower order modes. However, at small angles to the jet axis the only appreciable energy content was in the lower order modes. This change was also noticeable in the pressure spectrum shapes at small and large angles to the jet axis. At the smaller angles there was a peak in the spectrum and the autocorrelation function showed a distinct periodicity. At the higher angles, $\theta > 45°$, the autocorrelation function decayed very rapidly and the pressure spectrum showed no peak. Thus, many of the measured features of the near field showed the anticipated characteristic features of the jet far field, with noise radiation at small angles being dominated by wave-like disturbances with low azimuthal mode numbers.

The reduced data at each measurement point enabled contour plots of equal pressure power spectral density by frequency and azimuthal mode number to be drawn. These are shown in Figure 3E.7 through 3E.12. The contours are obtained by fitting a curve of the form

$$\text{power spectral density} = A + Bx + Cx^2 + Dxy + Ey + Fy^2,$$

using a least squares multiple regression scheme. The contour plots are very similar for the m = 0 and the m = 1 modes though, for these jet operating conditions, the m = 0 mode has a generally higher level. The maximum levels for the highest frequency occur close to the jet exit and those for the lowest frequency occur further downstream. The contours cover only a relatively small area where hydrodynamic pressure fluctuations dominate. This explains the qualitative correspondence between these measurements and the calculations of the near field by Morris [3.11].

In summary the experiments showed that the near field of an axisymmetric jet may be conveniently divided into two regions. For angles to the jet axis greater than 45 degrees, there is no preferred azimuthal mode structure to the near field as it is probably related to random turbulent motions. For angles to the jet axis less than 45 degrees, most of the fluctuating energy is concentrated at the lowest mode numbers and the pressure has a strong periodic component. The frequency of this preferred period decreases with distance from the jet exit. The pressure fluctuations in this region of the near field may be readily associated with the large-scale instabilities of the axisymmetric jet.

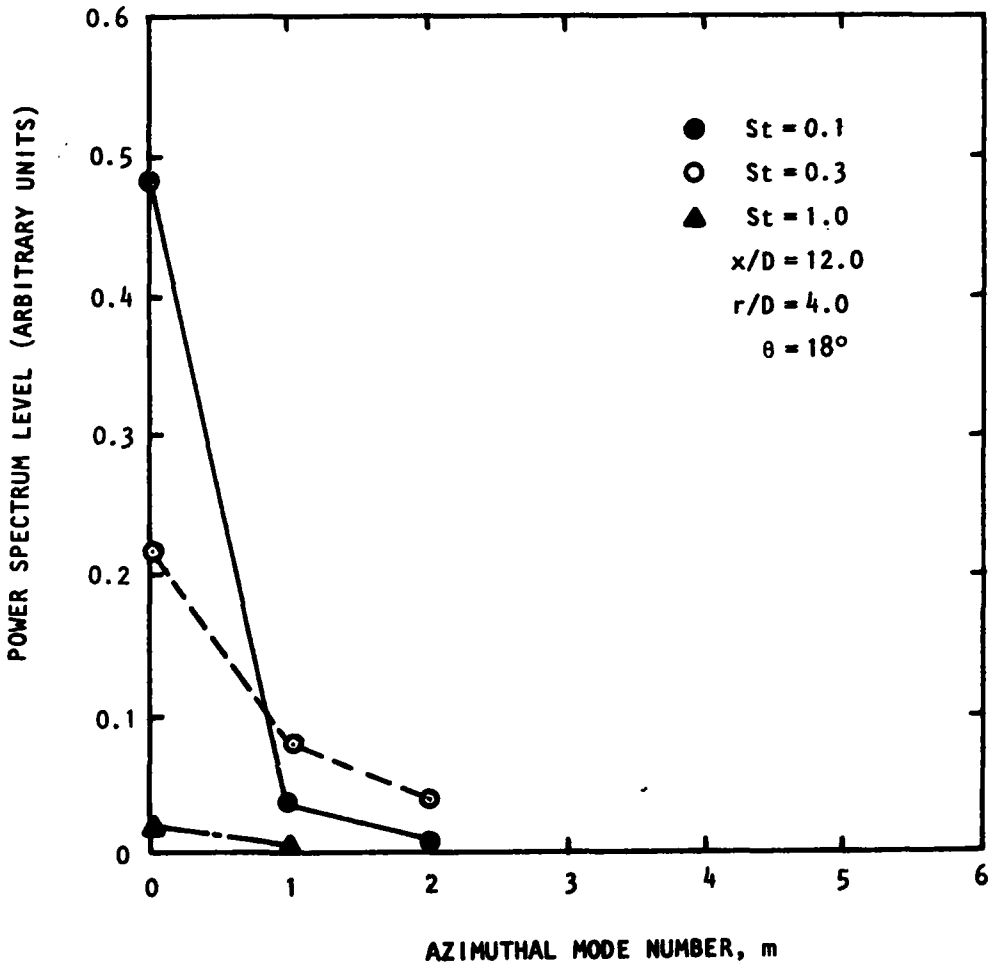

Figure 3E.2 Variation of Near-Field Spectrum Level With Mode Number.

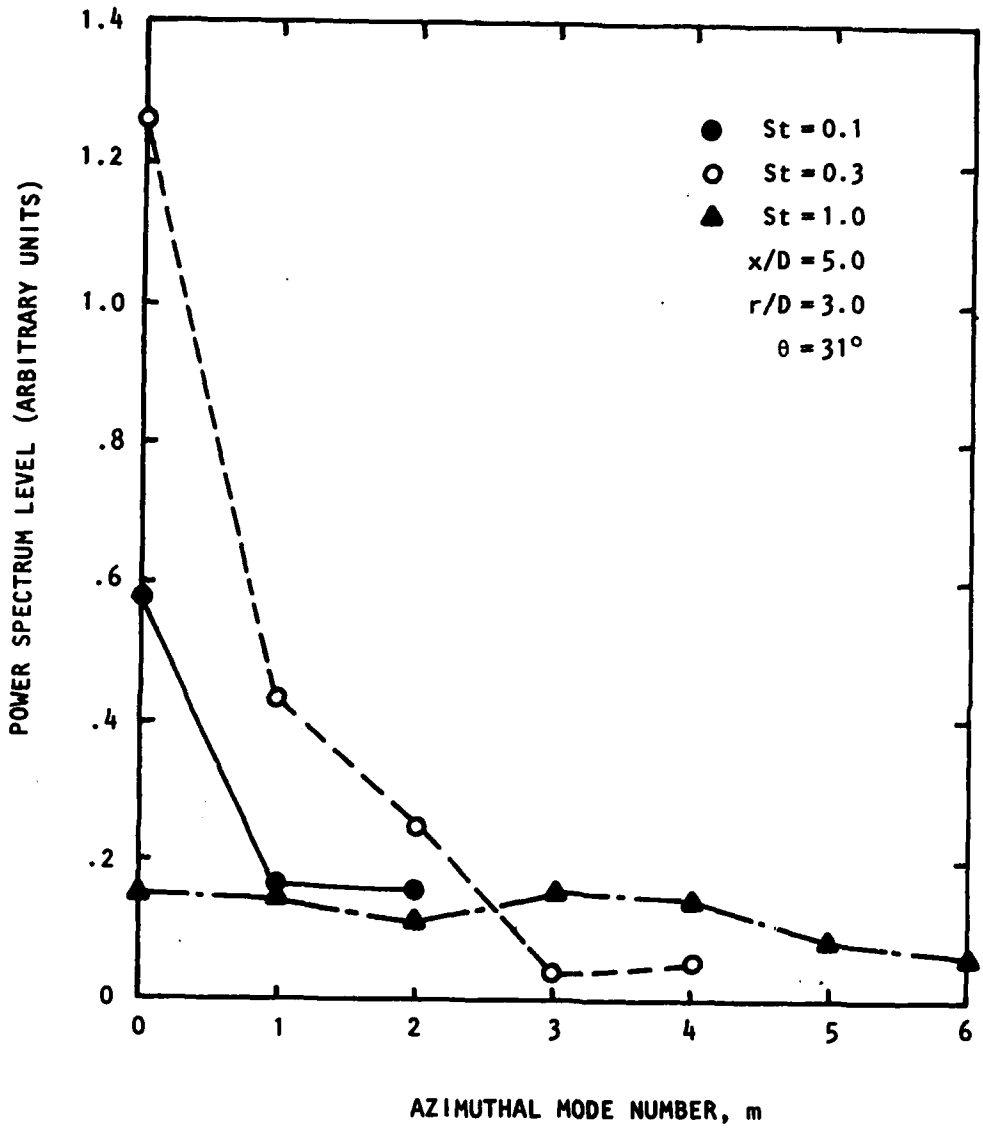

Figure 3E.3 Variation of Near-Field Spectrum Level with Mode Number.

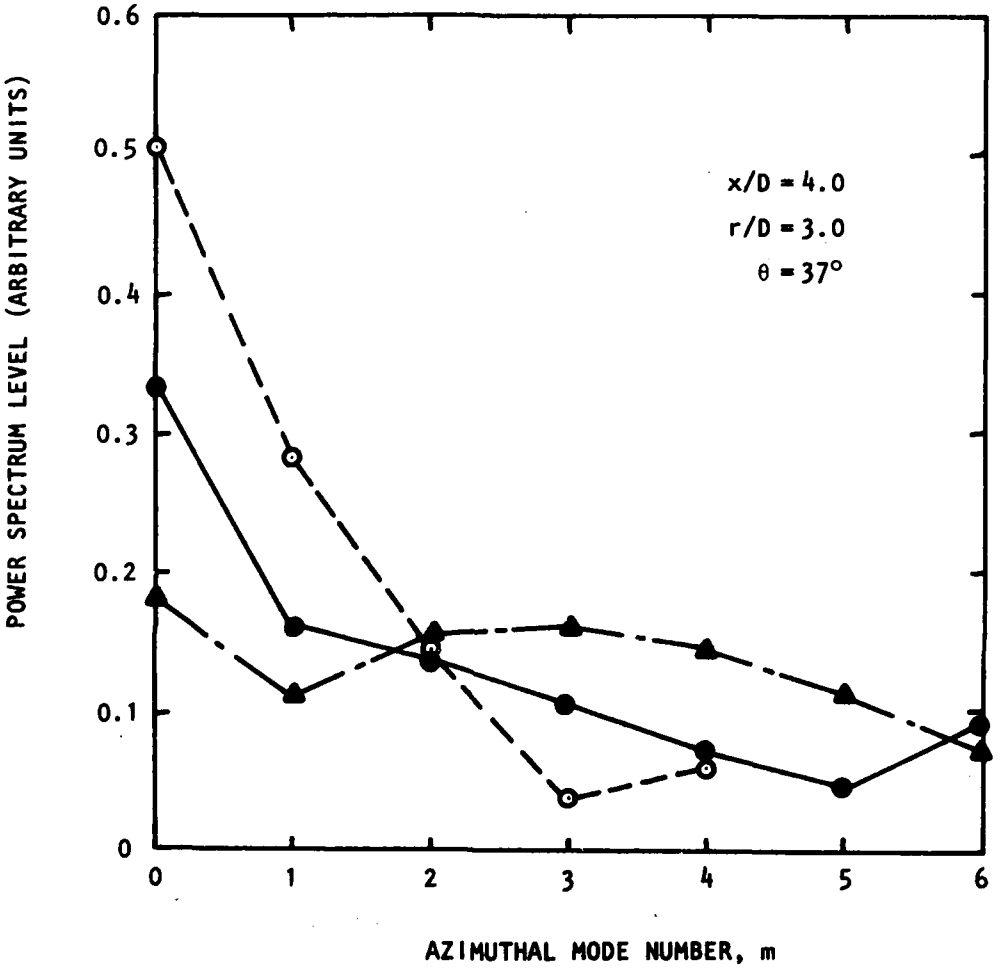

Figure 3E.4 Variation of Near-Field Spectrum Level with Mode Number.

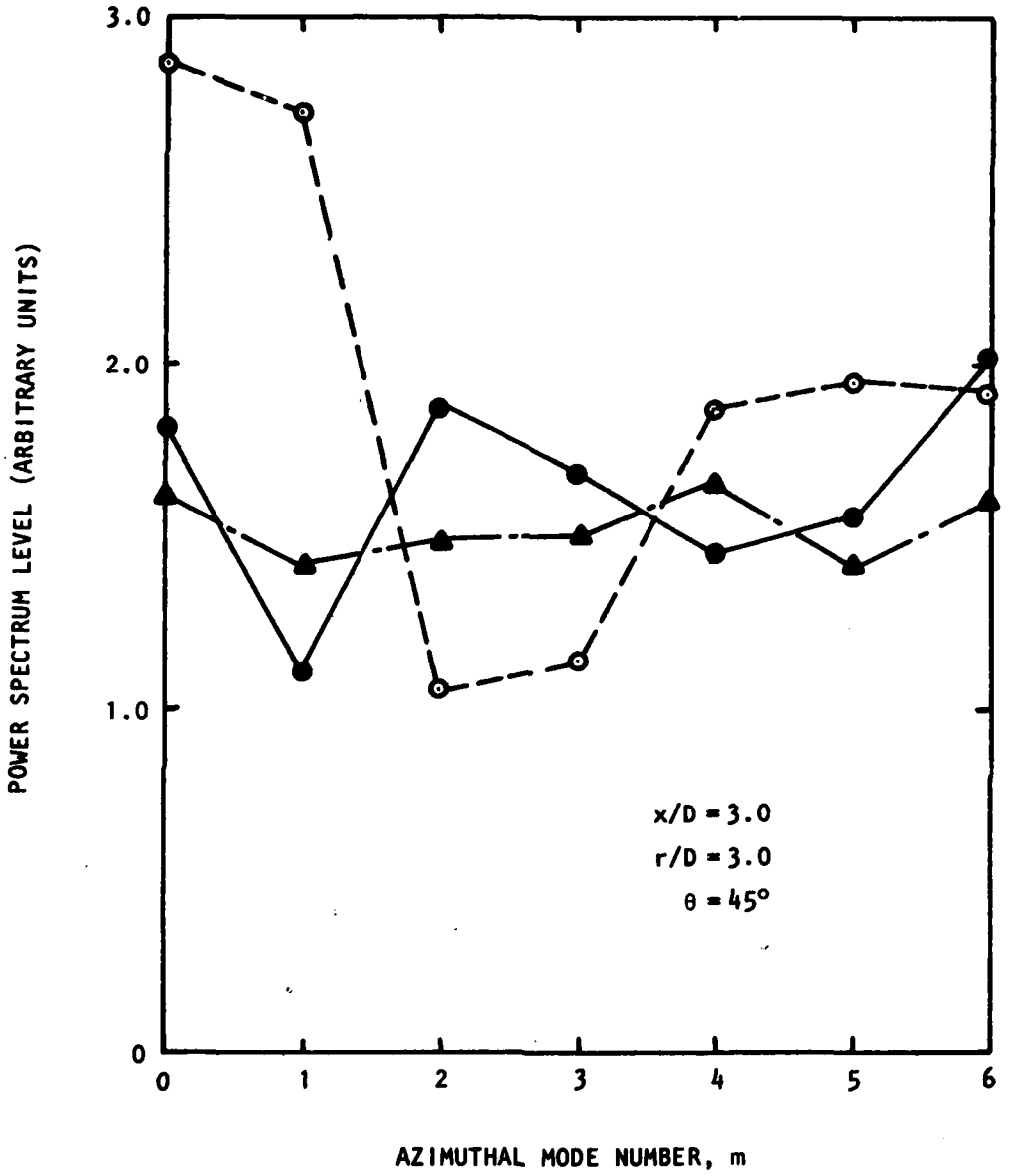

Figure 3E.5 Variation of Near-Field Spectrum Level With Mode Number

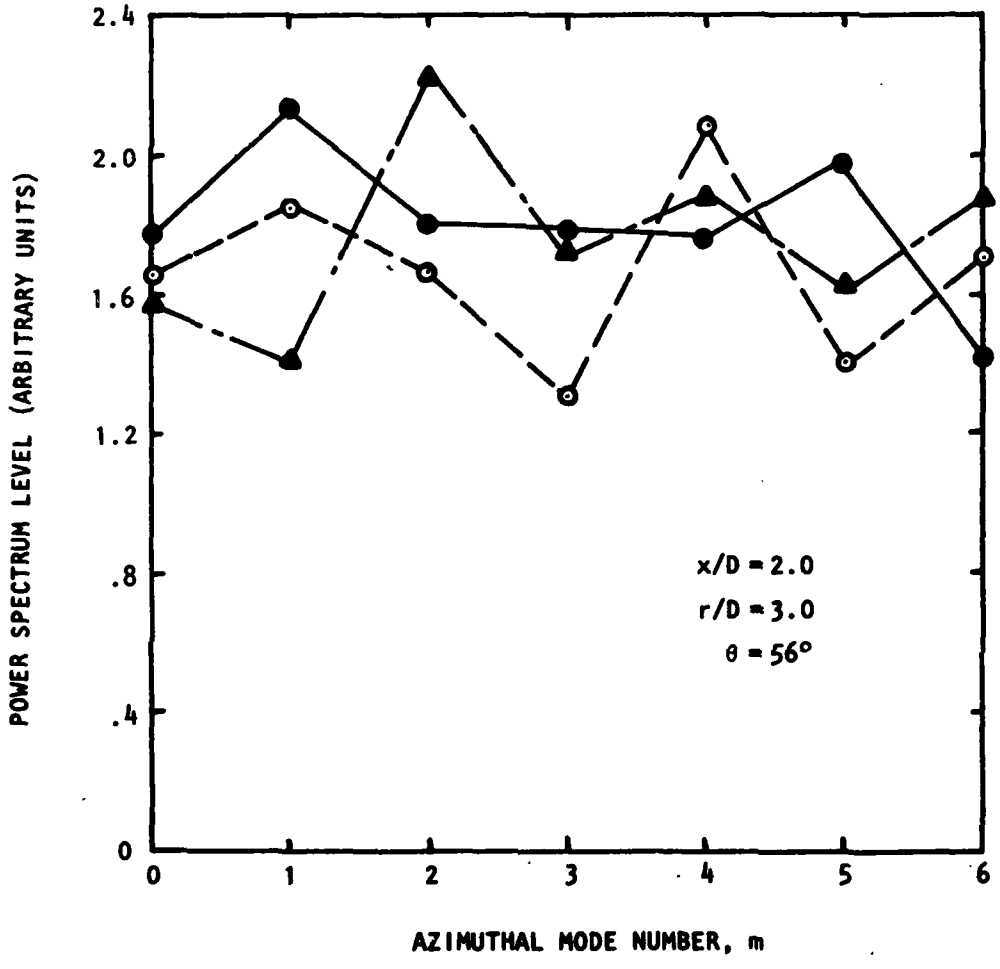

Figure 3E.6 Variation of Near-Field Spectrum Level with Mode Number.

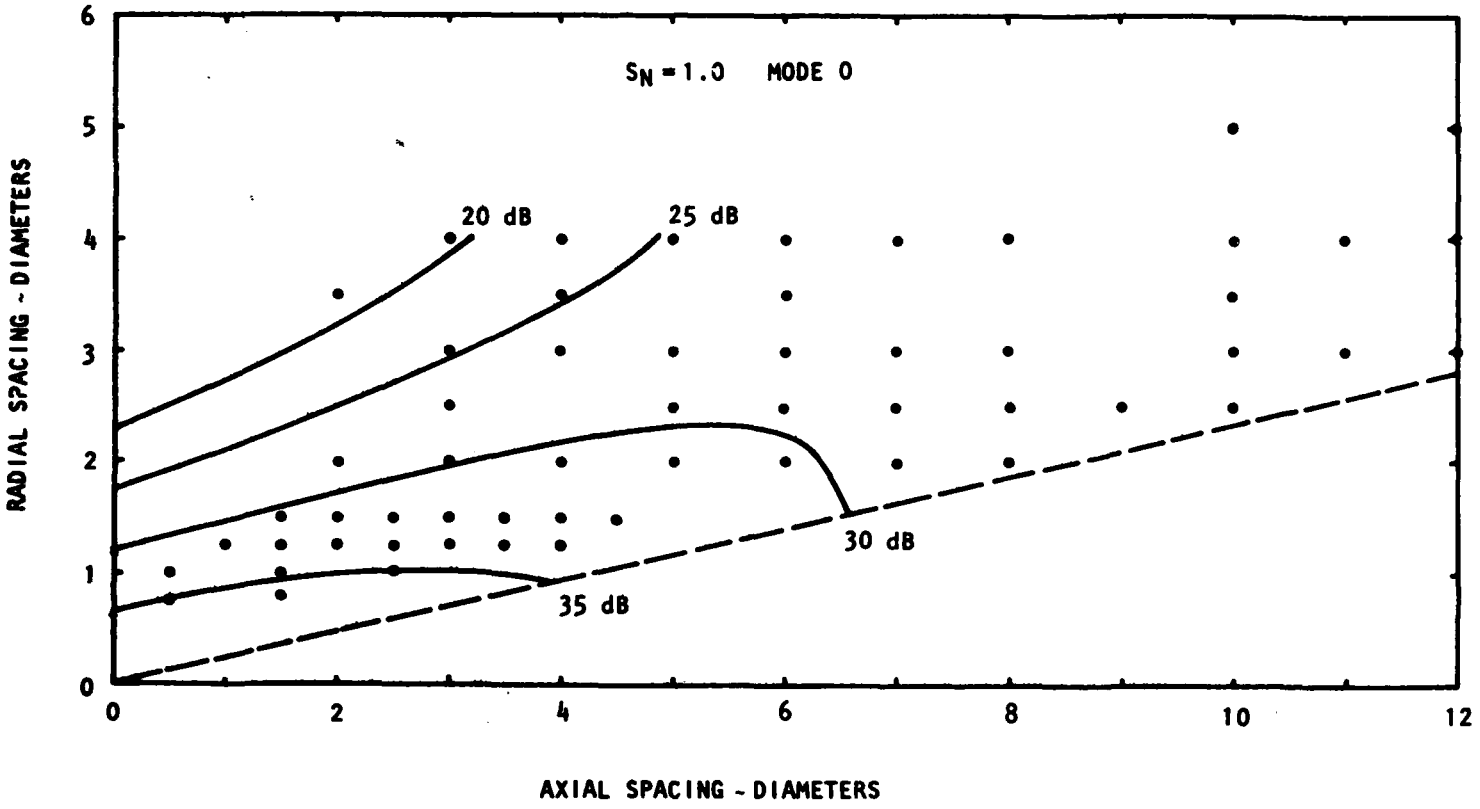

Figure 3E.7 Measured Contours of Equal SPL

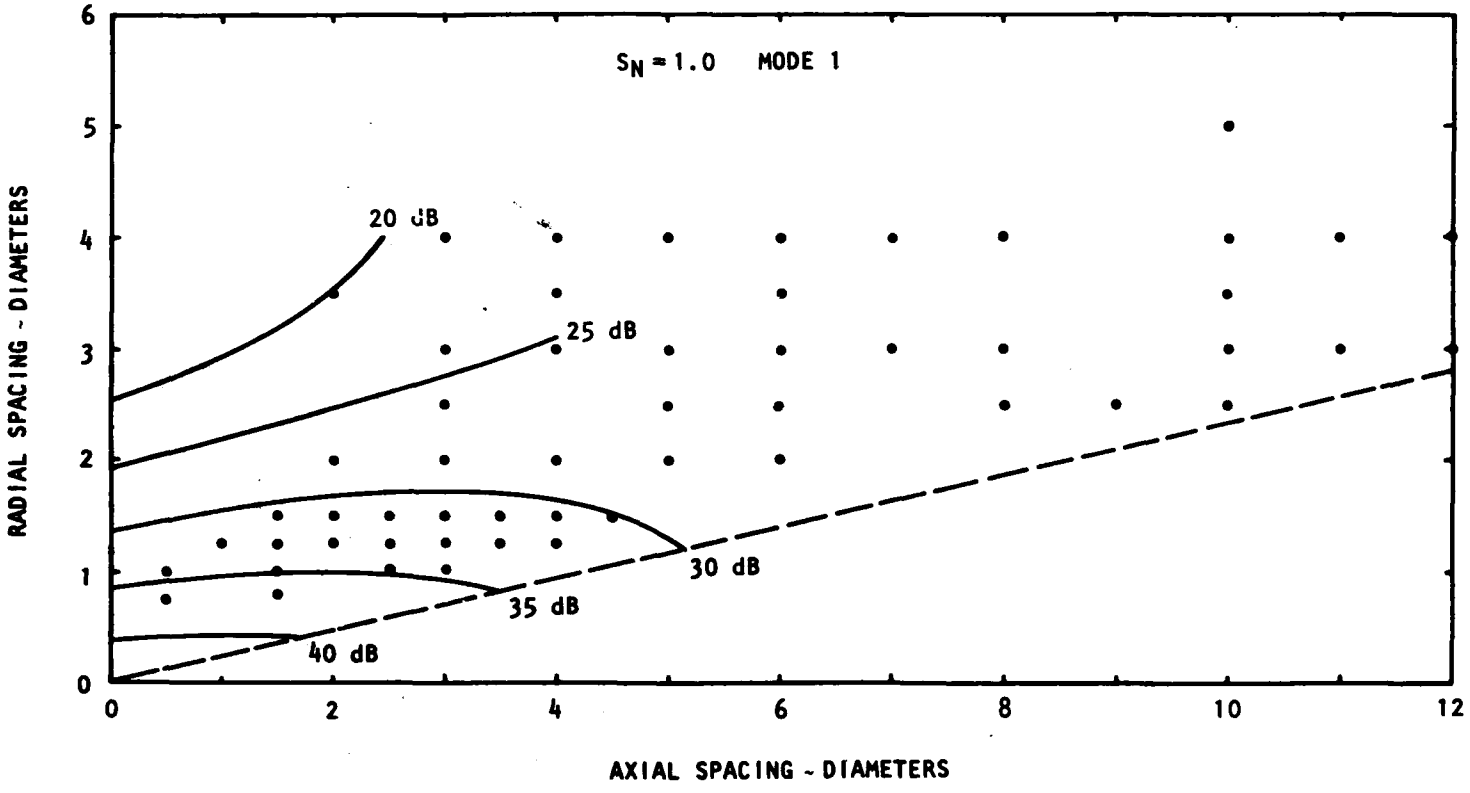

Figure 3E.8 Measured Contours of Equal SPL

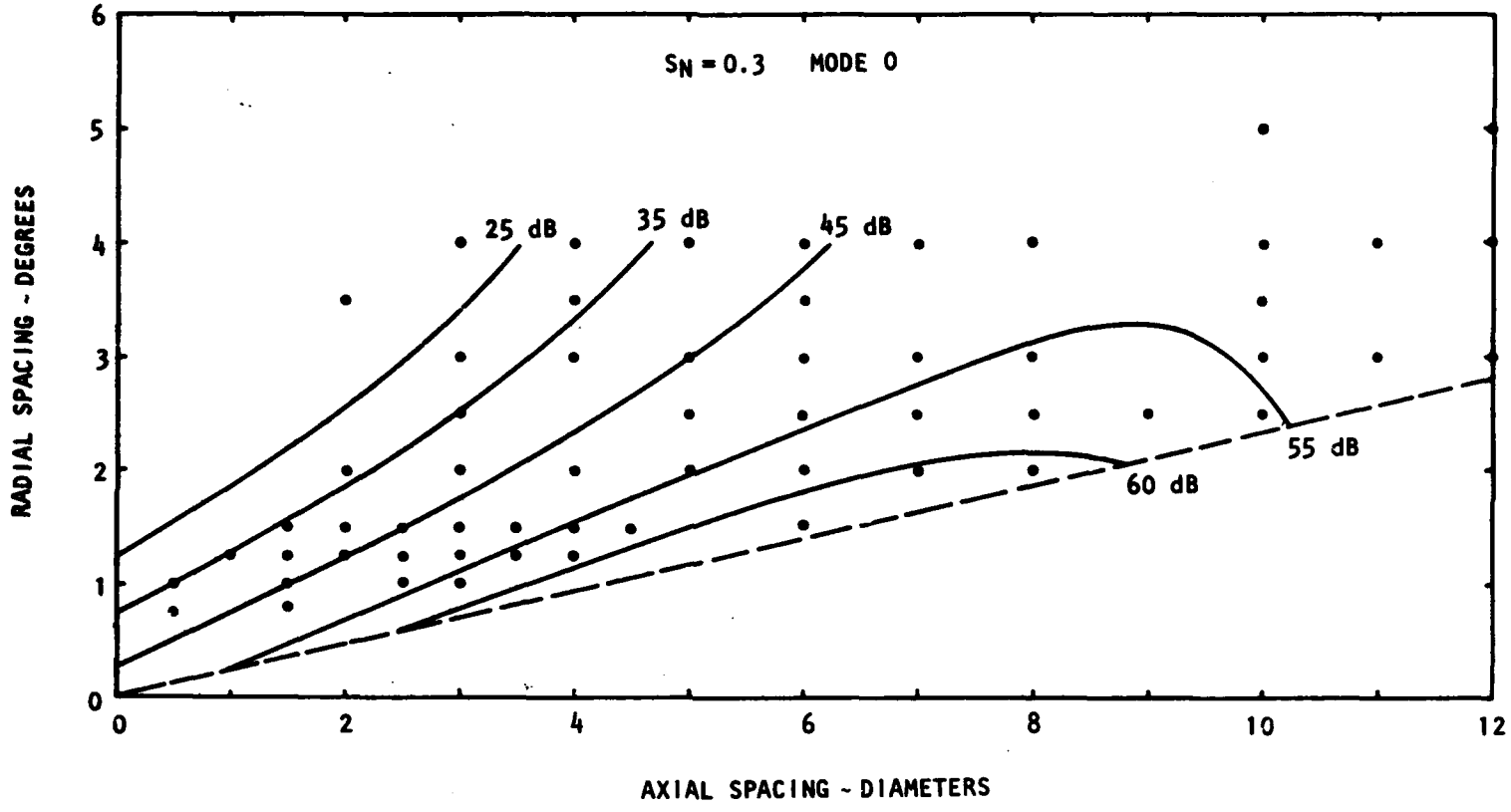

Figure 3E.9 Measured Contours of Equal SPL

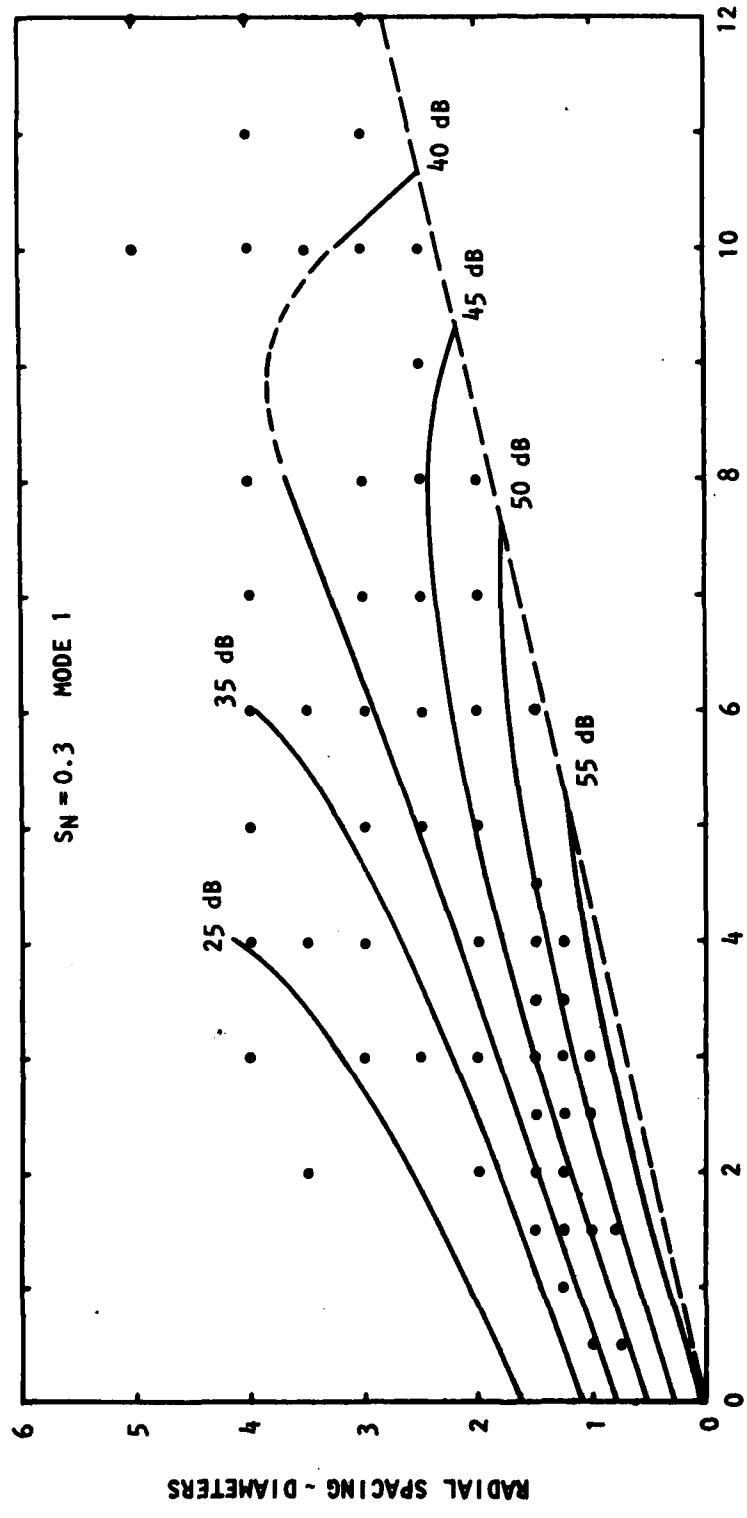

Figure 3E.10 Measured Contours of Equal SPL

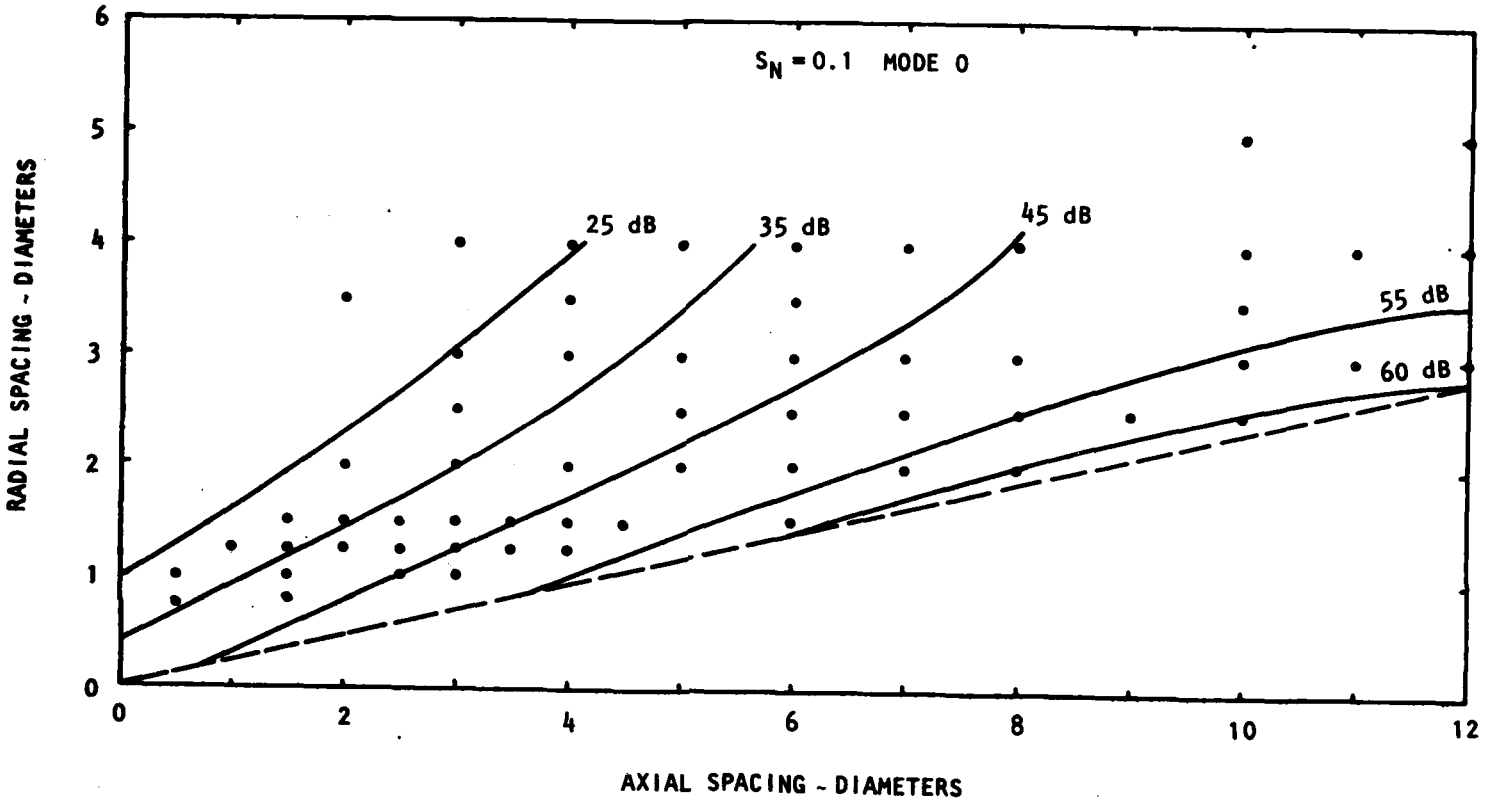

Figure 3E.11 Measured Contours of Equal SPL

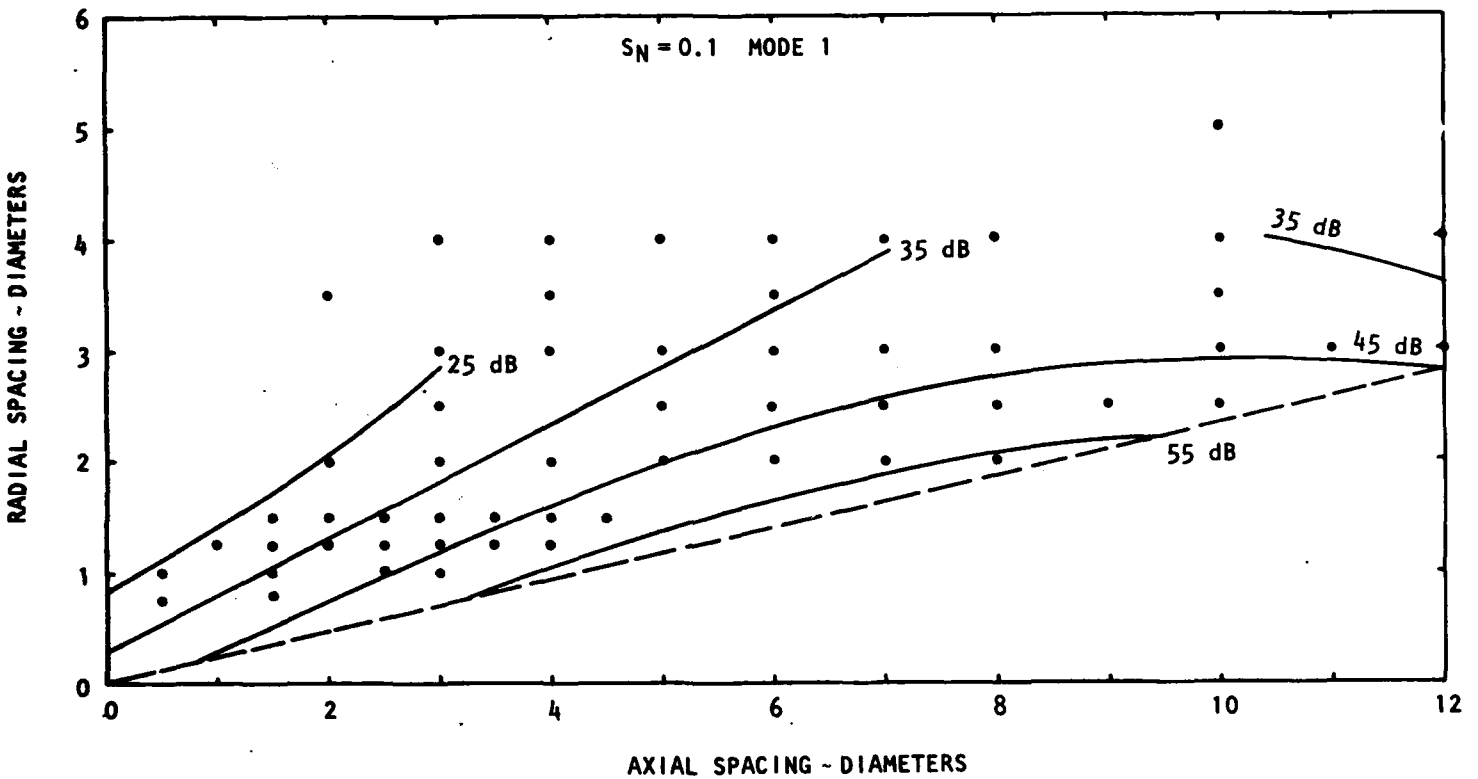

Figure 3E.12 Measured Contours of Equal SPL

REFERENCES

2.1. Lilley, G. M.: Generation of Sound in a Mixing Region. In Vol. IV, Theory of Turbulence Generated Jet Noise, Noise Radiation from Upstream Sources and Combustion Noise. AFAPL-TR-72-53, 1972.

2.2. Plumblee, H. E. (Editor): The Generation and Radiation of Supersonic Jet Noise, Vol. II, Studies of Jet Noise, Turbulence Structure and Laser Velocimetry. AFAPL-TR-76-65-Vol. II, 1976. (See also ref. [2.26].)

2.3. Ribner, H. S.: The Generation of Sound by Turbulent Jets. *Adv. in Applied Mech.*, Vol. 8, pp. 103-182, 1964.

2.4. Mani, R.: The Influence of Jet Flow on Jet Noise (Parts 1 and 2). *J. Fluid Mech.*, Vol. 73, Pt. 4, pp. 753-793.

2.5. Morfey, C. L.: Amplification of Aerodynamic Noise by Convected Flow Inhomogeneities. *J. Sound Vib.*, Vol. 31, pp. 391-397, 1973.

2.6. Mani, R. et al.: High Velocity Jet Noise Source Location and Reduction. Task 2 - Theoretical Developments and Basic Experiments. Report No. FAA-RD-76-79, II, 1977.

2.7. Ffowcs Williams, J. E.: Noise from Turbulence Convected at High Speed. *Phil. Trans. Roy. Soc.* Vol. A255, pp. 469-503.

2.8. Maestrello, L.: Use of Turbulent Model to Calculate the Vibration and Radiation Responses of a Panel, with Practical Suggestions for Reducing Sound Level. *J. Sound Vib.*, Vol. 5, No. 3, pp. 407-448, 1967.

2.9. Gradshteyn, I. S.; and Ryzhik, I. M.: *Table of Integrals, Series and Products.* Fourth Ed., Academic Press, 1965.

2.10. Plumblee, H. E. (Editor): Effects of Forward Velocity on Turbulent Jet Mixing Noise. NASA CR-2702, 1976.

2.11. Szewczyk, V. M.: The Role of Flow-Acoustic Interactions in Jet Noise Studies. Ph.D. Thesis, University of Southampton, 1978. (See also refs. [2.27] and [2.28].)

2.12. Fisher, M. J.; and Szewczyk, V. M.: Flow-Acoustic Interaction Effects in Jet Noise. ARC Paper No. 35 212 N897, 1974.

2.13. Tester, B. J.; Burrin, R. H.: On Sound Radiation from Sources in Parallel Sheared Jet Flows. AIAA Paper No. 74-57, 1974.

2.14. Tanna, H. K.; Dean, P. D.; and Burrin, R. H.: The Generation and Radiation of Supersonic Jet Noise, Vol. III, Turbulent Mixing Noise Data. AFAPL-TR-76-65-Vol. III, 1976.

2.15. Fisher, M. J.; Harper-Bourne, M.; and Glegg, S. A. L.: Jet Engine Noise Source Location: The Polar Correlation Technique. *J. Sound Vib.*, Vol. 51, No. 2, pp. 23-54, 1977.

2.16. Laufer, J.; Kaplan, R. E.; and Chu, W. T.: On Noise Produced by Subsonic Jets. Proceedings of the Second Interagency Symposium on University Research in Transportation Noise, Vol. 1, pp. 50-58, 1974.

2.17. Grosche, F. R.: Distribution of Sound Source Intensities in Subsonic and Supersonic Jets. AGARD CP-131, Noise Mechanisms (see also AIAA Paper No. 73-989), 1973.

2.18. Bradshaw, P.; Ferris, D. H.; and Johnson, R. F.: Turbulence in the Noise-Producing Region of a Circular Jet. *J. Fluid Mech.*, Vol. 19, 1964, p. 591.

2.19. Abramowitz, M.; and Stegun, I. A.: *Handbook of Mathematical Functions.* National Bureau of Standards, Applied Mathematics Series 55, June 1964.

2.20. SAE Committee A-21, Aircraft-Noise Measurement: Gas Turbine Jet Exhaust Prediction. Appendix A – Predictions of Single Stream Jet Mixing Noise from Shock-Free Circular Nozzles. SAE ARP 876, 1978.

2.21 Ahuja, K. K.; Tester, B. J.; and Tanna, H. K.: Calculation of Far-Field Jet Noise Spectra from Near-Field Measurements Using True Source Location. AIAA Paper No. 78-1153, 1978.

2.22. Witze, P. O.: Centerline Velocity Decay of Compressible Jets. *AIAA Journal*, Vol. 12, 1974, p. 417.

2.23. Morris, P. J.: Near- and Far-Field Noise from Large-Scale Instabilities of Axisymmetric Jets: AIAA Paper No. 77-1351, 1977.

2.24. Proc. Conference NASA Langley Research Center: *Free Turbulent Shear Flows. Vol. II - Summary of Data.* NASA SP-321, 1973.

2.25. Corrsin, S.; and Uberoi, M. S.: Further Experiments on the Flow and Heat Transfer in a Heated Turbulent Air Jet. NACA Report 998, 1951.

2.26. Tester, B. J.; and Morfey, C. L.: Developments in Jet Noise Modelling-Theoretical Predictions and Comparisons with Measured Data. *J. Sound Vib.*, Vol. 46, No. 1, pp. 79-103, 1976.

2.27. Morfey, C. L.; and Szewczyk, V. M.: Jet Noise Modelling by Geometric Acoustics, Parts I, II and III. University of Southampton ISVR Technical Reports Nos. 91, 92 and 93, 1977.

2.28. Morfey, C. L.; Tester, B. J.; and Szewczyk, V. M.: New Scaling Laws for Hot and Cold Jet Mixing Noise Based on a High-Frequency Model. AIAA Paper No. 77-1287, 1977.

3.1. Lilley, G. M.: Generation of Sound in a Mixing Region. In Vol. IV, Theory of Turbulence Generated Jet Noise, Noise Radiation from Upstream Sources and Combustion Noise. AFAPL-TR-72-53, 1972.

3.2. Lighthill, M. J.: The Bakerian Lecture, Sound Generated Aerodynamically. *Proc. Roy. Soc.*, Vol. A267, pp. 147-182, 1962.

3.3. Phillips, O. M.: On the Generation of Sound by Supersonic Turbulent Shear Layers. *J. Fluid Mech.*, Vol. 9, pp. 1-28, 1960.

3.4. Lilley, G. M.; Morris, P. J.; and Tester, B. J.: On the Theory of Jet Noise and its Application. AIAA Paper No. 73-987, 1973.

3.5. Morris, P. J.: The Structure of Turbulent Shear Flow. Ph.D. Thesis, University of Southampton, 1971.

3.6. Landahl, M. T.: A Wave-Guide Model for Turbulent Shear Flow. *J. Fluid Mech.*, Vol. 29, Pt. 3, pp. 441-459, 1967.

3.7. Reynolds, W. C.; and Hussain, A.K.M.F.: The Mechanics of An Organized Wave in Turbulent Flow. Pt. 3, Theoretical Models and Comparison With Experiment. *J. Fluid Mech.*, Vol. 54, pp. 263-288, 1972.

3.8. Morris, P. J.: A Model for the Structure of Jet Turbulence as a Source of Noise. AIAA Paper No. 74-1, 1974.

3.9. Morris, P. J.: The Spatial Viscous Instability of Axisymmetric Jets. *J. Fluid Mech.*, Vol. 77, pp. 511-529, 1976.

3.10. The Generation and Radiation of Supersonic Jet Noise. Vol. II, Studies of Jet Noise, Turbulence Structure, and Laser Velocimetry. AFAPL-TR-76-65, 1976.

3.11. Morris, P. J.: Flow Characteristics of the Large-Scale Wave-Like Structure of a Supersonic Round Jet. *J. Sound Vib.*, Vol. 53, 1977.

3.12. Tam, C. K. W.; and Morris, P. J.: The Radiation of Sound by the Instability Waves of a Compressible Plane Turbulent Shear Layer. To be published, *J. Fluid Mech.*, 1978.

3.13. Sedel'nikov, T. K.: The Frequency Spectrum of the Noise of a Supersonic Jet. *Phy. Aero. Noise*, Moscow: Nauka (Trans. 1969 NASA TTF-538, 71-75), 1967.

3.14. Tam, C. K. W.: Directional Acoustic Radiation from a Supersonic Jet Generated by Shear Layer Instability. *J. Fluid Mech.* Vol. 46, pp. 757-768, 1971.

3.15. Tam, C. K. W.: On the Noise of a Nearly Ideally Expanded Supersonic Jet. *J. Fluid Mech.*, Vol. 51, pp. 69-95, 1972.

3.16. Tam, C. K. W.: Supersonic Jet Noise Generated by Large-Scale Disturbances. *J. Sound Vib.*, Vol. 38, pp. 51-79, 1975.

3.17. Bishop, K. A.; Ffowcs Williams, J. E.; and Smith, W.: On the Noise Sources of the Unsuppressed High Speed Jet. *J. Fluid Mech.*, Vol. 50, pp. 21-31, 1971.

3.18. Morris, P. J.: The Generation and Radiation of Supersonic Jet Noise. Vol. II, The Flow and Acoustic Characteristics of the Large-Scale Wave-Like Structure of an Axisymmetric Jet. AFAPL-TR-76-65, 1976.

3.19. Liu, J. T. C.: Developing Large-Scale Wave-Like Eddies and the Near-Field Noise Field. *J. Fluid Mech.*, Vol. 62, pp. 437-464, 1974.

3.20. McLaughlin, D. K.; Morrison, G. L.; and Troutt, T. R.: Experiments on the Instability Waves in a Supersonic Jet and Their Acoustic Radiation. *J. Fluid Mech.*, Vol. 69, pp. 73-95, 1975.

3.21. McLaughlin, D. K.; Morrison, G. L.; and Troutt, T. R.: Reynolds Number Dependence in Supersonic Jet Noise. *AIAA Journal*, Vol. 15, pp. 526-532, 1977.

3.22. Dahan, C.; and Elias, G.: Source Structure Pattern in a Hot Jet by Infrared-Microphones Correlations. AIAA Paper 76-542, 1976.

3.23. Chan, Y. Y.: Spatial Waves in Turbulent Jets. *Physics of Fluids*, Vol. 17, pp. 46-53, 1974.

3.24. Chan, Y. Y.: Spatial Waves in Turbulent Jets. *Physics of Fluids*, Vol. 17, pp. 1667-1670, 1974.

3.25. Chan, Y. Y.: Spatial Waves of Higher Order Modes in an Axisymmetric Turbulent Jet. *Physics of Fluids*, Vol. 19, pp. 2042-2043, 1976.

3.26. Moore, C. J.: The Role of Shear Layer Instability Waves in Jet Exhaust Noise. *J. Fluid Mech.*, Vol. 80, pp. 321-367, 1977.

3.27. Chan, Y. Y.: Nonlinear Spatial Wave Development in an Axisymmetric Turbulent Jet. Aero. Report LR-585, National Research Council, Canada, National Aeronautical Establishment, 1975.

3.28. Merkine, L.; and Liu, J. T. C.: On the Development of Noise-Producing Large-Scale Wave-Like Eddies in a Plane Turbulent Jet. *J. Fluid Mech.*, Vol. 70, pp. 353-368, 1975.

3.29. Bouthier, M.: Stabilité Linéaire des Écoulements Presque Parallèles. Partie I, *J. de Mécanique*, Vol. 11, pp. 599-621, 1972.

3.30. Bouthier, M.: Stabilité Linéaire des Écoulements Presque Parallèles, Partie II, La Couche Limite de Blasius. *J. de Mécanique*, Vol. 12, pp. 75-95, 1973.

3.31. Gaster, M.: On the Effects of Boundary Layer Growth on Flow Stability. *J. Fluid Mech.*, Vol. 66, pp. 465-480, 1974.

3.32. Saric, W. S.; and Nayfeh, A. H.: Nonparallel Stability of Boundary Layer Flows. *Physics of Fluids*, Vol. 18, pp. 945-950, 1975.

3.33. Crighton, D. B.; and Gaster, M.: Stability of Slowly Diverging Jet Flow. *J. Fluid Mech.*, Vol. 77, pp. 397-413, 1976.

3.34. Lees, L.; and Lin, C. C.: Investigation of the Stability of the Laminar Boundary Layer in a Compressible Fluid. NACA TN 1115, 1946.

3.35. Lin, C. C.: On the Stability of Laminar Mixing Region Between Two Parallel Streams in a Gas. NACA TN 2887, 1953.

3.36. Gropengieser, H.: Bietrag zur Stabilität freier Grenzschichten in kompressiblen Medien. Deutsch Luft-und Raumfahrt FB 69-25, Berlin, 1969.

3.37. Blumen, W.: Shear Layer Instability of an Inviscid Compressible Fluid. *J. Fluid Mech.*, Vol. 40, pp. 769-781, 1970.

3.38. Blumen, W.: Jet Flow Instability of an Inviscid Compressible Fluid. *J. Fluid Mech.*, Vol. 46, pp. 737-747, 1971.

3.39. Dosanjh, D. S.; and Yu, J. C.: Noise from Underexpanded Axisymmetric Jet Flow Using Radial Jet Flow Impingement. Proceedings of AFOSR-UTIAS Symposium on Aerodynamic Noise, Toronto, Canada, 1968.

3.40. Liepmann, H. W.; and Laufer, J.: Investigations of Free Turbulent Mixing. NACA TN 1257, 1947.

3.41. Boyce, W. E.; and DiPrima, R. C.: *Elementary Differential Equations.* Third Edition, John Wiley and Sons, 1977.

3.42. Van Dyke, M.: *Perturbation Methods in Fluid Mechanics.* The Parabolic Press, Stanford, California, 1975.

3.43. Lau, J. C.; Morris, P. J.; and Fisher, M. J.: Turbulence Measurements in Subsonic and Supersonic Jets Using a Laser Velocimeter. AIAA Paper No. 76-348, 1976.

3.44. Patel, R. P.: An Experimental Study of a Plane Mixing Layer. *AIAA Journal*, Vol. 11, pp. 67-71, 1973.

3.45. Michalke, A.: Instabilität eines kompressiblen runden Freistrahls unter Berücksichtigung des Einflusses der Strahlgrenzchichtdicke. *Z. Flugwiss*, Vol. 19, pp. 319-328, 1971.

3.46. Betchov, R.; and Criminale, W. O.: *Stability of Parallel Flows.* Academic Press, 1967.

3.47. Brigham, E. O.; and Morrow, R. E.: The Fast Fourier Transform. *IEEE Spectrum*, December, pp. 63-70, 1967.

3.48. Eggers, J. M.: Velocity Profiles and Eddy Viscosity Distributions Downstream of a Mach 2.22 Nozzle Exhausting into Quiescent Air. NASA TND-3601, 1966.

3.49. Birch, S. F.; and Eggers, J. M.: A Critical Review of the Experimental Data for Developed Turbulent Free Shear Layers. Proc. NASA Conf. on Free Turbulent Shear Flows, Vol. 1, NASA SP-321, p. 11, 1972.

3.50. Yu, J. C.; and Dosanjh, D. S.: Noise Field of Coaxial Interacting Supersonic Jet Flows. AIAA Paper No. 71-152, 1971.

3.51. Abramowitz, M.; and Stegun, I. A.: *Handbook of Mathematical Functions*, National Bureau of Standards, Washington, D. C.

4.1. "The Generation and Radiation of Supersonic Jet Noise" (4 Volumes). Technical Report AFAPL-TR-76-65, June 1976.

4.2. Harper-Bourne, M.; and Fisher, M. J.: "The Noise from Shock Waves in Supersonic Jets." AGARD-CP-131, 1973.

5.1. Laurence, J. C.: Intensity, Scale and Spectra of Turbulence in Mixing Region of Free Subsonic Jets. NACA Rep. No. 1292, 1956.

5.2. Corrsin, S.; and Uberoi, M. S.: Further Experiments on the Flow and Heat Transfer in a Heated Turbulent Air Jet. NACA TR 998, 1950.

5.3. Davies, P.O.A.L.; Fisher, M. J.; and Barratt, M. J.: The Characteristics of the Turbulence in the Mixing Region of a Round Jet, *J. Fluid Mech.*, Vol. 15, p. 337, 1963.

5.4. Wygnanski, I.; and Fiedler, H.: Some Measurements in the Self-Preserving Jet. *J. Fluid Mech.*, Vol. 38, pp. 577-612, 1969.

5.5. Plumblee, H. E. Jr.: The Generation and Radiation of Supersonic Jet Noise. Vol. 1, Summary. AFFPL/TBC Tech. Report AFAPL-TR-76-65, 1976.

5.6. Birch, S. F.; and Egger, J. M.: A Critical Review of the Experimental Data for Developed Free Turbulent Shear Layers. NASA Conf. Proc. on Free Turbulent Shear Flows, Vol. 1, NASA SP-321, 1972.

5.7. Spencer, B. W.; and Jones, B. G.: Statistical Investigation of Pressure and Velocity Fields in the Turbulent Two-Stream Mixing Layer. AIAA Paper No. 71-613, 1971.

5.8. Brown, G. L.; and Roshko, A.: On Density Effects and Large Structure in Turbulent Mixing Layers. *J. Fluid Mech.* Vol. 64, p. 775, 1974.

5.9. Hussain, A. K. M. F.; and Zedan, M. F.: Effects of Initial Conditions on the Axisymmetric Free Shear Layer: Effect of Initial Fluctuation Level. *Phys. of Fluids* (to be published), 1978.

5.10. Korst, H. H.; and Chow, W. L.: The Compressible Turbulent Jet Mixing Between Two Streams at Constant Pressure. Univ. of Illinois Mechanical Engineering Report TN 393-2, 1962.

5.11. Abramovich, G. N.: *The Theory of Turbulent Jets*. MIT Press, 1963.

5.12. Batt, R. G.: Turbulent Mixing of Passive and Chemically Reacting Species in a Low-Speed Shear Layer. *J. Fluid Mech.*, Vol. 82, p. 53, 1977.

5.13. Witze, P. O.: Centerline Velocity Decay of Compressible Free Jets. *AIAA Journal*, Vol. 12, p. 417, 1974.

5.14. Kleinstein, G.: An Approximation Solution for the Axisymmetric Jet of a Laminar Compressible Fluid. *Quart. Appl. Math.* Vol. 20, p. 49, 1962.

5.15. Wilson, R. A. M.; and Danckwerts, P. V.: Studies in Turbulent Mixing – II, A Hot-Air Jet. *J. Chem. Eng. Sciences*, Vol. 19, p. 885, 1964.

5.16. Liu, C. H.; and Maestrello, L.: Propagation of Sound Through a Real Flow Field. AIAA Paper No. 74-5, 1974.

5.17. Davies, P.O.A.L.: Turbulence Structure in Free Shear Layers. *Journal of AIAA*, Vol. 4, p. 1971, 1966.

5.18. Lau, J. C.; Fisher, M. J.; and Fuchs, H. V.: The Intrinsic Structure of Turbulent Jets. *J. Sound Vib.*, Vol. 22, p. 379, 1972.

5.19. Whiffen, M. C.; Lau, J. C.; and Smith, D. M.: Design of LV Experiments for Turbulence Measurements. 3rd Intern. Workshop on Laser Velocimetry, Purdue Univ., 1978.

5.20. Lau, J. C.: The Vortex-Street Structure of "Turbulent" Jets. Part II. (submitted for publication), 1978.

5.21. Larson, R. S.; McColgan, C. J.; and Packman, A. B.: Jet Noise Source Modification Due to Forward Flight. AIAA Paper No. 77-58, 1977.

5.22. Lau, J. C.; and Fisher, M. J.: The Vortex-Street Structure of "Turbulent" Jets, Part I. *J. Fluid Mech.*, Vol. 67, p. 299, 1975.

5.23. Bradshaw, P.; Ferris, D. H.; and Johnson, R. H.: Turbulence in the Noise Producing Region of a Circular Jet. *J. Fluid Mech.*, Vol. 19, p. 591, 1964.

5.24. Jones, I. S. F.: Scale Pertinent to Noise Generation from a Jet. Proc. AFOSR-UTIAS Symp. on Aerodynamic Noise, Toronto, p. 69, 1968.

*U.S.Government Printing Office: 1979 — 657-002/360